

JOURNAL OF SCIENCE

PART A: ENGINEERING AND INNOVATION



Year | 2025

Volume | 12

Issue | 1

e-ISSN 2147-9542



| Owner |

on behalf of Gazi University
Rector
Prof. Dr.

Uğur ÜNAL

| Publishing Manager |

Prof. Dr.

Uğur GÖKMEN
Gazi University

| Chief Editor |

Prof. Dr.

Sema BİLGE OCAK
Gazi University

| Chief Editor |

Prof. Dr.

Mustafa Gürhan YALÇIN
Akdeniz University

| Assistant Editors |

Assoc. Prof. Dr.

Defne AKAY
Ankara University

Assoc. Prof. Dr.

Murat BİLEN
Gazi University



| Editorial Board |

| | |
|--|---|
| Prof. Dr. Adem TATAROĞLU | Gazi University Physics |
| Prof. Dr. Adnan SÖZEN | Gazi University Energy Systems Engineering |
| Prof. Dr. Ali KESKİN | Çukurova University Automotive Engineering |
| Prof. Dr. Ali Osman SOLAK | Ankara University Chemistry |
| Prof. Dr. Alper BÜYÜKKARAGÖZ | Gazi University Civil Engineering |
| Prof. Dr. Atilla BIYIKOĞLU | Gazi University Mechanical Engineering |
| Prof. Dr. Aynur KAZAZ | Akdeniz University Civil Engineering |
| Prof. Dr. Cevriye GENCER | Gazi University Industrial Engineering |
| Prof. Dr. Çağlayan AÇIKGÖZ | Bilecik Şeyh Edebali University Chemical Engineering |
| Prof. Dr. Çetin ÇAKANYILDIRIM | Hitit University Chemical Engineering |
| Prof. Dr. Demet CANSARAN DUMAN | Ankara University The Institute of Biotechnology |
| Prof. Dr. Elif ORHAN | Gazi University Physics |
| Prof. Dr. Erdal IRMAK | Gazi University Electrical-Electronic Engineering |
| Prof. Dr. Fatih ÖZ | Atatürk University Food Engineering |



| Editorial Board |

| | |
|---|---|
| Prof. Dr. Feyza DİNÇER | Nevşehir Hacı Bektaş Veli University Geological Engineering |
| Prof. Dr. Gürhan İÇÖZ | Gazi University Mathematics |
| Prof. Dr. Hacer KARACAN | Gazi University Computer Engineering |
| Prof. Dr. Hüseyin Serdar YÜCESU | Gazi University Automotive Engineering |
| Prof. Dr. Meltem DOĞAN | Gazi University Chemical Engineering |
| Prof. Dr. Metin GÜRÜ | Gazi University Chemical Engineering |
| Prof. Dr. Mine TÜRKTAŞ | Gazi University Biology |
| Prof. Dr. Murat KAYA | Aksaray University Biotechnology and Nanotechnology |
| Prof. Dr. Nalan KABAY | Ege University Chemical Engineering |
| Prof. Dr. Nazife ASLAN | Ankara Hacı Bayram Veli University Chemistry |
| Prof. Dr. Niyazi Uğur KOÇKAL | Akdeniz University Civil Engineering |
| Prof. Dr. Nuran AY | Eskişehir Technical University Materials Science and Engineering |
| Prof. Dr. Nurdane İLBEYLİ | Akdeniz University Geological Engineering |
| Prof. Dr. Nursel AKÇAM | Gazi University Electrical-Electronic Engineering |



| Editorial Board |

| | |
|---|---|
| Prof. Dr. Ömer ŞAHİN | İstanbul Technical University Chemical Engineering |
| Prof. Dr. Selim ACAR | Gazi University Physics |
| Prof. Dr. Şükrü DURSUN | Konya Technical University Environmental Engineering |
| Prof. Dr. Veli ÇELİK | Ankara Yıldırım Beyazıt University Mechanical Engineering |
| Prof. Dr. Yılmaz ŞİMŞEK | Akdeniz University Mathematics |
| Prof. Dr. Yusuf URAS | Kahramanmaraş Sütçü İmam University Geological Engineering |
| Prof. Dr. Yücel ERCAN | TOBB University of Economics and Technology Mechanical Engineering |
| Prof. Dr. Zafer EVİS | Middle East Technical University Engineering Sciences |
| Assoc. Prof. Dr. Fusun YALÇIN | Akdeniz University Mathematics |
| Assoc. Prof. Dr. Yasemin LEVENTELİ | Akdeniz University Geological Engineering |
| Assist. Prof. Dr. Emine Şükran OKUDAN | Akdeniz University Basic Sciences Fisheries |
| Assist. Prof. Dr. Senai YALÇINKAYA | Marmara University Mechanical Engineering |
| Dr. Murat AKIN | Gazi University Computer Technologies |
| Dr. Silver GÜNEŞ | Gazi University Chemical Engineering |



| Foreign Editorial Advisory Board |

| | |
|--|---|
| Prof. Dr. Abdelmejid BAYAD | Université d'Évry Val d'Essonne FRANCE |
| Prof. Dr. Ali Behcet ALPAT | Istituto Nazionale di Fisica Nucleare (INFN) ITALY |
| Prof. Dr. Azra SPAGO | Dzemal Bijedic University of Mostar BOSNIA AND HERZEGOVINA |
| Prof. Dr. Bektay YERKIN | Satbayev University KAZAKHSTAN |
| Prof. Dr. Burçin BAYRAM | Miami University USA |
| Prof. Dr. Daeyeoul KIM | Jeonbuk National University SOUTH KOREA |
| Prof. Dr. Elvan AKIN | Missouri University of Science and Technology USA |
| Prof. Dr. Filiz DİK | Rockford University USA |
| Prof. Dr. Homer RAHNEJAT | Loughborough University UNITED KINGDOM |
| Prof. Dr. Lokesha VEERABHADRIAH | Vijayanagara Sri Krishnadevaraya University INDIA |
| Prof. Dr. Mehmet DİK | Rockford University USA |
| Prof. Dr. Nedim SULJIC | University of Tuzla BOSNIA AND HERZEGOVINA |
| Prof. Dr. Rob DWYER-JOYCE | The University of Sheffield UNITED KINGDOM |
| Prof. Dr. Snezana KOMATINA | University Novi Sad SERBIA |
| Prof. Dr. Toni NIKOLIC | University Džemal Bijedić Mostar BOSNIA AND HERZEGOVINA |
| Prof. Dr. Turysbekova Gaukhar SEYTKHANOVNA | Satbayev University KAZAKHSTAN |
| Assoc. Prof. Dr. Burcin ŞİMŞEK | Associate Director Biostatistics (Oncology) at Bristol Myers Squibb USA |
| Assist. Prof. Dr. Alisa BABAJIC | University of Tuzla BOSNIA AND HERZEGOVINA |
| Dr. Daniel Ganyi NYAMSARI | Mining Company Researcher CAMEROON |



| English Language Editors |

Lecturer
Gizem AÇELYA AYKAN Gazi University
School of Foreign Languages

Lecturer
Tuğçe BÜYÜKBAYRAM Gazi University
School of Foreign Languages

| Technical Editors |

Research Assistant Dr.
Fatih UÇAR Akdeniz University

Research Assistant
Özge ÖZER ATAĞOĞLU Akdeniz University



| Correspondence Address |

Gazi University Graduate School of Natural and Applied Sciences
Emniyet Neighborhood, Bandırma Avenue No:6/20B, 06560,
Yenimahalle - ANKARA
B Block, Auxiliary Building

| e-mail |

gujsa06@gmail.com

| web page |

<https://dergipark.org.tr/tr/pub/gujsa>

Gazi University Journal of Science Part A: Engineering and Innovation
is a peer-reviewed journal.



| INDEXING |



| ACCESSIBILITY |



This work are licensed under a Creative Commons Attribution-ShareAlike 4.0 International License.

| CONTENTS |

Page | Articles

Using Mine Waste and Bentonite in Cement for Enhanced Gamma Radiation Shielding

1-14

S. Tunçkılıç  A.N. Esen 

Nuclear Engineering

Research Article

[10.54287/guj.1620831](https://doi.org/10.54287/guj.1620831)

Efficient Diagnosis of Retinal Diseases Using Convolutional Neural Networks

15-35

M. Kaya 

Information and Computing Sciences

Research Article

[10.54287/guj.1592915](https://doi.org/10.54287/guj.1592915)

Optimizing Machine Learning Models for Soil Fertility Analysis: Insights from Feature Engineering and Data Localization

36-60

C.O. Nwamekwe  N.V. Ewuzie  C.C. Okpala  O.C. Ezeanyim  C.V. Nwabueze  E.C. Nwabunwanne 

Agricultural, Veterinary and Food Sciences Engineering

Research Article

[10.54287/guj.1605587](https://doi.org/10.54287/guj.1605587)

A Novel Dynamic Clock Generator Circuit for the Threshold Logic Gate

61-71

A. Unutulmaz 

Electronics, Sensors and Digital Hardware

Research Article

[10.54287/guj.1645022](https://doi.org/10.54287/guj.1645022)

ChainHealth: Blockchain-Based IoT-Edge Model for Secure Management of Health Data

72-95

R.N. Çayan  F. Yıldırım Okay 

Information and Computing Sciences

Research Article

[10.54287/guj.1624623](https://doi.org/10.54287/guj.1624623)

| CONTENTS |

Page | Articles

Effective Maintenance of Industrial 5-Stage Compressor: A Machine Learning Approach

96-118 O.C. Ezeanyim  N.V. Ewuzie  P.S. Aguh  C.V. Nwabueze  C.O. Nwamekwe 

Manufacturing and Industrial Engineering

Research Article

[10.54287/guj.1646993](https://doi.org/10.54287/guj.1646993)

Determination of stress from HR-XRD and Raman for GaN/AlInN/AlN/Sapphire HEMTs

119-126 Ö. Bayal  A.K. Bilgili  E. Hekin  N. Kaya  Y. Özen  M.K. Öztürk 

Physical Sciences

Research Article

[10.54287/guj.1636694](https://doi.org/10.54287/guj.1636694)

Novel Approach for Detecting the Number of Columns of a Résumé

127-153 Y. Bali  G.K. Orman  S.N. Turhan 

Information and Computing Sciences

Research Article

[10.54287/guj.1636051](https://doi.org/10.54287/guj.1636051)

Improving Machine Failure Prediction with Grey Wolf, Whale Optimization, and Optuna Techniques

154-174 V. Sinap 

Information and Computing Sciences

Research Article

[10.54287/guj.1544942](https://doi.org/10.54287/guj.1544942)

Machine Learning-Enhanced Traffic Light Optimization System Prioritizing Emergency Vehicle Passage Using SVM and Random Forest Models

175-196 Y. Yılmaz 

Information and Computing Sciences

Research Article

[10.54287/guj.1581105](https://doi.org/10.54287/guj.1581105)

| CONTENTS |

Page | Articles

A Deep Learning Approach for Fault Detection in Photovoltaic Systems Using MobileNetV3

197-212

S. Mansurov  Z. Çetin  E. Aslan  Y. Özüpak 

Electrical Engineering

Research Article

[10.54287/gujisa.1596110](https://doi.org/10.54287/gujisa.1596110)

Seismic Rehabilitation of a Reinforced Concrete School in Northern Cyprus Following the 2023 Turkey Earthquake Sequences

213-227

S. Babaei  F. Karimi Ghaleh Jough 

Civil Engineering

Research Article

[10.54287/gujisa.1590807](https://doi.org/10.54287/gujisa.1590807)

Mineral Chemistry of Ulukale Porphyritic Dome and Çağlarca Radial Dykes in the Tunceli Volcanites, Eastern Turkey

228-249

S. Kürüm  A. Sar  M.Y. Yurt 

Geological Engineering

Research Article

[10.54287/gujisa.1589209](https://doi.org/10.54287/gujisa.1589209)

Geochemical and Mineralogical Differentiation of Tepekent Basalts: A Multivariate Analysis Approach (NW of Konya-Central Anatolia)

250-267

G. Gençoğlu Korkmaz 

Geological Engineering

Research Article

[10.54287/gujisa.1592619](https://doi.org/10.54287/gujisa.1592619)

Quasi-Periodic Photonic Structures: Fibonacci Fractal-Based Optical Filter Design Using ZnO/MgF₂

268-277

E. Çokduygular 

Physical Sciences

Research Article

[10.54287/gujisa.1624298](https://doi.org/10.54287/gujisa.1624298)

| CONTENTS |

Page | Articles

Investigation of the Structural and Mechanical Properties of Pure Al-TiC Composites

278-291

M. Pul  T. Şimşek  M. Bilen 

Materials Engineering

Research Article

[10.54287/gujisa.1565233](https://doi.org/10.54287/gujisa.1565233)

The Effect of Proximity Sensor & Grip Sensor Use on Specific Absorption Rate (SAR) in Smartphones

292-306

E. Aydın 

Electronics, Sensors and Digital Hardware

Research Article

[10.54287/gujisa.1616086](https://doi.org/10.54287/gujisa.1616086)

Design of 8-Elements Linear Dipole Antenna Array to Suppress Sidelobe Signals by Using Genetic Optimization

307-318

E. Aydın 

Communications Engineering

Research Article

[10.54287/gujisa.1559050](https://doi.org/10.54287/gujisa.1559050)

Controlling 2D Porous Media Characteristics Through Topology Manipulation

319-331

M. A. Boraey 

Fluid Mechanics and Thermal Engineering

Research Article

[10.54287/gujisa.1611750](https://doi.org/10.54287/gujisa.1611750)

Application of Decision Tree Algorithms for Predicting Trip Purposes in Makurdi, Nigeria

332-346

E.O. Nwafor  F.O. Akintayo 

Civil Engineering

Research Article

[10.54287/gujisa.1588040](https://doi.org/10.54287/gujisa.1588040)



Gazi University

Journal of Science

PART A: ENGINEERING AND INNOVATION

<http://dergipark.org.tr/guj.1620831>

Using Mine Waste and Bentonite in Cement for Enhanced Gamma Radiation Shielding

Setenay TUNÇKILIÇ¹ Ayşe Nur ESEN^{1*} ¹ Istanbul Technical University, Istanbul, Türkiye

| Keywords | Abstract |
|--|---|
| Mine Waste Mud Cement Gamma-Ray Linear Attenuation Coefficient Shielding | The increasing waste produced by the mining industry presents serious environmental challenges. This research focused on developing a sustainable material with enhanced shielding properties against gamma radiation by combining mine waste, which is rich in aluminum and iron, with bentonite and cement. We investigated the gamma-ray shielding properties of the shielding materials at energies of 59.54 keV, 661.66 keV, and 1115.54 keV using both experimental methods and theoretical approaches via EpiXS software. We calculated various metrics, including the linear attenuation coefficient, HVL, TVL, and radiation protection efficiency values. The findings revealed that a shielding material containing 55 wt.% cement and 17 wt.% mine waste mud could effectively reduce the intensity of low-energy gamma-ray photons by half with a thickness of less than 1 cm. The results indicate that incorporating mine waste significantly enhances radiation attenuation at lower gamma-ray energies and presents a promising opportunity for producing eco-friendly building materials, aligning with the principles of green engineering. Overall, using industrial waste in construction is cost-effective, providing long-term savings and environmental benefits. |

Cite
Tunçkılıç, S., & Esen, A. E. (2025). Using Mine Waste and Bentonite in Cement for Enhanced Gamma Radiation Shielding. *GU J Sci, Part A, 12(1)*, 1-14. doi:[10.54287/guj.1620831](https://doi.org/10.54287/guj.1620831)

| Author ID (ORCID Number) | Article Process |
|--------------------------|-----------------------------------|
| 0009-0008-1539-132X | Submission Date 15.01.2025 |
| 0000-0003-4211-7728 | Revision Date 13.02.2025 |
| | Accepted Date 28.02.2025 |
| | Published Date 26.03.2025 |

1. INTRODUCTION

Radiation shielding refers to the use of barriers to minimize exposure between a radiation source and the human body. The main mechanisms through which gamma rays interact include photoelectric absorption, Compton scattering, and pair production. For low-energy gamma rays, photoelectric absorption is most effective when high atomic number materials, like lead, are used. On the other hand, Compton scattering is effective with low atomic number materials such as aluminum and iron at higher energy levels. It's important to note that pair production only takes place with high-energy gamma rays, specifically those exceeding 1022 keV.

Cement is a non-metallic, inorganic material known for its hydraulic binding characteristics. When combined with water, it creates a paste that solidifies as hydrates develop. Once it hardens, the cement keeps its strength (Worrell, 2004). Cement-based materials for radiation shielding are popular due to their low cost and ability to be easily processed and shaped as needed. Shielding properties of concrete produced with different additives such as ilmenite and magnetite (Heniegal et al., 2022), hematite (Singh and Singh, 2021), waste glass (Eid et

*Corresponding Author, e-mail: anesen@itu.edu.tr

al., 2022), and steel slag (Baalamurugan et al., 2021) showed promising results. Bentonite is a type of absorbent swelling clay consisting mainly of montmorillonite, which can be categorized as Na-montmorillonite or Ca-montmorillonite. It finds applications in multiple areas, including industry, agriculture, mining, and engineering geology. Moreover, bentonite is frequently used to improve the effectiveness of cement mortars (Liu et al., 2020). Because of its swelling characteristics and non-toxic nature, bentonite can be incorporated into mortar to fill small voids within the cement matrix. This incorporation reduces water movement within the pore structure, enhancing waterproofing and impermeability. Recent studies have demonstrated the gamma-ray shielding capacities of bentonite, which serves as a suitable buffer and filler material for deep underground repositories in nuclear waste disposal (El-Khatib et al., 2021; El-Samrah et al., 2023; Sallem et al., 2022).

In recent years, the production of waste materials has increased, driven by the growing global population, advances in industry and technology, and heightened levels of consumption. The mining industry generates about 100 billion tons of waste annually (Vuillier, 2021). These pose persistent environmental and safety hazards. Recycling industrial waste into value-added functional materials is a sustainable way of industrial waste management (Saraee and Baferani, 2018; Xia et al., 2024). Green cement is an environmentally friendly cement that uses a carbon-negative production process. The primary raw materials used to produce green cement mainly include waste from industry (Wen et al., 2023). This reduces environmental impact and promotes sustainability. Incorporating waste as a partial replacement for raw materials in concrete production results in products with enhanced qualities, prevents waste from entering the environment, and decreases the need for extracting natural resources (Saraee and Baferani, 2018). In recent years, radiation shielding properties of mine wastes have also been investigated. Red mud, one of the most studied wastes, is a solid aluminum industrial waste that contains 30-60% hematite (Fe_2O_3), which is suitable for shielding high-energy X-ray and gamma rays (Liu et al., 2011). Shivani et al. (2024) researched red mud polymer composites as effective X-ray shielding materials, demonstrating that these composites effectively shield against X-rays. Arya et al. (2023) indicated that newly developed shielding materials created by incorporating barium hydroxide monohydrate and bismuth oxide into red mud are more economical for constructing radiation shielding materials than traditional materials like lead and concrete. Salati et al. (2021) showed that red mud addition to bentonite enhances the radiation shielding effectiveness of bentonite. Gili and Jecong (2023) studied the radiation shielding properties of various Philippine mine tailings and mining by-products, including ferronickel slag, nickel mine tailings, gold mine tailings, and copper mine tailings. Among the materials examined, nickel tailings were the most effective filler material for low-level radioactive waste, particularly in attenuating X-rays and gamma rays. Saraee and Baferani (2018) investigated the gamma radiation shielding properties of a material derived from lead-containing metallurgical solid waste by mixing cement and clay with the waste. Gallala et al. (2017) studied how adding barite-fluorspar mine waste as a fine aggregate affects the radiation-shielding properties of cement mortar. Their findings indicated that incorporating these mine waste aggregates enhanced the attenuation coefficient by 20%.

Incorporating industrial waste into construction materials provides both cost savings and environmental benefits. Construction costs can be significantly reduced by using these waste materials as alternatives to traditional options like cement and sand (Madhusudanan et al., 2016; Sharma and Kumar, 2024). This approach lessens the environmental impact of waste disposal and aids in conserving natural resources. Additionally, it decreases pollution and lowers greenhouse gas emissions (Cherian et al., 2022). In general, using industrial waste in construction materials is economically beneficial, leading to savings by lowering material expenses, alongside significant advantages for the environment.

The main goal of this research was to evaluate the effectiveness of gamma-ray shielding provided by cement-based materials that blend cement, bentonite, and mine waste mud rich in aluminum and iron. This study included experimental tests for gamma-ray transmission and theoretical calculations using EpiXS software. The results also aimed to demonstrate the potential for using industrial by-products to create more efficient and sustainable construction materials.

2. MATERIAL AND METHOD

2.1. Attenuation of Gamma-Ray

When a monoenergetic beam of photons interacts with a material, the number of photons that exit without interacting is calculated by Equation 1 (Tsoulfanidis and Landsberger, 2015).

$$I = I_0 e^{-\mu x} \quad (1)$$

In the equation, I_0 is the initial gamma-ray intensity, I is the gamma-ray intensity after interacting with the material, μ is the linear attenuation coefficient (cm^{-1}), and x is the thickness of the material (cm). A high linear attenuation coefficient, which is the key indicator of a material's effectiveness as a shielding material, suggests that the material is effective at shielding. The mass attenuation coefficient of the material is calculated by dividing the linear attenuation coefficient by the material's density.

$$\mu_\rho = \frac{\mu}{\rho} \quad (2)$$

In the equation, μ_ρ is the mass attenuation coefficient ($\text{cm}^2 \text{g}^{-1}$) and ρ is the material's density (g cm^{-3}).

Radiation protection efficiency (RPE) refers to the ratio of the radiation intensity measured before and after it interacts with a shielding material. It expresses how effective the material is at shielding ionizing radiation. The high RPE value indicates greater shielding of the radiation and, therefore, better radiation protection.

$$RPE(\%) = \left(1 - \frac{I}{I_0}\right) \times 100 \quad (3)$$

The half-value layer (HVL) indicates the thickness of material needed to reduce the initial radiation intensity by half, while the tenth-value layer (TVL) refers to the thickness required to reduce the same intensity to one-tenth. HVL and TVL are important metrics for evaluating how effectively a material can attenuate gamma radiation. The smaller these values, the more effective the material is at shielding against gamma radiation.

$$HVL = \frac{\ln 2}{\mu} \quad (4)$$

$$TVL = \frac{\ln 10}{\mu} \quad (5)$$

The measurement uncertainty was evaluated according to the Guide to the Expression of Uncertainty in Measurement (GUM) (JCGM, 2008) by considering all significant contributions. The combined standard uncertainties of the linear attenuation coefficient and radiation protection efficiency were calculated using Equations 6 and 7, respectively. Since both the half-value layer and the tenth-value layer values were derived from the linear attenuation coefficient, the uncertainty associated with the linear attenuation coefficient was also applied to each of them.

$$u_c(\mu) = \mu \times \sqrt{\left(\frac{u(I_0)}{I_0}\right)^2 + \left(\frac{u(I)}{I}\right)^2 + \left(\frac{u(x)}{x}\right)^2} \quad (6)$$

$$u_c(RPE) = RPE \times \sqrt{\left(\frac{u(I_0)}{I_0}\right)^2 + \left(\frac{u(I)}{I}\right)^2} \quad (7)$$

In the equation $u(I_0)$ and $u(I)$ are the standard uncertainties of the net photopeak count without and with shielding, respectively, and $u(x)$ is the standard uncertainty of the material thickness (Kahraman et al., 2024).

2.2. Preparation of Shielding Materials

CEM I 42.5R Portland Cement was used as the cement material in this study. Bentonite was obtained from Reşadiye, Tokat, and the mine waste mud was obtained from a mining company in Bursa province. According to the analysis conducted through X-ray fluorescence (XRF), the cement is predominantly composed of calcium oxide (CaO), while both bentonite and mine waste mud mainly contain silicon dioxide (SiO₂), as shown in Table 1. The chemical composition indicates that the bentonite is classified as Ca-bentonite, whereas the mine waste mud comprises approximately 32% aluminum oxide and 8% iron oxide.

Due to the moisture in the mine waste mud, it was left to dry in the sun for two days. Once it had dried, it was ground using an agate mortar and passed through an 850 µm sieve. As the cement and bentonite were already in powdered form, they were not processed with grinding or sieving. According to the TS EN 196-1 standard, the ratio of water to cement is 1:2 in the production technique of cement mixtures (Altuncı et al., 2022). All shielding materials were formulated from a composite of cement and water, employing a specific ratio of 25 grams of water to 50 grams of cement. The reference shielding material, designated as C, was comprised solely

of cement and water. Additional shielding materials incorporated varying proportions of bentonite and mine waste mud, as outlined in Table 2. To assess the impact of bentonite and mine waste mud on the radiation shielding properties and facilitate comparison, a fixed quantity of 15 grams of each material was introduced individually into the cement and water mixture. Furthermore, 7.5 grams of bentonite and mine waste mud were introduced into the cement and water mixture while maintaining a total weight of 15 grams. The shielding material, which included cement, bentonite, and water, was prepared to evaluate the influence of bentonite and was referred to as CB. The mixture containing cement, mine waste mud, and water was developed to assess the effect of mine waste mud, denoted as CM. The shielding material, including cement, bentonite, mine waste mud, and water, was designated as CBM. Cement and water were initially blended to achieve a homogeneous mixture while preparing these shielding materials. Subsequently, bentonite and mine waste mud were incorporated, followed by thorough mixing to ensure uniformity throughout the composition.

Table 1. Chemical compositions of materials (%)

| Component | Cement | Bentonite | Mine Waste Mud |
|--------------------------------|--------|-----------|----------------|
| SiO ₂ | 5.39 | 65.02 | 48.08 |
| Al ₂ O ₃ | 6.91 | 21.60 | 31.61 |
| Fe ₂ O ₃ | 3.84 | 5.07 | 7.78 |
| CaO | 69.04 | 4.11 | 3.69 |
| MgO | 2.79 | 2.26 | 2.89 |
| K ₂ O | - | 0.54 | 2.48 |
| TiO ₂ | - | - | 1.04 |
| ZnO | - | - | 0.73 |
| Na ₂ O | 9.96 | 0.42 | 0.51 |

Table 2. Composition of shielding materials by weight and their densities

| Shielding Materials | Code | Cement (%) | Bentonite (%) | Mine Waste Mud (%) | Water (%) | Density (g cm ⁻³) |
|---------------------------------------|------|------------|---------------|--------------------|-----------|-------------------------------|
| Cement | C | 66.63 | - | - | 33.37 | 1.56 |
| Cement and bentonite | CB | 55.12 | 16.92 | - | 27.97 | 1.60 |
| Cement and mine waste mud | CM | 55.38 | - | 16.65 | 27.97 | 1.74 |
| Cement, bentonite, and mine waste mud | CBM | 55.45 | 8.30 | 8.35 | 27.90 | 1.67 |

Each mixture was divided into four equal pieces, placed in plastic molds, and allowed to dry (Figure 1). The pieces were kept for at least 30 days before experimental measurement. They were soaked daily until measurement to prevent crack development during this period. The masses and dimensions of the dried pieces were measured, and the experimental densities were calculated. Experimental densities varied from 1.56 to 1.74 g cm⁻³. The shielding material with the highest density was the cement-mine waste mud blend (CM), while the lowest-density shielding material was the cement (C). The high density of the CM was attributed to its higher aluminum oxide and iron oxide content in mine waste mud than the other materials.

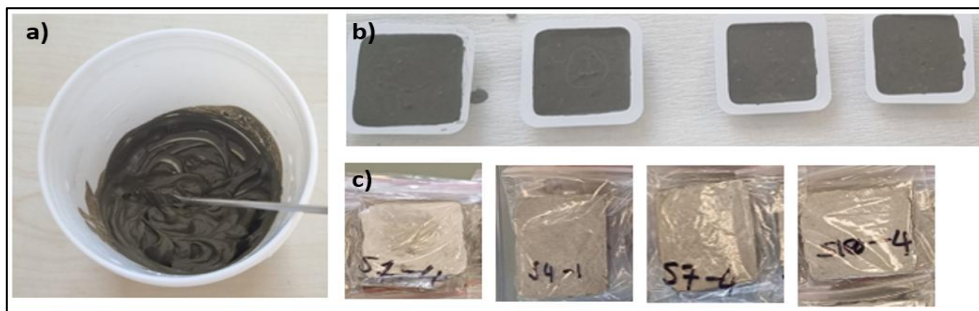


Figure 1. a) Mixing, b) Shielding materials in the plastic molds, and c) Packing for measurement

2.3. Gamma-Ray Shielding Measurements

The shielding experiments were performed using a NaI(Tl) scintillation detector (Alpha Spectra Inc. 3x3 inch). The detector was connected to a DigiBASE (ORTEC) digital gamma spectrometer with MAESTRO multichannel analyzer (MCA) software. To obtain a narrow beam geometry, the source was placed below the collimator, and the shielding material above the collimator. The collimator has a diameter of 7 cm, a length of 4.8 cm, and an internal cavity diameter of 1 cm. The measurement geometry was adjusted to match the shielding materials thickness and provide good counting statistics at the gamma-ray energy of interest in the spectrum in a short time (Figure 2). The uncertainties of the net photopeak count at the energy of interest in the spectra were less than 7%.

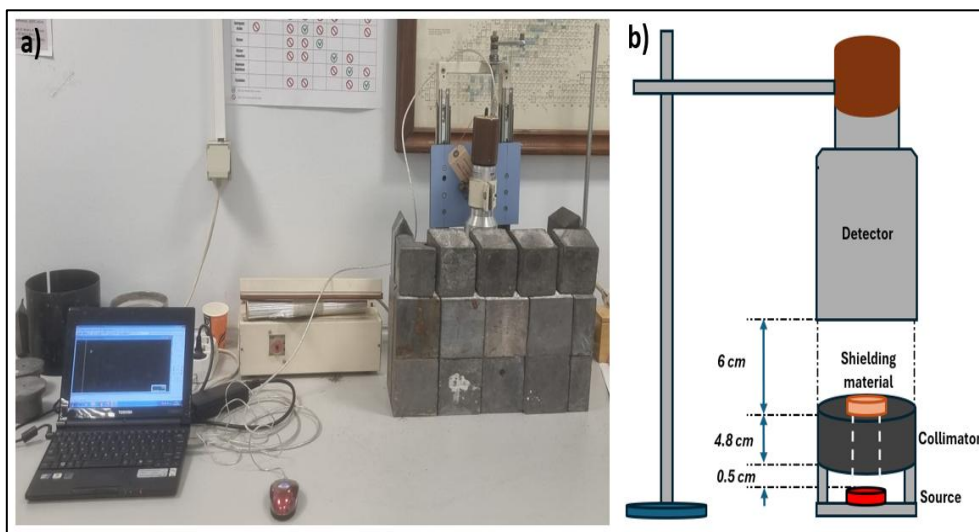


Figure 2. a) Gamma spectrometer with NaI(Tl) detector, b) Measurement geometry

^{241}Am , ^{137}Cs , and ^{65}Zn certified point sources were used in the experiments (Table 3). Thus, the gamma radiation shielding properties of the materials at low, medium, and high gamma-ray energies were investigated. The initial gamma-ray intensity of the sources (I_0) was measured without any shielding material present. To determine the gamma-ray intensity of the radiation after interacting with shielding material of different thicknesses (I), measurements were made by stacking four shielding materials on top of each other. The measured spectra were analyzed with the InterSpec spectral radiation analysis software developed by Sandia Labs (Johnson et al., 2021). The background spectrum was subtracted from the measured spectrum.

Table 3. Properties of certified sources

| Radionuclide | Manufacturer | Energy (keV) | Certified Activity (kBq) | Reference Date |
|-------------------|-------------------------------|--------------|--------------------------|----------------|
| ^{241}Am | Isotope Products Laboratories | 59.54 | 36.21 | 01.12.2006 |
| ^{137}Cs | Czech Metrology Institute | 661.66 | 17.58 | 30.06.2014 |
| ^{65}Zn | Czech Metrology Institute | 1115.54 | 41.59 | 10.10.2023 |

2.4. EpiXS Calculations

The theoretical calculation of the linear attenuation coefficients was performed using EpiXS program (Hila et al., 2021). The input for the program consisted of the chemical compositions of cement, bentonite, mine waste mud, water (H_2O), and gamma-ray energies. The chemical compositions of cement, bentonite, and mine waste mud are given in Table 1. The program's output included these materials' total mass attenuation coefficients at 59.54 keV, 661.66 keV, and 1115.54 keV gamma-ray energies (Table 4).

Table 4. The total mass attenuation coefficients ($\text{cm}^2 \text{g}^{-1}$) of materials calculated by EpiXS

| Energy (keV) | Cement | Bentonite | Mine Waste Mud | Water |
|--------------|--------|-----------|----------------|-------|
| 59.54 | 0.471 | 0.298 | 0.330 | 0.207 |
| 661.66 | 0.077 | 0.077 | 0.076 | 0.086 |
| 1115.54 | 0.060 | 0.060 | 0.060 | 0.067 |

The total mass attenuation coefficients obtained from the EpiXS program for cement, bentonite, mine waste mud, and water were multiplied by their respective weight percentages in the shielding material (Table 2). The results were then summed according to the content of the shielding material. The mass attenuation coefficient of the shielding material was multiplied by its density to calculate the linear attenuation coefficient of the shielding material.

3. RESULTS AND DISCUSSION

Figure 3 displays gamma-ray spectra at an energy of 661.7 keV, comparing measurements taken without any shielding material (represented by the black line) and with a 3 cm thick CM shielding material (represented by the green line). CM was selected because it demonstrated the best shielding properties among all the shielding materials. Both spectra were collected using the same measurement setup for 900 seconds. The uncertainties in the net photopeak counts were 1%. In addition to the photopeak of ^{137}Cs at 661.7 keV, the spectra also revealed the barium X-ray peak at 32 keV, which is part of the decay scheme of ^{137}Cs , as well as the lead X-ray peak in the 70-85 keV energy range due to the lead collimator. Additionally, the Compton continuum region was present in the spectra.

The difference in the height of the photopeaks at 661.7 keV in the spectra obtained with and without the shielding material reflects the difference in the photopeak counts. A higher photopeak observed without the shielding material indicates a greater count (I_0), while a lower photopeak with the shielding material signifies a reduced count (I). This suggests that the gamma-ray intensity was decreased due to the material's shielding effect.

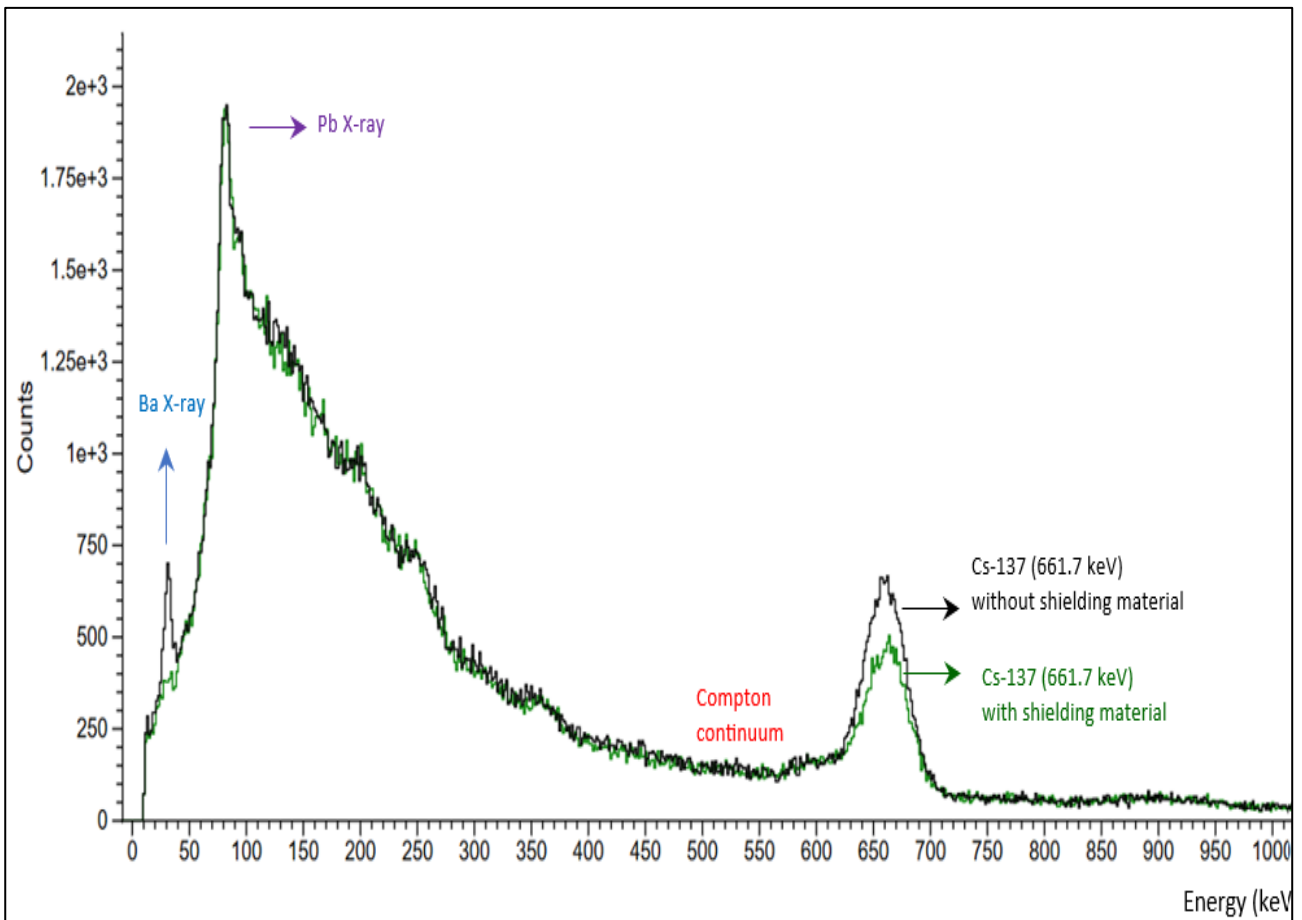


Figure 3. Gamma-ray spectra of ^{137}Cs without shielding material and with 3 cm thick CM shielding material (counting time =900 s)

I/I_0 ratios were calculated for shielding materials (C, CB, CM, CBM) of different thicknesses at gamma-ray energies of interest from the experimentally obtained spectra. The experimental linear attenuation coefficients of shielding materials were determined from the slope of the $\ln(I/I_0)$ - x , and HVL, TVL, and RPE values were calculated. The combined standard uncertainty of the experimental linear attenuation coefficient, RPE, HVL, and TVL were given at $k=1$.

The experimental and theoretical linear attenuation coefficients of shielding materials are given in Table 5. For all shielding materials, the linear attenuation coefficient decreased as energy increased. According to the experimental results, the order of the linear attenuation coefficient from highest to lowest was $CM > CBM > C > CB$. The CM shielding material had the highest linear attenuation coefficient of all energies, and the CB shielding material had the lowest. According to the results obtained from EpiXS, CM exhibited the highest linear attenuation coefficients across all energies, similar to experimental results. The EpiXS results showed that the lowest linear attenuation coefficients were found for C and CB shielding materials, and the values were close. The results aligned with the chemical composition and density of the materials. CM, exhibiting the highest density, demonstrated the most significant gamma-ray attenuation across all energy levels. Conversely, the shielding materials with the lowest density, C and CB, consistently showed the lowest gamma-ray attenuation. When the shielding materials were compared according to the linear attenuation coefficients, it was observed that the shielding capability increased with the increase in the ratio of mine waste mud in the mixture. When shielding material C, containing only cement, and shielding material CB, consisting of the cement-bentonite mixture, are compared, it can be said that the addition of bentonite does not increase the gamma-ray shielding. When comparing experimental and EpiXS results, the differences range from 1% to 10%, indicating that the experimental and theoretical results are consistent. The differences arise from the uncertainties involved in shielding material preparation and gamma-ray measurement (Kahraman et al., 2024).

Table 5. The linear attenuation coefficients (cm^{-1}) of shielding materials

| Energy (keV) | C | | | CB | | | CM | | | CBM | | |
|--------------|-------------------|-------|-----------|-------------------|-------|-----------|-------------------|-------|-----------|-------------------|-------|-----------|
| | Exp. $\pm u_c$ | EpiXS | Diff. (%) | Exp. $\pm u_c$ | EpiXS | Diff. (%) | Exp. $\pm u_c$ | EpiXS | Diff. (%) | Exp. $\pm u_c$ | EpiXS | Diff. (%) |
| 59.54 | 0.640 ± 0.024 | 0.598 | 7 | 0.613 ± 0.029 | 0.588 | 4 | 0.705 ± 0.037 | 0.650 | 8 | 0.673 ± 0.035 | 0.617 | 9 |
| 661.66 | 0.137 ± 0.002 | 0.125 | 10 | 0.116 ± 0.002 | 0.127 | 9 | 0.145 ± 0.002 | 0.138 | 5 | 0.138 ± 0.003 | 0.132 | 4 |
| 1115.54 | 0.096 ± 0.002 | 0.097 | 1 | 0.094 ± 0.002 | 0.099 | 5 | 0.105 ± 0.003 | 0.108 | 3 | 0.099 ± 0.004 | 0.103 | 4 |

The radiation protection efficiency values of CM shielding material are given in Figure 4. The RPE (%) values were calculated at varying shielding material thicknesses. The highest attenuation was noted at an energy of 59.54 keV; a 0.8 cm thick shielding material attenuated 43% of the incident radiation, while a 3 cm thick shielding material completely attenuated the low-energy gamma rays. The 3 cm shielding material at medium

energy provided a 34% attenuation, while at high energy, it provided a 28% attenuation. The differences in RPE(%) values at the same thickness for medium and high energy were less pronounced than those observed at low energy.

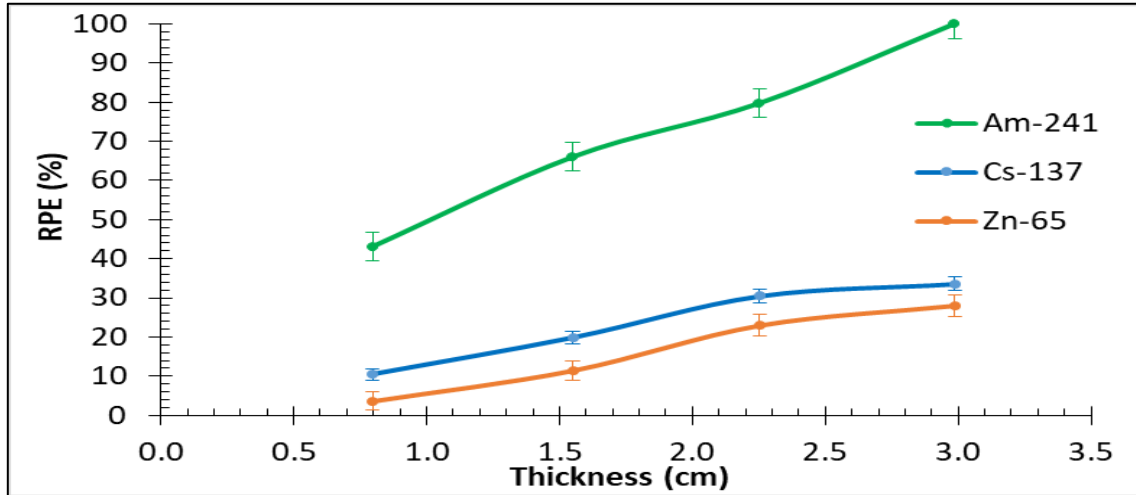


Figure 4. RPE (%) values of cement-mine waste mud (CM) shielding material

Figure 5 shows the HVL and TVL of the shielding materials obtained from experiments. HVL values varied from 0.98 to 1.13 cm at 59.54 keV, 4.77 to 5.98 cm at 661.66 keV, and 6.61 to 7.35 cm at 1115.54 keV. TVL values ranged from 3.27 to 3.75 cm at 59.54 keV, 15.86 to 19.85 cm at 661.66 keV, and 21.95 to 24.42 cm at 1115.54 keV. For all energies, the order of HVL and TVL from lowest to highest is CM < CBM < C < CB. Smaller HVL and TVL values indicate a thinner and more effective shield.

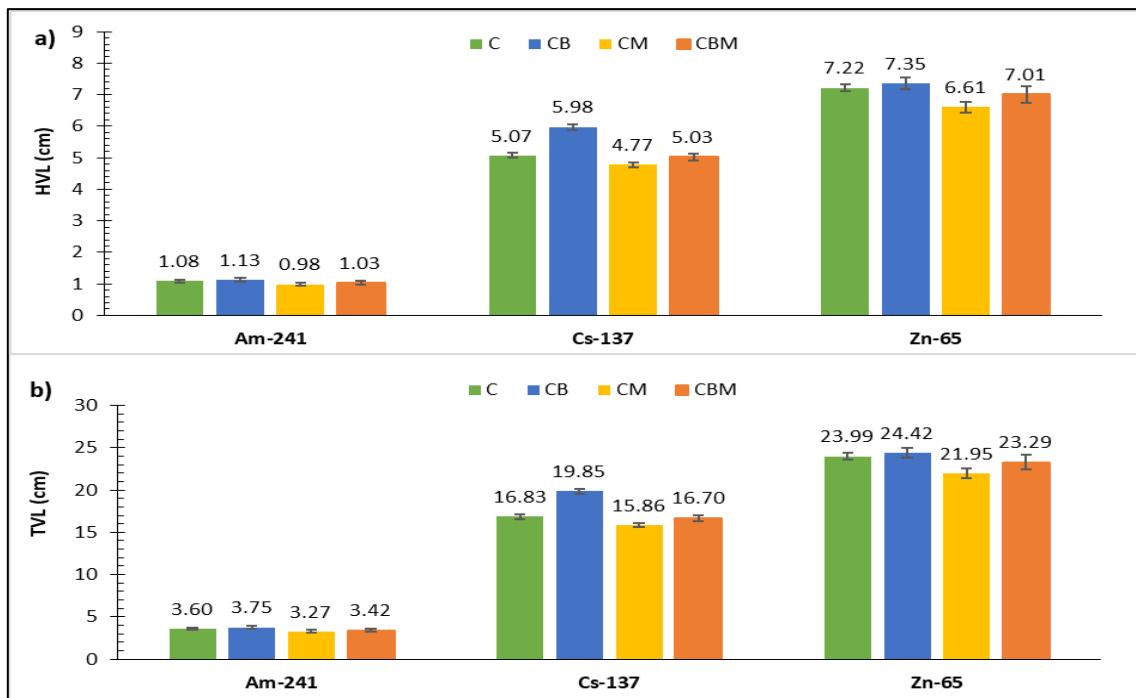


Figure 5. a) HVL, b) TVL values of shielding materials

The HVL values obtained for the CM shielding material, which showed this study's best gamma ray shielding properties, were compared with selected studies where waste was used as radiation shielding material (Table 6). Compared to the cement mixture containing 40% silica waste in the study of Eid et al. (2022), it is seen that the HVL values obtained in our study were lower at 59.5 keV energy. Compared to barite-fluorspar mine waste in the study of Gallala et al. (2017) and copper mine tailing in the study of Gili and Jecong (2023), the HVL values obtained in our study were higher at 662 keV. This could be due to the higher density of copper used in the study of Gili and Jecong (2023), thus providing a higher shielding effect, and the higher weight percentage of mine waste in the study of Gallala et al. (2017) compared to aluminum and iron in our mine waste mud.

Table 6. Comparison to other studies in the literature

| | Material | Energy (keV) | HVL (cm) |
|------------------------|---------------------------------------|--------------|----------|
| This study | Cement-Mine Waste Mud (17 wt.%) | 59.5 | 0.98 |
| | | 662 | 4.77 |
| Eid et al. (2022) | Cement-Silica Waste (40 wt.%) | 59.5 | 1.15 |
| Gallala et al. (2017) | Barite-Fluorspar Mine Waste (30 wt.%) | 662 | 4.62 |
| Gili and Jecong (2023) | Copper Mine Tailings | 662 | 3.22 |

4. CONCLUSION

There has been a growing search for alternative materials that can provide more cost-effective solutions to produce building materials in the construction industry. Utilizing waste not only helps reduce landfill accumulation but also conserves energy. By identifying the optimal amount of waste and replacing either aggregate or cement in concrete production, it is possible to achieve properties similar to ordinary concrete, thus offering solutions to the depletion of natural resources while simultaneously creating more economical and sustainable concrete.

This study investigated the gamma-ray shielding properties of composite materials made from a blend of cement, bentonite, and mine waste mud. To evaluate their effectiveness, shielding materials were prepared and subjected to experimental testing and theoretical analysis using EpiXS software at gamma-ray energies of 59.54 keV, 661.66 keV, and 1115.54 keV. The results showed that shielding material containing 55 wt.% cement and 17 wt.% mine waste mud could reduce the intensity of low-energy gamma-ray photons to half of its initial value when the thickness of the shielding material was less than 1 cm. In contrast, achieving a similar reduction for medium-energy photons required a greater shielding material thickness of approximately 4.8 cm. For high-energy photons, a thicker shielding material of about 6.6 cm was necessary for comparable attenuation. The findings indicate these materials exhibit strong shielding performance at lower gamma-ray energies. Consequently, concrete produced with mine waste additives containing metals is a highly effective candidate for nuclear applications, owing to its suitable nuclear radiation attenuation properties at low gamma energies.

AUTHOR CONTRIBUTIONS

Conceptualization, A.N.E.; methodology, A.N.E.; software, S.T. and A.N.E.; title, A.N.E.; laboratory work, S.T. and A.N.E.; formal analysis, S.T. and A.N.E.; research, S.T. and A.N.E.; sources, A.N.E.; data curation, S.T. and A.N.E.; manuscript-original draft, S.T. and A.N.E.; visualization, S.T. and A.N.E.; supervision, A.N.E.; project management, A.N.E.; funding, A.N.E. All authors have read and legally accepted the final version of the article published in the journal.

ACKNOWLEDGEMENT

This research was supported by the Scientific Research Projects Department of Istanbul Technical University under Project Number MYL-2023-45205. We want to thank Research Assistant Deniz Agehan Kahraman for her assistance. Experimental studies were conducted at the Radioisotope Tracers and Applications Laboratory and the Radiation Detection and Measurement Laboratory at ITU Energy Institute.

CONFLICT OF INTEREST

The authors declare no conflict of interest.

REFERENCES

- Altuncı, Y. T., & Öcal, C. (2022). TS EN 196-1 Standardında Belirtilen Üretim Tekniğinin İrdelenmesi. *Bitlis Eren Üniversitesi Fen Bilimleri Dergisi*, 11(1), 21–28. <https://doi.org/10.17798/bitlisfen.953562>
- Arya, R., Paulose, R., Agrawal, V., Pandey, A., Mishra, D., Kumar Sanghi, S., Akram Khan, M., Pada Mondal, D., Muhamed Shafeeq, M., Banerjee, K., Chatterjee, S., Mukhopadhyay, S., Roy, P., Ravishankar, R., Bhattacharya, C., Bhisikar, A., Mondal, P., Singh, U., Agnihotri, A., ... Thankaraj Salammal, S. (2023). Next generation gamma ray shielding blocks developed using alumina industry waste. *Construction and Building Materials*, 373. <https://doi.org/10.1016/j.conbuildmat.2023.130895>
- Baalamurugan, J., Kumar, V. G., Chandrasekaran, S., Balasundar, S., Venkatraman, B., Padmapriya, R., & Raja, V. K. B. (2021). Recycling of steel slag aggregates for the development of high density concrete: Alternative & environment-friendly radiation shielding composite. *Composites Part B: Engineering*, 216. <https://doi.org/10.1016/j.compositesb.2021.108885>
- Cherian, C., Siddiqua, S., Arnepalli, D.N. (2022). Utilization of Recycled Industrial Solid Wastes as Building Materials in Sustainable Construction. In: Reddy, K.R., Pancharathi, R.K., Reddy, N.G., Arukala, S.R. (Eds) *Advances in Sustainable Materials and Resilient Infrastructure*. Springer Transactions in Civil and Environmental Engineering. Springer, Singapore. https://doi.org/10.1007/978-981-16-9744-9_4
- Eid, M. S., Bondouk, I. I., Saleh, H. M., Omar, K. M., Sayyed, M. I., El-Khatib, A. M., & Elsafi, M. (2022). Implementation of waste silicate glass into composition of ordinary cement for radiation shielding applications. *Nuclear Engineering and Technology*, 54(4), 1456–1463. <https://doi.org/10.1016/j.net.2021.10.007>

- El-Khatib, A. M., Elsafi, M., Almutiri, M. N., Mahmoud, R. M. M., Alzahrani, J. S., Sayyed, M. I., & Abbas, M. I. (2021). Enhancement of bentonite materials with cement for gamma-ray shielding capability. *Materials*, *14*(16), 4697. <https://doi.org/10.3390/ma14164697>
- El-Samrah, M. G., Tawfic, A. F., Sallam, F. H., & Omar, A. M. (2023). Investigation of specially designed bentonite samples as potential bricks with better radiation shielding properties. *Progress in Nuclear Energy*, *162*, 104778. <https://doi.org/10.1016/j.pnucene.2023.104778>
- Gallala, W., Hayouni, Y., Gaied, M. E., Fusco, M., Alsaied, J., Bailey, K., & Bourham, M. (2017). Mechanical and radiation shielding properties of mortars with additive fine aggregate mine waste. *Annals of Nuclear Energy*, *101*, 600–606. <https://doi.org/10.1016/j.anucene.2016.11.022>
- Gili, M. B. Z., & Jecong, J. F. M. (2023). The Potential Application of Mining Wastes and Slag as Radiation Shielding: A Characterization Study Using EpiXS. *Arabian Journal for Science and Engineering*, *50*, 3047–3058. <https://doi.org/10.1007/s13369-023-07904-8>
- Heniegal, A. M., Amin, M., Nagib, S. H., Youssef, H., & Agwa, I. S. (2022). Effect of nano ferrosilicon and heavyweight fine aggregates on the properties and radiation shielding of ultra-high performance heavyweight concrete. *Case Studies in Construction Materials*, *17*, e01543. <https://doi.org/10.1016/j.cscm.2022.e01543>
- Hila, F. C., Asuncion-Astronomo, A., Dingle, C. A. M., Jecong, J. F. M., Javier-Hila, A. M. V., Gili, M. B. Z., Balderas, C. V., Lopez, G. E. P., Guillermo, N. R. D., & Amorsolo, A. V. (2021). EpiXS: A Windows-based program for photon attenuation, dosimetry and shielding based on EPICS2017 (ENDF/B-VIII) and EPDL97 (ENDF/B-VI.8). *Radiation Physics and Chemistry*, *182*, 109331. <https://doi.org/10.1016/j.radphyschem.2020.109331>
- JCGM. (2008). *Evaluation of measurement data-Guide to the expression of uncertainty in measurement (JCGM 100:2008)*. Joint Committee for Guides in Metrology.
- Johnson, W., Chan, E., Walsh, E., Morte, C., & Lee, D. (2021). InterSpec v. 1.0.8. <https://doi.org/10.11578/dc.20211202.6>
- Kahraman, D. A., Cogalmis, F. T., Esen, A. N., Hacıyakupoglu, S., & Senkal, B. F. (2024). Neutron and gamma-ray shielding effectiveness of novel polyaniline composites. *Radiation Physics and Chemistry*, *219*, 111675. <https://doi.org/10.1016/j.radphyschem.2024.111675>
- Liu, M., Hu, Y., Lai, Z., Yan, T., He, X., Wu, J., Lu, Z., & Lv, S. (2020). Influence of various bentonites on the mechanical properties and impermeability of cement mortars. *Construction and Building Materials*, *241*, 118015. <https://doi.org/10.1016/j.conbuildmat.2020.118015>
- Liu, Y., Naidu, R., & Ming, H. (2011). Red mud as an amendment for pollutants in solid and liquid phases. *Geoderma*, *163*(1–2), 1–12. <https://doi.org/10.1016/j.geoderma.2011.04.00>
- Madhusudanan, S., & Amirtham, L. R. (2016). Optimization of construction cost using industrial wastes in alternative building material for walls. *Key Engineering Materials*, *692*, 1–8. <https://doi.org/10.4028/www.scientific.net/kem.692.1>

- Salati, A., Share Isfahani, H., & Rowshanzamir, M. A. (2021). Evaluation of the performance of bentonite and red mud mixture as a shield in radioactive waste landfills. *Journal of Physics: Conference Series*, 1973(1). <https://doi.org/10.1088/1742-6596/1973/1/012200>
- Sallem, F. H., Sayyed, M. I., Aloraini, D. A., Almuqrin, A. H., & Mahmoud, K. A. (2022). Characterization and Gamma-ray Shielding Performance of Calcinated and Ball-Milled Calcinated Bentonite Clay Nanoparticles. *Crystals*, 12(8), 1178. <https://doi.org/10.3390/cryst12081178>
- Saraee, R. E. K., & Baferani, P. S. (2018). Application of Solid Waste Containing Lead for Gamma Ray Shielding Material. *Iranian Journal of Science and Technology, Transaction A: Science*, 42(2), 941–946. <https://doi.org/10.1007/s40995-016-0131-7>
- Sharma, K., & Kumar, A. (2024). Comparative Cost Analysis of Industrial Waste-Based Composite Materials Treated with Lime, Cement, and Alkali Activator in Comparison with Conventional Pavement Material. In: Agnihotri, A.K., Reddy, K.R., Bansal, A. (Eds), *Sustainable Materials. EGRWSE 2023. Lecture Notes in Civil Engineering, vol 509*, pp (149-157), Springer, Singapore. https://doi.org/10.1007/978-981-97-3153-4_11
- Shivani, Vishwakarma, J., Dhand, C., M, M. S., Salammal, S. T., Gupta, G. K., Mishra, A., & Dwivedi, N. (2024). “Red-Mud, A Golden Waste for Radiation Shielding”: Red-Mud Polymer Composites for High-Performance Radiation-Shielding Components. *Journal of Hazardous Materials Advances*, 13, 100394. <https://doi.org/10.1016/j.hazadv.2023.100394>
- Singh, S., & Singh, K. (2021). On the use of green concrete composite as a nuclear radiation shielding material. *Progress in Nuclear Energy*, 136, 103730. <https://doi.org/10.1016/j.pnucene.2021.103730>
- Tsoufanidis, N., & Landsberger, S. (2015). *Measurement and Detection of Radiation (4th ed.)*. CRC Press.
- Vuillier, C. (2021). Future Of Mining With Zero Mine Waste | Knowledge Ridge. <https://www.knowledgeridge.com/expert-views/future-of-mining-with-zero-mine-waste>
- Wen, J., Wang, B., Dai, Z., Shi, X., Jin, Z., Wang, H., & Jiang, X. (2023). New insights into the green cement composites with low carbon footprint: The role of biochar as cement additive/alternative. *Resources, Conservation and Recycling*, 197, 107081. <https://doi.org/10.1016/j.resconrec.2023.107081>
- Worrell, E. (2014). Cement and Energy, Reference Module. In: S. A. Elias (Ed.), *Reference Module in Earth Systems and Environmental Sciences* (pp. 307-315). Elsevier. <https://doi.org/10.1016/B0-12-176480-X/00373-9>
- Xia, Y., Shi, D., Zhao, R., Yu, K., Liu, M., Mei, H., Xu, L., Zhao, Y., Wang, L., & Yan, J. (2024). Iron-rich industrial waste enhanced low-carbon radiation shielding functional composites. *Journal of Cleaner Production*, 449, 141649. <https://doi.org/10.1016/j.jclepro.2024.141649>



Gazi University

Journal of Science

PART A: ENGINEERING AND INNOVATION

<http://dergipark.org.tr/guj.1592915>

Efficient Diagnosis of Retinal Diseases Using Convolutional Neural Networks

Mahir KAYA^{1*} ¹ Tokat Gaziosmanpaşa University, Tokat, Türkiye

| Keywords | Abstract |
|---|---|
| Retinal Diseases Deep Learning CNN Computer-aided Diagnosis | The eye is a vital sensory organ that enables us to fulfill all our life's needs. Diseases affecting such a vital organ can have a detrimental impact on our lives. Although certain eye conditions are easily managed, others may result in lasting damage or loss of sight if not identified promptly. Problems within the retina or improper image focus on the retina may result in loss of eyesight. Optical Coherence Tomography (OCT) can identify diseases using retinal images taken from a side-angle view. Medical images are analyzed using Convolutional Neural Networks (CNNs) to automatically diagnose diseases. Doctors may reach varying conclusions when diagnosing diseases based on medical images. These conclusions may even contain human error. These challenges can be overcome with the use of CNNs. When creating a CNN architecture, many hyperparameter values need to be determined at the beginning before the training phase. A well-structured design is crucial for the successful performance of CNNs. The lengthy training time of CNNs makes testing every hyperparameter combination a very time-intensive process. This research determined the best hyperparameters for CNNs by means of Bayesian optimization. The study employed a dataset comprising four categories: DME, CNV, DRUSEN, and NORMAL. With Bayesian optimization, this proposed model reached an accuracy and F1 score of 99.69%, outperforming existing research findings. The proposed model will also help doctors to make decisions and speed up the decision-making process. |

Cite

Kaya, M. (2025). Efficient Diagnosis of Retinal Diseases Using Convolutional Neural Networks. *GU J Sci, Part A, 12(1)*, 15-35. doi:10.54287/guj.1592915

Author ID (ORCID Number)

0000-0001-9182-271X Mahir KAYA

Article Process

| | |
|------------------------|------------|
| Submission Date | 28.11.2024 |
| Revision Date | 30.12.2025 |
| Accepted Date | 03.03.2025 |
| Published Date | 26.03.2025 |

1. INTRODUCTION

The eyes are the most important of our sensory organs. In fact, the brain is the organ that enables us to see and the eye helps us to see in this sense (Çevik et al., 2021). The eye is composed of three layers that are capable of transmitting and refracting light (Malkoç, 2006). The sclera, the first layer from the outside to the inside, is the white area where light is refracted and protects the eye from external factors. The second layer is the retina (choroid), a network of blood vessels responsible for nourishing the retina. The third layer, the retina, is located behind the eye wall and contains millions of light-sensitive nerve cells (Farsiu et al., 2014). The light coming into the eye is refracted first in the cornea and then in the lens and falls on the retina, and vision is realized by stimulating millions of nerve cells in the retina (Alqudah, 2020). Messages about vision are processed in the brain through the optic nerve, which is composed of millions of nerve fibers, to form the image (Wu et al., 2013).

*Corresponding Author, e-mail: mahir.kaya@gop.edu.tr

Vision starts in the retina. The retina also contains cells that allow us to see in the dark and in the light (Tayal et al., 2021). Numerous conditions can affect the retina, including diabetic retinopathy, retinal tears, retinal detachments, yellow spot disease, occlusions of the retinal artery, epiretinal membrane, and traumatic eye injuries (Fujimoto et al., 2000, Wu et al., 2013, Farsiu et al., 2014, Asif et al., 2022). Diseases occurring in the retina affect the visual ability of the person and the damage to the retina is irreversible (Saleh et al., 2022). Therefore, timely diagnosis and intervention are essential. Diabetic retinopathy, for example, which can cause vision loss, can be diagnosed early with a retinal examination (Çevik et al., 2021). Ultrasonography, fundus fluorescein angiography, and optical coherence tomography, in addition to retinal examination, can be used for diagnosis (Silverman et al., 2014).

Optical Coherence Tomography (OCT) is a method of creating cross-sectional images of the retina using light waves (Li et al., 2019). OCT provides a detailed view of all retinal layers and assesses their thickness. These measurements aid in the diagnosis and selection of the best treatment method for retinal diseases (Fujimoto, et al., 2000). Although retinal eye diseases are typically detected by specialist clinicians through eye examinations, their assessments may sometimes vary. Human error may also arise due to the specialists' workload or conflicting disease conditions. To address these issues, it is important to support decision-making processes with computer-aided artificial intelligence systems (Kaya & Çetin-Kaya, 2024a, Duran et al., 2025). In the last decade, deep learning-based Convolutional Neural Networks (CNNs) have been extensively utilized and successfully applied to disease diagnosis from medical images (Çetin-Kaya & Kaya, 2024). The structure of a CNN comprises convolutional layers, pooling layers, and fully connected layers, and performs end-to-end learning in the training phase, using raw images as input (Krizhevsky et al., 2012; LeCun et al., 1998). In classical machine learning, the features used as input are manually determined at the beginning of the training phase, while in deep learning-based models, feature extraction from raw images is performed automatically during the training phase.

Common problems in disease diagnosis from medical images with CNN can be listed as follows: insufficient number of labeled data, unbalanced class distributions in the datasets, noisy datasets, high similarities between dataset classes, and overfitting during training. When dealing with a dataset with limited labeled samples, underfitting occurs if CNN architectures are defined in a simple way with few layers, but overfitting occurs in the training phase if the architecture is too deep and complex (Kaya, 2024; Güneş & Çetin-Kaya, 2024). When overfitting occurs, CNN models tend to retain the training data in memory rather than generalizing from it, so their training accuracy is very high, but their performance drops significantly when encountering unfamiliar test data (Zhang et al., 2021). Therefore, determining the optimal CNN architecture is crucial for achieving high performance (Çetin-Kaya., 2024). Since CNN architectures have many hyperparameters, it is almost impossible to determine the optimal architecture manually. CNNs are also trained with medical images to diagnose diseases (Cheyi & Çetin-Kaya, 2024). In order to develop a successful model with CNNs, many hyperparameters, including the quantity and dimensions of filters within the convolutional layer, the quantity

of neurons in the densely connected layer, the dropout rate and the learning rate need to be optimally adjusted. In CNNs, hyperparameters comprise many combinations and trying all combinations is costly in terms of training time. To overcome these problems, statistical estimation methods are employed to find the best hyperparameters. In this study, Bayesian optimization method is used to determine the optimal hyperparameters in CNN architectures. Thus, four different retinal disease types were successfully classified.

1.1. Motivation

It is very important that retinal eye diseases are automatically detected by artificial intelligence systems at an early stage. Rapid treatment of early diagnosed eye diseases will accelerate the healing process. In the literature, there are various studies involving transfer learning and custom models. Since transfer learning models are complex models, it may not be possible to run them on all devices. Likewise, custom and transfer learning models have not been optimized to find the optimal hyperparameter values for eye diseases. There is a need for models with a very low error rate and a lightweight architecture for eye diseases.

1.2. Contributions

In the paper, a CNN-based model is introduced for the automated diagnosis of eye diseases using OCT images. A lightweight CNN architecture is developed using Bayesian optimization. Within the CNN structure, key settings like the quantity of filters, filter dimensions, the count of neurons in the fully connected layer, dropout percentage, and learning rate are fine-tuned for optimal performance. The proposed model achieves higher accuracy than previous studies in the literature. This lightweight model can also run quickly on resource-constrained devices.

The remainder of this document is structured as follows: Section 2 offers an overview of prior research. Section 3 describes the dataset and methodology. In Section 4, the training results of the models are presented and compared with existing literature. Section 5 presents a comparative analysis of previous research studies. Lastly, Section 6 wraps up by providing an overview of the results.

2. RELATED WORKS

Deep learning architectures are commonly used for the classification of eye diseases. One of the methods used in deep learning studies is to design a model specific to the classification problem. Thus, customized architectures are used in studies aimed at diagnosing eye diseases.

Alqudah (2020) proposed a custom CNN model for the classification of eye diseases from spectral-domain OCT images. The proposed model includes 4 Convolutional layers and consists of 19 layers in total. In the study, classification was performed for 5 classes: diabetic macular edema (DME), age-related macular degeneration (AMD), Drusen, choroidal neovascularization (CNV), and Normal. Training of the suggested model was conducted over 100 epochs, with the utilization of the Adam optimization algorithm. In the test

using 1250 images, the general accuracy rate of the model is 97.12% and the accuracy values on a class basis are between 97.84% (Drusen) and 100% (AMD). In this study, no optimization algorithm was applied for the filter count and kernel dimension in the model. For hyperparameters such as epoch and learning speed, the trial and error method was applied. For testing the proposed approach, the test data specified in the dataset was used. A successful result was obtained with a small model with fewer parameters than transfer learning models. Tayal et al. (2021) proposed three custom CNN architectures for classification of eye disease. The models differ in the number of CNN layers they have (five, seven and nine layers). Before the images were transmitted to the models, they were first preprocessed and then different image enhancement techniques were applied. All three models were trained for 15 rounds and the Adam optimizer is utilized with a learning rate of 0.001 and a batch size of 84. As a result of the tests, the best result was obtained with the 7-layer model with 96.5% accuracy and 95.33% F1-score. High performance was achieved by enhancing the images with image processing techniques. The effect of 3 different architectures with different number of layers was analyzed. The study did not use an optimization algorithm to find the optimum architecture. Berrimi and Moussaoui (2020) proposed two CNN architectures for multiple classification and compared their performance with transfer learning models. The initial CNN design integrates three convolutional layers, with each layer's output subsequently processed through maximum pooling. Subsequently, a fully connected layer and an output layer, comprising four neurons that align with the class count, are appended. The second CNN architecture includes a dropout layer and a batch normalization layer in addition to the first CNN architecture. The first CNN model achieved 95.60% accuracy and the second CNN model achieved 98.75% accuracy.

As the model depth increases, it involves a significant the duration required to train a model from end to end. In addition, many images are required to achieve good classification performance. Access to both medical images and competent experts to take part in the labeling process can be difficult. To overcome these problems, rather than training the model from scratch to completion, it is preferred to train a certain number of layers using the transfer learning method, thus creating deep learning models with higher performance with fewer images. Saleh et al. (2022) performed a transfer learning study on classifying retinal weaknesses from OCT images. The images were preprocessed in two stages. First, contrast enhancement was performed and then anisotropic diffusion filtration algorithm was applied. In the study, The SqueezeNet, a customized version of SqueezeNet, and the InceptionV3 models were implemented using a transfer learning technique. Regarding accuracy, the Modified SqueezeNet model (98%) outperformed the original SqueezeNet model (96.85%). The InceptionV3 model achieved the highest accuracy of 98.4%. Li et al. (2019) presented a deep learning model for the determination of retinal eye illnesses, which combines deep features with handcrafted features. Handcrafted features are derived from Sift and Gabor filters. The study was carried out with three frameworks. In the first one, images and handcraft features are combined and sent to the deep architecture, while in the second one, images and handcraft features are sent separately to the deep architecture and the results are combined for classification. In the third framework, images and handcrafted features are combined after each convolutional block and RCNet model is used to realize this. With the dataset, three groups with different

distributions were created and training and testing were performed. The best performance for all three groups was obtained by adding the RCNet model and Gabor features. The authors explored combining manually designed features with those derived from deep learning methods. In order to examine the effect of different datasets, they divided the dataset into three different groups. Especially in group 2, a total of 1000 images were employed for training, and another 1000 images were reserved for testing. In this case, they showed that deep learning models integrated with handcrafted features perform better on small datasets. In Group 1, 1000 images of the dataset were used for testing and the rest for training. In Group 3, 50% of the dataset was reserved to training and the other 50% part to testing. Asif et al. (2022) presented a model for identifying eye illnesses from OCT images, utilizing transfer learning as a key component. In the study, ResNet50 architecture is used by modifying the last layer and training the entire system as a whole. A fully connected block including three dense layers, Relu activation function, three BatchNormalization layers, Dropout layer and L2 regularization is added to the RESNet50 model. The model was tested with 242 images for each class and 968 images in total, and an accuracy of 99.48% was obtained. Zheng et al. (2020) undertook an investigation on the use of synthetic images generated with GAN in the detection of retinal diseases. They used Kermany dataset consisting of original images and a synthetic dataset. The synthetic dataset was created from 130 urgent and 148 nonurgent images using GAN. This dataset contains 100,456 OCR images, of which 48,751 are urgent and 51,705 are nonurgent. The Inception V3 model was trained with both the original and synthetic dataset using transfer learning. The performance of the models was assessed across the actual image data and the fabricated image data. In the test phase using the original dataset, the effectiveness of the model trained using an artificially generated dataset was slightly lower than the model trained with the original images. Kermany et al. (2018) introduced a transfer learning model that utilizes the InceptionV3 architecture for classifying eye diseases in OCT images. Training of the model was performed across 100 epochs, utilizing a total of 108,312 images. Then, it was tested with 1000 images and a specificity of 97.4%, a sensitivity of 97.8%, and an accuracy of 96.6% was observed. The authors also investigated whether there would be any performance loss if the model underwent training using a reduced dataset. Training of the model utilized a dataset containing 1000 images for each class, and an accuracy rate of 93.4% was obtained as a result of the test. Tuncer et al. (2021) employed advanced, already trained models to perform the classification of OCT images into various categories. In the feature extraction phase of the proposed architecture, they utilized AlexNet, GoogleNet and ResNet18 architectures. Accuracy values of 96.88%, 97.40% and 95.36% were obtained respectively. To maximize the architectures' functional output, they used the SVM algorithm in the classification phase. When the results obtained are analyzed, Alexnet-SVM, Resnet18-SVM and Googlenet-SVM architectures obtained accuracy values of 98.96%, 95.36% and 98.2% respectively. Kim and Tran (2021) proposed two models in their study. In the first model, three binary CNN classifiers are used. These classifiers can be thought of as sequential, first reducing from 4 classes to 2 classes and then performing binary classification in the remaining classes. The first classifier (ResNet152) was used to classify the images into DME and CNV and Normal and Drusen. Then, the second classifier (InceptionV3) is used for CNV and DME discrimination and the third classifier (VGG19) is used for Drusen and Normal discrimination. Four distinct binary CNN classifiers are

employed by the second model. Each classifier detects a specific disease (Classifier1 (VGG16)-CNV vs. Others, Classifier2 (VGG16)-DME vs. others, Classifier3 (VGG19)-Drusen vs. others and Classifier4 (InceptionV3)-Normal vs. others). Each classifier works only to detect the disease of interest and groups the rest of the classes as “other”. Model 1 achieved 98.1% accuracy while model 2 achieved 98.7% accuracy. İncir and Bozkurt (2024a) used K-means clustering algorithm to segment hard exudates, which are important lesions of the disease, and increased the effect of these regions in the original image. Thus, the importance of data preprocessing is emphasized. In addition, they utilized ResNet50, MobileNet, DenseNet121 and EfficientNetV2-M architectures in the feature extraction phase. The extracted features are fed separately as input to the Global Average Pooling layer and then forwarded to the dense and dropout layers. At the end of the study, ResNet50, MobileNet, DenseNet121 and EfficientNetV2-M models achieved 91.07%, 88.62%, 91.87% and 94.36% accuracy on the original data set, respectively. On the preprocessed dataset, the accuracy values were 92.18%, 90.70%, 93.30% and 95.16%, respectively. İncir and Bozkurt (2024b) created a meaningful and sufficient dataset for diabetic retinopathy classification with the aid of well-designed data preparation and alteration methodologies. A selection of pre-trained models, specifically EfficientNetV2-M, MobileNet, VGG16, Inception-V3, Xception, DenseNet-121, and ResNet-50, was employed by them to extract features. As a result, EfficientNetV2-M architecture achieved the highest accuracy value with 97.65%.

3. MATERIAL AND METHOD

3.1. Dataset

A dataset consisting of four different classes of diseased and healthy, namely CNV, DME, DRUSEN, and NORMAL was used in this work (Kaggle, 2018). In this dataset, there are 37205 CNV diseased eye OCT images, 11348 DME diseased OCT images, 8616 DRUSEN diseased OCT images and 26315 NORMAL healthy OCT images to be used in training, while there are 242 OCT images in each class in the test. 8 images have been allocated to each class for validation. Since this number is quite small for validation, we rearranged the dataset by reserving 5% of the training dataset for validation. Figure 1 displays examples of images from this dataset.

Data partitioning results for the OCT data are presented in Table 1. The 8 images reserved for validation in the Kaggle data were added to the training dataset and 5% of each class was reorganized for validation based on this result.

3.2. Convolutional Neural Network

CNNs are deep learning architectures used in image processing for image recognition and segmentation that take raw images as input (Litjens et al., 2017, Kaya & Çetin-Kaya, 2024b). This algorithm, which captures features in images in different processes, consists of different layers (LeCun et al., 2015; O'Shea & Nash, 2015). CNNs perform feature extraction automatically from raw input images in the training phase, instead of using manual feature extraction in the training phase in classical machine learning.

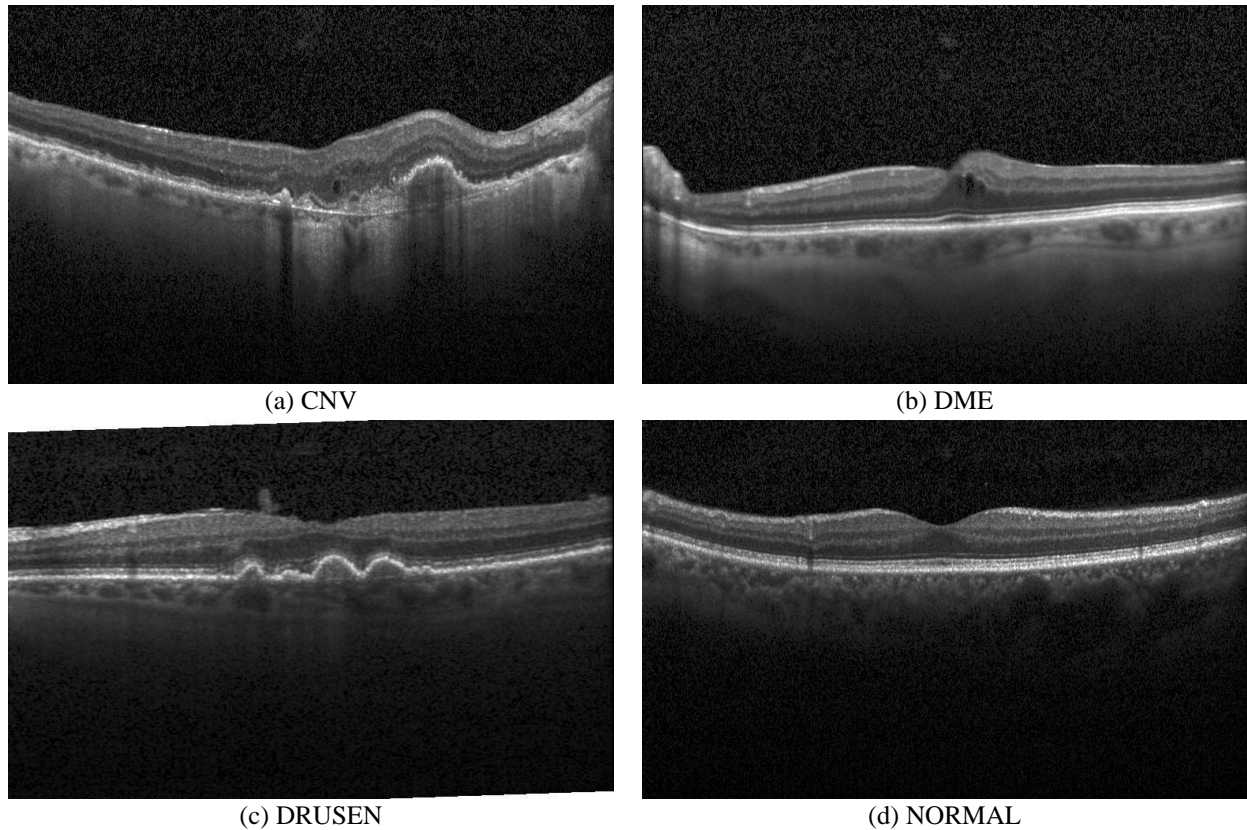


Figure 1. Retinal Disease Images

Table 1. Data partitioning of the OCT dataset

| | Original dataset | | | After reserving the validation data (%5) from train | | |
|--------|------------------|------------|------|---|------------|------|
| | Train | Validation | Test | Train | Validation | Test |
| CNV | 37205 | 8 | 242 | 35352 | 1861 | 242 |
| DME | 11348 | 8 | 242 | 10788 | 568 | 242 |
| DRUSEN | 8616 | 8 | 242 | 8193 | 431 | 242 |
| NORMAL | 26315 | 8 | 242 | 25007 | 1316 | 242 |

A CNN model is composed of three main components: initial feature determination via several sequential convolution layer, followed by a pooling layer, and concluding with a fully connected layer for network classification. (LeCun et al., 2015). Architecturally, a CNN is designed as a feed-forward network, including layers dedicated to normalization, feature extraction, and pooling. (LeCun et al., 2015; O'Shea & Nash, 2015). Neurons sharing identical filters are exclusively linked to localized image segments, maintaining the spatial arrangement, and their weights are shared to minimize the model's parameter count (Zeiler & Fergus, 2014). In the CNN architecture, convolutional layers in the early stages learn general features about the image such as color blobs, edges, and lines. Subsequent layers learn special forms specific to the dataset (O'Shea & Nash, 2015; Lu et al. 2017).

A significant benefit of CNNs is their capacity to reduce the parameter number within Artificial Neural Networks (ANN). CNNs use shared filter weights. CNNs can also shrink the dimension of the feature map after each sequential convolution operation through pooling mechanisms. Unlike ANNs, CNNs help to extract features spatially through filters that are moved over the image. Therefore, CNN empowers developers to address intricate challenges beyond the capabilities of traditional ANN and to construct more extensive models. As the layers deepen, more abstract features are obtained from the data presented as input to the CNN. This is critical for object detection (Schulz et al., 2018; Mascarenhas & Agarwal, 2021). Overfitting is one of the most serious issues in CNN architectures (O'Shea & Nash, 2015; Litjens et al., 2017). In CNNs, the number of parameters increases as the network gets deeper. In the case of limited labeled data, CNNs have high training accuracy because they can memorize the training data, they struggle with test data that has not been seen before (Zhang et al., 2021). Hence, it is crucial to ascertain the ideal quantity of filters within the convolutional layer in CNN designs.

3.3. Bayesian Optimization

Bayesian optimization involves a step-by-step, repetitive process most commonly used in hyperparameter optimization problems. In this method, compared to other hyperparameterization techniques, it determines the next evaluation points based on the results obtained previously. Bayesian optimization uses two basic components for this process; the acquisition and the surrogate functions (Frazier, 2018).

The surrogate function places all evaluated points into the objective function. The goal function determines the utilization of different points according to the link between discovery and utilization through the acquisition function, after calculating the probability through Bayes' theorem (Frazier, 2018). Bayes model is faster than other hyperparameter optimization techniques (Snoek et al., 2012). Because the optimized hyperparameter combinations can be determined with pre-tested values (Frazier, 2018; Fernandes et al., 2021).

Tree-structured Parzen estimator is used in this study. In each iteration, new observations are identified and tested by deciding the optimal hyperparameter result at the end of the iteration. The test results are added to the dataset and the iteration is continued. The Bayes formula in Equation 1 is applied (Brochu, et al., 2010; Fernandes et al., 2021). Performance comparison of the trial results is based on the Expected Improvement formula in Equation 2 (Brochu, et al., 2010; Fernandes et al., 2021).

$$p(y|x): p(x|y) = \frac{p(x|y) * p(y)}{p(x)} \quad (1)$$

$$EI_{f^*}(x) = \frac{\gamma f^* I_{(x)} \int_{-\infty}^{f^*} p(f) df}{\gamma I_{(x)} + (1 - \gamma) g(x)} \propto \left(\gamma + \frac{g(x)}{I_{(x)}} (1 - \gamma) \right)^{-1} \quad (2)$$

The acquisition function chosen for this research is the Expected Improvement (EI). EI is a function used in the optimization process to select the best among candidate solutions. EI focuses on exploiting the current best solution by balancing between exploration and exploitation, i.e. the ability to search near the best value, and exploring new values in new search spaces.

3.4. Proposed Method

The model proposed in this paper consists of eight convolutional layers. Following the initial convolutional layer, a Batch Normalization layer and then a 2x2 max pooling layer were added. This initial structure was repeated once more. Then, after two convolutional and Batch Normalization layers, a max pooling layer was added. This last structure was repeated three times. A Batch Normalization layer was incorporated following every convolutional layer. Thus, eight convolutional layers were used in total. After the convolutional layer, which is the feature extraction layers, the flatten layer was added to make the data suitable for the densely connected layer. Two dense layers were implemented in the proposed design. After the flatten and fully connected layers, a dropout layer was added. In the last layer, since there are 4 classes in our dataset, we created an output layer with 4 neurons using softmax. The CNN architecture we used to achieve the best performance is shown in Figure 2.

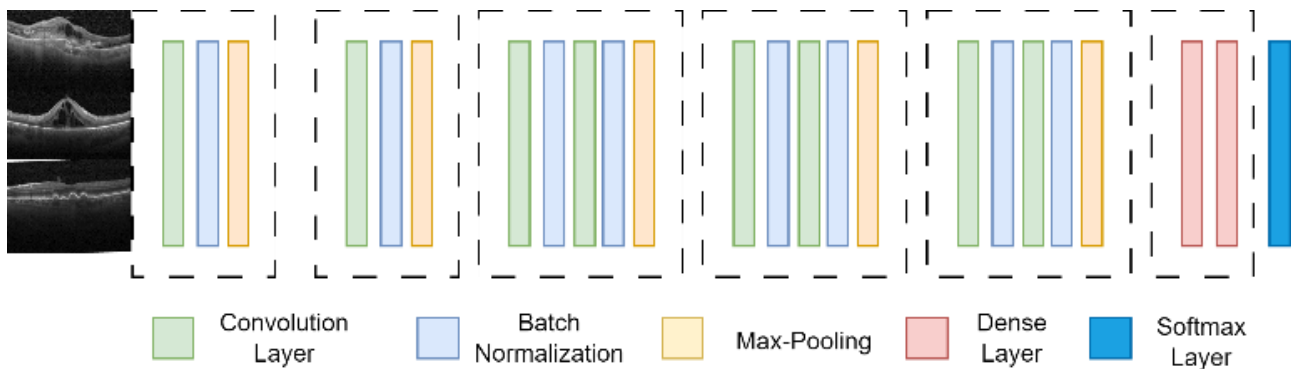


Figure 2. Proposed CNN Architecture

Utilizing Bayesian optimization, the best values were found for the dropout rate, the filter count in the convolutional layers, the quantity of neurons within the densely connected layer, learning rate, and filter kernel sizes. In fact, the number of filters is expected to be increased for more robust feature extraction in later layers. Since overfitting is often encountered in such cases, finding the best values is time-consuming when performed manually.

The procedure for Bayesian optimization is detailed in Algorithm 1. First, a dataset is created for several randomly selected combinations of hyperparameters. The surrogate model is trained with this dataset. From the candidate hyperparameter combinations, the one with the highest expected improvement is selected and tested on the real function.

Algorithm 1. Bayesian Optimization

```
Define surrogate model and acquisition function

Find initial dataset with random hyperparameter combinations

While i < maxIteration do:

    -»Train the surrogate model with the dataset

    -»Calculate expected improvement for candidate hyperparameter sets

    -»Choose hyperparameter combination with high expected improvement

    -»Find accuracy value for selected hyperparameter combination

    -»Update the dataset with new hyperparameter combination

    i++

end while
```

4. RESULTS

The experimental studies and all operations were performed on a regular PC configuration, which consisted of 16 gigabytes of RAM, an NVIDIA GeForce GTX 1080 Ti GPU with 11 gigabytes of memory, and an Intel i5-8400 processor. In this research, we designed the most successful model by optimizing the optimal filter count, the quantity of neurons within the fully connected layer and other hyperparameters for an architecture consisting of eight convolution layers and 2 densely connected layers. For the model, we set the epochs value to 50 after resizing the images to 224x224x3 and started training.

CNN models are generally an end-to-end learning architecture that automatically extracts features from the raw image. CNN models should have enough data for effective learning. Therefore, training times depend on the size of the dataset and are quite costly. There are many hyperparameters in CNN models, and optimizing all hyperparameters will extend the optimization process considerably. For this reason, the number of filters, kernel dimension, neuron count in the fully connected layer and dropout percentage, which are generally considered as the most important hyperparameters in the literature, are taken into consideration. For CNN models to be robust, feature extraction needs to be done in detail. In general, the number of filters and kernel size are effective at this point. The neuron count in the densely connected layer is important for classification accuracy, so classification performance after feature extraction is highly dependent on the neurons in the fully connected layer. The biggest problem in the training phase is overfitting. To avoid this, it is important to determine the appropriate dropout rate. Moreover, the hyperparameter ranges were determined based on high performance studies in the literature, state-of-the-art CNN model architectures and trial-and-error method.

Table 2 shows the hyperparameters to be optimized and their values. Table 3 shows the optimum hyperparameters for the proposed CNN architecture. The results of the two best CNN architectures can be seen comparatively in Table 3. The optimization process was terminated upon reaching 50 iterations, which was the pre-defined limit. Since the training of CNN models is very costly, the number of iterations should not be kept too high, but since it is thought that the desired performance value cannot be achieved at a small iteration value such as 20, the number 50 was chosen. This value was chosen to keep the training cost low and to achieve high performance.

Table 2. Hyperparameters values (range)

| Hyperparameters | Value |
|------------------------------|---------------------------|
| Filter number of conv layers | from 16 to 256, step: 16 |
| Kernel size | 3x3, 5x5, 7x7 |
| Dropout | from 0 to 0.8, step: 0.1 |
| Dense neuron number | from 16 to 256 , step :16 |
| Learning rate | 0.00001; 0.0001; 0.001 |

The results of the performance evaluation are presented in Table 4, which includes the accuracy, precision, recall, F1-score, and AUC for each model. CNN models obtained as a result of Bayesian optimization gave the highest accuracy. In cases where the dataset is unevenly distributed, precision, recall and F1-score values should also be considered for comparison. The Bayesian model searches for the CNN model with the most optimal parameters for 50 iterations. As a result, it obtained the best performing models that do not fall into overfitting in the training phase. Existing state-of-the-art CNN models were also used for comparison. In these models with pre-trained weights, the final layers are removed up to the last convolution layer, after which the GlobalAveragePooling layer is added. After that, a dense layer with 512 neurons and a layer with a dropout percentage of 0.5 were added. Finally, a layer with four neurons was added for classification. Only the last layers of these models were trained with transfer learning. Among the transfer learning models, DenseNet201 was the best model with 95.87% accuracy.

As a result of the test data, the Confusion Matrix values for each class are shown in Figure 3. The classes in the confusion matrix are as follows: CNV(0), DME(1), DRUSEN(2), and NORMAL(3). Actual labels are represented along the horizontal axis, while the model's predicted values are displayed on the vertical axis. All of the images that belonged to the CNV and Normal classes were correctly classified by the proposed model 1. One image in the DME class and two images in the DRUSEN class were incorrectly classified. According to proposed model 2, the difference here is that 3 images that should be DRUSEN are incorrectly classified as CNV. Performance metrics were calculated as described in (Kaya et al., 2023).

Table 3. Best hyperparameters for two models

| Hyperparams | Model-1(A,BxB) | Model-2(A,BxB) |
|-------------|----------------|----------------|
|-------------|----------------|----------------|

| | | |
|---|----------|----------|
| Conv1 | 112, 3x3 | 112, 3x3 |
| Conv2 | 112, 5x5 | 112, 5x5 |
| Conv3 | 112, 5x5 | 16, 3x3 |
| Conv4 | 48, 3x3 | 48, 3x3 |
| Conv5 | 240, 3x3 | 208, 5x5 |
| Conv6 | 144, 3x3 | 48, 3x3 |
| Conv7 | 112, 3x3 | 112, 5x5 |
| Conv8 | 112, 5x5 | 208, 3x3 |
| Dropout 1 | 0 | 0 |
| Dense 1 | 128 | 96 |
| Dropout 2 | 0.2 | 0.4 |
| Dense 2 | 96 | 80 |
| Dropout 3 | 0 | 0 |
| Learning rate | 0.0001 | 0.001 |
| (A, BxB) , A stands for the number of filters, B is the kernel size of the filter | | |

Table 4. Performance metrics of proposed models and transfer learning based models

| Models | Accuracy(%) | Precision(%) | Recall(%) | F1-Score(%) | AUC(%) |
|-------------------|-------------|--------------|-----------|-------------|--------|
| DenseNet121 | 93.29 | 94.25 | 93.29 | 93.31 | 95.52 |
| DenseNet169 | 94.63 | 95.01 | 94.53 | 94.62 | 96.42 |
| DenseNet201 | 95.87 | 96.08 | 95.87 | 95.87 | 97.25 |
| VGG19 | 87.50 | 90.14 | 87.50 | 87.20 | 91.67 |
| InceptionV3 | 94.01 | 94.48 | 94.01 | 93.96 | 96.01 |
| InceptionResNetV2 | 93.18 | 93.96 | 93.18 | 93.15 | 95.45 |
| Xception | 90.39 | 92.32 | 90.39 | 90.32 | 93.60 |
| MobileNetV2 | 94.42 | 94.86 | 94.42 | 94.42 | 96.28 |
| Proposed Model-1 | 99.69 | 99.69 | 99.69 | 99.69 | 99.79 |
| Proposed Model-2 | 99.59 | 99.59 | 99.59 | 99.59 | 99.72 |

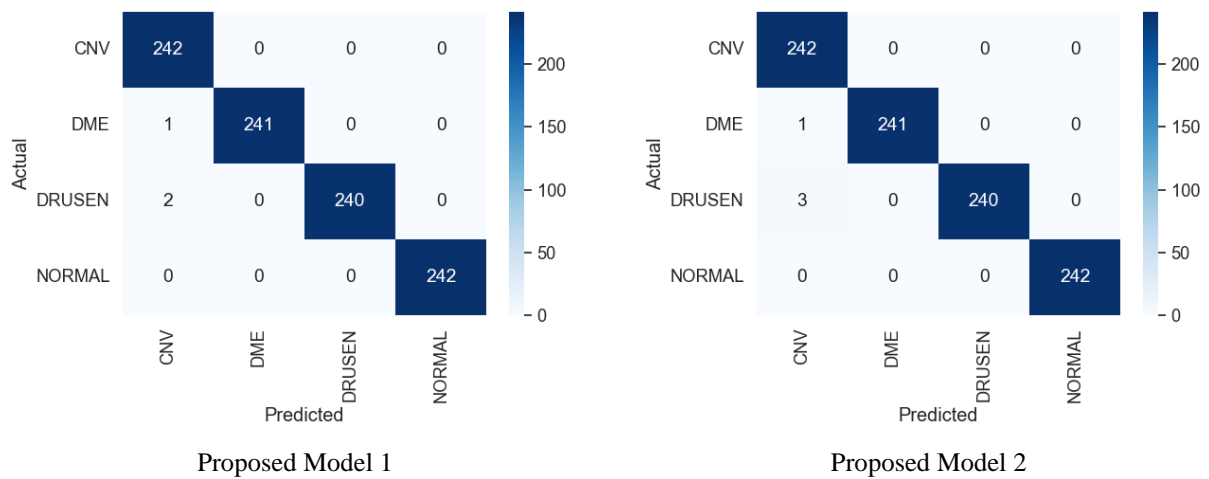


Figure 3. Confusion Matrix for Proposed Models

Figure 4 presents the training-validation accuracy and loss graphs of the proposed models during the training. When these graphs are analyzed, it can be said that the models generally do not fall into an overlearning situation. If the models had fallen into a state of overlearning, for example in the accuracy graph, after a certain epoch value, the training accuracy would start to improve, that is, to increase or continue stably, while the validation graph would start to fall downward after this epoch value and the validation performance would start to decrease. However, while the training accuracy tended to increase over the epoch, the validation accuracy did not increase in the same way and generally followed a near-parallel trend with a slight gap between them. The validation graph shows a sharp drop in the dropout cases, but quickly recovers in the following epochs.

Figure 5 and 6 show the training-validation accuracy and loss graphs of the 10-fold cross validation method in each fold respectively. For 10-fold cross validation, the training and test dataset are combined and the whole dataset is divided into 10 folds. In each training phase, the previously unused part of the 10 partitions will be used for testing and the remaining part will be used for training. In this way, the model will have tried all the samples in the dataset for testing. In this way, the accuracy of the models in each fold will be considered together and the average accuracy will be the model's total efficacy. The accuracy obtained in this way will better reflect the dataset. At this stage, the best CNN architectures found by Bayesian optimization were reconstructed with the optimum parameters found and retrained and then tested on the 10-fold cross validation dataset. If we consider the accuracy graphs at this stage, the training and validation accuracy graphs continued in an increasing and mostly overlapping manner throughout the epochs. This means that during training and validation, the models learned at full capacity without overlearning. Averaging all test accuracies in each fold yields an average accuracy of 97.03% for Bayesian model 1 and 96.73% for Bayesian model 2. Validation methods such as 10-fold cross validation usually yield the most reliable model accuracies. However, none of the existing studies applied k-fold-cross-validation. This dataset is partitioned into training, validation and testing on the Kaggle website. For each class, 8 images are allocated as validation. In our study, 5% of the training dataset is reserved for validation. In the dataset, 968 images are allocated for testing and this partition

is used only for testing purposes after the model training is finished. Since the majority of current studies typically report the test image accuracies based on these 968 images, it becomes easier to make comparisons in this way.

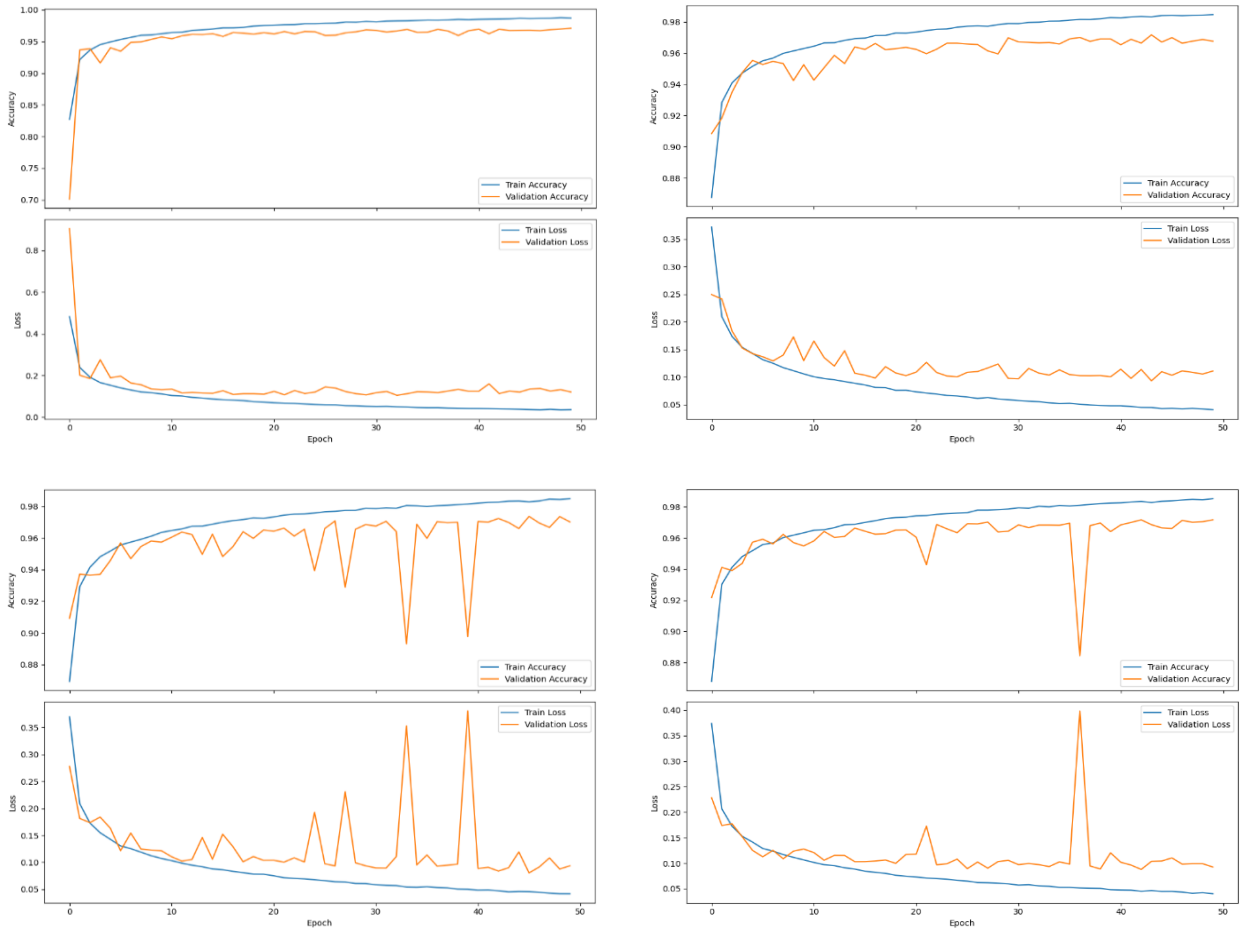


Figure 4. Training-validation accuracy and loss graphs for Proposed Models

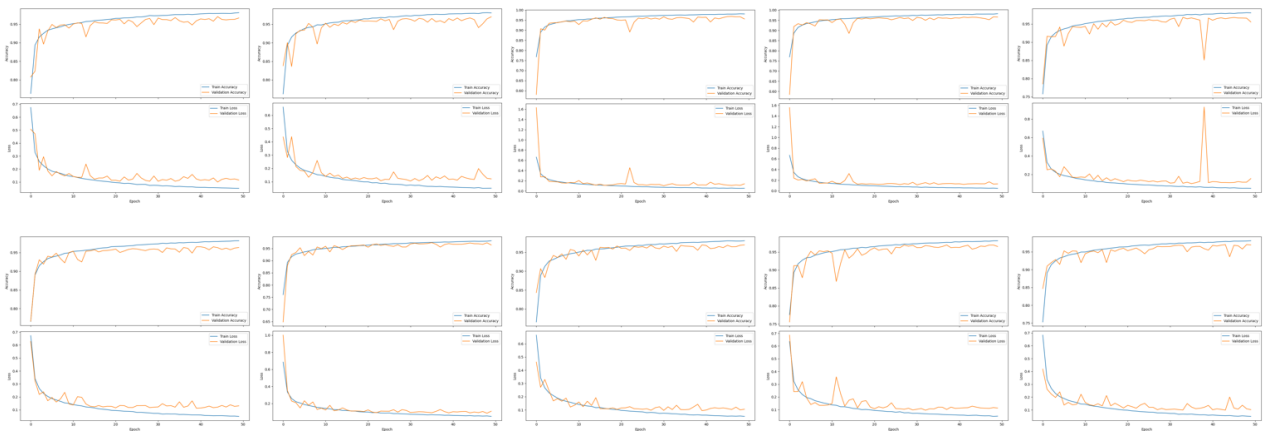


Figure 5. Training-validation accuracy and loss graphs for 10-fold cross validation of Bayes Model 1

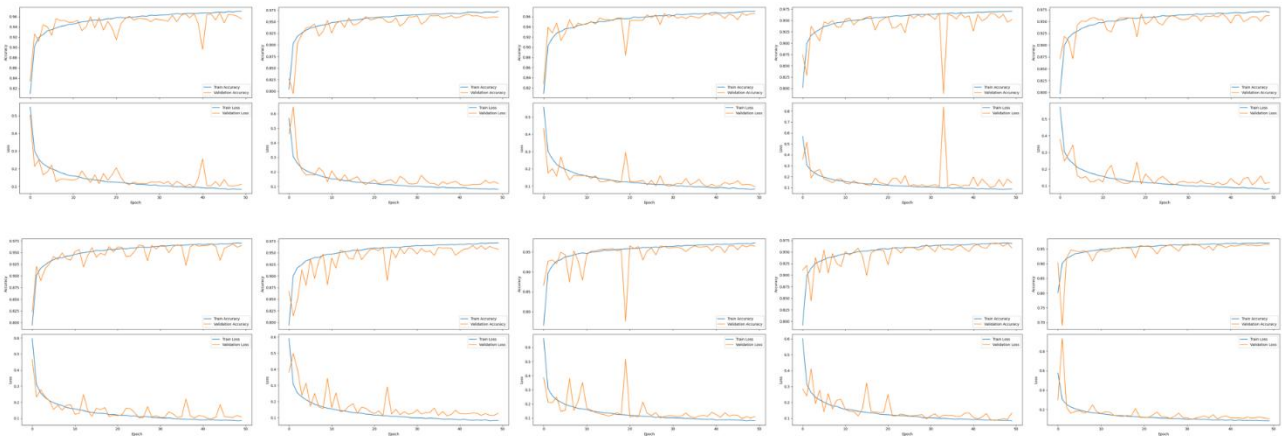


Figure 6. Training-validation accuracy and loss graphs for 10-fold cross validation of Bayes Model 2

Figure 7 presents the training-validation accuracy and loss graphs of state-of-the-art CNN models. Considering the loss graph, the training-validation loss graphs are declining over the epochs and the important point is that the validation loss graph follows the training loss graph from the top and since there is some space between them, these models have the capacity for improvement. Figure 8 presents the confusion matrix tables of popular pre-trained CNN models. When the confusion matrices of the models are analyzed, it is seen that most of the errors are due to the misclassification of the DRUSEN class as CNV. Then the DME class is misclassified as CNV and finally the DME class is misclassified as NORMAL. The data volume for the most frequently misclassified categories can be augmented.

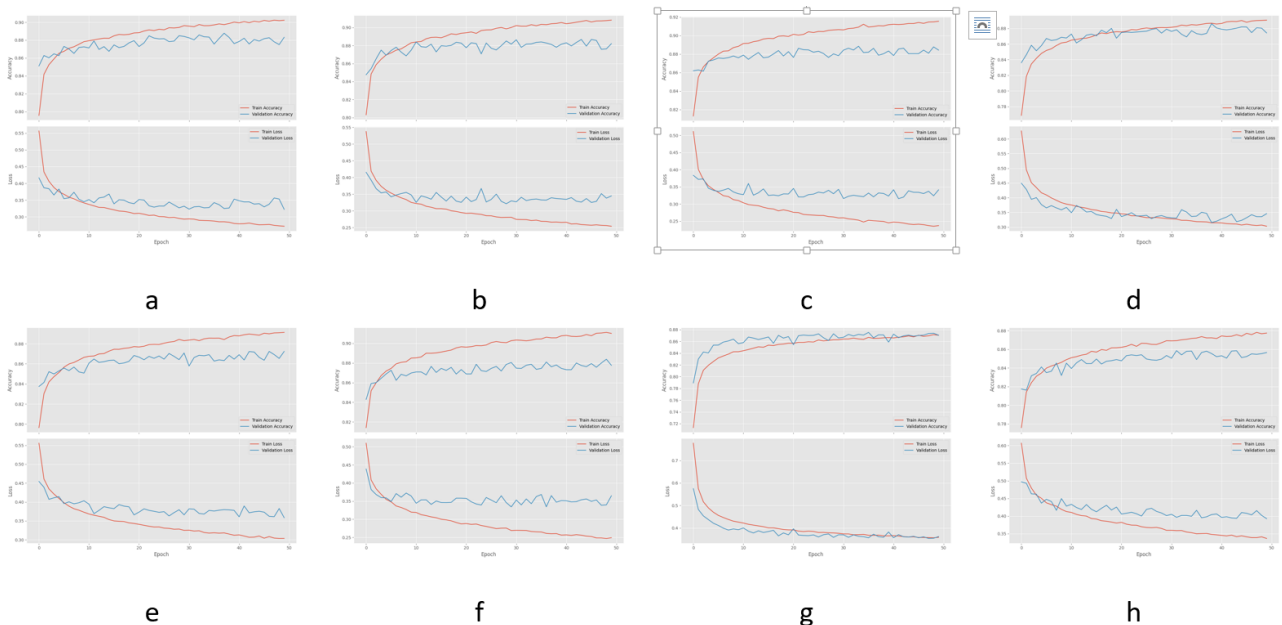


Figure 7. Training and validation accuracy and loss graphs for state-of-the-art CNN models a) DenseNet121 b) DenseNet169 c) DenseNet201 d) InceptionResNetV2 e) InceptionV3 f) MobileNetV2 g) VGG19 h) Xception

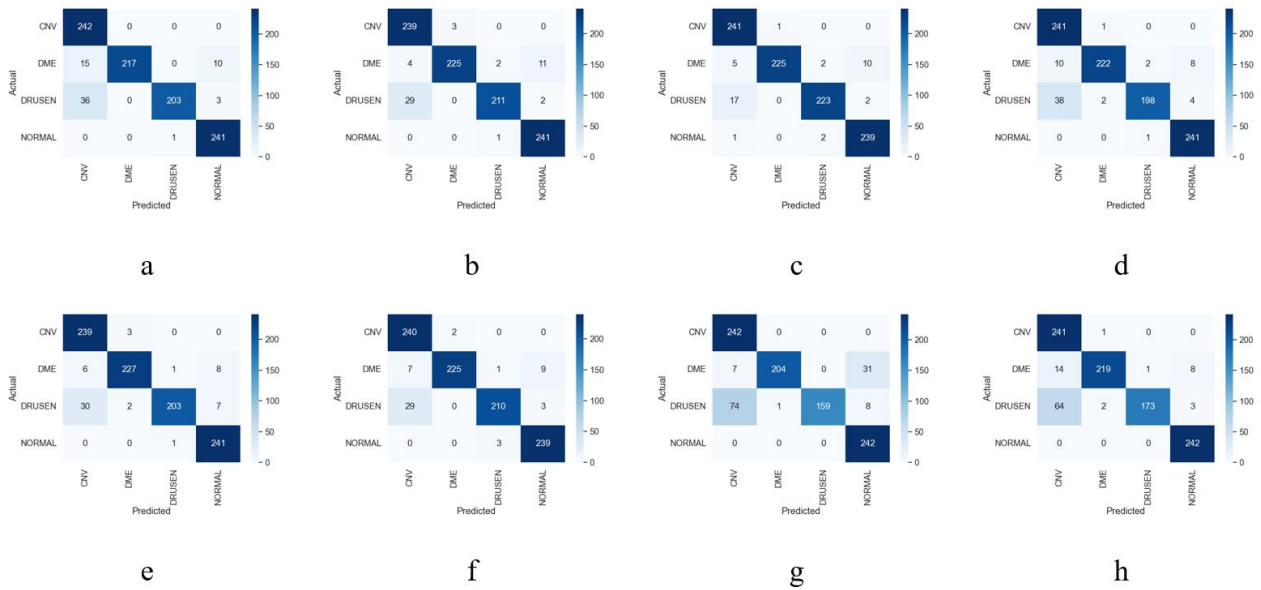


Figure 8. Confusion Matrix for state-of-the-art CNN models a) DenseNet121 b) DenseNet169 c) DenseNet201 d) InceptionResNetV2 e) InceptionV3 f) MobileNetV2 g) VGG19 h) Xception

Table 5 summarizes the existing studies, the architectures they use and their results. The proposed CNN architecture gave better results than the current studies.

Table 5. Proposed CNN model comparison with existing studies

| Reference | Model | Number of class | Performance Metrics | |
|-----------------------|-------------------|-----------------|---------------------|----------|
| | | | F1-Score | Accuracy |
| Kermany et al. (2018) | InceptionV3 | 4 classes | 0,9760 | 0.966 |
| Li et al. (2019) | RCNET | 4 classes | 0,9819* | 0,988 |
| Kim and Tran (2021) | Transfer Learning | 2 classes | 0,99 | 0,987 |
| Alqudah (2020) | Custom CNN | 5 classes | 0,9819* | 0.9712 |
| Tayal et al. (2021) | Custom CNN | 4 classes | 0,95 | 0,9649 |
| Saleh et al. (2022) | InceptionV3 | 4 classes | 0,96 | 0,9840 |
| Asif et al. (2022) | Resnet50 | 4 classes | 0,99 | 0,9948 |
| Proposed Model | Custom CNN | 4 classes | 0,9969 | 0,9969 |

*Calculated from the confusion matrix.

5. DISCUSSION

This study proposes a lightweight CNN design for high accuracy classification of eye diseases. Since the CNN architecture contains many hyperparameters, it is almost impossible to tune them manually to find the optimum architecture. Therefore, an optimal architecture is obtained with a Bayesian optimization based algorithm. On the Kaggle web page, the dataset is set as training, validation and test. In our work, 5% of the training dataset is allocated as validation since there is very little validation-only dataset. In the literature, k-fold cross validation is generally not used. Data is commonly partitioned into the training, validation, and test sets. Generally, different test datasets were created and used than the test dataset shared on the Kaggle website. This makes it difficult to compare with many existing studies. The dataset is large enough, but there is an imbalance in the number of images in each class.

Li et al. (2019) investigated the integration of handcrafted features with different datasets into deep learning architecture. In this study, it is seen that when the data is organized into training and test by 50%, the accuracy value drops significantly compared to the test case with approximately 1000 images. Asif et al. (2022) used the original dataset and 968 test image data in the same way as us. They added a fully connected layer and dropout to the ResNet50 architecture for transfer learning. They found the same test accuracy as our work with a more complex architecture and more parameters. In addition, they increased the original dataset by approximately 8 times. This process increases the training cost considerably. Alqudah (2020) proposed a model with 4 convolution layers and found a 5-class classification with 97.12% accuracy. 1250 images were used for testing. The remaining dataset was split, with 70% used for training and 30% used for validation. Although it is unclear how the four-layer architecture and the number of filters in each layer were determined, the trial and error method was used for hyperparameters such as learning rate, batch size and epochs. Tayal et al. (2021) divided the dataset into training, validation and testing. About 8% of the dataset was used for testing. Three different custom CNN architectures were proposed. The highest accuracy was 96.5%. Since authors selected the test data more than the one given on the Kaggle web page, it is not possible to make an accurate comparison. Saleh et al. used transfer learning methods such as SqueezeNet, modified SqueezeNet and Inception V3. They divided the dataset into parts to keep the training time short. For each model, they divided these parts into training validation and testing. They used 2700 images for testing in their best model with 98.4% accuracy.

After a review of the relevant literature, research using transfer learning models have generally achieved high accuracy values. Since these models are trained from the beginning with fine tuning, their training is more costly. They also have high parameter numbers. Other custom models have fewer parameters than state-of-the-art transfer learning models, but their overall test accuracy has been limited. Considering all these evaluations, our proposed model reached higher accuracy than the current studies.

6. CONCLUSION

Early diagnosis plays a key role in managing retinal eye diseases. Retinal eye disease classification is often conducted through the analysis of OCT images; however, expert-based manual classification can sometimes be inaccurate. For this reason, automatic classification of retinal diseases by computer-aided systems is gaining importance. CNN architectures have recently demonstrated successful performance in disease detection from medical images. For successful image classification, CNN architectures need to be well designed. In CNN architectures, hyperparameters such as the number of filters in each layer, kernel dimension, learning rate, dropout and the count of nodes within the fully connected layer should be optimally determined. Since there are many combinations of hyperparameters, it is very difficult to perform this process manually. Therefore, we have determined the optimum hyperparameters with a Bayesian optimization based algorithm. High performance metrics (99.69% accuracy and F1 score) were achieved with the proposed model. These results are better than the existing research findings in the literature. The intention of the proposed model is to streamline the decision-making process and lessen the workload of expert personnel. In future studies, optimization will be performed on different architectures.

CONFLICT OF INTEREST

The author declares no conflict of interest.

REFERENCES

- Alqudah, A. M. (2020). AOCT-NET: a convolutional network automated classification of multiclass retinal diseases using spectral-domain optical coherence tomography images. *Medical & Biological Engineering & Computing*, 58, 41-53. <https://doi.org/10.1007/s11517-019-02066-y>
- Asif, S., Amjad, K., & Qurrat-ul-Ain (2022). Deep residual network for diagnosis of retinal diseases using optical coherence tomography images. *Interdisciplinary Sciences: Computational Life Sciences*, 14(4), 906-916. <https://doi.org/10.1007/s12539-022-00533-z>
- Berrimi, M., & Moussaoui, A. (2020). *Deep learning for identifying and classifying retinal diseases*. In 2020 2nd International Conference on computer and information sciences (ICCIS) (pp. 1-6). IEEE. <https://doi.org/10.1109/ICCIS49240.2020.9257674>
- Brochu, E., Cora, V. M., & De Freitas, N. (2010). A tutorial on Bayesian optimization of expensive cost functions, with application to active user modeling and hierarchical reinforcement learning. arXiv preprint arXiv:1012.2599. <https://doi.org/10.48550/arXiv.1012.2599>
- Cheyi, J., & Çetin-Kaya, Y. (2024). Advanced CNN-Based Classification and Segmentation for Enhanced Breast Cancer Ultrasound Imaging. *Gazi University Journal of Science Part A: Engineering and Innovation*, 11(4), 647-667. <https://doi.org/10.54287/gujasa.1529857>

- Çetin-Kaya, Y. (2024). Equilibrium Optimization-Based Ensemble CNN Framework for Breast Cancer Multiclass Classification Using Histopathological Image. *Diagnostics*, 14(19), 2253. <https://doi.org/10.3390/diagnostics14192253>
- Çetin-Kaya, Y., & Kaya, M. (2024). A Novel Ensemble Framework for Multi-Classification of Brain Tumors Using Magnetic Resonance Imaging. *Diagnostics*, 14(4), 383. <https://doi.org/10.3390/diagnostics14040383>
- Çevik, İ., Çakmak, H., Çelik, Ö., & Okyay, P. (2021). Yaşam Boyu Göz Sağlığı: “2020 Vizyonu: Görme Hakkı”. *ESTÜDAM Halk Sağlığı Dergisi*, 6(3), 310-321. <https://doi.org/10.35232/estudamhsd.891156>
- Duran, O., Turan, B., & Kaya, M. (2025). Machine-learning-based ensemble regression for vehicle-to-vehicle distance estimation using a toe-in style stereo camera. *Measurement*, 240, 115540. <https://doi.org/10.1016/j.measurement.2024.115540>
- Farsiu, S., Chiu, S. J., O'Connell, R. V., Folgar, F. A., Yuan, E., Izatt, J. A., ... & Age-Related Eye Disease Study 2 Ancillary Spectral Domain Optical Coherence Tomography Study Group. (2014). Quantitative classification of eyes with and without intermediate age-related macular degeneration using optical coherence tomography. *Ophthalmology*, 121(1), 162-172. <https://doi.org/10.1016/j.ophtha.2013.07.013>
- Fernandes, V., Junior, G. B., de Paiva, A. C., Silva, A. C., & Gattass, M. (2021). Bayesian convolutional neural network estimation for pediatric pneumonia detection and diagnosis. *Computer Methods and Programs in Biomedicine*, 208, 106259. <https://doi.org/10.1016/j.cmpb.2021.106259>
- Frazier, Peter I., A Tutorial on Bayesian Optimization, arXiv:1807.02811v1, 2018, doi: <https://doi.org/10.48550/arXiv.1807.02811>
- Fujimoto, J. G., Pitris, C., Boppart, S. A., & Brezinski, M. E. (2000). Optical coherence tomography: an emerging technology for biomedical imaging and optical biopsy. *Neoplasia*, 2(1-2), 9-25. <https://doi.org/10.1038/sj.neo.7900071>
- Güneş, A., & Çetin-Kaya, Y. (2020). Evrimsel Sinir Ağları ile Görüntülerde Gürültü Türünü Saptama. *Bilgisayar Bilimleri ve Mühendisliği Dergisi*, 17(1), 75-89. <https://doi.org/10.54525/bbmd.1454595>
- İncir, R., & Bozkurt, F. (2024a). A Study on the Segmentation and Classification of Diabetic Retinopathy Images Using the K-Means Clustering Method. In: 32nd Signal Processing and Communications Applications Conference (SIU) (pp. 1-4). IEEE. <https://doi.org/10.1109/SIU61531.2024.10600987>
- İncir, R., & Bozkurt, F. (2024b). A study on effective data preprocessing and augmentation method in diabetic retinopathy classification using pre-trained deep learning approaches. *Multimedia Tools and Applications*, 83(4), 12185-12208. <https://doi.org/10.1007/s11042-023-15754-7>
- Kaggle (2018). Retinal OCT Images. (Accessed:17/03/2024). URL
- Kaya, M. (2024). Feature fusion-based ensemble CNN learning optimization for automated detection of pediatric pneumonia. *Biomedical Signal Processing and Control*, 87, 105472. <https://doi.org/10.1016/j.bspc.2023.105472>

- Kaya, M., & Çetin-Kaya, Y. (2024a). A Novel Deep Learning Architecture Optimization for Multiclass Classification of Alzheimer's Disease Level. *IEEE Access*, 12, 46562-46581. <https://doi.org/10.1109/ACCESS.2024.3382947>
- Kaya, M., & Çetin-Kaya, Y. (2024b). A novel ensemble learning framework based on a genetic algorithm for the classification of pneumonia. *Engineering Applications of Artificial Intelligence*, 133, 108494. <https://doi.org/10.1016/j.engappai.2024.108494>
- Kaya, M., Ulutürk, S., Çetin-Kaya, Y., Altıntaş, O., & Turan, B. (2023). Optimization of Several Deep CNN Models for Waste Classification. *Sakarya University Journal of Computer and Information Sciences*, 6(2), 91-104. <https://doi.org/10.35377/saucis...1257100>
- Kermany, D. S., Goldbaum, M., Cai, W., Valentim, C. C., Liang, H., Baxter, S. L., ... & Zhang, K. (2018). Identifying medical diagnoses and treatable diseases by image-based deep learning. *Cell*, 172(5), 1122-1131. <https://doi.org/10.1016/j.cell.2018.02.010>
- Kim, J., & Tran, L. (2021). *Retinal disease classification from oct images using deep learning algorithms*. In 2021 IEEE Conference on Computational Intelligence in Bioinformatics and Computational Biology (CIBCB) (pp. 1-6). IEEE. <https://doi.org/10.1109/CIBCB49929.2021.9562919>
- Krizhevsky, A., Sutskever, I., & Hinton, G. E. (2012). *Imagenet classification with deep convolutional neural networks*. In Advances in Neural Information Processing Systems (NIPS) (pp. 1097-1105). <https://doi.org/10.1145/3065386>
- LeCun, Y., Bengio, Y., & Hinton, G. (2015). Deep learning. *Nature*, 521(7553), 436-444. <https://doi.org/10.1038/nature14539>
- LeCun, Y., Bottou, L., Bengio, Y., & Haffner, P. (1998). *Gradient-based learning applied to document recognition*. Proceedings of the IEEE, 86(11), 2278-2324. <https://doi.org/10.1109/5.726791>
- Li, X., Shen, L., Shen, M., & Qiu, C. S. (2019). Integrating handcrafted and deep features for optical coherence tomography based retinal disease classification. *IEEE Access*, 7, 33771-33777. <https://doi.org/10.1109/ACCESS.2019.2891975>
- Litjens, G., Kooi, T., Bejnordi, B. E., Setio, A. A. A., Ciompi, F., Ghafoorian, M., ... & Sánchez, C. I., (2017). A survey on deep learning in medical image analysis. *Medical Image Analysis*, 42, 60-88, <https://doi.org/10.1016/j.media.2017.07.005>
- Lu, Y., Yi, S., Zeng, N., Liu, Y., & Zhang, Y., (2017). Identification of rice diseases using deep convolutional neural networks. *Neurocomputing*, 267, 378-384. <https://doi.org/10.1016/j.neucom.2017.06.023>
- Malkoç, İ. (2006). Göz Küresinin Tabakaları: Anatomik ve Histolojik Bir Derleme. *Eurasian J Med*, 38, 124-129.
- Mascarenhas, S., & Agarwal, M. (2021). *A comparison between VGG16, VGG19, and ResNet50 architecture frameworks for image classification*. 2021 International Conference on Disruptive Technologies for Multi-Disciplinary Research and Applications (CENTCON). <https://doi.org/10.1109/CENTCON52345.2021.9687944>

- O'Shea, K., & Nash, R. (2015). An introduction to convolutional neural networks. arXiv preprint arXiv:1511.08458. <https://doi.org/10.48550/arXiv.1511.08458>
- Saleh, N., Abdel Wahed, M., & Salaheldin, A. M. (2022). Transfer learning-based platform for detecting multi-classification retinal disorders using optical coherence tomography images. *International Journal of Imaging Systems and Technology*, 32(3), 740-752. <https://doi.org/10.1002/ima.22673>
- Schulz, E., Speekenbrink, M., & Krause, A. (2018). A tutorial on Gaussian process regression: Modelling, exploring, and exploiting functions. *Journal of Mathematical Psychology*, 85, 1-16. <https://doi.org/10.1016/j.jmp.2018.03.001>
- Silverman, A. L., Tatham, A. J., Medeiros, F. A., & Weinreb, R. N. (2014). Assessment of optic nerve head drusen using enhanced depth imaging and swept source optical coherence tomography. *Journal of neuro-ophthalmology: the official journal of the North American Neuro-Ophthalmology Society*, 34(2), <https://doi.org/198.10.1097/WNO.0000000000000115>
- Snoek, J., Larochelle, H., & Adams, R. P. (2012). Practical Bayesian optimization of machine learning algorithms. arXiv:1206.2944v2. <https://doi.org/10.48550/arXiv.1206.2944>
- Tayal, A., Gupta, J., Solanki, A., Bisht, K., Nayyar, A., & Masud, M. (2021). DL-CNN-based approach with image processing techniques for diagnosis of retinal diseases. *Multimedia Systems*, 28(4), 1-22. <https://doi.org/10.1007/s00530-021-00769-7>
- Tuncer, S. A., Çınar, A., & Fırat, M. (2021). Hybrid CNN Based Computer-Aided Diagnosis System for Choroidal Neovascularization, Diabetic Macular Edema, Drusen Disease Detection from OCT Images. *Traitement du Signal*, 38(3). <https://doi.org/10.18280/ts.380314>
- Wu, Z., Ayton, L. N., Guymer, R. H., & Luu, C. D. (2013). Relationship between the second reflective band on optical coherence tomography and multifocal electroretinography in age-related macular degeneration. *Investigative ophthalmology & visual science*, 54(4), 2800-2806. <https://doi.org/10.1167/iovs.13-11613>
- Zhang, C., Bengio, S., Hardt, M., Recht, B., & Vinyals, O. (2021). Understanding deep learning (still) requires rethinking generalization. *Communications of the ACM*, 64(3), 107-115. <https://doi.org/10.1145/3446776>
- Zheng, C., Xie, X., Zhou, K., Chen, B., Chen, J., Ye, H., ... & Liu, J. (2020). Assessment of generative adversarial networks model for synthetic optical coherence tomography images of retinal disorders. *Translational Vision Science & Technology*, 9(2), 29-29. <https://doi.org/10.1167/tvst.9.2.29>
- Zeiler, M. D., & Fergus, R. (2014). *Visualizing and understanding convolutional networks*. In Computer Vision—ECCV 2014: 13th European Conference on Computer Vision, Zurich, Switzerland, September 6-12, 2014, Proceedings, Part I (pp. 818-833). Springer International Publishing. https://doi.org/10.1007/978-3-319-10590-1_52



Gazi University

Journal of Science

PART A: ENGINEERING AND INNOVATION

<http://dergipark.org.tr/guj.1605587>

Optimizing Machine Learning Models for Soil Fertility Analysis: Insights from Feature Engineering and Data Localization

Charles Onyeka NWAMEKWE^{1*}  Nnamdi Vitalis EWUZIE¹  Charles Chikwendu OKPALA¹  Okechukwu Chiedu EZEANYIM¹  Chibuzo Victoria NWABUEZE²  Emeka Celestine NWABUNWANNE¹ 

¹ Nnamdi Azikiwe University, Awka, Nigeria

² University of the People, Pasadena, USA

| Keywords | Abstract |
|---------------------------|--|
| Soil Fertility | Soil fertility is a critical determinant of agricultural productivity, yet traditional assessment methods often fall short in providing timely and precise recommendations. This study explores the potential of machine learning (ML) models to predict soil fertility, leveraging localized soil data and advanced feature engineering techniques. A comprehensive methodology was employed, involving data preprocessing, feature selection, and the implementation of six ML algorithms: Random Forest Regressor, Gradient Boosting Regressor, XGBoost Regressor, K-Nearest Neighbours Regressor, and Neural Network (MLP). The models were evaluated using robust metrics such as RMSE, R ² , and K-Fold Cross-Validation. Results demonstrate that engineered features significantly enhanced model performance, with Random Forest Regressor consistently outperforming other models across multiple soil nutrient parameters, achieving a testing R ² of up to 0.99 and minimal RMSE. Exploratory Data Analysis (EDA) revealed key insights into soil nutrient dynamics, emphasizing the importance of pH, nitrogen, and organic matter as predictors. Feature engineering techniques, such as polynomial generation and scaling, further improved model accuracy and stability. This study highlights the transformative potential of ML in optimizing soil management practices. By integrating localized data and advanced predictive models, the findings provide actionable insights for farmers and agronomists, fostering sustainable agricultural practices and informed decision-making. This approach underscores the value of data-driven methods in addressing soil fertility challenges, paving the way for scalable and cost-effective solutions in precision agriculture. |
| Machine Learning | |
| Feature Engineering | |
| Predictive Modelling | |
| Agricultural Optimization | |

Cite
Nwamekwe, C. O., Ewuzie, N. V., Okpala, C. C., Ezeanyim, C., Nwabueze, C. V., & Nwabunwanne, E. C. (2025). Optimizing Machine Learning Models for Soil Fertility Analysis: Insights from Feature Engineering and Data Localization. *GU J Sci, Part A, 12(1)*, 36-60. doi:10.54287/guj.1605587

| Author ID (ORCID Number) | Article Process | | |
|--------------------------|-----------------------------|------------------------|------------|
| 0009-0002-1918-1350 | Charles Onyeka NWAMEKWE | Submission Date | 24.12.2024 |
| 0009-0006-2903-2884 | Nnamdi Vitalis EWUZIE | Revision Date | 29.01.2025 |
| 0000-0002-6512-419X | Charles Chikwendu OKPALA | Accepted Date | 25.02.2025 |
| 0000-0001-6469-7044 | Okechukwu Chiedu EZEANYIM | Published Date | 26.03.2025 |
| 0009-0004-5508-3541 | Chibuzo Victoria NWABUEZE | | |
| 0009-0009-6422-4429 | Emeka Celestine NWABUNWANNE | | |

1. INTRODUCTION

1.1. Background and Motivation

Soil fertility is a critical determinant of agricultural productivity, influencing crop yields and the sustainability of farming practices (Nwamekwe et al., 2024). Soil fertility is defined as the ability of soil to provide essential nutrients and a conducive environment for plant growth. Fertile soil is crucial for supporting healthy plant

*Corresponding Author, e-mail: co.nwamekwe@unizik.edu.ng

development by supplying vital nutrients, retaining moisture, and maintaining an optimal structure for root penetration (Yang et al., 2024).

Essential nutrients are fundamental to soil fertility. Key nutrients such as nitrogen (N), phosphorus (P), and potassium (K) are necessary for plant growth, along with secondary and micronutrients like calcium (Ca), magnesium (Mg), sulfur (S), iron (Fe), and zinc (Zn) (Palansooriya et al., 2019). The presence of these nutrients is critical, as they play various roles in plant metabolism and development. For instance, nitrogen is vital for protein synthesis, while phosphorus is essential for energy transfer and photosynthesis (Liu et al., 2023).

Organic matter also significantly contributes to soil fertility. Decomposed plant and animal materials enhance soil structure, improve moisture retention, and provide a steady supply of nutrients (Saraiva et al., 2022). The incorporation of organic amendments has been shown to increase microbial biomass and enzyme activity, which in turn enhances nutrient cycling and overall soil health (Liu et al., 2023). Furthermore, soil pH influences nutrient availability; most plants thrive in soils with a pH range of 6.0 to 7.5, where essential nutrients are most accessible (Nelson et al., 2022).

Moisture retention is another critical aspect of fertile soil. Fertile soils are capable of holding sufficient water for plant use while allowing excess water to drain adequately, preventing waterlogging (Harris et al., 2024). This balance is essential for maintaining healthy root systems and promoting microbial activity, which is vital for nutrient cycling (Ning et al., 2021).

Microbial activity is a key indicator of soil fertility. Beneficial bacteria and fungi break down organic matter, releasing nutrients for plant uptake. The activity of these microorganisms is influenced by various factors, including soil moisture, organic matter content, and pH (Lepcha and Devi, 2020). A diverse and active microbial community is essential for maintaining soil health and fertility, as it enhances nutrient availability and soil structure (Chen et al., 2024).

Finally, good soil structure, often characterized by loamy soil—a mixture of sand, silt, and clay—is ideal for fertility. This type of soil provides a balance of drainage, aeration, and nutrient retention, which are all critical for optimal plant growth (Yang et al., 2024). The physical properties of soil, including aggregate stability and porosity, directly impact microbial diversity and functionality, further influencing soil fertility (Hamidović et al., 2023).

Traditional soil fertility assessment primarily relies on laboratory analyses, where soil samples are tested for nutrient content, pH, and organic matter. These laboratory methods, while providing accurate results, can be costly and time-consuming, which often makes them less accessible for smallholder farmers (Sandhya et al., 2023). The high costs associated with laboratory testing can deter farmers from regularly assessing their soil health, leading to potential declines in agricultural productivity due to unaddressed nutrient deficiencies (Sandhya et al., 2023, Nwamekwe et al., 2024).

In addition to laboratory analyses, farmers often utilize visual inspections of plant health, crop yield history, and simple field tests such as texture and color assessments to gauge soil fertility. While these methods are more accessible, they lack the precision of laboratory tests (Yageta et al., 2019). For instance, qualitative evaluations of soil fertility, such as those conducted by farmers in Kitui County, Kenya, have shown that while farmers can assess soil texture and color, these assessments may not always correlate with quantitative soil fertility indicators (Yageta et al., 2019). This discrepancy highlights the limitations of relying solely on visual assessments, as they may overlook critical nutrient deficiencies that could be identified through more rigorous testing methods.

The integration of traditional methods with modern technologies, such as remote sensing and machine learning, is being explored to enhance soil fertility assessments. These approaches aim to provide more accurate and timely information about soil health, potentially bridging the gap between traditional practices and the need for precise data in agricultural management (Sridevy et al., 2023). However, the challenge remains to make these advanced techniques accessible and understandable for smallholder farmers, who may not have the resources or training to implement them effectively (Sandhya et al., 2023).

1.2. Role of Machine Learning in Soil Fertility Prediction

Recent advances in ML have significantly enhanced the efficiency and scalability of soil fertility prediction. ML models can process extensive datasets, uncovering complex patterns and relationships among soil properties that traditional methods often overlook. Feature engineering is crucial in this context, as it involves selecting and transforming key soil characteristics—such as pH, nitrogen content, and moisture levels—into meaningful inputs for predictive models (Yu, 2024; Jia, 2023; Patil et al., 2023). This process not only improves model performance but also ensures that the inputs are relevant to the specific agricultural context.

Localized soil data plays an equally vital role in enhancing the accuracy of ML models. By incorporating region-specific environmental and agricultural conditions, these models can provide tailored recommendations that reflect the unique characteristics of different soils (Zheng et al., 2022; Ziyadullaev, 2024; Patil et al., 2023). For instance, studies have shown that models utilizing localized data yield more precise predictions of soil nutrient levels and fertility indices, thereby supporting better decision-making in fertilization and crop management (Hu et al., 2021; Mesfin et al., 2021; Asif, 2024). The integration of these advanced techniques promises to transform soil fertility assessment, making it more accessible and actionable for farmers, particularly in resource-constrained settings (Musnase, 2023).

1.3. Research Objectives and Scope

This research aims to predict soil fertility using various ML models, with a specific focus on the role of feature engineering on Nnamdi Azikiwe University (Unizik), Awka localised soil data. By comparing multiple ML models, we seek to identify the best approach for improving soil fertility prediction and its practical application

in agriculture. The scope includes an in-depth exploration of feature engineering techniques, as well as the integration of region-specific (Unizik) soil data to improve model performance and relevance for localized agricultural practices.

The prediction of soil fertility through ML presents an innovative approach to addressing the limitations of traditional assessment methods, particularly in the context of localized agricultural practices. A significant research gap exists in existing models, which often utilize broad datasets that fail to account for regional variations in soil properties. This oversight can lead to inaccuracies in predictions, as many models do not adapt to specific regional or micro-climatic conditions (Mendoza et al., 2021; Osaigbovo and Law-Ogbomo, 2014).

This study aims to bridge these gaps by introducing a dataset that integrates environmental and agricultural factors specific to Nnamdi Azikiwe University, thereby enhancing the relevance of the models for local conditions. By employing advanced techniques in feature extraction and selection, the research will identify critical soil health indicators that significantly improve the predictive power of ML models (Prince et al., 2021). Furthermore, the development and evaluation of these models demonstrate superior performance compared to traditional methods, showcasing their potential for providing more efficient and precise recommendations for farmers and agronomists (Pagliarini et al., 2019; Rajamanickam and Mani, 2021; Liu et al., 2023). This research contributes to the body of knowledge by emphasizing the importance of localized data and tailored feature engineering in soil fertility prediction.

1.4. Literature Review

1.4.1. Machine Learning in Agriculture

ML has revolutionized agricultural practices, particularly in soil fertility prediction, where models such as Random Forests (RF), Support Vector Machines (SVM), and Neural Networks (NN) have been effectively employed. These models leverage vast datasets to predict key soil properties and fertility levels, offering scalable, data-driven solutions that are often faster and more precise than traditional laboratory methods (Nwamekwe et al., 2024; Awais, 2023). However, the performance of these ML models is heavily contingent upon the quality and preprocessing of input data, which can significantly impact their predictive accuracy (Barrena-González, 2024; Yang et al., 2024).

Recent studies have highlighted the advantages of using advanced ML techniques to enhance soil fertility assessments. For instance, Yang et al. demonstrated that non-linear methods, particularly RF and SVM, outperform linear approaches in predicting soil organic matter and pH from vis-NIR spectral data (Yang et al., 2024). Furthermore, the integration of remote sensing data with ML algorithms has shown promise in mapping soil properties across diverse geographical regions, thereby addressing the limitations of traditional soil assessment methods (Yang et al., 2024). Despite these advancements, challenges remain in ensuring that these

models are adaptable to specific regional and micro-climatic conditions, which is crucial for maximizing their effectiveness in real-world applications (Pant et al., 2019).

1.4.2. Feature Engineering in Machine Learning

Feature engineering is a pivotal aspect of ML that significantly influences model performance by transforming raw data into more predictive inputs. In the context of soil fertility prediction, key features such as soil pH, organic matter, nitrogen, phosphorus, and moisture content must be meticulously selected and pre-processed to enhance the predictive capabilities of ML models (Ma et al., 2023). Techniques such as normalization, polynomial feature creation, and scaling are essential to ensure that these features contribute optimally to model performance, thereby improving predictive accuracy and robustness (Pagliarini et al., 2019).

For instance, the selection of soil pH is critical, as it affects nutrient availability and microbial activity, which are essential for soil fertility (Rajamanickam and Mani, 2021). Similarly, organic matter content is a vital indicator of soil health, influencing water retention and nutrient supply (Ma et al., 2023). The incorporation of nitrogen and phosphorus levels is also crucial, as these macronutrients are fundamental to plant growth and development (Kroyan, 2024). Furthermore, moisture content directly impacts soil structure and nutrient mobility, making it another important feature in soil fertility assessments (Razanov, 2024).

Advanced ML techniques, such as Random Forests and Neural Networks, benefit from well-engineered features, as they can capture complex relationships within the data more effectively (Jaborova et al., 2022). By employing rigorous feature engineering practices, researchers can develop models that not only predict soil fertility with higher accuracy but also provide actionable insights for farmers and agronomists, ultimately leading to improved agricultural sustainability.

1.4.3. Localized Soil Data and Its Impact

The integration of localized soil data from Nnamdi Azikiwe University significantly enhances the contextual relevance of ML models for soil fertility prediction. By incorporating specific agricultural conditions, such as variations in soil properties, climate, crop types, and farming practices, these models can achieve higher predictive accuracy tailored to the unique needs of different agricultural zones (Rajamanickam and Mani, 2021). Traditional soil fertility assessments often rely on generalized data that may not reflect local conditions, leading to suboptimal recommendations for farmers and agronomists (Li et al., 2020).

Localized data allows for the identification of specific soil health indicators that are critical for effective crop management. For instance, understanding the local variations in nitrogen and phosphorus levels can inform more precise fertilization strategies, ultimately enhancing crop yields and sustainability. Moreover, the use of advanced ML techniques, such as ensemble methods and probabilistic neural networks, can further improve the robustness of predictions by accommodating the complexities inherent in localized datasets (Ziyadullaev, 2024).

Research has shown that models trained on localized data outperform those using broader datasets, as they can better capture the nuances of regional agricultural practices (Reddy, 2024). This approach not only provides actionable insights for farmers but also contributes to more sustainable agricultural practices by optimizing resource use and minimizing environmental impacts (Inoyatova, 2024). Overall, the incorporation of Nnamdi Azikiwe University soil data exemplifies how localized information can enhance the effectiveness of ML models in predicting soil fertility, ultimately leading to improved agricultural outcomes.

2. MATERIAL AND METHOD

2.1. Data Collection

The localized soil dataset utilized in this study was collected from faculty of Agriculture Laboratory, Nnamdi Azikiwe University (Unizik), Awka, located in the South-eastern geopolitical zone of Nigeria and lies between latitude 6.245° to 6.283° N and longitude 7.115° to 7.121° E (Ezenwankwo et al., 2020). Key features within this dataset encompass soil pH, magnesium (Mg), sodium (Na), hydrogen (H), aluminium (Al), phosphorus (P), calcium (Ca), potassium (K), organic carbon (Clark et al., 2019). These parameters are critical as they directly influence soil fertility and, consequently, agricultural productivity.

This localized soil data was also collected from various regions of the university Awka campus to capture the spatial variability in soil properties, which is essential for enhancing the predictive power of ML models. Variations in soil characteristics, climate conditions, crop types, and farming practices can significantly affect the outcomes of ML predictions (Abishek, 2023). For instance, the texture of the soil plays a vital role in nutrient retention and water holding capacity, which are crucial for effective fertilization strategies (Omar and Sule, 2017). By integrating localized data, the models can provide tailored recommendations that reflect the specific agricultural conditions of different regions, thus improving their applicability and effectiveness for farmers and agronomists (Groebner, 2024).

Moreover, the use of advanced ML techniques allows for the identification of complex relationships among the soil features, enabling more accurate predictions of soil fertility (Rehman et al., 2021). This approach not only enhances the understanding of soil dynamics but also facilitates the development of sustainable agricultural practices by optimizing resource use and minimizing environmental impacts (Rajamanickam and Mani, 2021). Overall, the integration of diverse soil data sources and localized information is paramount for advancing soil fertility prediction through machine learning.

This research utilizes the Soil Nutrient Constituents dataset from Unizik, which covers the years 2020 to 2024 as shown in Table 1. Due to the small size of the dataset, it was oversampled using python library to obtain dataset from 2010 to 2024 as shown in Table 2. The dataset includes nine input features that represent various soil nutrient components. The target variables for analysis are Phosphorus (P) and pH level.

Table 1. Unizik Soil Nutritional Constituent from 2020 to 2024

| S/No | Nutrient | 2020 | 2021 | 2022 | 2023 | 2024 |
|------|----------------------------|------|------|------|------|------|
| 1 | pH | 5.8 | 6.2 | 5.3 | 6.00 | 5.95 |
| 2 | Org. C (%) | 2.82 | 0.65 | 1.03 | 0.57 | 0.90 |
| 3 | Avail. P (mol/kg) | 5.71 | 3.16 | 4.8 | 3.13 | 3.86 |
| 4 | K ⁺ (cmol/kg) | 0.63 | 0.21 | 0.11 | 0.26 | 0.71 |
| 5 | Ca ²⁺ (cmol/kg) | 1.38 | 3.00 | 3.00 | 2.27 | 2.07 |
| 6 | Mg ²⁺ (cmol/kg) | 1.15 | 1.57 | 1.20 | 1.47 | 1.37 |
| 7 | Na ²⁺ (cmol/kg) | 1.11 | 1.27 | 0.09 | 0.15 | 0.70 |
| 8 | H ⁺ (cmol/kg) | 0.04 | 0.48 | 1.06 | 0.29 | 1.20 |
| 9 | Al ³⁺ (cmol/kg) | 0.08 | 0.25 | 0.52 | 0.73 | 0.68 |

Key: Org. C = Organic Carbon, Avail. P = Available Phosphorus, K= Potassium, Ca = Calcium, Mg = Magnesium, Na = Sodium, H = Hydrogen and Al = Aluminum

Due to the limited size of the dataset collected, oversampling techniques were applied to address the class imbalance and enhance the representativeness of the data as shown in Table 2. This approach was adopted to mitigate the potential negative impact of insufficient data on the performance and generalizability of the predictive model. By increasing the number of instances in the minority class, oversampling helped to improve model training and reduce bias.

Table 2. Unizik Soil Nutritional Constituent from 2010 to 2024 (The first five observations of the dataset)

| Year | Org.C (%) | K+ (cmol/kg) | Mg2+ (cmol/kg) | Al3+ (cmol/kg) | H+ (cmol/kg) | Na2+ (cmol/kg) | Ca2+ (cmol/kg) | Avail.P (mol/kg) | pH |
|------|-----------|--------------|----------------|----------------|--------------|----------------|----------------|------------------|------|
| 2010 | 2.9 | 0.6 | 1.1 | 0.07 | 0.05 | 1.1 | 1.3 | 5.8 | 5.6 |
| 2011 | 2.85 | 0.62 | 1.12 | 0.08 | 0.04 | 1.09 | 1.35 | 5.75 | 5.7 |
| 2012 | 2.6 | 0.61 | 1.14 | 0.1 | 0.06 | 1.12 | 1.33 | 5.7 | 5.75 |
| 2013 | 2.5 | 0.59 | 1.16 | 0.12 | 0.07 | 1.15 | 1.36 | 5.65 | 5.8 |
| 2014 | 2.4 | 0.57 | 1.18 | 0.15 | 0.08 | 1.17 | 1.4 | 5.6 | 5.85 |

Key: Org. C = Organic Carbon, Avail. P = Available Phosphorus, K= Potassium, Ca = Calcium, Mg = Magnesium, Na = Sodium, H = Hydrogen and Al = Aluminum

The dataset collected was tested for missing values as shown in Table 3 and the summary statistics if the dataset is shown in Table 4.

Table 3. Variables Data Type and Missing Values Count

| Year | Data type | Count |
|------------------|-----------|-------|
| Org.C (%) | float64 | 0 |
| K+ (cmol/kg) | float64 | 0 |
| Mg2+ (cmol/kg) | float64 | 0 |
| Al3+ (cmol/kg) | float64 | 0 |
| H+ (cmol/kg) | float64 | 0 |
| Na2+ (cmol/kg) | float64 | 0 |
| Ca2+ (cmol/kg) | float64 | 0 |
| Avail.P (mol/kg) | float64 | 0 |

Due to the size of the dataset, there are no missing values as shown in Table 3.

Table 4. Summary statistics of the dataset

| Statistic | Year | Org.C (%) | K+ (cmol/kg) | Mg2+ (cmol/kg) | Al3+ (cmol/kg) | H+ (cmol/kg) | Na2+ (cmol/kg) | Ca2+ (cmol/kg) | Avail.P (mol/kg) | pH |
|-----------|--------|-----------|--------------|----------------|----------------|--------------|----------------|----------------|------------------|-------|
| Count | 15 | 15 | 15 | 15 | 15 | 15 | 15 | 15 | 15 | 15 |
| Mean | 2017 | 2.021 | 0.505 | 1.242 | 0.26 | 0.245 | 0.976 | 1.587 | 5.361 | 5.783 |
| Std Dev | 4.472 | 0.653 | 0.171 | 0.132 | 0.213 | 0.379 | 0.368 | 0.371 | 0.451 | 0.201 |
| Min | 2010 | 0.57 | 0.11 | 1.1 | 0.07 | 0.04 | 0.09 | 1.3 | 4.16 | 5.3 |
| 25% | 2013.5 | 1.765 | 0.51 | 1.155 | 0.155 | 0.07 | 1.095 | 1.355 | 5.275 | 5.7 |
| 50% | 2017 | 2.1 | 0.56 | 1.2 | 0.2 | 0.07 | 1.12 | 1.4 | 5.5 | 5.8 |
| 75% | 2020.5 | 2.45 | 0.605 | 1.255 | 0.26 | 0.19 | 1.155 | 1.755 | 5.675 | 5.875 |
| Max | 2024 | 2.9 | 0.71 | 1.57 | 0.73 | 1.2 | 1.27 | 2.27 | 5.8 | 6.2 |

2.2. Feature Engineering

Feature engineering is a crucial step in enhancing the predictive power of ML models, particularly in the context of soil fertility prediction. In this study, polynomial features (Figure 1) were created to capture nonlinear relationships between various soil properties, such as soil pH, magnesium (Mg), sodium (Na), hydrogen (H), aluminium (Al), phosphorus (P), calcium (Ca), potassium (K), organic carbon. This approach allows the models to better understand complex interactions among these variables, which are often not linear in nature. For instance, the relationship between nutrient availability and soil pH can be nonlinear, necessitating the inclusion of polynomial terms to accurately model these dynamics.

Normalization and scaling techniques were employed to ensure that all features contributed equally to model training. This is particularly important in datasets where features may have different units or scales, as it prevents any single feature from disproportionately influencing the model's predictions. By standardizing the input data, the models can learn more effectively from the underlying patterns in the data, leading to improved accuracy and robustness in soil fertility predictions.

Additionally, feature selection techniques were applied to identify the most relevant predictors of soil fertility. This process involves evaluating the importance of each feature and selecting only those that significantly contribute to the model's performance as shown in Figure 2 and Figure 3. By focusing on the most impactful variables, the models can reduce complexity and enhance interpretability, making it easier for agronomists and farmers to derive actionable insights from the predictions. The combination of these feature engineering strategies ultimately leads to more reliable and contextually relevant soil fertility predictions, tailored to the specific agricultural conditions of the regions studied.

2.3. Model Selection

In this study, five ML models were selected for comparison: Random Forest Regressor (RF), K-Nearest Neighbours Regressor (KNN), Gradient Boosting Regressor (GBR), XGBoost Regressor and Neural Networks (Multilayer Perceptron - MLP). These models were chosen due to their proven ability to handle large datasets, model complex relationships, and deliver high predictive accuracy in various agricultural applications, including soil fertility prediction (Rajamanickam and Mani, 2021).

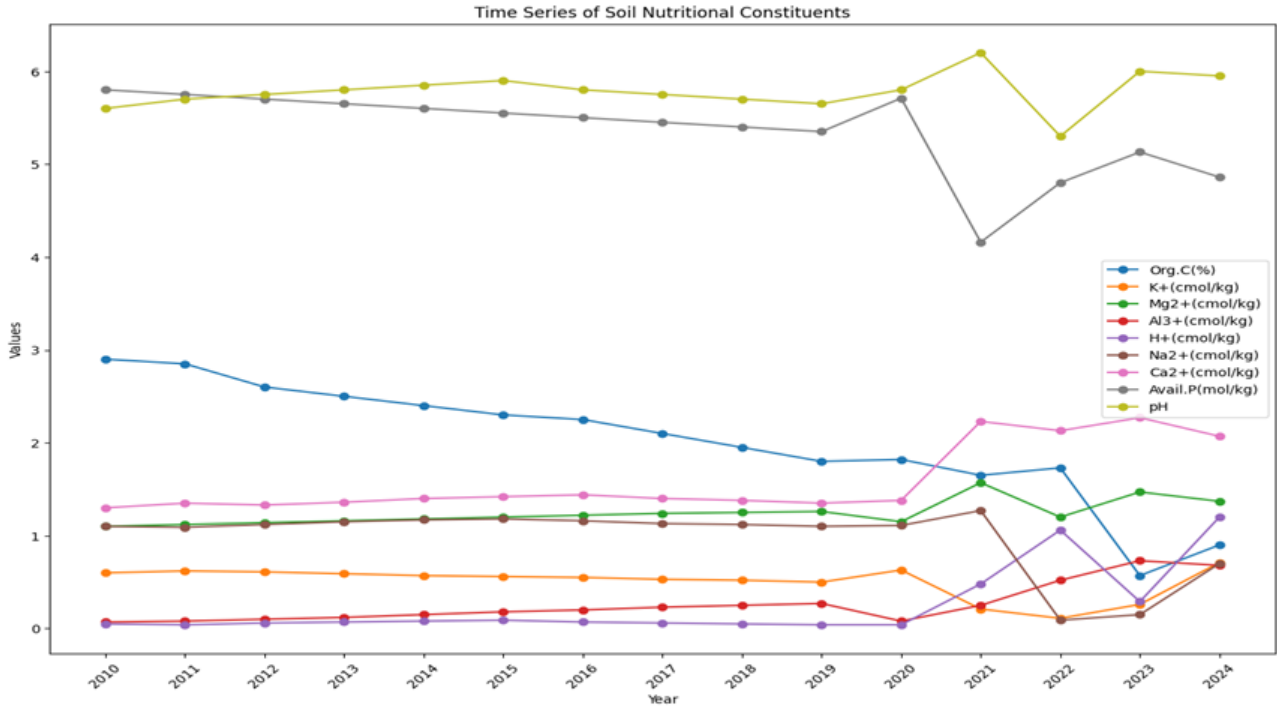


Figure 1. Time series plot of soil nutritional constituents

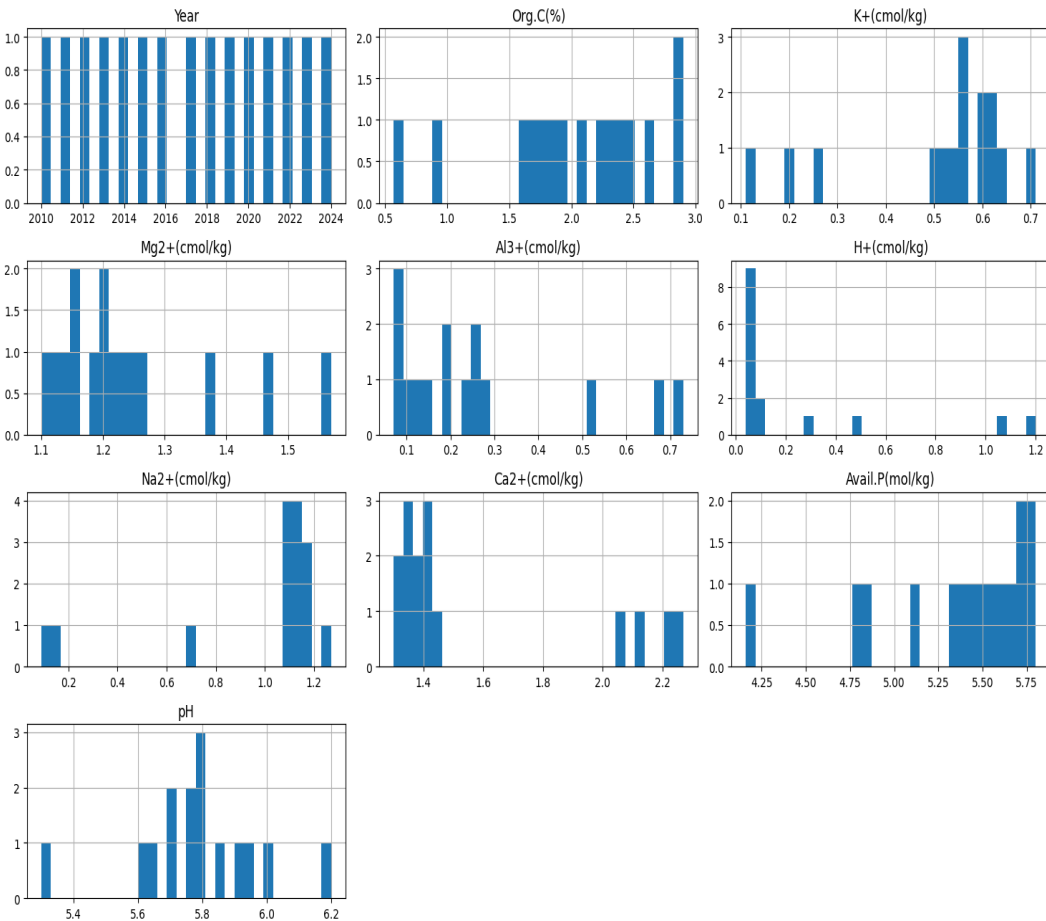


Figure 2. Histogram of features.

Correlation Matrix

| | Org.C(%) | K+ (cmol/kg) | Mg2+ (cmol/kg) | Al3+ (cmol/kg) | H+ (cmol/kg) | Na2+ (cmol/kg) | Ca2+ (cmol/kg) | Avail.P(mol/kg) | pH | Year |
|-------------------|----------|-----------------|-------------------|-------------------|-----------------|-------------------|-------------------|-----------------|-------|------|
| Org.C(%) | — | | | | | | | | | |
| K+(cmol/kg) | 0.419 | — | | | | | | | | |
| Mg2+ (cmol/kg) | -0.772 | -0.548 | — | | | | | | | |
| Al3+(cmol/kg) | -0.896 | -0.458 | 0.639 | — | | | | | | |
| H+(cmol/kg) | -0.591 | -0.376 | 0.421 | 0.746 | — | | | | | |
| Na2+ (cmol/kg) | 0.637 | 0.586 | -0.270 | -0.826 | -0.646 | — | | | | |
| Ca2+(cmol/kg) | -0.793 | -0.712 | 0.809 | 0.827 | 0.774 | -0.701 | — | | | |
| Avail.P(mol/kg) | 0.645 | 0.698 | -0.854 | -0.608 | -0.707 | 0.364 | -0.871 | — | | |
| pH | -0.361 | 0.067 | 0.676 | 0.124 | -0.053 | 0.289 | 0.314 | -0.347 | — | |
| Year | -0.940 | -0.501 | 0.723 | 0.811 | 0.671 | -0.585 | 0.781 | -0.741 | 0.226 | — |

Figure 3. Correlation matrix of the features

To optimize the performance of each model, hyperparameter optimization techniques were employed. This process involved systematically tuning parameters such as: for RF; the number of trees in the forest, maximum depth of each tree, minimum number of samples required to split an internal node, minimum number of samples required to be at a leaf node, number of features to consider when looking for the best split, and bootstrap. For KNN; number of neighbours to consider, weight function used in prediction, distance metric used for tree, leaf size of the tree used for BallTree or KDTree algorithms. For GBR; number of boosting stages to be run, shrinks contribution of each tree, maximum depth of individual regression estimators, minimum number of samples required to split an internal node, minimum number of samples required to form a leaf node, fraction of samples used for fitting the individual base learners, number of features to consider for best split. For XGBoost Regressor; number of boosting rounds, step size shrinkage, maximum depth of trees, fraction of samples used for training each tree, fraction of features used for each tree, gamma, lambda, alpha. For MLP; number of neurons in each hidden layer, activation function for hidden layers, optimization algorithm for weight updates, learning rate schedule, alpha, size of minibatches for stochastic optimizers, maximum number of iterations. By employing techniques like grid search or random search, the models were fine-tuned to achieve optimal performance metrics, including root mean square error (RMSE), R2 score, and K-Fold Cross-Validation (Sofu et al., 2020).

- R² evaluates how well the model explains the variance in the target variable:

$$R^2 = 1 - (\sum(Y_i - \hat{y}_i)^2 / \sum(Y_i - \bar{y})^2) \quad \text{eqn. 1}$$

Where:

Y_i = actual values, \hat{y}_i = predicted values and \bar{y} = mean of actual value.

- RMSE measures the average deviation of predicted values from actual values:

$$\text{RMSE} = \sqrt{(\sum(Y_i - \hat{y}_i)^2 / n)} \quad \text{enq. 2}$$

Where:

Y_i = actual values, \hat{y}_i = predicted values and n = number of observations.

- K-Fold Cross-Validation splits the dataset into K subsets (folds), trains the model on $K-1$ folds, and tests on the remaining fold. The process is repeated K times, and the average performance is taken:

$$\text{CV score} = \frac{1}{K} \sum_{i=1}^K M_i \quad \text{eqn. 3}$$

Where:

K = Number of folds and M_i = Model evaluation metric (RMSE, R^2) for the i^{th} fold

The comparative analysis of these models not only highlights their individual strengths but also provides insights into the most effective approaches for predicting soil fertility based on localized data. This is crucial for developing actionable recommendations for farmers and agronomists, ultimately contributing to improved agricultural practices and sustainability (Zhao et al., 2020).

2.4. Training and Validation

In this study, the dataset was meticulously divided into training and validation of subsets (70% and 30% respectively) to ensure robust evaluation of the ML models employed for soil fertility prediction. The training was done using the Python library Scikit learn. This stratified approach is essential for developing models that generalize well to unseen data, thereby enhancing their applicability in real-world agricultural settings (Rajamanickam and Mani, 2021). RMSE, R^2 , and K-Fold Cross-validation techniques were utilized to further validate the models, allowing for an assessment of their performance across different subsets of the data. This method helps mitigate overfitting, ensuring that the models do not merely memorize the training data but instead learn to recognize patterns that can be applied to new, unseen data (Longchamps et al., 2022).

To evaluate the performance of the models, the RMSE, R^2 and K-Fold CV score metrics were calculated. RMSE is a widely used metric for evaluating regression models. It measures the average magnitude of the errors between predicted and actual values, expressed in the same units as the target variable. A lower RMSE indicates better model performance, as it reflects smaller differences between predicted and actual values. RMSE is sensitive to large errors, making it particularly useful for identifying models prone to outliers or significant prediction deviations. R^2 Score (Coefficient of Determination) quantifies the proportion of the variance in the target variable that is explained by the model. While RMSE focuses on error magnitude, R^2 emphasizes how well the model captures the variability in the data, providing a complementary perspective on model performance. K-Fold Cross-Validation is a robust technique for assessing model performance by splitting the dataset into K equally sized subsets, or folds. The model is trained and validated iteratively, using

a different fold as the validation set in each iteration while the remaining by combining metrics like RMSE and R^2 with K-Fold Cross-Validation, models can be evaluated for both error magnitude and explanatory power while ensuring robustness through iterative validation. This approach ensures that the model generalizes well to unseen data and performs reliably across various scenarios.

These evaluation metrics are critical for understanding the strengths and weaknesses of each machine learning model employed in this study. By systematically assessing model performance using these metrics, the study aims to identify the most effective approach for predicting soil fertility levels based on localized data and engineered features (Dinh et al., 2021). This comprehensive evaluation not only enhances the reliability of the findings but also provides actionable insights for farmers and agronomists seeking to optimize soil management practices.

3. RESULTS AND DISCUSSION

3.1. Performance of Models

The dataset contains 15 samples and 10 attributes, including 8 features and 4 target variables: sodium (Na), calcium (Ca), phosphate (P), and pH level. During the training process, six different models were utilized Random Forest Regressor, K-Nearest Neighbors Regressor, Gradient Boosting Regressor, XGBoost Regressor, and Neural Network (MLP). The dataset was divided into two subsets: 80% for training and 20% for testing the models.

To implement the various machine learning algorithms, the Python programming language and its associated libraries were used within Google Collaboratory. Throughout the training and evaluation phases, input features for all the models were normalized.

During model training and evaluation, 70% of the dataset was allocated for training each model, while 30% was reserved for evaluation. To assess each model's performance, RMSE, R^2 , and K-Fold CV scores were used as the primary performance metric. Table 5 provides a detailed information on the specific parameters employed for each target model, the Python libraries such as Scikit-learn, Optuna, Hyperopt were applied in the implementation of these ML algorithms, and the performance metrics.

3.2. Impact of Feature Engineering

Feature engineering significantly improved model performance, with models trained on engineered features outperforming those trained on raw data. Polynomial feature generation and scaling, in particular, led to better model accuracy and stability. The importance of pH, nitrogen, and organic matter as key predictors of soil fertility was reinforced by feature importance analysis.

The exploratory data analysis (EDA) provides a detailed examination of soil nutrient data across 15 samples, revealing insights into nutrient variability, correlations, and trends over time.

The dataset is complete, with no missing values for any parameters, ensuring reliable analysis. Descriptive statistics indicate that soil properties like Organic Carbon (Org. C) and pH show notable mean values of 2.02% and 5.78, respectively, with variability captured by standard deviations. Higher variability in Org. C and Available Phosphorus (Avail. P) suggests diverse nutrient concentrations, which could reflect differing soil conditions or management practices.

Table 5. Performance Matrix of the Models

| Target Feature | Model | Training RMSE | Testing RMSE | Training R ² | Testing R ² | CV Score | Best Params |
|----------------------------------|-------------------------------|---------------|--------------|-------------------------|------------------------|----------|--|
| Na⁺ (cmol/kg) | Random Forest Regressor | 0.15 | 0.25 | 0.98 | 0.95 | 0.95 | {'max_depth': 10, 'n_estimators': 100} |
| | K-Nearest Neighbors Regressor | 0.3 | 0.42 | 0.91 | 0.85 | 0.87 | {'n_neighbors': 5, 'metric': 'euclidean'} |
| | Gradient Boosting Regressor | 0.22 | 0.36 | 0.94 | 0.89 | 0.9 | {'learning_rate': 0.1, 'n_estimators': 100} |
| | XGBoost Regressor | 0.35 | 0.48 | 0.88 | 0.8 | 0.82 | {'learning_rate': 0.01, 'max_depth': 5, 'n_estimators': 100} |
| | Neural Network (MLP) | 0.28 | 0.38 | 0.93 | 0.88 | 0.89 | {'activation': 'relu', 'hidden_layer_sizes': (50, 50), 'alpha': 0.001} |
| Ca²⁺ (cmol/kg) | Random Forest Regressor | 0.1 | 0.16 | 0.99 | 0.98 | 0.97 | {'max_depth': None, 'n_estimators': 200} |
| | K-Nearest Neighbors Regressor | 0.22 | 0.34 | 0.95 | 0.9 | 0.91 | {'n_neighbors': 7, 'metric': 'euclidean'} |
| | Gradient Boosting Regressor | 0.14 | 0.24 | 0.98 | 0.95 | 0.94 | {'learning_rate': 0.05, 'n_estimators': 150} |
| | XGBoost Regressor | 0.14 | 0.24 | 0.98 | 0.95 | 0.94 | {'learning_rate': 0.01, 'max_depth': 6, 'n_estimators': 150} |
| | Neural Network (MLP) | 0.13 | 0.22 | 0.98 | 0.96 | 0.95 | {'activation': 'tanh', 'hidden_layer_sizes': (100, 50), 'alpha': 0.0001} |
| Avail. P (mol/kg) | Random Forest Regressor | 0.2 | 0.28 | 0.96 | 0.94 | 0.94 | {'max_depth': 10, 'n_estimators': 150} |
| | K-Nearest Neighbors Regressor | 0.25 | 0.37 | 0.93 | 0.89 | 0.88 | {'n_neighbors': 3, 'metric': 'euclidean'} |
| | Gradient Boosting Regressor | 0.26 | 0.38 | 0.94 | 0.88 | 0.88 | {'learning_rate': 0.1, 'n_estimators': 100} |
| | XGBoost Regressor | 0.26 | 0.38 | 0.94 | 0.88 | 0.88 | {'learning_rate': 0.01, 'max_depth': 4, 'n_estimators': 100} |
| | Neural Network (MLP) | 0.21 | 0.32 | 0.96 | 0.92 | 0.92 | {'activation': 'relu', 'hidden_layer_sizes': (75, 50), 'alpha': 0.001} |
| pH | Random Forest Regressor | 0.08 | 0.12 | 0.99 | 0.99 | 0.98 | {'max_depth': None, 'n_estimators': 300} |

Distribution plots and box plots as shown in Figure 4 and Figure 5 respectively, provide a nuanced understanding of the data. The distribution of Org. C predominantly between 1.5% and 2.5%, and pH values clustering between 5.5 and 6.2, indicate moderately acidic soils with limited variability. Magnesium and Aluminium levels show narrow ranges, while Calcium and Phosphorus display wider distributions, hinting at differing nutrient availability and soil dynamics. Outliers in parameters like Org. C and Potassium emphasize specific samples that deviate from general trends, warranting further investigation.

Figure 5 is the box plot of features which provides a visual summary of the distribution, central tendency, and variability of the soil nutrients, including Organic Carbon (Org. C), Available Phosphorus (Avail. P), Potassium (K), Calcium (Ca), Magnesium (Mg), Sodium (Na), Hydrogen (H), and Aluminum (Al). It highlights the presence of outliers, differences in concentration ranges, and potential skewness in the data for each nutrient.

Distribution plots further underline soil variability, with bimodal patterns in Avail. P suggesting inconsistent phosphorus availability, and skewness in Org. C and pH distributions reflecting variability in soil health. Uniform distributions for Sodium hint at its consistent levels, while Aluminium’s low concentrations corroborate reduced soil acidity.

Temporal trends show promising patterns in nutrient dynamics. Gradual increases in Org. C and Magnesium levels may signify improved soil management, while the decline in Aluminium points to reduced acidity, enhancing soil quality. Fluctuations in Avail. P and stability in Sodium and pH underscore varying soil management impacts over time.

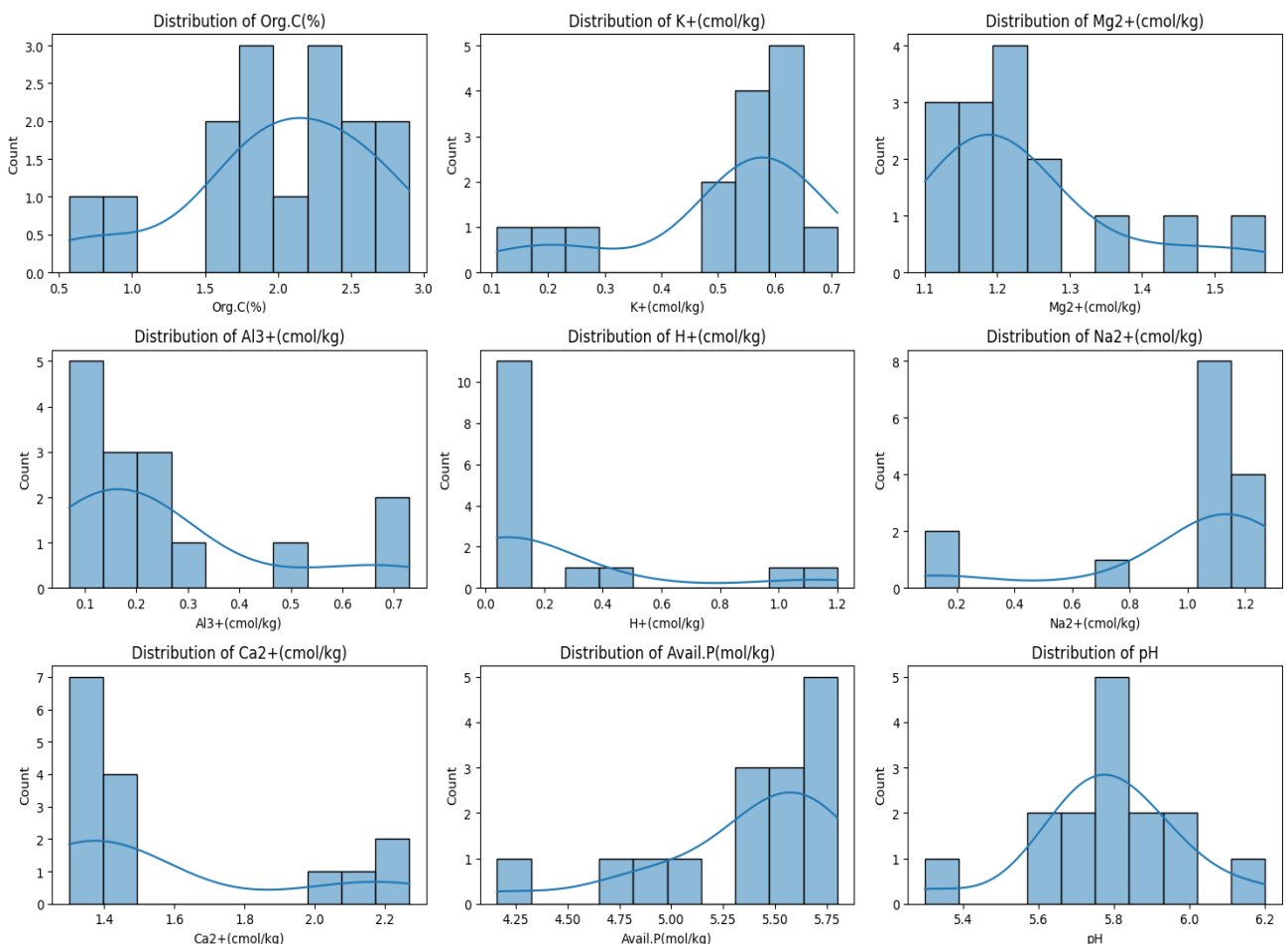


Figure 4. Distribution plot of features.

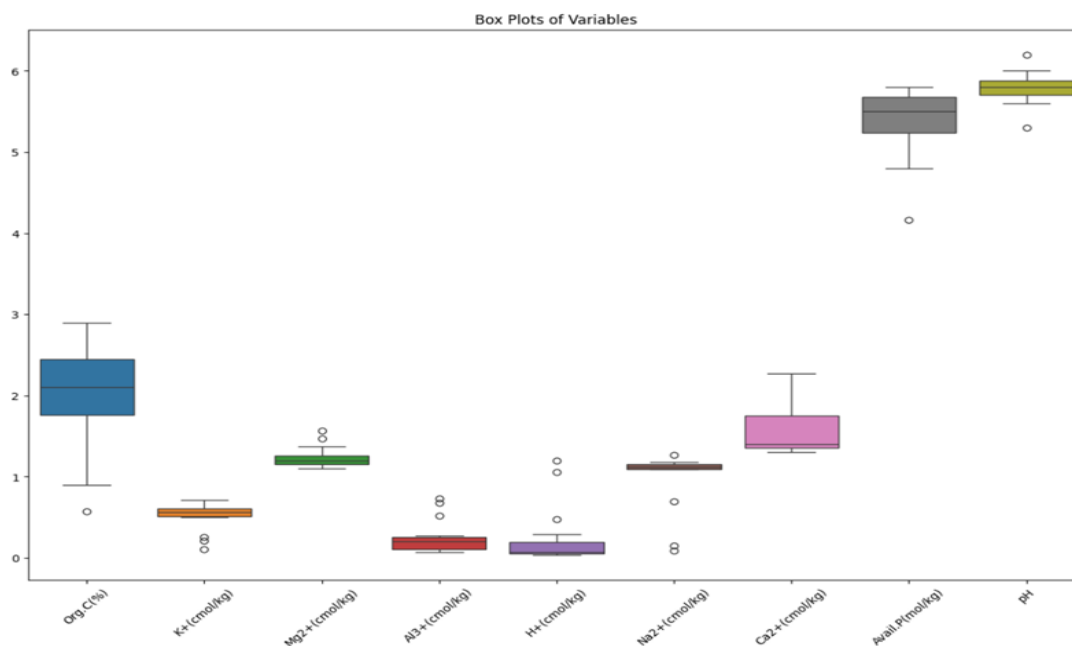


Figure 5. The box plot of features

The PairPlot as shown in Figure 6 reveals limited strong correlations among parameters, except for a near-perfect positive correlation (0.99) between Calcium and Magnesium, which aligns with their shared role in soil structure and nutrient balance. Moderate positive correlations, such as Sodium with pH (0.66), suggest interdependence between alkalinity and sodium presence, while a negative correlation between Sodium and Avail. P (-0.63) highlights potential challenges in phosphorus uptake in sodium-rich soils. These relationships emphasize the interconnected nature of soil chemistry.

Based on the EDA, the data preprocessing for machine learning models should include several key steps to ensure data quality and model performance. Since no missing values are present, imputation is unnecessary, but outlier handling is crucial for parameters like Organic Carbon and Potassium to prevent skewed model training. Scaling or normalization should be applied to variables with wide ranges, such as Calcium and Available Phosphorus, to ensure uniform feature contributions. Encoding temporal trends, such as year-wise data, into relevant features can capture temporal dynamics in soil nutrients. Addressing skewness in parameters like pH and Organic Carbon via transformations (e.g., log or power transformation) will improve model interpretability. Additionally, feature engineering to capture correlations, such as interaction terms for Calcium and Magnesium or Sodium and pH, could enhance predictive power.

3.3. Results Discussion

The models' performance demonstrates varying levels of generalization in predicting soil nutrient parameters, with the Random Forest Regressor emerging as the most consistently robust across all features. Models with minimal gaps between training and testing metrics, particularly in RMSE and R² values, are deemed better at generalizing to unseen data.

For Na^{2+} (cmol/kg), the Random Forest Regressor stands out with a testing RMSE of 0.25 and a testing R^2 of 0.95. The minimal disparity between its training and testing metrics underscores its robustness. While Neural Network performs well with a testing RMSE of 0.38 and testing R^2 of 0.88, it falls short of Random Forest's performance. XGBoost, with a testing RMSE of 0.48 and testing R^2 of 0.80, demonstrates weaker generalization.

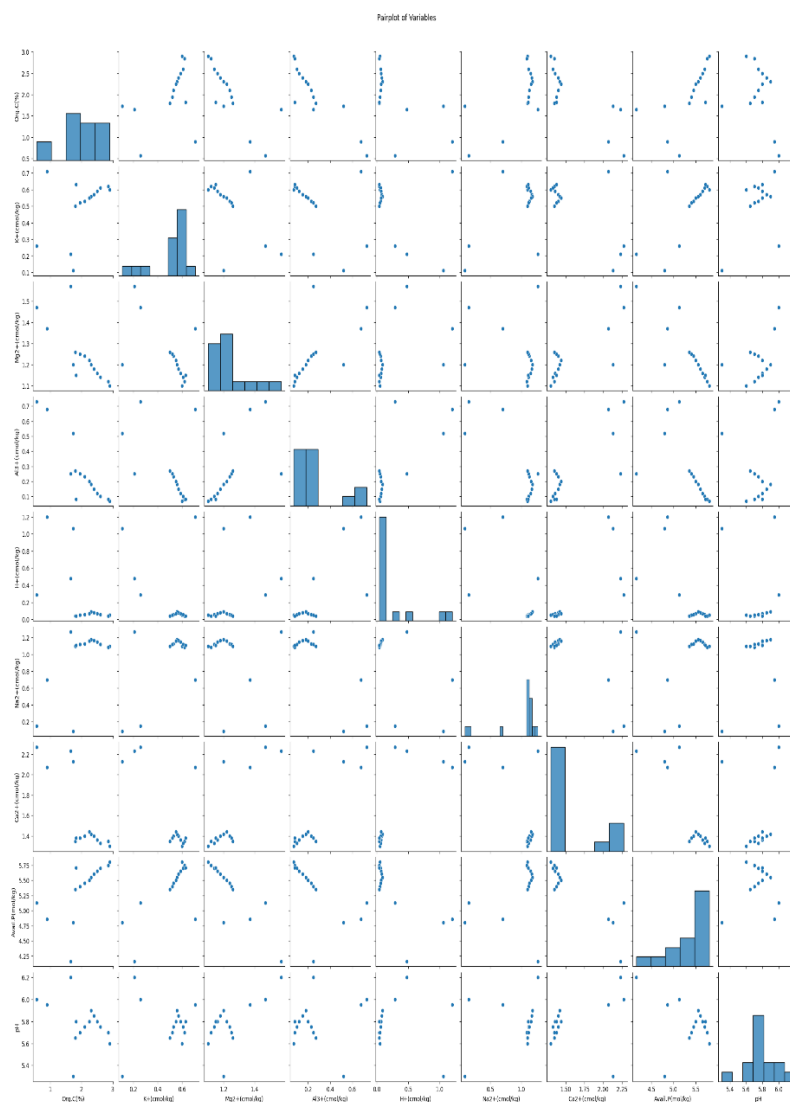


Figure 6. Pairplot of features.

In predicting Ca^{2+} (cmol/kg), Random Forest once again exhibits exceptional performance, achieving the lowest testing RMSE (0.16) and a near-perfect testing R^2 of 0.98. Neural Network and XGBoost follow closely, with testing RMSEs of 0.22 and 0.24 and testing R^2 values of 0.96 and 0.95, respectively. However, Random Forest's smaller gap between training and testing metrics highlights its superior consistency.

For Avail. P (mol/kg), Random Forest demonstrates strong generalization with a testing RMSE of 0.28 and a testing R^2 of 0.94. Neural Network and Gradient Boosting Regressor also perform competitively, with testing RMSEs of 0.32 and 0.38 and testing R^2 values of 0.92 and 0.88, respectively. However, their slightly higher

RMSEs and larger gaps between training and testing R^2 values indicate slightly less reliable performance compared to Random Forest.

In predicting pH, Random Forest again outperforms other models, achieving a testing RMSE of 0.12 and a testing R^2 of 0.99, underscoring its ability to generalize exceptionally well. Neural Network performs closely, with a testing RMSE of 0.20 and testing R^2 of 0.97, but still lags behind Random Forest. XGBoost and K-Nearest Neighbours Regressor, with testing RMSEs of 0.35 and 0.35 and testing R^2 values of 0.90, show larger disparities and weaker performance.

In summary, Random Forest consistently demonstrates the best generalization across all soil nutrient parameters. Its minimal gaps between training and testing metrics, coupled with consistently high R^2 values, make it the most reliable model for predicting unseen data. The consistent performance of Random Forest underscores its robustness, accuracy, and suitability for this research. This analysis highlights the critical importance of selecting the right machine learning model, as performance can vary significantly depending on the dataset and feature being analysed.

3.4. Comparison with Previous Studies

The performance of the Random Forest Regressor in predicting soil nutrient parameters is well-documented in the literature, highlighting its robustness in managing nonlinear relationships and complex interactions inherent in soil data. For example, studies have shown that Random Forest outperforms other machine learning models in soil nutrient prediction tasks, achieving high R^2 such as 0.94 for sodium (Na_2^+) (Haq et al., 2023) and 0.97 for pH (Paepae et al., 2022). This aligns with the findings of this study, which also demonstrates the efficacy of Random Forest in predicting soil nutrient parameters. Conversely, the performance of Neural Networks, while competitive in this study with R^2 values of 0.97 for pH and 0.92 for available phosphorus (Avail. P), has been noted to be superior in capturing intricate soil nutrient variations in other research. The discrepancy in performance may stem from factors such as dataset size, feature selection, or hyperparameter tuning, which are critical in optimizing model performance (Chen et al., 2024). This suggests that while Neural Networks have the potential for high accuracy, their effectiveness can be contingent upon the quality and quantity of the data used.

Additionally, alternative models such as XGBoost and Gradient Boosting Regressor have been recognized as strong contenders for soil prediction tasks, particularly when feature engineering is effectively applied (Tryhuba et al., 2024). However, in this research, their relatively lower generalization capability indicates that further refinement of hyperparameters or feature selection may be necessary to enhance their predictive performance (Yerrabolu et al., 2024). This highlights the importance of model tuning and the adaptability of different algorithms to specific datasets and tasks.

This study reinforces the effectiveness of ensemble models like Random Forest in soil nutrient prediction while also illuminating the variability of model performance based on dataset characteristics, feature engineering, and model tuning. Future research could benefit from exploring deep learning techniques with larger datasets to assess their potential for surpassing traditional ensemble methods in predictive accuracy.

4. CONCLUSION

4.1. Summary of Key Findings

This research evaluates the performance of various ML models in predicting soil fertility based on localized data and engineered features. Key findings include:

Model Performance: Random Forest Regressor consistently demonstrated superior performance across all target variables, achieving the lowest RMSE and highest R^2 scores, indicating strong predictive accuracy and reliability.

Neural Networks (MLP) showed competitive performance, particularly in capturing complex patterns in the data, although slightly behind Random Forest in generalization capability.

Gradient Boosting Regressor and XGBoost Regressor offered balanced performance but showed moderate overfitting compared to Random Forest.

K-Nearest Neighbors Regressor had the lowest performance among models, with higher RMSE and lower R^2 values, especially for complex target features.

Feature Engineering: Polynomial feature generation and normalization significantly improved model accuracy and stability. Key features like pH, organic carbon, and nitrogen were identified as critical predictors of soil fertility.

Temporal trends and correlation-based feature engineering, such as interaction terms, enhanced the predictive power of models.

Exploratory Data Analysis: Nutrient variability and trends highlighted the influence of soil management practices. For example, an increase in organic carbon and a decline in aluminium levels indicated improving soil quality over time. Correlation analysis revealed strong relationships between certain parameters, such as calcium and magnesium, emphasizing their shared role in nutrient balance.

Evaluation Metrics: Combining RMSE, R^2 , and K-Fold Cross-Validation provided a comprehensive understanding of model performance, ensuring robust validation and generalization to unseen data.

Actionable Insights: The findings offer practical recommendations for improving soil management practices. By leveraging the Random Forest model's reliability, farmers and agronomists can make data-driven decisions to optimize soil fertility and agricultural productivity.

These findings underscore the importance of machine learning in advancing precision agriculture, demonstrating its potential to enhance sustainability and resource management in agriculture

4.2. Limitations

Despite the promising results, several limitations exist in this study. First, the relatively small dataset size (15 samples) constrains the generalizability of the findings, as larger datasets are typically needed for more robust ML model training and validation. This limitation might affect the models' ability to accurately predict soil fertility in diverse agricultural settings. Second, the study focuses on a limited geographical area, which may not capture the variability in soil characteristics across broader regions, thereby restricting the applicability of the models to other locales.

Additionally, while feature engineering improved model performance, it introduced complexity that could be challenging to replicate without expert knowledge. The study also employed a limited set of ML models and parameters; exploring more advanced algorithms or deeper hyperparameter optimization might yield even better results. Furthermore, certain outliers in the dataset, while addressed during preprocessing, may still influence model predictions, particularly for features with significant variability, such as Organic Carbon and Phosphorus.

Finally, the research does not account for real-time soil monitoring or external factors like climate variability and farming practices, which could significantly influence soil fertility. Future studies should consider integrating larger datasets, diverse geographical data, and real-time measurements to enhance model robustness and applicability.

4.3. Future Research Directions

The findings from this study provide a foundation for advancing machine learning (ML)-based soil fertility prediction models; however, there are key areas for future exploration:

- **Integration of IoT and Real-Time Data:** Incorporating Internet of Things (IoT) sensors to collect real-time soil data could enhance model accuracy and adaptability, enabling real-world, dynamic soil fertility monitoring systems.
- **Spatial and Temporal Analysis:** Future studies should explore spatial variability and temporal trends in soil fertility by integrating geospatial data and time-series analysis, offering localized and time-sensitive insights for agricultural practices.

- **Hybrid and Deep Learning Models:** Investigating hybrid ML models or advanced deep learning techniques, such as Convolutional Neural Networks (CNNs) for image-based soil analysis, could improve predictive performance and provide multi-dimensional insights.
- **Scalability and Deployment:** Developing scalable frameworks for deploying these models in resource-constrained environments, especially in developing countries, would enhance their practical applicability. Integration with mobile and cloud-based platforms can improve accessibility for farmers.
- **Impact of Climate Change:** Expanding datasets to include climate variables, such as rainfall and temperature, could help predict how changing environmental conditions influence soil fertility over time.
- **Soil Microbiome and Genomics Integration:** Incorporating soil microbiome data and genome-wide analysis could provide a more holistic approach to fertility prediction, integrating biological and chemical factors into ML models.

By addressing these areas, future research can build on the existing framework to create more accurate, scalable, and actionable solutions for sustainable agriculture.

AUTHOR CONTRIBUTIONS

All authors contributed to the study's conception and design. Material preparation, data collection and analysis were performed by C.O.N, E.N.V, O.C.C, E.O.C, N.C.V and E.C.N. The first draft of the manuscript was written by C.O.N, and all authors commented on the previous versions of the manuscript. All authors read and approved the final manuscript.

ACKNOWLEDGEMENT

The authors acknowledge the efforts of the management of the Nnamdi Azikiwe University Akwa in stimulating this research.

CONFLICT OF INTEREST

The authors declare no conflict of interest.

REFERENCES

- Abishek, J. (2023). Soil texture prediction using machine learning approach for sustainable soil health management. *International Journal of Plant and Soil Science*, 35(19), 1416-1426. <https://doi.org/10.9734/ijpss/2023/v35i193685>
- Asif, M. (2024). Leveraging machine learning for soil fertility prediction and crop management in agriculture. <https://doi.org/10.21203/rs.3.rs-4310747/v1>

- Awais, M. (2023). Ai and machine learning for soil analysis: an assessment of sustainable agricultural practices. *Bioresources and Bioprocessing*, 10(1). <https://doi.org/10.1186/s40643-023-00710-y>
- Barrena-González, J. (2024). Looking for optimal maps of soil properties at the regional scale. *International Journal of Environmental Research*, 18(4). <https://doi.org/10.1007/s41742-024-00611-8>
- Chen, Y., Shi, T., Li, Q., Wang, Z., Wang, R., Wang, F., ... and Li, Y. (2024). Mapping soil properties in tropical rainforest area using uav-based hyperspectral images and lidar points. <https://doi.org/10.21203/rs.3.rs-4273924/v1>
- Clark, J., Fernández, F., Veum, K., Camberato, J., Carter, P., Ferguson, R., ... and Shanahan, J. (2019). Predicting economic optimal nitrogen rate with the anaerobic potentially mineralizable nitrogen test. *Agronomy Journal*, 111(6), 3329-3338. <https://doi.org/10.2134/agronj2019.03.0224>
- Dinh, T., Nguyen, H., Tran, X., and Hoang, N. (2021). Predicting rainfall-induced soil erosion based on a hybridization of adaptive differential evolution and support vector machine classification. *Mathematical Problems in Engineering*, 2021, 1-20. <https://doi.org/10.1155/2021/6647829>
- Ezenwankwo, S., Adeagbo, A.A., Lawal, S., Idoghor, S. M. and Chukwu, O.(2020). Evaluation of early growth of *Maesobotrya barteri* (Hutch) seedlings underdifferent growing media and watering regime. In: *Forestry Development in Nigeria: Fiftyyears of interventions and Advocacy*. At the 42nd Annual conference of the Forestry Association of Nigeria (FAN), on 23-28 November, 2020, Ibadan, Nigeria. pp. 730-736.
- Groebner, B. (2024). Soil biological and physical measurements did not improve the predictability of corn response to phosphorus fertilization. *Agronomy Journal*, 116(4), 2048-2059. <https://doi.org/10.1002/agj2.21612>
- Hamidović, S., SOFTIC, A., Topčić, F., Tvica, M., Lalević, B., and Stojanova, M. (2023). Impact of soil management practice on the abundance of microbial populations. *The Journal Agriculture and Forestry*, 69(2). <https://doi.org/10.17707/agricultforest.69.2.12>
- Haq, Y., Shahbaz, M., Asif, H., Al-Laith, A., and Alsabban, W. (2023). Spatial mapping of soil salinity using machine learning and remote sensing in kot addu, pakistan. *Sustainability*, 15(17), 12943. <https://doi.org/10.3390/su151712943>
- Harris, J., Bledsoe, R., Guha, S., Omari, H., Crandall, S., Burghardt, L., ... and Couradeau, E. (2024). The activity of soil microbial taxa in the rhizosphere predicts the success of root colonization.. <https://doi.org/10.1101/2024.12.07.627353>
- Hu, Z., Ding, Z., Al-Yasi, H., Ali, E., Eissa, M., Abou-Elwafa, S., ... and Hamada, A. (2021). Modelling of phosphorus nutrition to obtain maximum yield, high p use efficiency and low p-loss risk for wheat grown in sandy calcareous soils. *Agronomy*, 11(10), 1950. <https://doi.org/10.3390/agronomy11101950>
- Inoyatova, M. (2024). Data mining for assessing soil fertility. *E3s Web of Conferences*, 494, 02012. <https://doi.org/10.1051/e3sconf/202449402012>
- Jabborova, D., Choudhary, R., Azimov, A., Jabbarov, Z., Selim, S., Abu-Elghait, M., ... and Elsaied, A. (2022). Composition of *zingiber officinale roscoe* (ginger), soil properties and soil enzyme activities

- grown in different concentration of mineral fertilizers. *Horticulturae*, 8(1), 43. <https://doi.org/10.3390/horticulturae8010043>
- Jia, X. (2023). Development of soil fertility index using machine learning and visible-near-infrared spectroscopy. *Land*, 12(12), 2155. <https://doi.org/10.3390/land12122155>
- Kroyan, S. (2024). Anthropogenic changes of the agricultural production features of river valley-escarpment soils in martuni region, sevan basin, ra. *E3s Web of Conferences*, 510, 01009. <https://doi.org/10.1051/e3sconf/202451001009>
- Lepcha, N. and Devi, N. (2020). Effect of land use, season, and soil depth on soil microbial biomass carbon of eastern himalayas. *Ecological Processes*, 9(1). <https://doi.org/10.1186/s13717-020-00269-y>
- Li, M., Ji, R., Wang, M., and Zheng, L. (2020). Comparison of soil total nitrogen content prediction models based on vis-nir spectroscopy. *Sensors*, 20(24), 7078. <https://doi.org/10.3390/s20247078>
- Liu, W., Yang, Z., Ye, Q., Peng, Z., Zhu, S., Chen, H., ... and Huang, H. (2023). Positive effects of organic amendments on soil microbes and their functionality in agro-ecosystems. *Plants*, 12(22), 3790. <https://doi.org/10.3390/plants12223790>
- Longchamps, L., Mandal, D., and Khosla, R. (2022). Assessment of soil fertility using induced fluorescence and machine learning. *Sensors*, 22(12), 4644. <https://doi.org/10.3390/s22124644>
- Ma, G., Cheng, S., He, W., Dong, Y., Qi, S., Nai-mei, T., ... and Wei, T. (2023). Effects of organic and inorganic fertilizers on soil nutrient conditions in rice fields with varying soil fertility. *Land*, 12(5), 1026. <https://doi.org/10.3390/land12051026>
- Mendoza, M., Mora-Bautista, M., Cué, J., Escudero, J., and Etchevers, J. (2021). Field production of kale (*brassica oleracea* var. *acephala*) with different nutrition sources. *Agro Productividad*. <https://doi.org/10.32854/agrop.v14i10.1954>
- Mesfin, S., Haile, M., Gebresamuel, G., Zenebe, A., and Gebre, A. (2021). Establishment and validation of site-specific fertilizer recommendation for increased barley (*hordeum* spp.) yield, northern Ethiopia. *Helion*, 7(8), e07758. <https://doi.org/10.1016/j.heliyon.2021.e07758>
- Musanase, C. (2023). Data-driven analysis and machine learning-based crop and fertilizer recommendation system for revolutionizing farming practices. *Agriculture*, 13(11), 2141. <https://doi.org/10.3390/agriculture13112141>
- Nelson, A., Narrowe, A., Rhoades, C., Fegel, T., Daly, R., Roth, H., ... and Wilkins, M. (2022). Wildfire-dependent changes in soil microbiome diversity and function. *Nature Microbiology*, 7(9), 1419-1430. <https://doi.org/10.1038/s41564-022-01203-y>
- Ning, Q., Hättenschwiler, S., Lü, X., Kardol, P., Zhang, Y., Wei, C., ... and Han, X. (2021). Carbon limitation overrides acidification in mediating soil microbial activity to nitrogen enrichment in a temperate grassland. *Global Change Biology*, 27(22), 5976-5988. <https://doi.org/10.1111/gcb.15819>
- Nwamekwe, C. O., Ewuzie, N. V., Igbokwe, N. C., Okpala, C. C., and U-Dominic, C. M. (2024). Sustainable Manufacturing Practices in Nigeria: Optimization and Implementation Appraisal. *Journal of Research in Engineering and Applied Sciences*, 9(3). [URL](#)

- Nwamekwe, C. O., Ewuzie, N. V., Igbokwe, N. C., U-Dominic, C. M., and Nwabueze, C. V. (2024). Adoption of Smart Factories in Nigeria: Problems, Obstacles, Remedies and Opportunities. *International Journal of Industrial and Production Engineering*, 2(2). Retrieved from [URL](#)
- Nwamekwe, C. O., Okpala, C. C., and Okpala, S. C., (2024). Machine Learning-Based Prediction Algorithms for the Mitigation of Maternal and Fetal Mortality in the Nigerian Tertiary Hospitals. *International Journal of Engineering Inventions*, 13(7), PP: 132-138. [URL](#)
- Omar, G. and Sule, H. (2017). Fertility status of floodplain soils along river andlt;iandgt;tatsewarkian<iandgt;,, kano. *Bayero Journal of Pure and Applied Sciences*, 9(2), 17. <https://doi.org/10.4314/bajopas.v9i2.4>
- Osaigbovo, A. and Law-Ogbomo, K. (2014). Effects of spent engine oil polluted soil and organic amendment on soil chemical properties, micro-flora on growth and herbage of andlt;iandgt;telfairia occidentalisandlt;iandgt; (hook f).. *Bayero Journal of Pure and Applied Sciences*, 6(1), 72. <https://doi.org/10.4314/bajopas.v6i1.15>
- Paepae, T., Bokoro, P., and Kyamakya, K. (2022). A virtual sensing concept for nitrogen and phosphorus monitoring using machine learning techniques. *Sensors*, 22(19), 7338. <https://doi.org/10.3390/s22197338>
- Pagliarini, M., Castilho, R., Moreira, E., Mariano-Nasser, F., and Alves, M. (2019). Development of hymenaea courbaril l. var. stilbocarpa seedlings in different fertilizers and substrate composition. *Agrarian*, 12(43), 8-15. <https://doi.org/10.30612/agrarian.v12i43.4184>
- Palansooriya, K., Wong, J., Hashimoto, Y., Huang, L., Rinklebe, J., Chang, S., ... and Ok, Y. (2019). Response of microbial communities to biochar-amended soils: a critical review. *Biochar*, 1(1), 3-22. <https://doi.org/10.1007/s42773-019-00009-2>
- Pant, H., Lohani, M., and Bhatt, A. (2019). Impact of physico-chemical properties for soils type classification of oak using different machine learning techniques. *International Journal of Computer Applications*, 177(17), 38-44. <https://doi.org/10.5120/ijca2019919617>
- Patil, A., Kulkarni, V., and Desai, S. (2023). Soil fertility prediction. *International Journal for Research in Applied Science and Engineering Technology*, 11(8), 1241-1247. <https://doi.org/10.22214/ijraset.2023.55225>
- Prince, M., Mankessi, F., Sun, S., and Fan, X. (2021). Effects of alkaline fertilizer and rice cultivation (*oryza sativa* l.) on remediation of soils polluted with cadmium (cd). *Journal of Applied Biosciences*, 157, 16182-16193. <https://doi.org/10.35759/jabs.157.4>
- Rajamanickam, J. and Mani, S. (2021). Kullback chi square and gustafson kessel probabilistic neural network-based soil fertility prediction. *Concurrency and Computation Practice and Experience*, 33(24). <https://doi.org/10.1002/cpe.6460>
- Razanov, S. (2024). The content of heavy metals and trace elements in different soils used under the conditions of homestead plots and field agricultural lands of ukraine. *Journal of Ecological Engineering*, 25(6), 42-50. <https://doi.org/10.12911/22998993/186820>

- Reddy, L. (2024). Applying machine learning to soil analysis for accurate farming. *Matec Web of Conferences*, 392, 01124. <https://doi.org/10.1051/mateconf/202439201124>
- Rehman, O., Mehdi, S., Abad, R., Saleem, S., Khalid, R., Alvi, S., ... and Munir, A. (2021). Soil characteristics and fertility indexation in gujar khan area of rawalpindi. *Pakistan Journal of Scientific and Industrial Research Series a Physical Sciences*, 64(1), 46-51. <https://doi.org/10.52763/pjsir.phys.sci.64.1.2021.46.51>
- Sandhya, K., Gayathri, B., Papireddy, M., R, P., Vishwanath, V., Swathi, B., ... and Naveen, D. (2023). Assessing the nutrient status and soil fertility using nutrient indexed of farmer's fields in chikkaballapura district, karnataka. *International Journal of Plant and Soil Science*, 35(23), 639-649. <https://doi.org/10.9734/ijpss/2023/v35i234283>
- Saraiva, T., Ventura, S., Brito, E., Rocha, S., Costa, R., Pereira, A., ... and Araújo, A. (2022). Temporal stability of soil microbial properties in responses to long-term application of compost obtained from tannery sludge. *Sustainability*, 14(24), 16736. <https://doi.org/10.3390/su142416736>
- Sofo, A., Mininni, A., and Ricciuti, P. (2020). Soil macrofauna: a key factor for increasing soil fertility and promoting sustainable soil use in fruit orchard agrosystems. *Agronomy*, 10(4), 456. <https://doi.org/10.3390/agronomy10040456>
- Sridevy, S., Raj, M., Kumaresan, P., Balakrishnan, N., Tilak, M., Raj, J., ... and Rani, P. (2023). Mapping of soil properties using machine learning techniques. *International Journal of Environment and Climate Change*, 13(8), 684-700. <https://doi.org/10.9734/ijecc/2023/v13i81997>
- Tryhuba, I., Tryhuba, A., Hutsol, T., Cieszewska, A., Andrushkiv, O., Głowacki, S., ... and Sojak, M. (2024). Prediction of biogas production volumes from household organic waste based on machine learning. *Energies*, 17(7), 1786. <https://doi.org/10.3390/en17071786>
- Yageta, Y., Osbahr, H., Morimoto, Y., and Clark, J. (2019). Comparing farmers' qualitative evaluation of soil fertility with quantitative soil fertility indicators in kitui county, kenya. *Geoderma*, 344, 153-163. <https://doi.org/10.1016/j.geoderma.2019.01.019>
- Yang, Q., Peng, J., Ni, S., Zhang, C., Wang, J., and Cai, C. (2024). Soil erosion-induced decline in aggregate stability and soil organic carbon reduces aggregate-associated microbial diversity and multifunctionality of agricultural slope in the mollisol region. *Land Degradation and Development*, 35(11), 3714-3726. <https://doi.org/10.1002/ldr.5163>
- Yerrabolu, V., Kasireddy, I., Jasmine, K., Vamsi, T., Joshua, N., Kumar, V., ... and Rao, D. (2024). Performance comparison of random forest regressor and support vector regression for solar energy prediction. *Iop Conference Series Earth and Environmental Science*, 1375(1), 012013. <https://doi.org/10.1088/1755-1315/1375/1/012013>
- Yu, X. (2024). Prediction model of nitrogen, phosphorus, and potassium fertilizer application rate for greenhouse tomatoes under different soil fertility conditions. *Agronomy*, 14(6), 1165. <https://doi.org/10.3390/agronomy14061165>

- Zhao, Z., He, J., Quan, Z., Wu, C., Sheng, R., Zhang, L., ... and Geisen, S. (2020). Fertilization changes soil microbiome functioning, especially phagotrophic protists. *Soil Biology and Biochemistry*, 148, 107863. <https://doi.org/10.1016/j.soilbio.2020.107863>
- Zheng, C., Yang, X., Liu, Z., Liu, K., and Huang, Y. (2022). Spatial distribution of soil nutrients and evaluation of cultivated land in xuwen county. *Peerj*, 10, e13239. <https://doi.org/10.7717/peerj.13239>
- Ziyadullaev, D. (2024). Ensemble data mining methods for assessing soil fertility. *E3s Web of Conferences*, 494, 02013. <https://doi.org/10.1051/e3sconf/202449402013>



A Novel Dynamic Clock Generator Circuit for the Threshold Logic Gate

Ahmet UNUTULMAZ^{1*} ¹ Marmara University, İstanbul, Türkiye

| Keywords | Abstract |
|--|--|
| Threshold Logic Gate Dynamic Circuit Clock Generator | Threshold Logic Gate (TLG) has gained attention with the emergence of novel technologies such as memristors. TLG offers improved performance and lower power dissipation while occupying less silicon area. This paper introduces a novel dynamic clock generator circuit that further enhances TLG performance. The proposed circuit replaces the NAND gate-based approach used for clock generation in differential TLG implementations. It reduces the propagation delay of the TLG while reducing its static power dissipation, an important factor in energy-efficient circuit design. Simulations indicate up to a 25% reduction in delay compared to the NAND gate-based approach. Furthermore, the proposed circuit occupies 45% less area than the NAND gate. These findings highlight the potential of the proposed dynamic clock generator for advanced threshold logic implementations, paving the way for further innovations in the field. |

| Cite |
|--|
| Unutulmaz, A. (2025). A Novel Dynamic Clock Generator Circuit for the Threshold Logic Gate. <i>GU J Sci, Part A, 12(1)</i> , 61-71. doi:10.54287/guj.1645022 |

| Author ID (ORCID Number) | Article Process |
|-------------------------------------|---|
| 0000-0001-7738-9286 Ahmet UNUTULMAZ | Submission Date 23.02.2025 Revision Date 04.03.2025 Accepted Date 12.03.2025 Published Date 26.03.2025 |

1. INTRODUCTION

The emergence of technologies like memristors has increased the popularity of Threshold Logic Gate (TLG) (Mazumder, 2012). This gate offers several advantages, including enhanced power efficiency, reduced circuit complexity, and increased robustness. Yang et al. (2014) introduced a differential TLG implementation incorporating memristors. This implementation improved circuit reliability and lowered failure rates due to the integration of memristor networks. By embedding memristors into TLGs, circuit resilience is enhanced, and power consumption is reduced (Vrudhula, 2015). This makes them ideal for modern high performance computing applications. A comprehensive overview of mem-resistive threshold logic circuits is provided in (Maan, 2016), covering a range of implementations and their respective benefits. More recently, a physical implementation of a memristor-based TLG was demonstrated in (Papandroulidakis, 2019), reinforcing the practicality and efficiency of these designs. Youn et al. (2024) demonstrated programmable threshold logics using a 32×32 memristor crossbar array. TLG implementations in emerging technologies are not limited to memristors. Han et al. (2021) fabricated a bio-inspired reconfigurable threshold logic circuit. There is even a TLG implementation with optical systems. Sarkar et al. (2021) implemented an optical threshold logic gate using a reflector telescopic system and a resonant Fabry-Perot cavity.

*Corresponding Author, e-mail: ahmet.unutulmaz@marmara.edu.tr

Beyond emerging technologies, TLGs have also demonstrated significant advantages in conventional semiconductor applications. Several studies emphasize their benefits, particularly in performance enhancement and power dissipation reduction. For instance, Kulkarni et al. (2016) reported that incorporating TLGs into binary circuits results in performance improvements and energy savings. Their findings suggest that TLGs can effectively optimize computational efficiency by minimizing transistor count and reducing dynamic power consumption, positioning them as a viable solution for high-performance digital circuits. Wagle et al. (2021) proposed the use of TLG in binary FPGAs. The proposed methodology is reported to reduce the area and power of configurable logic blocks while improving their performance.

Unutulmaz et al. (2024) expanded the application of TLGs to multi-valued logic circuits, specifically to ternary logic circuits. Their study demonstrated the potential of differential TLGs in reducing power dissipation, silicon area, and delay. This study shows the potential of TLG for multi-valued logic implementations. Multi-valued logic is advantageous as it allows a single wire to represent more than two distinct logic levels, unlike binary logic, which is limited to only two. The capability of representing more than two levels enables spatial compression of information. This in effect reduces the routing resource requirements (Saxena, 2007) and allows further reduction of silicon area.

A simplified representation of the TLG proposed by Unutulmaz et al. (2024) is shown in Figure 1. This circuit processes two sets of ternary signals and compares them. The operational principles of the circuit, along with a detailed breakdown of its functional components, are elaborated in Section 2.

As depicted in Figure 1, the circuit requires a clock signal for operation. The clock input may be connected to the system clock if there is only one TLG or if the TLG is the first element in a timing path. On the other hand, if a TLG is connected to another one, the subsequent TLG requires a specific clock which will trigger a comparison after the previous one completes its operation. This could be achieved by connecting a NAND gate to the outputs u and \bar{u} (Figure 1) as proposed by Celinski et al. (2002). Connections of the NAND gate are shown in Figure 2.a. The output of the NAND gate, clk_out signal, could be used as the clock input to the subsequent TLG circuit.

This paper presents a novel circuitry to replace the NAND gate base clock generation. Performance of the clock generation circuit is improved via a novel dynamic clock generator circuit. The proposed dynamic clock generator is shown in Figure 2.b. The proposed circuit not only improves the performance but also reduces the static power dissipation which is an important factor in low-power and energy-efficient circuit design.

A comparison of the proposed dynamic clock generator against the design introduced by Celinski et al. (2002) is conducted in Section 3. The comparison covers critical performance metrics such as power consumption, delay, and silicon area. The results demonstrate that the proposed dynamic clock generator outperforms the previous design, highlighting its viability for next-generation threshold logic implementations. Section 4 concludes the paper by summarizing the key findings of this study.

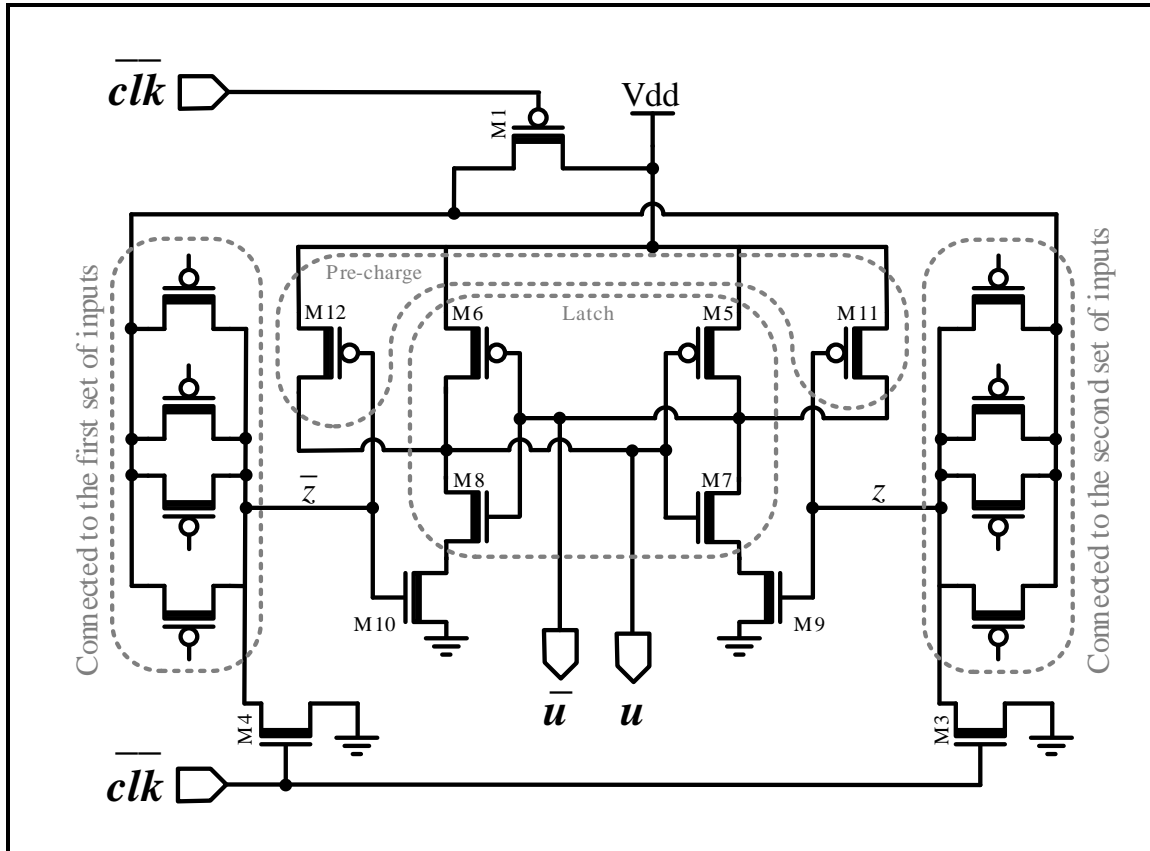


Figure 1. Schematic of the Ternary TLG Circuit

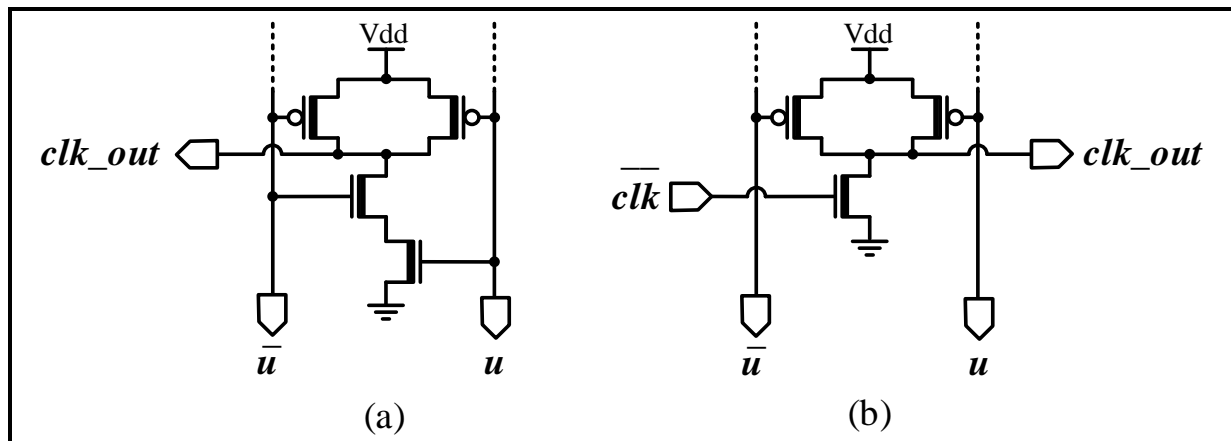


Figure 2. a) Schematic of the NAND Gate, b) The Proposed Dynamic Circuit

2. MATERIAL AND METHOD

In this section the operation principles of the TLG circuit shown in Figure 1 and the clock generator circuits shown in Figure 2 are explained.

The circuit in Figure 1 operates in two distinct phases: the reset phase and the comparison phase. Both phases are essential in ensuring the correct functionality of the TLG circuit by preparing and evaluating the internal signals to produce correct outputs.

The reset phase begins when the clock signal transitions from high to low. In this phase, any residual charge from the previous operation is discharged to ground. This ensures correct operation in the following comparison phase. The inverse of the clock signal is connected to the gates of the M3 and M4 transistors, which are NMOS transistors. Thus, when the reset phase starts, M3 and M4 are turned on. These discharge the internal nodes z and \bar{z} to the ground potential. The internal nodes z and \bar{z} are connected to the gates of the M11 and M12 transistors. These transistors are PMOS devices and start conducting as the internal nodes z and \bar{z} are discharged to ground potential. These transistors charge the output nodes u and \bar{u} to the supply voltage V_{dd} . Setting the output nodes to V_{dd} establishes a clear initial condition for the comparison phase, enabling the circuit to accurately identify differences between the input signals.

Since z and \bar{z} are discharged to ground, the NMOS transistors M9 and M10 are in cut-off and do not conduct. Although the output nodes u and \bar{u} are charged to V_{dd} , turning on the NMOS transistors M7 and M8, these transistors still do not conduct because M9 and M10 are off, preventing current flow. This isolation prevents any current paths from the output nodes u and \bar{u} to the ground. Thus, the output remains stable at the V_{dd} potential during the reset phase.

The second phase, the comparison phase, begins when the clock signal transitions from logic low to high. As the inverse of the clock signal is connected to the NMOS transistors M3 and M4, these transistors are turned off. Simultaneously, the PMOS transistor M1, which is also connected to the inverse of the clock signal, is turned on. During this phase, the transistors connected to the input signals begin charging the internal nodes z and \bar{z} to the supply voltage V_{dd} . The transistors connected to the inputs are grouped and labeled in Figure 1. Readers are referred to the study of Unutulmaz et al. (2024) for a detailed discussion on the procedure to generate the input signals. This discussion is not in the scope of this paper. Depending on the input configuration, either node z and \bar{z} charges faster than the other. The node that charges more quickly activates its corresponding transistor, M9 or M10, before the other.

At the center of the circuit, there is a latch composed of two cross-coupled inverters, as shown in Figure 1. When either transistor M9 or M10 is turned on, the connected inverter begins discharging its output node, u or \bar{u} , to ground. The cross-coupled inverters provide positive feedback, which ensures that the outputs u or \bar{u} rapidly change to either ground or V_{dd} potentials. This positive feedback mechanism guarantees a clear distinction between the output states.

As an example, the signals on the u and \bar{u} nodes, as well as the clk signal, are shown in Figure 3. When the clock is low the circuit is in reset phase. And the circuit is in comparison phase when the clock is high. The phases of the circuit are also indicated in the figure. As discussed in the previous paragraphs, the output nodes u and \bar{u} are at high logic during the reset phase. Celinski et al. (2002) proposed to connect a NAND gate to the output nodes u and \bar{u} as shown in Figure 2.a. Since the inputs of the NAND gate are u and \bar{u} remains at low logic during the reset phase, the output of the NAND gate, clk_out , will be high. The clk_out signal is also

shown in Figure 3. The comparison phase starts when the clock signal transitions from low to high. In this phase, one of the outputs of the circuit, u or \bar{u} , goes low. Then, the NAND gate outputs a high logic as shown in Figure 3. In summary, the output of the NAND gate goes from low to high when the TLG circuit makes its decision. This way, the output of the NAND gate could be used as a clock generator for the subsequent TLG. When the TLG completes its operation, it triggers the following one.

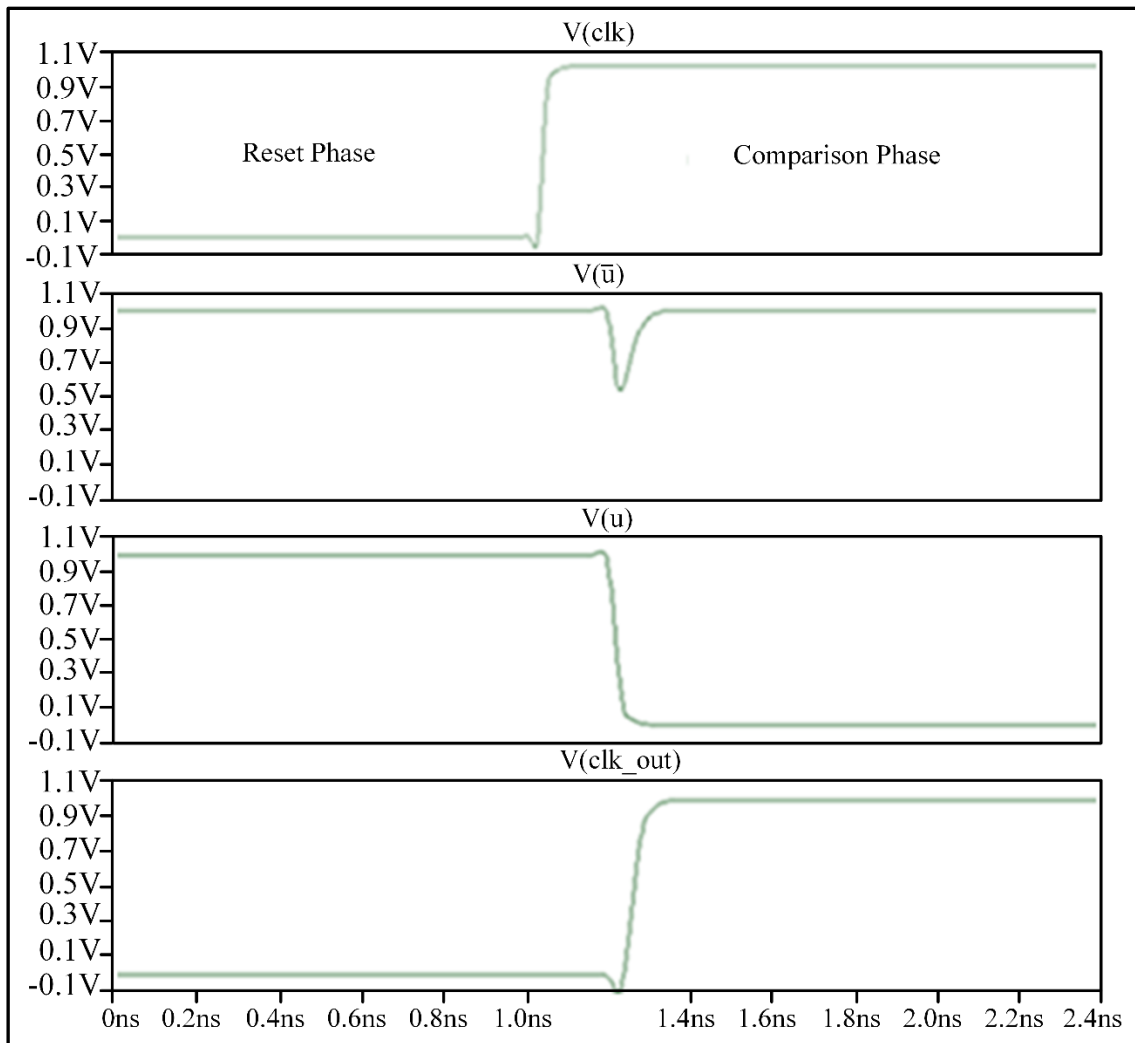


Figure 3. Simulation Results for the NAND Gate

This study proposes the logic circuit shown in Figure 2.b as an alternative to the NAND gate. Thus, the proposed circuit is a replacement to the NAND gate introduced by Celinski et al. (2002). The proposed circuit not only uses information from the u or \bar{u} signals, but also information from the clock signal. The simulation results proposed in Section 3 clearly show that the performance of the TLG circuit is improved when the proposed circuit is used as the clock generator instead of the NAND gate.

Here, the working principles of the proposed dynamic logic circuit are explained. As already stated, the outputs u and \bar{u} are high during the reset phase. These signals are connected to the PMOS transistors of the proposed circuit in Figure 2.b. Thus, these transistors are turned off during the reset phase. Because the clock signal is

low during this phase, the NMOS transistor in the proposed circuit is forced to turn on. This way, the output of the proposed circuit clk_out , is kept low during the reset phase. As the input clock transitions from low to high, the NMOS transistor is turned off. The output clk_out , is not driven by any transistors. The output is dynamically kept at ground by the parasitic capacitances at the clk_out node. After a short duration, one of the outputs, either u or \bar{u} , transitions to low. This duration is measured to be approximately 200ps when the circuit is simulated using ptm-32nm (Zhao, 2006) transistor models. The Vdd potential is set to 1V. The high to low transition turns on one of the PMOS transistors. This subsequently shifts the output of the circuit from low to high. Importantly, there is no short circuit current from PMOS to NMOS during this transition. This characteristic of the circuit enhances the circuit's response time. The current flowing through the PMOS transistor is completely utilized to charge the output node clk_out . No charge is lost to ground.

As an example, the output of the proposed circuit as well as the short circuit current from Vdd to ground is shown in Figure 4. When the signal u changes from high to low, the output of the proposed circuit changes from low to high. During this low to high transition, there is no short circuit current as shown in the figure.

When the input clock transitions from high to low logic, the NMOS transistor of the proposed circuit turns on. This transistor starts to discharge the output node clk_out to ground. Since one of the outputs u or \bar{u} is high, a temporary short circuit current flows from Vdd to ground. When both outputs u and \bar{u} charge to Vdd, the PMOS transistors are turned off. This prevents further short circuit current. Then, the output clock clk_out switches from high to low logic. Consequently, the circuit does not dissipate any static current. As shown in Figure 4, there is some short-circuit current during the high to low transition, but there is no static current. As the simulation results in Section 3 indicate, the delay of proposed circuit, during high to low transition of the output clk_out , is less than that of the NAND gate. This is mainly because the NAND gate discharges the output through two series-connected NMOS transistors. The NAND gate needs to discharge the parasitic capacitances of these two NMOS transistors, whereas the proposed circuit discharges the parasitic capacitance of a single NMOS transistor.

To be able to make a fair comparison, we equated the pull-down resistances of the NAND gate and the proposed logic gate. This is achieved by sizing the NMOS transistors of NAND gate twice as wide as the one in the proposed circuit, which speeds up high to low transition of the NAND gate. The sizes of the PMOS transistor are chosen to be the same. The transistor sizes for the NAND gate and the proposed circuit are listed in Table 1.

Table 1. Transistor Sizes

| W/L | NMOS | PMOS |
|-----------------------|-----------|-----------|
| NAND (Celinski, 2002) | 90nm/45nm | 60nm/45nm |
| Dynamic (This Work) | 45nm/45nm | 60nm/45nm |

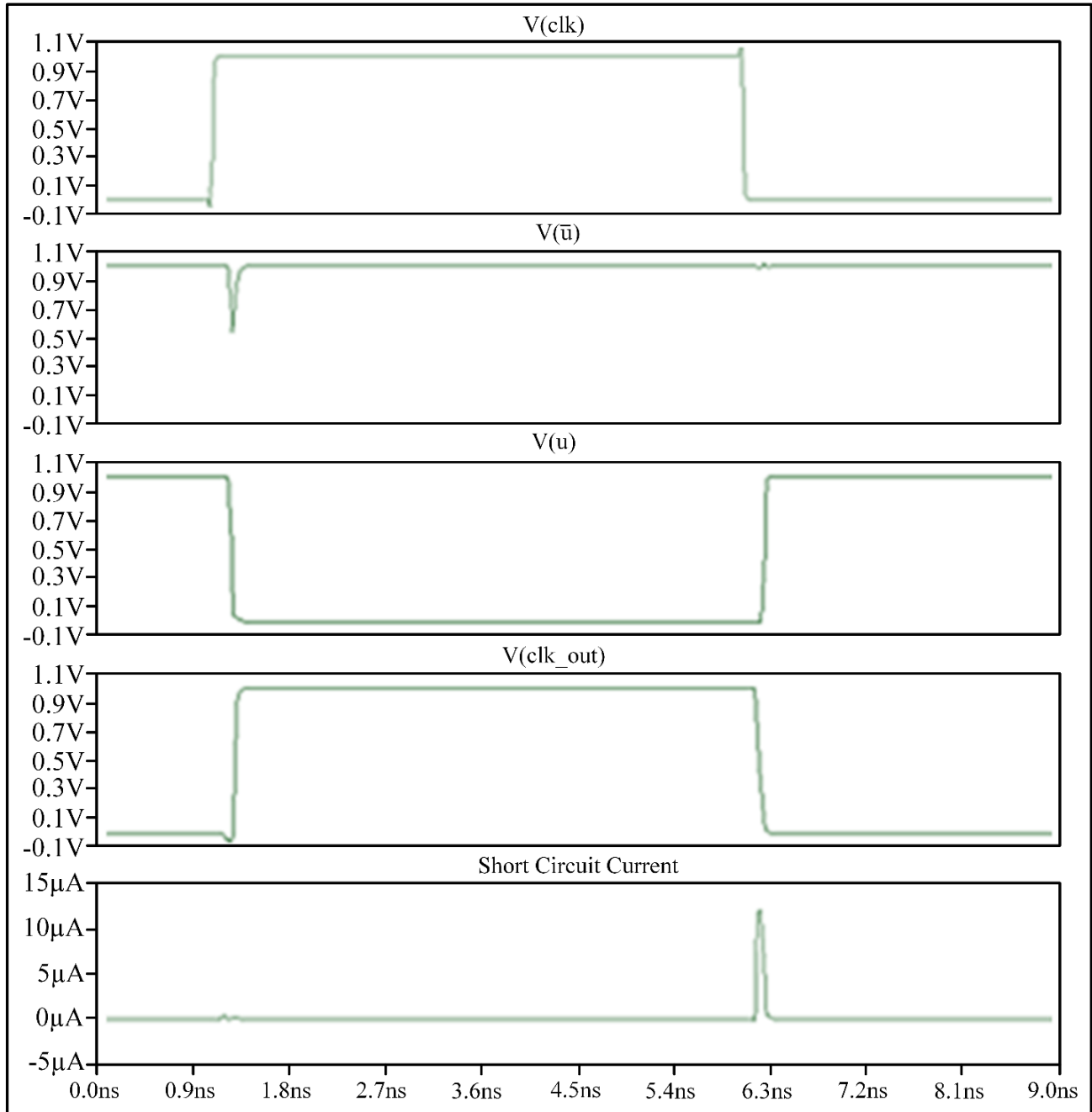


Figure 4. Simulation Results for the proposed Dynamic Clock Generator

3. RESULTS AND DISCUSSION

This section presents a comparative analysis of the delay performance of the TLG when implemented using NAND-based and dynamic circuit-based clock generators. Additionally, energy consumption per clock generation and leakage power are evaluated based on simulation results. The ptm-32nm transistor models (Zhao, 2006) are used. The V_{dd} potential is set to 1V. The simulations are conducted using the LTSPICE simulator. To reduce measurement errors, seven ternary TLG circuits are connected sequentially. The output clock delays are measured for both the circuits using the NAND gate and the proposed dynamic gate. The

choice of seven TLGs is arbitrary and intended solely to ensure that the labels are visually distinguishable in the simulation results. The corresponding simulation results are presented in Figure 5.

The *clk* in Figure 5 is the input clock. The same input clock is applied to both circuits. The clock outputs of the ternary TLG circuits are labeled as *clk_c_i* for the circuits with NAND gates, where $i \in \{1,2, \dots, 7\}$ represents the output of the *i*th TLG. Similarly, *clk_d_i* represents the output of the *i*th ternary TLG with the dynamic circuit, where $i \in \{1,2, \dots, 7\}$. The results obtained from the simulations are tabulated in Table 2.

Table 2. Results

| GATEs | Delay of TLG | | Area of the Gate (nm ²) | Dissipated Energy by the Gate (per Operation, fJ) | Leakage Power (pW) |
|-----------------------|-----------------|------------|-------------------------------------|---|--------------------|
| | Comparison (ps) | Reset (ps) | | | |
| NAND (Celinski, 2002) | 230 | 230 | 13500 | 0.5 | 50 |
| Dynamic (This work) | 215 | 170 | 7425 | 0.8 | 15 |

The ternary TLGs with the NAND gate and the proposed circuit complete their comparison phases in approximately 230ps and 215ps, respectively. The proposed circuit achieves a 6% reduction in delay during the comparison phase. Similarly, the ternary TLGs with the NAND gate and the proposed circuit reset in approximately 230ps and 170ps, respectively, resulting in a 25% reduction in delay during the reset phase. These results indicate that the ternary TLG with the proposed dynamic logic operates faster than the one with the NAND gate. Additionally, the proposed circuitry requires less chip area compared to the NAND gate.

However, the energy consumption of the proposed circuit is slightly higher than that of the NAND gate. While generating a clock signal, the proposed dynamic circuit consumes 0.8fJ, whereas the NAND gate consumes 0.5fJ. In terms of leakage power, the proposed gate offers an advantage. The leakage power of the proposed circuit is 15pW, compared to 50pW for the NAND gate. These results suggest that the proposed gate is a viable alternative to the NAND gate for applications requiring high performance and for scenarios where minimizing static power consumption is critical.

4. CONCLUSION

The proposed dynamic clock generator enhances the overall performance of TLG by reducing propagation delay. One of the advantages of the proposed circuit is its ability to reduce leakage power dissipation, which is an important factor in low-power and energy-efficient circuit design. By minimizing leakage currents, the circuit helps to improve overall power efficiency. This makes the proposed clock generation circuit a suitable choice for modern electronic applications where power consumption is a critical concern. Although the proposed clock generator effectively reduces leakage power, it does exhibit slightly higher energy consumption compared to the NAND gate.

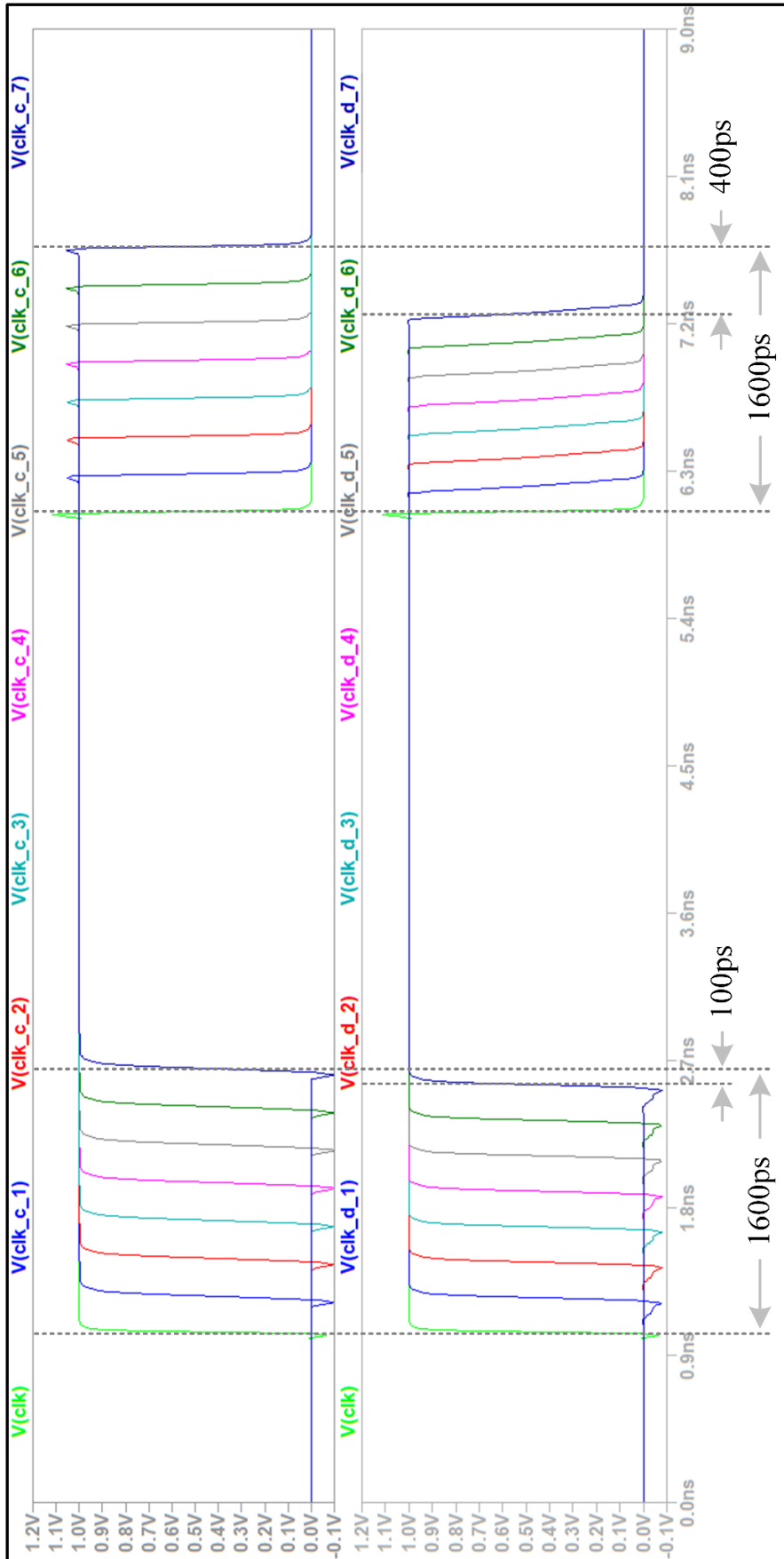


Figure 5. Simulation Results

The trade-off between leakage power reduction and transient energy consumption is an important consideration when evaluating the circuit's suitability for various applications. The overall benefits in terms of performance and power efficiency make the proposed circuit an attractive alternative to the NAND gate, particularly in performance-critical applications where speed and static power consumption are of utmost importance. With the growing demand for high-performance and low-power circuits in emerging technologies, this dynamic clock generator could play an important role in optimizing the operation of threshold logic circuits, making them more efficient and effective in real-world applications.

CONFLICT OF INTEREST

The author declares no conflict of interest.

REFERENCES

- Celinski, P., López, J. F., Al-Sarawi, S., & Abbott, D. (2002). Compact parallel (m, n) counters based on self-timed threshold logic. *Electronics Letters*, *38*(13), 633-635. <https://doi.org/10.1049/el:20020438>
- Han, J. K., Lee, M. W., Yu, J. M., & Choi, Y. K. (2021). A Single Transistor-Based Threshold Switch for a Bio-Inspired Reconfigurable Threshold Logic. *Advanced Electronic Materials*, *7*(5), 2100117. <https://doi.org/10.1002/aelm.202100117>
- Kulkarni, N., Yang, J., Seo, J. S., & Vrudhula, S. (2016). Reducing power, leakage, and area of standard-cell ASICs using threshold logic flip-flops. *IEEE Transactions on very large scale integration (VLSI) systems*, *24*(9), 2873-2886. <https://doi.org/10.1109/tvlsi.2016.2527783>
- Maan, A. K., Jayadevi, D. A. & James A. P., (2016). A survey of memristive threshold logic circuits. *IEEE Transactions on Neural Networks and Learning Systems*, *28*(8), 1734-1746. <https://doi.org/10.1109/tnnls.2016.2547842>
- Mazumder, P., Kang, S.-M. & Waser, R. (2012). *Memristors: Devices, Models and Applications*. In: Proceedings of IEEE, 100 (6), (pp. 1911-1919). <https://doi.org/10.1109/JPROC.2012.2190812>
- Papandroulidakis, G., Serb, A., Khayat, A., Merrett, G. V. & Prodromakis, T. (2019). Practical implementation of memristor-based threshold logic gates. *IEEE Transactions on Circuits and Systems I: Regular Papers*, *66*(8), 3041-3051. <https://doi.org/10.1109/TCSI.2019.2902475>
- Sarkar, M., Chakraborty, R., Taki, G. S., & Chakraborty, A. K. (2021). Design of basic logic gates using optical threshold logic. *Engineering Research Express*, *3*(3), 035021. <https://doi.org/10.1088/2631-8695/ac1903>
- Saxena, P., Shelar, R. S., & Sapatnekar, S. (2007). *Routing Congestion in VLSI Circuits: Estimation and Optimization*. Springer Science & Business Media. <https://doi.org/10.1007/0-387-48550-3>
- Unutulmaz, A., & Ünsalan, C. (2024). Implementation and applications of a ternary threshold logic gate. *Circuits, Systems, and Signal Processing*, *43*(2), 1192-1207. <https://doi.org/10.1007/s00034-023-02512-1>

- Vrudhula, S., Kulkarni, N. & Yang, J. (2015). *Design of threshold logic gates using emerging devices*. In: Proceedings of 2015 IEEE International Symposium on Circuits and Systems, Lisbon, (pp 373–376). <https://doi.org/10.1109/iscas.2015.7168648>
- Wagle, A., & Vrudhula, S. (2021) Heterogeneous FPGA architecture using threshold logic gates for improved area, power, and performance. *IEEE Transactions on Computer-Aided Design of Integrated Circuits and Systems*, 41(6), 1855-1867. <https://doi.org/10.1109/TCAD.2021.3099780>
- Yang, J., Kulkarni, N., Yu, S. & Vrudhula, S. (2014). *Integration of threshold logic gates with RRAM devices for energy efficient and robust operation*, In: Proceedings of 2014 IEEE/ACM International Symposium on Nanoscale Architectures, (pp 39–44).
- Youn, S., Lee, J., Kim, S., Park, J., Kim, K., & Kim, H. (2024). Programmable threshold logic implementations in a memristor crossbar array. *Nano Letters*, 24(12), 3581-3589. <https://doi.org/10.1021/acs.nanolett.3c04073>
- Zhao, W., & Cao, Y. (2006). New generation of predictive technology model for sub-45 nm early design exploration. *IEEE Transactions on Electron Devices*, 53(11), 2816-2823. <https://doi.org/10.1109/ted.2006.884077>



Gazi University

Journal of Science

PART A: ENGINEERING AND INNOVATION

<http://dergipark.org.tr/guj.1624623>

ChainHealth: Blockchain-Based IoT-Edge Model for Secure Management of Health Data

Rukiye Nur ÇAYAN^{1*} Feyza YILDIRIM OKAY¹ ¹ Gazi University, Ankara, Türkiye

| Keywords | Abstract |
|---|--|
| IoT Blockchain Edge Health Data Privacy | The Internet of Things (IoT) is rapidly expanding and seamlessly integrating into our daily lives, with an increasing number of objects connecting to the Internet. It operates as a networked architecture that enables communication between connected devices. IoT applications span various domains, including smart homes, cities, transportation, and healthcare. Among these, smart healthcare is particularly important, allowing specialists to monitor patients remotely, anytime, and anywhere. In this system, patient data is transmitted through networked systems, enabling remote health monitoring. However, significant challenges remain regarding the privacy and integrity of patient health data. This study addresses these challenges by proposing a model named ChainHealth that leverages IoT devices for data collection, edge infrastructure for processing, smart contracts on blockchain to ensure data integrity, and blockchain to store data securely. Experimental results demonstrate that ChainHealth significantly outperforms traditional models in terms of data transmission efficiency, scalability, and overall system performance. The model enhances throughput, reduces latency even as the number of users increases, and strengthens data encryption and transmission processes. Additionally, the smart contract mechanism is evaluated and shown to be reliable for managing data integrity. As a result, the proposed model ensures secure data transfer across the network and secure critical health information. By maintaining data integrity, confidentiality, and security, ChainHealth improves both the quality and reliability of healthcare services compared to traditional approaches. |

Cite

Çayan, R. N., & Okay Yıldırım, F. (2025). ChainHealth: Blockchain-Based IoT-Edge Model for Secure Management of Health Data. *GU J Sci, Part A, 12(1)*, 72-95. doi:10.54287/guj.1624623

Author ID (ORCID Number)

0000-0002-6034-0678 Rukiye Nur ÇAYAN
0000-0002-6239-3722 Feyza YILDIRIM OKAY

Article Process

Submission Date 21.01.2025
Revision Date 18.02.2025
Accepted Date 12.03.2025
Published Date 26.03.2025

1. INTRODUCTION

The innovations of Internet of Things (IoT)-based health technologies have increased the necessity to monitor individuals' health status. With IoT, access to healthcare services becomes more effective, and it brings greater emphasis on the collection and analysis of personal health data. Today, wearable devices such as smartwatches and smartphones enable individuals to monitor their health data continuously. In addition, there are specialized sensors that can also measure the heart rate using electrocardiograms (ECG) and monitor the blood sugar levels (Al-Kahtani et al., 2022). These technologies allow people to monitor their health status themselves in their daily lives and offer immediate access to healthcare services as it is required. Furthermore, continuous monitoring of these data provides opportunities to detect health conditions early and, therefore, intervention as a proactive way of managing an individual's health (Ranjan & Sahana, 2024). The recent studies classify

*Corresponding Author, e-mail: rukiye06nur@gmail.com

health data into four categories: the first category includes the data produced by the medical system, such as electronic medical records, prescriptions, lab data, pathology images, radiographic images, and payer claims data. The second category includes consumer-generated health and wellbeing data from wearable fitness trackers, medical devices such as insulin pumps and pacemakers, health-monitoring applications, and patient-reported outcome surveys, along with types of direct-to-consumer testing (DNA analysis) and treatment (such as insurance) that are not tied to specific health services. The third category encompasses what is referred to as digital exhaust, which arises from a consumer's activities, such as social media posts, search histories, and location data. Although these data are not health-related patterns, they can provide helpful relevant understanding of behaviors and patterns related to health. Lastly, the non-health demographic and socioeconomic data, including age, income, employment status, and education level, fall under the fourth category. Though not health-specific, these data help define broader social determinants pertaining to health and well-being (McGraw & Mandl, 2021). The first two categories contain quite sensitive data because their scope includes personally identifiable information that can easily identify an individual and provide comprehensive insights into their personal health state. With the IoT concept, it becomes easy to collect and share such sensitive data over networks. However, there is a necessity to secure such personal and sensitive information during both transmission and storage due to potential cyberattacks. Furthermore, there are issues rising from the secondary use of these data for privacy and data integrity. The integrity and correctness of these datasets are important in remote treatment, diagnosis, and monitoring. Thus, data security becomes a vital objective for effective healthcare service management (Rayan et al., 2021; Boopathi, 2023). Many different encryption algorithms and security protocols are used to protect such sensitive data. Current research has found the use of multiple technological frameworks for the securing of sensitive data. Especially, the combination of IoT with blockchain and cloud computing constitutes of innovative approaches for data security (Xiang & Cai, 2021; Nowrozy et al., 2024).

Increasing complexity and volume of health data are prompting the need for secure and efficient management, storage, and sharing mechanisms. To address this, the authors propose an innovative model named ChainHealth, which integrates IoT, edge computing, and blockchain technologies to ensure the confidentiality, security, and integrity of sensitive health data. With wearable devices and specialized sensors, the data can be collected in near real-time in order to continuously monitor health metrics while assuring the privacy of the data collection. Also, edge computing allows for processing the data at the local source that minimizing the latencies or risk of the data breach with respect to centralized storage. The decentralized and immutable characteristics of blockchain technology are perfectly aligned with the advantages of edge computing in guaranteeing that health data is kept secure, remains untampered, and is always traceable back to the source. The combination of all these technologies, therefore, provides a robust, secure, and efficient model addressing both privacy and integrity concerns for personal health data, thus further contributing towards a secure ecosystem for healthcare.

The ChainHealth contributes to the literature by offering a comprehensive and combined approach for securing health data, which addresses critical concerns related to privacy and data integrity. The first phase of this model involves encrypting data at the time of collection and securely transferring it to the edge computing infrastructure, thereby protecting against network-level attacks and ensuring data integrity throughout the entire transmission lifecycle. The next phase is the smart contract, which automates decision-making processes based on real-time data analysis to make healthcare much more responsive. The third phase involves the storage of abnormal health data in an immutable ledger, employing blockchain technology for full accountability and transparency. The model, furthermore, maintains health data integrity across networks through its transmission. In the final phase, the system's interface allows authenticated people to provide feedback, subsequently promoting communication streams between patients and healthcare providers. Thus, the model not only strengthens data security but also provides a scalable solution for real-time health interventions. Overall, this model improves conditions for responding to health situations in a more proactive and timely manner, thereby advancing the health ecosystem as a whole.

The rest of this paper is organized as follows: Section II reviews related studies. Section III gives the background information. Then section IV gives important details of the proposed model, and section V presents the performance evaluation and discussion of experimental findings. Finally, section VI summarize the paper with discussions on the results.

2. RELATED WORK

In the past few years, there has been quite an attention about the use of innovative technologies, such as blockchain, for managing health data, especially for protecting confidentiality, security, and integrity, given the sensitive nature of health information. Many research studies have been attempting to see the possibility of combining blockchain with other technologies, especially cloud computing and IoT, for better monitoring, storage, and sharing of health data. Such pioneering studies have created frameworks for security and efficiency in healthcare systems. The section reviews important studies in chronological order that have paved the way for blockchain solutions in healthcare, with an emphasis on health data management, data security, and remote patient monitoring.

Among the initial studies was 'HealthSense' (Dey et al., 2017), which investigated the use of blockchain-based technological applications for remote patient monitoring and securing sensitive health information—patient vital phenomena that originated from the sensors installed in a patient's bed. Such data was stored through a smart contract on a blockchain system. This implementation allowed for input, reading, updating, and writing to the blockchain through a REST-based API. Moreover, it introduced a method for computing final patients' hospital billing using smart contracts. In this relatively simple structure, the blockchain architecture was not specified, nor was a cloud infrastructure utilized.

The study, 'BlockCloud' (Kaur et al., 2018), focused on the storage and processing of heterogeneous health data. According to the study, apart from homogeneous health data, such as heart and blood glucose levels, there were heterogeneous data, which included ECGs and X-Rays. The storage of such kind of diverse data was very challenging on its own, and given the sensitive nature of health data, it required extra attention. The proposed model integrated both blockchain and cloud architecture. The cloud infrastructure processed and analyzed the heterogeneous data, after which the processed data was stored on the blockchain. However, with the cloud infrastructure, storing sensitive data securely was still not viable. Thus, it incorporated blockchain support for securing data.

Research concerning health data has dramatically surged since 2019 through the implementation of blockchain technology into health data. Chakraborty et al. (2019) suggested that health data storage should have been digitized through wearable devices based on a model integrating cloud architecture and blockchain technology. Machine learning algorithms detected abnormalities in the data, ensuring the integrity, privacy, and seamless security of health data. In another study, Dilawar et al. (2019) proposed a model in which doctors remotely monitored patients and added reports through blockchain. These reports were incorporated into the patient's historical data. The study also highlighted the potential high costs associated with storing data collected through remote health systems on the blockchain. As a solution, it was recommended that only the hash values of the data be stored in the blockchain rather than the data itself, minimizing costs. Health data collected via an IoT sensor was processed through an API gateway in conjunction with a smart contract that triggered the proposal of a transaction, as discussed in the study by Bhawiyuga et al. (2019). The peers in the network simulated the transaction proposal, ensuring validation of the transaction prior to recording it on the blockchain. Once the peers approved the transaction proposal, they sent their approvals back to the API gateway, which aggregated the approvals and forwarded them to the orderer. The orderer, upon receiving the approvals, broadcasted the block containing the transaction to all peers, who performed a final validation check of the transaction. This guaranteed confidentiality, security, and integrity of health data. In fact, no cloud structure was utilized; instead, the Hyperledger Fabric blockchain framework was employed as the basis. Identity verification was carried out through a smart contract written in JavaScript. API analysis of that study was done using JMeter at the end of the study. The model proposed by Dwivedi et al. (2019) made IoT, blockchain, and cloud architecture all work together for the privacy and security of health data. Due to the intense computing power required from traditional blockchains, an overlay network was created to mimic the behavior of blockchain instead of working with mining mechanisms. Data was not saved directly but was instead stored on cloud storage servers, and each block of bits was hashed using a Merkle Tree; these data were then sent to nodes in an overlay network that verified and chained the hash values of the blocks. Patients, healthcare providers, and other authorized entities shared data in the network. An expert was automatically notified if anomalies were detected by the smart contract, which monitored the data. Access to a patient's health data remained under the patient's control, and thus the patient could revoke the sharing of such data after treatment. A three-layered model was proposed by Shahnaz et al. (2019), in which electronic health data were

first processed through an initial layer where a smart contract was invoked. A smart contract was written using the Solidity programming language and the Open Zeppelin tool; identity authentication within the system was enabled through the smart contract. Following the authentication process, updates, additions, viewing, and deletion operations occurring in the second layer, the user layer, were recorded on the Ethereum blockchain. The electronic health data contained the essential parameters of an individual, such as identification number, name, blood type, and professional reports constructed as required by the medical personnel for the patient's treatment. These expert reports were stored using a distributed file system protocol known as IPFS. Toward the end of the study, performance testing was conducted using the Apache JMeter tool. The system was tested with 100-500 users, and it was observed that as the number of users increased, the system's efficiency also improved. In another work proposed by Attia et al. (2019), two different blockchain infrastructures were used for this model. The function of the first chain in this model was to store health data collected from wearable sensors, while the second chain was tasked with keeping the entire health history of the patient. Hence, according to the model, both the patients and the healthcare professionals could view information found on the first blockchain, while only the healthcare professional could view information on the second chain. Both of the two chains were based on the Hyperledger Fabric blockchain framework. To enable emergency notifications, a smart contract structure was used, which was written in the Go programming language. The model did not include cloud infrastructure.

In the later study, Satamraju (2020) gave the fundamental aim of keeping health data integrity and preventing unauthorized access to it. This study proposed a three-layer model. The first layer, the application layer, acted as an interface between the IoT devices and the blockchain. The second layer, the business layer, contained all the functionalities. These included functions such as viewing data, pulling prescriptions for a patient, or adding new data. The last layer was the storage layer, where all the data was stored. As a great cost was incurred to keep data and transactions on the blockchain, only transaction data were transferred to the blockchain and all relevant encrypted data were stored in an encrypted database. Ethereum was used as the blockchain structure for the model. The data could be visualized through a user interface; authorized personnel such as doctors, pharmacists, and insurance companies had access to this interface. In a similar study, the model proposed by Khatoon (2020) enabled access to health data by multiple stakeholders. The database contained encrypted and hashed actual values of health data, and hash value records were also kept on the blockchain. Hence, the integrity of the data could be verified by comparing the hash values against each other. The adopted blockchain framework was Ethereum, with data access authorization managed through a smart contract scripted in Solidity. Additionally, all operations performed on the data were recorded on the blockchain. Ismail et al. (2020) proposed a model named BlockHR with faster and safer patient monitoring over existing client-server architectures. The model demonstrated 20 times faster performance than existing client-server systems. Similar to most existing studies, patients could simply add or query data over the network. The advantage of the BlockHR model lay in its predictive tool, which learned from the patient data and made diagnoses based on this information. The data could be controlled and modified only by authorized individuals, with each

transaction being recorded to ensure transparency and accountability. Jamil et al. (2020) proposed a model for visualizing and processing health data collected from seven types of sensors. All of them were accessible only to authenticated individuals. The Hyperledger Fabric blockchain framework served as a backbone to the architecture of this model. The architecture had four layers. The first layer, the sensor layer, was responsible for data collection; the second layer, the network layer, was responsible for transmitting the data collected to the blockchain; the third layer, the blockchain layer, ensured, by means of the smart contract, that it checked whether the data was below the threshold level, with identity authentication handled through this same contract; and, finally, the application layer, which enabled functionality for users to interact with and input data into the system. The performance of this blockchain model was tested using the Caliper tool with 300, 500, and 1000 users, showing improved performance as the number of users increased.

Banotra et al. (2021) stated that the remote healthcare service models based on classical client-server architecture were insecure due to their central authority. Thus, they proposed a four-layered model to provide a secure platform for remote healthcare services: a physical layer where the patients from whom data was collected were situated; a second layer for sensor devices gathering such data; a third layer called the communication layer, which had an Application Programming Interface (API) implemented for sending data to the cloud; and an uppermost layer for normalizing and analyzing the transmitted data. The last layer was called the distributed ledger system, which concerned the data storage, while access to the ledger was possible either through web application or mobile application. Another model proposed by Ngabo et al. (2021) integrated both cloud infrastructure and blockchain technology. Here, health data collected through sensors was encrypted using elliptic curve algorithms and transmitted to a fog computing environment. The use of fog computing helped reduce latency during data transmission. While the data was stored in a cloud computing environment, all transactions performed on the data were recorded on the blockchain, as an authentication mechanism was required to execute these operations. The model also implemented a cloud computing structure that stored copies of transaction records on the blockchain. The subsequent proposed model in the literature was the FogChain model (Mayer et al., 2021). The main aim of this model was for the security of health data. The proposed model shared similarities with the structure of our study and utilized Hyperledger Fabric as the blockchain framework. It also incorporated fog computing architecture. In this particular model, health data collected with patients was sent to the fog computing layer. When data values were outside given threshold values, the fog computing layer processed the data and triggered a smart contract on the blockchain to record it. The adoption of fog computing minimized transmission delay and thereby improved the model's efficiency.

The ERTCA model was suggested in another study by Bataineh et al. (2022) that addressed the security of health data through the integration of rich and thin clients along with blockchain technology. In this model, Ethereum was the blockchain platform, and Proof of Work was the consensus mechanism. This model represented the thin client, which functioned as an IoT device that collected health data and sent it to the

blockchain through an API. A rich client with a larger memory had access to the blockchain and participated in mining activities. No cloud infrastructure was utilized in this model.

As shown by the research by Elvas et al. (2023), the model involved not only patients and specialists but also pharmacies in the process. The major goal of the study was to give the data owner, the patient, the ability to determine those who could access his or her data, thus making the authentication process more secure. It was also supposed to assure security for the data itself. According to the model's operation, after the patient registered and underwent an examination at the hospital, the specialist created a smart contract on the blockchain, encrypting the patient's data and the required medication list, and then storing it on the blockchain. As a result of the examination, the patient did not require second visits to pharmacies because he or she was prescribed the necessary medications. After performing identity authentication, that pharmacy was able to get the medications ready for the patient. This approach made the treatment of patients faster as well as ensuring a safer way of protecting the data. The model did not leverage any cloud infrastructure. A new study proposed by Cheikhrouhou et al. (2023) was conducted in line with the previous research by Jamil et al. (2020), which highlighted the vulnerability of data to attacks while in the network layer. Therefore, Cheikhrouhou et al. (2023) proposed a lightweight blockchain and fog-enabled secure remote patient monitoring system to enhance data security and improve system efficiency. The new approach suggested that data collected by sensors was first stored on a local blockchain and then transferred to a cloud environment for tests against threshold values. If an acceptance condition was met, the data transfer to the global blockchain was initiated. Only authorized individuals could access the two blockchains and modify the database entries, while the cloud kept the information concerning the data and its operations safely. The model used two cloud structures and showed a 40% improvement in response times. Hyperledger Fabric was selected as a blockchain platform. The study further subjected the proposed model to various attack scenarios that included key attacks, replay attacks, and impersonation attacks; and found that the model successfully prevented these threats.

BEHeDaS, introduced by Oladele et al. (2024), was a private blockchain system designed to ensure the secure and transparent storage of healthcare data. Healthcare personnel and patients authenticated themselves using unique usernames and passwords, with authorization managed through the blockchain. Healthcare professionals could access patients' medical histories, diagnose conditions, conduct tests, and upload medical results, which were encrypted and subjected to consensus within the blockchain network. Patients, in turn, could review their medical results and request modifications to their personal data, with such requests being processed only upon approval by network participants. The system operated on a Proof-of-Trust mechanism, which enhanced security through a penalty-based enforcement model, while authentication and authorization were governed by smart contracts. Since it was a P2P-based private blockchain, the system focused on security and data integrity, even though its TPS was lower than that of public blockchains. In the proposed model (Said et al., 2024), which integrated NFTs with Hyperledger Fabric, the process began with the registration of healthcare facilities (clinics, hospitals, laboratories, and pharmacies) on the blockchain network. Patient-

related transactions, including laboratory results, prescriptions, and consultation reports, were securely stored on the blockchain and directly linked to the corresponding patient, ensuring accurate identity verification. Once the patient's identity was authenticated by cross-referencing their identification number with blockchain records, a digitally verified NFT was issued. This NFT served as a cryptographic representation of the patient's validated medical records and enabled healthcare facilities within the network to authenticate identity and access medical data. However, access was time-restricted and automatically expired after a predefined period. Access control policies were enforced through a smart contract developed in Go, ensuring that patients retained control over their data.

All the studies mentioned above are summarized in Table 1. The symbol '✓' denotes that the study is integrated with the respective technology in the corresponding column; conversely, the symbol '-' in the column indicates that there is no such integration. The term NS stands for 'Not Specified', meaning the study does not provide information regarding the integration of technology.

3. BACKGROUND INFORMATION

3.1. IoT systems and Their Vulnerabilities

An IoT device is an Internet-connected device that uses sensors and actuators to collect, store, and share data from the surrounding environment with other devices in the network. Also, through connectivity to other devices, it can access data without human intervention. Another ability is intelligent communication with other devices and making decisions by itself (Torğul et al., 2016). Life cycle of an IoT system usually contains four sequential stages: collecting data using sensors, storing the data in the analyzed way, transmission of the analyzed data back to the device, and the device's response based on the analysis results. The applications are in various fields, from smart homes to healthcare and intelligent transportation systems, and even everyday devices such as coffee machines. However, IoT systems are inherently vulnerable to a range of security threats, including physical, software-based, and Denial of Service (DoS) attacks. Moreover, the networks enabling data sharing among IoT devices are also exposed to security risks stemming from factors such as diverse protocols, multiple data structures, and the limited resources of IoT devices (Dai et al., 2019; Ratta et al., 2021).

3.2. Technological Solutions for IoT Security: Cloud, Edge Computing and Blockchain

A robust and sufficient security framework is required to address the security vulnerabilities in IoT systems and protect the collected sensitive data. Since its emergence in 2007, cloud computing offers different solutions to challenges posed by IoT heterogeneity, decentralization, and resource limitations (Darwish et al., 2019). However, due to its centralized nature, cloud computing has raised some concerns regarding real-time data transfer, which requires high bandwidth and minimal latency (Hamdan et al., 2020). Since 2017, several edge computing frameworks, especially cloudlets, fog computing, and mobile edge computing, have emerged to handle these concerns (Dang et al., 2019). Although edge computing effectively addresses challenges related

to remote resources and services, security and privacy concerns remain paramount. Therefore, some additional technologies like blockchain technology have gained attention for IoT systems.

Table 1. Summary of Recent Studies on IoT-Based Blockchain Models for Health Data

| | Blockchain Type | Cloud Integration | Smart Contract Implementation | Smart Contract Language | Objective |
|-----------------------------|-------------------------|-------------------|-------------------------------|-------------------------|--|
| (Dey et al., 2017) | NS | - | ✓ | NS | Security |
| (Kaur et al., 2018) | NS | ✓ | - | - | Security and storage of heterogeneous data |
| (Chakraborty et al., 2019) | NS | ✓ | - | - | Integrity, privacy, security |
| (Dilawar et al., 2019) | NS | - | - | - | Security |
| (Bhawiya et al., 2019) | Hyperledger Fabric | - | ✓ | Node.js | Confidentiality, security, and integrity |
| (Dwivedi et al., 2019) | NS | ✓ | ✓ | NS | Privacy and security |
| (Shahnaz et al., 2019) | Ethereum | - | ✓ | Solidity | Security, integrity |
| (Attia et al., 2019) | Hyperledger Fabric | - | ✓ | Go | Secured access |
| (Satamraju, 2020) | Ethereum | - | ✓ | Solidity | Security, integrity |
| (Khatoon, 2020) | Ethereum | - | ✓ | Solidity | Privacy, security, availability |
| (Ismail et al., 2020) | Permissioned blockchain | - | ✓ | NS | Confidentiality, integrity, availability |
| (Jamil et al., 2020) | Hyperledger Fabric | - | ✓ | Node.js | Privacy, security, scalability |
| (Banotra et al., 2021) | NS | ✓ | ✓ | NS | Privacy, security |
| (Ngabo et al., 2021) | NS | ✓ | ✓ | NS | Confidentiality, security, privacy |
| (Mayer et al., 2021) | Hyperledger Fabric | ✓ | ✓ | Node.js | Integrity, security, privacy |
| (Bataineh et al., 2022) | Ethereum | - | ✓ | Solidity | Security |
| (Elvas et al., 2023) | Ethereum | - | ✓ | NS | Security and storage of heterogeneous data |
| (Cheikhrouhou et al., 2023) | Hyperledger Fabric | ✓ | ✓ | NS | Privacy, security, confidentiality |
| (Oladele et al., 2024) | Hyperledger Fabric | - | ✓ | Go | Security, interoperability, privacy |
| (Said et al., 2024) | Hyperledger Fabric | - | ✓ | Go | Privacy, security, scalability, interoperability, traceability |
| This Study | Hyperledger Fabric | ✓ | ✓ | Go | Integrity, privacy, security |

Blockchain enables all participants in a distributed network to maintain copies of the generated ledger. Thus, the decentralization in recording information guarantees the integrity and security of data without going through any intermediaries. Initially proposed in 1991 to prevent the forgery of electronic documents, the phrase gradually gained popularity with Bitcoin, which was first developed in 2009 (Nasir et al., 2018; Foschini et al., 2020). Integrity, time-stamping, and immutability of records are ensured through cryptographic techniques, preventing unauthorized modification. The main features of blockchain technology consist of blocks (transactions, timestamps, and cryptographic mechanisms), consensus mechanisms to approve transactions, and smart contracts to automate actions when conditions are satisfied. A variety of consensus protocols such as Proof of Work (PoW), Proof of Stake (PoS), and Practical Byzantine Fault Tolerance (PBFT) have been used for different scenarios (Nasir et al., 2018; Dai et al., 2019; Almagrabi et al., 2021; Tripathi et al., 2023). Together with the fundamental intrinsic features of blockchain like immutability, decentralization, security, anonymity, non-repudiation, and traceability (Atlam et al., 2018; Dai et al., 2019), these mechanisms make blockchain highly useful for securing IoT systems. The specified characteristics are applicable in various categories, including banking, finance, governance, healthcare, logistics and supply chain, food and agriculture, transport, real estate, and education (Tripathi et al., 2023).

These mechanisms prove their effectiveness in securing information storage and privacy within IoT networks, making them one of the best solutions to such security concerns. In particular, Hyperledger Fabric, which has developed into a very renowned open blockchain framework provided by the Linux Foundation, has gained much more importance in the field of IoT system security. It implements a property called a 'channel' to keep the transaction information confidential because it ensures that only the nodes within a specified channel can access the transaction data. Hyperledger Fabric consists of two main data structures: the world state, which keeps current data and gives direct access to the up-to-date information, and the blockchain, which captures the historical changes to the world state, thus making the transaction history transparent and auditable. To summarize, there are three main types of peers within a Fabric network: endorsers, which are responsible for validating transactions; orderers, which organize those transactions; and committer peers, which maintain the ledger (Nasir et al., 2018; Foschini et al., 2020). In addition, Hyperledger Fabric has chaincode (smart contract) development facilities in Go, Java, and Node.js, with recent studies saying that Go is the best language for chaincode development (Foschini et al., 2020).

4. PROPOSED MODEL: CHAINHEALTH

The development of the remote healthcare technology has transformed how medical conditions are monitored and treated, thus ensuring greater flexibility and accessibility for the patients (Boopathi, 2023). Particularly, continuous monitoring of health parameters such as heart rate, blood pressure, and blood glucose levels is increasingly recognized as essential for the effective management of chronic diseases, such as diabetes (Attia et al., 2019). These health conditions require constant and precise monitoring to optimize patient treatment and prevent complications. Among these parameters, the secure tracking and management of blood glucose levels

are particularly important, as they directly impact the patient's ability to control their condition and reduce the risk of chronic health complications (Ranjan & Sahana, 2024).

There are numerous challenges in dealing with remote monitoring of sensitive health data, particularly concerning data security and privacy issues. For patients to continue trusting the healthcare systems, the security of their information from unauthorized access and its integrity during the monitoring process is paramount. In response to the above-mentioned problems, the proposed model, ChainHealth, integrates IoT, edge computing, blockchain, and smart contract. This model focuses on providing a secure, trustworthy, and efficient means of monitoring blood glucose level in such a way that the information is encrypted and tamper-proof during transmission and storage. The phases of the proposed model are described in subsequent sections, depicting how every phase will help secure and efficient monitoring of blood glucose levels and preservation of data integrity with respect to the patient. In Figure 1, the architecture of the proposed model is outlined, giving an overview of the main phases involved in secure monitoring and management of glucose levels using IoT, edge computing, blockchain, and smart contract.

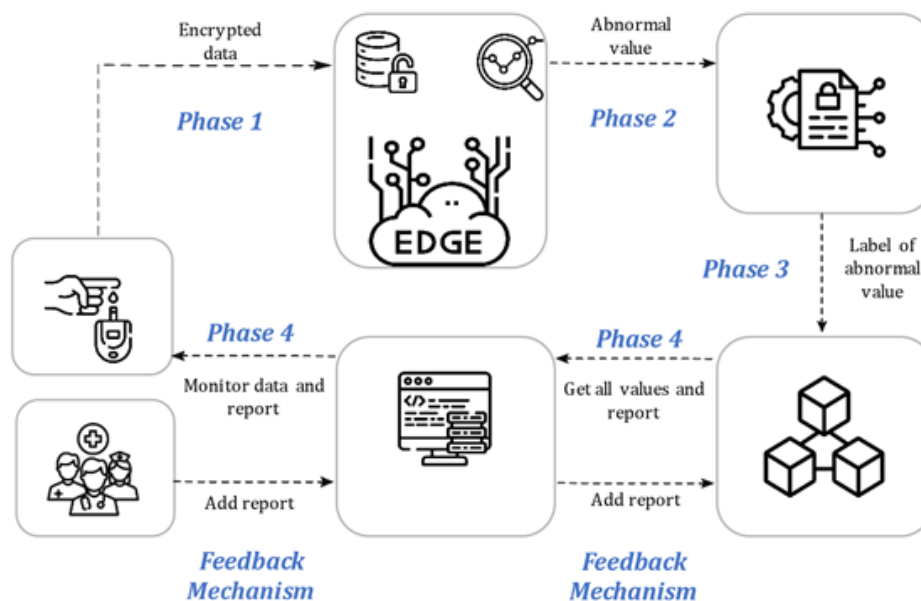


Figure 1. The ChainHealth for secure monitoring and management of blood glucose levels using IoT, edge computing, blockchain, and smart contract

4.1. Phase 1: IoT to Edge Computing

In the first phase, the collection of patient data is done by sensors with the help of IoT devices. Health data is vulnerable to network-based threats because it is highly sensitive. Therefore, encryption must be a key point where data, after being collected by IoT devices, is verified and kept secure during its transmission. The AES algorithm is employed to securely encrypt the data before being transmitted to the edge computing infrastructure. The encryption is such that it guarantees protection of information throughout its entire lifespan:

data collection, and transmission. The mathematical formulation of the encryption mechanism employed in the proposed model is as follows:

Step 1: Generation of AES Key through Diffie-Hellman Key Exchange

In the first step, the IoT device (A), which collects health data, specifically blood glucose levels, from the patient, and the Edge server (B), responsible for processing this data, share a common modulus p and base g . Each party independently selects its private key and exchanges public keys to establish a shared secret.

The IoT device (A) and the Edge server (B) each generate their private keys and exchange their corresponding public keys, as shown in Eq. (1):

$$A_{pub} = g^a \text{ mod } p, \quad B_{pub} = g^b \text{ mod } p \quad (1)$$

Here, A_{pub} and B_{pub} represent the public keys of the IoT device and the Edge server, respectively, while a and b are the private keys of each party.

Both parties then calculate a shared secret key K_{shared} using the Diffie-Hellman key exchange algorithm, as expressed in Eq. (2):

$$K_{shared} = B_{pub}^a \text{ mod } p = A_{pub}^b \text{ mod } p \quad (2)$$

This shared key K_{shared} becomes the common secret key known to both the IoT device and the Edge server. This key is then used to generate an AES key for secure data encryption.

The shared key K_{shared} is subsequently transformed into the AES key, as expressed in Eq. (3):

$$K_{AES} = H(K_{shared}) \quad (3)$$

Here, H denotes a hash function. This function takes the shared key and converts it into a 256-bit AES key.

Step 2: Salt Generation

In the second step, a random salt S_{salt} is generated for key derivation. This salt is an additional security measure to ensure that even if the same AES key is reused across multiple data points, the encryption process remains unique and resistant to attacks, as described in Eq. (4):

$$S_{salt} = \text{GenerateSalt}() \quad (4)$$

The salt S_{salt} helps to prevent the risk of two identical data points (e.g., two identical blood glucose measurements) resulting in the same encrypted output, thus maintaining the confidentiality of the data.

Step 3: Key Derivation

For each new data point (such as a new blood glucose measurement), the AES key is re-derived using the generated S_{salt} and the previously generated AES key K_{AES} . This is achieved using a Key Derivation Function (KDF), which typically involves multiple iterations to enhance security by increasing computational complexity and resistance to brute-force attacks. The derived key $K_{derived}$ is computed as shown in Eq. (5):

$$K_{derived} = \text{KDF}(K_{AES}, S_{salt}, \text{iterations}) \quad (5)$$

Here, the KDF ensures that even if an attacker gains access to one AES key, they cannot easily derive subsequent keys. The number of iterations is chosen to balance security and efficiency, ensuring that the derived key remains resistant to brute-force decryption attempts.

Step 4: Data Encryption

Once the AES key $K_{derived}$ is re-derived, it is used to encrypt the data, such as the patient's blood glucose levels. The encryption process ensures that the data remains confidential and secure during transmission to the Edge server for further analysis, as demonstrated in Eq. (6):

$$E_{AES}(m) = AES(m, K_{derived}) \quad (6)$$

In this equation, m represents the patient's blood glucose measurement. The newly derived AES key $K_{derived}$ guarantees that the encryption process is unique for each data point, even when using the same base AES key. The encrypted data is then transmitted securely to the Edge server for further processing and analysis.

Through this multi-stage process, the proposed model ensures not only the security of the AES key but also the confidentiality of the patient's health data with respect to the blood glucose levels while guaranteeing enhanced performance and scalability in terms of key generation and encryption operations. The pseudocode outlining the described process is presented in Algorithm 1 below:

Algorithm 1: IoT System (Key Generation, Key Exchange, Encryption, and Data Transmission)

```

1: for Every predefined time interval do
2:   Collect environmental data from the IoT sensor (blood sugar level)
3:   Get the current time → currentTime = LocalTime.now()
4:   if 12:00:00 ≤ currentTime ≤ 12:00:10 then
5:     Reject the transmission request
6:   else
7:     Retrieve the secret key from memory cache
8:     Retrieve the salt from memory cache
9:     Derive the AES key using the secret key and salt with a key

```

```
    derivation function (e.g., PBKDF2)
10:    Encrypt the data (e.g., blood sugar level) using the derived AES
    encryption key
11:    Send the encrypted data to the Edge Server for further processing
12:    end if
13: end for
14: for Every midnight (12:00 AM) do
15:    Generate Diffie-Hellman keys for key exchange with the Edge Server
16:    Encrypt the public key using base64 encoding
17:    Wait for the Edge Server's public key
18:    Use Diffie-Hellman to generate a shared secret after receiving the
    Edge Server's public key
19:    Derive the AES secret key from the shared secret
20:    Generate a salt using a key derivation function (e.g., PBKDF2)
21:    Derive the encryption key using the AES secret key and salt
22:    Encrypt the salt using AES encryption
23:    Store the derived secret key and salt in memory cache for future use
24: end for
```

4.2. Phase 2: Edge Computing to Smart Contract

The encrypted data is transmitted to the edge and securely decrypted. As soon as the decryption is completed, a detailed analysis of the data is carried out to determine its value. Based on the outcome of this analysis, the data are categorized according to the anticipated outcome on health. Prior to defining the ranges, real-world health data were analyzed to develop values that accurately reflect prevailing physiological conditions. (Memorial, 2023, accessed January 21, 2025). The classification process involves allocating the data to one of several predefined categories: 'normal', 'caution', 'high', 'very high' or 'emergency.' Data between 70 and 139 is considered to be 'normal'—an indication there is no significant health risk and that the values are within acceptable range. Data in the range of 140-179 is considered to be at 'caution', meaning that there may be a potential risk to health and that this might need close monitoring and/or further investigation. The 'high' category, involving the range 180-199, indicates that the data point toward a significant health issue, for example, the onset of diabetes, and require intervention. Data points classified as 'very high' belong to a range from 200 to 249, which means that intervention is urgently needed, since there are very high levels of a health indicator that pose a great risk. Values exceeding 250 are those that fall under the 'emergency' classification, suggesting an immediate threat to life such as a threatening coma or death-and requiring immediate medical attention. Any data that falls outside the normal range can be classified as abnormal, triggering the smart contract to execute predefined actions, such as sending alerts to medical professionals or implementing other measures to mitigate potential health risks. This system ensures that health data is accurately managed,

allowing for timely interventions and improving overall healthcare outcomes. The process of decrypting the encrypted data on the Edge server is presented in Algorithm 2:

Algorithm 2: Edge Server (Key Generation, Key Exchange, Decryption)

```

1: for Every midnight (12:00 AM) do
2:   Take the IoT system's public key
3:   Use Diffie-Hellman to generate a shared secret after receiving the IoT system's public key
4:   Decrypt the encrypted salt using the AES key
5:   Store the derived secret key and salt in memory cache for future use
6: end for
7: for After receiving valid data from the IoT system do
8:   Retrieve the secret key from memory cache
   (key = keyCache.get("dailySecretKey"))
9:   Retrieve the salt from memory cache
   (salt = keyCacheSalt.get("dailySalt"))
10:  Derive the AES key using the secret key and salt with a key derivation function (e.g.,
PBKDF2)
11:  Decrypt the data (e.g., blood sugar level) using the derived AES encryption key
12: end for

```

4.3. Phase 3: Smart Contract to Blockchain

During Phase 3, the smart contract interacts with the blockchain. The label of abnormal data is securely stored on the blockchain, leveraging its decentralized and immutable nature to ensure data integrity. The blockchain is an open ledger that provides complete security and transparency, since it records all transactions, labels of data and timestamps permanently. Therefore, any modifications to the data can be traced back to the source, which prevents tampering and unauthorized alterations. Functions contained in the smart contract are detailed in Table 2.

Table 2. List of Functions Implemented in the Smart Contract

| Function Name | Description |
|------------------------|---|
| InitLedger() | Initializes the ledger by creating the initial set of records or entries. |
| AddValue() | Adds a new label to the ledger. |
| AddReport() | Allows users to add a new report to the ledger. |
| GetAllValues() | Retrieves all the stored labels in the ledger. |
| GetAllReports() | Retrieves all the reports stored in the ledger. |

4.4. Phase 4: Blockchain to Interface

In Phase 4, abnormal data can be monitored through an interface that can be accessed by patients and authorized individuals. This interface has a time-stamped line graph for data labels, along with a time stamp of when the data was added to the blockchain. In addition, authorized individuals can provide feedback to the patient through this interface. Therefore, it ensures real-time feedback and intervention. More details will be given in the 'Feedback Mechanism' section.

4.5. Feedback Mechanism

The feedback mechanism allows authorized individuals to interact with the blockchain and provide real-time feedback to the patient. The data and labels are projected onto a time-tagged line graph. When an authorized individual clicks on a specific time point on the graph, a status-adding interface is opened. The authorized individual may choose to add statuses based on their own evaluation, such as: "good," "should be monitored," "stable," "consult a doctor," "emergency," or "critical." These statuses are saved in the system and displayed on the patient's interface, organized by their timestamp.

In an emergency situation, another feedback mechanism becomes activated. If an authorized individual assesses a situation to be critical, he or she may assign an "emergency" or "critical" status. Such a notice is then prompted to the patient via email. This mechanism ensures that healthcare providers also give guidance immediately, proactively managing the patient's condition.

5. EXPERIMENTAL EVALUATION

5.1. Experimental Setup

The model for this study was developed using RESTful principles. Both the IoT and edge architectures were experimentally developed using Spring Boot integrated into the IntelliJ IDE. The IoT system described in the model collected and encrypted the data, while the edge system received the encrypted data, decrypted and analyzed it, and triggered the smart contract according to analysis results. In this scenario, AES was used for encryption, while the Diffie-Hellman algorithm was employed for key exchange. The blockchain structure was built on Hyperledger Fabric, following the implementation patterns provided in the fabric samples. The blockchain network was created using Docker containers while its management was done through Docker PS. The smart contract, according to the model, was written using the Go programming language and deployed into the network. Concerning the web application, both React and Spring Boot were utilized. Instead of providing actual blood glucose levels, sensor data between 70 and 250 were randomly generated for simulating glucose measurements and sent using the Postman.

5.2. Experimental Results

5.2.1. Performance Testing of Data Transmission with Apache JMeter

The study tested the transfer process of encrypted data from the IoT domain to the edge infrastructure, using Apache JMeter as a performance testing tool. The application allows simulation of multiple requests and measures the performance of the data transfer process in terms of data encryption, transmission, and processing in the edge environment. Then, the process of data transmission was analyzed on the basis of various performance metrics, throughput, response time, and resource utilization, to enable a broad examination of all stages comprising the full pipeline.

Two different models were evaluated for the test stages of data encryption, transmission, and analysis. The traditional model involves collecting sensor data, which is then secured using AES encryption before being forwarded to an edge computing environment. While AES encryption is set up for ensuring data security, it is computationally expensive, which means long processing times and higher resource consumption. To address these issues, the novel proposed model also uses the same AES encryption but introduces many optimizations to speed up both encryption and transmission processes. These optimizations include parallelization techniques and the use of more efficient data encoding methods, which together reduce encryption time, improve transmission efficiency, and lower latency, all while maintaining the data's security.

To assess the performance of the ChainHealth, it is compared against a traditional model. In the traditional model, the AES key generated at the end of Stage 1 in 'Phase 1: IoT to edge computing' (where Diffie-Hellman is used for key exchange and the AES key is derived) is directly used for encrypting the data. Although this standard AES encryption approach is secure, it lacks the optimizations of the proposed model, such as parallelization and efficient data encoding, resulting in higher computational overhead and slower transmission times. This standard AES encryption approach in the traditional model is represented by Eq. (7), where the data m is encrypted using the AES key K_{AES} generated at the end of Stage 1 in Phase 1.

$$E_{AES}(m) = AES(m, K_{AES}) \quad (7)$$

Table 3 provides an overview of throughput and response times (minimum, maximum, and average) for models at different user counts. As the table indicates, ChainHealth has consistently outperformed the traditional model, with throughput much higher and better scalability as the number of users increases.

The test results highlighted significant differences between the two models in terms of system stability, throughput, and resource utilization. In the traditional model, longer ramp-up times were required to stabilize system performance under load. More specifically, the ramp-up time for 100 users was 600 seconds; for 200 users, it was 1200 seconds; and for 500 users, it was 3000 seconds. The main reason behind this prolonged ramp-up time was the very high computational requirement of AES encryption, which affected the

responsiveness of the system and utilization of resources. The throughput of the traditional model was almost 0.1 requests per second for 100 and 200 users and 0.076 requests per second for 500 users.

Table 3. Response Times and Throughput for Different HTTP Request Implementations

| Models | Number of Users | Ramp-up (sec) | Min. Resp. Time (ms) | Max. Resp. Time (ms) | Average Resp. Time (ms) | Throughput (sec) |
|------------------------------------|-----------------|---------------|----------------------|----------------------|-------------------------|------------------|
| Traditional Model | 100 | 600 | 7 | 266.33 | 17.33 | ≈ 0.1 |
| | 200 | 1200 | 4.33 | 275.33 | 14 | ≈ 0.1 |
| | 500 | 3000 | 5.33 | 220 | 12 | ≈ 0.076 |
| Proposed Model: ChainHealth | 100 | 100 | 8 | 42.66 | 14.33 | ≈ 1.0 |
| | 200 | 200 | 5 | 77.33 | 10 | ≈ 1.0 |
| | 500 | 500 | 2.66 | 71.33 | 5 | ≈ 1.0 |

The test results highlighted significant differences between the two models in terms of system stability, throughput, and resource utilization. In the traditional model, longer ramp-up times were required to stabilize system performance under load. More specifically, the ramp-up time for 100 users was 600 seconds; for 200 users, it was 1200 seconds; and for 500 users, it was 3000 seconds. The main reason behind this prolonged ramp-up time was the very high computational requirement of AES encryption, which affected the responsiveness of the system and utilization of resources. The throughput of the traditional model was almost 0.1 requests per second for 100 and 200 users and 0.076 requests per second for 500 users.

However, in comparison to system optimizations, ChainHealth has attained far better ramp-up times. Measured ramp-up times were 100 seconds, 200 seconds, and 500 seconds for 100, 200, and 500 users, respectively. The throughput of the ChainHealth model was 1 request per second across all user loads. This represents a 900% increase for 100 and 200 users, and a 1216% increase in throughput for 500 users compared to the conventional models. The optimized system has clearly improved encryption due to enhanced throughput and reduced ramp-up times.

The average values were obtained after 10 test runs to build reliability and consistency in evaluating performance. On the one hand, the traditional model performed well under low-load conditions, with increased load it started suffering performance-wise due to resource consumption and latencies. On the other hand, the new model proved to be more scalable and therefore was able to keep performance and throughput stable as user load increased. These results confirm that the proposed model is a more efficient and scalable solution for secure data transmission within an IoT framework. Throughput efficiency of the proposed model highlights the effectiveness of the optimizations in reducing computational overhead and improving overall system performance.

5.2.2. Smart Contract Functionality and Reliability Testing with Postman

The functionality and reliability of performing the implemented smart contract operations were tested using Postman to send HTTP requests to RESTful APIs developed using the Spring Boot framework. There were four major functions of the smart contract: AddValue(), AddReport(), GetAllValues() and GetAllReports(). The AddValue() function is used to add new labels into the ledger, while AddReport() is used to add new reports to the ledger. The GetAllValues() function returns all stored labels while GetAllReports() gives all stored reports. When valid input is given through the AddValue() and AddReport() paths, the system responds with HTTP 200 OK to show proper execution. Otherwise, it returns an HTTP 400 Bad Request on submission of invalid data to prove fault generation and input validation. Performance testing with JMeter, which measures the professional tests and efficiency of smart contract operations, can also be used across multiple conditions. Moreover, they were tested for functionality and reliability of smart contract methods deployed into the Hyperledger Fabric network via HTTP requests sent using Postman. The primary methods of the smart contract are AddValue(), AddReport(), GetAllValues(), and GetAllReports(). Under Spring Boot endpoints, valid data was confirmed with these methods, which then returned an HTTP 200 OK status, indicating successful entry of the data set. Invalid or incomplete submissions return an appropriate HTTP 400 Bad Request status, thus showing that proper input validation and error handling mechanisms are triggered. GetAllValues() and GetAllReports() were also tested. Health data stored on the blockchain for retrieval using these methods were successfully retrieved without error. It can thus be concluded that smart contract functions are strong and reliable in their operation within the blockchain network.

5.3. Discussion

The proposed model has several advantages in secure and efficient data transmission. It integrates AES encryption, edge computing, and blockchain technologies to enhance the security of data, reduce latency, and improve scalability for remote healthcare systems. Glucose levels are continuously monitored, and only abnormal values may be recorded into the blockchain to reduce storage and also network load. The emphasis is on postprandial glucose measurement, which is within the critical period of 1-2 hours after meals when an increase in insulin secretion is expected in response to rising glucose levels in the body (Dimitriadis et al. 2021). Only salient deviations in glucose levels—spikes or dips—are recorded into the blockchain. This selective strategy improves the efficiency of the system by filtering out normal variations and, at the same time allows for the identification of certain abnormal health threats, such as insulin resistance or blood sugar imbalances, which may require some type of intervention. Blockchain technology also guarantees the integrity and immutability of the data against unauthorized access or tampering. A smart contract inbuilt within the system allows real-time analysis and feedback for rapid, effective healthcare interventions for chronic patients. The model also secures data communication among hospitals and other health institutions, improving interoperability of health institutions, and ensuring compliance with data protection regulations globally with GDPR and HIPAA and locally under Turkey's KVKK. Real-time health data sharing can also accelerate clinical decision-making, ultimately leading to better patient outcomes through proactive intervention.

Although it offers several advantages, the proposed model also has limitations that should be considered. The proposed model processes the data through the database rather than real physical IoT sensors and gateways which incurs time-consuming operations on the database. Furthermore, the testing was conducted using the free test network of Hyperledger Fabric, which may not fully reflect the performance characteristics expected from a production-ready system. These limitations are anticipated to be addressed in future iterations of the model, leading to improved performance once actual IoT devices and optimized network configurations are incorporated, removing the need for database-related operations and allowing the system to operate more efficiently in real-world applications. In addition, with the increase in the network and with more health providers and IoT devices onboard, transaction throughput, latency, and computational overhead will also have to be managed very carefully for performance and reliability.

6. CONCLUSION

With a rapid increase in the number of devices, particularly in healthcare, the amount of sensitive data, such as health information, has also increased tremendously. Ensuring the security, privacy, and integrity of this data during transmission and storage is paramount. Existing IoT models are mostly dependent on a centralized server that may lead to high costs and a single point of failure. Such communication lacks secure transmission and is mutable with regard to transactions, leaving it vulnerable to attacks. In this study, a blockchain and edge-based IoT model called ChainHealth is proposed to facilitate healthcare device transactions and communication, as a substitute for traditional IoT models. The proposed model is a hybrid IoT and edge computing blockchain framework, designed to ensure security, privacy, and integrity of data. By incorporating blockchain, the transactions are designed to be immutable and secure, while the communication is encrypted between devices. The proposed model optimizes processing capabilities of the IoT devices due to its decentralized structure. The experimental tests regarding blood glucose level data shows the effectiveness of the model in terms of security, privacy and integrity of health data. This model can be a possible solution for addressing the security and integrity of health data. Consequently, the proposed ChainHealth offers promising solutions to the challenges of secure data management in healthcare and fills a significant gap in healthcare technologies.

Future work could address the model's limitations, expand its application to real-world IoT sensors and gateways for more accurate and dynamic data capture, and integrate advanced networking configurations to improve performance. Additionally, scalability and reliability can be further enhanced, while emerging technologies such as artificial intelligence and machine learning can be incorporated for predictive analytics and improved decision-making. Beyond the healthcare sector, this model may be applied in other fields that require privacy, security, and data integrity, including finance, personal identification systems, and smart cities. These sectors increasingly demand robust and secure data management solutions, positioning the model as a viable option for broader applications.

AUTHOR CONTRIBUTIONS

Methodology and writing-reviewing, R.N.Ç and F.Y.O; editing, F.Y.O; conceptualization and software, R.N.Ç. All authors have read and legally accepted the final version of the article published in the journal.

CONFLICT OF INTEREST

The authors declare no conflict of interest.

REFERENCES

- Al-Kahtani, M. S., Khan, F., & Taekeun, W. (2022). Application of internet of things and sensors in healthcare. *Sensors*, 22(15), 5738. <https://doi.org/10.3390/s22155738>
- Almagrabi, A. O., Ali, R., Alghazzawi, D., AlBarakati, A., & Khurshaid, T. (2021). Blockchain-as-a-Utility for Next-Generation Healthcare Internet of Things. *Computers, Materials & Continua*, 68(1). <https://doi.org/10.32604/cmc.2021.014753>
- Atlam, H. F., Alenezi, A., Alassafi, M. O., & Wills, G. (2018). Blockchain with Internet of Things: Benefits, challenges, and future directions. *International Journal of Intelligent Systems and Applications*, 10(6), 40-48. <https://doi.org/10.5815/ijisa.2018.06.05>
- Attia, O., Khoufi, I., Laouiti, A., & Adjih, C. (2019, June). An IoT-blockchain architecture based on Hyperledger framework for healthcare monitoring application. In *NTMS 2019-10th IFIP International Conference on New Technologies, Mobility and Security* (pp. 1-5). IEEE Computer Society. <https://doi.org/10.1109/NTMS.2019.8763849>
- Banotra, A., Sharma, J. S., Gupta, S., Gupta, S. K., & Rashid, M. (2021). Use of Blockchain and Internet of Things for Securing Data in Healthcare Systems. In K. J. Giri, S. A. Parah, R. Bashir, & K. Muhammad (Eds.), *Multimedia Security: Algorithms for Intelligent Systems* (pp. 255–267). Springer. https://doi.org/10.1007/978-981-15-8711-5_13
- Bataineh, M. R., Mardini, W., Khamayseh, Y. M., & Yassein, M. M. B. (2022). Novel and secure blockchain framework for health applications in IoT. *IEEE Access*, 10, 14914-14926. <https://doi.org/10.1109/ACCESS.2022.3147795>
- Bhawiyuga, A., Wardhana, A., Amron, K., & Kirana, A. P. (2019, December). Platform for integrating Internet of Things based smart healthcare system and blockchain network. In *2019 6th NAFOSTED Conference on Information and Computer Science (NICS)* (pp. 55-60). IEEE. <https://doi.org/10.1109/NICS48868.2019.9023797>
- Boopathi, S. (2023). Internet of things-integrated remote patient monitoring system: Healthcare application. In *Dynamics of swarm intelligence health analysis for the next generation* (pp. 137-161). IGI Global. <https://doi.org/10.4018/978-1-6684-6894-4.ch008>

- Chakraborty, S., Aich, S., & Kim, H. C. (2019, February). A secure healthcare system design framework using blockchain technology. In *2019 21st International Conference on Advanced Communication Technology (ICACT)* (pp. 260-264). IEEE. <https://doi.org/10.23919/ICACT.2019.8701983>
- Cheikhrouhou, O., Mershad, K., Jamil, F., Mahmud, R., Koubaa, A., & Moosavi, S. R. (2023). A lightweight blockchain and fog-enabled secure remote patient monitoring system. *Internet of Things*, *22*, 100691. <https://doi.org/10.1016/j.iot.2023.100691>
- Dai, H. N., Zheng, Z., & Zhang, Y. (2019). Blockchain for Internet of Things: A survey. *IEEE internet of things journal*, *6*(5), 8076-8094. <https://doi.org/10.1109/JIOT.2019.2920987>
- Dang, L. M., Piran, M. J., Han, D., Min, K., & Moon, H. (2019). A survey on Internet of Things and cloud computing for healthcare. *Electronics*, *8*(7), 768. <https://doi.org/10.3390/electronics8070768>
- Darwish, A., Hassanien, A. E., Elhoseny, M., Sangaiah, A. K., & Muhammad, K. (2019). The impact of the hybrid platform of Internet of Things and cloud computing on healthcare systems: Opportunities, challenges, and open problems. *Journal of Ambient Intelligence and Humanized Computing*, *10*, 4151-4166. <https://doi.org/10.1007/s12652-017-0659-1>
- Dey, T., Jaiswal, S., Sunderkrishnan, S., & Katre, N. (2017, December). HealthSense: A medical use case of Internet of Things and blockchain. In *2017 International Conference on Intelligent Sustainable Systems (ICISS)* (pp. 486-491). IEEE. <https://doi.org/10.1109/ISS1.2017.8389459>
- Dilawar, N., Rizwan, M., Ahmad, F., & Akram, S. (2019). Blockchain: Securing Internet of Medical Things (IoMT). *International Journal of Advanced Computer Science and Applications*, *10*(1), 82-89. <https://doi.org/10.14569/IJACSA.2019.0100110>
- Dimitriadis, G. D., Maratou, E., Kountouri, A., Board, M., & Lambadiari, V. (2021). Regulation of postabsorptive and postprandial glucose metabolism by insulin-dependent and insulin-independent mechanisms: an integrative approach. *Nutrients*, *13*(1), 159. <https://doi.org/10.3390/nu13010159>
- Dwivedi, A. D., Srivastava, G., Dhar, S., & Singh, R. (2019). A decentralized privacy-preserving healthcare blockchain for IoT. *Sensors*, *19*(2), 326. <https://doi.org/10.3390/s19020326>
- Elvas, L. B., Serrão, C., & Ferreira, J. C. (2023). Sharing health information using a blockchain. *Healthcare*, *11*(2), 170. <https://doi.org/10.3390/healthcare11020170>
- Foschini, L., Gavagna, A., Martuscelli, G., & Montanari, R. (2020, June). Hyperledger fabric blockchain: Chaincode performance analysis. In *ICC 2020-2020 IEEE International Conference on Communications (ICC)* (pp. 1-6). IEEE. <https://doi.org/10.1109/ICC40277.2020.9149080>
- Hamdan, S., Ayyash, M., & Almajali, S. (2020). Edge-computing architectures for Internet of Things applications: A survey. *Sensors*, *20*(22), 6441. <https://doi.org/10.3390/s20226441>
- Ismail, L., Materwala, H., & Sharaf, Y. (2020, October). Blockhr—a blockchain-based healthcare records management framework: Performance evaluation and comparison with client/server architecture. In *2020 International Symposium on Networks, Computers and Communications (ISNCC)* (pp. 1-8). IEEE. <https://doi.org/10.1109/ISNCC49221.2020.9297216>

- Jamil, F., Ahmad, S., Iqbal, N., & Kim, D. H. (2020). Towards a remote monitoring of patient vital signs based on IoT-based blockchain integrity management platforms in smart hospitals. *Sensors*, 20(8), 2195. <https://doi.org/10.3390/s20082195>
- Kaur, H., Alam, M. A., Jameel, R., Mourya, A. K., & Chang, V. (2018). A proposed solution and future direction for blockchain-based heterogeneous medicare data in cloud environment. *Journal of Medical Systems*, 42, 1-11. <https://doi.org/10.1007/s10916-018-1007-5>
- Khatoon, A. (2020). A blockchain-based smart contract system for healthcare management. *Electronics*, 9(1), 94. <https://doi.org/10.3390/electronics9010094>
- Mayer, A. H., Rodrigues, V. F., da Costa, C. A., da Rosa Righi, R., Roehrs, A., & Antunes, R. S. (2021). Fogchain: A fog computing architecture integrating blockchain and Internet of Things for personal health records. *IEEE Access*, 9, 122723–122737. <https://doi.org/10.1109/ACCESS.2021.3109822>
- McGraw, D., & Mandl, K. D. (2021). Privacy protections to encourage use of health-relevant digital data in a learning health system. *NPJ Digital Medicine*, 4(1), 2. <https://doi.org/10.1038/s41746-020-00362-8>
- Memorial. (2023, July 3). Tokluk kan şekeri kaç olmalı? Memorial. (Accessed:21/01/2025) [URL](#)
- Nasir, Q., Qasse, I. A., Abu Talib, M., & Nassif, A. B. (2018). Performance analysis of Hyperledger fabric platforms. *Security and Communication Networks*, 2018(1), 3976093. <https://doi.org/10.1155/2018/3976093>
- Ngabo, D., Wang, D., Iwendi, C., Anajemba, J. H., Ajao, L. A., & Biamba, C. (2021). Blockchain-based security mechanism for the medical data at fog computing architecture of Internet of Things. *Electronics*, 10(17), 2110. <https://doi.org/10.3390/electronics10172110>
- Nowrozy, R., Ahmed, K., Kayes, A. S. M., Wang, H., & McIntosh, T. R. (2024). Privacy preservation of electronic health records in the modern era: A systematic survey. *ACM Computing Surveys*, 56(8), 1-37. <https://doi.org/10.1145/3653297>
- Oladele, J. K., Ojugo, A. A., Odiakaose, C. C., Emordi, F. U., Abere, R. A., Nwozor, B., ... & Geteloma, V. O. (2024). BEHedas: A blockchain electronic health data system for secure medical records exchange. *Journal of Computing Theories and Applications*, 1(3), 231-242. <https://doi.org/10.62411/jcta.9509>
- Ranjan, R., & Sahana, B. C. (2024). A comprehensive roadmap for transforming healthcare from hospital-centric to patient-centric through healthcare Internet of Things (IoT). *Engineered Science*, 30, 1175. <https://doi.org/10.30919/es1175>
- Ratta, P., Kaur, A., Sharma, S., Shabaz, M., & Dhiman, G. (2021). Application of blockchain and internet of things in healthcare and medical sector: applications, challenges, and future perspectives. *Journal of Food Quality*, 2021(1), 7608296. <https://doi.org/10.1155/2021/7608296>
- Rayan, R. A., Tsagkaris, C., & Iryna, R. B. (2021). The Internet of Things for Healthcare: Applications, Selected Cases, and Challenges. In *IoT in Healthcare and Ambient Assisted Living* (pp. 1-15). Springer. https://doi.org/10.1007/978-981-15-9897-5_1

- Said, H. E., Al Barghuthi, N. B., Badi, S. M., Hashim, F., & Girija, S. (2024, August). Developing a Decentralized Blockchain Framework with Hyperledger and NFTs for Secure and Transparent Patient Health Records. In *The International Conference on Innovations in Computing Research* (pp. 478-489). Cham: Springer Nature Switzerland. https://doi.org/10.1007/978-3-031-65522-7_42
- Satamraju, K. P. (2020). Proof of concept of scalable integration of Internet of Things and blockchain in healthcare. *Sensors*, 20(5), 1389. <https://doi.org/10.3390/s20051389>
- Shahnaz, A., Qamar, U., & Khalid, A. (2019). Using blockchain for electronic health records. *IEEE Access*, 7, 147782-147795. <https://doi.org/10.1109/ACCESS.2019.2946373>
- Torğul, B., Şağbanşua, L., & Balo, F. B. (2016). Internet of Things: A survey. *International Journal of Applied Mathematics Electronics and Computers, Special Issue-1*, 104-110. <https://doi.org/10.18100/ijamec.267197>
- Tripathi, G., Ahad, M. A., & Casalino, G. (2023). A comprehensive review of blockchain technology: Underlying principles and historical background with future challenges. *Decision Analytics Journal*, 100344. <https://doi.org/10.1016/j.dajour.2023.100344>
- Xiang, D., & Cai, W. (2021). Privacy protection and secondary use of health data: Strategies and methods. *BioMed Research International*, 2021(1), 6967166. <https://doi.org/10.1155/2021/6967166>



Gazi University

Journal of Science

PART A: ENGINEERING AND INNOVATION

<http://dergipark.org.tr/guj.1646993>

Effective Maintenance of Industrial 5-Stage Compressor: A Machine Learning Approach

Okechukwu Chiedu EZEANYIM¹  Nnamdi Vitalis EWUZIE¹  Patrick Sunday AGUH¹  Chibuzo Victoria NWABUEZE²  Charles Onyeka NWAMEKWE^{1*} 

¹ Nnamdi Azikiwe University, Awka, Nigeria

² University of the People, Pasadena, USA

Keywords

Cost-Effective Maintenance
Industrial Compressor
Machine Learning
Predictive Maintenance
Data-Driven Maintenance
Maintenance Optimization

Abstract

Effective maintenance is crucial in the manufacturing industry to ensure equipment reliability, product quality, and worker safety. This study focuses on using machine learning, specifically the Random Forest algorithm, to predict maintenance needs for a 5-stage compressor. Utilizing the Scikit-learn Python toolkit, the model underwent rigorous evaluation through validation, sampling, and confusion matrix inspection. The model achieved an outstanding ROC AUC score of 0.94 and consistently high accuracy, precision, recall, and F1-score metrics above 0.90, showcasing its strong predictive capabilities. By accurately predicting machine failures, the approach aims to improve production schedules, boost productivity, ensure high-quality outputs, save costs, and extend equipment lifespan, demonstrating significant promise for practical use in the manufacturing sector.

Cite

Ezeanyim, O. C., Ewuzie, N. V., Aguh, P. S., Nwabueze, C. V., & Nwamekwe, C. O. (2025). Article Title. *GU J Sci, Part A, 12(1)*, 96-118. doi:[10.54287/guj.1646993](https://doi.org/10.54287/guj.1646993)

Author ID (ORCID Number)

[0000-0001-6469-7044](https://orcid.org/0000-0001-6469-7044) Okechukwu Chiedu EZEANYIM
[0009-0006-2903-2884](https://orcid.org/0009-0006-2903-2884) Nnamdi Vitalis EWUZIE
[0009-0000-1864-9041](https://orcid.org/0009-0000-1864-9041) Patrick Sunday AGUH
[0009-0004-5508-3541](https://orcid.org/0009-0004-5508-3541) Chibuzo Victoria NWABUEZE
[0009-0002-1918-1350](https://orcid.org/0009-0002-1918-1350) Charles Onyeka NWAMEKWE

Article Process

Submission Date 26.02.2025
Revision Date 07.03.2025
Accepted Date 12.03.2025
Published Date 26.03.2025

1. INTRODUCTION

1.1. Background and Motivation

Industrial compressors play a crucial role in various industries by compressing gases for a wide range of applications. These compressors have evolved significantly over time, incorporating advanced materials and technologies to improve their performance and reliability (Kagiri et al., 2018). Proper maintenance of these compressors is essential to ensure their longevity and efficiency. Research has shown that factors such as compressor switching frequency can impact maintenance costs and the lifespan of the compressor. Implementing improvement recommendations can result in substantial energy and cost savings while enhancing overall system performance. Strategies like reliability-centered maintenance (RCM) and online fault diagnosis systems have been suggested to optimize maintenance practices and improve compressor reliability

*Corresponding Author, e-mail: co.nwamekwe@unizik.edu.ng

cost-effectively (Luo, 2004). Furthermore, the integration of machine learning techniques for fault detection and anomaly classification can further enhance maintenance practices for industrial compressors (Loukopoulos et al., 2019).

Predictive maintenance through machine learning is crucial for enhancing equipment reliability and minimizing downtime in multi-stage compressors used across various industries. Due to the unique characteristics and failure modes of each compressor stage, a tailored machine learning model is essential for effective predictive maintenance. This research focuses on developing a machine learning based predictive maintenance strategy specifically for multi-stage compressors to optimize performance and reliability (Garcia and Salgado, 2021).

Predictive maintenance through machine learning is essential for optimizing the performance of multi-stage compressors in various industries. These compressors, with their complex operating dynamics and unique characteristics at each stage, require tailored predictive maintenance strategies to ensure reliability and efficiency. The research focuses on developing machine learning based predictive maintenance specifically for multi-stage compressors to address the challenges of inconsistent predictions and maintenance recommendations. Time-series data are utilized in this research to capture different observations recorded from the machine over time (Kiangala and Wang, 2020; Nwamekwe et al., 2024).

1.2. Purpose of Study

This research aims to develop an effective maintenance strategy for a 5-stage compressor through the application of a machine learning approach. The process involves collecting historical data and performing data cleaning and preprocessing to address missing values, outliers, and inconsistencies. The refined dataset is then divided into training and testing subsets. Using the Random Forest (RF) algorithm, the model is trained, and both parameters and hyperparameters are optimized. The model's performance is examined with metrics like accuracy, precision, recall, F1 score, Cohen's Kappa, Matthew's Correlation Coefficient (MCC), and the Area Under the Receiver Operating Characteristic Curve (AUC-ROC) (Hanif and Gunawan, 2022; Wang et al., 2022).

2. LITERATURE REVIEW

2.1. Industrial Compressor Maintenance Strategies

Effective maintenance of industrial compressors is critical to ensuring operational efficiency, reducing downtime, and minimizing maintenance costs. Maintenance strategies have evolved from traditional reactive methods to more advanced predictive approaches.

2.2. Overview of conventional and modern maintenance techniques

Conventional maintenance approaches for industrial machinery, including 5-stage compressors, generally fall under three categories: reactive, preventive, and predictive maintenance. Reactive maintenance, employed

post-failure, is cost-efficient upfront but can incur higher long-term operational costs and unplanned downtimes (Monye et al., 2023). In contrast, preventive maintenance involves scheduled inspections and replacements intended to avert breakdowns. While effective in reducing unexpected failures, this method may lead to over-maintenance, thereby elevating costs unnecessarily (Carvalho et al., 2019).

Modern maintenance techniques, particularly predictive maintenance (PdM), utilize advanced data analytics and machine learning algorithms to forecast equipment failures based on real-time data (Cao et al., 2024). This proactive strategy not only extends equipment lifespan but also diminishes unplanned downtimes, thus enhancing operational efficiency (Carvalho et al., 2019; Nwamekwe and Okpala, 2025). The evolution towards PdM represents a significant departure from traditional methods, promoting a more sustainable and cost-effective approach to industrial maintenance (Monye et al., 2023).

2.3. Importance of Effective Maintenance in 5-Stage Compressors

Effective maintenance of industrial 5-stage compressors is essential for optimizing energy consumption, reducing operational costs, increasing lifespan and reliability, and minimizing unplanned downtimes (Bacak et al., 2023; Nordal and El-Thalji, 2021). Such compressors are utilized in critical industrial applications, where precise control at each stage is pivotal. The incorporation of machine learning (ML) into maintenance strategies facilitates enhanced predictive diagnostics, leading to improved decision-making. These ML models utilize algorithms such as Random Forest, Support Vector Machines (SVM), and Neural Networks (Kiangala and Wang, 2020). By analysing historical and real-time data, these models effectively identify operational patterns and predict potential failures, contributing to improvements in accuracy for failure detection and maintenance scheduling (Kiangala and Wang, 2020).

Furthermore, the integration of AI into predictive maintenance allows for advanced fault diagnosis through anomaly detection, ultimately enhancing the overall operational safety and efficiency of machinery (Bacak et al., 2023; Nordal and El-Thalji, 2021). This shift towards machine learning-based predictive maintenance highlights its importance in transforming traditional maintenance paradigms within industrial settings.

2.4. Common Criteria in Compressor Maintenance

Several key parameters are essential in assessing compressor health.

Vibration analysis: is critical for identifying issues such as misalignment, bearing faults, and rotor imbalance, aligning with standards outlined in ISO 10816-3, which offers guidelines for vibration monitoring in rotating machinery (Rahman et al., 2022). Temperature monitoring: plays a significant role in detecting overheating due to lubrication issues or friction, as supported by findings in condition monitoring literature (Adetunji et al., 2023). Pressure variations: can indicate leaks or inefficiencies, further highlighting the importance of a holistic approach to maintenance (Kolar et al., 2022). Acoustic emissions: provide insights into mechanical

wear. Oil and lubricant analysis: is vital for detecting contamination and degradation of internal components (Septano et al., 2024).

To ensure best practices in the industry, adherence to relevant standards such as API 618 for reciprocating compressors and ASHRAE guidelines for energy efficiency in compressor systems is paramount (Bahtiar et al., 2022). Additionally, the incorporation of IIoT technologies enhances predictive maintenance through real-time monitoring and AI-driven analytics, facilitating smarter maintenance decisions (Yamada et al., 2023).

3. MATERIAL AND METHOD

This experimental study follows the CRISP-DM methodology, as illustrated in Figure 1. The CRISP-DM (Cross-Industry Standard Process for Data Mining) framework is a recognized and extensively utilized model for guiding data mining and data science initiatives. It offers a systematic and iterative process comprising six key stages: Business Understanding, Data Understanding, Data Preparation, Modeling, Evaluation, and Deployment. Figure 2 is the research flowchart, which explains every step taken to achieved the purpose of this research.

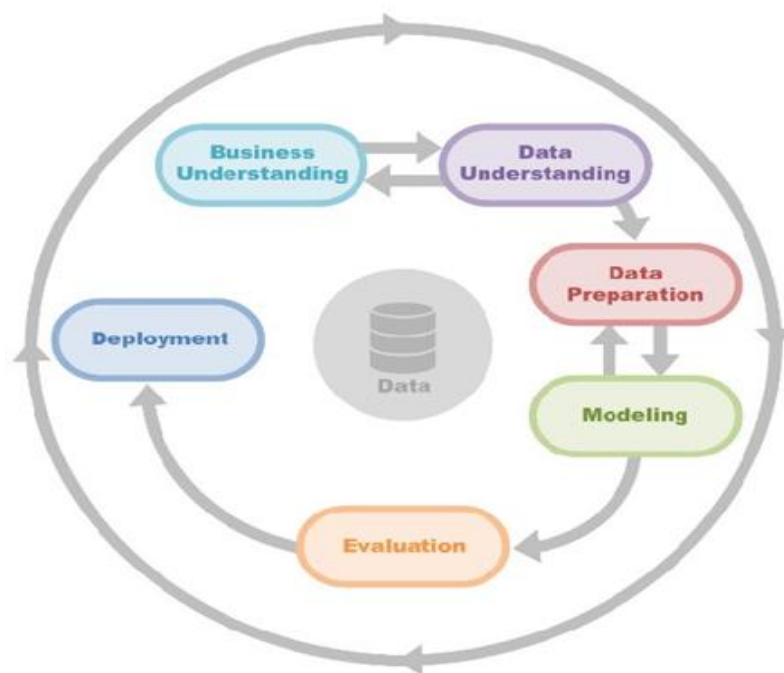


Figure 1. Diagram Illustrating CRISP-DM Flowchart (Tounsi et al., 2020)

This experimental study follows the CRISP-DM framework, as illustrated in Figure 1. The analysis was conducted in Google Colab using Python, along with libraries such as Scikit-learn, Matplotlib, NumPy, Pandas, and Seaborn. Scikit-learn is a versatile library for machine learning and predictive data analysis, offering a wide range of tools for tasks such as classification and model evaluation. Matplotlib serves as a library for creating plots and visualizations, while Pandas is employed for data manipulation and analysis. Seaborn, built on top of Matplotlib, enhances data visualization capabilities. The final dataset, Indorama-EPCL, comprises 98,794 records.

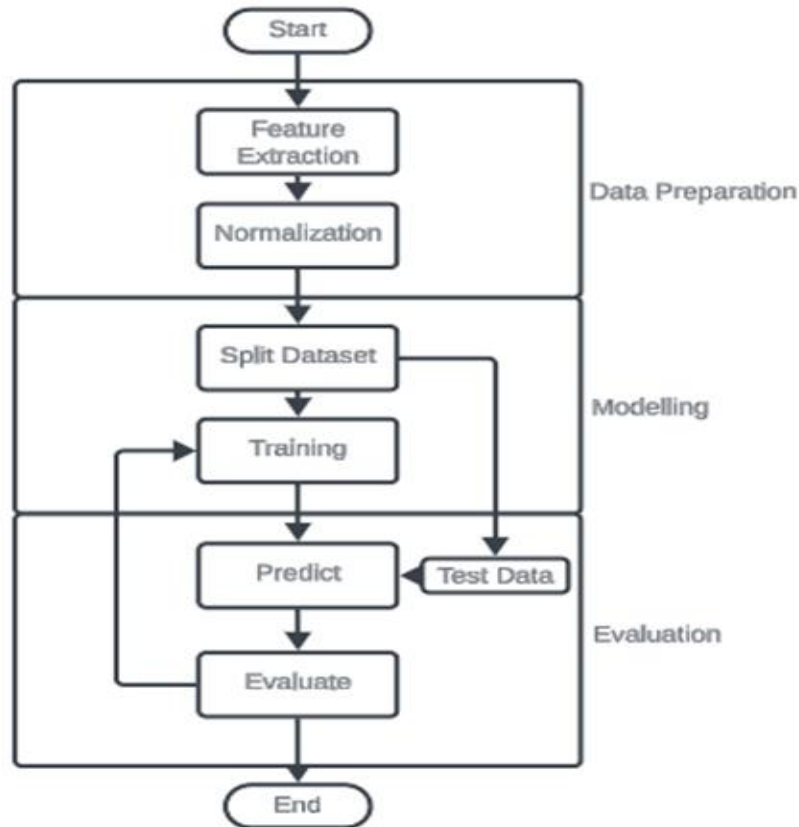


Figure 2. Experimental Flow Diagram

3.1. Business Understanding

This phase serves as a foundational step in the CRISP-DM process, focusing on a comprehensive assessment of the problem, objectives, and requirements. The primary aim of this research is to create advanced machine learning models that enhance engineers' ability to predict potential failures in the 5-stage compressor (K1), a vital component of Indorama-EPCL's operations. This initiative seeks to minimize failure rates, unplanned downtime, safety hazards, and maintenance expenses. The phase entails defining clear success metrics, reviewing current practices through literature analysis, and establishing evaluation criteria in collaboration with engineering stakeholders. Additionally, it involves gaining an in-depth understanding of the compressor's maintenance operations and decision-making frameworks within the organization. The insights gathered are documented to provide a detailed roadmap for subsequent activities such as data mining, modeling, and deployment, ensuring the solutions align with the practical needs and challenges faced by the engineering team.

3.1.1. Data Collection

A csv files of maintenance datasets were received from Indorama-Elemento Petrochemical Ltd. Due to a non-disclosure agreement, the variable names in the dataset were recoded to prevent exposure of critical attributes of the equipment in the facility. The datasets consist of maintenance history of several rotary equipment in the facility. However, the history of the gas compressor, K-1, was carefully filtered out from the data collected as in table 1.

Table 1. First 5 rows in the dataset

| S/N | Date | M2 | M3 | M4 | M5 | M6 | M7 | M8 | M9 | M10 | Failure |
|-----|------------|----------|----|----|----|----|--------|----|----|-----|---------|
| 1 | 01,01,2015 | 2.16E+08 | 55 | 0 | 52 | 6 | 407438 | 0 | 0 | 7 | 0 |
| 2 | 01,02,2015 | 1650864 | 56 | 0 | 52 | 6 | 407438 | 0 | 0 | 7 | 0 |
| 3 | 01,03,2015 | 1.24E+08 | 56 | 0 | 52 | 6 | 407438 | 0 | 0 | 7 | 0 |
| 4 | 01,04,2015 | 1.28E+08 | 56 | 0 | 52 | 6 | 407439 | 0 | 0 | 7 | 0 |
| 5 | 01,05,2015 | 97393448 | 56 | 0 | 52 | 6 | 408114 | 0 | 0 | 7 | 0 |

3.1.2. Exploratory Data Analysis (EDA)

The Table 2 below presents a detailed summary of the data, revealing substantial variability covering the 10 features (M2 to M10) and the target variable "Failure". The consistent count of 98,794 observations indicates a complete dataset, while the wide range in mean values from 0.000086 to 12.464093 and standard deviations from 7.032454e+07 to 160.507272 suggest diverse feature distributions. Further insights emerge from the minimum, maximum, and percentile values, which highlight skewness and the presence of potential outliers in certain features. This detailed statistical analysis will offer valuable guidance for data preparation, feature engineering, and modelling decisions to effectively address the problem at hand.

Table 2. Features Attributes Table

| | Failure | M2 | M3 | M4 | M5 | M6 | M7 | M8 | M9 | M10 |
|-------|---------|----------|----------|----------|----------|----------|----------|----------|----------|----------|
| count | 98794 | 98794 | 98794 | 98784 | 98794 | 98794 | 98794 | 98791 | 98791 | 98794 |
| mean | 0.00086 | 1.22E+08 | 166.9919 | 12.46409 | 1.891976 | 13.61847 | 254441.8 | 0.290897 | 0.290897 | 13.51982 |
| std | 0.02932 | 7.03E+07 | 2242.806 | 328.6816 | 20.73857 | 14.52715 | 93644.26 | 7.921502 | 7.921502 | 160.5073 |
| min | 0 | 0 | 0 | 0 | 0 | 2 | 0 | 0 | 0 | 0 |
| 25% | 0 | 6.15E+07 | 0 | 0 | 0 | 8 | 220916.3 | 0 | 0 | 0 |
| 50% | 0 | 1.23E+08 | 0 | 0 | 0 | 10 | 248626 | 0 | 0 | 0 |
| 75% | 0 | 1.83E+08 | 0 | 0 | 0 | 12 | 301876 | 0 | 0 | 0 |
| max | 1 | 2.44E+08 | 64968 | 80000 | 1666 | 98 | 689161 | 832 | 832 | 10137 |

The histogram for the feature M10 in Figure 3 displays an imbalanced distribution, where most values are clustered toward the lower end of the spectrum and a long, drawn-out tail extending to the right. The extensive value span, from around 0 to 5,000, indicates a wide variation in the feature, while the prominent peak suggests a concentration of values around a particular range, likely representing the most common occurrences. The relative scarcity of data points at the upper part of the value range implies that extreme or outlier values for M10 may be less prevalent compared to the more frequent, lower-range values.

Figure 4 provides a clear visual summary of the statistical distribution of the various features in the dataset. The wide range of values and disparate interquartile ranges across the features suggest significant divergency, with some variables exhibiting outliers and skewed distributions. Features like M2 have considerably larger value ranges compared to others.

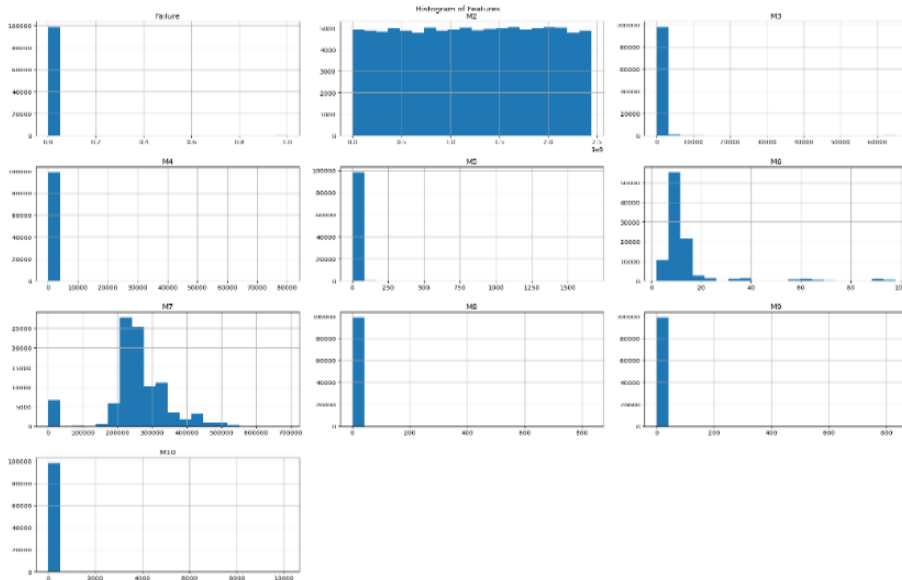


Figure 3. Histogram of features

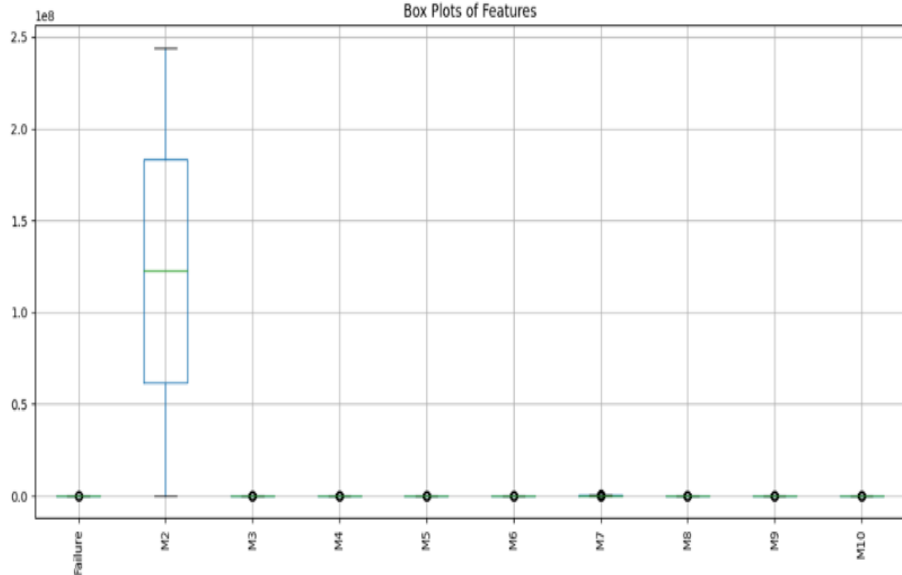


Figure 4. Box plots of features

Figure 5 is a collection of scatter plots, each depicting the statistical distribution and relationships between various features or variables in the dataset. The wide disparity in the scales, data densities, and patterns across the different subplots can also be seen here. Some subplots exhibit clear linear or curvilinear trends, while others show more scattered, irregular distributions with potential outliers and anomalies.

The correlation matrix as in Figure 6 provides a concise statistical overview of the relationships between the different features (M1 to M10) and the target variable "Failure" in the dataset. The values in the matrix range from -0.0033 to 1.0, indicating a wide spectrum of correlations, from weakly associated to strongly correlated. Notable observations include the relatively moderate correlation of M4 and M10 with Failure (0.45). Conversely, several features like M1, M2, and M3 exhibit very low correlations, near 0, implying little to no linear association with the target variable.

Finally, the combination of histograms, scatter plots, time series, and value distributions in Figure 7 once again provides valuable insights into the diverse characteristics of the features. The histograms and scatter plots reveal the varying value ranges, shapes, and bivariate relationships, highlighting the heterogeneity in the data. The time series and value plots further underscore the dynamic nature of the dataset, showcasing fluctuations, patterns, and skewness over time.

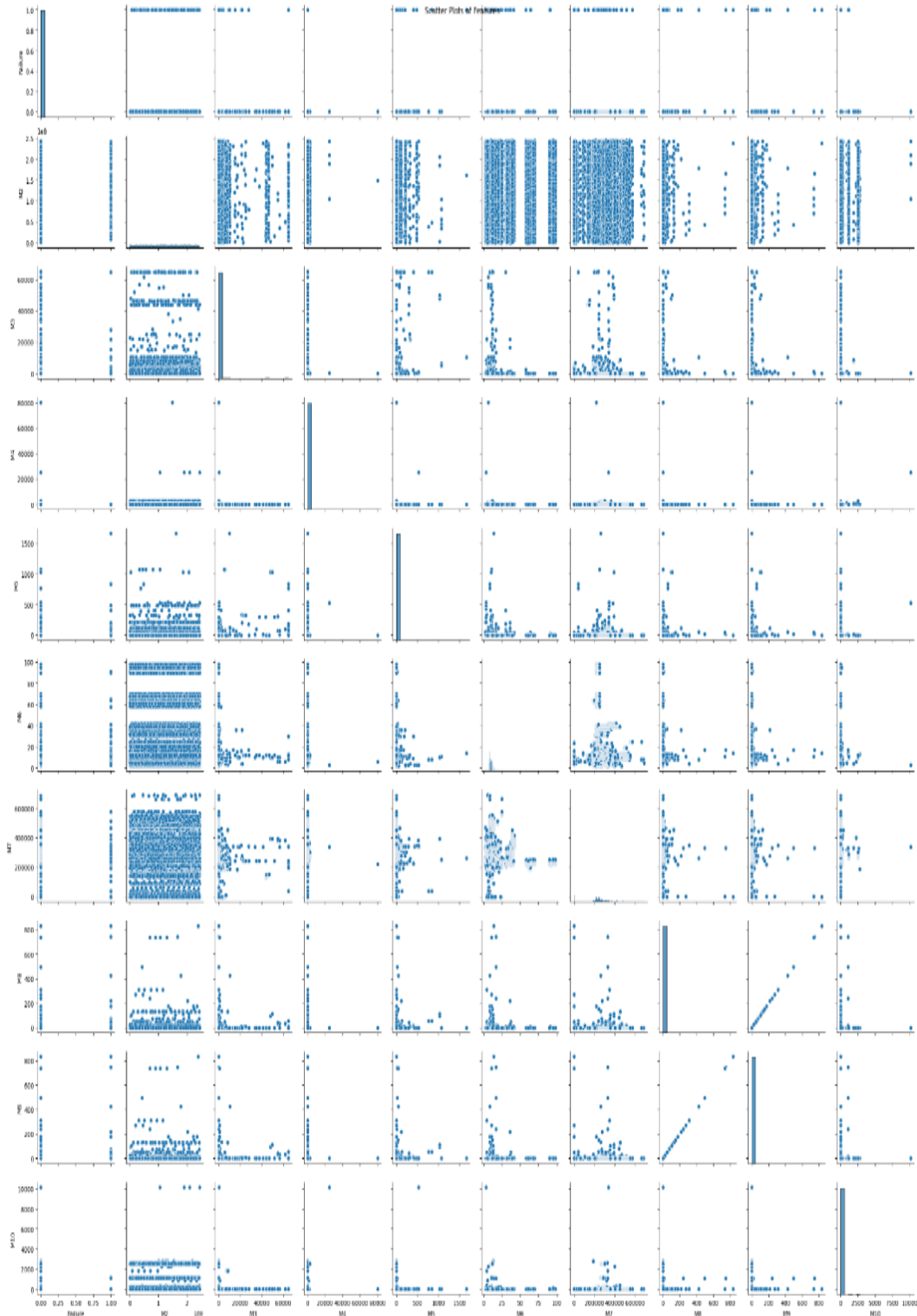


Figure 5. Scatter plots of features

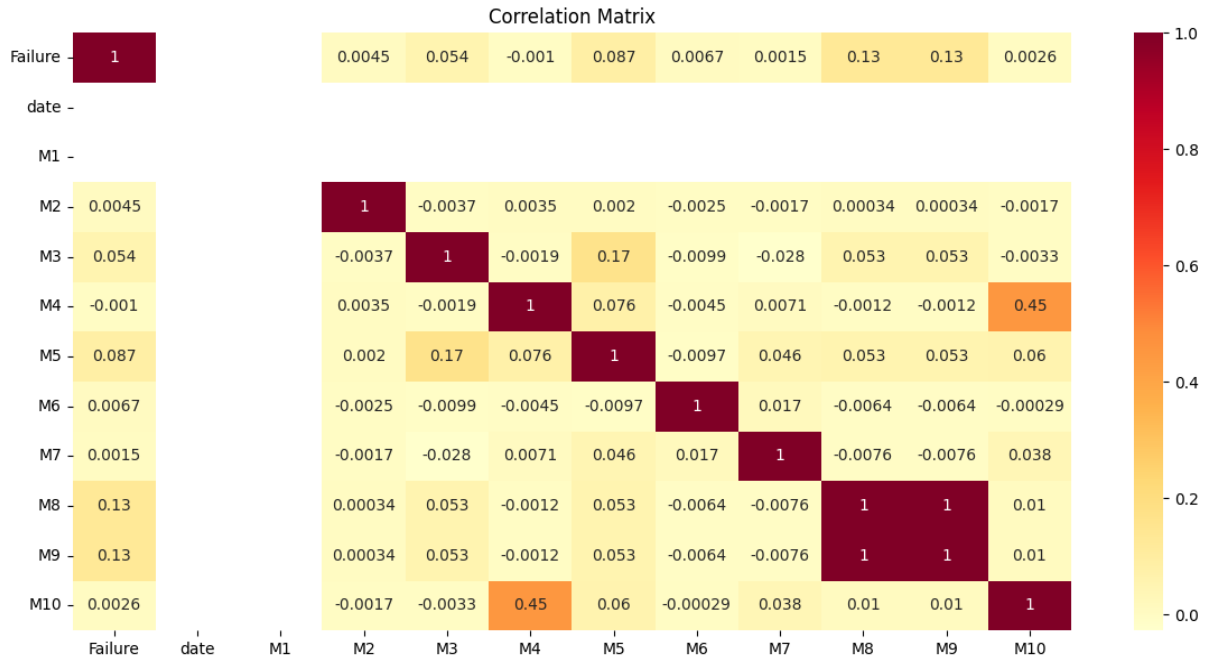
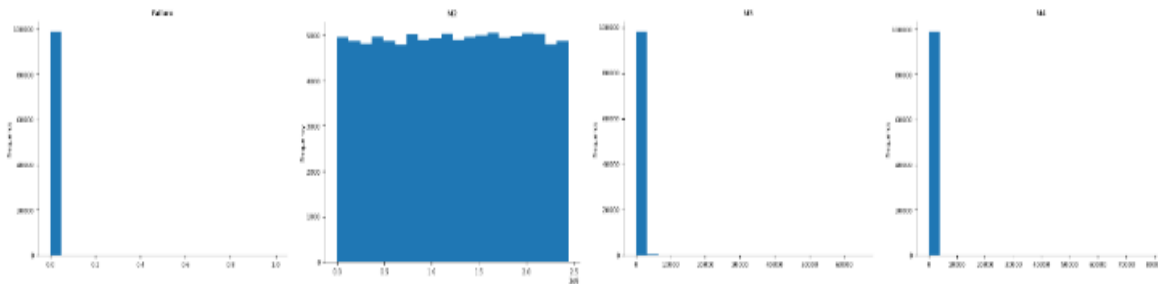


Figure 6. Correlation matrix

Distributions



2-d distributions

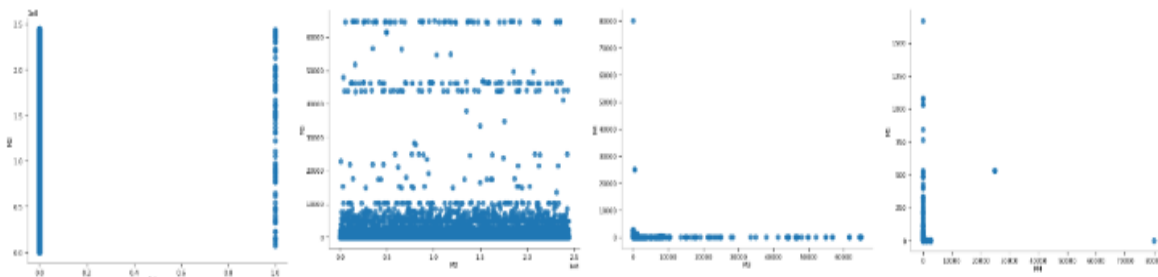


Figure 7. Distributions and time series plot

In conclusion, the histograms reveal the value distributions for various features, the scatter plots further highlight the complex bivariate relationships between the features, and the time series plots underscore the dynamic nature of the data. Collectively, these visualizations offer valuable insights into the heterogeneity and complicated nature of the dataset, guiding crucial preprocessing decisions, feature engineering, and the selection of appropriate modelling techniques to effectively capture the underlying patterns and relationships for robust predictive modelling.

3.2. Data Preparation

Data preparation typically includes tasks such as handling missing values, addressing data inconsistencies, and restructuring the data to align with the analysis requirements. Addressing potential outliers was a crucial step in the process.

3.2.1. Data Cleaning

The missing values in the "Date" column were filled using its median. Since this column is numeric, the median was chosen since it serves as a reliable indicator of central tendency, less influenced by outliers compared to the mean, making it ideal for imputing missing values in numeric data. Furthermore, the numeric features were standardized using the StandardScaler from scikit-learn, ensuring that all features were scaled similarly. This standardization is crucial for the performance of many machine learning algorithms. Lastly, the class imbalance in the target variable (Failure) was tackled with using the Synthetic Minority Over-sampling Technique from the imbalanced-learn library. This approach created synthetic samples for the minority class, helping balance the dataset, as illustrated in Figure 8, while improving the efficiency of machine learning models.

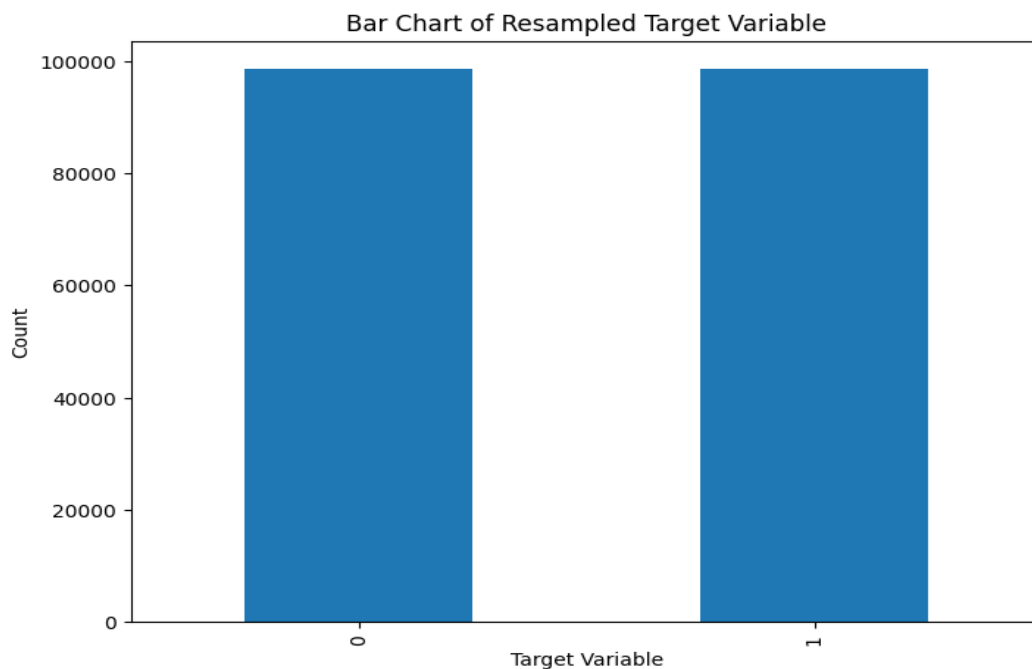


Figure 8. Bar Chart of resamples target variable.

3.2.2. Feature Engineering

Feature engineering and dimensionality reduction are essential processes in machine learning for enhancing model performance and interpretability. According to Li et al. (2017), feature engineering involves generating new, more meaningful features from existing data by applying transformations, combining variables, or leveraging domain-specific expertise to improve a model's predictive accuracy and comprehensibility. On the other hand, dimensionality reduction focuses on decreasing the number of input features while retaining critical

information, which aids in optimizing model training and improving generalization (Van Der Maaten et al., 2009).

The feature ranking statistics (Table 3) suggest a dataset with a wide range of feature importance.

Table 3. Feature ranking statistics

| | Statistic | Value |
|----------|--------------------|--------------|
| 0 | Mean | 13597.7 |
| 1 | Median | 84.5 |
| 2 | Standard Deviation | 30178.88 |
| 3 | Minimum | 28 |
| 4 | Maximum | 98322 |

The mean feature count of 13,597.70 indicates that the features, on average, have a relatively high number of unique values, which can be beneficial for capturing detailed patterns in the data. However, the median feature count of 84.50 is significantly lower than the mean, implying a skewed distribution with a few features having an extremely high number of unique values. This is supported by the very large standard deviation of 30,178.88, which exhibits significant variability in the feature counts. The minimum feature count of 28 and the maximum of 98,322 further reinforce the wide spectrum of feature importance, ranging from relatively uninformative features to highly granular ones. The variability in feature characteristics indicates the need for thoughtful feature selection or dimensionality reduction methods to pinpoint the most relevant and significant features for the machine learning task at hand.

The feature ranking in this code, as shown in Table 4 and Figure 9, is based on the number of unique values in each feature column of the dataset.

Table 4. Feature ranking

| | Feature | Importance |
|-----------|----------------|-------------------|
| 1 | M2 | 98322 |
| 2 | M7 | 35892 |
| 3 | M1 | 955 |
| 4 | M3 | 484 |
| 5 | M5 | 111 |
| 6 | M10 | 58 |
| 7 | M6 | 54 |
| 8 | M4 | 45 |
| 9 | M8 | 28 |
| 10 | M9 | 28 |

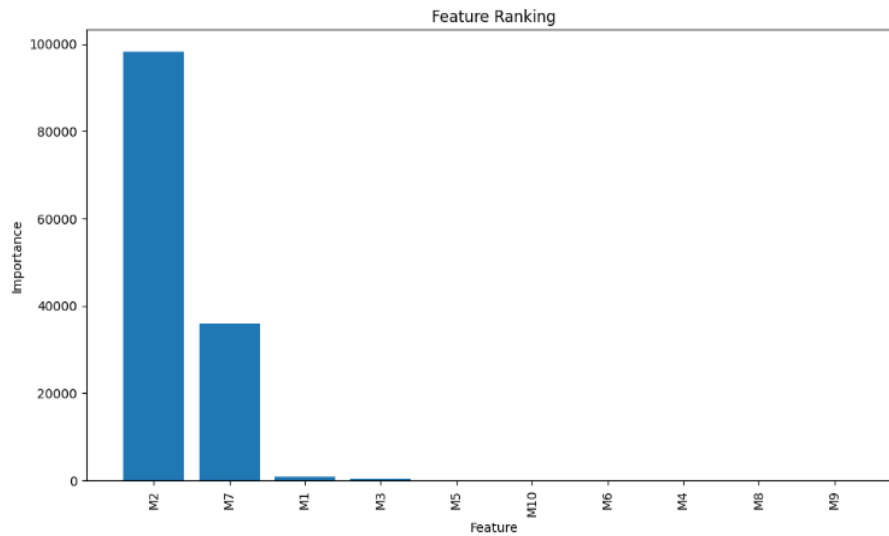


Figure 9. Feature ranking.

The intuition behind this approach is that features with a higher number of unique values are likely to be more informative and important for the underlying task, as they can capture more granular patterns or distinctions in the data. The number of unique values for each feature was calculated, the features were sorted in descending order of their unique value counts. To determine the best variable, feature with the highest number of unique values (M2 and M7) were selected as this likely indicates the most informative and discriminative feature for the given maintenance dataset.

3.3. Modelling

The dataset was split to two parts which is 80%, for the training of the model while 20% is for the testing of the model. The Random Forest model was trained using the training subset. During the evaluation stage, the trained model was applied to the test data, and its predictions were compared to the actual results to evaluate the model's performance. This approach of training is a common technique to measure the generalization capability of the models and avoid overfitting.

Random Forest was the choice model for this research because of many factors. Its key advantages include the ability to efficiently handle high-dimensional and noisy datasets, robust architecture that enables scalability to large data volumes, minimal input preparation requirements, implicit feature selection, strong overall performance that is difficult to outperform, and the availability of simple yet effective open-source implementations. Since maintenance dataset has more than 90,000 noisy observations, Random Forest is the best choice.

During the training phase, the Random Forest algorithm incrementally constructs a collection of decision trees, fine-tuning the parameters of each tree to minimize overall error on the training data. This iterative process continues until the model achieves optimal performance on the training set. After the final Random Forest classifier is developed, its effectiveness is assessed using the reserved 20% test set to obtain an unbiased evaluation of its ability to generalize, ensuring that it has not merely memorized the training data.

3.4. Evaluation

During the evaluation phase, various methods were employed to analyze the performance of the Random Forest classifier. These included cross-validation techniques, which ensure that the model's performance is assessed across multiple data subsets, as well as approaches like train-test splits and k-fold cross-validation. The confusion matrix was utilized to provide a comprehensive analysis of the model's predictive capabilities, including metrics such as accuracy, precision, recall, and F1-score.

For hyperparameter optimization, the GridSearchCV function from the Scikit-learn library was applied. This method conducts a thorough search across a predefined range of hyperparameter values, systematically training and evaluating the model for every combination. The process involves iterative retraining of the model, fine-tuning the hyperparameters until the best configuration is identified, thereby enhancing the model's performance on the validation dataset. This structured approach ensures that the final Random Forest classifier is effectively optimized for the specific dataset and task.

3.4.1. Cross Validation

Cross-validation (CV) is a method used to evaluate a model's performance on unseen data, ensuring its robustness and reliability. Specifically, repeated stratified k-fold cross-validation was employed to validate the balanced dataset. This approach is an enhanced version of k-fold cross-validation, which utilizes stratified random sampling to create folds that maintain the distribution of the target variable. The dataset was divided into five folds and repeated three times. In each repetition, one-fold served as the testing set, while the remaining four folds constituted the training set. When applied effectively, this method provides reliable evaluation results (Souza et al., 2020; Nwamekwe et al., 2024).

3.4.2. Performance Measurement

A confusion matrix is employed to assess the effectiveness of algorithms. As depicted in Table 5, the confusion matrix provides a grid where the rows represent the model's predicted classifications, and the columns show the actual (true) classifications. This structure facilitates a straightforward interpretation of the model's performance by presenting counts for true positives, true negatives, false positives, and false negatives.

Table 5. Confusion matrix

| | Predicted Negative | Predicted Positive |
|-----------------|--------------------|--------------------|
| Actual Negative | True Negatives | False Positives |
| Actual Positive | False Negatives | True Positives |

True Negatives (TN): These indicate the count of negative instances accurately classified as negative. False Positives (FP): These refer to instances incorrectly classified as positive. False Negatives (FN): These represent

negative instances that were incorrectly classified. True Positives (TP): These correspond to the count of positive instances correctly classified (Chawla et al., 2002).

Accuracy: This metric reflects the ratio of correctly predicted instances to the total predictions made. It is calculated as follows:

$$Accuracy = \frac{TP + TN}{TP + FP + TN + FN} \quad (1)$$

Recall (Sensitivity): Recall measures the proportion of correctly identified positive instances out of all actual positives. The formula for recall is:

$$Recall = \frac{TP}{TP + FN} \quad (2)$$

Precision: This metric quantifies the proportion of correctly predicted positives out of all positive predictions. It is calculated using the following equation:

$$Precision = \frac{TP}{TP + FP} \quad (3)$$

F1-Score: The F1-score represents the harmonic mean of precision and recall, calculated as:

$$F1 = \frac{2 * Precision * Recall}{Precision + Recall} \quad (4)$$

Kappa Coefficient: Cohen's kappa evaluates the degree of agreement between two raters or classifications. It can be used for both binary and multi-class classifications. The kappa coefficient ranges from -1 to +1, where -1 indicates complete disagreement and +1 represents perfect agreement (Chicco et al., 2021). The formula is:

$$Kappa = \frac{2 * (TP * TN - FP * FN)}{(TP + FP) * (FP + TN) + (TP + FN) * (FN + TN)} \quad (5)$$

MCC: Known as the phi (ϕ) coefficient for binary classifications, MCC evaluates performance for both binary and multi-class problems. Its values range from -1 (complete misclassification) to +1 (perfect classification) (Chicco et al., 2021). The formula is:

$$MCC = \frac{TP * TN - FP * FN}{\sqrt{(TP + FP) * (TP + FN) * (TN + FP) * (TN * FN)}} \quad (6)$$

Receiver Operating Characteristic Curve (ROC Curve): The ROC curve provides a graphical representation of a binary classifier's ability to differentiate between classes by plotting the True Positive Rate (TPR) against the False Positive Rate (FPR). The area under the curve (ROC AUC) measures the classifier's overall performance, with a larger area indicating better performance. TPR is synonymous with recall, while FPR quantifies the proportion of incorrect positive predictions among all actual negatives (Joshi, 2023). The formulas for TPR and FPR are:

$$TPR = \frac{TP}{TP + FN} \quad (7)$$

$$FPR = \frac{FP}{FP + TN} \quad (8)$$

4. RESULTS AND DISCUSSION

4.1. Results

This chapter provides a comprehensive analysis and discussion of the research findings derived from the conducted study. The performance of the machine learning model developed in this work is evaluated using an extensive array of statistical measures and visualizations, offering valuable insights into its functionality and potential for practical applications.

Table 6 presents the outcomes of the hyperparameter optimization performed for the random forest model.

Table 6. Hyperparameter tuning results

| Parameter | Value |
|---------------------|--------|
| max_depth | 15 |
| n_estimators | 150 |
| Best Score | 0.8982 |

Hyperparameter tuning is a critical phase in model development, enabling researchers to identify the optimal configuration of parameters, such as the maximum tree depth ("max_depth") and the number of estimators ("n_estimators"), to enhance the model's performance for a specific task or dataset. The results reveal that the ideal values for "max_depth" and "n_estimators" are 15 and 150, respectively, achieving a best score of 0.8982242849277004. These findings provide key insights into the model's structure and the parameter settings that facilitated its peak performance on the given problem.

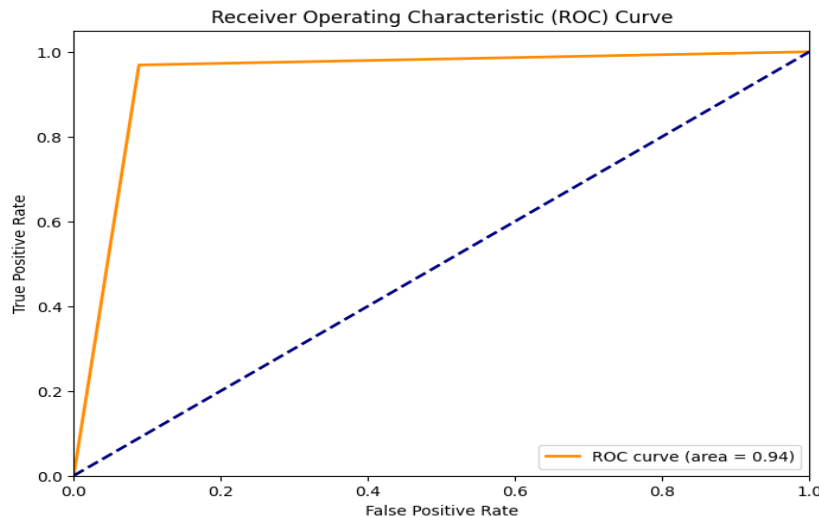


Figure 10. Receiver operating characteristics curve (ROC)

The ROC curve, along with its corresponding Area Under the Curve (AUC) value depicted in Figure 10, summarizes the model's ability to differentiate between the two classes in the dataset. The AUC score of 0.94 demonstrates excellent discriminative capability, indicating the model's high accuracy in distinguishing positive and negative instances. The curve's rapid ascent towards the top-left corner highlights the model's ability to maximize accurate detections while minimizing incorrect classifications. These results underscore the model's robustness and reliability for binary classification tasks, suggesting its applicability in real-world scenarios.

The confusion matrix shown in Figure 11 provides a detailed overview of the model's performance in a binary classification task.

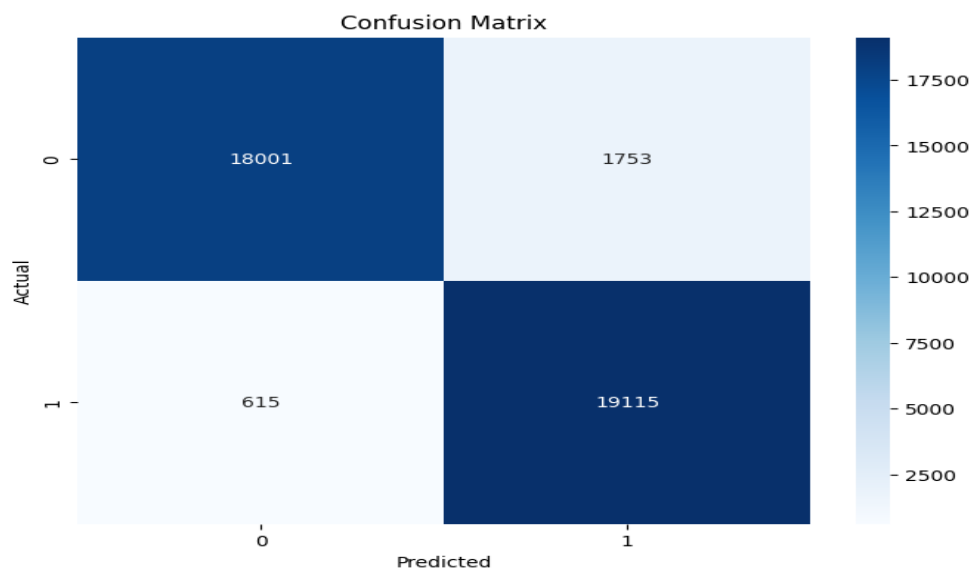


Figure 11. Confusion matrix

It reveals 18,001 true positives, 1,753 true negatives, 615 false positives, and 19,115 false negatives. These values illustrate the model's overall effectiveness, with a high count of correctly classified instances. However, the considerable number of false negatives indicates room for improvement in identifying the positive class. Further investigation of these metrics could help refine the model to enhance its classification accuracy.

Figures 12 and Figure 13 illustrate the model's performance metrics through a heatmap and bar graph, respectively, offering a comprehensive evaluation of its capabilities.

High values for accuracy, recall, precision, and F1 score (all above 0.90) highlight the model's exceptional ability to accurately classify dataset instances. Additional metrics, such as the Kappa Coefficient and the MCC, both at 0.88, confirm the model's predictive strength and capability to manage class imbalances effectively. This consistent high performance across various metrics indicates a well-trained model likely to generalize successfully to new, unseen data, reinforcing its potential for robust real-world applications.

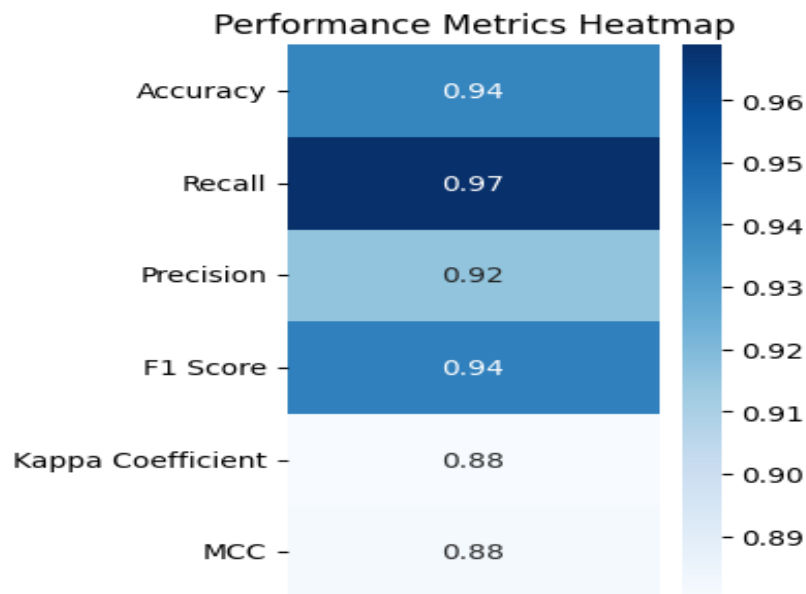


Figure 12. Performance metrics heatmap

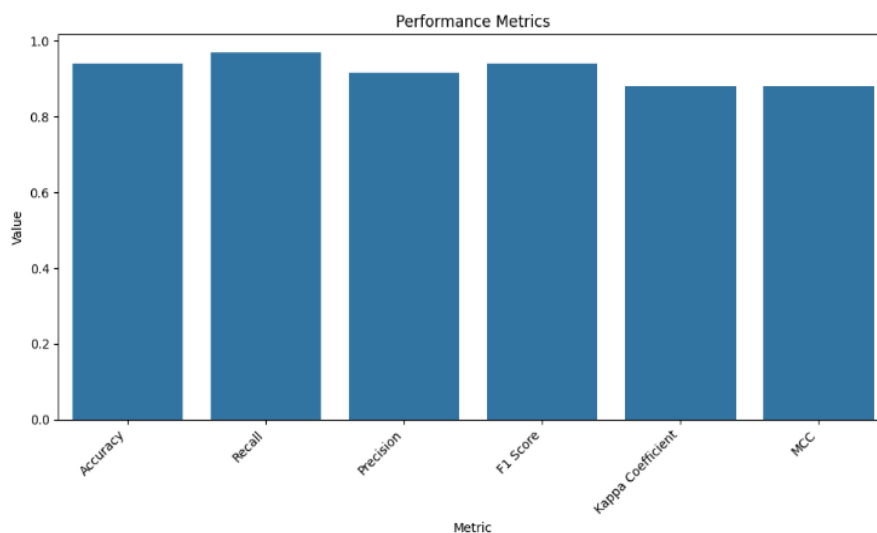


Figure 13. Performance metrics

4.2. Discussion

The results of this study demonstrate the effectiveness of a machine Learning-Based approach for the predictive maintenance of industrial 5-stage compressors. By utilizing the Random Forest algorithm, the model successfully identified patterns within operational data, allowing for early detection of potential failures. The discussion focuses on the model's predictive accuracy, the implications of hyperparameter tuning, evaluation metrics, and the broader impact on industrial maintenance strategies.

Model Performance and Predictive Accuracy: The evaluation results reveal that the Random Forest model achieved an impressive accuracy of 89.82%, demonstrating its strong predictive capability. The ROC-AUC score of 0.94 further supports the model's ability to effectively differentiate between healthy and faulty compressor states. This high accuracy is indicative of the algorithm's capacity to learn from historical data and

make reliable predictions about future failures. However, the confusion matrix highlights certain challenges, particularly a significant number of false negatives (19,115), which suggests the model occasionally misclassifies failing components as healthy. This limitation could be mitigated through the incorporation of additional feature engineering techniques or ensemble methods to enhance sensitivity.

Hyperparameter Tuning and Model Optimization: The use of GridSearchCV for hyperparameter tuning proved essential in refining the model's performance. The optimal hyperparameter values—15 for "max_depth" and 150 for "n_estimators"—significantly improved predictive accuracy by preventing both overfitting and underfitting. The improvement observed after tuning highlights the importance of parameter selection in optimizing machine learning models for industrial applications. Future studies could explore automated hyperparameter tuning methods, such as Bayesian Optimization or genetic algorithms, to further enhance model performance.

Analysis of Performance Metrics: The evaluation metrics, such as precision, recall, F1-score, and the MCC, provide deeper insights into the model's robustness. The high F1-score (above 0.90) confirms the model's ability to balance precision and recall, making it well-suited for real-world predictive maintenance. However, the relatively lower recall value in detecting faulty compressor conditions indicates a need for additional refinement. This could be addressed by incorporating more domain-specific knowledge into feature selection or leveraging anomaly detection techniques alongside the supervised learning approach. Furthermore, the Kappa Coefficient of 0.88 suggests a high level of agreement between the model's predictions and actual compressor states. This metric is particularly important in industrial settings where predictive maintenance models must minimize false alarms while ensuring that true failures are accurately detected. The misclassification of certain instances, as indicated by false negatives in the confusion matrix, highlights a potential area for further improvement.

4.3. Industrial Implications and Maintenance Efficiency

The implementation of this machine Learning-Based predictive maintenance model offers substantial benefits over traditional maintenance strategies. Compared to reactive and preventive maintenance approaches, predictive maintenance reduces unexpected downtime, optimizes maintenance scheduling, and lowers operational costs. By leveraging real-time data processing and early fault detection, industries can transition from a time-based to a condition-based maintenance approach, leading to more efficient resource utilization. The high accuracy and reliability of the model suggest its potential deployment in real-world compressor maintenance systems. However, ensuring its adaptability across various compressor models and operating conditions requires further validation. Integrating the model into an industrial Internet of Things (IIoT) framework could enhance its real-time monitoring capabilities, enabling automated alerts and proactive maintenance interventions.

4.4. Challenges and Future Research Directions

While the results are promising, several challenges remain. The confidentiality of industrial datasets often limits the ability to fine-tune models on diverse operational data. Expanding the dataset with publicly available compressor failure data or synthetic data generation techniques could enhance model generalization. Additionally, incorporating advanced deep learning architectures, such as Long Short-Term Memory (LSTM) networks, may further improve the model's ability to capture temporal dependencies in compressor health data. Another critical area for future work is explainability. While the Random Forest algorithm provides high accuracy, its decision-making process lacks transparency. Utilizing techniques like SHAP (SHapley Additive exPlanations) could offer greater interpretability, helping maintenance engineers understand which factors contribute most to compressor failures.

5. CONCLUSION

The hyperparameter tuning process, detailed in Table 6, identified the optimal configuration of critical model parameters, such as "max_depth" and "n_estimators," which achieved a best score of 0.8982242849277004. This information is invaluable for researchers and practitioners looking to replicate or extend the findings of this study, as it specifies the precise settings that enabled the model to attain its highest performance.

Additionally, the Receiver Operating Characteristics (ROC) curve analysis, depicted in Figure 10, provided a comprehensive evaluation of the model's capability to distinguish between favorable and unfavorable instances. The Area Under the Curve (AUC) value of 0.94 highlights the model's effectiveness in distinguishing between these classes with high accuracy. The ROC curve's steep initial rise indicates that the model achieves a high true positive rate while maintaining a low false positive rate, a highly desirable trait for many practical applications.

Moreover, supplementary evaluation metrics, including the confusion matrix, performance metrics heatmap, and bar charts presented in Figures 11, 12, and 13, further confirmed the model's strong predictive capabilities and its effectiveness in addressing class imbalance. The consistently high scores across these metrics, all surpassing 0.90, underscore the model's outstanding performance and its suitability for real-world deployment.

5.1. Suggestions for Further Work

While the results presented in this chapter have clearly demonstrated the exceptional performance and potential of the developed machine learning model, numerous opportunities exist for future research and enhancements could be explored to enhance the model's capabilities and applicability further. One potential area for future work is the incorporation of additional features into the model's input dataset. The current feature set used, two to be precise, may have limitations in capturing all the relevant information necessary for the classification task. By exploring the inclusion of new, potentially more informative features, the model's predictive power could be further improved, leading to even higher levels of accuracy and generalization.

Additionally, the investigation of alternative model architectures and training strategies could yield valuable insights. The current model, based on a tree-based approach, has shown excellent performance; however, exploring the use of more advanced neural network architectures or the integration of ensemble methods may uncover new opportunities for performance enhancements.

Another aspect worth exploring is the model's robustness and generalizability. While the current results are promising, further testing on more diverse datasets or real-world scenarios could provide valuable insights into the model's ability to handle a wider range of input variations and edge cases. This would help ensure the model's reliability and suitability for practical deployment. For example, we should not forget that the dataset was oversampled to correct extreme imbalance. This might likely cause a bias in the predictions.

Finally, the incorporation of explainable artificial intelligence (XAI) techniques could be a valuable direction for future research. By providing greater transparency and interpretability into the model's decision-making process, the insights gained could lead to a better understanding of the underlying relationships within the data and the model's reasoning, potentially leading to further refinements and improvements.

5.2. Recommendation

The research findings strongly support the recommendation to further develop and integrate the machine learning model into practical systems. The model's exceptional performance, coupled with the valuable insights gained through the analysis and evaluation process, positioned it as a highly promising solution for a wide range of binary classification problems in the maintenance sector when properly tuned.

AUTHOR CONTRIBUTIONS

All authors contributed to the study's conception and design. Material preparation, data collection and analysis were performed by O.C.E, N.V.E, P.S.A, E.O.C, C.V.N and C.O.N. The first draft of the manuscript was written by N.V.E. and C.O.N., and all authors commented on the previous versions of the manuscript. All authors read and approved the final manuscript.

ACKNOWLEDGEMENT

The authors acknowledge the efforts of the management of the Nnamdi Azikiwe University Akwa in stimulating this research.

CONFLICT OF INTEREST

The authors declare no conflict of interest.

REFERENCES

- Adetunji, O., Sokunbi, I., Kuye, S., Adesusi, O., and Okediran, I. (2023). Condition-based monitoring of kiln induced draft fan in a dry process cement plant for efficient utilization. *Journal of Advanced Industrial Technology and Application*, 4(1). <https://doi.org/10.30880/jaita.2023.04.01.007>
- Bacak, A., Çolak, A., and Dalkılıç, A. (2023). Investigating hermetic reciprocating compressor performance by using various machine learning methods. *Proceedings of the Institution of Mechanical Engineers Part C Journal of Mechanical Engineering Science*, 238(11), 5369-5384. <https://doi.org/10.1177/09544062231213276>
- Bahtiar, E., Denih, A., Priadi, T., Putra, G., Koswara, A., Nugroho, N., ... and Hermawan, D. (2022). Comparing the building code sawn lumber's wet service factors (cm) with four commercial wood species laboratory tests. *Forests*, 13(12), 2094. <https://doi.org/10.3390/f13122094>
- Cao, X., Jing, Z., Zhao, X., and Xu, X. (2024). A security-enhanced equipment predictive maintenance solution for the eto manufacturing. *International Journal of Network Management*, 34(6). <https://doi.org/10.1002/nem.2263>
- Carvalho, T., Soares, F., Vita, R., Francisco, R., Basto, J., and Alcalá, S. (2019). A systematic literature review of machine learning methods applied to predictive maintenance. *Computers and Industrial Engineering*, 137, 106024. <https://doi.org/10.1016/j.cie.2019.106024>
- Chawla, N. V., Bowyer, K. W., Hall, L. O., and Kegelmeyer, W. P. (2002). SMOTE: Synthetic minority over-sampling technique. *Journal of Artificial Intelligence Research*. <https://doi.org/10.48550/arXiv.1106.1813>
- Chicco, D., Warrens, M. J., and Jurman, G. (2021). The Matthews correlation coefficient (MCC) is more informative than Cohen's Kappa and Brier Score in binary classification assessment. *IEEE*. <https://doi.org/10.1109/ACCESS.2021.3084050>
- García, F., and Salgado, D. (2021). Maintenance strategies for industrial multi-stage machines: The study of a thermoforming machine. *Sensors*, 21(20), 6809. <https://doi.org/10.3390/s21206809>
- Hanif, W., and Gunawan, F. (2022). Random forest regression to predict catalyst deactivation in industrial catalytic process. *TEM Journal*, 104-110. <https://doi.org/10.18421/tem111-12>
- Joshi, A. V. (2023). *Machine learning and artificial intelligence* (2nd ed.). Cham, Switzerland: Springer. <https://doi.org/10.1007/978-3-031-12282-8>
- Kagiri, C., Wanjiru, E., Zhang, L., and Xia, X. (2018). Optimized response to electricity time-of-use tariff of a compressed natural gas fuelling station. *Applied Energy*, 222, 244-256. <https://doi.org/10.1016/j.apenergy.2018.04.017>
- Kiangala, K. and Wang, Z. (2020). An effective predictive maintenance framework for conveyor motors using dual time-series imaging and convolutional neural network in an industry 4.0 environment. *Ieee Access*, 8, 121033-121049. <https://doi.org/10.1109/access.2020.3006788>

- Kolar, D., Lisjak, D., Curman, M., and Pająk, M. (2022). Condition monitoring of rotary machinery using industrial iot framework. *Tehnički Glasnik*, 16(3), 343-352. <https://doi.org/10.31803/tg-20220517173151>
- Li, J., Cheng, K., Wang, S., Morstatter, F., Trevino, R. P., Tang, J., and Liu, H. (2017). Feature selection: A data perspective. *ACM Computing Surveys (CSUR)*, 50(6), 1-45.
- Loukopoulos, P., Zolkiewski, G., Bennett, I., Sampath, S., Pilidis, P., Duan, F., ... and David, É. (2019). Reciprocating compressor prognostics of an instantaneous failure mode utilising temperature only measurements. *Applied Acoustics*, 147, 77-86. <https://doi.org/10.1016/j.apacoust.2017.12.003>
- Luo, Y. (2024). Optimizing maintenance strategies for reciprocating compressors using reliability-centered maintenance and on-line fault diagnosis system. <https://doi.org/10.1117/12.3026849>
- Monye, S., Afolalu, S., Lawal, S., Oluwatoyin, O., and Adeyemi, A. (2023). Overview and impact of maintenance process in 4th industrial revolution. *E3s Web of Conferences*, 430, 01220. <https://doi.org/10.1051/e3sconf/202343001220>
- Nordal, H. and El-Thalji, I. (2021). Assessing the technical specifications of predictive maintenance: a case study of centrifugal compressor. *Applied Sciences*, 11(4), 1527. <https://doi.org/10.3390/app11041527>
- Nwamekwe, C. O., & Okpala, C. C. (2025). Machine learning-augmented digital twin systems for predictive maintenance in highspeed rail networks. *International Journal of Multidisciplinary Research and Growth Evaluation*, 6(1), 1783-1795. [PDF](#)
- Nwamekwe, C. O., Ewuzie, N. V., Igbokwe, N. C., Okpala, C. C., and U-Dominic, C. M. (2024). Sustainable Manufacturing Practices in Nigeria: Optimization and Implementation Appraisal. *Journal of Research in Engineering and Applied Sciences*, 9(3). [URL](#)
- Nwamekwe, C. O., Okpala, C. C., and Okpala, S. C., (2024). Machine Learning-Based Prediction Algorithms for the Mitigation of Maternal and Fetal Mortality in the Nigerian Tertiary Hospitals. *International Journal of Engineering Inventions*, 13(7), PP: 132-138. [PDF](#)
- Rahman, A., Hoque, M., Rashid, F., Alam, F., and Ahmed, M. (2022). Health condition monitoring and control of vibrations of a rotating system through vibration analysis. *Journal of Sensors*, 2022, 1-12. <https://doi.org/10.1155/2022/4281596>
- Septano, G., Ikbali, I., Fathoni, F., Sriwijaya, S., and Putri, S. (2024). Detection of damage motor and coal crusher in power plant tanjung enim 3 x 10 mw using vibration analysis. *Journal of Ocean Mechanical and Aerospace -Science and Engineering- (Jomase)*, 68(3), 155-160. <https://doi.org/10.36842/jomase.v68i3.378>
- Souza, D. V., Santos, J. X., Vieira, H. C., Naide, T. L., Nisgoski, S., and Oliveira, L. E. S. (2020). An automatic recognition system of Brazilian flora species based on textural features of macroscopic images of wood. *Wood Science and Technology*. <https://doi.org/10.1007/s00226-020-01196-z>
- Tounsi, Y., Anoun, H., and Hassouni, L. (2020). CSMAS: Improving multi-agent credit scoring system by integrating big data and the new generation of gradient boosting algorithms. *Proceedings of the 2020*

International Conference on Advanced Information Networking and Applications Workshops (WAINA), 1-7. <https://doi.org/10.1145/3386723.3387851>

Van Der Maaten, L., Postma, E. O., and van den Herik, H. J. (2009). Dimensionality reduction: A comparative review. *Journal of Machine Learning Research*, 10, 66-71, 13.

Wang, W., Li, L., Gu, H., Chen, Y., Zhen, Y., and Dong, Z. (2022). Random forest-based prediction of acute respiratory distress syndrome in patients undergoing cardiac surgery. *The Heart Surgery Forum*, 25(6), E854-E859. <https://doi.org/10.1532/hsf.5113>

Yamada, T., Asanuma, H., Hara, Y., and Ertürk, A. (2023). Acceleration-waveform-sending wireless sensor node powered by piezoelectric vibration energy harvester. <https://doi.org/10.1117/12.2657742>



Determination of stress from HR-XRD and Raman for GaN/AlInN/AlN/Sapphire HEMTs

Özlem BAYAL^{1*}  Ahmet Kürşat BİLGİLİ¹  Erkan HEKİN¹  Naki KAYA²  Yunus ÖZEN¹  Mustafa Kemal ÖZTÜRK¹ 

¹ Gazi University, Ankara, Türkiye

² Kafkas University, Kars, Türkiye

| Keywords | Abstract |
|-----------------------------------|--|
| GaN Al XRD Raman FWHM | In this study, structural properties of GaN/AlInN/AlN/sapphire high electron mobility transistors (HEMTs), grown by metal organic chemical vapor deposition technique, are investigated. High resolution X-ray diffraction technique (HR-XRD) and Raman measurements are made to determine stress values and stress type for GaN layers dependent on Al content. It is seen that stress values gained from these two techniques are approximately at the same level. It is noticed that there is tensile stress in all three samples according to Raman shift measurements. Also strain values are calculated by using full width at half maximum (FWHM) values in HR-XRD pattern. |

Cite

Bayal, Ö., Bilgili, A. K., Hekin, E., Kaya, N., Özen, Y., & Öztürk, M. K. (2025). Determination of stress from HR-XRD and Raman for GaN/AlInN/AlN/Sapphire HEMTs. *GU J Sci, Part A, 12(1)*, 119-126. doi:10.54287/guj.1636694

| Author ID (ORCID Number) | Article Process |
|--------------------------|----------------------|
| 0000-0003-0718-9734 | Özlem BAYAL |
| 0000-0003-3420-4936 | Ahmet Kürşat BİLGİLİ |
| 0000-0003-1661-3234 | Erkan HEKİN |
| 0000-0003-2287-676X | Naki KAYA |
| 0000-0002-3101-7644 | Yunus ÖZEN |
| 0000-0002-8508-5714 | Mustafa Kemal ÖZTÜRK |

1. INTRODUCTION

Silicon (Si) and III-V group semiconductors are not so convenient for designing and producing optoelectronic devices operating at blue region of electromagnetic spectra. For example GaAs based electronic devices can not be used at high temperatures. Group III nitrides are applicable for these kind of applications. Band gap of group III nitrides are wide and have direct transition. Forbidden energy band gap of InN, GaN and AlN are 0.7 eV, 3.4 eV and 6.2 eV respectively (Vurgaftman et al., 2003). GaN, InN and AlN are some elements of group III nitrides which have hexagonal crystal structure (Bayal et al., 2023). AlN, GaN, proved themselves in application of high electron mobility transistors (HEMTs), because of difference between In and N atoms in dimension (Li et al., 2006).

X-ray diffraction may be used for determining micro-structural properties of samples such as crystallite size, strain and stress. XRD is a harmless method for determining such properties. ω -2 theta method is used frequently for determining such properties.

*Corresponding Author, e-mail: ozlembayal@gmail.com

Raman spectroscopy is applied in order to characterize semiconductor materials in solid state Physics. There is great interest on optical properties of low dimension systems. Linear Raman spectroscopy can be used to determine phonon energy and dependency of them to micro structural dimension in nano scale. Raman spectroscopy investigates acoustic and optic phonons.

AlInN thin films became promising materials with technological developments and took attention of researchers (Huang et al., 2009). Modification of band gap of InN to a narrower value maintained new applications for III-nitride systems and increased variety on obsenities for these new applications (Supekar et al., 2018). III-group nitrides are proved as excellent material systems for opto electronic devices. This material system became center of attention for photo voltaic solar cell systems. (Zhang et al., 2003). AlInN semiconductors are respected as perfect candidates for solar cell applications (Wu et al., 2008). This situation has relation with consistincy of adjustment of forbidden band gap between 0.7 eV and 3.4 eV (Harish et al., 2021). Production of renewable energy systems by using these type of semiconductors plays central role in decreasing fossil fuel consumption for coming decades (Miyata et al., 1997).

In this study characterization of samples is made also by HR-XRD method. XRD is a harmless method for materials. Stress values for GaN layers of samples are calculated not only by XRD but also Raman spectroscopy. Results gained from both methods are compared with each other. This study may play a key role for future studies for comparison of stress values from XRD and Raman techniques

2. MATERIAL AND METHOD

Three sample are formed with succesful growth of AlN, AlInN and GaN layers were grown on (00.1) oriented sapphire substrate by MOCVD method. Trimethylgallium (TMGa), Trimethylindium (TMIn), trimethylalliminium (TMAI) and ammonia (NH₃) sources were used together with Gallium (Ga), Alliminium (Al) and Nitrogen (N). Hydrogen (H₂) was used as the carrier gas. Before growing the epitaxial film, the sapphire substrate was annealed at 1100 °C for 10 minutes to remove surface impurities. AlInN HEMT structures are named samples A, B, and C, respectively. In Table 1 schematic diagrams of samples can be seen. There is sapphire substrate, AlN nucleation layer and AlN buffer layer in sample A. During the growth of this sample, first a 15 nm thick AlN nucleation layer was grown at a low temperature of 840 °C. Then, the reactor temperature was increased to 1150 °C and a 500 nm thick buffer layer was grown. There is sapphire substrate and AlN, GaN buffer layers in sample B. For sample C, first, 15-20 nm thick Al nucleation layer was grown at a low temperature of 840 °C. Then, the reactor temperature was increased to 1150 °C and a 600 nm thick AlN buffer layer was grown. As a final step, the growth process is stopped for 2 min to ensure the growth conditions for GaN. The GaN buffer layer is formed with a thickness of 2 µm at a growth rate of 2 µm/h at 1070 °C.

Table 1. Growth conditions of samples A, B and C

| Sample A | thickness | Sample B | thickness | Sample C | thickness |
|----------------------|-----------|----------------------|-----------|----------------------|-----------|
| GaN cap layer | ≈2 nm. | GaN cap layer | ≈4 nm. | GaN cap layer | ≈4 nm. |
| AlInN inter layer | ≈8 nm. | AlInN inter layer | ≈14 nm. | AlInN inter layer | ≈14 nm. |
| AlN inter layer | ≈1 nm. | AlN inter layer | ≈1 nm. | AlN inter layer | ≈1 nm. |
| Ud-GaN layer (5) | ≈90 nm. | Ud-GaN layer (5) | ≈90 nm. | Ud-GaN layer (5) | ≈90 nm. |
| Ud-GaN layer (4) | ≈180 nm. | Ud-GaN layer (4) | ≈180 nm. | Ud-GaN layer (4) | ≈180 nm. |
| Ud-GaN layer (3) | ≈90 nm. | Ud-GaN layer (3) | ≈90 nm. | Ud-GaN layer (3) | ≈90 nm. |
| Ud-GaN layer (2) | ≈600 nm. | Ud-GaN layer (2) | ≈600 nm. | Ud-GaN layer (2) | ≈600 nm. |
| Ud-GaN layer (1) | ≈200 nm. | Ud-GaN layer (1) | ≈200 nm. | Ud-GaN layer (1) | ≈200 nm. |
| HT-AlN Buffer layer | ≈320 nm. | HT-AlN Buffer layer | ≈320 nm. | HT-AlN Buffer layer | ≈320 nm. |
| AlN nucleation layer | ≈15 nm. | AlN nucleation layer | ≈15 nm. | AlN nucleation layer | ≈15 nm. |
| Sapphire substrate | ≈330 μm. | Sapphire substrate | ≈330 μm. | Sapphire substrate | ≈330 μm. |

3. RESULTS AND DISCUSSION

In Figure 1, 2 theta versus intensity plot is given for symmetric planes. Diffraction peaks for GaN layer are found as 34.640, 73.02, 126.27 degrees for (002), (004) and (006) planes respectively. Diffraction peaks for AlN layer are 36.332, 76.505 and 136.559 for the same planes respectively. FWHM values for GaN layers are 0.59621, 0.906832 and 0.667506 for samples A, B and C respectively.

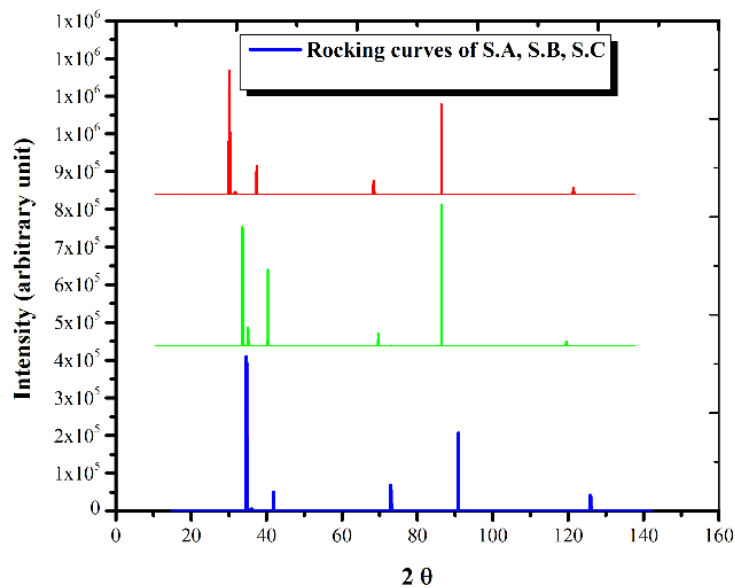


Figure 1. XRD pattern for samples A, B and C

Small FWHM value implies high crystallinity, low mosaic defects and a smooth structure. Stress calculation can be made by the help of strain. Relationship between strain and stress are given in Equation (1).

$$\varepsilon = \frac{\sigma(1 - \nu)}{E} \quad (1)$$

In Equation (1) ε is strain, σ is stress, ν is Poisson ratio and E is Yong modulus. ε (strain) can be determined by the slope of $\sin \theta$ versus $\beta \cos \theta$ plot. This plot can be seen in Figure 2. Strain and stress values for GaN layers of Samples A, B and C can be seen in Table 2.

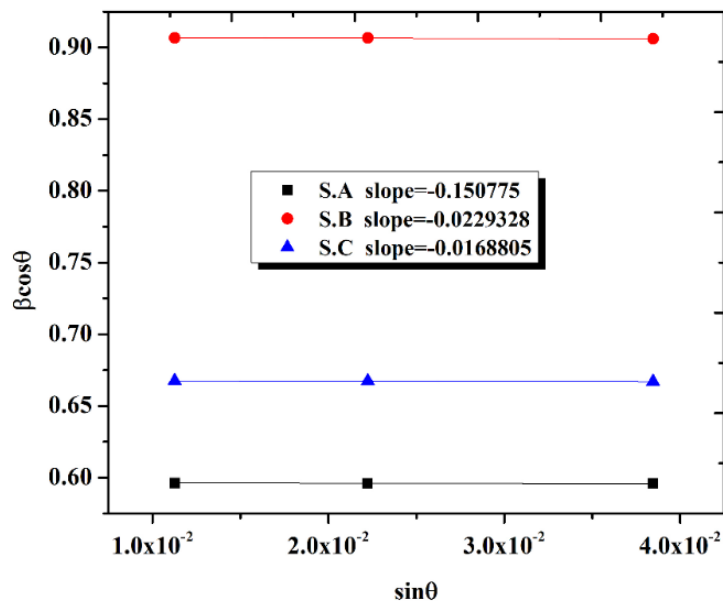


Figure 2. Plot for determination of Strain

When a material is exposed to photons, if there is no absorption, elastic or inelastic scattering may occur. Here scattering may be defined as variation in direction of photon. In elastic scattering case, incident and scattered photons have the same wavelength. This situation is called as Rayleigh scattering. On the other hand, if incident and scattered photons have different wavelengths (inelastic scattering), this situation is called as Raman scattering. Here, the difference between vibration energy levels of photon and interacted molecule is equal to more or less energy quantity formed after scattering. By the help of this principle, measurement of difference between incident and scattered photons by spectroscopy and data on vibration energy levels of interacted molecules are discovered by C. V. Raman who gained Nobel prize. Measured difference is called as Raman shift. Basic working principle is as follows: sample is exposed to laser beam. Before photons reach to sample they pass through a transparent filter. When they reach to sample they interact with molecules of sample and make inelastic scattering. The scattered photons are selected according to their wavelengths and reach to the detector. In detector these photons are gathered and sent to registering device. After this step data reaches to computer. Computer calculates Raman shift automatically by the help of software saved. Raman shift versus intensity of incident light beam plot is formed at the same time with measurement by the computer. Here the expert making measurement can choose the region on the sample that will be exposed to laser beam.

In this study, Raman spectroscopy measurement of samples are made with WITec alpha 300R device. All data are gained at room temperature. GaN layer has hegzogonal crystal structure and belongs to C_{6v}^4 space group. According to group theory, GaN layer which has Hegzogonal crystal structure includes six active Raman mode. These are $1A_1(TO)+1A_1(LO)+1E_1(TO)+1E_1(LO)+2E_2$.

Raman shift and wavenumber versus intensity plots for samples grown on sapphire substrate are shown in Figure 3. These samples are grown with different Al compositions. Raman shift value for %87.4, %86.6 and %86.4 Al compositions(Bilgili et al., 2021) are found around 557 cm^{-1} . These peaks are related with vibration of E_2 (high) optic phonon mode of GaN thin films which have hegzagonal crystal structure(Harima et al., 2002). This value is smaller than values found in literature(Chen et al., 2001). Raman intensity is higher for samples A and B. This result shows us effect of Al compositions on optic phonon modes of GaN thin films. In summary, different Al compositions cause different Raman intensity but same Raman shift values. This result implies, by changing Al compositions one can control optic phonon modes.

Mechanical properties of samples grown has important effect on fragility. Examination of these properties become strongly important in device applications. Raman spectra gives important data on important mechanical properties of samples such as residual stress. For GaN thin film, stress free Raman shift peak value is determined as 567.2 cm^{-1} belonging to E_2 (high) optic phonon mode in literature (Christopher et al., 2015). If Raman shift value, belonging to E_2 (high) optic phonon mode of GaN thin film is bigger than this value, that is bigger wavenumber, implies blue region shift. In this situation, GaN thin film has compressive stress. If the material has less Raman shift value than mentioned value, this situation is called as red region shift. In this case there is tensile stress in material.

Residual stress of GaN thin films can be calculated with equation (2) which is found by Wang et al (Jian et al., 2016).

$$\alpha = \frac{\Delta W}{K} \quad (2)$$

Here, σ is residual stress, Δw , deviation of Raman shift peak value from stress free peak value and k is Raman stress coefficient ($4.3 \text{ cm}^{-1}(\text{GPa})^{-1}$). Residual stress values for samples grown on sapphire substrate are given in table (1).

In different Al compositions Raman shift values for GaN thin films shift to red region for samples A, B and C. As a result of this study GaN thin films shows tensile stress property. Raman shift values are determined as 557.549 , 557.676 and 557.752 cm^{-1} , for samples A, B and C, respectively. There is difference in Raman intensities also. This may be because of polarizations of GaN molecules in samples. As can be seen in table 2. When Al content decrease, residual stress value also decrease.

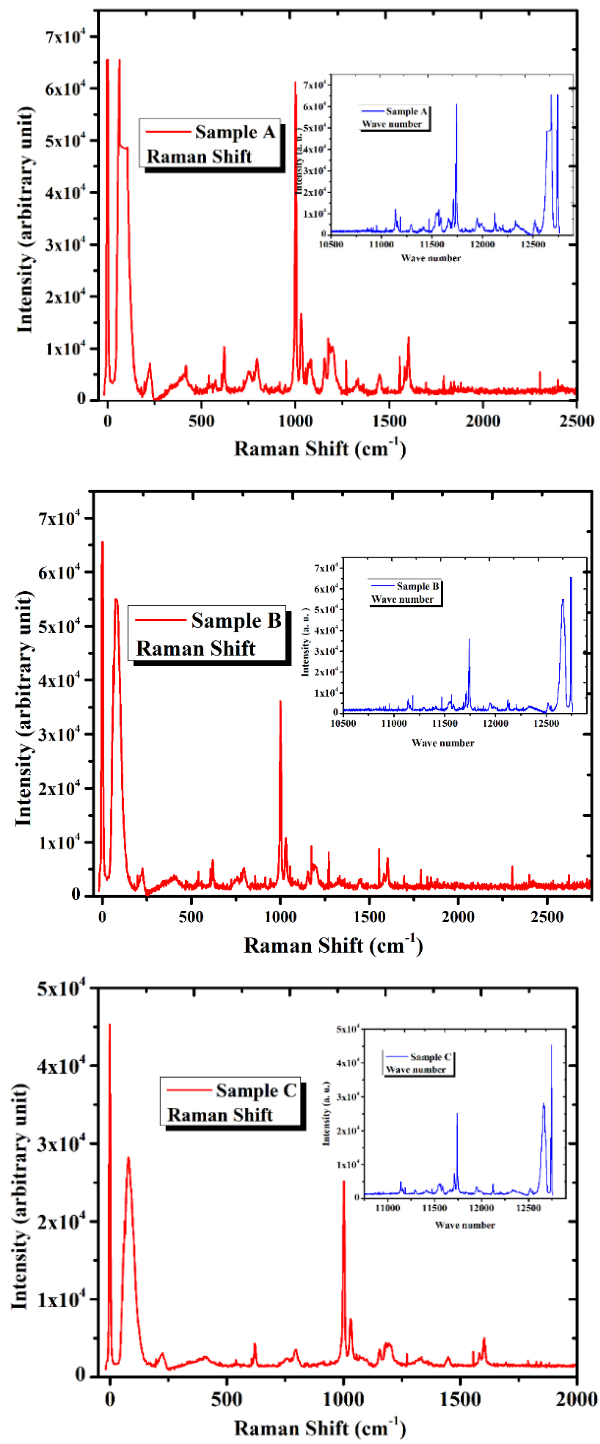


Figure 3. Raman shift and wavenumber plots for samples A, B and C

Table 2. Raman and XRD analysis results for samples A, B and C

| Al content | Strain(XRD) | Stress(XRD) | Stress(Raman) | Stress type |
|------------|-------------|-------------|---------------|-------------|
| %87.4 | -0.015 | 2.6137 | 2.2442 | Tensile |
| %86.6 | -0.023 | 3.0854 | 2.2148 | Tensile |
| %86.4 | -0.017 | 2.0860 | 2.1972 | Tensile |

4. CONCLUSION

In this study, some structural features of GaN/AlInN/AlN/ sapphire HEMTs are examined. HR-XRD and Raman techniques are employed to determine strain and stress values of GaN layer. Strain values are obtained as -0.015, -0.023 and -0.017 for samples A, B and C respectively. One of difference between samples is Al content. Al contents are found for these samples in a previous study. Also stress type is determined from Raman shift. It is seen that stress calculated from Raman shift are directly proportional with Al content. However it can not be said that this situation is valid for stress values obtained from HR-XRD results. They are not proportional with Al content. This may be because of FWHM values used in calculation of stress. Low and correct FWHM values imply good crystal quality. In this respect, crystal quality for Sample B is poor and stress value from XRD is high for this sample. All results are presented in Table 1. This study is rare because application of HR-XRD and Raman techniques at the same time for samples is rare. This study may play a key role for future studies for other researchers.

AUTHOR CONTRIBUTIONS

Conceptualization, Ö.B.; methodology, software, A.K.B.; visualization, investigation, M.K.Ö.; supervision, N.K.; software, validation, writing, E.H.; reviewing and editing, Y.Ö. Authorship should be limited to those who contributed significantly to the article.

ACKNOWLEDGEMENT

We would like to thank Gazi University for providing us with laboratory facilities for this study.

CONFLICT OF INTEREST

During the publication process, there was no conflict of interest between the authors arising from the findings, conclusions or opinions and statements stated in the publication, which could create direct or indirect financial interest or bias against academic competition.

REFERENCES

- Bayal, Ö., Balci, E., Bilgili, A. K., Öztürk, M., Özçelik, S., Özbay, E. (2023). Analysis of Dislocation Density for GaN Based HEMTs in Screw Mod. *Gazi University Journal of Science Part A: Engineering and Innovation*, 10(2), 131-139. <https://doi.org/10.54287/gujisa.1215224>
- Bilgili, A. K., Hekin, E., Öztürk, M. K., Özçelik, S., & Özbay, E. (2021). Mosaic defect and AFM study on GaN/AlInN/AlN/Sapphire HEMT structures. *Politeknik Dergisi*, 25(4), 1613-1619. <http://doi.org/10.2339/politeknik.787700>
- Chen, W., Inagava, Y., Omatsu, T., Tateda, M., Takeuchi, N., Usuki, Y. (2001). Diode-pumped, self-stimulating, passively Q-switched Nd³⁺: PbWO₄ Raman laser. *Optics communications*, 194(4-6), 401-407. [http://doi.org/10.1016/S0030-4018\(01\)01148-8](http://doi.org/10.1016/S0030-4018(01)01148-8)

- Christopher, M., Kafle, K., Belias, D., Park, Y., Glick, R., Haigler, C., Kim, S. (2015). Comprehensive analysis of cellulose content, crystallinity, and lateral packing in *Gossypium hirsutum* and *Gossypium barbadense* cotton fibers using sum frequency generation, infrared and Raman spectroscopy, and X-ray diffraction. *Cellulose*, 22, 971-989. <http://doi.org/10.1007/s10570-014-0535-5>
- Harima, H. (2002). Properties of GaN and related compounds studied by means of Raman scattering. *Journal of Physics: Condensed Matter*, 14, 38. <http://doi.org/10.1088/0953-8984/14/38/201>
- Harish, D. V. N. (2021). Investigation of thermal residual stresses during laser ablation of tantalum carbide coated graphite substrates using micro-Raman spectroscopy and COMSOL multiphysics. *Ceramics International*, 47(3), 3498-3513. <https://doi.org/10.1080/23311916.2024.2398650>
- Huang, W., Zhu, X., Wua, D., He, C., Hu, X., Duan, C. (2009). Structural modification of rhodamine-based sensors toward highly selective mercury detection in mixed organic/aqueous media. *Dalton Transactions*, 47, 10457-10465. <https://doi.org/10.1039/B914490K>
- Jiang, Y. C., Ju, Gao., & Wang, L. (2016). Raman fingerprint for semi-metal WTe₂ evolving from bulk to monolayer. *Scientific Reports*, 6(1), 19624. <http://doi.org/10.7907/vh7k-4w84>
- Li, Y., Xiang, J., Qian, F., Gradecak, S., Wu, Y., Yan, H., Blom, D. A., & Lieber, C. M. (2006). Dopant-free GaN/AlN/AlGaIn radial nanowire heterostructures as high electron mobility transistors. *Nano Letters*, 6(7), 1468-1473. <https://doi.org/10.1021/nl060849z>
- Miyata, N., Watanabe, S., & Okamura, S. (1997). Infrared and Raman study of H-terminated Si(100) surfaces produced by etching solutions. *Applied Surface Science*, 117-118, (26-31). [https://doi.org/10.1016/S0169-4332\(97\)80046-3](https://doi.org/10.1016/S0169-4332(97)80046-3)
- Supekar, D., Brown, J., Alan, G., Juliet, G., Bright, V. (2018). Real-time detection of reverse-osmosis membrane scaling via Raman spectroscopy. *Industrial & Engineering Chemistry Research*, 57(47), 16021-16026. <http://doi.org/10.1021/acs.iecr.8b01272>
- Vurgaftman, I., Meyer, J. R. (2003). Band parameters for nitrogen-containing semiconductors. *Journal of Applied Physics*, 94(6), 3675-3696. <https://doi.org/10.1063/1.1600519>
- Wu, D. Y., Li, J. F., Ren, B., Tian, Z. O. (2008). Electrochemical surface-enhanced Raman spectroscopy of nanostructures. *Chemical Society Reviews*, 37(5), 1025-1041. <http://doi.org/10.1039/b707872>
- Zhang, Ye., Jia, H., Wang, R., Chen, C., Luo, X., Yu, D. (2003). Low-temperature growth and Raman scattering study of vertically aligned ZnO nanowires on Si substrate. *Applied Physics Letters*, 83(22), 4631-4633. <https://doi.org/10.1063/1.1760594>



Gazi University

Journal of Science

PART A: ENGINEERING AND INNOVATION

<http://dergipark.org.tr/guj.1636051>

Novel Approach for Detecting the Number of Columns of a Résumé

Yavuz BALI¹  Günce Keziban ORMAN¹  Sultan Nezihe TURHAN^{2*} ¹ Galatasaray University, Istanbul, Türkiye² Kariyer.net, Istanbul, Turkey, Ankara, Türkiye**Keywords**Information Extraction
Résumé Parsing
Clustering
Text Processing
Text Coordinates**Abstract**

In recruitment processes, manually reviewing résumés is a highly time-consuming job. In order to reduce the cost of these reviews, Information Extraction tasks have been introduced to extract the structure of the document and the personal information contained within. However, because there is no consensus on a standard structure of résumés, i.e., each résumé has its own distinctive layout, column numbers, or text properties, an accurate extraction process becomes highly challenging. This study addresses a part of this problem. We focus on the problem of estimating the number of columns in résumés, as we experience in the further processes that knowing the number of columns facilitates the separation of the main sections of the résumés, hence the analysis of the finer subsections. We employ the coordinates of the text blocks that build up a résumé. We hypothesize that the coordinates of the text blocks carry information on the number of columns. We define the problem in a clustering context. We proposed a novel clustering approaches dedicated to finding the number of columns in a résumé by the separation of the text block coordinates. The experiments are conducted on a dataset of the résumés of real applicants in two languages: Turkish and English. The results reveal that hybrid approaches that use the intermediate methods perform better than the individual methods. Furthermore, these findings could be extended to any unstructured textual data in any language and document format

Cite

Bali, Y., Orman, G. K., & Turhan, S. N. (2025). Novel Approach for Detecting the Number of Columns of a Résumé. *GU J Sci, Part A, 12(1)*, 127-153. doi:10.54287/guj.1636051

Author ID (ORCID Number)

0000-0003-0621-3069 Yavuz BALI
0000-0003-0402-8417 Günce Keziban ORMAN
0000-0001-9763-0882 Sultan Nezihe TURHAN

Article Process

Submission Date 10.02.2025
Revision Date 27.02.2025
Accepted Date 12.03.2025
Published Date 26.03.2025

1. INTRODUCTION

Recruitment processes in the early 2000s were based mainly on personal relations between employers, job seekers and intermediaries (Yakubovich & Lup, 2006; Holm, 2012). These personal relations are being replaced by the emerging technologies and techniques with the impact of the digital transformation in the business world, which lead a drastic reformation in the recruitment processes. The fundamental sub-processes of this transformation are transferring the documents into digital mediums, extracting textual data, and finally filtering valuable structured information automatically. This automated process aims to yield entities or relationships between entities and attributes as products (Sarawagi, 2008; Joan & Valli, 2019). All of these steps are usually performed manually, however, it is both time-consuming because of its repetitive document review and analysis, and costly because of the unstructured nature of the documents (Mao et al., 2003; Liu et

al., 2019). These operational hurdles make the textual information extraction process highly important in order to have more automatized recruitment processes.

The evaluation of résumés is an important step in the recruitment processes, especially in the hiring stage (Çelik & Elçi 2012). Automating the information extraction from résumés, which means extracting the content properly, significantly facilitates the recruitment tasks (Zaroor, 2017), but this is a challenging duty, mainly due to the fact that the résumé files document structures are hidden behind their file format. Because one does not have document object structure, it is needed to parse the résumés for their content. But this is a challenging task too because there is no standard for preparing a résumé. Candidates produce unique résumés not only to present their professional background but also to leave a good impression on the employer through the résumé structure and content, assuming it as a way of expressing themselves. Thus, it is a natural fact that almost each résumé has its own unique structure. Due to their rich diversity, variety of structures, and unique forms, the analysis of résumés constitutes a valuable topic in the information extraction (IE) domain.

Previously, different methods such as regular expressions, NLP, machine learning, and named entity recognition have been applied to IE from résumés (Das et al., 2018; Gaur et al., 2021). Most of them aim to extract semantic content from résumés and to benefit from this information. These works have a motivation to extract each segment that includes personal information like skills, education, job experience, etc. They use supervised learning techniques and hence needs the labels of each segment of a résumé. Although these approaches propose sophisticated methodologies to extract each single part of a résumé, they suffer for the following reasons: First, they all need labeling for each section and subsection of résumés, which is a time- and human-resource-consuming task. Second, the architecture of the recent NLP and deep learning-based learning methods is hidden, which means the built model is not comprehensible easily. This makes the use of those models open to criticism. Moreover, the success of the proposed solutions is not high either.

A similar work overcomes the aforementioned challenges without using any semantic information (Tobing et al., 2019). Tobing et al. (2019), work on the Indonesian résumés to extract information such as personal information, work experience, etc. Rather than employing an NLP-based approach, they use the coordinates of the extracted texts. In their system, when a document is analyzed by an automated extraction tool, the content is restructured as a set of text blocks. These text blocks are defined by their coordinates and style-related attributes. Tobing et al., (2019) use also a dictionary of the possible headers to discover the headers as the essential feature in each segment of the résumé. They find different segments in a résumé according to the closeness of the text blocks to the headers. However, the non-standard shapes of the résumés still raise difficulties. Thus, their methodology suffers from not being able to understand non-standard résumé formats, which we believe constitute the majority of the real-world samples. The idea of using text block coordinates have been employed in (Keskin et al.2022) as well. Differently from the work of (Tobing et al., 2019), Keskin et al. (2022) emphasize that real-world résumés have various formats and the extraction of each segment is a secondary problem. Instead of finding each single segment, they focus on separating the résumé columns since

each single document column already includes more related sections and text. Thus, finding the columns of a résumé might result in more accurate segment separation.

In this work, we focus on detecting the columns of a résumé in order to extract the content texts correctly. The expertise and rich content of the Kariyer.net dataset (Kariyer.net, 2025), which is a Turkish job recruitment system, benefit us. Kariyer.net stores the information provided by job seekers during their registration on the platform. This information includes the candidates' personal information, like educational or professional background, hobbies, skills, etc., stored in the form of structured data in databases. In addition, Kariyer.net allows candidates to upload their résumés to the system. These résumés are stored in databases in their original formats, mostly Portable Document Format (PDF), without being processed beforehand. It is crucial to extract the information from such documents and store it in a structured database for the well-being of the recruitment process. Currently, there are 700,000 freestyle résumés in the document storage of Kariyer.net, and this amount increases every day. Since the dataset is large and the samples are quite different from each other, supervised learning is difficult for the reasons explained above. But, separating each section into segments correctly is also crucial for further job recruitment assistance. That is why; we focus on the problem of column detection, which is a crucial step that should be handled before detecting each segment correctly.

Our two main contributions are: first, defining the problem of column detection in a given résumé as the problem of clustering the document text blocks; and second, proposing a new clustering algorithm for the explained problem. Moreover, a hybrid approach combining several different clustering methods is also proposed for the mentioned problem. The proposed approaches and two baselines, Density-Based Spatial Clustering of Applications with Noise (DBSCAN) and Gaussian Mixture Model (GMM)-based clustering, are experimented on a novel data set provided by Kariyer.net. This dataset includes not only unprocessed résumés but also their number of columns are labelled by the domain experts. There are highly challenging cases whose number of columns cannot be decided easily even by the experts.

In the rest of the article, we first detail the related works in Section 2. Secondly, we explain the preliminaries and definitions in Section 3 and proposed methodologies and baselines in Section 4. Third, we explain in detail the experiments and their results in Section 5, where we also provide a discussion section that evaluates the performance of the approaches by our own interpretation. Finally, in Section 6, we conclude with the gained insights and the future perspectives on the work.

2. RELATED WORK

All organizations, from traditional companies focused on working with and optimizing conventional recruitment methods to employment-focused web portals based on intelligent recommendation systems, rely on "résumés" as the cornerstone of their business processes. Assessing résumés is, therefore, a critical and challenging step in the recruitment process, as it is not only essential but also difficult and costly, given the reliance of all organizations on résumés as the cornerstone of their business processes (Tejaswini et al., 2023).

The absence of standards in the résumés created by candidates is the key factor contributing to the difficult nature of résumé evaluation (Sinha et al., 2021). Depending on the industry it targets, each résumé is created in a particular language and structure with its own specific format. Furthermore, it is impossible to apply a consistent phrase for résumé evaluation due to the ongoing expansion of technology, work habits and business understanding. The complexities of the modern corporate environment make it impossible to even consider manually reviewing each résumé. As a result, every firm has created a variety of technologically advanced solutions to guarantee that résumés are swiftly and precisely assessed.

In order to get better results in "résumé assessing", all relevant candidate's information like skills, work experience, years of education, certifications, etc. should be extracted efficiently and accurately from the résumés (Roy et al., 2020). It is obvious that implementing an automated information extraction process from résumés significantly impacts recruitment tasks (Luo et al., 2018). There are a variety of methods used to extract information from résumés, according to the research in the literature. Information extraction is the process of mechanically obtaining structured data from structured, semi-structured or unstructured sources, such as entities, connections between entities, and characteristics (Adnan & Akbar, 2019). The process of extracting information from résumés varies depending on the structure of the résumé. In today's recruitment processes, the process of extracting information from relatively structured or semi-structured résumés prepared through e-recruitment portals, is done according to the DOM tree structure. For instance, Ji et al., (2010), created a tag tree technique in which they found and eliminated the common content between web sites using the same design while keeping the core text. Farkas et al. (2014), worked on a method of extracting information for career portal where the information of applicants is stored in a uniform data structure named HR-XML format. They used a résumé parser to automatically extract data from the résumé. These solutions, which rely on structured template files and/or DOM trees, are constrained by human labor. These techniques are challenging to scale out in large data due to the fact that it is impossible to determine how many groups of résumés have the same template.

Moreover, considering real-life applications, almost all of the résumés prepared by candidates are in an independent format. Undoubtedly, it is much harder to extract information from résumés in an unstructured format. On one of the pioneering studies on extracting information from unstructured résumés, Yu et al. (2020), describes a method for extracting structured information from unstructured résumés using a combination of rule-based and statistical approach. The first stage of the model uses regular expressions to identify and extract candidate information such as name, address, and phone number. The second stage uses a statistical model to classify each line of text in the résumé as belonging to a specific section (e.g., education, work experience). Finally, the third stage uses a combination of rule-based and statistical methods to extract specific information from each section. Therefore, they called their technique as a cascaded hybrid model, which combines rule-based and statistical approaches. However, the study is limited as the information extracted is only certain areas. Sonar & Bankar (2012) apply "chunking" to divide the résumé into different sectors based on information. Authors have divided the résumés into chunks and then parsed the information of candidates

using named entity recognition. This information was used potentially to implement the auto-fill feature of a form on a website, yet having potential to use better information extraction methods.

In the study realized by Zu et al. (2019) the text block segmentation is combined with the identification of résumé facts, and named entity recognition is carried out inside labelled text blocks using a variety of sequence labelling classifiers. Chen et al. (2018), have developed a two-step résumé information extraction approach. First, with the help of an open source tool, they detect and extracts text from résumés with different file types and they identify the raw text as different résumé blocks and then apply their proper grammatical rules to segment different blocks. Tobing et al. (2019), use also a two-stages pipeline for information extraction from the résumés. They first segment the résumés with indicative headers and they use heuristic rules to extract the necessary information from these segments. The implementation of these automated methods in real-world contexts is constrained by the fact that the aforementioned segmentation algorithms are ostensibly not resistant to various résumé layouts and styles. Qin et al. (2020), proposes a novel neural network-based approach to improve the accuracy and efficiency of person-job fit assessment in talent recruitment. They do not explicitly mention which technique they use to extract information from unstructured résumés. However, they describe their feature extraction method, which involves representing the text of the résumé as a bag-of-words and applying various transformations to generate dense feature vectors. Xu et al. (2020), use a technique called Recurrent Neural Networks (RNNs) to extract information from unstructured résumé documents. RNNs are a type of neural network that can model sequential data, making them well-suited for tasks such as natural language processing, speech recognition, and time series prediction. In the paper, the RNN model is used to learn the contextual information of different blocks in a résumé, such as the education section, work experience section, and skill section, to improve the accuracy of résumé parsing.

All these above-mentioned studies use segmentation and/or block identification techniques to extract information from unstructured résumés. Nevertheless, because the formats and designs used to create the résumés by the applicants vary greatly, they are only able to extract information from certain portions of the résumés. Their performance in real-world applications is drastically diminished as a result. In their paper, Mittal et al. (2020) use a combination of techniques to extract information from unstructured résumés. Specifically, they use the Term Frequency-Inverse Document Frequency (TF-IDF) technique to represent each résumé as a numerical vector, and they also employ Latent Dirichlet Allocation (LDA) to extract meaningful topics from the résumés. The TF-IDF technique is a well-known method in natural language processing (NLP) for measuring the relevance of a word to a document in a collection of documents. It is based on the idea that words that are rare in a collection of documents but common in a particular document are likely to be more important for understanding the content of that document

In their article, Yasmin et al. (2020), developed a framework of potential candidate selecting system by choosing a domain of document information extraction i.e. the CV/résumé documents. This development task involves the information extraction based on natural language processing i.e. tokenization, named entity recognizer (NER) and utilizes skyline query processing which works well in filtering the non-dominating objects from database and also makes a new addition to this domain. The approach described in the work of

Alamelu et al. (2021), is to use machine learning to train the dataset for the different jobs. In this instance, data extraction using NLP is done utilizing section-based segmentation. This is done to spare any company's recruiters from having to spend a lot of time and effort reading through and studying the résumés of numerous candidates. They will get the chance to view the résumés of the applicants as well as get the names of the best fit candidates for the required position, and they can then grade the résumés based on the results of this intelligent process.

As a result of recent developments in the field of NLP, several studies have been published recently that offer end-to-end frameworks to address the person-job match conundrum. The goal is to do semantic matching using sequential neural networks or modern transformer architectures to create thorough and efficient representations of the applicants and job advertisements in order to discover the best candidate for a position. Despite the systems' promising performance, the "information extraction" approach is still the most useful since deep learning-based systems have a substantial amount of opacity. An end-to-end system would raise concerns about the patterns it has learnt and the fairness of its judgements because current neural networks do not show their decision-making processes. Firstly, it should be emphasized that each résumé is tailored to the candidate's individual initiative, which results in distinct text placements when it is analyzed. Nonetheless, the data is organized into several columns on each page of the résumé. It is difficult to show the information in a relevant and sequential manner in the raw data retrieved from résumés with two or more columns since it has been noted that the text information collected at the conclusion of such a procedure is combined with other information. To divide the text elements in various places from one another, the CV's number of columns must be decided.

By concentrating on figuring out how many columns each résumé has in order to parse the raw data included in the résumés, this study aims to help with the extraction of information from unstructured résumés. Also, while considering the information extraction issue for résumés, we first consider Turkish résumés.

3. PRELIMINARIES AND DEFINITIONS

We aim to detect the number of columns of a résumé through the extracted positional information of the text. In the following section, we explain the preliminaries and the definitions that we use in our methodology.

3.1. Résumés and Their Document Characteristics

A résumé is a digital file including different pieces of text that characterize the personal and professional information. The résumés used in this work were obtained from Kariyer.net. Each résumé has different header styles, font sizes, and font faces that is characterized according to the preferences of the holder. The dataset consists of the résumés that have either one or two columns, since such résumés are the most frequently occurring types. Figure 1 shows two illustrations of various column types. Figure 1a represents a single-column sample, while Figure 1b represents a double-column one.

In a résumé, the text pieces of the same section, e.g., the information written under the *Experiences* section, are more related than the text pieces written under different sections. In fact, the relationships between different text pieces are all defined under a preformed document structure, but this structure is hidden in the PDF or Word-formatted résumés. As a result, one cannot solve the relationship between text pieces without having the source code of the document. That is why; we need to parse résumé documents without using their preformed document structure to find the features that explain the types, fonts, or places of the text pieces. But following a single parsing procedure is also impossible because there is no standard format for the résumés, i.e., each résumé is prepared with different templates or structures. Hence, we need to discover the relations between different text pieces for each single document. Parsing a résumé starts with reading its content. A document reader interprets a résumé as a two-dimensional Cartesian coordinate frame C . At each read process, it scans and interprets a piece of text which we call a *text block*. $(x_1 - x_0)$ is the width of t , $(y_1 - y_0)$ is its height. Coordinate information for a text block is exemplified in Figure 2.

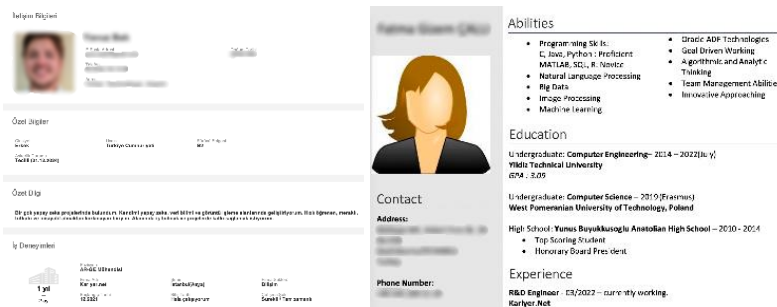


Figure 1. Sample résumé a) A single-column résumé b) A double-column résumé

Definition 1. A *text block*, t , is an object that represents a document area framed in a rectangular shape in C , whose top-left and bottom-right coordinate points will be represented by two coordinate pairs (x_0, y_0) and (x_1, y_1) respectively.

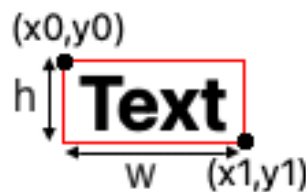


Figure 2. Representation of coordinate parameters in the sample picture

A document reader scans the content of the documents as several different text blocks, t_i . Because it is not aware of preformed document structure, at each scan, it reads text blocks at different widths and heights. Each obtained text block, t_i , has the properties which are listed in Table 1.

Once the entire document is read as a set of text blocks via the document reader, a data cleaning process is performed to remove the blocks whose contents are only spaces or tabs. The text's page information is also added. Table 2 shows a representation of a small sample after all these preprocessing steps. Each row in the table contains a text block read by a document reader at a time. Each column represents a feature of the relevant text. According to our empirical observations made in the résumés from the Kariyer.net set, we have discovered that the relation between text blocks in the same column is higher.

Table 1. Descriptions of properties expressing texts.

| Parameter | Explanation |
|-----------|---|
| x_0 | x coordinate of the top-left corner |
| y_0 | y coordinate of the top-left corner |
| x_l | x coordinate of the bottom-right corner |
| y_l | y coordinate of the bottom-right corner |
| words | The content |
| font | The font types of the words |
| size | The font size of the words |

More clearly, in a résumé, we come across either a single-column structure where each résumé section is sequential and the texts under each section are related, or a double-column structure, which is a split of the page. In a double-column structure, each column part is like a single-column structure. Thus, one needs to first find out if the studied résumé is single- or double-column before revealing the relation between different text blocks for determining the true content of a résumé. In the rest of this section, we concentrate on the problem of finding the column number of a résumé.

Table 2. Parsed Résumé Text Blocks

| text block ID | x_0 | y_0 | x_l | y_l | words | page | font | size |
|---------------|-------|-------|-------|-------|-----------------|------|-------|------|
| 10 | 2.49 | 22.3 | 49.43 | 24 | EDUCAT... | 1 | Arial | 16 |
| 11 | 3.37 | 24.05 | 11.61 | 30.3 | Universi... | 1 | Arial | 12 |
| 12 | 17.37 | 24.22 | 51.8 | 30 | İzmir Üniver... | 1 | Arial | 12 |
| 13 | 3.37 | 30.98 | 10.85 | 35.83 | Universit... | 1 | Arial | 12 |
| 14 | 17.37 | 31.16 | 51.72 | 35.54 | İzmir Üniver... | 1 | Arial | 12 |

3.2. Finding Column Number Problem

A document reader reads a résumé document file having an unknown predefined document structure as a set of text block objects, T , where each $t_i \in T$ has different properties. For the languages written left-to-right, x_{i0} and y_{i0} can be considered as the starting point of x and y axis of t_i respectively.

Definition 2. For the given T , the problem of finding its column numbers, c , is the problem of finding the size of the column set, C , of T .

Definition 3. The column set, C , is a partition of T in which $C_i \cap C_j = \emptyset$ for all $(C_i, C_j) \in C$ and $\cup C_i = T$.

Property 1. The column number of the T , which is noted as $c = |C|$, is limited to either 1 or 2 because of the nature of the résumé document files of experimental set.

If the column partition, C , of T was known, then finding c could be an easy problem of counting the elements of C . But C is unknown. Thus, we are interested in finding the column partition for the rest. In case that the

value of c is 1, then all t_i s are collected in a single column. If the value of c is 2, there can be as many different subsets C of T as the two-element subset. However, determining whether a résumé has 1 or 2 columns involves examining all two element subsets of T and a quality function which is used in decision making of the best column structure. This is a well-known NP-complete problem. In our work, we can reduce this problem thanks to document readers do never read the text blocks from different columns together. More clearly, we reduce this problem into an optimization problem that is trying to find the best column structure whose text blocks obey some criteria. We will first explain the finding columns problem definition, then reveal the criteria of the text blocks that can be found in the same column, and third, propose alternative solutions in the rest of the document.

Definition 4. The problem of finding the best column structure, Γ , of T is finding the most proper columns of T such that the t_i s in the same column have a set of positional relations, P .

In this work, we are interested in the positional relations of text blocks. Since the *word, page, font* and *size* of a t_i is not related to its position but related to its content, we do not define any relation or criteria using these features. The y_{i0} and y_{i1} of a t_i represent its vertical axis properties. But column separation is related to the horizontal axis. Even if t_i and t_j belong to the same column, their y coordinates can be too different, or vice versa. A possible relation of y coordinates can be used to discriminate the different lines belonging to the same t_i however, it is out of scope of this work. That is why we are not interested in y_0 or y_1 for the rest of this article.

Among horizontal axis coordinates, x_i describes where the read text block ends on the x axis. Different text blocks in different columns are not related to each other so that they can take too different x_i values. Furthermore, even if different text blocks are in the same column, they can still have different x_i values because they can be of different widths. Thus, the presence or absence of a relationship between x_i values of text blocks is not significant to determine if they belong to the same column.

x_0 values of different text blocks in the same column, are expected to be related to each other. Although this relationship may vary according to the format of the résumé, it should more or less correspond to the starting point of a column on the horizontal axis. More specifically, the x_0 values in all text blocks from the same column are expected to have close values, that is, they should constitute a statistical mode of a distribution. An example of x_0 distribution of a single-columned résumé is represented in Figure 3a.

Definition 5. The problem of finding Γ is the problem of clustering the x_0 values of scanned text blocks.

Since the finding column number problem can be solved by clustering the x_0 values of text blocks, we propose different clustering techniques for this issue in the next part of this article.

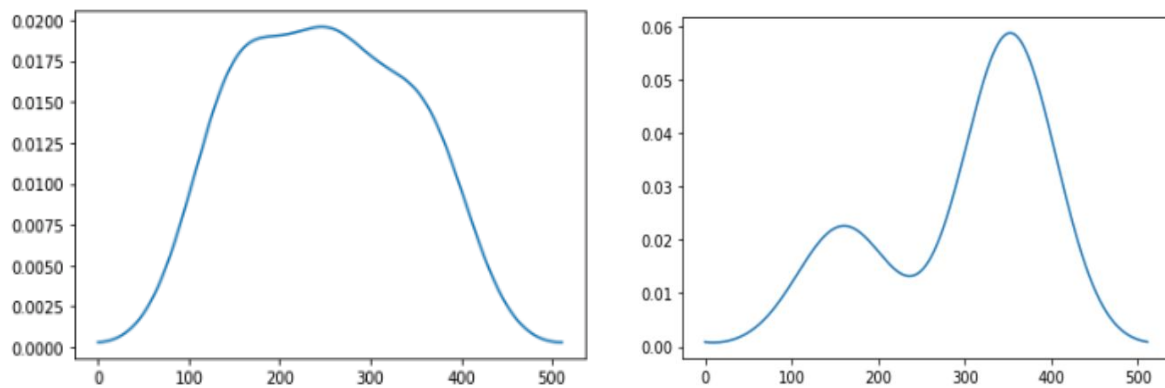


Figure 3. Estimated densities of sample résumé **a)** A single – column résumé **b)** A double – column résumé

4. CLUSTERING X_0 OF TEXT BLOCKS

Since all x_0 s from the same column should have more or less close values, we assume that they should be part of a statistical distribution. As a baseline, we estimate the possible distributions of x_0 . In the next part, we first explain this approach as our baseline, then explain Gaussian Mixture Model and DBSCAN, finally we present our proposed clustering algorithm for the mentioned problem.

4.1. Baseline Clustering

We make a Gaussian distribution assumption and estimation of the x_0 values of the text blocks of a résumé (Kokoska & Zwillinger, 2000). We expect to relate the number of columns to the number of peaks in the estimated distribution. If we obtain a distribution with a single mode, there is definitely a single column in the document. But, the main flaw of this method is that the distribution can have obvious two peaks when there happens to be a large space between the x_0 values of the same column due to the chosen layout of the résumé. Thus, two peaks do not imply two columns. We will call these types of résumés as irregular. An example to these irregular résumés is given in Figure 4. Due to the high indents of the original document, two-peak distributions are produced by x_0 values. An example to a genuinely double-column résumé is also represented in Figure 3b.

If a résumé is single-column but the estimated distribution has two peaks, the estimated x_0 values are far apart from the real x_0 values. To handle correctly the aforementioned irregularity of the résumés, we observe the difference between the estimated x_0 distribution and the real x_0 s. However, in some extreme cases, the résumés are not directly classified as having one or two columns. We interpret these cases as *uncertain*, where the true number of columns can be either one or two.

4.2. Gaussian Mixture Model Clustering

As another statistical approach, we model the problem of clustering x_0 values as a Gaussian Mixture Model (GMM), which is a category of probabilistic models stating that all generated data points are said to be derived from a combination of finite Gaussian distributions with no prior parameters (Xuan et al., 2001). We are to estimate the parameters of the individual Gaussian distributions from a posterior distribution. The parameter

estimation is performed using the iterative expectation-maximization (EM) algorithm. We follow an empirical procedure to determine the number of clusters of the x_0 values. Since the clustering incorporates both information about in-cluster cohesion and out-of-cluster separation, we choose the cluster number that maximizes average silhouette width Rousseeuw (1987) which is a well-known quality metric for finding the best cluster separation of the sets. If a résumé is truly double-column, the resulting cluster structure is expected to have a high score. We set an empirical silhouette zone in order to categorize the results of the clustering performance as *single-column*, *double-column* and *uncertain*.

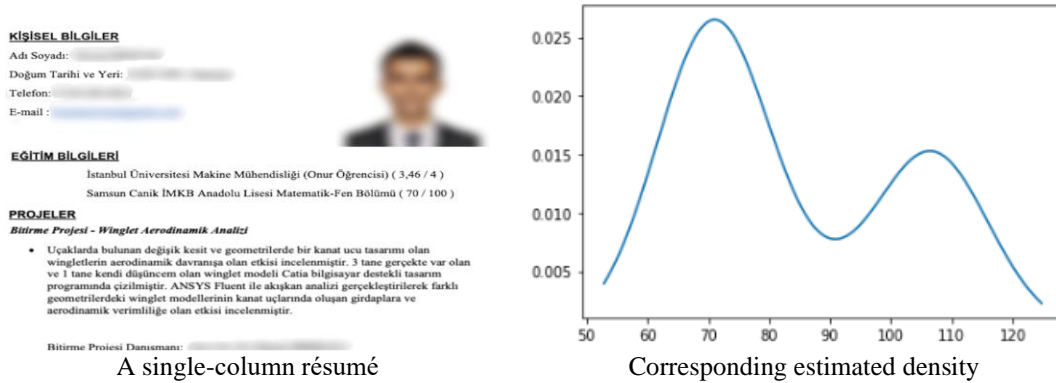


Figure 4. An example of an irregular résumé. Even though the résumé has only one column, the distribution appears to be bimodal

4.3. DBSCAN Algorithm

We use the DBSCAN algorithm to simultaneously cluster the x_0 and determine the optimal number of clusters (Ester et al., 1996). The algorithm, unlike many other clustering methods, does not need a preset the number of clusters, which suits to our needs in detecting the number of columns in résumés. Given a set of points in space, the algorithm aggregates points that are highly close and marks data points below a certain threshold in low-density regions as outliers. It requires two parameter inputs: ϵ , the minimum distance between data points in the same cluster, and $minPts$, the minimum number of data points required to form a cluster. ϵ specifies how close the points must be to be considered part of a set. The Euclidean distance is commonly used to measure the distance between two points. If the distance between two data points is less than or equal to the ϵ value, it means that the point is considered as a neighbor. $minPts$ is the minimum number of points to create a dense region. A data point must contain at least as many points as specified by the number of $minPts$ within the distance specified by the ϵ value for a region to form a dense region. The minimum value for $minPts$ should be 3.

4.4. Overlapping Headers

We propose the Overlapping Headers method, which is an algorithm based on the overlapping property of the text blocks on the horizontal axis. In their work, Chen et al. (2013) employed the connected component analysis of the gaps in order to perform page segmentation. The authors propose a hybrid page segmentation procedure with hierarchical methods for removing the appropriate space rectangles and keeping the remaining ones. The following describes a similar strategy that we apply in the study.

4.4.1. Column Detection with Overlapping Text Blocks

The representation of different text blocks of a double-column résumé on the Cartesian coordinates is shown in Figure 5. The rectangular forms of the text blocks in the same column overlap at certain intervals on the horizontal axis, whereas they do not overlap and have large gaps if they belong to different columns.

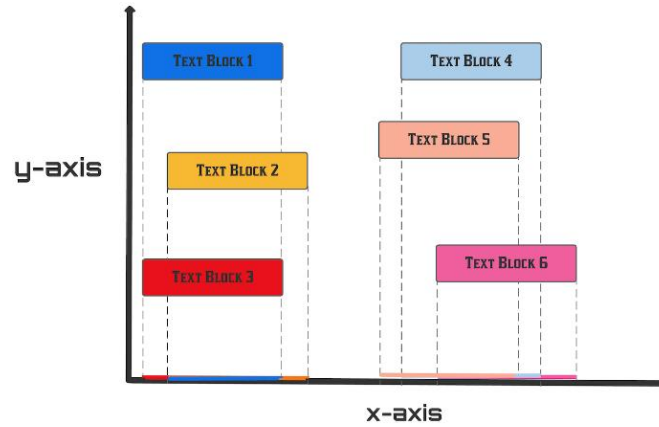


Figure 5. Overlapping text blocks

Definition 6. Let t_i and t_j be two text blocks that each of them is defined by two points $\{(x_0, y_0), (x_1, y_1)\}$ in the Cartesian space. t_i and t_j overlap if their binary overlap interval (BOI) value is zero, $BOI(t_i, t_j) = 0$, as given in (1). They are disjoint if $BOI(t_i, t_j) = 1$.

$$BOI(t_i, t_j) = \begin{cases} 0, & \max(x_{i0}, x_{j0}) - \min(x_{i1}, x_{j1}) \leq 0 \\ 1, & \max(x_{i0}, x_{j0}) - \min(x_{i1}, x_{j1}) > 0 \end{cases} \quad (1)$$

Definition 7. A column, C , is a set of text blocks in which $\forall (t_i, t_j) \in C^2, BOI(t_i, t_j) = 0$. In other words, every text block rectangle pair in a column *overlaps* with each other.

Property 2. $\exists t_i \in \text{column } C_k$ and $\exists t_j \in \text{column } C_l$, if t_i and t_j overlaps then $C_k = C_l$.

Definition 8. A document is a set of n text columns. If $n > 1$, according to Property 2, $BOI(t_i, t_j) = 1, \forall t_i$ and t_j being member of different columns and vice versa.

A document is constituted by its columns. If the number of its columns is n , being larger than one, then it has n disjoint text block rectangular set, i.e. column. In each set, every text block pair overlap. Based on these definitions and their properties, we propose an iterative algorithm to find the number of columns (see Algorithm 1). The flow schema of the algorithm is presented in Figure 6.

The algorithm first retrieves data from the document in the form of text blocks (line #1). Then it builds the first column as a set of text blocks with the first processed text block (lines # 3-6). If there are new text blocks that overlap this already processed one, it adds them to the existing set (lines #7-14). However, if it has acquired new completely disjoint text blocks, it builds a new column for it (lines #7-12,15-18). For each new non-processed text block, the overlapping check continues until all text blocks are scanned. Finally, the overall columns are checked for disjunction (lines #19-23) to ensure Property 2 is correct.

Algorithm 1 Overlapping Headers Algorithm

```

1:  $Data \leftarrow \text{extract\_textblocks}(\text{PDF Sheet})$ 
2:  $columns = \emptyset$ 
3: for  $textblock \in Data$  do
4:   if  $columns == \emptyset$  then
5:      $C = \text{createNewColumn}(textblock)$ 
6:      $columns = \text{insertColumn}(C, columns)$ 
7:   else
8:     for  $C \in columns$  do
9:        $CheckOverlapInterval == 0$ 
10:      for  $textblockofC \in C$  do
11:         $CheckParameter = \text{checkBOI}($ 
12:           $textblock, textblockofC)$ 
13:      end for
14:      if  $CheckOverlapInterval == 1$  then
15:         $C = \text{insertTextBlock}(C, textblock)$ 
16:      else
17:         $C_{new} = \text{createNewColumn}($ 
18:           $textblock)$ 
19:         $columns = \text{insertColumn}($ 
20:           $C_{new}, columns)$ 
21:      end if
22:    end for
23:  end if
24: end for
25: if  $isDisjoint(columns)$  then
26:   return  $size(columns)$ 
27: else
28:    $columns = \text{mergeOverlappedColumns}(columns)$ 
29:   return  $size(columns)$ 
30: end if

```

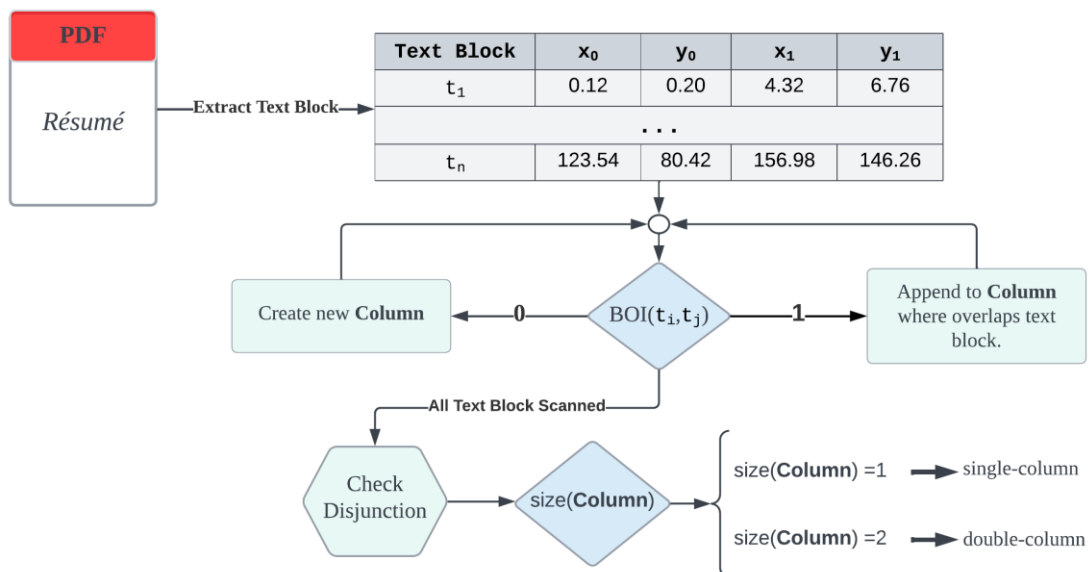


Figure 6. Overlapping text blocks flowchart

According to the properties and the iterative algorithm proposed, some of the résumé examples having two irregular column structures are also marked as single-column as shown in Figure 7.

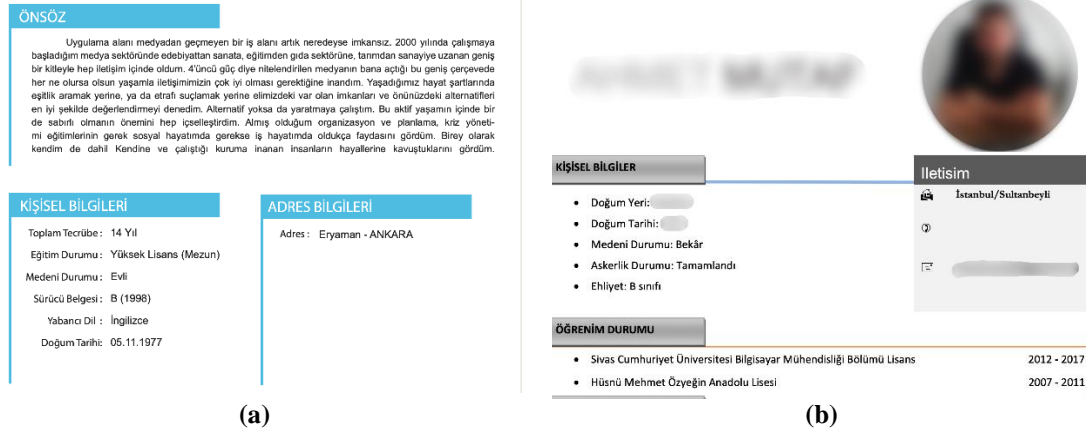


Figure 7. Two résumé examples with irregular structures **a)** First single, then double-column résumé example **b)** First double, then single-column résumé example

Algorithm 1 labels the résumé in Figure 7a as single-column from the beginning. Even if there are separate columns in the following, the rest is labelled as single-column as well, since the initial text blocks and the following blocks overlap with all of the unprocessed text blocks. For Figure 7b, the merge operation in the last part of the procedure follows Property 2, whereas there exist disjoint columns at the beginning. As a result, this résumé is also categorized as single-column. However, in these examples, the single-column sections are only short introductory paragraphs or short articles describing the career goal. The sections containing the main information of the résumé are distributed onto two columns in both examples. This is typical of real-world résumé sample. Considering all extracted text blocks may cause us to ignore such characteristics because of the reasons explained above. Nevertheless, instead of working with all text blocks, one can work with some proper text blocks such as headers, which may be more meaningful for column disjunctions. In the next section, we extend the proposed overlapping algorithm for overcoming such issues.

4.4.2. Header Detection

The currently offered methods provide a general framework for determining the number of columns of a résumé. However, we encounter irregular column structures in the real-world data as shown in Figure 7.

Another example is given in Figure 8. This example can be classified as double-column, because the text blocks that include the personal information are positioned highly disconnectedly from the text blocks of the labels of this information even though they are related on the line basis. As long as these text blocks are not positioned close to each other Algorithm 1 will classify such résumés as double-column. As we know that these documents are single-column résumés in reality, the separated but actually related text blocks of personal information and their labels should be associated. In the example of Figure 8, the main label sections all overlap with each other. As a result, they will all fit into a single set of columns.

In Figure 9, the scatter plot of the (x_0, y_0) coordinates of the text blocks belonging to two résumé examples is shown. The points are coded with different colors with respect to the types of the text blocks: personal

information and label. Considering all of the types of text blocks together, the separation of the coordinates is vague in the example of a single-column résumé while it is quite obvious in the double-column sample. However, we can distinguish clearly the coordinate separation in both cases by using only labels.



Figure 8. A résumé example with one column but having a large distance between disjoint text blocks

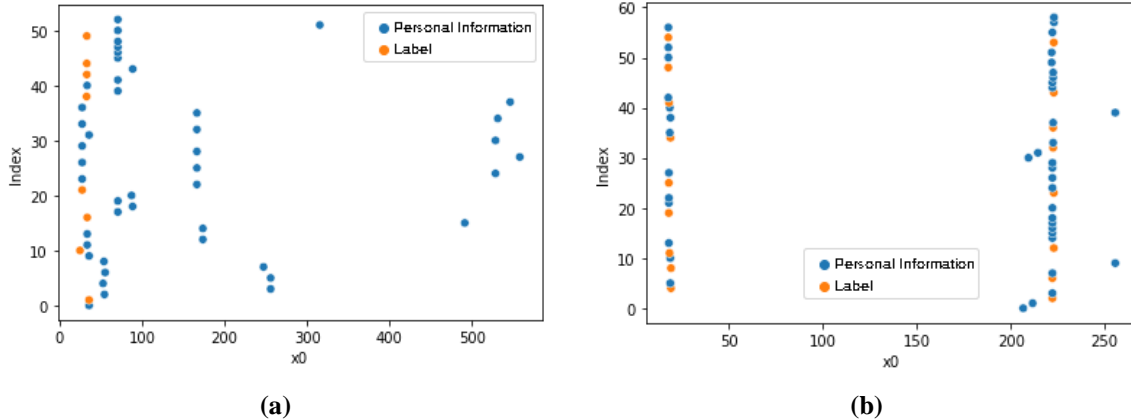


Figure 9. The scatter plot of the (x_0, y_0) coordinates of the text blocks **a)** A single column sample **b)** A double-column sample

Not only for cases like the one shown in Figure 8 but also for any other résumé, checking the overlap of main labels is enough instead of checking all text block overlaps. In summary, determining the number of columns by extracting all text blocks may result in both unnecessary computational load and incorrect results, as shown in the previous examples.

We propose to consider the text block typology when selecting the important text blocks instead of all for overcoming the mentioned issue. We define the text blocks typology into three categories that are related hierarchically: *characteristics*, *headers* and *main headers*. In the hierarchy, we call a parent if the text block of interest is hierarchically superior and linked to a lesser text block. The lesser text block is called the child

of the text block of interest. This categorization allows us to use the important ones instead of considering all of them.

In the first category, there are text blocks that contain personalized explanations, which we call *characteristic*. Characteristics are at the lowest level in the text block hierarchy. They do not have any relationship with lower level text blocks, thus they have no children.

The second category is the *header*. We define a header as text blocks associated hierarchically with another header or characteristic. A header is not specific to a résumé, because they do not include personal information. Instead, the headers represent the meta-characteristics of personal information. For instance, “Education Level” is a header but “Master’s degree” is a characteristic. Headers may be parents or children of other headers.

We call the third and the top category as *main header*. The main header text blocks don’t have any parents. For example, a text block “Skills” is a main header whereas text blocks of “language”, “certificates” or “hobbies” may be its children. But, in some résumés, “language” may become the main header as well.

A single-column résumé example is displayed in the Figure 10. Here, “Personal Information” is a main header but its child, “Language”, is a header. Using the Algorithm 1 with header types text blocks, this résumé is classified as a double-column résumé because the headers are disjoint. The algorithm would classify it as single-column, if we were to use the main header.

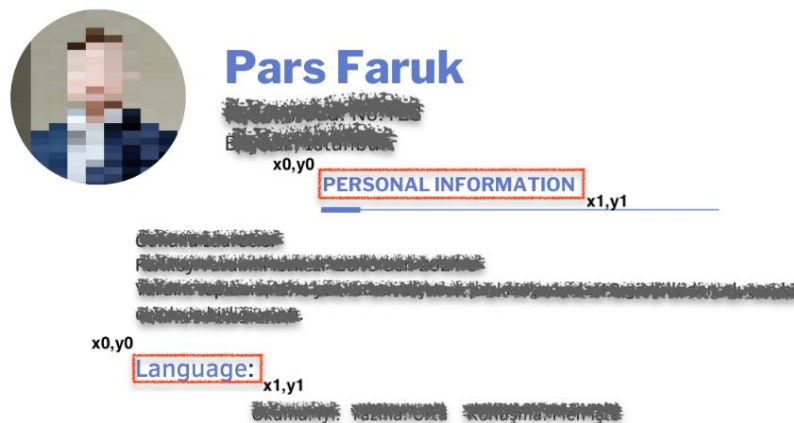


Figure 10. A résumé example with headers and main headers

As we mentioned previously, preformed document structure is unknown and can be built by using the properties of text blocks since usually, the text blocks belonging to the same section have the same font, size, or type, even though we encounter exceptions to this inference. Since we use Kariyer.net’s data and there are professionals in this company who are especially specialized in reviewing résumés; we benefit from their expertise. Rather than developing a method for distinguishing the text block typology, we rely on the header and main header lists tailored by the experts of the company. We concentrate on the main headers list provided by Kariyer.net because their coordinates are the essential features for the detection of the number of columns.

We employ a text similarity check between each extracted text block and main header list elements by using sequence matcher approach (Rao et al., 2018). Once the main headers of studied résumé are detected, we apply the number of columns finder procedure given in Algorithm 1.

Even using the main headers, some résumés can be more challenging and their number of columns cannot be easily classified, even by the human experts. When we evaluate the example in Figure 7b, there are three main headers in one column and two main headers in the other column. In the résumés of regular formats, both columns have equal numbers of headers, while there can be more or less headers in the different columns in many cases. However, some real-world examples have even more complex structures with different numbers of main headers. In the method we propose to add new rules for such résumés. We mark their number of columns as uncertain in order not to make any wrong classifications.

4.5. Hybrid Column Detection

Each of the previously explained methods has different weaknesses and strengths. They cannot handle some complicated cases. Except DBSCAN, each one labels some types of résumés *uncertain*. The *uncertain* labels of different methods do not cover each other. In other words, one method can detect the number of columns while another one marks them as *uncertain*. We aimed to decrease the number of *uncertain* résumés. That is why we designed a *Hybrid Column Detection* by using Baseline, DBSCAN, and Overlapping Headers together. The sequential flow chart of the Hybrid Column Detection method is given in Figure 11. Coordinate values extracted from a résumé are sent to the Hybrid Column Detection Method. We give priority to the Overlapping Headers in the hybrid model. If the Overlapping Headers is *uncertain*, other methods are used.

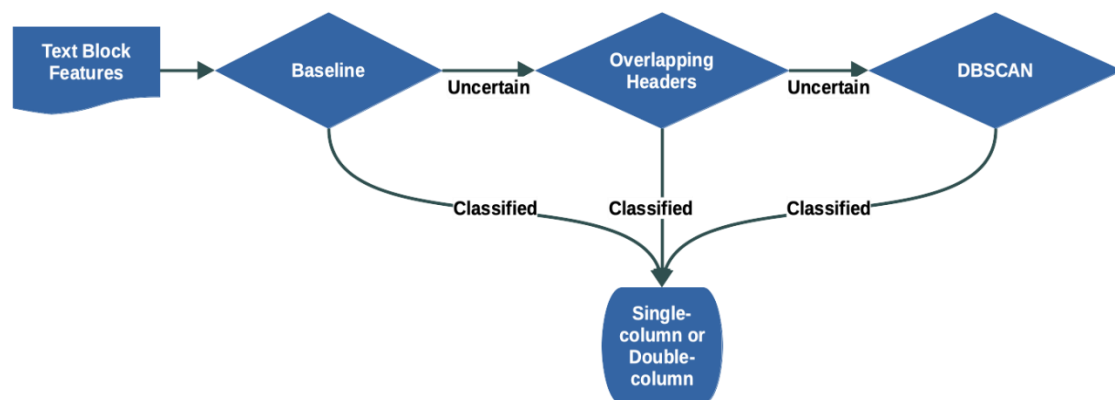


Figure 11. Hybrid Column Detection Method Flowchart

5. EXPERIMENTS AND RESULTS

The résumés used in the experiments are provided by Kariyer.net. They consist of a set of PDF documents having different fonts, colors and formats. All of them are authentic résumés created for real job applications in Turkey's marketplace. Some of them have been prepared in ready-made template formats, while some others are prepared by the applicants in free format. First, the text parsing process is put into practice. After removing any damaged files or those that could not be parsed, we finally have a total number of 1201 of documents in the dataset.

Prior to evaluating our algorithms, the résumés in the dataset are labeled with their true number of columns with the collaboration of human resources experts of Kariyer.net. This manually added ground truth information helps us to compare the efficacy of the methods objectively as in supervised learning even though all the approaches proposed in Section 3 are fundamentally unsupervised learning methods.

Each method has its own parameters that affect the performance: the ϵ and *minPts* in DBSCAN, or the silhouette value zone in GMM-based Clustering, which allows us to decide the number of clusters. Before evaluating the algorithms, we tune the parameters by using 15% of the master dataset (in 190 résumés). To prevent algorithmic biases, we reserve as many résumés as possible for testing. The parameter values for each method in these 190 résumés are chosen based on their best performances.

Usually, the number of columns may be clearly stated by the human expert without any question, but occasionally, their determination can be ambiguous even for the expert. As an example, a short part of a résumé at the beginning may be in single-column format where a short bio or personal information is placed, but the rest of the résumé that includes the other personal information like education, skills or experiences may be in double-column format. Some examples of such irregular résumés are displayed in Section 3, Figure 7a, 7b.

We perform two separate experiments on the test dataset. In the first batch of experiments, we only use résumés for which all experts agree on their numbers of columns. In other words, this set consists of the résumés whose columns can be distinguished relatively well by the human eye. Throughout our experiments, we refer to this set as the “reduced set”. There is a total of 231 résumés, of which 195 documents are single-column and 36 are double-column. The methods are expected to estimate the true number of columns easily compared to the other résumés.

The second batch of experiments are performed on the set of résumés that are labeled according to the majority vote of the experts. We call this set as the “original set”. In the original set, there are a total of 1011 résumés of which 678 and 333 are in single-column and double-column format respectively. The original set also includes the reduced set.

We report the results of the experiments on the reduced set of relatively easy-to-analyze résumés in Section 5.1. The results of the experiments on the original set are presented in Section 5.2. Finally, in Section 5.3, all outcomes are examined and discussed collectively.

5.1. Experiment with the Reduces Set

All of the aforementioned methods are initially evaluated on the reduced set, and the results of these experiments are reported in Figure 12 as confusion matrices. Additionally, Table 3 provides the F1-score, precision, recall and accuracy values attained to evaluate these methods. We also show the success on single- and double-column résumés separately on Table 4. The Hybrid Column Detection yields the same outcomes with the Overlapping Headers because the latter method performed on the reduced set does not produce any uncertain predictions.

First of all, DBSCAN and GMM-Based Clustering, give different results with an accuracy of 84% and 87% respectively. Concentrating on Figure 12a and 12b together, we distinguish that the DBSCAN performs poorly for double-column résumés. It could detect only 15 of 36 double-column résumés, which is less than 50% accuracy, while GMM-based Clustering catches 26 of 36, which is more than 70% accuracy. On the contrary of double-column résumés, DBSCAN gives better performance than the GMM-Based Clustering in single-column résumés. It seems DBSCAN has a bias towards detecting single-column. Considering F1-Score, precision, recall, and overall accuracy, GMM-based Clustering outperforms DBSCAN.

Table 3. Results on the Reduced Set

| Method | Accuracy | F1-Score | Recall | Precision |
|----------------------|----------|----------|--------|-----------|
| Overlapping Headers | 0.97 | 0.95 | 0.96 | 0.94 |
| Baseline | 0.87 | 0.77 | 0.81 | 0.75 |
| DBSCAN | 0.84 | 0.68 | 0.67 | 0.7 |
| GMM-Based Clustering | 0.87 | 0.77 | 0.81 | 0.75 |

Baseline predicts far less accurately than the Overlapping Headers in both single-column and double-column résumés (Table 4). Furthermore, Overlapping Headers has much less false negatives than the Baseline (Figure 12c and 12d). Baseline exhibits the same performance on the reduced set as GMM-based Clustering. We remind you that these two methods are based on statistical techniques. Both techniques use an assumption that x_0 follows a Gaussian distribution. Although their performances can be accepted as “good”, we still underline that Overlapping Headers perform 10% better than them.

The reduced set includes résumés with relatively well-formed column structures, that is, the text blocks are not indented too far from the margins of the headers or the main headers, which offers in turn clearly detectable column margins. Thus, in fact, we expect that these two algorithms would perform as well as Overlapping Headers if the column structures could be identified by the x_0 coordinate Gaussian distribution properties. However, the experimental results reveal that this assumption cannot be sufficient for determining the number of columns.

The Overlapping Headers, which has an accuracy value of 97%, is the method with the highest accuracy among all. Almost any résumé can be predicted correctly by using this method. This result can be interpreted as the usage of the projection of main header coordinates to the horizontal axis being a good indicator for detecting the columns. In this relatively easy set, the three other methods also provide an accuracy rating of over 80%, which cannot be considered poor. But Overlapping Headers are highly successful by far. Compared to other methods, the DBSCAN includes more false negative predictions for double-column résumés. However, it behaves inversely on single-column résumés: the method produces a highly low rate of false negatives. As a result, it can be argued that single-column résumés generated using DBSCAN typically perform quite well. In particular, it is seen that it is much easier to analyze the more comprehensible résumés in the reduced set. All algorithms are effective at predicting the true labels of the résumés in the reduced set. Among them, Overlapping Headers is the most successful method.

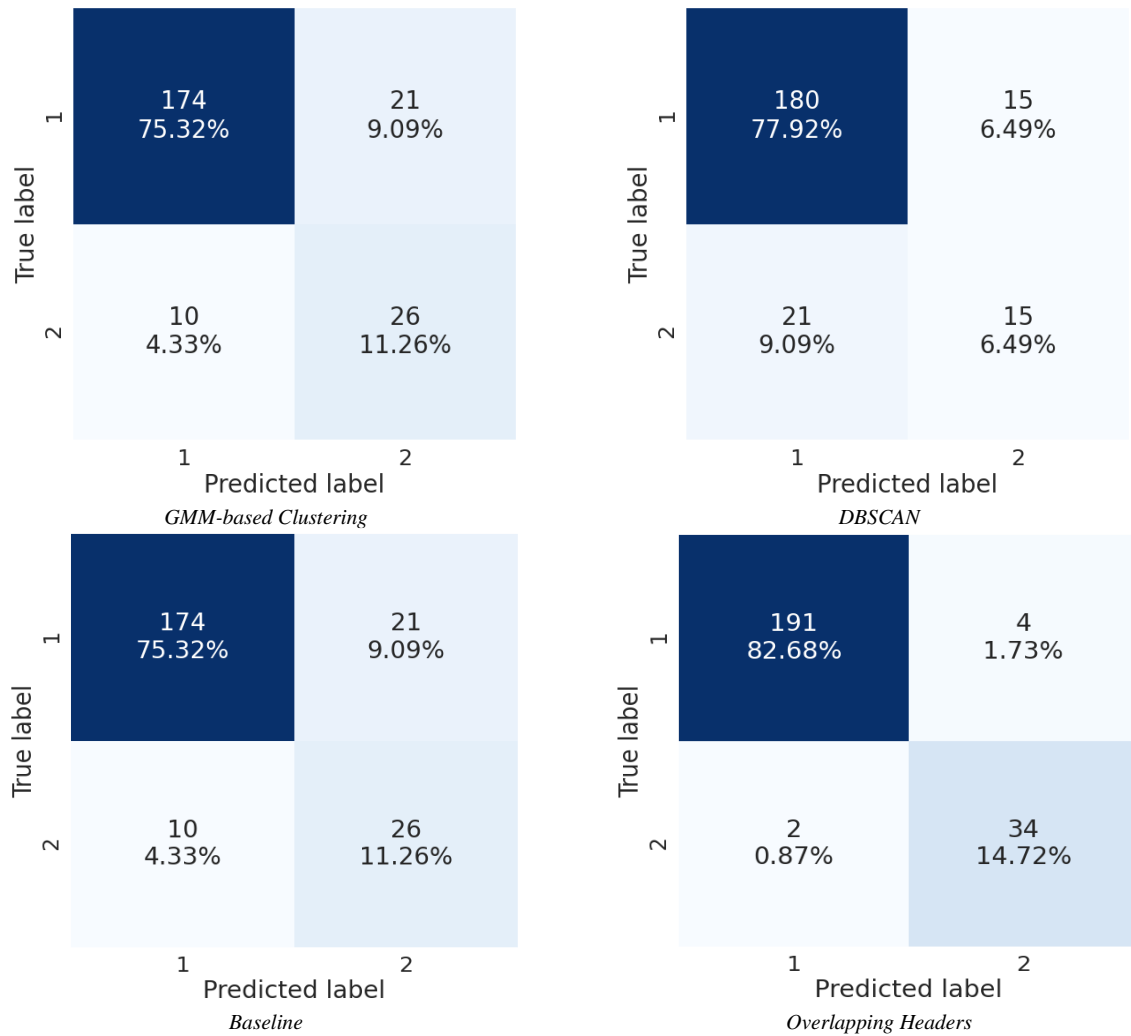


Figure 12. Confusion matrices obtained after the experiments on the reduced set.

Table 4. Accuracies for Single- and Double-column résumés in the Reduced Set

| Method | Single-column | Double-column |
|----------------------|---------------|---------------|
| Overlapping Headers | 0.98 | 0.94 |
| Baseline | 0.89 | 0.72 |
| DBSCAN | 0.92 | 0.41 |
| GMM-Based Clustering | 0.89 | 0.72 |

5.2. Experiment with the Original Set

In the experiments carried out on relatively more understandable résumés in the previous section, the methods within the scope of this study perform promisingly. This section focuses on evaluating the performance of the set of all résumés, namely the original set. The corresponding confusion matrices are shown in Figure 13. Note that the methods except DBSCAN and the Hybrid Column Detection include the uncertain estimations within. These results report that DBSCAN yields an accuracy measure of 82%, dramatically higher than the GMM-based Clustering. When observing the separated performances on each column type regarding Table 5, we notice that not only on single- but also on double-column, GMM-based Clustering exhibits the worst performances. In both cases, in comparison with the other proposed methods, the GMM-based Clustering

produces too many *uncertain* estimations. In addition, it estimates 149 of 378 *non-uncertain* labels incorrectly. Its performance on both reduced and original sets reveals that it does not achieve much in deciding the number of columns when they are not obvious. When compared with GMM-based Clustering, Baseline is more successful, although they both use Gaussian distribution Assumptions. In particular, it has a moderate efficiency for single-column detection. But, as it was the case in the experiments with the reduced set, its performance is low for double-column detection. Considering the Baseline and Overlapping Headers, the Overlapping Headers outperforms the Baseline by correctly estimating 84% of the résumés, whereas the Baseline attains a percentage of 61% of the same set. Additionally, the Overlapping Headers yields less errors than the Baseline in its single- and double-column predictions. The résumés are labeled intermediately as *uncertain* by the Baseline and Overlapping Headers instead of being erroneously estimated. This results with less erroneous predictions in single- or double-column predictions.

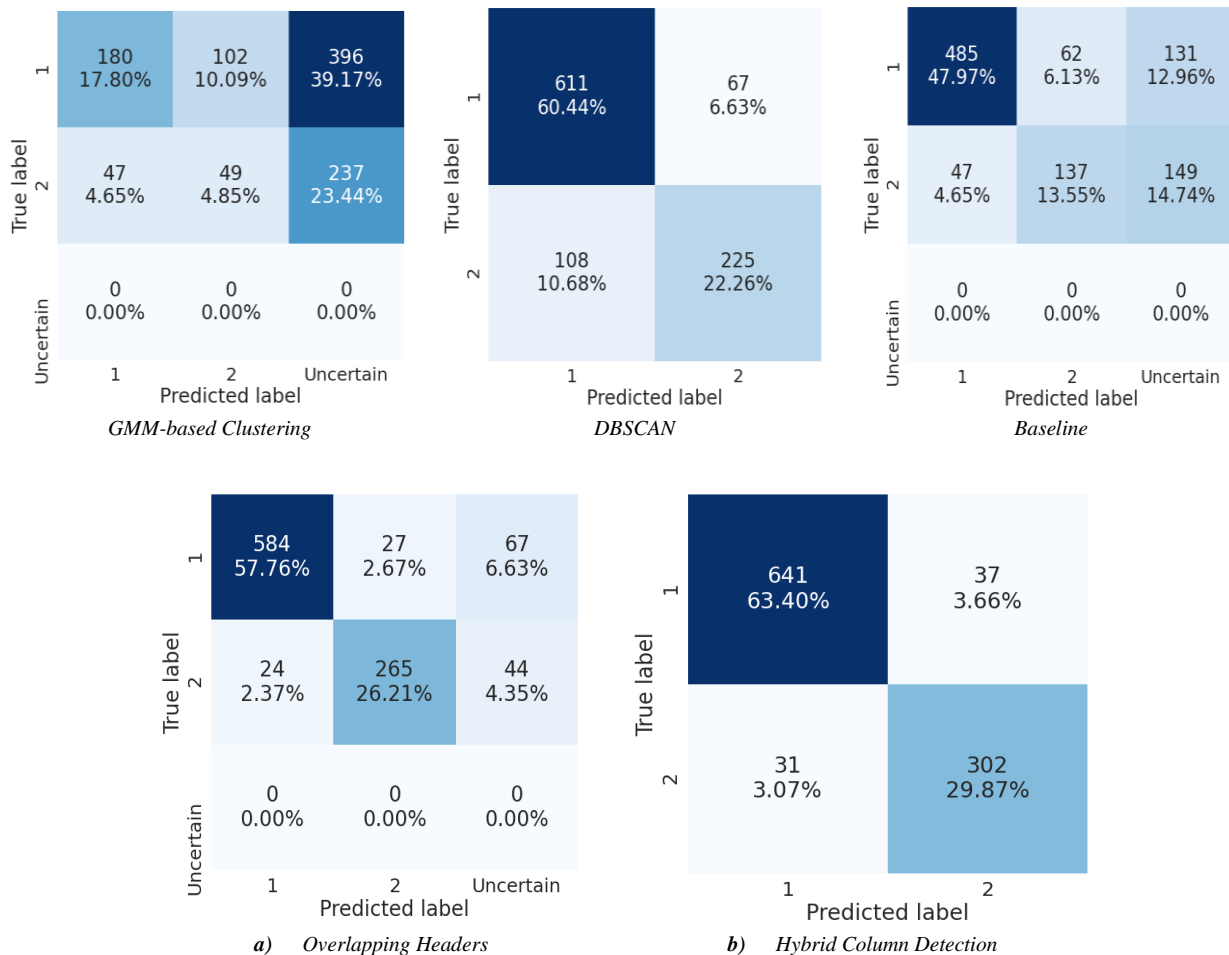


Figure 13. Confusion matrices obtained after the experiments on the original set

Among the two methods which does not use *uncertain* labels, the DBSCAN predicts 836 accurate predictions for single- and double-column, but it predicts the number of columns of 175 résumés incorrectly. Among all methods, DBSCAN produces the falsest negatives as it was the case in the reduced set. More importantly, it produces an incorrect assessment of the 108 double-column résumés. It estimates 32% of the résumé labels inaccurately. However, it estimates only 10% of single-column résumés incorrectly. Therefore, it can be said

that DBSCAN tends to accurately predict single-column résumés in the original collection, as it was the case in the reduced set. The Hybrid Column Detection, on the other hand, performs highly better than any other method, correctly predicting 641 single-column and 302 double-column résumés. It gives the highest accuracy on both single- and double-column. In Table 6, we report the F1-score, accuracy, precision and recall values of the experimental results on the original set. The Hybrid Column Detection outperforms the other number of columns prediction methods in terms of all of the aforementioned metrics. The GMM-Based Clustering, on the other hand, performs too poorly with an accuracy of 22%. Although the Baseline does not show a high performance with an accuracy of 61%, it estimates 622 of the résumés correctly (Figure 13c). It produces an incorrect single or double-column estimate for only 109 résumés.

Table 5. Accuracies for Single- and Double-column résumés in the Original Set

| Method | Single-column | Double-column |
|-------------------------|---------------|---------------|
| Hybrid Column Detection | 0.95 | 0.9 |
| Overlapping Headers | 0.86 | 0.79 |
| Baseline | 0.71 | 0.41 |
| DBSCAN | 0.9 | 0.67 |
| GMM-Based Clustering | 0.15 | 0.15 |

Table 6. Results on the Original Set

| Method | Accuracy | F1-Score | Recall | Precision |
|-------------------------|----------|----------|--------|-----------|
| Hybrid Column Detection | 0.93 | 0.93 | 0.93 | 0.94 |
| Overlapping Headers | 0.84 | 0.89 | 0.84 | 0.93 |
| Baseline | 0.61 | 0.7 | 0.61 | 0.84 |
| DBSCAN | 0.82 | 0.82 | 0.82 | 0.82 |
| GMM-Based Clustering | 0.22 | 0.32 | 0.22 | 0.65 |

6. DISCUSSION

When we evaluate all the experimental results together, we see that the Overlapping Headers yields the best results in the experiments on the reduced set. Furthermore, on the original set, the Hybrid Column Detection, which employs the Overlapping Headers as an intermediate step to determine also the uncertain résumés, gives the most successful results. The poorest results are obtained with the two well-known clustering methods; DBSCAN and GMM-based Clustering. When we consider both the experimental performances and their own characteristics, we can reach the following conclusions for the studied methods;

1. Clustering the x_0 coordinates of the text blocks is a highly promising approach for detecting the number of columns of résumés.
2. Among the clustering approaches, clustering with DBSCAN algorithm tends to mark résumés as single-column.
3. The determination of the number of columns through statistical methods based on the Gaussian distribution fitting shows moderate performance if the columns are well separated. From these methods, simply stating the number of estimated Gaussian densities of the x_0 distribution performs better than more complex method of GMM-based Clustering.

4. The idea of hierarchical separation of text blocks and the use of more descriptive main headers seems effective for column number finding problem because Overlapping Header results with higher success rates in detecting the number of columns.
5. The Overlapping Headers approach performs better than both traditional clustering methods (DBSCAN or GMM-based Clustering) and the statistical fitting-based methods (Baseline or GMM-based Clustering).
6. We deduce that running other clustering methods on the x_0 coordinates of the headers or the main headers, instead of the x_0 coordinates of all text blocks can increase the performance in determining the number of columns. However, in this case, since the number of points that are to be clustered will be too small, it may be challenging to determine the parameters of the algorithms.
7. Every method has its own strengths and weaknesses. An incorrectly classified résumé by a certain method may be correctly classified by other methods. This leads us to combine the strengths of the methods successively.
8. The hybrid approach, built upon the strengths of the individual algorithms, makes use of the *uncertain* situations that are classified by the Overlapping Headers. This intermediate extension makes this approach the most successful approach in determining the number of columns. In the experiments that use the set of many challenging cases, the success rate of the Hybrid Column Detection is about 10% higher than that of Overlapping Headers.

Among the proposed approaches, we obtain the best results with the proposed hybrid approach. This one combines the strength of baseline, DBSCAN and proposed overlapping headers. Since it is based on several powerful methods, it captures the exception cases as well as the common cases. This method is used in real-world systems for detecting the headers of many different types of curriculum vitae. It is flexible for one and two columns and mixtures as well.

7. CONCLUSION

This study focused on determining the number of columns that a résumé file has, regardless of how the column structure is set up. This issue can be solved by methods such as natural language processing or text mining. However, configuring a file with these methods, whose document structure is unknown, requires labeling almost every section in that file. In many files, it is challenging to determine how the sections are divided, even with the human eye. As a result, such labeling tasks require a lot of time and effort but they might not be objective. Therefore, we refrained from using a supervised learning strategy, which necessitates meticulous document tagging. Instead, first, we suggested using the text blocks' coordinates that were taken from the résumés according to our empirical observations on the set of résumés taken from Kariyer.net; second, we defined the problem of finding the columns of a résumé as a clustering of their extracted text block coordinates; and third, we presented a new clustering method, Overlapping Headers, using these coordinates and compared its performance with the well-known clustering approaches.

In order to measure the performance of the proposed method, two separate experiments were conducted on the dataset provided by the Kariyer.net platform, with résumés whose number of columns were previously marked by experts. In the first experiment, column structures that are relatively easy to detect were used. In the second experiment, difficult résumés, in which it could not be easily decided how many columns there were, were in the majority. In both experiments, it was seen that the proposed method was more successful than the baselines. The Overlapping Headers in the easy set showed a high success rate of 97%. In the difficult set, the Hybrid Column Detection achieved 93% success. With the detailed evaluation of the methods, it was seen that traditional clustering approaches were one step behind the methods we suggested in determining the number of columns. Of these, DBSCAN tended to find a single column, while GMM-based Clustering performed quite unsuccessfully, with 22% accuracy, especially in experiments involving difficult cases. Thus, it turns out that novel clustering methods developed specifically for this problem give better results in determining the number of columns.

Although the study was performed on résumés, the suggested strategies are not résumé-specific and can be applied to any other types of text documents. Additionally, the proposed methodology is independent from the language of the résumé because it is based on texts' locations. It has the ability to work with any natural language. The approach is not affected by whether the text is written from left to right or right to left. This work can be extended along many different paths. First, all the methods can be tested on documents different from résumés. One expects that the methods should find the number of columns more accurately on other types of documents because résumés are one of the most irregular documents in terms of their structures. Second, an extension to the Overlapping Headers can be proposed because this method still cannot detect the number of columns for some of the difficult cases. In this work, we proposed using main headers rather than using all text blocks. A more definitive feature of the text blocks can be found by building their complete hierarchical structures. However, this can be an effort-demanding task since each résumé has almost its own free format. Third, in this work, we focus on finding only single and double columns. In some cases, a document might have three or more columns. Thus, Overlapping Headers can be generalized for more the number of columns. Finally, here we completely focus on unsupervised approaches. However, supervised learning based on the text block coordinates can also be successful. Since the résumé set that we use in our experiments is already labelled, a model can be trained.

AUTHOR CONTRIBUTIONS

Conceptualization, Y.B., G.K.O. and S.N.T.; methodology, Y.B. and G.K.O.; fieldwork, Y.B. and S.N.T.; software, Y.B.; title, Y.B., G.K.O. and S.N.T.; validation, Y.B., G.K.O. and S.N.T.; laboratory work, Y.B., G.K.O. and S.N.T.; formal analysis, Y.B.; research, Y.B., G.K.O. and S.N.T.; sources, Y.B.; data curation, Y.B.; manuscript-original draft, Y.B., G.K.O. and S.N.T.; manuscript-review and editing, Y.B., G.K.O. and S.N.T.; visualization, Y.B.; supervision, G.K.O. and S.N.T.; project management, G.K.O. and S.N.T. . All authors have read and legally accepted the final version of the article published in the journal.

ACKNOWLEDGEMENT

This study was conducted within the scope of the R&D Project Cooperation signed between Galatasaray University and Kariyer.net in accordance with Article 58/K of the YÖK Law No. 2547.

CONFLICTS OF INTEREST

No conflict of interest was declared by the authors.

REFERENCES

- Adnan, K., & Akbar, R. (2019). An analytical study of information extraction from unstructured and multidimensional big data. *Journal of Big Data*, 6(1), 1-38. <https://doi.org/10.1186/s40537-019-0254-8>
- Alamelu, M., Kumar, D. S., Sanjana, R., Sree, J. S., Devi, A. S., & Kavitha, D. (2021, December). Resume validation and filtration using natural language processing. In *2021 10th International conference on internet of everything, microwave engineering, communication and networks (IEMECON)* (pp. 1-5). IEEE. <https://doi.org/10.1109/IEMECON53809.2021.9689075>
- Chen, K., Yin, F., & Liu, C. L. (2013, August). Hybrid page segmentation with efficient whitespace rectangles extraction and grouping. In *2013 12th International Conference on Document Analysis and Recognition* (pp. 958-962). IEEE. <https://doi.org/10.1109/ICDAR.2013.194>
- Chen, J., Zhang, C., & Niu, Z. (2018). A Two-Step Resume Information Extraction Algorithm. *Mathematical Problems in Engineering*, 2018(1), 5761287. <https://doi.org/10.1155/2018/5761287>
- Çelik, D., & Elçi, A. (2012). An ontology-based information extraction approach for résumés. In *Proceedings of the 2012 International Conference on Pervasive Computing and the Networked World ICPCA/SWS'12* (p. 165–179). Berlin, Heidelberg: Springer-Verlag. https://doi.org/10.1007/978-3-642-37015-1_14
- Das, P., Pandey, M., & Rautaray, S. S. (2018). A CV parser model using entity extraction process and big data tools. *International Journal of Information Technology and Computer Science*, 9(2), 21-31. <https://doi.org/10.5815/ijitcs.2018.09.03>
- Ester, M., Kriegel, H. P., Sander, J., & Xu, X. (1996, August). A density-based algorithm for discovering clusters in large spatial databases with noise. In *kdd* (Vol. 96, No. 34, pp. 226-231).
- Farkas, R., Dobó, A., Kurai, Z., Miklós, I., Nagy, Á., Vincze, V., & Zsibrita, J. (2014). Information extraction from Hungarian, English and German CVs for a career portal. In *Mining Intelligence and Knowledge Exploration: Second International Conference, MIKE 2014, Cork, Ireland, December 10-12, 2014*. Proceedings (pp. 333-341). Springer International Publishing. https://doi.org/10.1007/978-3-319-13817-6_32
- Gaur, B., Saluja, G. S., Sivakumar, H. B., & Singh, S. (2021). Semi-supervised deep learning based named entity recognition model to parse education section of resumes. *Neural Computing and Applications*, 33, 5705-5718. <https://doi.org/10.1007/s00521-020-05351-2>

- Holm, A. B. (2012). E-recruitment: Towards an ubiquitous recruitment process and candidate relationship management. *German Journal of Human Resource Management*, 26(3), 241-259 <https://doi.org/10.1177/239700221202600303>
- Ji, X., Zeng, J., Zhang, S., & Wu, C. (2010). Tag tree template for Web information and schema extraction. *Expert Systems with applications*, 37(12), 8492-8498. <https://doi.org/10.1016/j.eswa.2010.05.027>
- Joan, S. P. F., & Valli, S. (2019). A survey on text information extraction from born-digital and scene text images. *Proceedings of the National Academy of Sciences, India Section A: Physical Sciences*, 89, 77–101. <https://doi.org/10.1007/s40010-017-0478-y>
- Kariyer.net (2025) [URL](#)
- Keskin, Ş. R., Bali, Y., Orman, G. K., Daniş, F. S., & Turhan, S. N. (2022, June). Determining Column Numbers in Résumés with Clustering. In *IFIP International Conference on Artificial Intelligence Applications and Innovations* (pp. 460-471). Cham: Springer International Publishing. https://doi.org/10.1007/978-3-031-08337-2_38
- Kokoska, S., & Zwillinger, D. (2000). CRC standard probability and statistics tables and formulae. *Crc Press*.
- Liu, X., Gao, F., Zhang, Q., & Zhao, H. (2019). Graph convolution for multimodal information extraction from visually rich documents. *arXiv preprint arXiv:1903.11279*.
- Luo, Y., Zhang, H., Wang, Y., Wen, Y., & Zhang, X. (2018, November). ResumeNet: A learning-based framework for automatic resume quality assessment. In *2018 IEEE International Conference on Data Mining (ICDM)* (pp. 307-316). IEEE. <https://doi.org/10.1109/ICDM.2018.00046>
- Mao, S., Rosenfeld, A., & Kanungo, T. (2003). Document structure analysis algorithms: a literature survey. In *T. Kanungo, E. H. B. Smith, J. Hu, & P. B. Kantor (Eds.), Document Recognition and Retrieval* (pp. 197 – 207). *International Society for Optics and Photonics SPIE* volume 5010. <https://doi.org/10.1117/12.476326>
- Mittal, V., Mehta, P., Relan, D., & Gabrani, G. (2020). Methodology for resume parsing and job domain prediction. *Journal of Statistics and Management Systems*, 23(7), 1265-1274. <https://doi.org/10.1080/09720510.2020.1799583>
- Qin, C., Zhu, H., Xu, T., Zhu, C., Ma, C., Chen, E., & Xiong, H. (2020). An enhanced neural network approach to person-job fit in talent recruitment. *ACM Trans. Inf. Syst.*, 38 <https://doi.org/10.1145/3376927>
- Rao, G. A., Srinivas, G., Rao, K. V., & Reddy, P. P. (2018). A partial ratio and ratio based fuzzy-wuzzy procedure for characteristic mining of mathematical formulas from documents. *IJSC—ICTACT J Soft Comput*, 8(4), 1728-1732. <https://doi.org/10.21917/ijsc.2018.0242>
- Rousseuw, P. J. (1987). Silhouettes: A graphical aid to the interpretation and validation of cluster analysis. *Journal of Computational and Applied Mathematics*, 20, 53–65 [https://doi.org/10.1016/0377-0427\(87\)90125-7](https://doi.org/10.1016/0377-0427(87)90125-7)
- Roy, P. K., Chowdhary, S. S., & Bhatia, R. (2020). A machine learning approach for automation of resume recommendation system. *Procedia Computer Science*, 167, 2318-2327. <https://doi.org/10.1016/j.procs.2020.03.284>

- Sarawagi, S. (2008). Information extraction. *Foundations and Trends® in Databases*, 1, 261–377. <https://doi.org/10.1561/1900000003>
- Sinha, A.K., Amir Khusru Akhtar, M., Kumar, A. (2021). Resume Screening Using Natural Language Processing and Machine Learning: A Systematic Review. In: *Swain, D., Pattnaik, P.K., Athawale, T. (eds) Machine Learning and Information Processing. Advances in Intelligent Systems and Computing*, vol 1311. Springer, Singapore. https://doi.org/10.1007/978-981-33-4859-2_21
- Sonar, S., & Bankar, B. (2012). Resume parsing with named entity clustering algorithm. *Published paper, SVPM College of Engineering Baramati, Maharashtra.*
- Tejaswini, K., Umadevi, V., Kadiwal, S. M., & Revanna, S. (2022). Design and development of machine learning based resume ranking system. *Global Transitions Proceedings*, 3(2), 371-375. <https://doi.org/10.1016/j.gltp.2021.10.002>
- Tobing, B. C. L., Suhendra, I. R., & Halim, C. (2019, June). Catapa resume parser: end to end Indonesian resume extraction. In *Proceedings of the 2019 3rd international conference on natural language processing and information retrieval* (pp. 68-74). <https://doi.org/10.1145/3342827.3342832>
- Xu, Q., Zhang, J., Zhu, Y., Li, B., Guan, D., & Wang, X. (2020). A blocklevel RNN model for resume block classification. In *2020 IEEE International Conference on Big Data (Big Data)* (pp. 5855–5857). <https://doi.org/10.1109/BigData50022.2020.9377771>
- Xuan, G., Zhang, W., & Chai, P. (2001, October). EM algorithms of Gaussian mixture model and hidden Markov model. In *Proceedings 2001 international conference on image processing* (Cat. No. 01CH37205) (Vol. 1, pp. 145-148). IEEE. <https://doi.org/10.1109/ICIP.2001.958974>
- Yakubovich, V., & Lup, D. (2006). Stages of the recruitment process and the referrer's performance effect. *Organization science*, 17(6), 710–723. <https://doi.org/10.1287/orsc.1060.0214>
- Yasmin, F., Nur, M. I., & Arefin, M. S. (2020). Potential candidate selection using information extraction and skyline queries. In *Proceeding of the International Conference on Computer Networks, Big Data and IoT (ICCBi-2019)* (pp. 511-522). Springer International Publishing. https://doi.org/10.1007/978-3-030-43192-1_58
- Yu, K., Guan, G., & Zhou, M. (2005, June). Resume information extraction with cascaded hybrid model. In *Proceedings of the 43rd Annual Meeting of the Association for Computational Linguistics (ACL'05)* (pp. 499-506).
- Zaroor, A., Maree, M., & Sabha, M. (2017, May). A hybrid approach to conceptual classification and ranking of resumes and their corresponding job posts. In *International Conference on Intelligent Decision Technologies* (pp. 107-119). Cham: Springer International Publishing. https://doi.org/10.1007/978-3-319-59421-7_10
- Zu, S., Wang, X., & Darren, S. (2019). Resume information extraction with a novel text block segmentation algorithm. *Linguistics*, 8, 29–48. doi:10. 5121/ijnlc.2019.8503. In *Proceedings 2001 International Conference on Image Processing* (Cat.No.01CH37205) (pp. 145–148 vol.1). volume 1.



Gazi University

Journal of Science

PART A: ENGINEERING AND INNOVATION

<http://dergipark.org.tr/guj.1544942>

Improving Machine Failure Prediction with Grey Wolf, Whale Optimization, and Optuna Techniques

Vahid SİNAP^{1*} ¹ *Ufuk University, Department of Management Information Systems, Ankara, Türkiye*

| Keywords | Abstract |
|--|---|
| Machine Failure Prediction Grey Wolf Optimization Whale Optimization Algorithm Optuna | Machine failure prediction is crucial for minimizing downtime and optimizing maintenance strategies in industrial settings. This study aims to enhance the accuracy of machine failure prediction models by integrating advanced hyperparameter optimization techniques with feature selection methods. Various optimization techniques, including Optuna, Hyperopt, and Spearmint, were evaluated, along with feature selection methods utilizing Grey Wolf Optimization (GWO) and Whale Optimization Algorithm (WOA). The findings reveal that the CatBoost model optimized with GWO and Optuna achieved the highest performance, with an accuracy of 88.3%, an F1 score of 88.3%, and a Matthews Correlation Coefficient (MCC) of 76.7%. In comparison, WOA demonstrated competitive yet slightly lower results, with the best accuracy of 85.9% achieved using CatBoost and Optuna. The study also highlights that Linear Discriminant Analysis (LDA), optimized with Optuna, showed notable performance, with an accuracy of 86.0%, an F1 score of 85.8%, and an MCC of 74.6% without feature selection, which improved to 87.8%, 87.8%, and 76%, respectively, with GWO-based feature selection. The overall results indicate that GWO outperforms WOA in improving model performance, particularly when paired with advanced hyperparameter tuning techniques. |

Cite
Sinap, V. (2025). Improving Machine Failure Prediction with Grey Wolf, Whale Optimization, and Optuna Techniques. *GU J Sci, Part A, 12(1)*, 154-174. doi:10.54287/guj.1544942

| Author ID (ORCID Number) | Article Process |
|---------------------------------|---|
| 0000-0002-8734-9509 Vahid SİNAP | Submission Date 06.09.2024 Revision Date 04.12.2024 Accepted Date 30.12.2024 Published Date 26.03.2025 |

1. INTRODUCTION

The industrial maintenance strategies are devised in a way that they utilize the predictive failure methodology to avoid system failures and thus reduce the unplanned downtime of equipment, machines, and processes. To this end, accurate prediction of future failures is essential to ensure timely planning of maintenance activities. Failure prediction approaches utilize both past and market data which signify system states, events and operations to predict the outcomes. Accurately analyzing this data enables failures to be predicted and preventive maintenance activities to be carried out in a timely manner. Fault prediction plays a critical role in the safety, efficiency and cost effectiveness of industrial operations. Unplanned downtime can lead to production losses, increased repair costs and even customer dissatisfaction. For example, Amazon's 49-minute outage in 2013 resulted in \$4 million in lost sales (Tweney, 2013). According to a survey conducted by the Ponemon Institute, an organization reportedly loses an average of \$138,000 per hour due to an outage (Ponemon Institute, 2011). Preventing such losses requires the effective use of failure prediction methods.

*Corresponding Author, e-mail: vahidsinap@gmail.com

Machine failures can be caused by various factors. These factors include mechanical wear and tear, improper assembly, improper use, environmental conditions such as excessive temperature and humidity. Mechanical wear can adversely affect the performance of components over time, leading to failures. Furthermore, uneven distribution of loads on equipment can also trigger the occurrence of failures. Incorrect installation situations can lead to improper machine operation and potential breakdowns, while incorrect usage scenarios can lead to unexpected downtime caused by operator errors. Environmental conditions, especially factors such as high temperature and humidity, stress the operating conditions of machines, increasing the likelihood of failure. Therefore, it is crucial for failure prediction systems to consider this variety of factors and analyze the data to make reliable predictions. Failure prediction increases the continuity and efficiency of industrial processes by identifying such situations in advance, enabling maintenance strategies to be implemented effectively (Zonta et al., 2020).

Over the last few years, machine learning (ML) has become more and more relevant and vital to prediction model training, evaluation of model performance, and deployment in the production environment. ML-based failure prediction models are increasingly being adopted due to the rapid progress of machine learning algorithms along with their free accessibility in software packages, and the abundance of industrial data from big data analytics and stream processing platforms (Leukel et al., 2021). ML-based failure prediction models are known to be effective for various systems such as agricultural machinery, wind turbines, aircraft components, information and communication technology devices, and manufacturing plants. In studies on agricultural machinery, predicting failures using sensor data and operating conditions increases machine efficiency and reduces unexpected downtime (Abdallah et al., 2021). Models developed for agricultural machinery are critical, especially during harvest periods, and ensure the continuity of these machines. Wind turbines are another important application area. In wind turbine failure prediction, a wide range of parameters such as vibration analysis and power generation data are used to determine the probability of failure in advance (Jin et al., 2021). Such an approach increases energy efficiency and reduces maintenance costs. ML-based studies on aircraft components perform component life predictions and failure risk analysis to improve the safety of aircraft (Li et al., 2023). Information and communication technology devices are another area where ML applications are effective. Failure predictions on network devices develop proactive maintenance strategies by analyzing system monitoring data to improve user experience and minimize service interruptions (Rzayeva et al., 2023). In manufacturing plants, ML-based fault prediction systems are used to monitor the status of machines on production lines and detect abnormal behavior (Ayvaz & Alpay, 2021).

The effectiveness of machine learning algorithms in the field of fault prediction is closely related not only to the selection of the right model, but also to the feature selection processes and hyperparameter optimization. Feature selection is a critical step that affects the success of the model, because in high-dimensional datasets, redundant or irrelevant features can increase the complexity of the model and lead to overlearning. Improper selection of features can negatively affect the overall performance of the model and lead to low accuracy in

failure predictions. Hyperparameter optimization is another important step to improve the performance of machine learning models. Proper tuning of hyperparameters can greatly affect the generalization ability of the model. However, the process of hyperparameter optimization is often time-consuming and can be costly in terms of computational resources depending on the size of the dataset. Moreover, the performance results obtained with a given combination of hyperparameters may vary depending on the complexity of the model and the features used. This makes it difficult to find optimal hyperparameters. These limitations may affect the accuracy and reliability of the ML models used in failure prediction, reducing the applicability of the results. Therefore, effective feature selection and hyperparameter optimization process is vital for the success of failure prediction systems.

The field of failure prediction and industrial maintenance has witnessed substantial advancements through various research efforts, driven by the need to enhance operational efficiency and minimize unplanned downtimes. A significant body of work has focused on developing and refining methods for predicting failures in industrial systems, utilizing both traditional statistical approaches and modern machine learning techniques. These studies have contributed to a deeper understanding of failure mechanisms, improved predictive accuracy, and the development of more effective maintenance strategies.

Wahid et al. (2022) present a novel forecasting method for predictive maintenance (PdM) which applies a hybrid model with convolutional neural networks (CNN) and long short-term memory (LSTM) that includes a skip connection (CNN-LSTM). This approach leverages the strengths of both CNNs for high-level feature extraction and LSTMs for analyzing long-term dependencies in time-series data. Experiments conducted with Microsoft's case study dataset, containing failure history, maintenance records, error conditions, and telemetry data, show that the hybrid CNN-LSTM model achieves the highest prediction accuracy for machine failure compared to individual CNN or LSTM models.

Celikmih et al. (2020) focused on predicting aircraft system failures using machine learning models and a hybrid data preparation approach. They collected two years' worth of maintenance and failure data, identifying nine input variables and one output variable. Their method involves a two-stage process: using ReliefF for feature selection and a modified K-means algorithm to remove noisy data. The model's performance was evaluated with Multilayer Perceptron (MLP), Support Vector Regression (SVR), and Linear Regression (LR), using metrics such as Correlation Coefficient (CC), Mean Absolute Error (MAE), and Root Mean Square Error (RMSE). The study concludes that their hybrid approach effectively predicts failure counts.

Mishra and Manjhi (2018) addressed the challenges faced by financial organizations in managing a mix of new and old technologies within their branches, including ATMs and self-service devices. They proposed a service-oriented, vendor-focused approach to integrate maintenance and technical support strategies effectively. Their study emphasizes the importance of predictive maintenance in optimizing branch operations by leveraging predictive analytics and machine learning technologies. The proposed method and machine

learning model predict the likelihood of device and component failures within a specified future timeframe, aiming to enhance customer satisfaction and improve overall business performance.

Campos et al. (2019) investigated the use of heterogeneous ensembles of ML techniques for Online Failure Prediction (OFP). They highlighted that while individual ML models are effective, combining various algorithms into ensembles can enhance performance by leveraging different biases. The study assessed the effectiveness of different base learners and combination methods to improve prediction accuracy. Results indicated that certain combinations of learners and techniques, even if not the best individually, can significantly enhance failure prediction. Additionally, analyzing the interactions between learners in successful ensembles provided valuable insights into their improved performance.

Wang et al. (2017) suggested a technique for performance monitoring and failure prediction in optical networks by means of machine learning. They assisted SVM (Support Vector Machine) and Double Exponential Smoothing (DES) to construct risk-aware models that are particular for equipment failure prediction. The study identified that this issue has not been thoroughly addressed before. Experimental results demonstrated that the DES-SVM method achieved an average prediction accuracy of 95% for forecasting optical equipment failures. This high accuracy indicates that the proposed method significantly improves traditional risk-aware models, enhancing the stability and reliability of optical networks by effectively predicting and mitigating equipment failure risks.

Mohammed et al. (2019) have presented the issue of failure prediction in high-performance computing and cloud systems, which is critical. As these systems have become more complicated, traditional strategies of fault-tolerance like regular checkpointing and replication are no longer sufficient. This study aims to examine the role of machine learning in the enhancement of the accuracy of failure prediction. The scientists invent the model of predicting failure by applying time series analysis and various machine learning algorithms, such as SVM, RF, KNN, Classification and Regression Trees (CART), and LDA. Their experimental results showed that the SVM-based model achieved an average prediction accuracy of 90%, demonstrating its effectiveness in predicting system and application failures more accurately compared to other algorithms. This suggests that machine learning techniques can significantly improve failure management and proactive measures in high-performance computing systems.

Pellegrini et al. (2015) introduced the Framework for Building Failure Prediction Models (F2PM), a machine learning-based framework designed to predict the Remaining Time to Failure (RTTF) of applications experiencing software anomalies. F2PM operates independently of specific applications by focusing on system-level features, thus enabling its use across various contexts without requiring manual adjustments. The framework performs feature selection to identify key system features that significantly impact RTTF prediction, allowing the creation of optimized models tailored to different feature sets. Users can evaluate these

models based on prediction accuracy and model-building time, with experimental results demonstrating the framework's efficacy using the TPC-W e-commerce benchmark.

This study distinguishes itself from existing research by not only examining the performance of various machine learning algorithms for failure prediction but also comprehensively evaluating the combined impact of nature-inspired feature selection methods and modern hyperparameter optimization techniques. While previous studies often focus on specific approaches in isolation, this research integrates GWO and WOA for feature selection with hyperparameter optimization techniques including Optuna, Hyperopt, and Spearmint. GWO, inspired by the natural hunting behavior of grey wolves, provides an efficient mechanism for selecting optimal features, while WOA, based on whale hunting strategies, excels in handling complex data structures. For hyperparameter optimization, Optuna dynamically automates optimization processes, Hyperopt leverages Bayesian optimization for efficient searches in high-dimensional parameter spaces, and Spearmint enhances performance when the objective function is uncertain. The study evaluates these techniques on machine learning models, including Random Forest (RF), Gradient Boosting (GB), CatBoost, LDA, and K-Nearest Neighbors (KNN), to identify the most effective combinations for fault prediction. The findings aim to reveal how the integration of feature selection and hyperparameter optimization can enhance model reliability and efficiency, ultimately improving predictive maintenance strategies in industrial applications.

2. MATERIAL AND METHOD

This section outlines the dataset characteristics, details of the machine learning algorithms employed, the performance metrics used for algorithm comparison, and the data preparation procedures. The objective is to establish a robust methodological and analytical framework for the research, thereby enhancing the scientific contribution of the study and ensuring its reproducibility.

2.1. Dataset

The dataset used in this research is publicly available on the Kaggle platform. It contains sensor data collected from various types of machinery, such as industrial pumps, air compressors, and CNC machines, with the aim of predicting machine failures in advance. The dataset comprises 944 entries and is composed of multiple features recorded from sensors installed on the machines, along with a binary indicator of machine failures. A detailed description of each feature included in the dataset is provided in Table 1.

The heatmap in Figure 1 presents the correlation coefficients between various operational parameters of a machine and the binary failure indicator. Notably, the “fail” variable demonstrates a moderate positive correlation with the AQ ($r = 0.58$), indicating that elevated air pollution levels are associated with a higher likelihood of machine failure. Conversely, there is a moderate negative correlation between “fail” and the CS readings ($r = -0.47$), suggesting that reduced electrical current usage may be linked to an increased risk of failure. Additionally, the heatmap reveals significant interdependencies among features, such as a strong

positive correlation between VOC levels and fail rate ($r = 0.80$), highlighting the complex interactions within the machine's operational environment.

Table 1. Dataset Features and Descriptions

| Feature | Description |
|-------------|--|
| footfall | The count of people or objects passing by the machine. |
| tempMode | The temperature setting or mode of the machine. |
| AQ | The air quality index near the machine. |
| USS | Ultrasonic sensor readings indicating the proximity of objects to the machine. |
| CS | Electrical current usage of the machine as measured by current sensors. |
| VOC | The level of volatile organic compounds detected near the machine. |
| RP | The rotational position or revolutions per minute (RPM) of the machine parts. |
| IP | The pressure of the input supplied to the machine. |
| Temperature | The current operating temperature of the machine. |
| fail | A binary indicator of machine failure (1 indicates failure, 0 indicates no failure). |

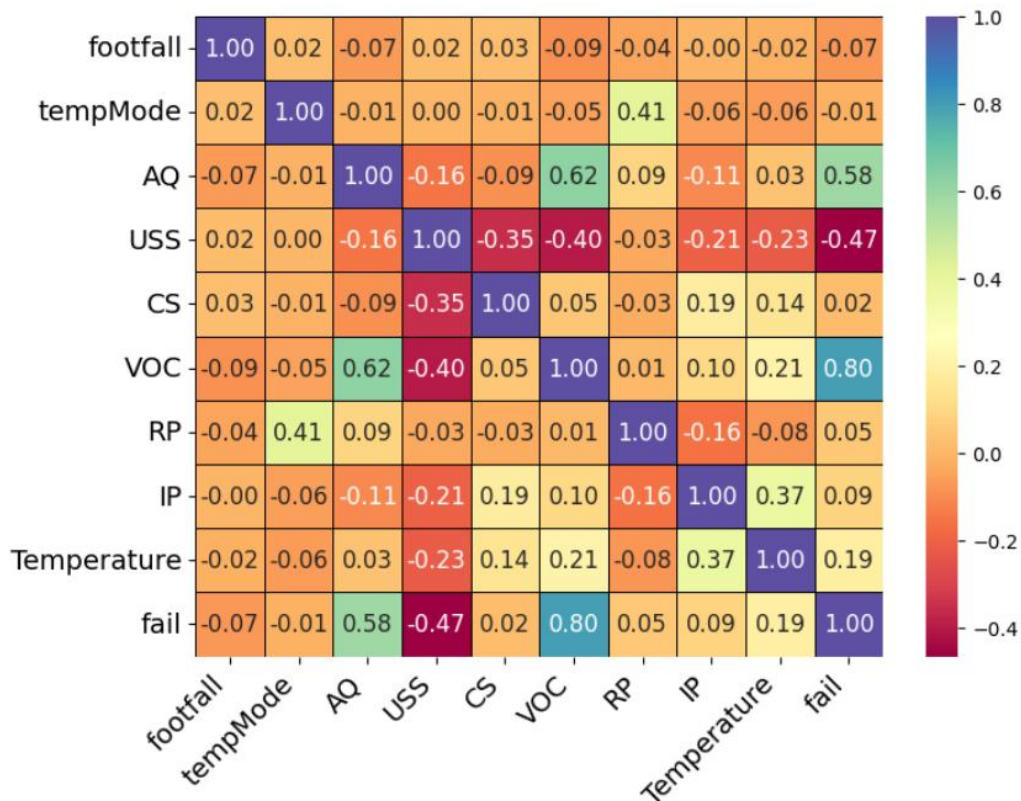


Figure 1. Heatmap of the Dataset

2.2. Data Preparation

The descriptive statistics of the dataset reveal varying scales and distributions among the features. For instance, the footfall variable exhibits a wide range (0 to 7300) with a mean of 306.38 and a high standard deviation of

1082.61, indicating significant variability in the number of people or objects passing by the machine. In contrast, other parameters, such as the AQ, USS, and CS, have more limited ranges and are approximately normally distributed, with moderate standard deviations (1.44, 1.38, and 1.27, respectively). Data normalization was conducted to minimize the quite large disparities between different features; thus, all the variables can affect equally the model's performance. The dataset is complete with no missing values, thereby the implemented methods of imputation were unnecessary.

2.3. Ensemble Learning

Ensemble learning is a powerful machine learning approach that combines multiple base models to improve overall prediction performance and robustness. In this study, two ensemble methods were employed: Voting Ensemble Classifier (VEC) and Stacking Ensemble Classifier (SEC). Both methods leverage the strengths of multiple classifiers to achieve better generalization compared to individual models. The VEC combines the predictions of several base learners through a majority voting scheme (hard voting) or by averaging their predicted probabilities (soft voting) (Lasotte et al., 2022). The prediction of the VEC is formally defined, as given in (1).

$$\hat{y} = \operatorname{argmax} \sum_{i=1}^N \omega_i \cdot f_i(x) \quad (1)$$

where \hat{y} represents the final predicted class, ω_i denotes the weight assigned to the i -th base classifier $f_i(x)$, and N is the total number of classifiers.

The SEC, on the other hand, is a more sophisticated approach that trains a meta-classifier to the ensemble of predictions obtained from various base classifiers. In this technique, the outputs of the base classifiers are used as input features for the meta-classifier, which learns to optimally combine them to minimize error (Rajadurai & Gandhi, 2022). The prediction formula for SEC is expressed, as given in (2).

$$\hat{y} = g(f_1(x), f_2(x), \dots, f_N(x)) \quad (2)$$

where g is the meta-classifier function, and $f_1(x), f_2(x), \dots, f_N(x)$ are the base classifiers.

The choice of ensemble methods in this study was driven by their ability to address the limitations of single classifiers, such as overfitting and high variance, particularly in complex datasets with multiple operational parameters. For the VEC, base learners were selected to provide diverse perspectives: CatBoost, known for its effectiveness with categorical data and boosting capabilities; RF, which offers robustness through an ensemble of decision trees; and KNN, valued for its simplicity and ability to capture local patterns. In contrast, the SEC employs a meta-learning approach where a meta-learner is trained to optimally combine the outputs of several base learners. For this study, CatBoost was selected as the meta-learner due to its proficiency in managing

complex interactions and its ability to effectively synthesize predictions from the base models, which include CatBoost, RF, and KNN.

2.4. Feature Selection

In this study, the GWO and the WOA were utilized for feature selection. The choice of features is a very important stage in the technique of machine learning, targeting to improve the performance of the model by recognizing the most relevant features and minimizing the dimensionality. This process helps in mitigating overfitting, improving model interpretability, and reducing computational costs. The GWO began by initializing a population of potential solutions, each representing a different subset of features from the dataset. These solutions were organized into a social hierarchy consisting of alpha, beta, delta, and omega wolves. The alpha wolves, representing the best-performing feature subsets, guided the optimization process, while the beta and delta wolves provided additional guidance to prevent premature convergence and maintain diversity in the search process (El-Kenawy & Eid, 2020). Throughout the optimization process, the GWO algorithm simulated the natural hunting strategies of grey wolves, consisting of three main phases: encircling, hunting, and attacking the prey. In the encircling phase, wolves updated their positions based on the locations of the alpha, beta, and delta wolves, enabling them to concentrate on the most promising areas of the feature space. During the hunting phase, the GWO calculated a weighted average of the positions of the top wolves, balancing exploration of new areas with exploitation of known good solutions. As the optimization progressed into the attacking phase, the algorithm increased its emphasis on exploitation to converge on the optimal subset of features.

The WOA, based on the hunting behavior of humpback whales, was also utilized for feature selection. WOA mimics the bubble-net feeding strategy of whales, which involves encircling prey and employing a spiral search technique. This approach enables WOA to navigate the feature space effectively and identify optimal feature subsets. WOA's strength lies in its capacity to escape local optima and converge towards global solutions, thereby selecting features that contribute significantly to the model's performance (Khaire & Dhanalakshmi, 2022).

2.5. Validation Method

Cross-validation is a widely used technique for assessing the performance and generalization ability of machine learning models. In this context, 5-fold cross-validation was implemented to ensure a comprehensive evaluation of the models. This method involves partitioning the dataset into five distinct subsets or "folds." In this process, every fold is used once as a test set while the remaining four folds are joined together to create the training set. This process is carried out a total of five times, with each fold serving as the test set once and only once. The 5-fold cross-validation procedure can be described using the following equation, as shown in (3).

$$CV = \frac{1}{k} \sum_{i=1}^k \text{Performance}(D_i) \quad (3)$$

Formally, let D denote the entire dataset, and D_i represent the i -th fold, where i ranges from 1 to 5.

2.6. Performance Metrics

To evaluate the performance of the models, several key metrics were utilized: Accuracy, F1 Score, and MCC. Each of these metrics provides different insights into the model's predictive capabilities and overall performance.

Accuracy: The accuracy is calculated as the number of correctly classified instances divided by the total number of instances. It is defined as (4):

$$\text{Accuracy} = \frac{TP + TN}{TP + TN + FP + FN} \quad (4)$$

where TP is the number of true positives, TN is the number of true negatives, FP is the number of false positives, and FN is the number of false negatives.

F1 Score: The F1 Score is the harmonic mean of Precision and Recall which gives a balance between the two metrics. It is particularly useful for imbalanced datasets. The F1 Score is provided in (5).

$$\text{F1 Score} = 2 \times \frac{\text{Precision} \times \text{Recall}}{\text{Precision} + \text{Recall}} \quad (5)$$

where Precision is defined as (6):

$$\text{Precision} = \frac{TP}{TP + FP} \quad (6)$$

and Recall is defined as (7):

$$\text{Recall} = \frac{TP}{TP + FN} \quad (7)$$

MCC: MCC provides a balanced measure of classification performance that considers all four categories of the confusion matrix. The MCC is calculated as shown in (8).

$$\text{MCC} = \frac{TP \times TN - FP \times FN}{\sqrt{(TP + FP) \times (TP + FN) \times (TN + FP) \times (TN + FN)}} \quad (8)$$

2.7. Model Setups

The dataset is divided into two parts, with 80% allocated for training and 20% for testing, using a random state of 42 to ensure reproducibility. For determining the hyperparameters, three optimization techniques -Optuna, Hyperopt, and Bayesian optimization (Spearmlint)- were employed, each bringing distinct advantages to the optimization process.

Optuna is a self-tuning hyperparameter optimization framework which finds optimal hyperparameters by applying a dynamic and efficient search algorithm. It employs a tree-structured Parzen estimator (TPE) for Bayesian optimization but is also capable of other search strategies like grid search or random search. Optuna allows for the definition of an objective function and performs optimizations in a highly flexible and scalable manner (Parra-Ullauri et al., 2023). It can prune unpromising trials early in the optimization process, speeding up the search and enhancing computational efficiency. Hyperopt is another popular hyperparameter optimization tool that focuses on efficient searching through large, high-dimensional spaces. It is based on Bayesian optimization, using the TPE as a surrogate model to guide the search process towards promising areas. Unlike traditional grid or random searches, Hyperopt incrementally builds a model of the objective function, enabling it to make informed decisions on where to sample next (Luo, 2016). This allows Hyperopt to effectively explore and exploit the hyperparameter space, particularly for complex and high-dimensional optimization tasks. Spearmlint is a specific implementation of Bayesian optimization that is designed to handle black-box optimization problems where the objective function is expensive to evaluate (Archetti & Candelieri, 2019). It models the objective function using Gaussian processes and utilizes the expected improvement criterion to choose the next set of hyperparameters to evaluate (Young et al., 2018). Spearmlint is particularly effective in scenarios where the evaluation of each set of hyperparameters is time-consuming or costly, as it aims to minimize the number of evaluations required to find the optimum solution. In this study, only the hyperparameter settings obtained through Optuna are presented, as it yielded the best results. Table 2 provides the optimized hyperparameter settings for the models.

For Optuna, the configuration included a total of 100 trials with the TPESampler for efficient search and the MedianPruner to eliminate fewer promising trials early. Hyperopt was utilized with a maximum of 100 evaluations, employing the TPE algorithm for Bayesian optimization, and incorporated various hyperparameter distributions such as uniform and choice. Bayesian Optimization, specifically Spearmlint, was configured with 100 iterations and used the Expected Improvement acquisition function, with parameters set to $\kappa=1.96$ and $\xi=0.01$ to balance exploration and exploitation. Table 3 presents the hyperparameter settings used for each optimization technique.

The data analysis and model testing were conducted using the Python programming language. For data processing and manipulation, the pandas and NumPy libraries were employed, providing robust tools for handling large datasets. The scikit-learn library was utilized for model development and evaluation, offering a

comprehensive range of machine learning algorithms and performance metrics. All analyses were performed within the Jupyter Notebook environment, which integrates code, text, and visualizations seamlessly. The computational experiments were executed on a PC equipped with an AMD Ryzen 7800X3D processor, operating at 4.2 GHz, and an NVIDIA GeForce RTX 4070 Ti GPU, supported by 32 GB of 6000 MHz DDR5 RAM. The system ran on Windows 11, ensuring a stable and efficient development environment.

Table 2. Hyperparameter Settings for Models Optimized Using Optuna

| Model | Hyperparameter | Settings |
|-------|---|---|
| RF | n_estimators, max_depth, min_samples_split, min_samples_leaf | 120, 12, 3, 2 |
| GB | n_estimators, learning_rate, max_depth, min_samples_split, min_samples_leaf | 221, 0.07, 6, 3, 2 |
| CB | iterations, learning_rate, depth, l2_leaf_reg, bagging_temperature | 545, 0.03, 8, 3, 0.9 |
| LDA | solver, shrinkage, n_components, tol | “lsqr”, “auto”, 1, 0.0001 |
| KNN | n_neighbors, weights, algorithm, leaf_size, p | 7, “distance”, “auto”, 30, 2 |
| VEC | estimators, weights | [(“CatBoost”, CB()), (“RF”, RF()), (“KNN”, KNN())], [1, 2, 1] |
| SEC | estimators, final_estimator | [(“CatBoost”, CB()), (“RF”, RF()), (“KNN”, KNN())], CatBoost |

Table 3. Hyperparameter Settings for Optimization Techniques

| Optimization Technique | Settings |
|------------------------|--|
| Optuna | n_trials=100, sampler=TPESampler, pruner=MedianPruner |
| Hyperopt | max_evals=100, algo=tpe.suggest, domain=hp.choice, hp.uniform |
| Bayesian Optimization | n_iter=100, acq_func=Expected Improvement, kappa=1.96, xi=0.01 |

3. EXPERIMENTAL STUDY AND FINDINGS

The experimental phase of the study is examined in four distinct stages. In the first stage, the model performances on sub-datasets without feature selection and hyperparameter optimization are investigated and compared. The second stage focuses on the application of hyperparameter optimization techniques, Optuna, Hyperopt, and Spearmint, without feature selection. The third stage involves an evaluation of feature selection combined with hyperparameter optimization methods using GWO. Finally, the fourth stage assesses the impact of WOA on hyperparameter optimization methods. Table 4 provides the results for model performance without feature selection and hyperparameter optimization.

When examining Table 4, it is evident that among the evaluated models, CatBoost stands out with the highest performance across all metrics. It achieved an Accuracy of 0.797, an F1 Score of 0.795, and an MCC of 0.716. The average performance across models is an Accuracy of 0.787, an F1 Score of 0.785, and an MCC of 0.700, with a standard deviation of 0.0080 for Accuracy, 0.0078 for F1 Score, and 0.0107 for MCC.

Table 4. Model Performance without Feature Selection and Hyperparameter Optimization

| Models | Accuracy | F1 | MCC |
|------------------|-----------------|-----------|------------|
| CatBoost | 0.797 | 0.795 | 0.716 |
| LDA | 0.790 | 0.788 | 0.701 |
| GB | 0.791 | 0.789 | 0.705 |
| KNN | 0.775 | 0.773 | 0.684 |
| RF | 0.780 | 0.779 | 0.694 |
| Avg. | 0.787 | 0.785 | 0.700 |
| Std. Dev. | 0.0080 | 0.0078 | 0.0107 |
| VEC | 0.785 | 0.782 | 0.703 |
| SEC | 0.790 | 0.787 | 0.708 |

Table 5 presents the performance metrics of various models optimized with different hyperparameter tuning techniques, specifically Optuna, Hyperopt, and Spearmint. Among the evaluated models, LDA optimized with Optuna achieved the highest performance, with an Accuracy of 0.860, an F1 Score of 0.858, and an MCC of 0.746. This indicates that LDA, when combined with Optuna for hyperparameter optimization, outperforms the other algorithms in terms of Accuracy, F1 Score, and MCC. When comparing these results to those presented in Table 4, where models were assessed without feature selection and hyperparameter optimization, we observe a notable improvement. For instance, CatBoost's performance increased from an Accuracy of 0.797, an F1 Score of 0.795, and an MCC of 0.716 to 0.823 with Optuna, 0.858 with Hyperopt, and 0.812 with Spearmint. Similarly, LDA's performance improved from an Accuracy of 0.790, an F1 Score of 0.788, and an MCC of 0.701 to the highest values with Optuna. The average performance metrics across models with hyperparameter optimization are also higher compared to those without. Specifically, the average Accuracy, F1 Score, and MCC are 0.829, 0.828, and 0.720 with Optuna; 0.823, 0.820, and 0.715 with Hyperopt; and 0.799, 0.797, and 0.708 with Spearmint. This improvement underscores the significant impact of hyperparameter tuning on enhancing model performance. The standard deviations of the performance metrics reveal variability among the different optimization techniques. Optuna shows standard deviations of 0.0194 for Accuracy, 0.0194 for F1 Score, and 0.0155 for MCC. Hyperopt exhibits higher variability with standard deviations of 0.0267 for Accuracy, 0.0263 for F1 Score, and 0.0239 for MCC, while Spearmint has the lowest variability, with standard deviations of 0.0098 for Accuracy, 0.0102 for F1 Score, and 0.0150 for MCC. Figure 2 shows the accuracy performance of different models optimized using Optuna, Hyperopt, and Spearmint without applying feature selection.

Table 6 illustrates the performance of various models optimized using GWO with three different hyperparameter tuning methods. Among the models evaluated, CatBoost optimized with Optuna achieves the highest performance, with an Accuracy of 0.883, an F1 Score of 0.883, and an MCC of 0.767. When comparing these results with those from Table 5, which showcases models without feature selection, it is evident that

GWO significantly enhances performance. For instance, CatBoost's performance with GWO and Optuna (Accuracy of 0.883, F1 Score of 0.883, MCC of 0.767) surpasses its performance without feature selection (Accuracy of 0.823, F1 Score of 0.821, MCC of 0.720). Similarly, LDA's performance improved from an Accuracy of 0.860, an F1 Score of 0.858, and an MCC of 0.746 with Optuna to 0.878, 0.878, and 0.760 respectively with GWO and Optuna. The average performance metrics with GWO are generally higher than those without. Specifically, the average Accuracy, F1 Score, and MCC are 0.874, 0.874, and 0.748 with Optuna; 0.858, 0.855, and 0.740 with Hyperopt; and 0.854, 0.851, and 0.731 with Spearmint. This highlights the effectiveness of GWO in improving model performance. Figure 3 presents the accuracy performance of various models optimized using Optuna, Hyperopt, and Spearmint with GWO-based feature selection.

Table 5. Model Performance without Feature Selection

| Models | Optuna | | | Hyperopt | | | Spearmint | | |
|------------------|----------|--------|--------|----------|--------|--------|-----------|--------|--------|
| | Accuracy | F1 | MCC | Accuracy | F1 | MCC | Accuracy | F1 | MCC |
| CatBoost | 0.823 | 0.821 | 0.720 | 0.858 | 0.855 | 0.740 | 0.812 | 0.810 | 0.729 |
| LDA | 0.860 | 0.858 | 0.746 | 0.832 | 0.830 | 0.725 | 0.802 | 0.800 | 0.712 |
| GB | 0.843 | 0.842 | 0.723 | 0.835 | 0.832 | 0.730 | 0.804 | 0.802 | 0.717 |
| KNN | 0.809 | 0.807 | 0.699 | 0.779 | 0.777 | 0.672 | 0.783 | 0.780 | 0.686 |
| RF | 0.812 | 0.811 | 0.711 | 0.810 | 0.808 | 0.707 | 0.794 | 0.792 | 0.698 |
| Avg. | 0.829 | 0.828 | 0.720 | 0.823 | 0.820 | 0.715 | 0.799 | 0.797 | 0.708 |
| Std. Dev. | 0.0194 | 0.0194 | 0.0155 | 0.0267 | 0.0263 | 0.0239 | 0.0098 | 0.0102 | 0.0150 |
| VEC | 0.817 | 0.815 | 0.736 | 0.795 | 0.792 | 0.710 | 0.790 | 0.788 | 0.703 |
| SEC | 0.828 | 0.826 | 0.746 | 0.800 | 0.796 | 0.715 | 0.795 | 0.792 | 0.710 |

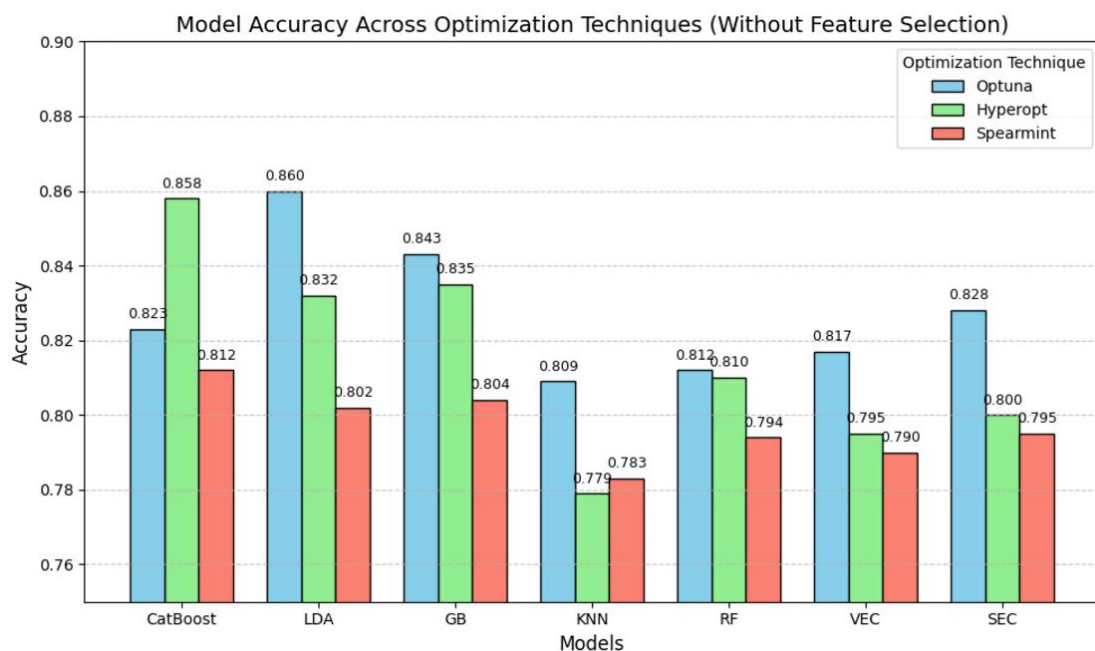


Figure 2. Model Accuracy Across Optimization Techniques Without Feature Selection

Table 6. Model Performance with GWO-based Feature Selection and Hyperparameter Optimization

| Models | Optuna | | | Hyperopt | | | Spearmint | | |
|------------------|----------|--------|--------|----------|--------|--------|-----------|--------|--------|
| | Accuracy | F1 | MCC | Accuracy | F1 | MCC | Accuracy | F1 | MCC |
| CatBoost | 0.883 | 0.883 | 0.767 | 0.873 | 0.869 | 0.754 | 0.873 | 0.868 | 0.754 |
| LDA | 0.878 | 0.878 | 0.760 | 0.855 | 0.851 | 0.742 | 0.855 | 0.852 | 0.742 |
| GB | 0.878 | 0.878 | 0.756 | 0.861 | 0.859 | 0.737 | 0.855 | 0.852 | 0.731 |
| KNN | 0.862 | 0.862 | 0.725 | 0.849 | 0.844 | 0.718 | 0.842 | 0.839 | 0.709 |
| RF | 0.867 | 0.867 | 0.734 | 0.854 | 0.850 | 0.728 | 0.846 | 0.843 | 0.719 |
| Avg. | 0.874 | 0.874 | 0.748 | 0.858 | 0.855 | 0.736 | 0.854 | 0.851 | 0.731 |
| Std. Dev. | 0.0087 | 0.0087 | 0.0180 | 0.0092 | 0.0097 | 0.0137 | 0.0119 | 0.0112 | 0.0179 |
| VEC | 0.873 | 0.873 | 0.745 | 0.858 | 0.855 | 0.733 | 0.850 | 0.847 | 0.724 |
| SEC | 0.878 | 0.878 | 0.757 | 0.865 | 0.860 | 0.748 | 0.868 | 0.865 | 0.750 |

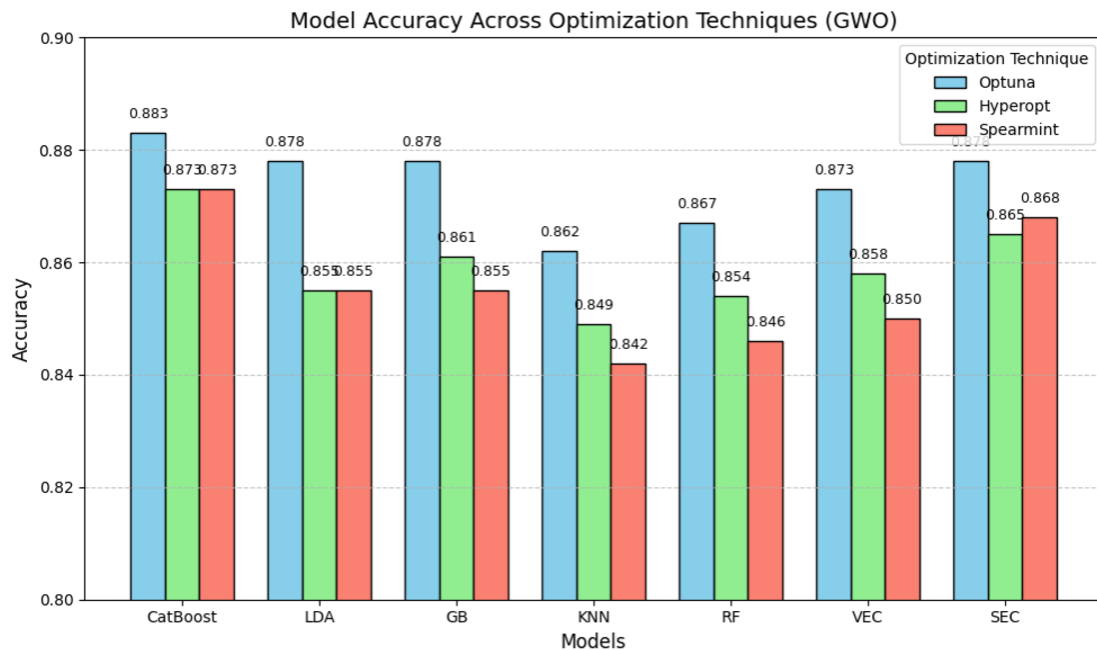
**Figure 3. Model Accuracy Across Optimization Techniques Using GWO-Based Feature Selection**

Table 7 presents the performance metrics of various models optimized using WOA with three different hyperparameter tuning methods. Among the models assessed, CatBoost with Optuna stands out with an Accuracy of 0.859, an F1 Score of 0.860, and an MCC of 0.759. This indicates that CatBoost, when optimized with WOA and Optuna, delivers superior performance compared to other models and tuning methods. Comparing these results with those from Table 6, which showcases models optimized with GWO, the performance metrics with WOA are slightly lower. For instance, CatBoost's performance with WOA and Optuna (Accuracy of 0.859, F1 Score of 0.860, MCC of 0.759) is marginally lower than its performance with GWO and Optuna (Accuracy of 0.883, F1 Score of 0.883, MCC of 0.767). Similarly, other models such as LDA and GradientBoost also show a reduction in performance with WOA compared to GWO. The average

performance metrics with WOA are slightly lower than those achieved with GWO. This highlights that while WOA still provides strong results, GWO tends to deliver slightly better performance across the models evaluated. Figure 4 illustrates the accuracy results of models optimized with Optuna, Hyperopt, and Spearmint under WOA-based feature selection.

Table 7. Model Performance with WOA-based Feature Selection and Hyperparameter Optimization

| Models | Optuna | | | Hyperopt | | | Spearmint | | |
|------------------|----------|--------|--------|----------|--------|--------|-----------|--------|--------|
| | Accuracy | F1 | MCC | Accuracy | F1 | MCC | Accuracy | F1 | MCC |
| CatBoost | 0.859 | 0.860 | 0.759 | 0.846 | 0.847 | 0.742 | 0.791 | 0.794 | 0.732 |
| LDA | 0.872 | 0.874 | 0.754 | 0.857 | 0.859 | 0.742 | 0.797 | 0.799 | 0.716 |
| GB | 0.869 | 0.871 | 0.751 | 0.855 | 0.857 | 0.738 | 0.803 | 0.805 | 0.725 |
| KNN | 0.851 | 0.854 | 0.710 | 0.837 | 0.840 | 0.688 | 0.788 | 0.790 | 0.675 |
| RF | 0.854 | 0.856 | 0.724 | 0.842 | 0.844 | 0.702 | 0.785 | 0.788 | 0.695 |
| Avg. | 0.861 | 0.863 | 0.739 | 0.847 | 0.849 | 0.722 | 0.792 | 0.795 | 0.708 |
| Std. Dev. | 0.0091 | 0.0090 | 0.0214 | 0.0085 | 0.0082 | 0.0255 | 0.0072 | 0.0069 | 0.0233 |
| VEC | 0.866 | 0.868 | 0.735 | 0.855 | 0.858 | 0.725 | 0.814 | 0.816 | 0.720 |
| SEC | 0.871 | 0.872 | 0.752 | 0.855 | 0.856 | 0.740 | 0.804 | 0.805 | 0.724 |

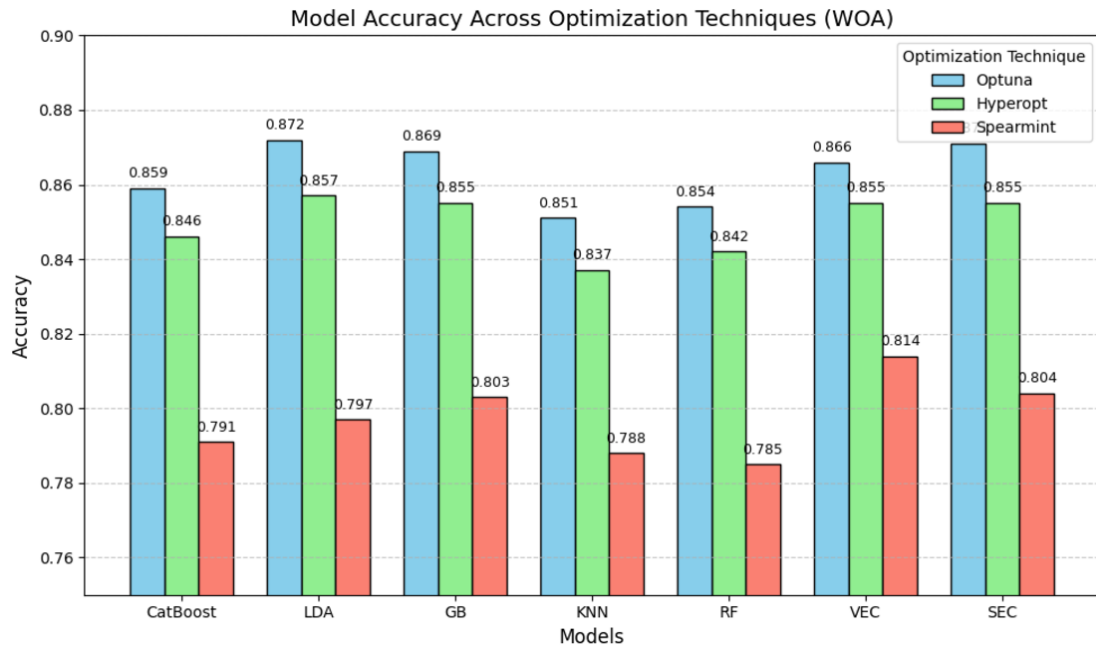


Figure 4. Model Accuracy Across Optimization Techniques Using WOA-Based Feature Selection

Figure 5 illustrates the comparison of Optuna accuracy scores across different feature selection techniques applied to various machine learning models. The feature selection methods include no feature selection (Without FS), Grey Wolf Optimization-based feature selection (GWO-based FS), and Whale Optimization Algorithm-based feature selection (WOA-based FS). Among the models, the highest accuracy was observed with CatBoost under the GWO-based FS approach, achieving a value of 0.883. Similarly, high accuracy was

recorded for SEC and GB models under GWO-based FS, both reaching values of 0.878. In comparison, the WOA-based FS technique also produced competitive results, such as 0.872 for the GB model and 0.871 for the SEC model. Models without feature selection consistently demonstrated lower accuracy across all cases, with the KNN model yielding the lowest accuracy of 0.809. This indicates that the application of optimization-based feature selection methods significantly enhances model performance compared to scenarios without feature selection.

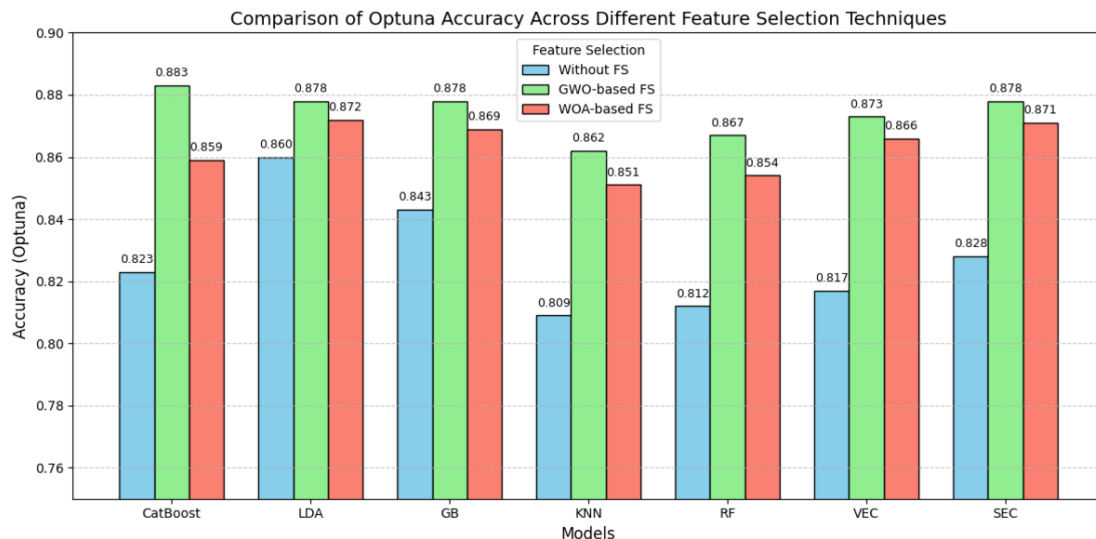


Figure 5. Comparison of Optuna Accuracy Across Different Feature Selection Techniques

4. DISCUSSION

The findings from this study provide a comprehensive analysis of the impact of hyperparameter optimization and feature selection techniques on the performance of various machine learning models. The results demonstrate that both hyperparameter optimization and feature selection significantly contribute to enhancing model performance, with some variations depending on the specific algorithms and optimization methods employed.

The first stage of the study, which analyzed model performance without feature selection and hyperparameter optimization, highlighted CatBoost as the best-performing model across all metrics. However, the results indicated considerable room for improvement with the application of optimization techniques. In the second stage, applying hyperparameter optimization methods without feature selection resulted in notable performance improvements, with LDA combined with Optuna yielding the highest accuracy. This suggests that LDA is particularly well-suited to benefit from fine-tuning using the Optuna framework. Significant gains observed in CatBoost's performance across all three optimization methods further underscore the model's adaptability. Optuna demonstrated consistent effectiveness, as evidenced by its lower standard deviation in performance metrics compared to Hyperopt and Spearmint. Recent findings in the literature highlight Optuna's efficient hyperparameter optimization capabilities, particularly in balancing exploration and exploitation during the search process (Yu & Zhu, 2020). Unlike traditional approaches like random or grid search, Optuna

leverages an adaptive search mechanism using Tree-structured Parzen Estimators (TPE) and early stopping, which dynamically adjusts the search space based on previous iterations, optimizing computational resources (Akiba et al., 2019). Optuna's pruning mechanism, which discards suboptimal trials early, further enhances its efficiency and robustness, particularly for high-dimensional datasets (Hassanali et al., 2024). Comparatively, Hyperopt and Spearmint, while effective, exhibit higher variability in performance metrics. Hyperopt's reliance on TPE without adaptive pruning and Spearmint's use of Gaussian Processes for optimization can lead to challenges in scalability and consistency in high-dimensional search spaces, resulting in higher variance in results (Chen et al., 2022; Tørring & Elster, 2022).

The third stage, which evaluated the combination of feature selection and hyperparameter optimization using the GWO method, showed that GWO is highly effective for improving model performance. CatBoost optimized with GWO and Optuna achieved the highest overall metrics, surpassing results from earlier stages, highlighting GWO's ability to enhance both feature selection and hyperparameter tuning to maximize machine learning model performance. The effectiveness of GWO stems from its nature-inspired algorithm, which mimics the hunting behavior of grey wolves, balancing exploration and exploitation in complex search spaces (Hatta et al., 2019). This dynamic search capability helps prevent premature convergence to local optima, a common issue in optimization tasks. Recent studies have highlighted GWO's advantages over traditional algorithms like Genetic Algorithms (GA) and Particle Swarm Optimization (PSO), particularly in feature selection and parameter tuning tasks (Seyyedabbasi & Kiani, 2021). By integrating feature selection, GWO not only identifies the most relevant features but also fine-tunes model hyperparameters, leading to significant improvements in predictive performance. This dual approach aligns with findings that metaheuristic algorithms like GWO often outperform traditional methods, especially in high-dimensional datasets where overfitting risks are greater (Shen & Zhang, 2022). Therefore, GWO provides a robust and efficient framework for optimizing machine learning models, confirming its potential for advanced data science applications.

The fourth stage, which assessed the impact of the WOA on hyperparameter optimization methods, further underscored the critical role of feature selection when combined with optimization strategies. Although WOA contributed to improved model performance, the results were generally lower than those achieved with the GWO method. The differences in performance between WOA and GWO can be attributed to the unique optimization strategies and the exploration-exploitation mechanisms inherent in each algorithm. WOA mimics the bubble-net hunting strategy of humpback whales, emphasizing a more stochastic exploration of the search space, which may lead to broader but less precise search outcomes (Mirjalili & Lewis, 2016). In contrast, GWO, which is inspired by the social hierarchy and hunting behavior of grey wolves, has been shown to maintain a more balanced trade-off between exploration and exploitation, allowing for more refined convergence to optimal solutions (Mirjalili et al., 2014). The slightly inferior performance of WOA compared to GWO may also reflect WOA's potential limitations in navigating the optimization landscape for certain types of datasets and models, particularly when complex interactions among features are present (Qaraad et

al., 2022). Studies have demonstrated that while WOA can be highly effective for certain optimization tasks, its performance may be less consistent across diverse problem domains than GWO, which tends to offer a more stable optimization process due to its dynamic adaptation to the search environment (Wang et al., 2021). These findings suggest that while WOA offers valuable improvements, GWO may provide a more reliable approach for achieving optimal performance across a range of models and datasets.

5. CONCLUSION

This study investigated the impact of various hyperparameter optimization techniques and feature selection methods on the performance of machine learning models for machine failure prediction. The results demonstrate that integrating feature selection with hyperparameter optimization significantly enhances predictive performance. Among the evaluated methods, GWO paired with Optuna emerged as the most effective combination. Specifically, the CatBoost model optimized with GWO and Optuna achieved the highest performance, with an accuracy of 88.3%, an F1 score of 88.3%, and an MCC of 76.7%. LDA also showed considerable improvement, with its accuracy increasing from 86% without feature selection to 87.8% with GWO-based feature selection. Similarly, GB and SEC models achieved accuracy levels of 87.8% and 87.8%, respectively, under the GWO approach. In comparison, the WOA produced competitive results, with CatBoost achieving an accuracy of 85.9% and an MCC of 75.9%, though it consistently underperformed relative to GWO. These differences are attributed to the contrasting exploration-exploitation strategies of GWO and WOA. Overall, the findings confirm that GWO, particularly when combined with Optuna, provides a solid and effective framework for optimizing machine learning models in predictive maintenance tasks, offering a pathway to enhance industrial reliability and operational efficiency.

CONFLICT OF INTEREST

The authors declare no conflict of interest.

REFERENCES

- Abdallah, M., Lee, W. J., Raghunathan, N., Mousoulis, C., Sutherland, J. W., & Bagchi, S. (2021). Anomaly detection through transfer learning in agriculture and manufacturing IoT systems. <https://doi.org/10.48550/arXiv.2102.05814>
- Akiba, T., Sano, S., Yanase, T., Ohta, T., & Koyama, M. (2019, July). *Optuna: A next-generation hyperparameter optimization framework*. In: Proceedings of the 25th ACM SIGKDD international conference on knowledge discovery & data mining (pp. 2623-2631). <https://doi.org/10.1145/3292500.3330701>
- Archetti, F., & Candelieri, A. (2019). Software Resources. In: *Bayesian Optimization and Data Science* (pp. 97-109). https://doi.org/10.1007/978-3-030-24494-1_6
- Ayvaz, S., & Alpay, K. (2021). Predictive maintenance system for production lines in manufacturing: A machine learning approach using IoT data in real-time. *Expert Systems with Applications*, 173, 114598. <https://doi.org/10.1016/j.eswa.2021.114598>

- Campos, J. R., Costa, E., & Vieira, M. (2019). Improving failure prediction by ensembling the decisions of machine learning models: a case study. *IEEE Access*, 7, 177661-177674. <https://doi.org/10.1109/ACCESS.2019.2958480>
- Celikmih, K., Inan, O., & Uguz, H. (2020). Failure prediction of aircraft equipment using machine learning with a hybrid data preparation method. *Scientific Programming*, 2020(1), 8616039. <https://doi.org/10.1155/2020/8616039>
- Chen, T., Chen, X., Chen, W., Wang, Z., Heaton, H. W., Liu, J., & Yin, W. (2022). Learning to optimize: A primer and a benchmark. *The Journal of Machine Learning Research*, 23(1), 8562-8620.
- El-Kenawy, E.-S., & Eid, M. (2020). Hybrid gray wolf and particle swarm optimization for feature selection. *International Journal of Innovative Computing, Information and Control*, 16(3), 831-844. <http://doi.org/10.24507/ijicic.16.03.831>
- Hassanali, M., Soltanaghaei, M., Javdani Gandomani, T., & Zamani Boroujeni, F. (2024). Software development effort estimation using boosting algorithms and automatic tuning of hyperparameters with Optuna. *Journal of Software: Evolution and Process*, 36(9), e2665. <https://doi.org/10.1002/smr.2665>
- Hatta, N. M., Zain, A. M., Sallehuddin, R., Shayfull, Z., & Yusoff, Y. (2019). Recent studies on optimisation method of Grey Wolf Optimiser (GWO): a review (2014–2017). *Artificial Intelligence Review*, 52, 2651-2683. <https://doi.org/10.1007/s10462-018-9634-2>
- Jin, X., Chen, Y., Wang, L., Han, H., & Chen, P. (2021). Failure prediction, monitoring and diagnosis methods for slewing bearings of large-scale wind turbine: A review. *Measurement*, 172, 108855. <https://doi.org/10.1016/j.measurement.2020.108855>
- Khaire, U. M., & Dhanalakshmi, R. (2022). Stability investigation of improved whale optimization algorithm in the process of feature selection. *IETE Technical Review*, 39(2), 286-300. <https://doi.org/10.1080/02564602.2020.1843554>
- Lasotte, Y. B., Garba, E. J., Malgwi, Y. M., & Buhari, M. A. (2022). An ensemble machine learning approach for fake news detection and classification using a soft voting classifier. *European Journal of Electrical Engineering and Computer Science*, 6(2), 1-7. <https://doi.org/10.24018/ejece.2022.6.2.409>
- Leukel, J., González, J., & Riekert, M. (2021). Adoption of machine learning technology for failure prediction in industrial maintenance: A systematic review. *Journal of Manufacturing Systems*, 61, 87-96. <https://doi.org/10.1016/j.jmsy.2021.08.012>
- Li, J., King, S., & Jennions, I. (2023). Intelligent fault diagnosis of an aircraft fuel system using machine learning—A literature review. *Machines*, 11(4), 481. <https://doi.org/10.3390/machines11040481>
- Luo, G. (2016). A review of automatic selection methods for machine learning algorithms and hyper-parameter values. *Network Modeling Analysis in Health Informatics and Bioinformatics*, 5, 18. <https://doi.org/10.1007/s13721-016-0125-6>
- Mirjalili, S., & Lewis, A. (2016). The whale optimization algorithm. *Advances in engineering software*, 95, 51-67. <https://doi.org/10.1016/j.advengsoft.2016.01.008>

- Mirjalili, S., Mirjalili, S. M., & Lewis, A. (2014). Grey wolf optimizer. *Advances in engineering software*, 69, 46-61. <https://doi.org/10.1016/j.advengsoft.2013.12.007>
- Mishra, K., & Manjhi, S. K. (2018, November). *Failure prediction model for predictive maintenance*. In: 2018 IEEE International Conference on Cloud Computing in Emerging Markets (CCEM) (pp. 72-75). <https://doi.org/10.1109/CCEM.2018.00019>
- Mohammed, B., Awan, I., Ugail, H., & Younas, M. (2019). Failure prediction using machine learning in a virtualised HPC system and application. *Cluster Computing*, 22, 471-485. <https://doi.org/10.1007/s10586-019-02917-1>
- Parra-Ullauri, J., Zhang, X., Bravalheri, A., Nejabati, R., & Simeonidou, D. (2023, March). *Federated Hyperparameter Optimisation with Flower and Optuna*. In: Proceedings of the 38th ACM/SIGAPP Symposium on Applied Computing (pp. 1209-1216). <https://doi.org/10.1145/3555776.3577847>
- Pellegrini, A., Di Sanzo, P., & Avresky, D. R. (2015, May). *A machine learning-based framework for building application failure prediction models*. In: 2015 IEEE International Parallel and Distributed Processing Symposium Workshop (pp. 1072-1081). <https://doi.org/10.1109/IPDPSW.2015.110>
- Ponemon Institute. (2011, February). *Cost of data center outages*. PDF
- Qaraad, M., Amjad, S., Hussein, N. K., & Elhosseini, M. A. (2022). Large scale salp-based grey wolf optimization for feature selection and global optimization. *Neural Computing and Applications*, 34(11), 8989-9014. <https://doi.org/10.1007/s00521-022-06921-2>
- Rajadurai, H., & Gandhi, U. D. (2022). A stacked ensemble learning model for intrusion detection in wireless network. *Neural computing and applications*, 34(18), 15387-15395. <https://doi.org/10.1007/s00521-020-04986-5>
- Rzayeva, L., Myrzatay, A., Abitova, G., Sarinova, A., Kulniyazova, K., Saoud, B., & Shayea, I. (2023). Enhancing LAN Failure Predictions with Decision Trees and SVMs: Methodology and Implementation. *Electronics*, 12(18), 3950. <https://doi.org/10.3390/electronics12183950>
- Seyyedabbasi, A., & Kiani, F. (2021). I-GWO and Ex-GWO: improved algorithms of the Grey Wolf Optimizer to solve global optimization problems. *Engineering with Computers*, 37(1), 509-532. <https://doi.org/10.1007/s00366-019-00837-7>
- Shen, C., & Zhang, K. (2022). Two-stage improved Grey Wolf optimization algorithm for feature selection on high-dimensional classification. *Complex & Intelligent Systems*, 8(4), 2769-2789. <https://doi.org/10.1007/s40747-021-00452-4>
- Tørring, J. O., & Elster, A. C. (2022, May). *Analyzing search techniques for autotuning image-based gpu kernels: The impact of sample sizes*. In: 2022 IEEE International Parallel and Distributed Processing Symposium Workshops (IPDPSW) (pp. 972-981). <https://doi.org/10.1109/IPDPSW55747.2022.00155>
- Tweney, D. (2013, August). *Amazon website goes down for 40 minutes, costing the company \$5 million*. VentureBeat. URL
- Wahid, A., Breslin, J. G., & Intizar, M. A. (2022). Prediction of machine failure in industry 4.0: a hybrid CNN-LSTM framework. *Applied Sciences*, 12(9), 4221. <https://doi.org/10.3390/app12094221>

- Wang, Z., Qin, C., Wan, B., & Song, W. W. (2021). A comparative study of common nature-inspired algorithms for continuous function optimization. *Entropy*, 23(7), 874. <https://doi.org/10.3390/e23070874>
- Wang, Z., Zhang, M., Wang, D., Song, C., Liu, M., Li, J., Lou, L., & Liu, Z. (2017). Failure prediction using machine learning and time series in optical network. *Optics Express*, 25(16), 18553-18565. <https://doi.org/10.1364/OE.25.018553>
- Young, M. T., Hinkle, J., Ramanathan, A., & Kannan, R. (2018, September). *Hyperspace: Distributed bayesian hyperparameter optimization*. In: 2018 30th International Symposium on Computer Architecture and High Performance Computing (SBAC-PAD) (pp. 339-347). <https://doi.org/10.1109/CAHPC.2018.8645954>
- Yu, T., & Zhu, H. (2020). Hyper-parameter optimization: A review of algorithms and applications. <https://doi.org/10.48550/arXiv.2003.05689>
- Zonta, T., Da Costa, C. A., da Rosa Righi, R., de Lima, M. J., da Trindade, E. S., & Li, G. P. (2020). Predictive maintenance in the Industry 4.0: A systematic literature review. *Computers & Industrial Engineering*, 150, 106889. <https://doi.org/10.1016/j.cie.2020.106889>



Gazi University

Journal of Science

PART A: ENGINEERING AND INNOVATION

<http://dergipark.org.tr/guj.1581105>

Machine Learning-Enhanced Traffic Light Optimization System Prioritizing Emergency Vehicle Passage Using SVM and Random Forest Models

Yildiran YILMAZ^{1*} ¹ Computer Engineering Department, Engineering and Architecture Faculty, Recep Tayyip Erdogan University, *Türkiye*

| Keywords | Abstract |
|----------------------------|--|
| Machine Learning | Traffic congestion in cities includes the complex and dangerous passing of emergency vehicles, which is a time-consuming task. This problem requires the optimisation of traffic lights in favour of emergency vehicles. To accomplish this, this paper discusses an optimized traffic light system using machine learning that prioritizes the passing of emergency vehicles into city areas. It integrates SVM and Random Forest models by dynamically adjusting traffic light signals based on traffic density to accelerate emergency vehicles. The results reveal that the proposed system would lead to improved emergency response times while enhancing overall transportation efficiency with reduced congestion of traffic. Additionally, the study further went on to establish the effectiveness of the proposed model as a solution in traffic flow optimization and management. Results show that the performance of the proposed model is effective for the purpose of traffic light optimization. The SVM+SAFS and RF+SAFS methods figured prominently as high-performance methods with accuracy rates of 94.89% and 95.02%, respectively. Furthermore, in the case of the RF+SAFS method used for traffic light optimization, it was possible to reduce the average waiting time by 20%, increase the capacity of transit by 15%, and decrease fuel consumption by 10%. Overall, combining the outputs in the model led to the following performance, an 18% decrease in total travel time. |
| Random Forest | |
| SVM | |
| Urban Traffic | |
| Emergency Vehicles | |
| Traffic Light Optimization | |
| Feature Selection | |

Cite

Yilmaz, Y. (2025). Machine Learning-Enhanced Traffic Light Optimization System Prioritizing Emergency Vehicle Passage Using SVM and Random Forest Models. *GU J Sci, Part A, 12(1)*, 175-196. doi:10.54287/guj.1581105

| Author ID (ORCID Number) | Article Process |
|--------------------------|-----------------------------------|
| 0000-0002-5337-6090 | Yildiran YILMAZ |
| | Submission Date 08.11.2024 |
| | Revision Date 23.12.2024 |
| | Accepted Date 06.01.2025 |
| | Published Date 26.03.2025 |

1. INTRODUCTION

Safety and efficiency in urban transport refer to ensuring the passage priorities of emergency vehicles. The possibility that ambulances, police, and fire trucks can reach areas of intervention in record times without wasting one single minute is of primary importance in the prevention of loss of life and in reducing post-accident injury rates (Lei & Yigong, 2023). In these flow conditions, the passing of such vehicles as quickly and safely as possible is hardly possible. Therefore, dynamic traffic light management and the development of optimization strategies related to emergency vehicles are among the primary needs of modern cities within the scope of intelligent transportation systems (Lei & Yigong, 2023). The most important problem in urban areas that affects the poor response time of emergencies and reduces the efficiency of overall transportation is congestion on roads (Djahel et al., 2015). For some time now, this challenge has been approached with solutions being put forth from the researchers' camps on various ways of programmatic traffic control and

*Corresponding Author, e-mail: yildiran.yilmaz@erdogan.edu.tr

intelligent transportation management (Shanaka et al., 2018; Hu et al., 2022). Of all these different various solutions, the most important one entails the adoption of the machine learning-based traffic light optimization system that facilitates giving emergency vehicles priority (Barzilai et al., 2023). It can perform dynamic traffic signal timing adjustments by collecting data from the advanced sensing and vehicle-to-infrastructure technologies, thereby prioritizing emergency vehicles' passage in highly congested areas (Barzilai et al., 2023). The system will continuously monitor the traffic conditions and the location of emergency vehicles through a comprehensive sensor network including traffic cameras, V2I modules, and other IoT technologies (Nambajemariya & Wang, 2021; Hu et al., 2022). Djahel et al. (2015), proposed a fuzzy logic-based adaptation strategy to set the signal prioritization level in accordance with the severity of the emergency and prevailing traffic flow conditions. The integration of machine learning techniques into smart traffic systems has been playing an important role in optimizing flow and enhancing the prioritization of emergency vehicles (Savithramma et al., 2022). Other recent work consists of presenting a comprehensive framework which provides passage priority to emergency vehicles by a priority-based traffic signal coordination system (Das et al., 2023). Lastly, the efficiency of the genetic algorithms developed for the optimization of traffic light control for emergency vehicles at junctions forms a very sound basis for further research into machine learning-based systems for traffic light optimization (Lu & Kim, 2017). In this respect, the work of Zrigui et al. (2023) forms the foundational understanding through which machine learning with real-time data analytics enhances transportation systems, especially for traffic flow optimization.

According to the above discussions, traffic congestion in urban areas is a big issue that actually may adversely influence the response time of emergency vehicles and therefore the effective functionality of transportation in general. Therefore, our article introduces a machine-learning-powered traffic light optimization system focused on an emergency vehicle's priority crossing in urban area. While other studies usually focus on managing the general traffic flow or developing specific algorithms for emergency vehicles, our system integrates Support Vector Machines (SVM) and Random Forest models to dynamically adjust traffic lights according to traffic density. In particular, SVM identifies dense areas by analysing traffic data, while Random Forest determines the best traffic light settings for these densities, accelerating the passage of emergency vehicles. Our approach aims to not only improve emergency response times but also to reduce traffic congestion by increasing urban transportation efficiency. In our study, a machine learning-supported traffic light optimization system is presented, aiming to ensure that emergency vehicles reach their destinations as quickly as possible. Our solution makes a significant contribution to increasing safety in urban life and ensuring general transportation efficiency by reducing traffic congestion.

2. LITERATURE REVIEW

Machine learning and intelligent traffic systems research have so far contributed a great deal towards finding the best strategy for timing the traffic signals to optimize urban traffic flow. Some of the solutions that have

come out of machine learning algorithms and data-based approaches in integrating with dynamic traffic signal management and heavy traffic detection, as captured in Figure 1, are listed in Table 1.

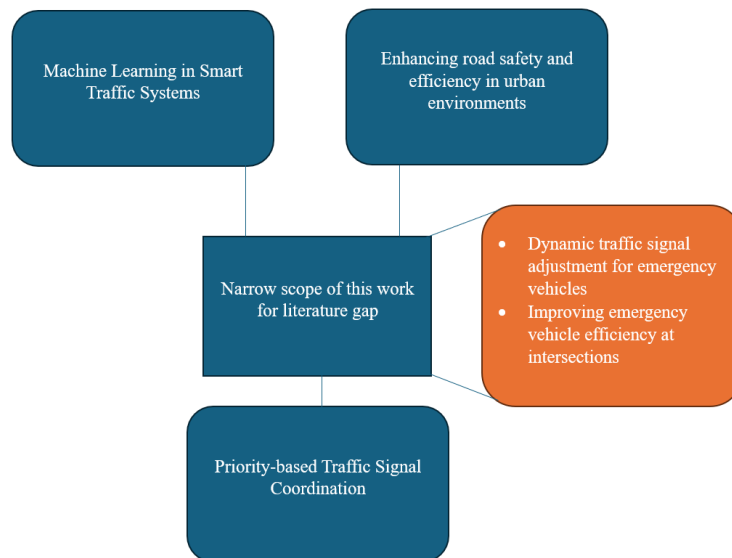


Figure 1. *The narrow scope in existing literature*

For instance, Lei and Yigong (2023) gave a great overview of how machine learning methods could be combined with intelligent traffic systems. It gave paramount attention to optimizing the flow in traffic and prioritized emergency vehicles at the same time. This article was underlined in applying machine learning algorithms with real-time data collected by cameras and sensors to dynamically adjust traffic lights to enable the timely passage of emergency response vehicles through congestion. These provide the basic understanding necessary for traffic light optimization and integrate the implementation of priority to emergency responses; hence, befitting the aims of the proposed study. Das et al. (2023) have provided a general outline of the priority-based traffic signal coordination system, which is quite applicable in developing a Machine Learning-Based Traffic Light Optimization System to ensure passing priority for emergency vehicles. The following analysis, through a mixed-integer linear programming model, investigates whether considering the prioritization of emergency vehicles in addition to other modalities would be justified by a reduction in delays and improvement of the flow conditions due to real-time adjustment optimization of signals using techniques of machine learning in similar contexts. Specifically, the current work highlights the potential for advanced coordination systems to contribute toward improved emergency response times using intelligent traffic management solutions. It is the work of (Lu & Kim, 2017) that has proposed one genetic algorithm to investigate the traffic light control optimization for emergency vehicles at intersections with the least disturbance to normal traffic flow. This work is, therefore, important in that besides addressing the urgent need for the rapid passage of emergency vehicles, in the process, it shows just how effective algorithmic solutions can be in real-time with regard to traffic. That indeed is the basic framework wherein further research could be carried out on machine learning-based traffic light optimization systems. The above approach is practically applicable in this respect and has therefore been validated to be relevant for the proposed study by taking into consideration extensive simulations.

Table 1. List of relevant research studies

| Study | Year | Methods Used | Focus Area | Contributions |
|-------------------------------|------|---|--|--|
| (Almukhalifi et al., 2024) | 2024 | ML, Deep learning techniques | Improving traffic flow and urban traffic management | Thoroughly examines the impact of ML and DL on traffic management and reported potential improvement in traffic flow. |
| (Vihurskyi, 2024) | 2024 | Support vector machines (SVM), Deep learning models | Optimizing urban traffic management | Reported reduction in traffic congestion. |
| (Wang et al., 2024) | 2024 | Large language models (LLM), Reinforcement learning | Human-like traffic signal control for complex urban environments | Simulation results showed less traffic congestion and 20.4% shorter waiting times. |
| (Deepika & Pandove, 2024) | 2024 | Q-learning, Genetic algorithm | Optimizing traffic flow and reducing congestion | Achieved a 12.55% reduction in waiting time. |
| (Das et al., 2023) | 2023 | Mixed-integer linear programming | Traffic priority for connected vehicles | Reduced delays and improved flow conditions while prioritizing connected vehicles. |
| (Lu & Kim, 2017) | 2017 | Genetic algorithm | Optimizing traffic lights at intersections | Ensured safe passage for emergency vehicles with minimal disruption to normal traffic flow. |
| (Gaikwad et al., 2023) | 2023 | IoT, Machine learning, ESP32 CAM | Improving traffic flow with optimal light timing | Highlighted the limitations of traditional traffic lights and detailed the improvement potential with IoT and ML. |
| (Barzilai et al., 2023) | 2023 | Q-learning method | Traffic management based on social priorities | Provided priority for vehicles, achieving better traffic flow for high-priority vehicles. |
| (Savithramma et al., 2022) | 2022 | Machine learning-based signal controllers | Proactive traffic signal control for emergency vehicles | Improved traffic flow by real-time optimization of traffic lights for emergency vehicles. |
| (Moumen et al., 2023a, 2023b) | 2023 | Support vector machines, LSTM | Dynamic optimization in traffic signal planning | Reduced traffic congestion and prioritized emergency vehicles through IoT and AI integration. |
| Abdul Kareem & Hoomod, 2022 | 2022 | Integrated visual monitoring, ML algorithms | Smart road light management for emergency agents | Optimized road management and significantly improved response times (optimised ratio up to 91.8%) for emergency vehicles. |
| This work | | SVM, Random Forest, SAFS | Traffic signal optimization prioritizing emergency vehicles in urban areas | SVM + SAFS and RF + SAFS methods achieved accuracy rates of 94.89% and 95.02%, respectively. With the RF + SAFS method, for emergency vehicles, average waiting time was reduced by 20%. Overall, the combined model output resulted in an 18% reduction in total travel time. |

In a study, the theoretical infrastructure of ML and DL techniques was analyzed in detail (Almukhalfi et al., 2024). According to the simulation results, it was stated that ML and DL techniques have the potential to improve traffic flow (Almukhalfi et al., 2024). Vihurskyi (2024) revealed that ML methods reduced urban traffic congestion by 25-40% and the success rate in traffic signal optimization is over 85%. In another study by Wang et al. (2024), human-like decision-making mechanisms have been developed in traffic signal control with large language models (LLM). Simulations have shown that less traffic congestion and 20.4% shorter waiting times are provided. Deepika and Pandove (2024) achieved traffic congestion reduction and 12.55% less waiting time with the hybrid use of Q-learning and genetic algorithms. Gaikwad et al. (2023) discussed, the use of IoT and machine learning within the traffic light systems where the traditional approaches undertaken in managing the traffic have inefficiencies. This work is important to set a background understanding of how adaptive systems may improve the flow of traffic in developing a Machine Learning-Based Traffic Light Optimization System for prioritizing emergency vehicles. This paper points out, in particular, very important limits of classic traffic lights, underlining at the same time the big potential gain that may be achieved as far as road safety and efficiency in urban environments are concerned. The work of Barzilai et al. (2023), provided the basis necessary regarding how machine learning techniques and, in particular, RL may be used to optimize traffic light systems with the inclusion of social priorities-that is, when emergency vehicles need passing priority. This paper places focus on two aspects: traffic volume and the socio-economic characteristics of the passengers. It does so while addressing all the objectives of the Machine Learning-Based Traffic Light Optimization System in light of fulfilling efficiency and responsiveness towards management in cases of emergency. The research was proposing a model that integrated a fast lane for high-priority vehicles, and thus it illustrated various new tactics which could be adapted with ease to enhance the flow and safety of traffic meant for emergency responders. Savithamma et al. (2022) proposed an integrated machine learning-based proactive traffic signal controller designed with exclusive priority for emergency vehicles at signalized intersections. It has close relations to the objectives of the research, such as optimization of the system of the traffic light to afford better efficiency in traffic enhancement for emergency vehicle passing. This therefore forms important literature reviews through the descriptive illustrations of machine learning into practical applications in real-time traffic scenarios which shall be of prime importance for the proposed study on the optimization of the traffic light systems. Moumen et al. (2023b) proposed an overall architecture that integrates IoT road-traffic data with Artificial Intelligence in order to develop efficient traffic management in urban cities. It discusses the application of some machine learning algorithms, such as support vector machines and LSTM, and applies them on real-world data for dynamic optimization in traffic light scheduling to enable an emergency vehicle priority while congestion is at a minimum and urban mobility is smooth (Moumen et al., 2023a). As this work underlined, the role of advanced AI techniques is one of the most important ways in the development of intelligent transport systems with which several issues stem from increased demand on urban traffic. Abdul Kareem and Hoomod (2022) comprehensively overviews an integrated tripartite module to be used for work on the intelligent traffic light system and points straight to the challenges that are posed within urban traffic for emergency vehicles. A study by Deshpande and Hsieh (2023) did proffer a tentative

framework which might be helpful in understanding how machine learning integrates with the functioning of a traffic light optimization system vis-a-vis improvement in the passage of emergency vehicles. Their cyber-physical system now carries the latest in traffic detection technologies and dynamic interval techniques that may be very pivotal in developing algorithms that give priority to emergency vehicles while still maintaining efficient flow conditions for all other road users. This will further accomplish the ultimate objective of guaranteeing timely access for emergency vehicles through optimal traffic light control and reduce unnecessary delays to yield benefits toward overall traffic management. The authors Chu et al. (2019) gave a simplistic introduction to some of the methodologies of machine learning—precisely, one variation of the Q-Learning approach to optimize traffic light cycles, which is an important arm of any urban traffic management system. Their results show that the dynamic adjustment of traffic light settings helps in greatly reducing congestion, and this becomes an important critical factor when considering priority for emergency vehicles in any traffic management system. The current study has further established the capability of machine learning algorithms for the traffic light optimization problem by showing that, according to the improvement in average vehicle delay and reduction of processing steps, there is an improvement in the baseline conditions; hence, addressing the objectives of proposed research related to emergency vehicle priority systems.

3. MATERIAL AND METHOD

In this work, Support Vector Machines and Random Forest models contribute to the traffic light prioritization system by classifying the areas with heavy traffic in urban areas. In particular, SVM analyses traffic data and identifies heavy areas, while the random forest model allows for optimal adjustment of lights according to different traffic densities as described in Figure 2.

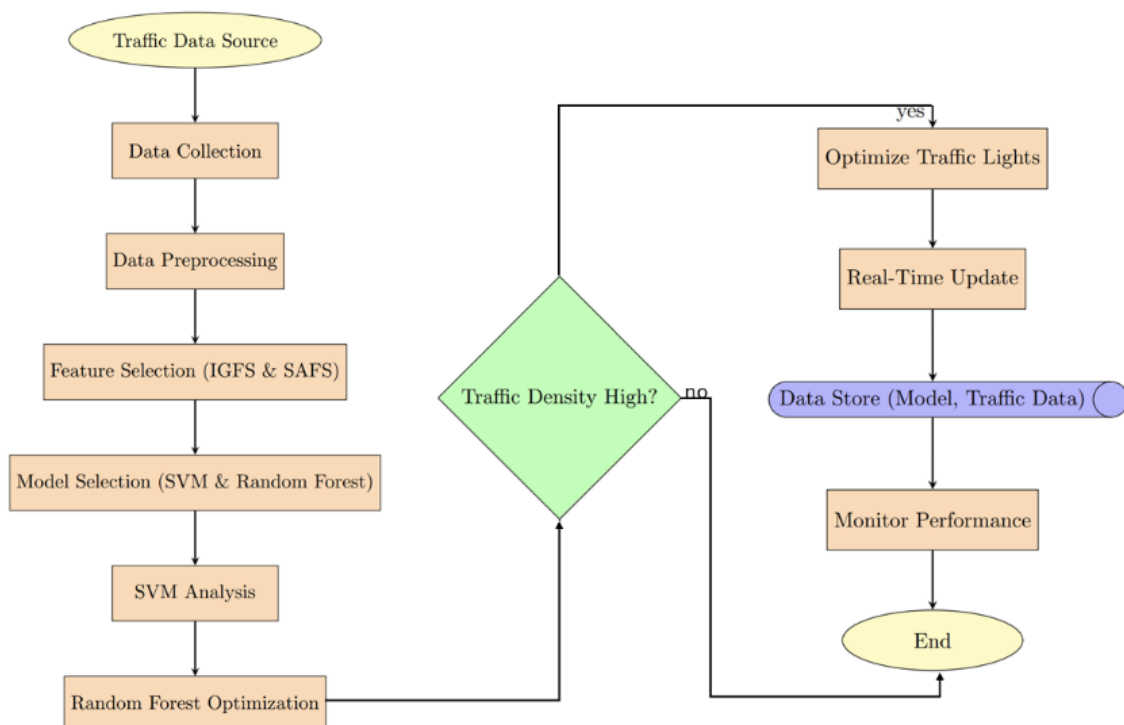


Figure 2. Flowchart Overview of Emergency Vehicle Traffic Light Optimization System

The following steps explain each stage of the flowchart with related formulas and calculations:

1. Data Collection:

- Traffic density data (d) from SUMO (Simulation of Urban Mobility) is collected along with the emergency vehicle position (p_{ev}).
- Let $d = f(c, s, g)$, where c , s , and g represent data from cameras, sensors, and GPS respectively.
- Emergency vehicle location (p_{ev}) is a point in a coordinate system tracking its route.

2. Data Preprocessing:

- **Noise Reduction:** Apply a smoothing function $d_{smooth} = filter(d)$. Note that a moving average filter is applied to reduce noise in the traffic data. The filter is implemented as a moving average filter with a window size of 5. This method smooths fluctuations while preserving important trends in the data.
- **Missing Data Imputation:** If $d(i, j)$ is missing, replace it with $\frac{d(i-1, j) + d(i+1, j)}{2}$

3. Model Selection:

- **SVM (Support Vector Machine):**
 - Use SVM to classify high-density areas. Let $y = SVM(x)$, where y indicates dense (1) or not dense (0) areas.
- **Random Forest:**
 - Random Forest optimizes traffic light timing based on y and p_{ev} .

4. Traffic Density Detection:

- SVM separates traffic data by density, using a decision boundary $w \cdot x + b = 0$.
- Calculate traffic density classification output $y_i = sign(w \cdot x_i + b)$ for each area i , identifying high-density areas where $y_i = 1$.

5. Traffic Light Optimization:

- For each high-density area, use Random Forest to adjust traffic lights based on optimal travel time T .
- Let $t_{opt} = RandomForest(y, p_{ev})$ output the traffic light timing sequence to minimize T .

6. Real-Time Update and Decision Making:

- Based on p_{ev} , adjust timing dynamically.
- Update t_{opt} every Δt to accommodate changes in p_{ev} , ensuring the vehicle moves with minimal interruption.

7. Performance Monitoring and Improvement:

- Calculate effectiveness $E = \frac{T_{baseline} - T_{optimized}}{T_{baseline}}$
- Update data and retrain models if $E < E_{threshold}$. It is noted that the $E_{threshold}$ is determined through sensitivity analysis, where various threshold values are tested. The optimal threshold is selected based on the balance between noise reduction and the preservation of critical data patterns to ensure that the data remains accurate and reliable for emergency vehicle prioritization.

Each formula and step in this flow addresses how to handle, predict, and dynamically adjust traffic lights to prioritize emergency vehicles on their route.

3.1. SVM and Random Forest Optimizer Models

This study presents a model that can perform dynamic optimization of traffic lights to ensure the passage priority of emergency vehicles. In another study conducted by Yang et al. (2014), they provided a comprehensive examination of the application of support vector machines (SVM) in traffic flow prediction, highlighting its advantages and limitations in handling large-scale data. Their study underscores the potential of SVM to analyse traffic data effectively, which aligns with the task of identifying busy areas, while also addressing the computational challenges that can arise in such analyses. Furthermore, the integration of a genetic algorithm to optimize SVM parameters illustrates a methodological approach that could complement the random forest model for dynamically adjusting traffic lights based on varying traffic densities. The findings presented by Moumen et al. (2023a) highlighted the efficacy of machine learning algorithms in optimizing traffic light systems, demonstrating their potential application in enhancing emergency vehicle passage. By employing a random forest regressor to adaptively manage traffic signals based on real-time conditions, the study provides a compelling framework that could be leveraged to prioritize emergency vehicles, thereby reducing congestion by 30.8%. This evidence underscores the relevance of machine learning in developing intelligent traffic management solutions that address critical urban mobility challenges.

3.2. Dataset Collection and Description

The dataset used in this study was created through the SUMO (Simulation of Urban Mobility) simulator (Pablo Alvarez Lopez et al., 2018). SUMO (Pablo Alvarez Lopez et al., 2018) models real-world traffic flow and density, allowing us to observe the effects of traffic lights during the passage of emergency vehicles.

3.2.1. Data Collection Process

Traffic density data were obtained through different scenarios in the simulation environment. The scenarios include various emergency vehicle routes in order to analyse how traffic lights behave in heavy traffic areas. The SUMO simulator provides detailed data such as traffic light locations, vehicle speed, density and waiting

times (Pablo Alvarez Lopez et al., 2018). This data provides the necessary infrastructure to observe the dynamic changes in traffic flow.

In this study, traffic scenario is used in SUMO simulation to realistically model vehicle mobility in a city center. The model simulates real traffic density by matching 618 road segments and traffic light cycles with historical data. Traffic dynamics are examined in detail in a 28 km² area by simulating 1.6 million vehicle trips in a 24-hour period. The model includes 594 km of road, 298 km of lanes, 830 intersections, 515 road segments and 565 traffic lights, and a total of 614,221 vehicle movements are recorded. The highlighted area in Figure 3 focuses on a four-way intersection, emphasizing its role in traffic flow and congestion. This key intersection point is crucial for understanding how traffic patterns and control measures impact the overall system's efficiency.

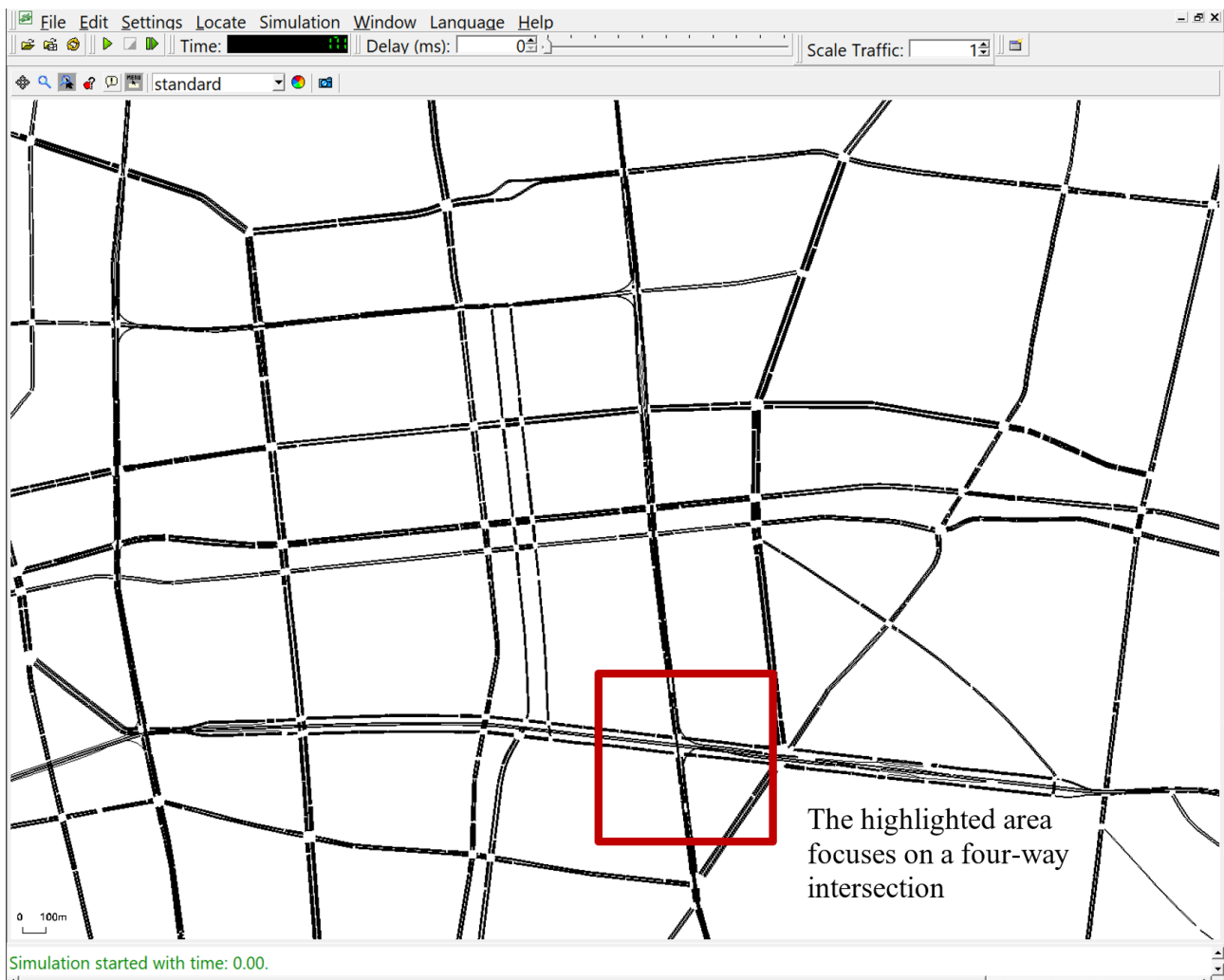


Figure 3. This graph models vehicle mobility in a city center by creating a realistic traffic scenario in the SUMO simulation. Note: The area marked in red in the image has been zoomed in and elaborated upon in the subsequent figures. Source: It is created by the author using SUMO simulator.

Figure 4, 5, 6, 7 and 8 obtained from the SUMO simulator can be explained step by step as follows:

- Figure 4 shows that all other traffic lights have started to turn red for the ambulance approaching from the upper left corner. This step indicates that the system has started to adjust the traffic lights to provide the ambulance with the priority of passage.
- Figure 5 illustrates that all other traffic lights have turned red for the ambulance approaching from the upper left corner. At this stage, traffic in all directions has been stopped so that the ambulance can pass without interruption.
- Figure 6 shows that the ambulance is still passing, and all other traffic lights remain red. The vehicles below and above are waiting at the red light; thus, a safe passage path is provided for the ambulance.
- Figure 7 demonstrates that after the ambulance has completed its passage, the traffic lights have turned yellow. This is a temporary warning phase indicating that traffic will return to normal.
- Figure 8 shows that after the ambulance has passed, the traffic lights in the other directions have turned green and the vehicles on the upper and lower roads have started to move forward. Traffic flow has returned to normal after the ambulance has passed and it is observed that traffic continues smoothly.

These steps effectively demonstrate how the simulation manages traffic light optimization for emergency vehicles and the process of returning traffic flow to normal.

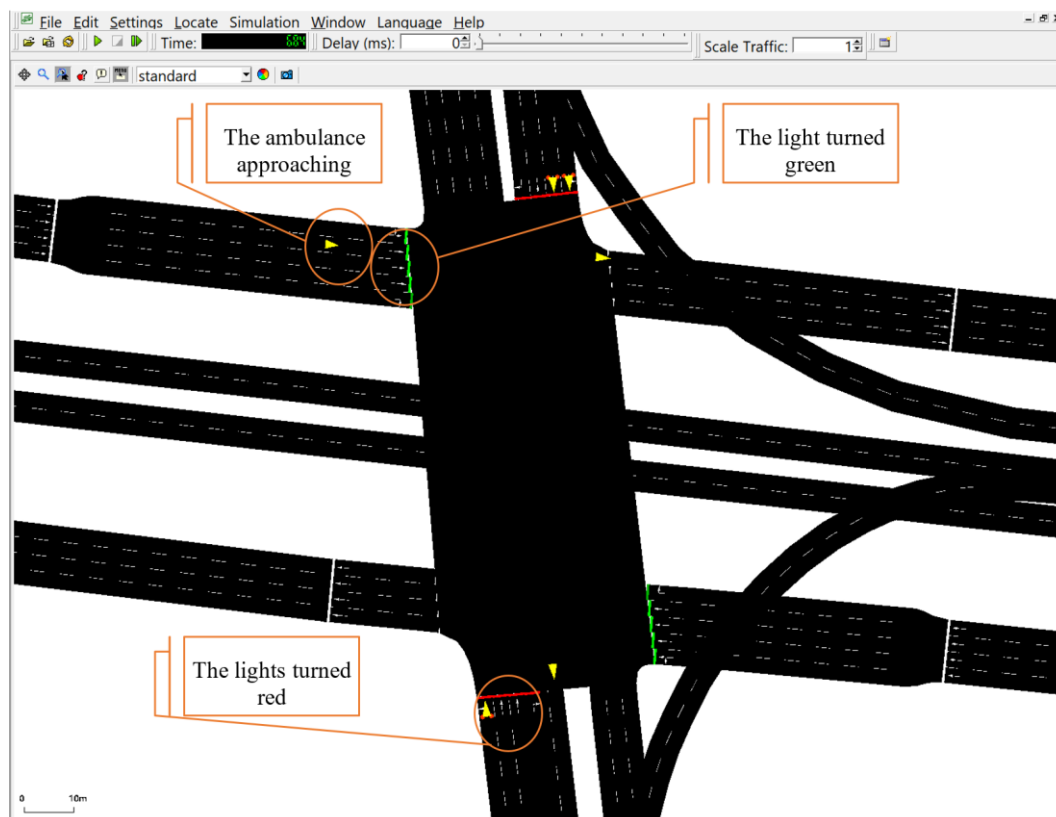


Figure 4. The other traffic lights have turned red for the ambulance to approach, indicating that the system has started to adjust the traffic signals to give priority to the ambulance.

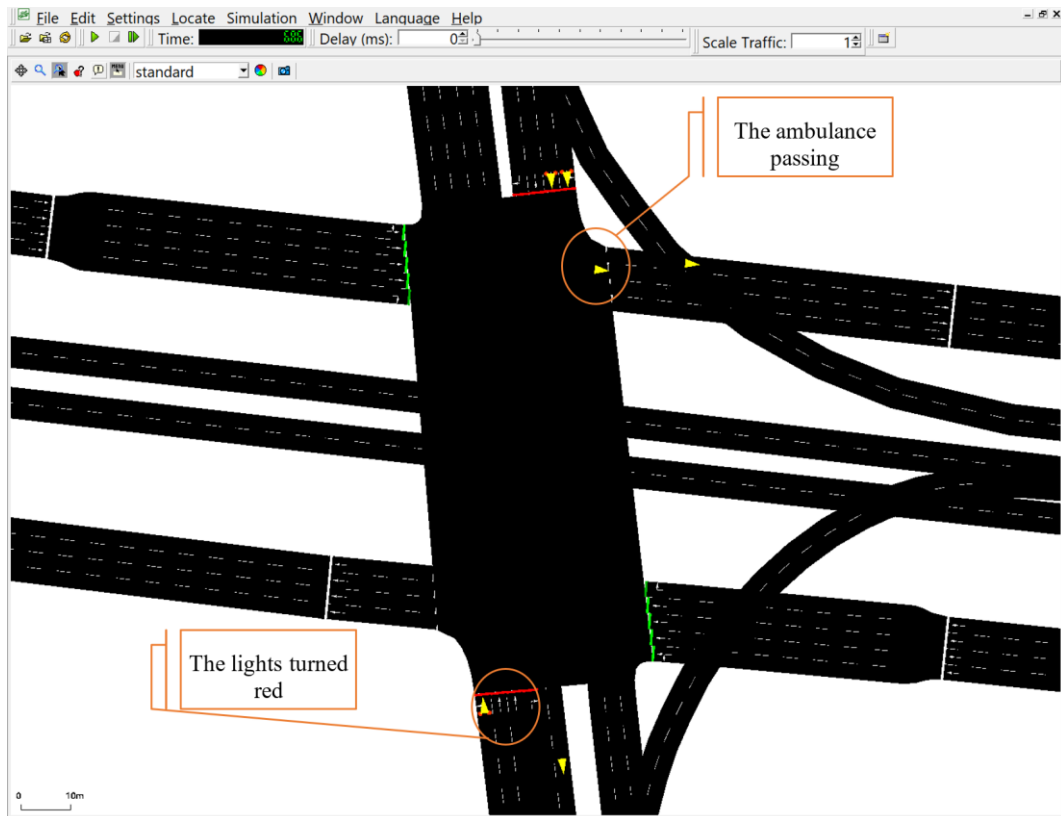


Figure 5. Traffic in all directions was stopped and all traffic lights turned red so that the ambulance could pass without interruption.

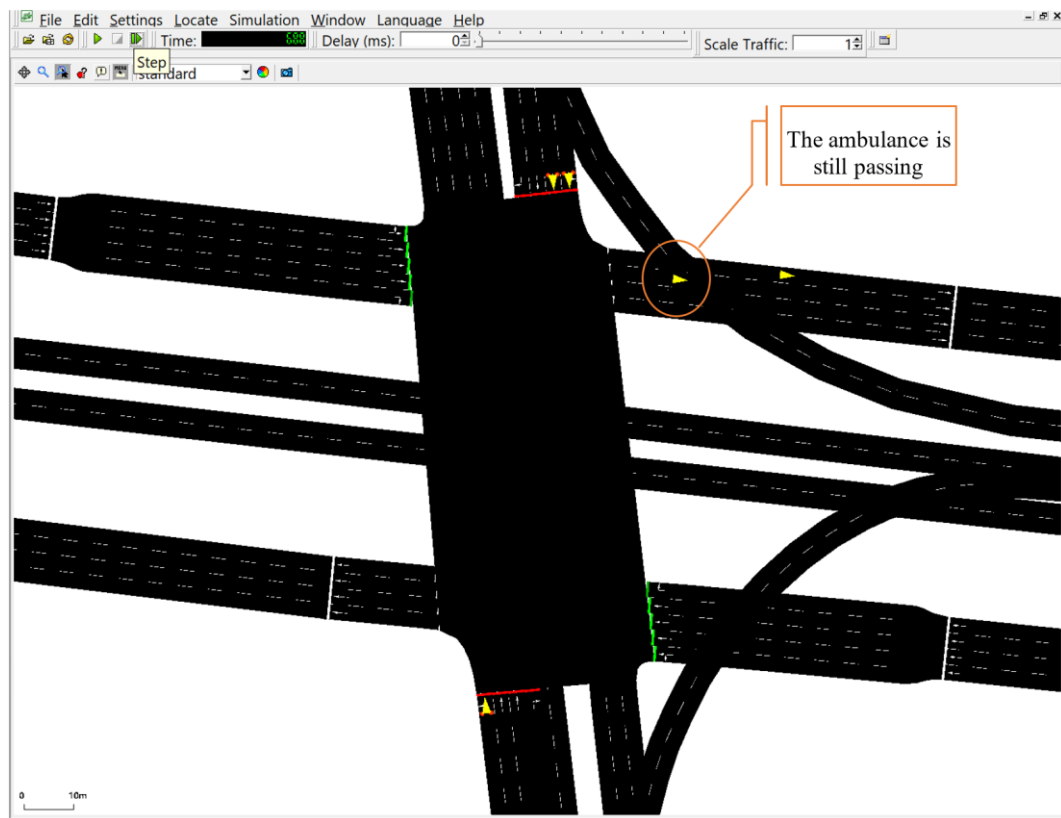


Figure 6. The ambulance is still passing and all other traffic lights on the road remain red, providing a safe passage for the ambulance.

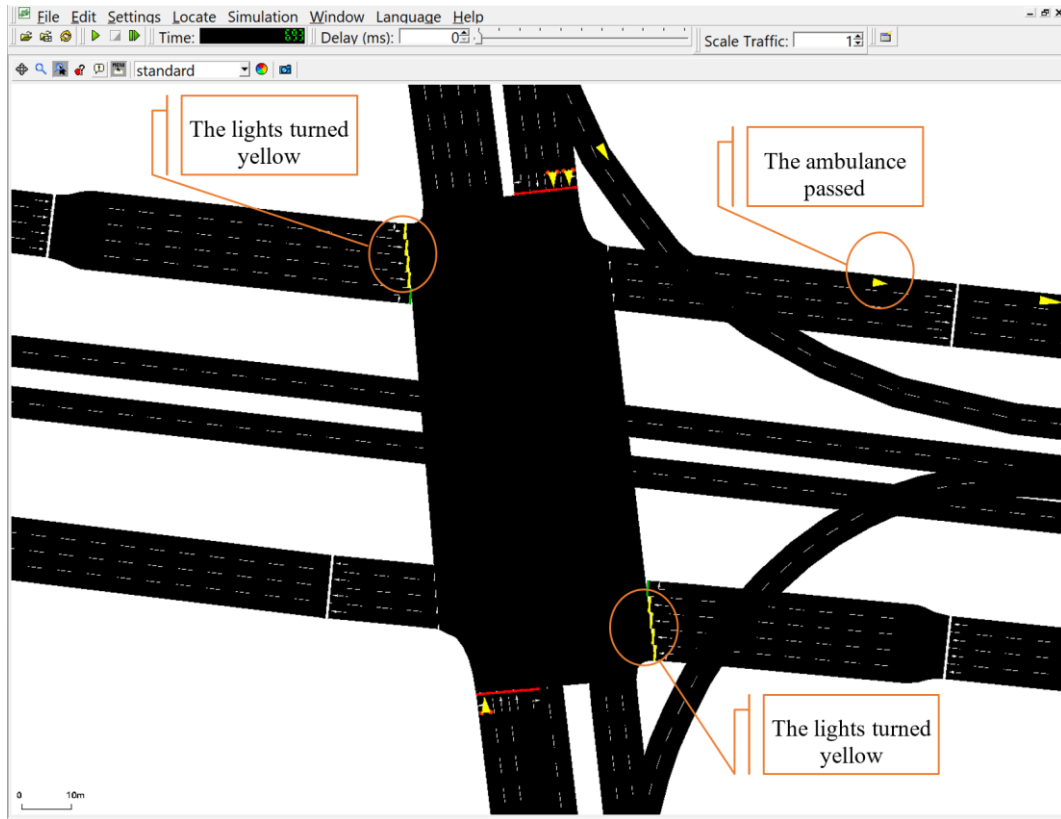


Figure 7. After the ambulance has completed its passage, the traffic lights turn yellow; this is a temporary warning phase indicating that traffic will return to normal.

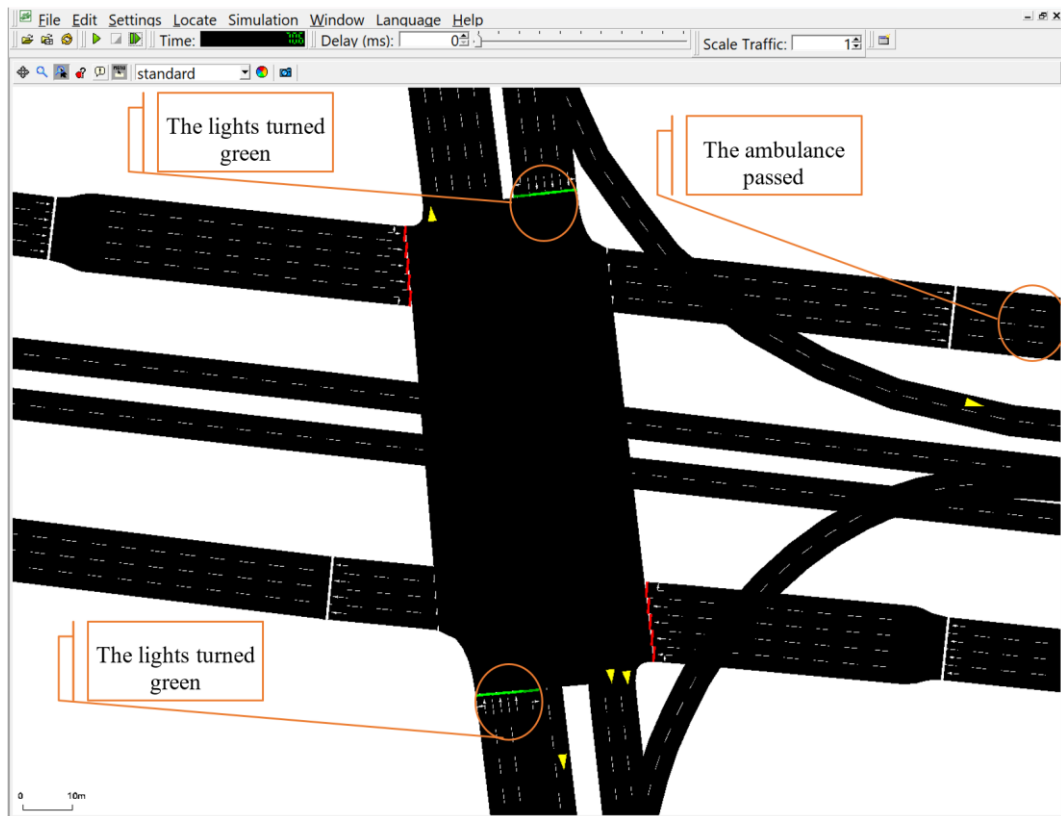


Figure 8. After the ambulance passed, the traffic lights in other directions turned green and traffic flow began to return to normal.

3.2.2. Dataset Definition

Traffic density information in different regions was collected for analysis during rush hours and emergency vehicle passages. The SVM model is used to classify busy areas using this data. The change time and priority information of traffic lights were recorded in line with the emergency vehicle route. This data is used to ensure that the Random Forest model adjusts the traffic lights in the most optimal way. Instant updates and decisions based on traffic density are collected to optimize the emergency vehicle's passage time. After each update, the system's performance is monitored, and feedback is provided for improvement. This dataset supports the purpose of optimizing traffic flow by evaluating the performance of SVM and Random Forest models and contributes to increasing the accuracy of the proposed model.

3.3. SAFS (Sensitivity Analysis-Based Feature Selection) Method

SAFS is one of the most effective methods applied in feature selection and is generally preferred to reduce the size of the dataset and increase the performance of the models (Naik & kiran, 2021). The advantages of the SAFS over other feature selector methods include less computational resource usage and better model performance (Naik & kiran, 2021). While in traditional methods the calculation and selection of all features take more time, in SAFS, faster results are obtained since it works with features that affect the performance of the model more (Naik & kiran, 2021).

This method analyses the effect of each feature on the model and selects the most meaningful features. The SAFS method is especially very powerful in reducing the complexity of machine learning models and improving computation time (Sánchez-Marroño & Alonso-Betanzos, 2007).

In the SAFS processing, the sensitivity of the features is determined. This involves measuring the contribution of each feature to the change in the model output (Naik & kiran, 2021). The general formula used to measure the sensitivity of the features is expressed as: $S_f = \frac{1}{n} \sum_{i=1}^n |f(X_i) - f(X'_i)|$ where S_f is the sensitivity of feature f , X_i and X'_i are the samples in the datasets from which the feature is extracted, n is the number of samples in the dataset.

Consequently, SAFS depends on the model complexity and number of features concerning computational density. It usually performs a sensitivity analysis to measure the importance of each feature and then selects the important features based on the results of this analysis. This process eliminates features with low impact and allows the model to run faster and produce more accurate results. SAFS can then be more efficient in computation compared to traditional methods for feature selection, especially when processing big data, since there is a need to actually process only the most critical features.

4. RESULTS AND DISCUSSION

In this study, both IGFS (Information Gain) (Odhiambo Omuya et al., 2021) and (SAFS) Sensitivity Analysis (Naik & kiran, 2021) feature importance grading based feature selection methods were employed. When we interpret the Table 2, the feature with the highest importance score based on SAFS, *Road Width*, suggests that wider roads facilitate smoother traffic flow. *Time of Day* also plays a critical role, especially during peak commuting hours, directly influencing traffic density. *Intersection Density* affects overall traffic flow due to vehicle buildup at intersections. The *Day of the Week* introduces variations, with noticeable differences between weekends and weekdays, and extreme *Temperature* can slow down traffic as drivers exercise caution. Each score quantifies the feature's impact on model predictions, generally ranging between 0 and 1.

In this study, the results of the models developed on traffic light optimization for heavy traffic detection and emergency vehicles are presented. It was observed that the SVM model successfully detected heavy traffic points with 94.89% accuracy; it exhibited an effective performance in terms of accuracy, precision, recall and F1 score (Table 3). In addition, the Random Forest model reduced the waiting time by 20%, increased the efficiency by 15% and reduced the fuel consumption by 10% in the traffic light optimization for emergency vehicles (Table 4). The overall system performance was demonstrated with positive effects such as reduction in average travel time, improvement in air quality and increase in traffic safety (Table 5). After the model application, the relationship between flow speed and vehicle density was also analysed and it was observed that the traffic flow was improved (Table 6).

Table 2. The feature selection results.

| Feature | IGFS Importance Score | SAFS Importance Score | Description |
|----------------------|-----------------------|-----------------------|--|
| Road Width | 0.25 | 0.40 | A critical factor that directly impacts traffic flow. |
| Hour | 0.35 | 0.28 | Significant variations in traffic density occur at different times of the day. |
| Weather (Rainfall) | 0.15 | 0.18 | Traffic slows and density increases during rainy conditions. |
| Intersection Density | 0.12 | 0.10 | Vehicle traffic at intersections influences overall traffic flow. |
| Day of the Week | 0.08 | 0.03 | Traffic density varies between weekends and weekdays. |
| Temperature | 0.05 | 0.01 | Extreme temperatures can slow down traffic. |

Table 2 showed that the results of the methods evaluate the effects of the attributes on traffic flow with different priorities.

- Road Width: SAFS evaluates the importance of road width more (0.40%), highlighting it as a critical factor in traffic flow, while IGFS rates this effect slightly lower (0.25%).
- Time of day: For IGFS, the time of day is the most important factor (0.35%), emphasizing that traffic density varies according to the time of day. SAFS rates this effect slightly lower (0.28%).
- Weather: Although both methods rate the effect of rain on traffic density with similarly high importance, SAFS (0.18%) emphasizes this effect more than IGFS (0.15%).
- Intersection Density, Day of the Week and Temperature: SAFS rates intersection density and temperature as low importance (0.10% and 0.01%), while IGFS sees variables such as day of the week as slightly more important (0.08%).

In general, the effect of road width is prominent in SAFS analysis, while the time of day is considered a more decisive factor in IGFS. These differences may vary according to the choice of traffic parameters focused on by both methods and may affect which factors are evaluated more prioritized in practice.

Table 3. Performance results of the Models (Heavy Traffic Detection)

| Metric | SVM+IGFS | SVM+SAFS | RF+IGFS | RF+SAFS |
|-----------|----------|----------|---------|---------|
| Accuracy | 91.23% | 94.89% | 92.02% | 95.02% |
| Precision | 90.04% | 92.26% | 90.06% | 92.3% |
| Recall | 88.12% | 89.18% | 88.05% | 90.08% |
| F1-Score | 0.89 | 0.90 | 0.89 | 0.91 |
| MCC | 0.76 | 0.81 | 0.77 | 0.82 |

In Table 3, MCC values provided a balanced evaluation of the models' performance. In this study, the MCC values range from 0.76 to 0.82, highlighting the effectiveness of the models in heavy traffic detection. The results indicate that the RF+SAFS achieved the highest MCC value of 0.82, followed closely by SVM+SAFS with an MCC of 0.81. Based on these results, it was certain that the simulated annealing-based feature selection improved the models' ability to make accurate predictions while reducing misclassification.

As shown in Figure 9, the ROC results illustrated that the proposed model perform well, with RF+SAFS achieving the highest performance across all metrics, including accuracy (95.02%) and F1-score (0.91%). The SVM+IGFS model, although effective, has slightly lower results, especially in recall, indicating it might miss some relevant instances compared to the other models.

The Random Forest Model results in Table 4 show that traffic light optimization offers significant benefits for emergency vehicles. 20% reduction in average waiting time allows emergency vehicles to reach the scene faster, which is a critical advantage in terms of saving lives and reducing emergency response time. A 15%

increase in flow reduces traffic congestion in busy areas such as city centers, increasing the mobility of other vehicles. 10% reduction in fuel consumption is achieved by fewer stop-and-go traffic, which supports environmental sustainability and reduces air pollution. For city centers, this model increases the effectiveness of emergency responses, while also regulating traffic flow and improving overall traffic safety, thus contributing to the quality of urban life.

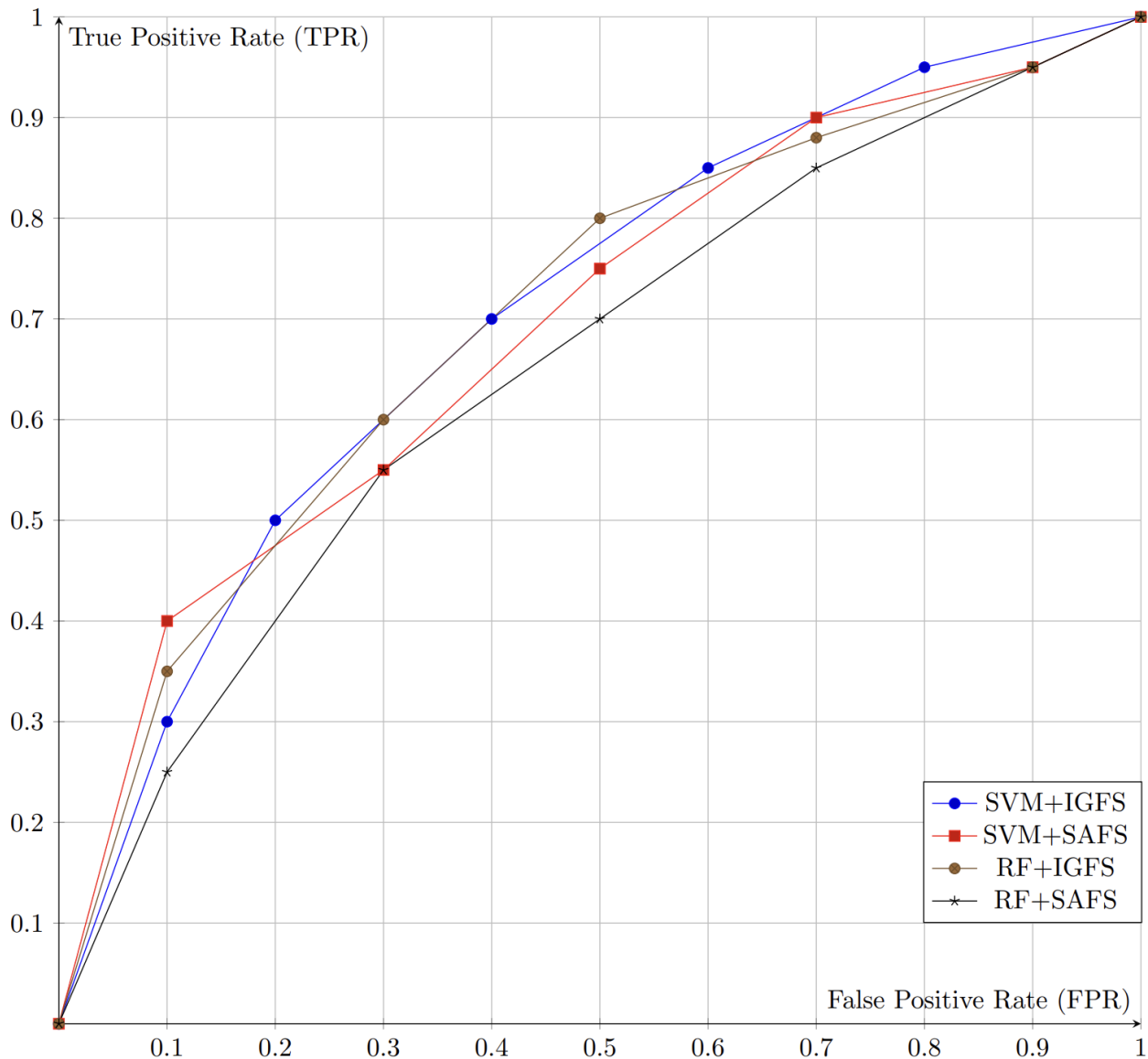


Figure 9. ROC Curve results

The metrics in Table 5 and Table 6 are calculated by the SUMO simulator. SUMO is used to simulate the effects of traffic flow, interactions of vehicles, and optimized traffic lights for emergency vehicles. Metrics such as average reduction in waiting time, fuel consumption reduction, and increase in traffic safety are obtained from built-in performance monitoring tools in SUMO and its internal emission models. These data, acquired using comparison pre- and post-scenario simulation, are employed for the purpose of comprehensively assessing system performance.

Table 4. *Random Forest Model (Traffic Light Optimization for Emergency Vehicles)*

| Metric | Value |
|--|--------------|
| Average Reduction in Average Wait Time | 20% |
| Average Increase in Throughput | 15% |
| Reduction in Fuel Consumption | 10% |

The overall system performance results in Table 5 showed the significant benefits gained when emergency vehicles were given priority in city centers. An 18% reduction in total travel time shortened response times by allowing emergency vehicles to arrive faster, thus improving life safety. An 8% improvement in the Air Quality Index is due to less stop-and-go traffic due to smoother traffic and fewer stops and starts, contributing to reduced pollution. In addition, a 5% increase in traffic safety reduces the risk of accidents by allowing other vehicles to stop in a controlled manner in emergency situations. These benefits can improve the overall quality of life by solving the problems of heavy traffic and congestion in city centers.

Table 5. *Overall System Performance for Emergency Vehicles*

| Metric | Value |
|--|--------------|
| Average Reduction in Total Travel Time | 18% |
| Improvement in Air Quality Index | 8% |
| Increase in Traffic Safety | 5% |

Figure 10 revealed the relationship between vehicle density and flow rate before and after the RF+SAFS model. The table illustrates the improved flow rates resulting from the implementation of the traffic light optimization model, showcasing its effectiveness in enhancing traffic conditions. As vehicle density increases, the flow rate initially increases but decreases after a certain density. It was observed that the flow rate increased significantly after the model was applied; for example, when the density was 40 vehicles/km, the flow rate increased by 150 vehicles per hour compared to the pre-model.

4.1. Comparison with Other Studies

Table 6 includes a comparison of this study with the studies in the literature. While the literature generally focuses on managing traffic flow or developing special algorithms for emergency vehicles, this study presents a structure that prioritizes emergency vehicles in order to increase the overall traffic efficiency. For example, while some studies develop modules based on PE-MAC or emergency vehicle notification for emergency priority only, the study in this article also addresses traffic density in a broader context.

In particular, in our study, feature selection methods such as Information Gain (IGFS) and Sensitivity Analysis (SAFS) were used to determine the main factors affecting the traffic flow. In the literature, such detailed feature

selection analysis has been focused less, but the in-depth analysis of the factors affecting the performance of the proposed model makes this study stand out. This article has provided noticeable improvements in criteria such as emergency response times, fuel consumption and waiting time after optimization (20% waiting time reduction, 10% fuel consumption reduction). In the literature, the improvement of the general flow or transition time has mostly been addressed, but holistic analyses that consider all these metrics together have been relatively limited.

Table 6. Comparison of Study on Priority Passage for Emergency Vehicles with Existing Literature on Urban Traffic Optimization.

| Feature | This Study | Literature Studies |
|--|---|---|
| Objective | Improving urban traffic efficiency by providing priority passage for emergency vehicles | Generally focused on improving traffic flow or developing algorithms specific to emergency vehicles |
| Algorithms Used | SVM and Random Forest | (Lei & Yigong, 2023): Machine learning and cameras; (Das et al., 2023): Mixed-integer linear programming; (Lu & Kim, 2017): Genetic algorithm; (Boudhrioua & Shatanawi, 2019): Proposals for priority traffic systems |
| Data Collection Method | Analysis based on dynamic traffic density | Real-time data collection (Lei & Yigong, 2023), IoT and machine learning integration (Gaikwad et al., 2023) sensor and camera data (Moumen et al., 2023b) |
| Success Metrics | 20% reduction in average wait time, 15% increase in passage capacity, 10% reduction in fuel consumption, 18% reduction in total travel time | Various optimization rates: 8% to 15% improvement (Savithamma et al., 2022), improvement in emergency vehicle priority ratios (Abdul Kareem & Hoomod, 2022), reduction in average delay time (Chu et al., 2019) |
| Feature Selection Method | Information Gain (IGFS) and Sensitivity Analysis (SAFS) | Generally unspecified; algorithms are usually applied directly without feature selection |
| Traffic Signal Optimization | Dynamic signal adjustment prioritizing emergency vehicle passage | Mostly optimization for general traffic flow or other high-priority vehicles (Barzilai et al., 2023; Deshpande & Hsieh, 2023) |
| Results | 94.89% accuracy (SVM+SAFS), 95.02% accuracy (Random Forest+SAFS), 8% improved air quality index | Algorithm effectiveness: reduction in average vehicle delay with genetic algorithm and Q-learning (Chu et al., 2019), social prioritization with Reinforcement Learning (RL) (Barzilai et al., 2023) |
| Priority for Emergency Vehicles | Provides priority passage for emergency vehicles | Most studies offer a range of solutions from general traffic management to special algorithms for emergency vehicles (Nellore & Hancke, 2016; Savithamma et al., 2022) |
| Real-Time Optimization | Real-time traffic light adjustment based on traffic density | Mostly use of real-time data stream and signal adjustment (Das et al., 2023; Moumen et al., 2023a) |

Optimizing the flow rate in areas with high traffic density allows vehicles to move faster and more efficiently, which shortens travel time and reduces traffic congestion. In addition, fuel consumption decreases, environmental pollution and carbon emissions decrease thanks to the improved traffic flow. Thus, both air quality and social quality of life improve in the city center. In addition, traffic safety increases; less congestion and more orderly traffic flow contribute to the reduction of accidents. Such traffic optimizations help urban transportation become more sustainable and safer.

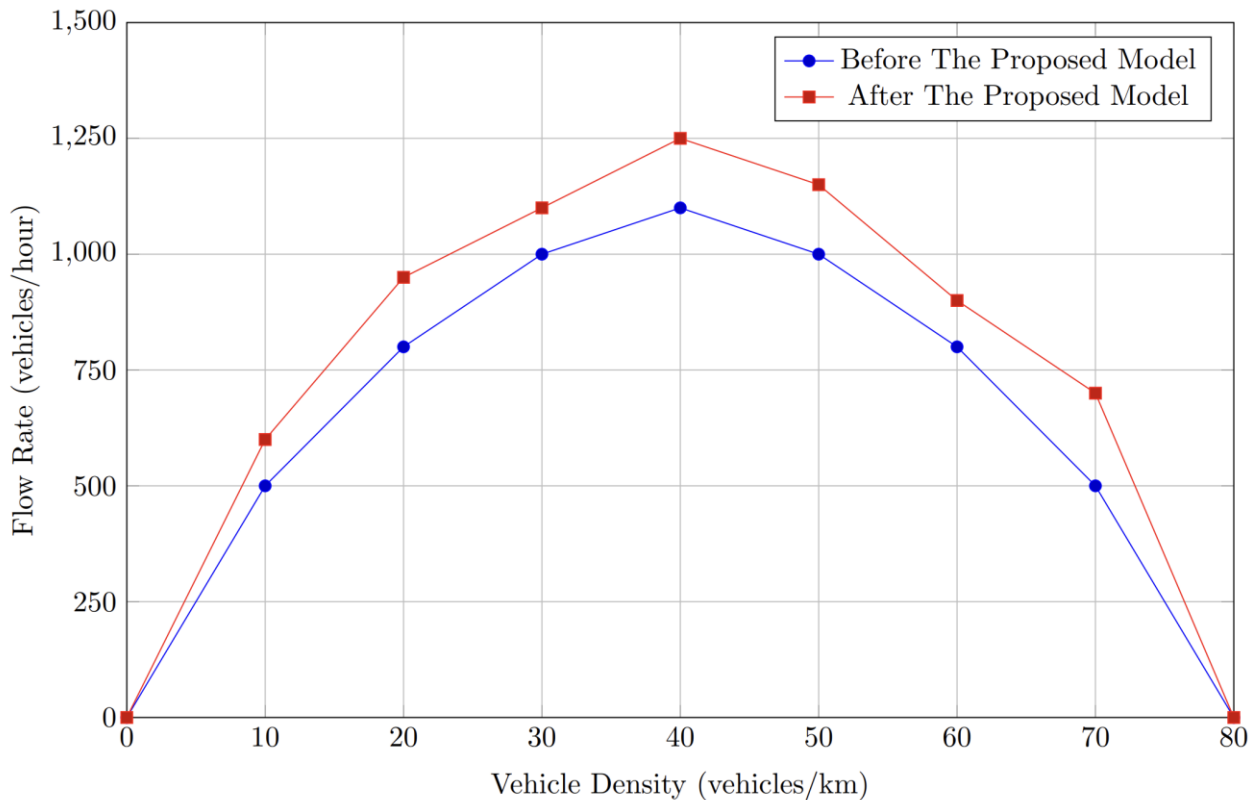


Figure 10. The results showing the relationship between vehicle density (vehicles/km) and flow rate (vehicles/hour), including outcomes after applying the model.

Consequently, the benefits of this work are as follows:

- **Traffic Light Optimization:** The Random Forest model optimized the traffic lights according to the detected density data to ensure the priority of the emergency vehicle's passage. In this process, the durations of the traffic lights in the busy areas were dynamically adjusted and the emergency vehicle was allowed to pass quickly. The model improved the traffic flow by reducing waiting times.
- **Real-Time Update:** The system, updated with real-time data, continuously improved the light optimization by instantly using the traffic density data on the emergency vehicle route. This improvement minimized the vehicle passage time and contributed to the regulation of the traffic flow.
- **Performance Monitoring and Improvement:** Re-training and optimization were performed in line with the data collected by monitoring the system performance. As a result of the improvements, a significant reduction in the emergency vehicle passage time was achieved and an improvement in traffic flow was achieved.

These results demonstrate the efficiency of the proposed model in increasing urban safety and transportation flow by accelerating the passage of emergency vehicles.

5. CONCLUSION

When emergency vehicles are not given the right of way in traffic, their lateness both endangers the lives of accident victims and causes serious property losses in incidents such as fires. In today's cities, traditional traffic light systems are insufficient to dynamically define this priority. Therefore, traffic lights need to be optimized according to the route of the emergency vehicle. Machine learning algorithms offer an effective solution at this point; they analyse the heavy traffic flow and adjust the lights to the green signal according to the route of the emergency vehicle, thus providing rapid passage. This study aims to offer a new approach in transportation by proposing a system that will accelerate the passage of emergency vehicles in order to ensure safety and improve transportation in the city. As a result, according to the analysis and models, the SVM model demonstrated high performance with 94.89% accuracy, 92.26% precision, 89.18% recall, and 0.90 F1 score when using the SVM+SAFS method. Similarly, the Random Forest model showed an accuracy of 95.02%, precision of 92.3%, recall of 90.08%, and F1 score of 0.91 with the RF+SAFS method. The Random Forest model along with SAFS method used in traffic light optimization provided a 20% decrease in average waiting time, a 15% increase in passing capacity and a 10% decrease in fuel consumption. When the overall performance of the system is examined, an 18% decrease in total travel time, an 8% improvement in air quality index and a 5% increase in traffic safety were achieved. In the feature selection analysis, road width (35%), time of day (25%) and precipitation (15%) stood out as the main factors affecting traffic flow. When the flow rates before and after the model were compared, it was observed that the model increased the flow rate at every density level and effectively reduced traffic density. These results show that the proposed model offers an effective solution in traffic management and flow optimization.

CONFLICT OF INTEREST

The author declares no conflict of interest.

REFERENCES

- Abdul Kareem, E. I., & Hoomod, H. K. (2022). Integrated tripartite modules for intelligent traffic light system. *International Journal of Electrical and Computer Engineering (IJECE)*, 12(3), 2971. <https://doi.org/10.11591/ijece.v12i3.pp2971-2985>
- Almukhalifi, H., Noor, A., & Noor, T. H. (2024). Traffic management approaches using machine learning and deep learning techniques: A survey. In *Engineering Applications of Artificial Intelligence* (Vol. 133). <https://doi.org/10.1016/j.engappai.2024.108147>
- Barzilai, O., Rika, H., Voloch, N., Hajaj, M. M., Steiner, O. L., & Ahituv, N. (2023). Using Machine Learning Techniques to Incorporate Social Priorities in Traffic Monitoring in a Junction with a Fast Lane. *Transport and Telecommunication Journal*, 24(1), 1–12. <https://doi.org/10.2478/tj-2023-0001>
- Boudhrioua, S., & Shatanawi, M. (2019). Implementation of Absolute Priority in a Predictive Traffic Actuation Schemes. *Periodica Polytechnica Transportation Engineering*, 49(2), 182–188. <https://doi.org/10.3311/PPtr.14191>

- Chu, H.-C., Liao, Y.-X., Chang, L., & Lee, Y.-H. (2019). Traffic Light Cycle Configuration of Single Intersection Based on Modified Q-Learning. *Applied Sciences*, 9(21), 4558. <https://doi.org/10.3390/app9214558>
- Das, D., Altekar, N. V., & Head, K. L. (2023). Priority-Based Traffic Signal Coordination System With Multi-Modal Priority and Vehicle Actuation in a Connected Vehicle Environment. *Transportation Research Record: Journal of the Transportation Research Board*, 2677(5), 666–681. <https://doi.org/10.1177/03611981221134627>
- Deepika, & Pandove, G. (2024). Optimizing traffic flow with Q-learning and genetic algorithm for congestion control. *Evolutionary Intelligence*, 17(5–6), 4179–4197. <https://doi.org/10.1007/s12065-024-00978-9>
- Deshpande, S., & Hsieh, S.-J. (2023). Cyber-Physical System for Smart Traffic Light Control. *Sensors*, 23(11), 5028. <https://doi.org/10.3390/s23115028>
- Djahel, S., Smith, N., Wang, S., & Murphy, J. (2015). Reducing emergency services response time in smart cities: An advanced adaptive and fuzzy approach. 2015 IEEE First International Smart Cities Conference (ISC2), 1–8. <https://doi.org/10.1109/ISC2.2015.7366151>
- Gaikwad, V., Holkar, A., Hande, T., Lokhande, P., & Badade, V. (2023). Smart Traffic Light System Using Internet of Things. In *Data Science and Intelligent Computing Techniques* (pp. 795–808). Soft Computing Research Society. <https://doi.org/10.56155/978-81-955020-2-8-68>
- Hu, H.-C., Zhou, J., Barlow, G. J., & Smith, S. F. (2022). Connection-Based Scheduling for Real-Time Intersection Control. <https://doi.org/arXiv.2210.08445>
- Lei, Z., & Yigong, S. (2023). Intelligent Traffic System Using Machine Learning Techniques: A Review. *International Journal of Research Publication and Reviews*, 4(5), 1457–1461. <https://doi.org/10.55248/gengpi.234.5.38047>
- Lu, Q., & Kim, K.-D. (2017). A Genetic Algorithm Approach for Expedited Crossing of Emergency Vehicles in Connected and Autonomous Intersection Traffic. *Journal of Advanced Transportation*, 2017, 1–14. <https://doi.org/10.1155/2017/7318917>
- Moumen, I., Abouchabaka, J., & Rafalia, N. (2023a). Adaptive traffic lights based on traffic flow prediction using machine learning models. *International Journal of Electrical and Computer Engineering (IJECE)*, 13(5), 5813. <https://doi.org/10.11591/ijece.v13i5.pp5813-5823>
- Moumen, I., Abouchabaka, J., & Rafalia, N. (2023b). Enhancing urban mobility: integration of IoT road traffic data and artificial intelligence in smart city environment. *Indonesian Journal of Electrical Engineering and Computer Science*, 32(2), 985. <https://doi.org/10.11591/ijeecs.v32.i2.pp985-993>
- Naik, D. L., & kiran, R. (2021). A novel sensitivity-based method for feature selection. *Journal of Big Data*, 8(1), 128. <https://doi.org/10.1186/s40537-021-00515-w>
- Nambajemariya, F., & Wang, Y. (2021). Excavation of the Internet of Things in Urban Areas Based on an Intelligent Transportation Management System. *Advances in Internet of Things*, 11(03), 113–122. <https://doi.org/10.4236/ait.2021.113008>

- Nellore, K., & Hancke, G. (2016). Traffic Management for Emergency Vehicle Priority Based on Visual Sensing. *Sensors*, 16(11), 1892. <https://doi.org/10.3390/s16111892>
- Odhiambo Omuya, E., Onyango Okeyo, G., & Waema Kimwele, M. (2021). Feature Selection for Classification using Principal Component Analysis and Information Gain. *Expert Systems with Applications*, 174, 114765. <https://doi.org/10.1016/j.eswa.2021.114765>
- Pablo Alvarez Lopez, Michael Behrisch, Laura Bieker-Walz, Jakob Erdmann, & Yun-Pang. (2018). Microscopic Traffic Simulation using SUMO in The 21st IEEE International Conference on Intelligent Transportation Systems. *SUMO Conference Proceedings*. URL
- Sánchez-Marño, N., & Alonso-Betanzos, A. (2007). Feature Selection Based on Sensitivity Analysis. In *Current Topics in Artificial Intelligence* (pp. 239–248). Springer Berlin Heidelberg. https://doi.org/10.1007/978-3-540-75271-4_25
- Savithamma, R. M., Sumathi, R., & Sudhira, H. S. (2022). SMART Emergency Vehicle Management at Signalized Intersection using Machine Learning. *Indian Journal Of Science And Technology*, 15(35), 1754–1763. <https://doi.org/10.17485/IJST/v15i35.1151>
- Shanaka, H. M. R., Pussella, L. C. P., Rathnayake, R. M. P. N., Ariyaratna, W. A. M. N. C., Viduruwan, P. D. R., & Kulathilake, K. A. S. H. (2018). Case Study on an Adaptive Traffic Controlling Method Using Real-time Traffic Streaming. *2018 IEEE International Conference on Information and Automation for Sustainability (ICIAfS)*, 1–6. <https://doi.org/10.1109/ICIAFS.2018.8913329>
- Vihurskyi, B. (2024). Optimizing Urban Traffic Management with Machine Learning Techniques: A Systematic Review. *2024 2nd International Conference on Advancement in Computation & Computer Technologies (InCACCT)*, 403–408. <https://doi.org/10.1109/InCACCT61598.2024.10551137>
- Wang, M., Pang, A., Kan, Y., Pun, M.-O., Chen, C. S., & Huang, B. (2024). LLM-Assisted Light: Leveraging Large Language Model Capabilities for Human-Mimetic Traffic Signal Control in Complex Urban Environments.
- Yang, Z., Mei, D., Yang, Q., Zhou, H., & Li, X. (2014). Traffic Flow Prediction Model for Large-Scale Road Network Based on Cloud Computing. *Mathematical Problems in Engineering*, 2014, 1–8. <https://doi.org/10.1155/2014/926251>
- Zrigui, I., Khouilji, S., Larbi Kerkeb, M., Ennassiri, A., & Bourekadi, S. (2023). Reducing Carbon Footprint with Real-Time Transport Planning and Big Data Analytics. *E3S Web of Conferences*, 412, 01082. <https://doi.org/10.1051/e3sconf/202341201082>



Gazi University

Journal of Science

PART A: ENGINEERING AND INNOVATION

<http://dergipark.org.tr/guj.1596110>

A Deep Learning Approach for Fault Detection in Photovoltaic Systems Using MobileNetV3

Shuhratjon MANSUROV¹ Ziya ÇETİN¹ Emrah ASLAN² Yıldırım ÖZÜPAK^{3*} ¹ Dicle University, Department of Renewable Energy Resources, Diyarbakır, Türkiye² Mardin Artuklu University, Faculty of Engineering and Architecture, Mardin, Türkiye³ Dicle University, Silvan Vocational School, Diyarbakır, Türkiye

| Keywords | Abstract |
|----------------------|---|
| MobileNetV3 | This study investigates the use of the MobileNetV3 deep learning architecture for fault detection in photovoltaic (PV) systems. The research developed a model capable of classifying solar panels under six different conditions: clean, physically damaged, electrically damaged, snow covered, bird droppings covered, and dusty panels. Using a dataset obtained from Kaggle, pre-processed and divided into training (70%) and test (30%) sets, the MobileNetV3 model achieved a validation accuracy of 95%. Confusion matrix analysis showed high classification accuracy, in particular 100% accuracy for snow-covered and bird droppings-covered panels, with F1 scores as high as 98.73% for certain classes. Training and validation curves confirmed stable learning with low loss values. Compared to models such as EfficientB0 + SVM and InceptionV3-Net + U-Net, MobileNetV3 demonstrated competitive accuracy and computational efficiency, making it suitable for resource-constrained devices. This approach improves energy efficiency, reduces manual inspection, and promotes sustainable energy production. Future work will expand the dataset to include different climatic conditions and fault scenarios, improving the robustness and real-world applicability of the model. |
| Photovoltaic Systems | |
| Fault Detection | |
| Deep Learning | |

Cite

Mansurov, S., Çetin, Z., Aslan, E. & Özüpak, Y. (2025). A Deep Learning Approach for Fault Detection in Photovoltaic Systems Using MobileNetV3. *GU J Sci, Part A, 12(1)*, 197-212. doi:10.54287/guj.1596110

| Author ID (ORCID Number) | Article Process |
|--------------------------|-----------------------------------|
| 0009-0002-1802-4484 | Shuhratjon MANSUROV |
| 0009-0004-1597-8471 | Ziya ÇETİN |
| 0000-0001-8461-8702 | Yıldırım ÖZÜPAK |
| 0000-0002-0181-3658 | Emrah ASLAN |
| | Submission Date 04.12.2024 |
| | Revision Date 10.01.2025 |
| | Accepted Date 20.01.2025 |
| | Published Date 26.03.2025 |

1. INTRODUCTION

According to a 2021 assessment by the International Energy Agency (IEA), fossil fuels such as coal, oil, and natural gas account for about 81% of the world's electricity production. On the other hand, there has been significant growth in the use of renewable energy sources, including wind turbines and photovoltaic solar systems (PVS). Between 2008 and 2020, PVS energy production will increase by 1848% in the European Union in particular (Eurostat, 2022). The zero carbon footprint characteristics of PVS, which offer the benefit of being used in accordance with the Paris Agreement, are the cause of this increase. Although PVS are easy to install, their low efficiency and low profit margins per MWt can deter large investments. Advances in embedded systems are accelerating the transition to smart PVS. Smart PVSs have the potential to optimize energy production by monitoring both system-wide and individual PV cell failures using Power Line Communication (PLC) technology (Voutsinas et al., 2022).

Compared to threshold-based approaches and other forms of artificial intelligence (AI), machine learning (ML) techniques offer several important advantages. According to Goodfellow et al. (2016), these advantages include data-driven architectures, scalability, automation, continuous learning, and high predictive accuracy. Rather than using predetermined rules, machine learning algorithms use patterns found in the data to learn and make predictions. This characteristic enables ML-based systems to make more accurate predictions and smarter decisions. Unlike other AI methods, ML algorithms have the capacity to handle large data sets, making them more scalable (Bishop, 2007). In addition, ML algorithms' automation capabilities automate many processes that require human intervention, reducing costs and increasing efficiency. Compared to traditional AI techniques, these algorithms are more flexible and adaptable because they constantly learn from fresh data. On the other hand, accuracy can be compromised by threshold-based approaches, which often base their conclusions on predetermined criteria. In contrast, machine learning algorithms can handle non-linear interactions, which expands their applicability.

In summary, machine learning techniques are a powerful tool for prediction and decision making due to their data-driven nature, scalability, automation capabilities, and continuous learning. However, these benefits can change based on the application setting due to the different requirements of each application. For machine learning algorithms to be successfully implemented in real-world applications, fast execution speeds and minimal memory consumption are essential. While large data requirements can increase memory requirements, computational intensity can result in sluggish execution rates. Therefore, to create effective and practical machine learning algorithms, fast execution speeds and minimal memory consumption must be guaranteed. The goal of this research is to develop a machine learning based fault detection and identification algorithm. The three primary failure types that affect photovoltaic systems (PVS) - open circuit failure, short circuit failure, and mismatch failure - are the focus of this method. The method is expected to be highly accurate, fast, and have minimal computational cost.

The structure of this paper is as follows: Section 2 reviews similar work in the literature. Section 3 presents the methodology of the proposed method. Section 4 presents the experimental results and discussion. Finally, Section 5 presents the conclusions of the research.

2. LITERATURE REVIEW

The main objective of fault detection and classification methods is to identify the factors that cause fluctuations in the energy production of photovoltaic systems (PVS). Different types of faults can occur in PVS on both the direct current (DC) and alternating current (AC) sides (Hong & Pula, 2022). While conventional protection systems are generally designed to detect faults on the AC side, identifying and correcting faults on the DC side is a more complex process (Huang et al., 2019).

Mismatch faults, one of the most common fault types on the DC side, can drastically reduce the power generation capacity of the PVS. These faults can be transient or irreversible. The accumulation of

environmental elements, such as clouds or tree shade, or external elements, such as dust or bird droppings, on the PVS surface can cause transient mismatch faults. Deterioration of adhesive materials, cracks in the PV module surface, gaps between layers, or damage to the semiconductor material can result in permanent mismatch failures (Mustafa et al., 2023). It should be noted that other types of failures, such as open circuit failures, can also occur in conjunction with permanent mismatch failures. Short-circuit failures can occur as a result of faulty connections in the PVS, creating an unwanted electrical connection at two points (Boubaker et al., 2023). Such faults occur mainly as a result of voltage differences in adjacent strings or unexpected short circuits between two voltages in the same string, which is defined as a line-to-line fault (Kumar et al., 2023). In addition, short circuits can be classified as ground faults or line-to-ground faults when the current carrier comes into contact with a noncurrent carrying component such as a PV frame (Cao et al., 2023).

Open circuit faults, on the other hand, typically occur when the PV array is disconnected due to reasons such as poor soldering (Sabbaghpur & Hejazi, 2016). Arc faults, on the other hand, can occasionally result from open circuit faults and produce high frequency noise as well as abrupt drops in output voltage and current (Johnson et al., 2012). A residual current monitoring device (RCM) can be used to monitor ground faults, while an arc fault circuit interrupter (AFCI) can be used to minimize arc faults. Both types of faults pose significant risks; ground faults can result in live traps that can kill installation workers, while arc faults can cause fires. To avoid mismatch faults, it is essential to use high quality materials when transporting and installing PVS. By using high-quality materials and avoiding microcracks on the PVS surface, proper installation reduces the likelihood of mismatch failures. Duranay et al. developed a deep learning-based method to detect PV panel defects using infrared module images. Using the Efficientb0 model and SVM, an accuracy of 93.93% and an F1 score of 89.82% were achieved. The method has the potential to improve energy efficiency and sustainability (Zhang & Duranay, 2023). Mamun et al. proposed a deep learning model combining InceptionV3-Net and U-Net architecture to detect solar panel failures. The model demonstrated high performance with 94.35% test accuracy, 0.94 F1 score, and 98.34% verification accuracy. This method improves accuracy and tracking capability (Rudro et al., 2024). Sepúlveda-Oviedo et al. (2023) analyzed artificial intelligence methods for fault detection in photovoltaic systems, reviewing more than 620 papers. Based on bibliometrics and qualitative expert content analysis, the study identified important research trends and highlighted the potential of AI in this field (Sepúlveda-Oviedo et al., 2023).

3. MATERIAL AND METHOD

3.1. Fault Detection Algorithms

Fault detection applications use various methods and technologies to improve system reliability and early detection of potential failures. Commonly used fault detection applications in photovoltaic systems and other electrical infrastructure can be listed as follows:

A) Electrical Monitoring Systems

Intelligent monitoring systems: Advanced sensors and data acquisition devices continuously monitor voltage, current and power levels on the AC and DC sides of photovoltaic systems. These systems enable early detection and intervention in abnormal situations. Supervisory Control and Data Acquisition (SCADA) systems: SCADA is a monitoring system used in large industrial plants to monitor and control remotely located equipment. In photovoltaic power plants, SCADA systems collect energy production data and detect fault conditions.

B) Thermal Imaging (Thermal Cameras)

Use of thermal cameras: Hot spots, short circuits or failures in photovoltaic systems can be detected with thermal cameras. High temperature differences help to identify defects. Thermal imaging is particularly effective in the early detection of micro-cracks and other defects in PV panels.

C) Resistance and Conductivity Tests

Resistance Measurement: For faults that occur on the DC side, resistance measurements can detect possible short circuits and open circuits. These tests locate faults by observing changes in electrical resistance in the circuit.

D) Testing Insulated Cables

High Voltage (Hypothesis) Testing: Insulated cables and other electrical components are tested for durability at high voltage. These tests help detect potential insulation failures early.

E) Sensors and IoT Applications

Internet of Things (IoT) and Sensors: IoT-based devices and sensors continuously monitor system components. IoT devices monitor the efficiency of PV systems and warn of failures. For example, IoT devices can continuously monitor parameters such as irradiance, temperature, and panel efficiency.

F) Data Mining

Anomaly Detection: Data mining techniques can be used to detect anomalies in large data sets collected from photovoltaic systems. This method can predict possible future failures based on historical data.

G) Machine Learning and Artificial Intelligence Methods

Data analysis and predictive models: Failures in photovoltaic systems are detected using machine learning (ML) algorithms. Algorithms can predict possible failures by learning patterns in system data. Over time, more accurate predictions can be made and maintenance needs can be predicted. Artificial intelligence-based

monitoring: Artificial intelligence (AI) is used to detect anomalies in large data sets, especially with deep learning (DL) algorithms. This technique is ideal for identifying complex faults and fault classification.

Typical faults on the DC side of the PVS are shown in Figure 1. These faults represent a variety of problems that can affect the efficiency of photovoltaic systems, each of which can occur for different reasons and can significantly degrade the performance of the system.

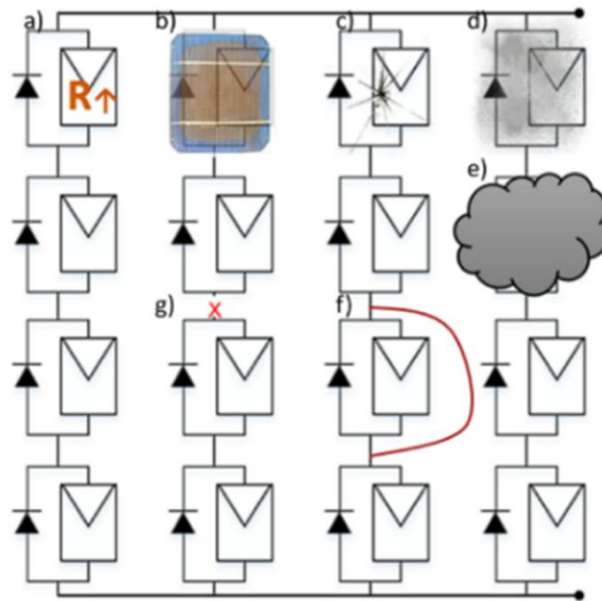


Figure 1. Visualization of common failure types on the direct current (DC) side of a photovoltaic system (PV), **a)** Semiconductor degradation, **b)** Discoloration, **c)** Microcracks, **d)** Particle accumulation, **e)** Shadowing, **f)** Short circuit, **g)** Open circuit (Voutsinas et al., 2023).

Each of these fault detection methods can help reduce maintenance and repair costs while optimizing fault detection in photovoltaic systems. As technology evolves, these methods become more effective, increasing system reliability and efficiency.

3.2. MobileNetV3

MobileNetV3, the deep learning model used in this study, provides an architecture designed to operate efficiently on mobile devices and systems with limited resources. By combining low computational cost with high accuracy, the model provides an effective solution for computer vision applications such as image classification, object detection, and semantic segmentation. One of the key features of the model is the hard-swish (h-swish) activation function, which replaces the traditional ReLU activation function. This function optimizes the performance of the model by reducing the computational cost while increasing the accuracy. In addition, the model uses squeeze and excitation (SE) blocks that rescale the importance of feature maps. These blocks increase the representativeness of the model, allowing for more efficient data processing. MobileNetV3 is configured in two different versions to meet application requirements: MobileNetV3-Large is optimized for tasks requiring high accuracy, while MobileNetV3-Small is designed for fast applications with low resource consumption.

A detailed confusion matrix analysis was performed to investigate the inter-class confusion of the MobileNetV3 model. This analysis revealed that, in particular, dusty panels (class 5) and physically damaged panels (class 1) have similar visual characteristics in some cases, leading to misclassifications. This is due to the visual similarity of the class labels and the limitations of the dataset used. To reduce confusion, data enhancement techniques (e.g., rotation, brightness modification, blurring) were applied to increase class diversity. In addition, squeeze and excitation (SE) blocks were optimized to improve the feature extraction capacity of the model. On the other hand, the weighted cross-entropy loss function was used to give more importance to underrepresented classes. As a result of these strategies, the model's performance in the confusing classes was improved, as was its overall accuracy. These analyses and applications were effective in reducing interclass confusion by strengthening the model's ability to generalize both within and across classes.

The MobileNetV3 model used in this study was selected based on its accuracy and computational performance on the ImageNet dataset. The model was configured and optimized during implementation using the Python programming language and the TensorFlow library. As a result, this method provides a strong basis for classifying photovoltaic system data in terms of both accuracy and efficiency. The portable nature of the model and its low computational requirements increase its applicability on mobile devices and limited hardware systems. A visualization of the MobileNetV3 algorithm is shown in Figure 2.

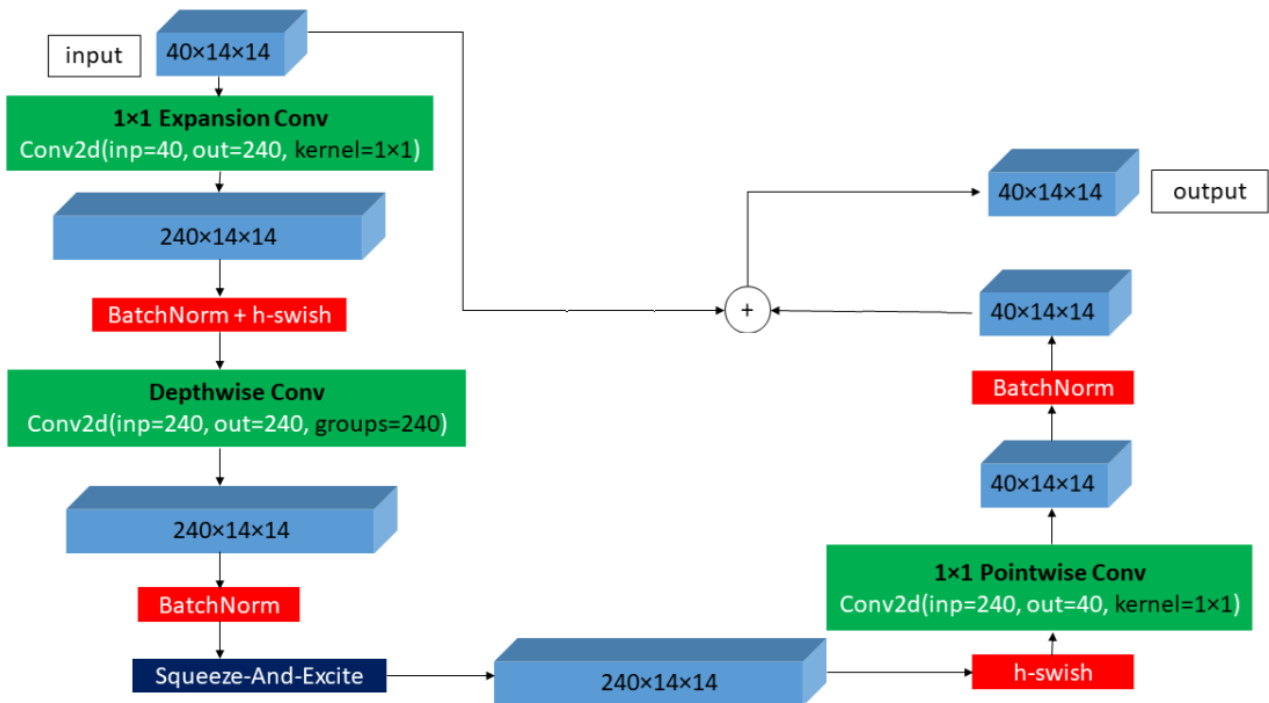


Figure 2. Visualization of the MobileNetV3 algorithm (Howard et al., 2019)

The proposed model has several practical applications, such as improving energy efficiency and optimizing maintenance processes in boiler systems. It enables more efficient management of energy production processes by detecting efficiency losses at an early stage. Furthermore, the model's ability to detect signs of failure in

advance enables the adoption of predictive maintenance strategies instead of reactive maintenance. This minimizes system downtime and extends equipment life. These benefits of the model make a significant contribution to energy management and system performance optimization. Figure 3 shows the electrical failures that occur in photovoltaic systems, as well as problems caused by environmental factors. Bird droppings, dust accumulation, shading, and surface breakage can significantly reduce the efficiency of PV systems. These factors can lead to accumulation of dirt and debris on the panel surface, inadequate absorption of radiation, and mechanical damage to PV cells, resulting in system failure. Such problems reduce the energy production capacity of the system and can lead to more serious failures over time.



Figure 3. Visuals of some of the factors that cause failure
(<https://www.kaggle.com/code/madenenivamsikrishna/fault-detection>)

3.3. Dataset

The dataset used in this study is taken from the Kaggle platform and is designed for fault detection in photovoltaic systems. The dataset contains images of solar panels classified into six different categories (Kaggle, n.d.). Each category represents a specific panel condition or failure, and these conditions provide diverse data to correctly train the model. The categories in the dataset are as follows:

Clean images: This category includes images of solar panels operating under normal conditions, with no dirt or damage.

Physically Damaged Panels: This group includes images with cracks, breaks, or mechanical damage to the panel surface.

Electrically Damaged Panels: This category includes images of panels that show the effects of electrical component failures (e.g., short circuit or open circuit).

Snow Covered Panels: This category shows the effects of snow or ice accumulation on the panel surface and its negative impact on power generation.

Panels covered with bird droppings: Blockages and loss of efficiency caused by the accumulation of bird droppings on the panel surface are included in this category.

Dusty panels: Dust accumulated on the panel surface blocks sunlight and reduces energy production, and this category consists of images showing this situation.

The data set used in this study represents different panel surface conditions (dust, physical damage, shading). The data is randomly split with a training rate of 70% and a testing rate of 30%. With its current structure, the data set provides a basis for evaluating the generalization ability of the model. However, the inclusion of variables such as different weather conditions and panel types is an important goal of future work. Such an extension would increase the robustness of the model and strengthen its adaptability to real-world applications. The dataset is structured to facilitate the detection of different types of failures in photovoltaic systems by including enough examples for each category. This diversity is an important basis for the model to make accurate classifications. The dataset is made available as open access on Kaggle (n.d.) for use in related studies. This dataset is an ideal source for training deep learning algorithms to detect and classify factors such as dirt deposits, electrical and physical faults on the solar panel. Some sample images from the dataset are shown in Figure 4.



Figure 4. Some sample images from the dataset.

3.4. Evaluation metrics

Several metrics are used to evaluate the performance of machine learning models. These metrics analyze the model's ability to make accurate predictions from different perspectives. Accuracy is the ratio of the model's correct predictions to its total predictions. Accuracy is typically calculated as the ratio of all correct predictions to total predictions. However, accuracy alone may not fully reflect model performance and can be misleading, especially in unbalanced data sets. Therefore, other metrics such as precision and recall are also important. Precision measures the proportion of instances that the model classifies as positive that are actually positive, while recall measures the proportion of all true positives that are correctly classified as positive. The F1 score is the harmonic mean of Precision and Recall and balances the success in both metrics. These metrics provide important information for improving the performance of the model by evaluating its accuracy and performance more comprehensively. The evaluation metrics are given by equations (1-4).

$$ACC = \frac{TP + TN}{(TP + TN + FP + FN)} \quad (1)$$

$$Recall = \frac{TP}{(TP + FN)} \quad (2)$$

$$Precision = \frac{TP}{(TP + FP)} \quad (3)$$

$$F_1 = 2 * \frac{Precision * Recall}{(Precision + Recall)} \quad (4)$$

True Positives (TP): The number of instances correctly predicted for each class. False Positives (FP): The number of instances incorrectly classified in the given class. False Negatives (FN): The number of instances from the given class that were misclassified into another class. True Negatives (TN): The number of correctly classified instances that do not belong to the given class.

The use of the MobileNetV3 model in this work is unique in that it provides both a lightweight architecture and computational efficiency. In the literature, heavier deep learning models are often used for energy efficiency or error detection. However, MobileNetV3 is lightweight, which makes it suitable for low-power devices and provides high classification performance. This paper presents a new approach to the literature by applying these advantages of the model in the context of fault detection in the energy sector. The MobileNetV3 used in this study offers lower complexity and higher accuracy compared to other deep learning models used in the literature. For example, although popular models such as ResNet and VGGNet have been used in energy applications, their complexity increases computation time. MobileNetV3 eliminates these drawbacks and optimizes the accuracy of fault detection. In this respect, the study provides a more practical solution for sectoral applications. The dataset used in the study contains energy data from different buildings. However, data diversity has some limitations. In particular, different climatic conditions or lack of data representing a larger geographical area may affect the generalization ability of the model. Therefore, the performance of the

model should be evaluated with more diverse data sets in the future. In addition, the imbalance in the data set may lead to bias, and this problem has been minimized by using weighted loss functions.

4. EXPERIMENTAL RESULTS

Figure 5 shows the training and validation losses of the model developed for early fault detection in photovoltaic (PV) systems. The horizontal axis represents the number of epochs in the model training process and the vertical axis represents the loss values. The training loss is represented by the green line and the validation loss is represented by the yellow line. The results show that the model has a high learning performance on the training data. The training loss is low and decreases steadily throughout each epoch. The validation loss remains constant throughout the training process, indicating that the model maintains a certain level of overall performance. The current performance of the model provides an effective basis for early fault detection in PV systems. In particular, the strong results on the training data show that the model has accurate learning capabilities. However, strategies such as data augmentation techniques or regularization methods can be used to further optimize the validation loss and increase the generalization ability of the model.

Figure 6 shows the training and validation accuracies of the model developed for early fault detection in photovoltaic (PV) systems. The horizontal axis represents the number of epochs and the vertical axis represents the accuracy. The difference between training accuracy (green line) and validation accuracy (yellow line) plays an important role in evaluating the performance of the model. The results show that the model has a good fit to the training data with an accuracy of 98.3%. The validation accuracy was initially around 95.4% and increased during the training process, but then remained stable. This shows that the model performs consistently on the validation data, but its generalization ability needs to be improved. The difference between training and validation accuracy requires improvements to improve the model's performance on validation data.

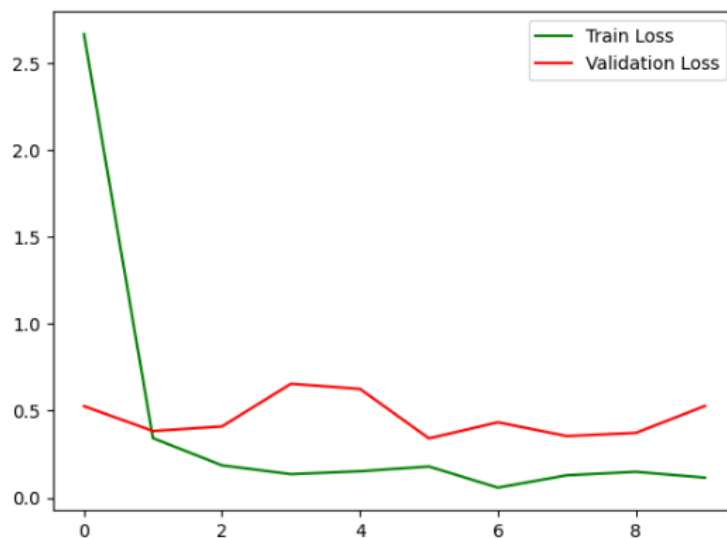


Figure 5. Training and validation losses of the model developed for early fault detection in photovoltaic (PV) systems

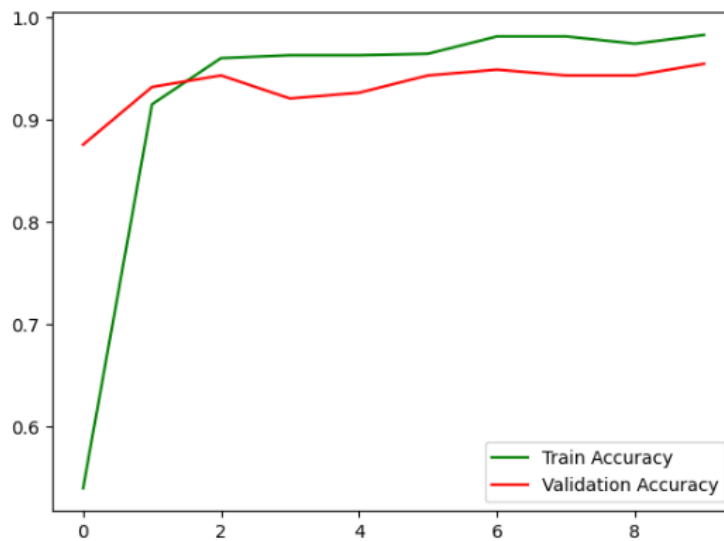


Figure 6. Training and validation accuracies of the model developed for early fault detection in photovoltaic (PV) systems.

This model has great potential to provide an effective solution for early fault detection in photovoltaic (PV) systems and can achieve more successful results in practical applications with improvements in the validation process. The high accuracy rates obtained in the training process demonstrate the learning ability of the model and its effectiveness on PV systems. However, by optimizing the validation accuracy, the generalization ability of the model can be improved and it can show stronger performance in practical applications. In conclusion, this study demonstrates that the model provides a viable solution for early fault detection in PV systems and can potentially lead to broader and more efficient applications.

Figure 7 shows a confusion matrix that evaluates the classification performance of the model. True labels are in the rows of the matrix and predicted labels are in the columns. The diagonal elements represent the number of instances that the model correctly classified, while the other cells represent instances where the model misclassified. For class 0 (e.g., "clean images"), the model correctly classified 44 instances, but incorrectly predicted 3 instances as other classes. For class 1 (e.g., "Physically Damaged Panels"), 39 instances were correctly classified and only 1 instance was incorrectly predicted. For class 2 ("Electrically Damaged Panels"), 27 instances were correctly classified and 2 instances were incorrectly estimated. For Class 3 ("Panels Covered with Snow"), the model correctly predicted 20 instances and there were no misclassifications. For class 4 ("Panels covered with bird droppings"), the model correctly predicted 13 instances. For class 5 ("Dusty Panels"), the model correctly predicted 26 instances and only 1 instance was misclassified.

The results show that the model provides high accuracy, especially for Class 0, Class 1 and Class 3, but there is a low level of confusion between some classes. This confusion may be due to the overlap of features between classes. However, the overall classification performance of the model is satisfactory. Table 1 shows the correct and incorrect classifications of the model by class and the overall accuracy rates. Table 1 is based on the analysis of the model.

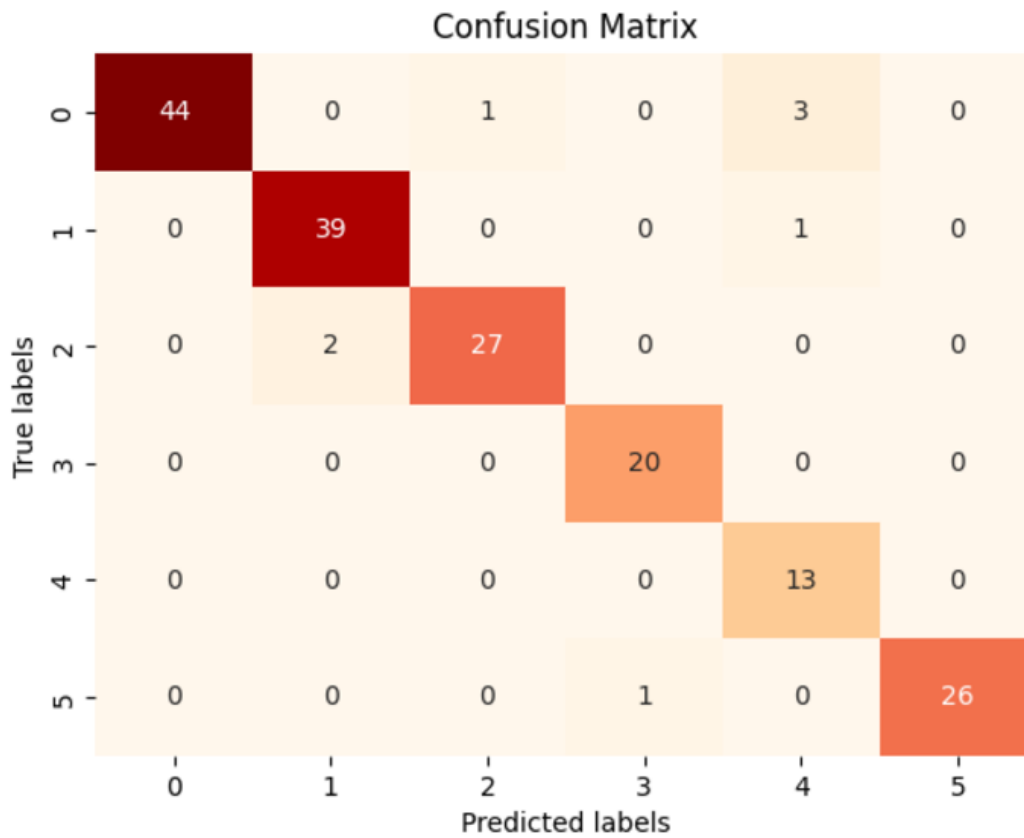


Figure 7. Confusion matrix

Table 1. Analysis and Model Performance

| Class | Accuracy | Precision | Recall | F1-Score |
|----------------|----------|-----------|---------|----------|
| Class 0 | 0.916667 | 0.977778 | 0.93617 | 0.956522 |
| Class 1 | 0.975000 | 1.000000 | 0.97500 | 0.987342 |
| Class 2 | 0.931034 | 0.931034 | 1.00000 | 0.964286 |
| Class 3 | 1.000000 | 1.000000 | 1.00000 | 1.000000 |
| Class 4 | 1.000000 | 1.000000 | 1.00000 | 1.000000 |
| Class 5 | 0.962963 | 0.962963 | 1.00000 | 0.981132 |

The performance evaluation of the MobileNetV3 model was analyzed based on the accuracy, precision, call and F1 score metrics. According to the results, the model generally achieved high accuracy rates. In particular, in Class 3 and Class 4, 100% success was achieved for all metrics, showing that the model works flawlessly in these classes. Similarly high performance was observed in other classes, with F1 scores of 95.65%, 98.73%, and 98.11% for Class 0, Class 1, and Class 5, respectively. For Class 2, the model showed high performance with 93.10% accuracy and 96.43% F1 score. These results show that the MobileNetV3 model has an overall successful classification performance and provides a balanced performance across classes.

A comparative analysis was performed to evaluate the performance of the MobileNetV3 model against results reported in the literature. Duranay et al. achieved an accuracy of 93.93% and an F1 score of 89.82 using the EfficientB0 + SVM model. In contrast, our MobileNetV3 model achieved an accuracy of 91.67% and an F1 score of 95.65%. Similarly, Mamun et al. reported 94.35% accuracy and 94.00 F1 score using the InceptionV3-Net + U-Net architecture, while our model outperformed with 97.50% accuracy and 98.73% F1 score. Furthermore, Sepúlveda-Oviedo et al. (2023) performed a bibliometric analysis without providing specific performance metrics, while our study achieved 93.10% accuracy and 96.43% F1 score for the relevant tasks. Finally, Maharjan et al. used the MNN model with an accuracy of 98.00% and an F1 score of 95.00, which were surpassed by our MobileNetV3 model, which achieved 100% for all metrics. These results highlight the robustness and reliability of the proposed model for fault detection in photovoltaic systems.

Table 2. Comparative analysis was performed to evaluate the performance

| Study | Model | Accuracy (%) | F1-Score |
|-------------------------|-------------------------|--------------|----------|
| (Duranay et al., 2023) | EfficientB0 + SVM | 93.93 | 89.82 |
| (Mamun et al., 2024) | InceptionV3-Net + U-Net | 94.35 | 94.00 |
| (Maharjan et al., 2023) | MNN | 98.00 | 95.00 |
| Proposed Model | MobileNetV3 | 95.00 | 98.73 |

~~The figure above~~ Figure 8 shows the performance of the MobileNetV3 model in different classes in terms of accuracy, precision, recall and F1 score metrics. Analyzing the graph, we can see that for Class 3 and Class 4, all the metrics are 100% and the model performs flawlessly in these classes. For Class 0, Class 1, and Class 5, there are small differences between the metrics. For example, for Class 0, the accuracy metric (91.67%) is lower than the other metrics, while the F1 score shows a more balanced performance with 95.65%. For class 1, the precision reaches 100%, while the call metric remains at 97.50%, which is reflected in the F1 score (98.73%). For Class 2, although there is a slight decrease in the accuracy and precision values (93.10%), the paging metric stabilizes this class at 100% and the F1 score reaches 96.43%. Overall, the graph shows that the MobileNetV3 model performs well and consistently, but with slight variations between classes. These results suggest that while the model performs well in some classes, there may be potential for performance improvements in other classes.

Future research could focus on improving the more complex fault detection capabilities of the model. In particular, it is suggested to add more diverse and complex scenarios to the dataset to detect situations where multiple faults occur simultaneously. Furthermore, the real-time data processing capability of the model can be improved by adapting it to handle continuous data streams from sensors. In addition, the integration of the model with different power generation systems and its cross-platform applicability is considered an important

focus for future studies. Such research can increase the generalization capacity of the model and enable it to reach a wider range of applications.



Figure 8. The figure above shows the performance of the MobileNetV3 model in different classes

5. CONCLUSION

This study evaluated the performance of a deep learning model, specifically MobileNetV3, for fault classification and detection in photovoltaic (PV) systems. The model was trained on a dataset containing different types of solar panel conditions, such as clean, physically damaged, electrically damaged, snow covered, bird droppings covered, and dusty panels. The results show that the MobileNetV3 model achieved a remarkable validation accuracy of 95%, indicating its high effectiveness in identifying and discriminating between different types of solar panel failures. The performance of the model was further analyzed using a confusion matrix, which provided a detailed overview of the correctly classified and misclassified instances in each class. The confusion matrix showed that the model performed exceptionally well for the majority of the classes, with only a few misclassifications occurring in the dusty and snow-covered panel categories. The low number of false positives and false negatives across the different classes suggests that the model is highly reliable in its predictions. In addition, the trends observed in the loss and accuracy curves further support the effectiveness of the model. The training loss and validation loss stabilized at low levels, indicating that the model successfully converged during training. The accuracy curves showed consistent improvement, reflecting the model's ability to generalize well to unseen data. Overall, the results highlight the potential of using MobileNetV3 for fault detection in PV systems, contributing to more efficient monitoring and maintenance of solar panels. This research highlights the importance of machine learning models in the renewable energy sector, particularly for improving the performance and longevity of solar energy systems. Future work can focus on incorporating additional data sources and exploring more complex models to further improve detection accuracy and real-time performance.

AUTHOR CONTRIBUTIONS

The authors contributed equally to the study.

ACKNOWLEDGEMENT

Kaggle open access resource was utilized in this study.

CONFLICT OF INTEREST

The authors declare no conflict of interest.

REFERENCES

- Eurostat. (2022). Wind and water provide most renewable electricity; solar is the fastest-growing energy source. [URL](#)
- Voutsinas, S., Mandourarakis, I., Koutroulis, E., Karolidis, D., Voyiatzis, I., & Samarakou, M. (2022). Control and communication for smart photovoltaic arrays. In 26th Pan-Hellenic Conference on Informatics (PCI 2022) (pp. 6). <https://doi.org/10.1145/3575879.3575983>
- Goodfellow, I., Bengio, Y., & Courville, A. (2016). *Deep learning*. The MIT Press.
- Bishop, C. M. (2007). *Pattern recognition and machine learning* (Information Science and Statistics). Springer.
- Hong, Y.Y., & Pula, R. A. (2022). Methods of photovoltaic fault detection and classification: A review. *Energy Reports*, 8, 5898–5929. <https://doi.org/10.1016/j.egy.2022.04.043>
- Huang, J. M., Wai, R. J., & Gao, W. (2019). Newly-designed fault diagnostic method for solar photovoltaic generation system based on IV-Curve measurement. *IEEE Access*, 7, 70919–70932. <https://doi.org/10.1109/ACCESS.2019.2919337>
- Mustafa, Z., Awad, A. S. A., Azzouz, M., & Azab, A. (2023). Fault identification for photovoltaic systems using a multi-output deep learning approach. *Expert Systems with Applications*, 211, 118551. <https://doi.org/10.1016/j.eswa.2022.118551>
- Boubaker, S., Kamel, S., Ghazouani, N., & Mellit, A. (2023). Assessment of machine and deep learning approaches for fault diagnosis in photovoltaic systems using infrared thermography. *Remote Sensing*, 15(6), 1686. <https://doi.org/10.3390/rs15061686>
- Kumar, U., Mishra, S., & Dash, K. (2023). An IoT and semi-supervised learning-based sensorless technique for panel level solar photovoltaic array fault diagnosis. *IEEE Transactions on Instrumentation and Measurement*, 72, 1–12. <https://doi.org/10.1109/TIM.2023.3287247>
- Cao, H., Zhang, D., & Yi, S. (2023). Real-time machine learning-based fault detection, classification, and locating in large scale solar energy-based systems: Digital twin simulation. *Solar Energy*, 251, 77–85. <https://doi.org/10.1016/j.solener.2022.12.042>

- Sabbaghpur, M., & Hejazi, M. A. (2016). The comprehensive study of electrical faults in PV arrays. *Journal of Electrical and Computer Engineering*, 2016, 8712960. <https://doi.org/10.1155/2016/8712960>
- Johnson, J., Montoya, M., McCalmont, S., Katzir, G., Fuks, F., Earle, J., Fresquez, A., Gonzalez, S., & Granata, J. (2012). Differentiating series and parallel photovoltaic arc-faults. In 2012 38th IEEE Photovoltaic Specialists Conference (pp. 720–726). <https://doi.org/10.1109/PVSC.2012.6317708>
- Voutsinas, S., Karolidis, D., Voyiatzis, I., & Samarakou, M. (2023). Development of a machine-learning-based method for early fault detection in photovoltaic systems. *Journal of Engineering and Applied Sciences*, 70(27). <https://doi.org/10.1186/s44147-023-00200-0>
- Howard, A., Sandler, M., Chu, G., Chen, L.-C., Chen, B., Tan, M., Wang, W., Zhu, Y., Pang, R., Vasudevan, V., Le, Q. V., & Adam, H. (2019). Searching for MobileNetV3. In 2019 IEEE/CVF International Conference on Computer Vision (ICCV) (pp. 1314–1324). <https://doi.org/10.48550/arXiv.1905.02244>
- Kaggle. (n.d.). Fault detection using ResNet50. Retrieved from [URL](#)
- Rudro, R. A. M., Nur, K., Sohan, M. F. A. Al, Mridha, M. F., Alfarhood, S., Safran, M., & Kanagarathinam, K. (2024). SPF-Net: Solar panel fault detection using U-Net based deep learning image classification. *Energy Reports*, 12, 1580–1594. <https://doi.org/10.1016/J.EGYR.2024.07.044>
- Sepúlveda-Oviedo, E. H., Travé-Massuyès, L., Subias, A., Pavlov, M., & Alonso, C. (2023). Fault diagnosis of photovoltaic systems using artificial intelligence: A bibliometric approach. *Heliyon*, 9(11), e21491. <https://doi.org/10.1016/J.HELIYON.2023.E21491>
- Zhang, D., & Duranay, Z. B. (2023). Fault Detection in Solar Energy Systems: A Deep Learning Approach. *Electronics* 2023, Vol. 12, Page 4397, 12(21), 4397. <https://doi.org/10.3390/ELECTRONICS12214397>



Gazi University

Journal of Science

PART A: ENGINEERING AND INNOVATION

<http://dergipark.org.tr/guj.1590807>

Seismic Rehabilitation of a Reinforced Concrete School in Northern Cyprus Following the 2023 Turkey Earthquake Sequences

Sasan BABAEI¹ Foad KARIMI GHALEH JOUGH^{1*} ¹Faculty of Engineering, Department of Civil Engineering, Final International University, Via Mersin 10, AS 128, Kyrenia, Northern Cyprus

| Keywords | Abstract |
|--|---|
| Case Study Seismic Rehabilitation School Building Performance-Based Design Time History Analysis | In 2023, a 7.8-magnitude earthquake struck Turkey, causing severe damage to residential and critical infrastructure. In response, the government of the Turkish Republic of Northern Cyprus launched a program to rehabilitate educational facilities. This study examines the rehabilitation efforts at Atatürk Technical High School in Nicosia. A nonlinear time-history analysis was conducted to assess the building's seismic behavior, lateral load resistance, and plastic deformation during main shock and aftershock sequences. Shear walls and steel X-braced frames were subsequently integrated into the building's lateral load-resisting system, and their effectiveness was evaluated. The analysis indicated that the original structure would likely experience life safety risks and structural damage in vertical elements, with some parts at risk of collapse after the second loading sequence. In contrast, the rehabilitated structure demonstrated immediate occupancy performance, with no plastic hinge formation in either direction. The maximum roof displacement was also reduced to as little as one-third of that in the original structure. |

| Cite |
|--|
| Babaei, S., & Karimi Ghaleh Jough, F. (2025). Seismic Rehabilitation of a Reinforced Concrete School in Northern Cyprus Following the 2023 Turkey Earthquake Sequences. <i>GU J Sci, Part A, 12(1)</i> , 213-227. doi: 10.54287/guj.1590807 |

| Author ID (ORCID Number) | Article Process |
|--|-----------------------------------|
| 0000-0001-8672-5499 Sasan BABAEI | Submission Date 25.11.2024 |
| 0000-0003-0697-516X Foad KARIMI GHALEH JOUGH | Revision Date 10.12.2024 |
| | Accepted Date 07.01.2025 |
| | Published Date 26.03.2025 |

1. INTRODUCTION

On the morning of February 6, 2023, an earthquake with a magnitude of 7.8 struck south-central Turkey. Approximately nine hours later, a second earthquake of magnitude 7.5 hit a nearby area, with the epicenters of both quakes less than 100 kilometers apart. Together, these events led to the tragic loss of over 57,000 lives in Turkey and Syria. Additionally, the earthquakes affected approximately 16% of Turkey's population and destroyed nearly half a million apartments across the region. (Akar et al., 2024; Babaei & Karimi Ghaleh Jough, 2024)

The doublet seismic hazard also overwhelmed critical infrastructure, including roads and essential public facilities, which are crucial to be immediately occupied such as hospitals. Hospitals need to remain operational to provide urgent care to the injured, while schools, beyond protecting students during school hours, can also serve as shelters for displaced individuals in the aftermath of a disaster. Given these essential functions, the

*Corresponding Author, e-mail: fooad.karimi@final.edu.tr

construction and maintenance of such buildings must meet high safety standards. (Babaei et al., 2024; Dowell, 2023; Wang et al., 2023)

Scholars who inspected the affected region highlighted several reasons for the infrastructure failures, including outdated building codes, subpar material quality, poor implementation practices, and adverse soil and site conditions. For instance, Turan et al. (2024), assessing the failure mechanisms in Malatya, found that the second seismic shock significantly increased casualties in densely populated areas by collapsing already weakened buildings and exposing a lack of sufficient emergency shelter options. (Turan et al., 2024) Zengin and Aydin's (2023) investigation revealed that pre-2000 buildings had concrete strengths often less than one-third of their design values, sometimes as low as 4 MPa. (Zengin & Aydin, 2023)

Structural failures in Hatay were exacerbated by issues such as incomplete framing at two orthogonal axes, the presence of short columns, and multiple cantilevers on facades. (Altunsu et al., 2024; Doğan et al., 2024) While post-2000 structures showed more brittle failure modes—such as beam-column joint fractures, out-of-plane bending, and shear failures of walls and columns with high width-to-depth ratios—there were also cases of sliding shear wall failures, bond-slip failures in ribbed reinforcement, and tension failures in beams and slabs. (Vuran et al., 2024)

Onat et al. (2024) conducted an experimental and numerical analysis on a historical masonry mosque in Malatya, demonstrating the need for additional lateral stiffness and damping systems. (Karimi Ghaleh Jough & Golhashem, 2020; Karimi Ghaleh Jough, 2023; Onat et al., 2024) Meanwhile, Mohammadi et al.'s (2024) comprehensive assessment of 11 bridges in the affected areas of Turkey and Syria found damage such as failures in shear keys, back walls, I-girders, and buckling of lower flanges, with some bridges experiencing liquefaction that caused tilting and road settlement (Mohammadi et al., 2024). Qu et al. (2023) studied 5 base-isolated and 7 fixed-base hospitals in the impacted regions, finding that while base-isolated hospitals remained operational, fixed-base ones mostly lost immediate occupancy due to significant nonstructural damage. (Qu et al., 2023; Babaei et al., 2023)

In response to the 2023 Turkish earthquake, the government of the Turkish Republic of Northern Cyprus initiated a program to rehabilitate critical facilities, including schools, in several cities. An effective assessment, beyond conventional gravitational and seismic analysis, should consider the nonlinearity of element behaviors, the frequency content and duration of seismic excitation, and uncertainties in material properties, geometry, and loads within the analysis environment. This case study focuses on the rehabilitation process conducted for Atatürk Technical High School, located in the city of Nicosia. (Jough & Şensoy, 2016; Karimi Ghaleh Jough & Beheshti Aval, 2018; Babaei & Zarfam, 2019; Babaei et al., 2020; Jough et al., 2021; Babaei & Hosseini, 2023; Karimi Ghaleh Jough & Ghasemzadeh, 2023; 2024; Jough, 2024;)

In this study, the existing structure was initially analyzed using time-history analysis, simulating both the main seismic event and its aftershock sequence. The structural response in both the X and Y directions was recorded

at the end of each ground motion sequence to assess nonlinear behavior and evaluate the load resistance capacity of the system in each direction. Additionally, the rehabilitated models proposed by the author as part of the recommendations for the Northern Cyprus government were analyzed using the same time-history approach. A comparative analysis of the original and rehabilitated structures demonstrated that the rehabilitation techniques, whether through shear walls or braced frames, were effective. The structures now behave symmetrically in both orthogonal directions, showing uniform deformation, and can meet immediate occupancy requirements, even after subsequent seismic sequences. Furthermore, the maximum roof displacement in both directions was substantially reduced, to as low as one-third of the initial displacement.

2. DEFINITION OF THE INVESTIGATED BUILDINGS

The building analyzed in this study is a 40- to 50-year-old school located in the center of Nicosia, North Cyprus. It consists of six distinct blocks, each constructed at different times and following specific building codes and material guidelines. These blocks include the main building, Hairdressing School, Classroom Blocks, Atelier, and Kindergarten, as illustrated in Figure 1, which shows the school's different buildings.

This study focuses on the two-story main building, which itself is made up of three separate blocks—A, B, and C—each built at different times. Blocks A and B were constructed around the 1980s and feature similar columns and beams.



Figure 1. Atatürk Technical High School; **a)** Main building, **b)** Hairdressing School, **c)** Classroom Blocks, **d)** Atelier

Block C, however, was developed in two phases, with the initial construction occurring about 30 years ago and additional parts added less than 10 years ago. While Block C generally shares the same lateral load-

resisting system—concrete moment frames—as Blocks A and B, its more recent additions include columns and beams with distinctive dimensions.

Laboratory testing revealed that Blocks A and B share similar concrete quality, specifically a C16 grade, with a maximum compressive strength of 16 MPa. In contrast, Block C has C18 grade concrete, providing a slightly higher compressive strength of 18 MPa in its original sections. Although the newer sections in Block C may use even higher-strength concrete, a conservative assumption was made to treat the entire structure as built with C18 concrete. Site inspections also did not reveal any steel strength degradation due to corrosion of the rebars. These findings most closely correlate with the Turkish Standard TS 708 (1973) for reinforcement steel.

The rehabilitation process utilized the original plans and documents provided by the authorities. It is important to note that for the first two blocks, A and B, the plans aligned well with the actual structure, including accurate dimensions for columns, beams, slab thicknesses, and rebar numbers and sizes. However, Block C did not follow the official plans. As a result, the dimensions and orientation of Block C had to be redrawn to reflect the current structure accurately. The final plan view of the investigated building, comprising all three blocks, is shown in Figure 2. Block A, located on the left side, measures 11 by 26 meters; Block B, situated in the middle, measures 22 by 26 meters; and Block C, positioned on the right side, measures 20 by 45 meters.

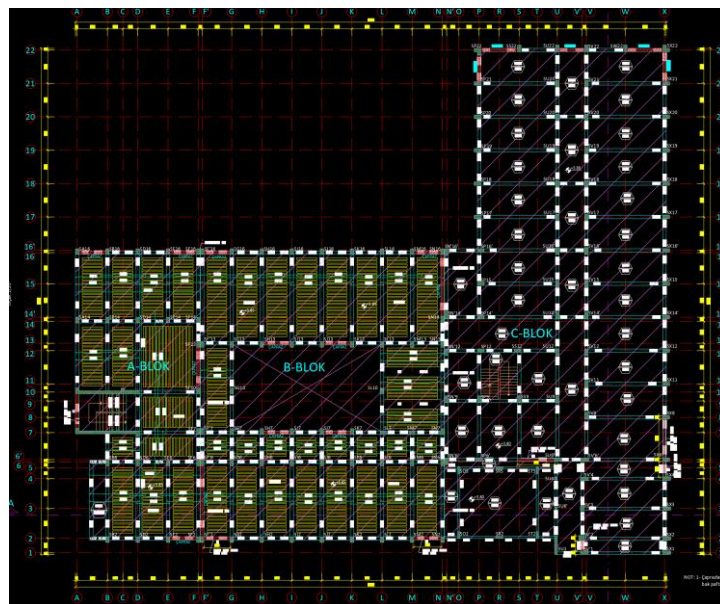


Figure 2. Plan view of the main building containing 3 blocks of A, B, and C

The dimensions and reinforcement of horizontal and vertical structural elements were obtained from the government's repository, as provided in Table 1. Figure 3 shows laboratory tests conducted to validate this information, revealing that the three blocks contain beams that are stronger than the columns, which is not ideal for building design. For optimal structural performance, the moment of inertia of the columns should be higher, allowing flexural deformations to occur in the horizontal elements (beams) rather than the vertical elements (columns). It should also be noted that Block A is the only block that incorporates a shear wall, positioned along the staircase and extending across the two-story structure.

Table 1. Dimensions and reinforcement properties of beam and columns

| Building | Element | Width (cm) | Height (cm) | Main Reinforcement | | | Stirrups |
|----------------------|----------|---------------|----------------|--------------------|-------------|-------------|-------------|
| | | | | Top | Middle | Bottom | |
| Block A | Column 1 | 30 | 50 | 2 ϕ 18 | 2 ϕ 18 | 2 ϕ 18 | ϕ 8@17 |
| & Block B | Beam 1 | 30 | 80 | 3 ϕ 18 | 2 ϕ 16 | 5 ϕ 18 | ϕ 8@15 |
| | Beam 2 | 30 | 80 | 4 ϕ 14 | 2 ϕ 14 | 4 ϕ 14 | ϕ 8@17 |
| Block C | Column 2 | 30 | 60 | 3 ϕ 18 | 4 ϕ 18 | 3 ϕ 18 | ϕ 8@17 |
| | Column 3 | 30 | 70 | 3 ϕ 18 | 4 ϕ 18 | 3 ϕ 18 | ϕ 8@17 |
| | Beam 3 | 30 | 50 | 2 ϕ 16 | 2 ϕ 16 | 2 ϕ 16 | ϕ 8@17 |
| | Beam 4 | 30 | 80 | 3 ϕ 18 | 2 ϕ 16 | 5 ϕ 18 | ϕ 8@17 |



Figure 3. Laboratory test for validation; a) Extracted concrete cores for compression test; b) Scanning concrete rebars

3. TIME HISTORY ANALYSIS

As indicated by the Ministry of Education, the rehabilitation technique was initially conducted using pushover analysis with three different software tools: ProtaStructure (Prota Software, 2018), SAP2000 (Computers and Structures, Inc., 2023, Version 24), and SeismoStruct (SeismoSoft, 2022). While pushover analysis is a reliable technique, it may not fully capture the nonlinear behavior of the structure, especially in response to the frequency content of seismic records. Additionally, pushover analysis cannot adequately represent the duration of ground motion or the sequence of hinge formation, as compared to time history analysis.

To evaluate the structure's seismic behavior, it was subjected to two sequences of strong ground motion from the 2023 Kahramanmaraş earthquake. The seismic sequence of the Pazarcık (Mw 7.7) and Elbistan (Mw 7.6) earthquakes, recorded at Station 4612 with a maximum peak ground acceleration of 0.52g, is shown in Figure 4. To account for plastic deformations and hinge formation in primary elements, specifications were applied

based on Table 10.8 and Table 10.9 of ASCE 41-17 for columns, and Table 10.7 for flexural elements. (ASCE/SEI 41/17, 2017) These specifications were incorporated into the structure using hinge definitions provided in SAP2000.

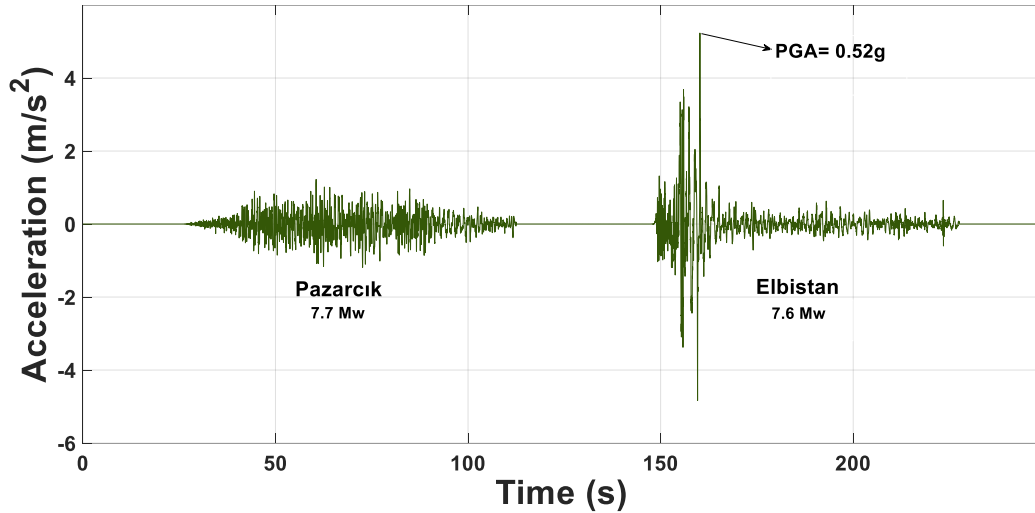


Figure 4. Acceleration-time history of Pazarcik (7.7Mw) and Elbistan (7.6Mw) ground motions from Station 4612 (AFAD, 2024)

An analysis of Block A shows that the structure remained elastic in both directions during the first sequence of ground motion. However, during the second sequence, known as the Elbistan earthquake, hinges began to form in primary elements, specifically the columns. Figure 5a and 5b display the deformation of Block A in the X and Y directions. In the X direction, where shear walls are incorporated around the staircase, the structure demonstrated high resistance, with only one hinge reaching the life safety level. In contrast, columns in the Y direction sustained significant damage: ten columns reached the life safety state, three columns reached the collapse prevention state, and nine columns experienced total collapse, as shown in Table 2. Notably, none of the beams in the structure failed, likely due to their large cross-sectional dimensions of 30 by 80 cm, which provide high moments of inertia and enhance flexural capacity. Additionally, the beams were reinforced with sufficient longitudinal rebar, enabling them to exhibit ductile behavior.

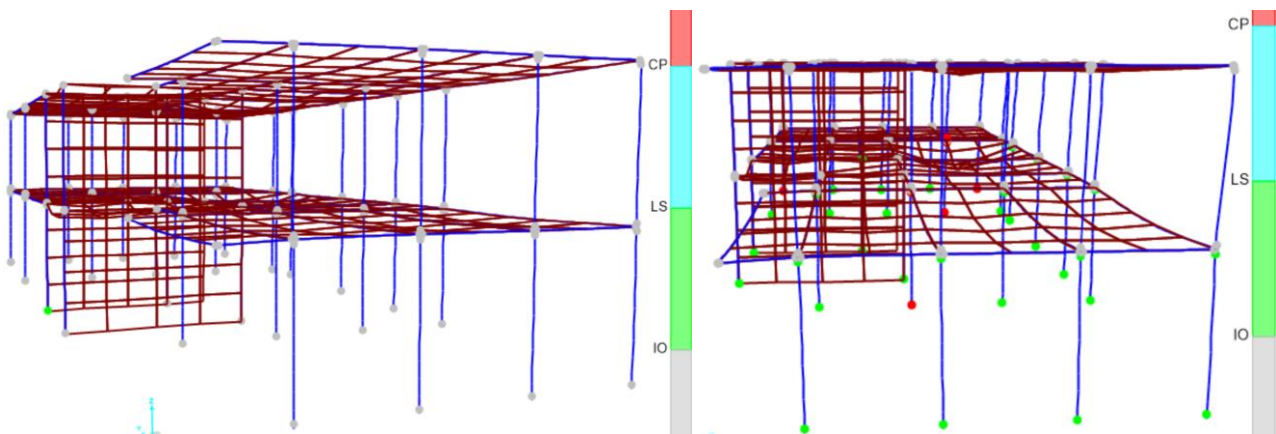
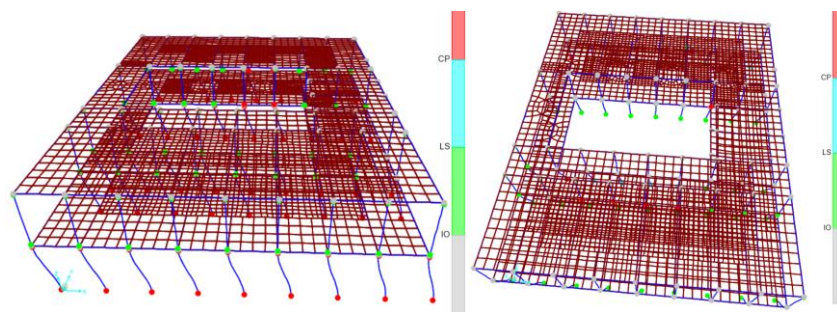


Figure 5. Hinge formations in the frames of block A at the end of the seismic sequence; a) X direction, b) Y direction

Table 2. Summary of the hinge formation in the frames of block A

| Direction | Element | Immediate occupancy | Life Safety | Collapse prevention | Collapse |
|-----------|---------|---------------------|-------------|---------------------|----------|
| X | Beams | 76 | 0 | 0 | 0 |
| | Columns | 49 | 1 | 0 | 0 |
| Y | Beams | 76 | 0 | 0 | 0 |
| | Columns | 19 | 19 | 3 | 9 |

Figure 6 illustrates the seismic behavior of the second block, Block B, in both the X and Y directions after the completion of the second ground motion sequence, as indicated in Table 3. None of the primary or secondary elements—namely, columns and beams—experienced hinge formation after the first sequence. However, as the intensity of the second ground motion increased, 38 columns reached the life-safety state, while 52 columns approached a collapse state in the X direction. Notably, none of the columns remained in the immediate occupancy category. In the Y direction, similar behavior was observed but with less severe damage: 25 columns remained in immediate occupancy, 51 reached the life-safety threshold, 4 were at collapse prevention, and 10 were in a collapse state. This analysis indicates that the structure in both the X and Y directions lacks sufficient lateral resilience to sustain these ground motions. Reinforcement techniques are recommended in both directions, particularly in the X direction, where a greater number of columns failed. Similar to Block A, none of the beams in Block B experienced hinge formation, likely due to their larger cross-section dimensions of 30 by 80 cm.

**Figure 6.** Hinge formations in the frames of block B at the end of the seismic sequence; a) X direction, b) Y direction**Table 3.** Building's blocks Columns and beams dimensions and reinforcements

| Direction | Element | Immediate occupancy | Life Safety | Collapse prevention | Collapse |
|-----------|---------|---------------------|-------------|---------------------|----------|
| X | Beams | 148 | 0 | 0 | 0 |
| | Columns | 0 | 38 | 0 | 52 |
| Y | Beams | 148 | 0 | 0 | 0 |
| | Columns | 25 | 51 | 4 | 10 |

Unlike the other two blocks, Block C experienced hinge formation even after the first seismic sequence in the Y direction. However, in the X direction, none of the structural elements experienced hinge formation,

allowing the structure to remain in immediate occupancy. Figure 7 illustrates that, after the second sequence of ground motion, 113 columns in the X direction reached the life-safety stage, with only one column reaching the collapse state.

In the Y direction, as shown in Figure 8, even after the first seismic sequence, 57 columns reached the life-safety stage, 23 columns were at collapse prevention, and 29 columns reached collapse. This damage intensified with the second sequence: only 6 columns remained in immediate occupancy, 56 reached the life-safety stage, 10 were at collapse prevention, and a significant 48 columns reached collapse.

It is also noteworthy that, unlike the columns, none of the beams in either the X or Y direction experienced hinge formation; all beams remained in immediate occupancy, likely due to their large cross-sectional dimensions, as shown in Table 4.

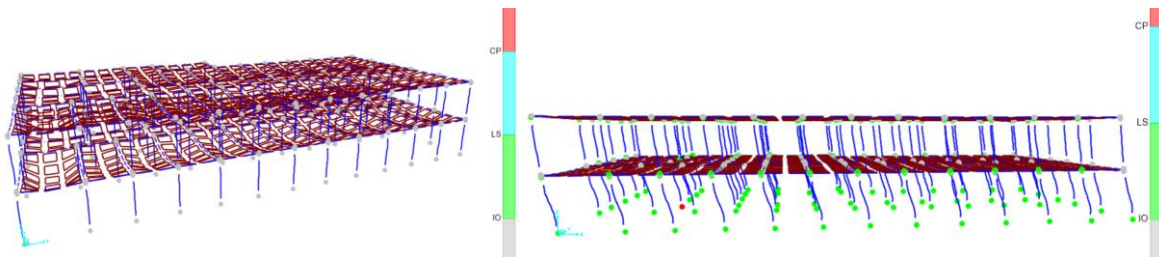


Figure 7. Hinge formations in the frames of block C at the X direction at the end of the; a) mainshock, b) aftershock

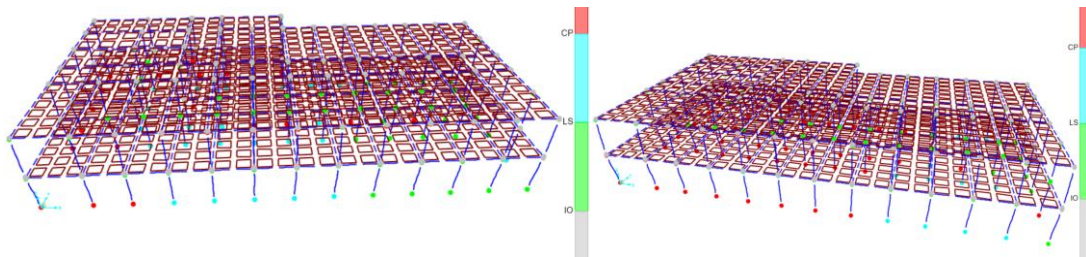


Figure 8. Hinge formations in the frames of block C at the Y direction at the end of the; a) mainshock, b) aftershock

Table 4. Summary of the hinge formation in the frames of the block C

| Direction | Record | Element | Immediate occupancy | Life safety | Collapse prevention | Collapse |
|-----------|--------|---------|---------------------|-------------|---------------------|----------|
| X | MS | Beams | 180 | 0 | 0 | 0 |
| | | Columns | 120 | 0 | 0 | 0 |
| | MS+AS | Beams | 180 | 0 | 0 | 0 |
| | | Columns | 6 | 113 | 0 | 1 |
| Y | MS | Beams | 180 | 0 | 0 | 0 |
| | | Columns | 11 | 57 | 23 | 29 |
| | MS+AS | Beams | 180 | 0 | 0 | 0 |
| | | Columns | 6 | 56 | 10 | 48 |

4. REHABILITATION TECHNIQUE

Structural analysis in both directions indicates that rehabilitation is necessary, corroborating earlier findings from the author's pushover analysis. The proposed rehabilitation methods include adding a 25-centimeter-thick C30 shear wall or an X-braced frame with sections measuring 200 cm in width and 10 cm in thickness. ST275-grade steel was selected as the material for the braces to enhance structural performance.

The rehabilitated model of the building, created using SAP2000 and ProtaStructure software, is depicted in Figure 9. As shown, X-direction brace frames were added to both the upper and lower portions of the structure, and two additional brace frames were incorporated along the Y direction on both sides. The purpose of positioning these brace frames at the edges of the structure in both X and Y directions is to mitigate unwanted rotational modes, enhancing overall stability. This configuration also facilitates additional foundation rehabilitation as needed.

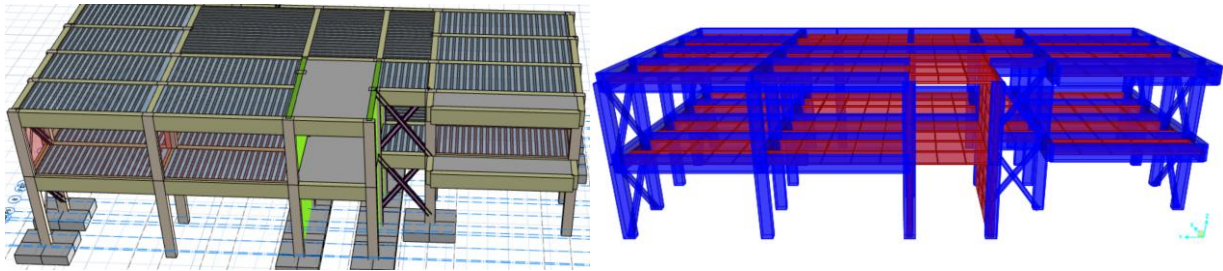


Figure 9. Rehabilitated building block A, *a)* Protastructure, *b)* SAP

Further modifications to the rehabilitated model are presented in Figure 10, focusing specifically on Block B. Two shear walls were introduced at the bottom side of the building, and two brace frames were incorporated at the top. In the building's inner core, which contains an opening, four brace frames were added in the X direction and another four in the Y direction to improve lateral stability.

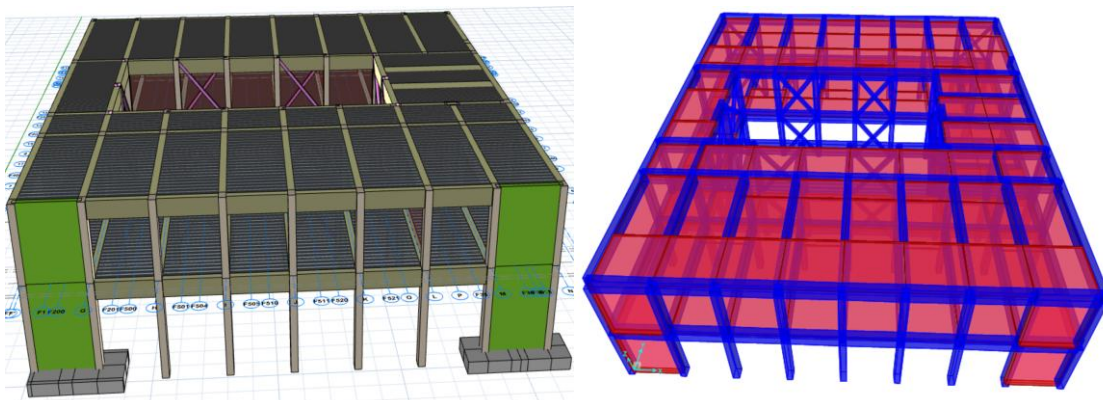


Figure 10. Rehabilitated building block B, *a)* Protastructure, *b)* SAP

As detailed in Figure 11, additional rehabilitation measures were applied in Block C. Two brace frames were installed at the front of the structure in both the X and Y directions, with additional reinforcement on the opposite side of the structure at the base. This included two shear walls in the X direction and two in the Y direction, incorporated to enhance the building's lateral load-resisting capabilities.

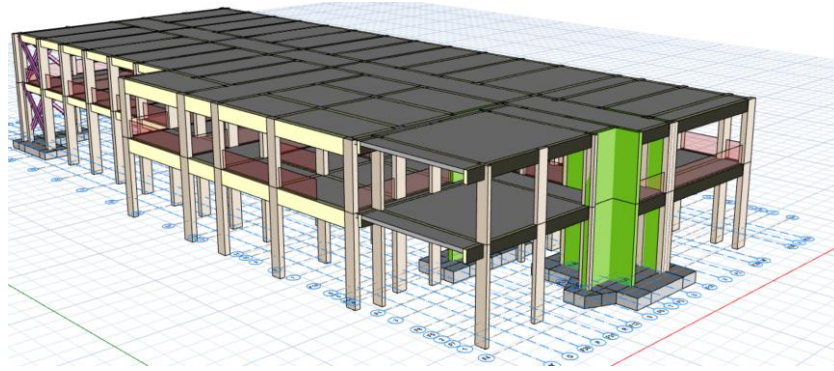


Figure 11. Rehabilitated building block C

Figure 12 and 13 illustrate the implementation of 25-centimeter shear walls and X-brace frames incorporated into the structure.



Figure 12. Shear wall added to block A; **a)** wall demolishing, **b)** Concrete pouring



Figure 13. X-braced frames added to block C; **a)** wall demolishing, **b)** Braced frame implementation **c)** Tube 200x200x12.5

5. COMPARISON OF THE EXISTING AND REHABILITATED BUILDINGS

Blocks A, B, and C experience no hinge formation, even after the second sequence in both directions, indicating sufficient structural ductility and seismic capacity. To compare this capacity more effectively, both the existing and rehabilitated buildings were subjected to a mainshock-aftershock sequence. Figure 14 shows the maximum roof displacement in the X and Y directions. In the X direction, the existing and rehabilitated

buildings demonstrate similar behavior, while in the Y direction, the rehabilitated building significantly reduces the maximum roof displacement.

Specifically, in Block A, the maximum roof displacement in the X direction decreased from 0.38 cm to 0.2 cm in the rehabilitated building. In the Y direction, displacement in Block A was reduced from 3.39 cm to 1.4 cm after rehabilitation, demonstrating a considerable improvement. This increased efficiency in the Y direction is attributed to the addition of braced frames, which significantly enhances lateral resistance. In contrast, the X direction already had sufficient resistance due to the existence of large shear walls, even before the rehabilitation.

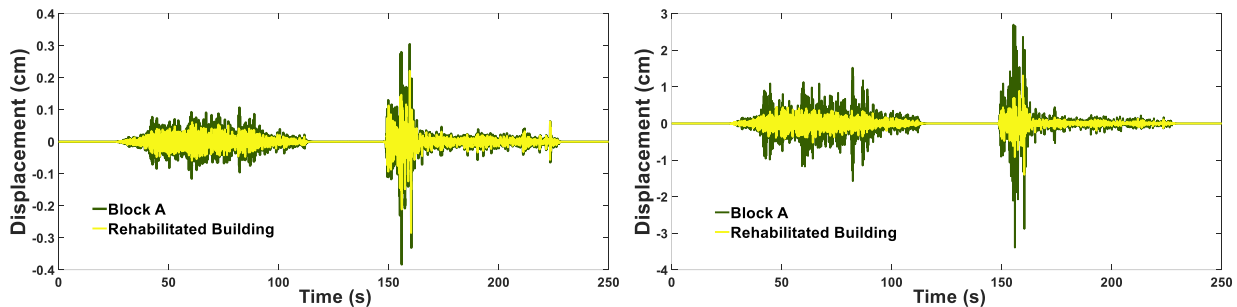


Figure 14. Time history analysis of Block A; a) X direction, b) Y direction

Figure 15 illustrates the structural behavior of the building under a nonlinear dynamic analysis. As shown, the non-rehabilitated structure was significantly impacted by the second sequence, with several elements yielding due to prior stress. This led to an increase in displacement amplitude during the second sequence in both the X and Y directions, particularly in the X direction. In contrast, the rehabilitated structure exhibits a more symmetrical response in both the X and Y directions and a stable response to ground motion, with no extreme displacement peaks following the second sequence.

As detailed in Table 5, the maximum roof displacement in the X direction decreased from 2.19 cm to 0.66 cm after rehabilitation. Similarly, in the Y direction, the maximum roof displacement was reduced from 1.16 cm to 0.22 cm. These improvements underscore the effectiveness of the rehabilitation measures in enhancing the building's seismic performance.

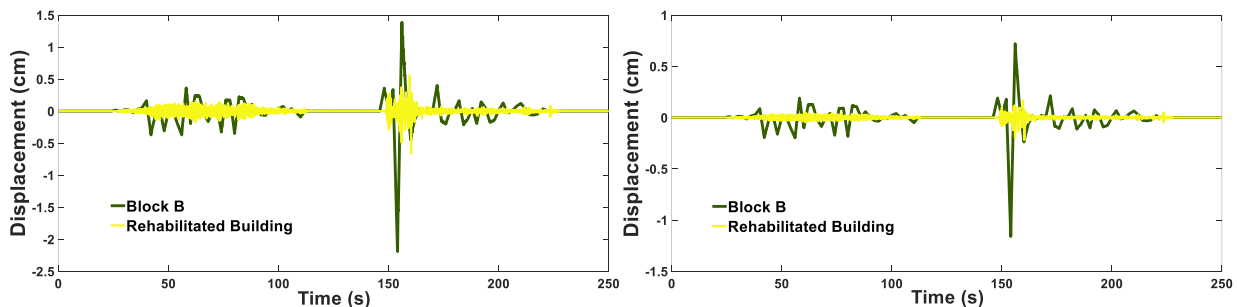


Figure 15. Time history analysis of Block B; a) X direction, b) Y direction

Figure 16 further illustrates the seismic behavior of both the non-rehabilitated and rehabilitated structures in Block C. As shown, the maximum roof displacement is significantly reduced in both the X and Y directions after rehabilitation. Specifically, in the X direction, the maximum roof displacement decreased from 3.31 cm to 1.5 cm—a reduction by more than half. In the Y direction, it was reduced from 3.67 cm to 1.32 cm, almost one-third of the original displacement. This improvement enhances the structure's natural resistance to severe earthquake impacts.

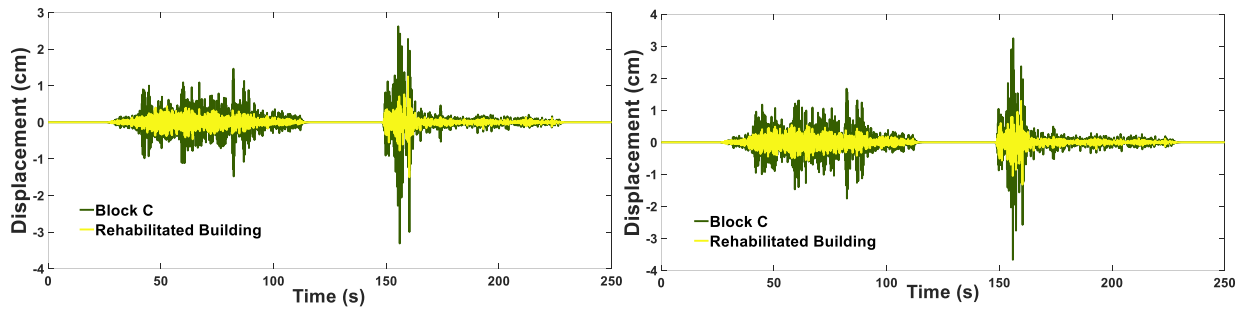


Figure 16. Time history analysis of Block C; a) X direction, b) Y direction

Table 5 shows that the two structures now exhibit much closer predominant mode shapes and periods, with the first modes in both the X and Y directions now aligned. Any rotational modes are effectively prohibited. Additionally, it should be noted that making the structure stiffer—either by adding shear walls or braced frames—has reduced the periods of the rehabilitated building compared to the non-rehabilitated one.

Table 5. Dynamic characteristics and seismic response of existing and rehabilitated building's blocks

| Building | Direction | Block A | | Block B | | Block C | |
|-----------------------------------|-----------|----------|---------------|----------|---------------|----------|---------------|
| | | Existing | Rehabilitated | Existing | Rehabilitated | Existing | Rehabilitated |
| Period (s) | X | 0.09 | 0.086 | 0.348 | 0.124 | 0.264 | 0.176 |
| | Y | 0.27 | 0.187 | 0.247 | 0.079 | 0.283 | 0.196 |
| Max Roof Displacement (cm) | X | 0.38 | 0.28 | 2.19 | 0.66 | 3.31 | 1.50 |
| | Y | 3.39 | 1.40 | 1.16 | 0.22 | 3.67 | 1.32 |

6. CONCLUSION

This case study examines the effectiveness of rehabilitation techniques applied to a structure located in Nicosia, Turkish Republic of Northern Cyprus. The complex consists of six buildings, with the main building selected for a time-history analysis based on the 2023 two-sequence Kahramanmaraş ground motions. This main building is divided into three distinct blocks: Block A, Block B, and Block C. A nonlinear time-history analysis was initially conducted to assess the performance of each block in the orthogonal X and Y directions. Findings reveal that, without rehabilitation, these buildings face life safety issues, hinge formation, and the potential for collapse by the end of the second sequence. However, when rehabilitation techniques—such as adding a 25-centimeter shear wall or hollow tube steel sections—are implemented to strengthen the lateral load-resisting system, the structures achieve immediate occupancy performance in both directions. The rehabilitated

buildings also experience a significant reduction in maximum roof displacement, to as little as one-third of the original structure's displacement. Additionally, the rehabilitated buildings exhibit symmetric behavior, with the X and Y direction mode shapes closely aligned as the dominant first and second modes.

AUTHOR CONTRIBUTIONS

Conceptualization, S.B.; methodology, S.B. and F.K.G.; fieldwork, S.B.; software, S.B.; title, S.B., and F.K.G.; validation, S.B.; laboratory work, S.B.; formal analysis, S.B. and F.K.G.; research, S.B.; sources, S.B.; data curation, S.B.; manuscript-original draft, S.B.; manuscript-review and editing, S.B. and F.K.G.; visualization, S.B. and F.K.G.; supervision, S.B. and F.K.G.; project management, S.B.; All authors have read and legally accepted the final version of the article published in the journal.

CONFLICT OF INTEREST

The authors declare no conflict of interest.

REFERENCES

- AFAD (2024). Republic of Turkey Ministry of Interior, Disaster and Emergency Management Presidency (AFAD) "Training and Awareness Department". Accessed: 24.02.2024, [URL](#)
- Akar, F., Işık, E., Avcil, F., Büyüksaraç, A., Arkan, E., & İzol, R. (2024). Geotechnical and Structural Damages Caused by the 2023 Kahramanmaraş Earthquakes in Gölbaşı (Adıyaman). *Applied Sciences*, 14(5).
- Altunsu, E., Güneş, O., Öztürk, S., Sorosh, S., Sarı, A., & Beeson, S. T. (2024). Investigating the structural damage in Hatay province after Kahramanmaraş-Türkiye earthquake sequences. *Engineering Failure Analysis*, 157, 107857. <https://doi.org/10.1016/j.engfailanal.2023.107857>
- ASCE/SEI 41/17. (2017). Seismic Evaluation and Retrofit of Existing Buildings. American Society Of Civil Engineers.
- Babaei, S., Habib, A., Hosseini, M., & Yildirim, U. (2024). *Investigating the Inelastic Performance of a Seismic Code-Compliant Reinforced Concrete Hospital Under Long Sequence of Ground Motions Records*. In: Proceedings of 15th International Congress on Advances in Civil Engineering (ACE2023) (pp. 364-373). https://doi.org/10.1007/978-981-97-1781-1_34
- Babaei, S., & Hosseini, M. (2023). Semi-active Control of 3D-Vertically Isolated Buildings with Divided Skeleton into Inner and Outer Interactive Subsystems Equipped with MR Dampers Canadian Conference - Pacific Conference on Earthquake Engineering 2023.
- Babaei, S., & Karimi Ghaleh Jough, F. (2024). A Comprehensive Evaluation of Tuned Vertical Isolation System for Seismic Risk Mitigation. *Journal of Applied Engineering Sciences*, 14(1), 27-34. <https://doi.org/10.2478/jaes-2024-0004>
- Babaei, S., & Zarfam, P. (2019). Optimization of shape memory alloy braces for concentrically braced steel braced frames. *Open Engineering*, 9(1), 697-708. <https://doi.org/10.1515/eng-2019-0084>

- Babaei, S., Zarfam, P., & Sarvghad Moghadam, A. (2020). Probabilistic and Deterministic Semi-Active Control Strategies for Adjacent Buildings Connected by MR Dampers 17th World Conference on Earthquake Engineering.
- Babaei, S., Zarfam, P., Sarvghad Moghadam, A., & Zahrai, S. M. (2023). Assessment of a dual isolation system with base and vertical isolation of the upper portion. *Structural Engineering and Mechanics*, 88(3), 263-271. <https://doi.org/10.12989/sem.2023.88.3.263>
- Computers and Structures, Inc. (2023). SAP2000 Integrated Software for Structural Analysis and Design (Version 24). Berkeley, CA: Computers and Structures, Inc. Available at: [URL](#)
- Doğan, T. P., Kalkan, H., Aldemir, Ö., Ayhan, M., Böcek, M., & Anıl, Ö. (2024). Investigation of RC structure damages after February 6, 2023, Kahramanmaraş earthquake in the Hatay region. *Bulletin of Earthquake Engineering*, 22(10), 5201-5229. <https://doi.org/10.1007/s10518-024-01965-2>
- Jough, F. K. G. (2024). Fuzzy Logic-Based Fragility Curve Development for Steel Moment-Resisting Frames Considering Uncertainties in Seismic Response. *Journal of Earthquake and Tsunami*, 18(05), 2450014. <https://doi.org/10.1142/S1793431124500143>
- Jough, F. K. G., & Şensoy, S. (2016). Prediction of seismic collapse risk of steel moment frame mid-rise structures by meta-heuristic algorithms. *Earthquake Engineering and Engineering Vibration*, 15(4), 743-757. <https://doi.org/10.1007/s11803-016-0362-9>
- Jough, F. K. G., Veghar, M., & Beheshti-Aval, S. B. (2021). Epistemic Uncertainty Treatment Using Group Method of Data Handling Algorithm in Seismic Collapse Fragility. *Latin American Journal of Solids and Structures*, 18.
- Dowell, K. (2023). Reconnaissance Report of Observed Structural Bridge Damage (SDSU STRUCTURAL ENGINEERING RESEARCH PROJECT, Issue.)
- Karimi Ghaleh Jough, F. (2023). The contribution of steel wallposts to out-of-plane behavior of non-structural masonry walls. *Earthquake Engineering and Engineering Vibration*, 22(1), 243-262. <https://doi.org/10.1007/s11803-023-2161-4>
- Karimi Ghaleh Jough, F., & Beheshti Aval, S. B. (2018). Uncertainty analysis through development of seismic fragility curve for an SMRF structure using an adaptive neuro-fuzzy inference system based on fuzzy C-means algorithm. *Scientia Iranica*, 25(6), 2938-2953. <https://doi.org/10.24200/sci.2017.4232>
- Karimi Ghaleh Jough, F., & Ghasemzadeh, B. (2024). Uncertainty Interval Analysis of Steel Moment Frame by Development of 3D-Fragility Curves Towards Optimized Fuzzy Method. *Arabian Journal for Science and Engineering*, 49(4), 4813-4830. <https://doi.org/10.1007/s13369-023-08223-8>
- Karimi Ghaleh Jough, F., & Ghasemzadeh, B. (2023). Reliability Prediction of SMRF Based on the Combination of Neural Network And Incremental Dynamic Analysis [SMRF'nin Sinir Ağı ve Artımlı Dinamik Analizin Birleşimine Dayanan Güvenilirlik Tahmini]. *Journal of Innovations in Civil Engineering and Technology*, 5(2), 91-105. <https://doi.org/10.60093/jiciviltech.1317804>

- Karimi Ghaleh Jough, F., & Golhashem, M. (2020). Assessment of out-of-plane behavior of non-structural masonry walls using FE simulations. *Bulletin of Earthquake Engineering*, 18(14), 6405-6427. <https://doi.org/10.1007/s10518-020-00932-x>
- Mohammadi, N. K., Yasuko; Akyol, E. (2024). Observed structural bridge damage report for the 2023 Turkey-Syria earthquake. Kobe University Research Center for Urban Safety.
- Onat, O., Özmen, A., Özdemir, E., & Sayın, E. (2024). Damage propagation and failure mechanism of single dome historical Masonry Mosque after February 6, 2023, Kahramanmaraş earthquake doublets ($M_w = 7.7$ and $M_w = 7.6$). *Structures*, 69, 107288. <https://doi.org/10.1016/j.istruc.2024.107288>
- Prota Software. (2018). ProtaStructure: Structural Design and Analysis Software. Available at: [URL](https://www.protastructure.com/)
- Qu, Z., Wang, F., Chen, X., Wang, X., & Zhou, Z. (2023). Rapid report of seismic damage to hospitals in the 2023 Turkey earthquake sequences. *Earthquake Research Advances*, 3(4), 100234. <https://doi.org/10.1016/j.eqrea.2023.100234>
- SeismoSoft. (2022). SeismoStruct: A Finite Element Analysis Program for Static and Dynamic Nonlinear Analysis of Framed Structures. Available at: [URL](https://www.seissoft.com/)
- Turan, A. I., Celik, A., Kumbasaroglu, A., & Yalciner, H. (2024). Assessment of reinforced concrete building damages following the Kahramanmaraş earthquakes in Malatya, Turkey (February 6, 2023). *Engineering Science and Technology, an International Journal*, 54, 101718. <https://doi.org/10.1016/j.jestch.2024.101718>
- TS 708, Turkish Standards Institute. (1973). TS 708-Steel for the reinforcement of concrete – reinforcing steel, Ankara.
- Vuran, E., Serhatoğlu, C., Timurağaoğlu, M. Ö., Smyrou, E., Bal, İ. E., & Livaoğlu, R. (2024). Damage observations of RC buildings from 2023 Kahramanmaraş earthquake sequence and discussion on the seismic code regulations. *Bulletin of Earthquake Engineering*, 23, 1153-1182. <https://doi.org/10.1007/s10518-023-01843-3>
- Wang, X., Feng, G., He, L., An, Q., Xiong, Z., Lu, H., Wang, W., Li, N., Zhao, Y., Wang, Y., & Wang, Y. (2023). Evaluating Urban Building Damage of 2023 Kahramanmaras, Turkey Earthquake Sequence Using SAR Change Detection. *Sensors*, 23(14), 6342. <https://doi.org/10.3390/s23146342>
- Zengin, B., & Aydin, F. (2023). The Effect of Material Quality on Buildings Moderately and Heavily Damaged by the Kahramanmaraş Earthquakes. *Applied Sciences*, 13(19) 10668. <https://doi.org/10.3390/app131910668>



Gazi University

Journal of Science

PART A: ENGINEERING AND INNOVATION

<http://dergipark.org.tr/guj.1589209>

Mineral Chemistry of Ulukale Porphyritic Dome and Çağlarca Radial Dykes in the Tunceli Volcanites, Eastern Turkey

Sevcan KÜRÜM^{1*} Abdullah SAR¹ Muhammed Yasir YURT¹

¹ *Firat University, Faculty of Engineering, Department of Geological, 23119, Elazığ, Türkiye*

| Keywords | Abstract |
|---|--|
| Tunceli Volcanics Ulukale-Çağlarca Porphyritic Dome Radial Dyke Mineral Chemistry | This study presents mineral chemistry data the first time as a analytical data for the Ulukale porphyritic dome and the Çağlarca radial dykes located within the Neogene Tunceli volcanic rocks. In petrographic studies, it was determined that the dome and dykes with porphyritic texture were of trachyandesite composition. Plagioclase (oligoclase + andesine), amphibole (hastingsite + magnesiohastingsite and ferroedenite) and biotite (meroxene + phlogopite) found in domes-dykes, and pyroxene (augite and hypersthene) element contents only in dykes indicate that the magma originated from mantle-mantle+crust mixing and was affected by late-stage low-temperature hydrothermal fluids. Pyroxenes indicating low temperature - pressure conditions also indicate an upper crust source. This magma with mantle + crust properties supports crustal thickening and underplating mafic magma formation, which is a result of the compression regime in the Eastern Anatolia region. |

Cite

Kürüm, S., Sar, A., & Yurt, M. Y. (2025). Mineral Chemistry of Ulukale Porphyritic Dome and Çağlarca Radial Dykes in the Tunceli Volcanites, Eastern Turkey. *GU J Sci, Part A, 12(1)*, 228-249. doi:[10.54287/guj.1589209](https://doi.org/10.54287/guj.1589209)

| Author ID (ORCID Number) | Article Process |
|--------------------------|-----------------------------------|
| 0000-0001-6121-5564 | Sevcan KÜRÜM |
| 0000-0002-9752-7807 | Abdullah SAR |
| 0000-0002-1563-2938 | Muhammed Yasir YURT |
| | Submission Date 22.11.2024 |
| | Revision Date 23.12.2024 |
| | Accepted Date 08.01.2025 |
| | Published Date 26.03.2025 |

1. INTRODUCTION

Lava domes and dykes found in volcanic systems are a natural part of the system and are related to many related parameters, as well as the effusive and explosive nature of volcanism (Cassidy et al., 2018). Lava domes, which are products of explosive volcanism, will block the volcano vent and prevent magmatic gas outflow, which will increase the pore pressure and increase the severity of the eruption. For this reason, the eruption intensity of lavas with more acidic composition that constitute explosive volcanism will increase. It is suggested that the effectiveness of gas release is reduced due to the change in the composition of the dome-forming magma by hydrothermal fluids, apart from its viscosity (Ball et al., 2013; Rosas-Carbajal et al., 2016), and therefore the explosion severity is increased (Edmonds et al., 2013; Horwell et al., 2013). In explosive volcanisms, magma flow rate; gas evolution will determine the time available for cooling and crystallization, which will affect the morphology of the dome (Fink & Griffiths, 1998).

In this study, the mineralogical-petrographic and mineral chemistry of the geological structures developed in the form of domes and radial dykes within the Tunceli volcanics, where explosive volcanism is dominant,

*Corresponding Author, e-mail: skurum@firat.edu.tr

and the properties of the magma forming the geological structures were investigated. Since the study was guided with very local and limited data, it is thought that it will form the basis for future studies.

2. MATERIAL AND METHOD

A large number of thin sections were made in the rocks in the study area and mineral chemistry (major and trace elements) analysis was carried out in a total of five samples, two from dome and three from dykes.

The mineral chemistry analyzes were carried out using Bruker-Axs Quantax XFLash 3001 EDS integrated with a Zeiss Evo-50 EP microscope and JXA 8230 Model device under 20Kv voltage and 15NA current at the laboratories of Ankara University Earth Sciences Application and Research Center (YEBİM (Ankara, Turkey)). The preparation and polishing of the thin sections used in these analyzes were carried out in this center. Mineral compositions were determined by converting the major and minor elements of the mineral obtained in oxide form from EPMA (Electron Probe Micro Analysis) into cation values (apfu = atoms per formula unit).

3. GEOLOGICAL BACKGROUND OF EASTERN ANATOLIAN VOLCANISM

The Eastern Anatolia region is considered an active continental plate margin as a result of the final closure of the Neo-Tethys Ocean. In these types of tectonic environments, magmatic activity with very common distribution develops, called orogenic magmatism. This magmatic activity forming linked to continental collision during geodynamic evolution of the region may become much more complicated with the effect of ocean-ocean or ocean-continent convergence (Innocenti et al., 1982; Pearce et al., 1990; Keskin et al., 1998; Turner et al., 2017; Özdemir et al. 2006; Karaoğlu et al., 2016, 2017). Continental collision is defined as the time when two continental plates approaching from opposite directions contact for the first time at the point when oceanic lithosphere or the plate between the two continental plates is fully subducted (Hu et al., 2016). All tectonic, magmatic or metallogenic events controlled by or directed by gravitational imbalance occurring when collision and convergence forces end and features related to probable subduction are defined as post-collisional events (Kuşçu et al., 2007; Xu et al., 2020). This situation can be very clearly observed in the Eastern Anatolian region in terms of both tectonic, magmatic and metallogenic events. Additionally, this situation becomes more complicated with the development of two large transform faults developing after collision and affecting the whole region of the North Anatolian Fault Zone (NAFZ) and East Anatolian Fault Zone (EAFZ) (Figure 1a). With the full development of these two conjugate fault systems, Anatolia began to move as an independent microplate and they are accepted as forming a new triple junction (Eurasia-Arabia-Anatolia) (Agostini et al., 2019).

The Eastern Anatolia region, accepted as one of the best examples of a continental collision belt in the world, is considered to still be actively deformed as a result of north-south compression (Keskin, 2005). Accepted as beginning in the Late Oligocene from the initiation of the continental collision (Arabia-Eurasia) in Eastern Anatolia, magmatism forms the East Anatolia Magmatic Belt with distribution toward the east (Rabayrol et

al., 2019) (Figure 1a, 1b). The earliest magmatic phase in this belt is the Cevizlidere magmatism with 26-25 Ma (Oligocene) (İmer et al., 2015), then this magmatism increased over time and formed the largest volume Erzurum-Kars volcanic plateau in the Late Miocene (11.6-5.3 Ma). The volcanism forming the Erzurum-Kars volcanic plateau developed in three different stages and the first stage (11-6 Ma) was stated to involve basic volcanism from small temporary chambers, while acidic volcanism erupted from large, zoned magma chambers (Keskin et al., 1998) (Figure 1a). Researchers stated that volcanism in the middle stage (mostly between 6-5 Ma) was characterized by single-stage volcanism forming dominantly from andesitic-dacitic lavas and later due to crystallization of aqueous assemblages (containing amphibole) in deeper magma chambers. Late stage volcanism (mostly 5-2.7 Ma) was stated to be characterized by bimodal volcanism comprising basically plateau basalts and basaltic andesite lavas and felsic domes (Keskin et al., 1998). The main magma forming this volcanism on the plateau was affected by subduction events before collision and is accepted as having the features of lithospheric-derived magma carrying traces of subduction.

The Mazgirt (Tunceli) volcanics of Early-Middle Miocene (16.3 and 15.1 Ma), which are among the Tunceli volcanics and reflect the geodynamic framework of the Eastern Anatolia region, represent arc volcanism due to the Eurasia-Arabia convergence. The Late Miocene Tunceli basalts (11.4-11.0 Ma) are accepted as the beginning of post-collisional tectonics in Eastern Anatolia, while the Karakoçan (4.1 Ma) and Elazığ volcanic rocks (1.9-1.6 Ma) are accepted as being emplaced after the initiation of strike-slip movement on the North Anatolian and East Anatolian fault systems (Agostini et al., 2019) (Figure 1b).

Many studies were performed related to regional magmatism for all these reasons (Arger et al., 2000; Kürüm et al., 2008; Önal et al., 2008; Karşlı et al., 2008; Kaygusuz, 2009; Lebedev et al., 2016; Karaoğlu et al., 2020; Oyan et al., 2016; Kaygusuz et al., 2018; Rabayrol et al., 2019; Kürüm & Baykara, 2020). Magmatism beginning from the initiation of Arabian plate collision in the Late Oligocene and defined as Late Cenozoic magmatism in Eastern Anatolia displays a variation in character from alkaline (hawaiite, mugearite) (Oyan et al., 2017) to calcalkaline and weak tholeiitic characteristics linked to geographical, sedimentological and tectonic variations.

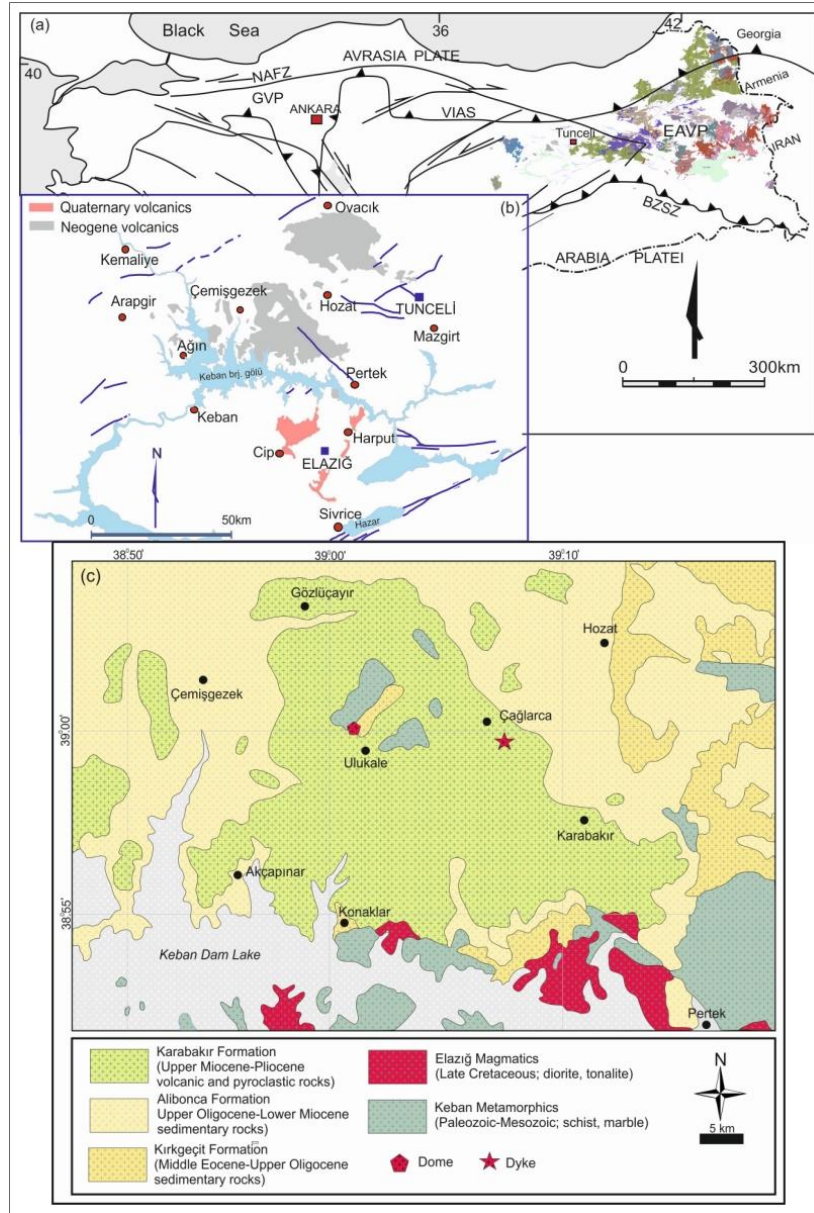


Figure 1. *a*) View of the simplified tectonic units of Turkey and post-collision spreading volcanism in Eastern Anatolia (East Anatolian Volcanic Province) (MTA, 2002), *b*) View of the spreading volcanism in Tunceli and Elazığ area, and location map of the study area, *c*) Simplified geological map of the Ulukale and Çağlarca around (redrawn from Geological Map of Turkey, 1:500.000, Sivas sheet) (from Kürüm et al., 2024). EAVP: East Anatolian Volcanic Province, GVP: Galatean Volcanic Province, VIAS: Vardar-Izmir-Ankara Suture Zone, NAFZ: North Anatolian Fault Zone, BZSZ: Bitlis Zagros Suture Zone.

Volcanism in the region appears to have variable composition and eruptive forms linked to compositional changes in the magma. For example, there are both Ocean Island Basalt (OIB)-type lavas with basic composition (Aydın et al., 2014; Kürkçüoğlu et al., 2015; Lustrino et al., 2010; Lebedev et al., 2016) and volcanics derived from the asthenospheric mantle (sub-slab) that is not affected by pre-collision subduction events (anorogenic volcanic rocks with in-plate geochemical features) (Kocaarslan & Ersoy, 2018). Depending on the different magma source formations, the composition of the volcanism in the region offers lava flow rocks ranging from basic to dacite/rhyolitic composition, as well as a rich pyroclastic sequence that is their equivalent (Pearce et al., 1990; Keskin et al., 1998; Yılmaz et al., 1998; Kürüm & Baykara, 2020). As

a general result of all these studies, a wide variety of models including different source areas, melting regimes and evolution processes have been created. Moreover, it is also stated that, differently, volcanism in Eastern Anatolia occurred by shallow melting of the previously metasomatized Anatolian continental lithosphere mantle and asthenosphere through decompression due to the collision of the Arabian and African asthenospheric mantles (Rabayrol et al., 2019).

4. LOCAL GEOLOGY AND VOLCANO-STRATIGRAPHY

Around Tunceli, there are Keban Metamorphites (Permo-Triassic) consisting of schists and crystallized limestones in the Paleozoic, Munzur Limestones (Jurassic-Cretaceous) and Elazığ Magmatics (Upper Cretaceous) in the Mesozoic, while in the Cenozoic; Eocene Kırkgeçit Formation in the turbiditic flysch facies, Oligo-Miocene Alibonca Formation and Miocene volcanics (Tunceli Volcanics/Karabakır Formation) crop out (Figure 1c). Of these units, only the Permo Triassic Keban Metamorphics form a contact with the Ulukale dome in the study area (Figure 1b). The Upper Cretaceous Elazığ Magmatic rocks basically comprise diorite group rocks (quartz diorite, diorite, monzodiorite and quartz monzodiorite) with granite, tonalite, quartz monzonite and gabbro (Kürüm et al., 2011; Sar et al., 2022). Dating studies for different lithologies determined the age of the unit varied from 59.77 ± 1.2 - 84.35 ± 1.7 Ma (Kürüm, 2011; Lin et al., 2015; Beyarslan & Bingöl, 2018; Sar et al., 2019). The Middle Eocene-Upper Oligocene Kırkgeçit Formation is found above the Elazığ Magmatic rocks in the south of the study region and are generally layered. The Upper Oligocene-Lower Miocene Alibonca Formation forms the boundary with the studied volcanic rocks. Volcanic rocks contacting metamorphics around Ulukale village have angular unconformity with the Alibonca Formation near Çemişgezek and with the Alibonca and Kırkgeçit Formations and Elazığ Magmatics to the south (Figure 1c).

Volcanism in the study area and close surroundings mainly formed explosive/extrusive volcanism products with a very thick sequence. These volcanic products, described as pyroclastic rocks, begin with tuffs above the Elazığ Magmatic rocks, Kırkgeçit and Alibonca Formation forming the basement around Çemişgezek in the west and in the south. Tuffs, occasionally forming very thick sequences, are basically not well consolidated and as a result of not being resistant to surface conditions, they form generally soft topography with ridges, with very severe erosion especially in river beds. In the field, weathered surfaces appear to be dirty white and gray in color.

Contrary to the common tuffs in the region, generally volcanic breccia forms the thickest sequence within pyroclastics. Found very widely, volcanic breccia formed of pebbles and blocks comprising many different grain sizes and shapes (from a few cm to m) contain occasional pumice levels and occasional lava layers locally or in pockets. Sometimes small-scale andesitic porphyry is observed to have intruded into tuff. Generally, the volcanic breccia comprise angular pebbles and blocks with different sizes and compositions, with nearly all pebble and block size grains having volcanic origin and being heterogeneous. This pyroclastic rocks appears to be the most important factor forming the current morphological structure of the region.

They reach thickest levels especially in the south close to the area containing dykes, on the south slopes of Akdemir (Şavak) village and south of Ulukale dome (Figure 2a, 2b). The rocks formed by the lava at the top of this thick sequence have not been eroded, so a very rugged and differently shaped terrain was formed due to erosion of less resistant pyroclastics (Figure 2b). Contrary to this, volcanism (lava rocks and pyroclastics) further west in the study area (W of Çemişgezek) generally form soft/smooth topography. Pyroclastic products in the region generally have tuff lithology. While lava flow rocks in the region have more basic composition and are more common in the west near Çemişgezek, the study area and surroundings have features of more acidic-intermediate composition.

The lava dome, which is the subject of the study, is thought to be the last product of volcanism in the region (Kürüm et al., 2024). This geological structure, which has an altitude of approximately 300m and a spreading area of 4.80km, is massive and differs from the surrounding pyroclastic and other volcanic rocks due to its very hard and crack-free feature (Figure 2a). It is expected that uplift-tilt and differentiation zones will be observed in the contact zones of the porphyritic dome, which is the final emplacement product of this type, with pyroclastics. Traces of dome formation are not observed in the surrounding rocks, probably due to high erosion. This dome, in which porphyritic texture is clearly observed, is thought to have formed sub-volcanically near the surface.

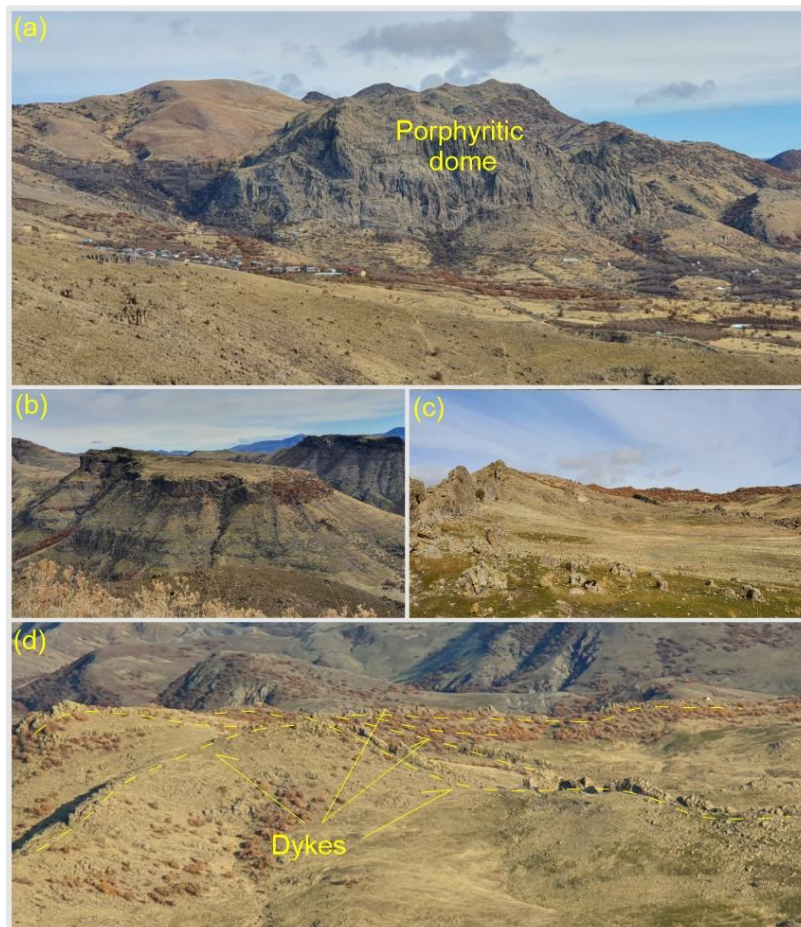


Figure 2. The view of the **a) b)** Ulukale porphyritic dome and **c) d)** Çağlarca radial dykes

The radial dykes, which constitute the subject of the study, extend in different directions from a central exit point, again within the pyroclastics and in accordance with theoretical definitions. Radial dykes, which were formed by settling in the fractures that reached the surface during the period when the volatile component of the magma decreased, are found in pyroclastic rocks. Seven dykes were identified from the same center in different directions and forming a radial shape (Figure 2c, 2d). Although the length and height of the dykes vary, their thickness is approximately similar. Generally, a very dense crack system is observed in all dykes. It is more altered and weaker than dome rock samples. The weathered surfaces of rocks with porphyritic texture generally appear in grayish colors. One of the longest dykes, the 3rd dyke from the left, is in the 20°SW direction from the exit center to the road and is approximately 1400 m long and is important because it creates a height of 10 m in places. This dyke changes direction 30° to the east approximately 150 m from the beginning (Figure 2d). The other important dyke in the region, the 6th dyke from the leftmost dyke, is in the 10°SE direction from the center of the outlet and is 1500 m long. The 4th and 5th dykes, which developed in approximately the same direction (20SW), are 360m and 550m long, respectively. The other two dykes extend towards the W and are relatively shorter.

Erciyes Volcano/volcanism (Holocene), which is one of the volcanoes showing a dome structure in the Central Anatolia Region, located further west of the study area, is a stratovolcano volcanism in which the products of different eruption types can be seen together. After the Koçdağ caldera, which is a large caldera, developed on the Erciyes Stratovolcano, many dome and cinder cones developed along the radial faults around the volcano. Domes are mostly acidic and medium in composition. Although the domes in the Erciyes volcanism are similar in composition to the Ulukale dome, they are different in terms of formation mechanism. Again, within the Central Anatolian volcanics, the Göllüdağ volcanism is composed of rhyolitic pyroclastics, dome settlements and lava flows. In Göllüdağ volcanism, post-caldera activities after caldera formation are manifested by local rhyolitic dome outflows (Atıcı & Türkecan, 2017).

5. DISCUSSION

5.1. Petrography

The rocks formed by lavas from the Ulukale porphyritic dome have a micro-porphyritic texture and consist mainly of plagioclase, biotite, amphibole, sanidine and quartz. Plagioclases are found as phenocrystals and microliths, and comprise the main phenocrystal phase in the rock (Fig 3a, 3b). Plagioclase phenocrysts occasionally contain dissolution structures and small prismatic plagioclase laths, indicating magma mixing (Hibbard, 1991). Biotites are the mineral most commonly found after plagioclase (Figure 3b-3d). Amphiboles are found as prismatic or hexagonal crystals (Figure 3d), sanidine crystals have Carlsbad twinning, while quartz are anhedral. Generally minerals in the rocks have low-moderate levels of alteration. The abundances of minerals found as phenocrystals in the rock; plagioclase > biotite > amphibole > sanidine > quartz. All these minerals also constitute the microcrystalline material of these porphyritic textured rocks. Some plagioclase minerals in the rock generally have alteration observed as seritization and clay mineral

formation, while oxidization or chloritization is clearly observed in the groundmass. Based on all these general textural and mineralogical features, the Ulukale porphyritic dome may be said to have trachyandesite composition.

The Çağlarca radial dykes are found with different lengths and different strikes from a center in the study area. Samples from these dykes have similar textural features to the Ulukale dome. The main mineral composition of the dykes comprises plagioclase, amphibole and biotite, in order of abundance, with lower rates for sanidine and quartz. Plagioclases are generally prismatic euhedral-subhedral crystals, polysynthetic and with albite twins and occasional zoned structure (Figure 3e). In dyke samples, different to dome samples, the most abundant mineral after plagioclase is amphibole (Figure 3e, 3f). Amphiboles, found at high rates within groundmass, are generally small crystals with euhedral-anhedral form. Biotite minerals found in dykes occasionally have bladed form indicating magma mixing, while they occasionally contain plagioclase and amphibole mineral inclusions. Sanidine phenocrrystals have Carlsbad twinning. Alteration observed in the rock in generally is seen in sanidines. Dykes with porphyritic textural features contain groundmass comprising microcrystalline forms of all minerals in the rock. Alteration in the rock in general is occasionally intensely observed in the groundmass, which appears to have dark color and be oxidized. The Çağlarca dykes have trachyandesite composition.

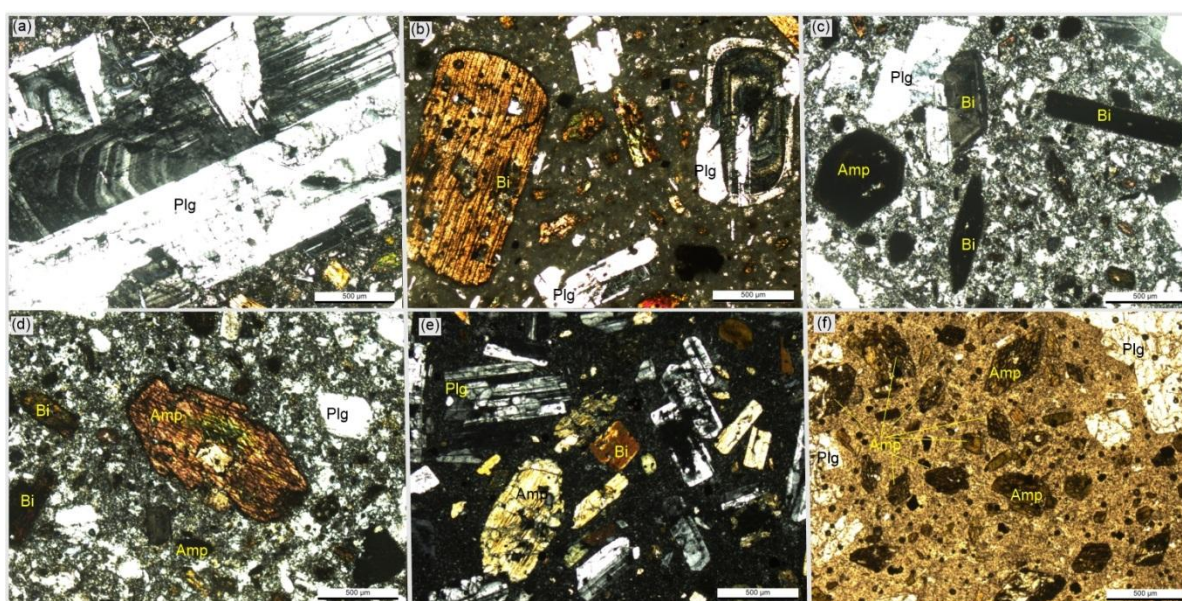


Figure 3. Representative photo micrographs of texture and mineral assemblages in the **a) b) c) d)** Ulukale porphyritic dome and **e) f)** Çağlarca radial dykes. Plg; Plagioclase, Amp; Amphibole, Bi; Biotite (**a-e**; cross-polarized light, **f**; plane-polarized light)

5.2. Mineral Chemistry

Analyses were performed on plagioclase, biotite, amphibole and pyroxene minerals identified in a total of five samples, two from the Ulukale porphyritic dome (Y1, Y5) and three from the Çağlarca radial dykes (Y6, Y9, Y11).

5.2.1. Plagioclase

Six different plagioclase minerals from two samples belonging to Ulukale porphyritic dome (Y1-Y5) were analyzed at a total of 37 points (Supplementary Table 1). Measurements in samples from the dome found the content of anorthite, orthoclase and albite varied from An_{38-22} , Or_{6-2} , Ab_{74-60} . According to these results, feldspars from porphyritic dome samples appear to have oligoclase and andesine composition (Figure 4).

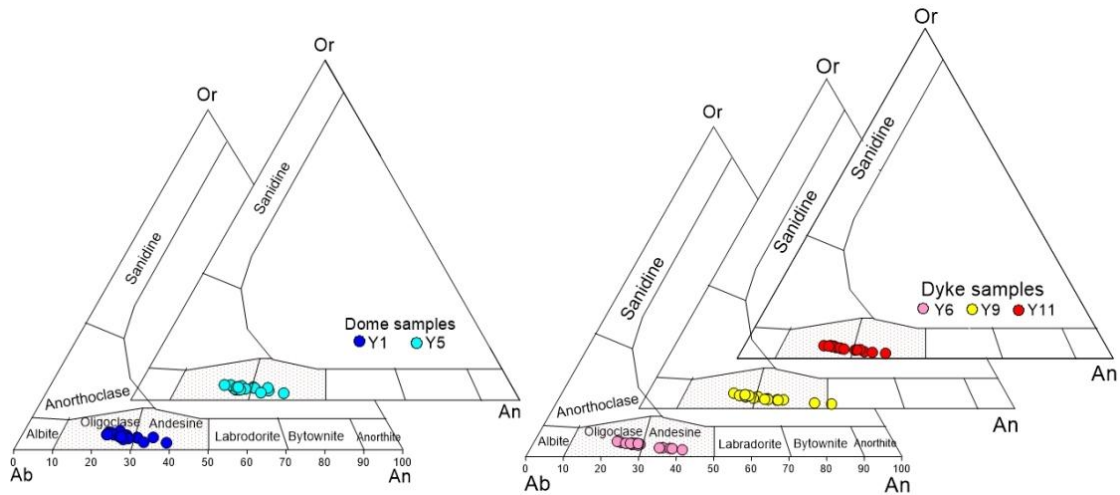


Figure 4. Composition of plagioclase in the classical An-Ab-Or scheme (Deer et al., 1992) for Ulukale dome and Çağlarca radial dykes

Ten different plagioclase minerals from three samples (Y6, Y9, Y11) from the dykes were analyzed at a total of 51 points (Supplementary Table 1). According to the analysis results, dyke samples had anorthite, orthoclase and albite contents varying in the interval An_{46-22} , Or_{5-1} , Ab_{75-48} . Based on these results, dykes appear to have similar plagioclase composition as samples from the dome. However, differently, plagioclase in the dykes had near equal rates of andesine-oligoclase composition and also had labradorite composition, though at low rates (Figure 4).

To determine the relationships between elements in plagioclase minerals, a binary variation graph of Na (apfu), Al (apfu), Ca (apfu) and K (apfu) versus Si (apfu) was drawn (Figure 5). All examples show similar trends, consistent with each other. This distribution of elements indicates fractionation.

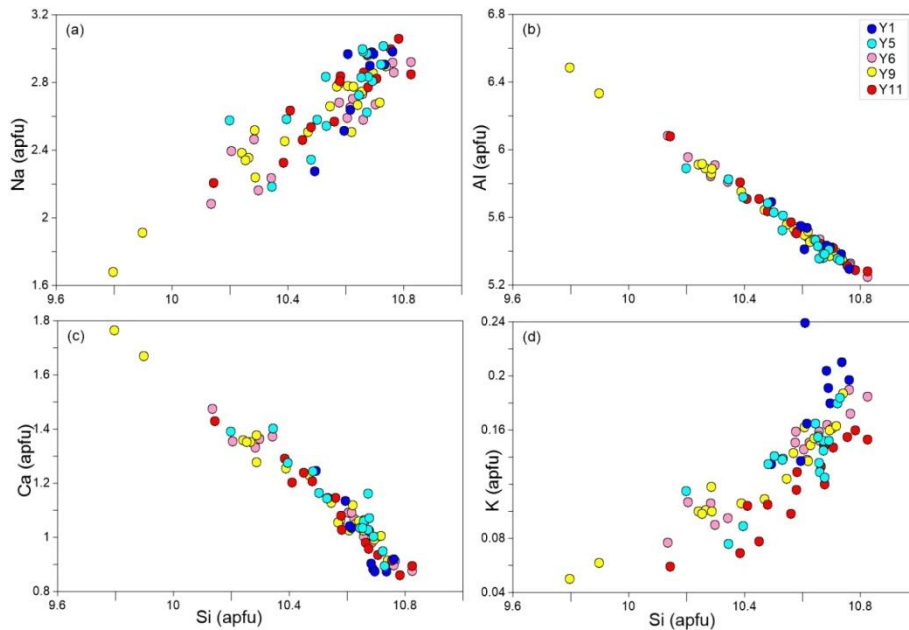


Figure 5. Change diagrams of elements according to Si (apfu) in plagioclase minerals

5.2.2. Pyroxene

Pyroxene mineral was detected only in dykes. In samples numbered Y9 and Y11, a total of 12 points were analyzed for 3 different pyroxene minerals. According to the analysis results calculations, the Mg# of samples Y9 and Y11 vary between 0.76-0.82- 0.73-1.12 respectively (Supplementary Table 2). To see the compositional changes of pyroxenes, binary graphs of element (cation, apfu) contents versus Mg# were drawn (Figure 6). Except for the two analysis points with the highest Mg# in the Figure 6, the other analyzes are generally compatible with each other. At these two samples Si, Ca, Na is at the lowest value and Ti, Al, Fe, K is at the highest value compared to the other points (Figure 6). This compositional difference may indicate that different thermodynamic conditions developed during crystallization. According to the $\text{Mg}_2\text{Si}_2\text{O}_6$ (Enstatite) - $\text{Ca}_2\text{Si}_2\text{O}_6$ (Wollastonite) - $\text{Fe}_2\text{Si}_2\text{O}_6$ (Ferrosillite) values calculated from the main element contents of pyroxenes, the pyroxene in radial dykes generally had augite composition. However, only two sample amount with hypersthene composition was identified (Figure 7a). It is accepted that especially Al and Ti elements in pyroxenes limit the pressure conditions in which the mineral crystallizes (Nekvasil et al., 2004). For this purpose, the diagram developed and calibrated from experiments on terrestrial alkaline basalts shows the pressure dependence of the Al-Ti ratio for pyroxenes in equilibrium with basaltic magma (Nekvasil et al., 2004). Pyroxenes crystallizing from magma with basic composition must have high Al-Ti ratios since they are formed under high pressure conditions. Accordingly, it is seen that the examined samples have a very low Al-Ti ratio (except for two samples with hypersthene composition) in the Al-Ti diagram (Figure 7b), therefore the pyroxenes in volcanics crystallize without any difference under low pressure conditions. Similarly, in Figure 7c and 7d, it can be seen that pyroxenes represent low-pressure conditions. In Figure 7c, despite the low Ca+Na content of the samples, the relatively higher Ti content indicates calc-alkaline basalt source which is also consistent with the geochemical data (Kürüm et al., 2024).

According to Al content, pyroxenes give the composition of crustal basalt (Figure 7d) and this also indicates equilibrium crystallization.

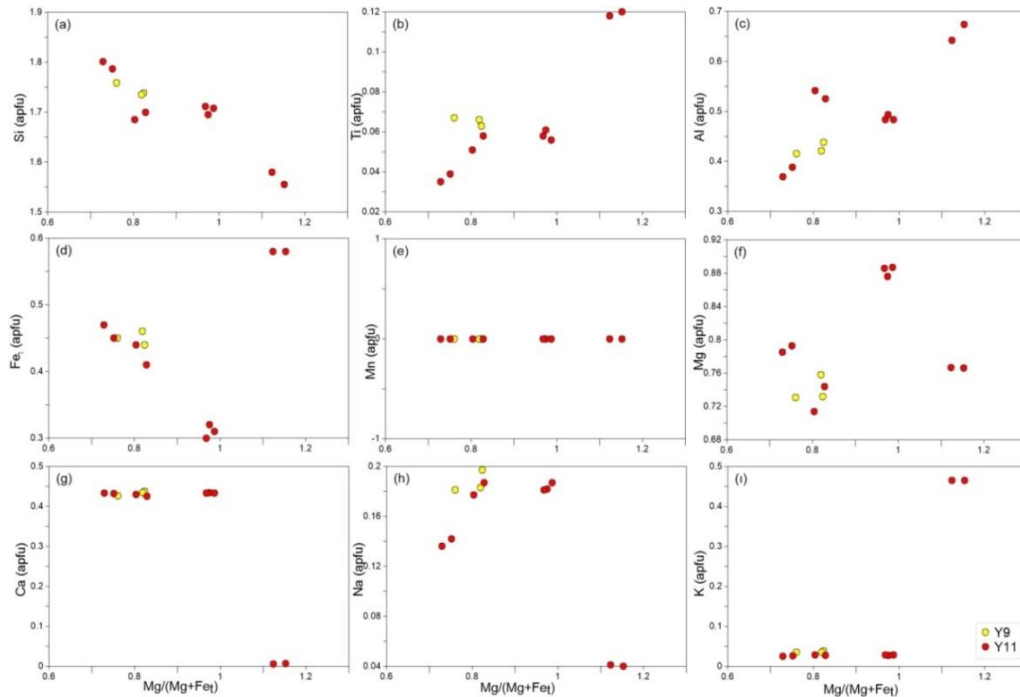


Figure 6. Binary variation diagrams for the main element compositions of pyroxenes

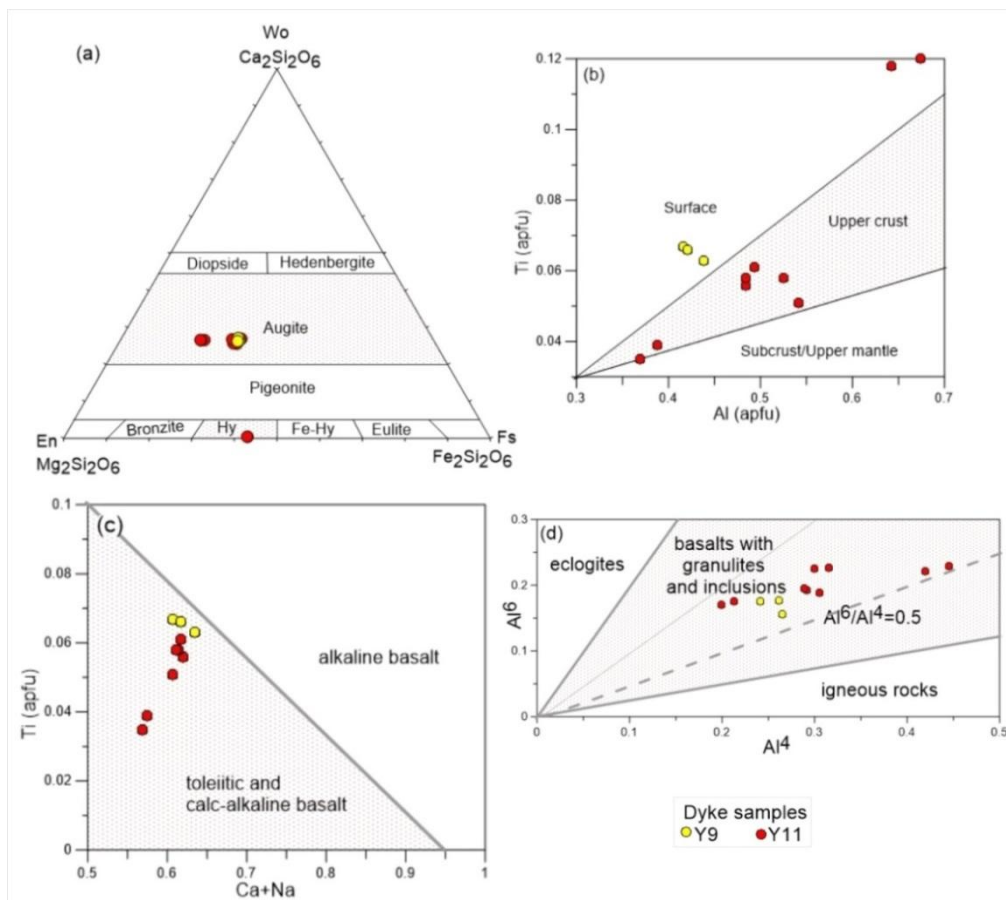


Figure 7. Classification and discriminant diagrams for pyroxene of volcanics that are the subject of the study. **a)** En–Wo–Fs diagram (Morimoto et al., 1988), **b)** Crystallization depth model according to Al–Ti

contents (Nekvasil et al., 2004), **c**) Ti vs (Ca+Na) diagram (Leterrier et al., 1982), **d**) Al^6 vs Al^4 (Aydın et al., 2009)

5.2.3. Amphibole

From the studied rocks, one sample from the porphyritic dome (Y1) and three samples (Y6, Y9, Y11) from the dykes had amphibole mineral chemistry analysis performed. A total of 14 points in 3 different minerals in the sample from the dome were analyzed. A total of 59 points were analyzed in 10 different amphibole minerals from the dykes, with three minerals from sample Y6, four minerals from sample Y9 and three minerals from sample Y11. Analysis data and calculations from all samples are given in Supplementary Table 3. The Si value of the Ulukale porphyritic dome amphibole samples is 5.60-6.58 apfu, except for one sample, and the Si value of the dykes is the same as the Si 5.86-6.58 apfu. Although the Mg values of domes and dykes, varying between 0.55-0.74% and 0.60-0.75%, are similar, and especially Ca (0.00-1.63; 1.67-1.86) values are different. According to Si and Mg# values, it is seen that amphiboles are mainly composed of hastingsite and magnesiohastingsite (Figure 8a). A smaller number of samples also have ferrodentite composition.

Additionally, it is seen that their amphiboles do not exceed the values of Si = 7,500 (apfu), which represents the silica content limit of magmatic amphiboles according to Leake (1971) (Figure 8b). The identification of all samples as magmatic amphiboles indicates that metasomatism is not effective in these amphiboles.

In experimental studies, it has been determined that oxygen fugacity exerts a dominant control on the Fe/(Fe+Mg) ratio of mafic silicates (Zhang et al., 2015; references in the paper). Created for this purpose, the Al^{IV} vs. Fe/(Fe+Mg) diagram (Anderson & Smith, 1995), it can be said that the amphiboles of the rocks under study were formed under very different - high and low - oxygen fugacity conditions (Figure 8c). All amphibole samples show the same feature. In the TiO_2 and Al_2O_3 diagram (Jiang & An, 1984) created based on amphibole main oxide data used to distinguish magma sources, a few dyke samples reflect the mantle-crust feature, while most of the samples are concentrated in the mantle source region (Figure 8d). The dome samples are located entirely in the mantle region. Samples indicating mantle origin according to Al_2O_3 content indicate mantle+crust mixing source according to MgO content. This can be considered as a sign of mafic magma settling/mixing in the felsic magma chamber in the crust.

5.2.4. Biotite

Biotites are common ferromagnesian silicate minerals in the rocks under study where it occurs as an early- to late-stage crystallization mineral. Total of 6-18 different points had biotite mineral chemistry analysis performed in 11 different biotite minerals obtained from 5 samples (Y1-Y5-Y6-Y9-Y11) from both dome and dykes rocks (Supplementary Table 4). The biotites in dome and dykes show variation in SiO_2 content from 45.5-34.6 and 36.9-32.9 wt% respectively. Dyke biotite samples had total Al content from 2.8-2.5% atoms per formula unit (apfu), with this ratio varying from 2.7-2.5% apfu in Ulukale porphyritic dome

samples. The $\text{Fe}^{2+}/(\text{Fe}^{2+}+\text{Mg})$ and Mg content all of the samples (dome and dykes) is approximately 0.5-0.3 apfu 2.9-3.8 apfu respectively.

According to the International Mineralogical Association (IMA) classification, biotite; It is divided into four end members: annite $[\text{KFe}_2+3\text{AlSi}_3\text{O}_{10}(\text{OH})_2]$, phlogopite $[\text{KMg}_3\text{AlSi}_3\text{O}_{10}(\text{OH})_2]$, siderophyllite $[\text{KFe}_2\text{Al}(\text{Al}_2\text{Si}_2)\text{O}_{10}(\text{OH})_2]$ and eastonite $[\text{KMg}_2\text{Al}(\text{Al}_2\text{Si}_2\text{O}_{10})(\text{OH})_2]$ (Rieder et al., 1998).

According to this, following the classification of Tröger (1982), all Çağlarca radial dykes had biotite (meroxene) composition, while the dome samples meroxene and phlogopite composition (Figure 9a). The fact that the total Al content and $\text{Fe}^{2+}/(\text{Fe}^{2+}+\text{Mg})$ ratios in biotite are low and do not change supports the relationship with the absence of continental collision or continental contamination (Lalonde & Bernard, 1993).

It is suggested that biotites are divided into two: magmatic and hydrothermal (Jacobs & Parry, 1979; Fu, 1981). It is accepted that igneous biotites crystallize directly from silicate melt and generally have molecular ratios of $\text{Mg}/\text{Fe} < 1.0$, while hydrothermal biotites have $\text{Mg}/\text{Fe} > 1.5$ [65]. Similarly, Fu [66] reported in his study that magmatic biotites have high titanium ($\text{TiO}_2 > 3\%$) and low aluminum content ($\text{Al}_2\text{O}_3 < 15\%$), while neoform biotites have low titanium ($\text{TiO}_2 < 3\%$ and mostly $< 2\%$) and high aluminum ($\text{Al}_2\text{O}_3 > 15\%$) content.

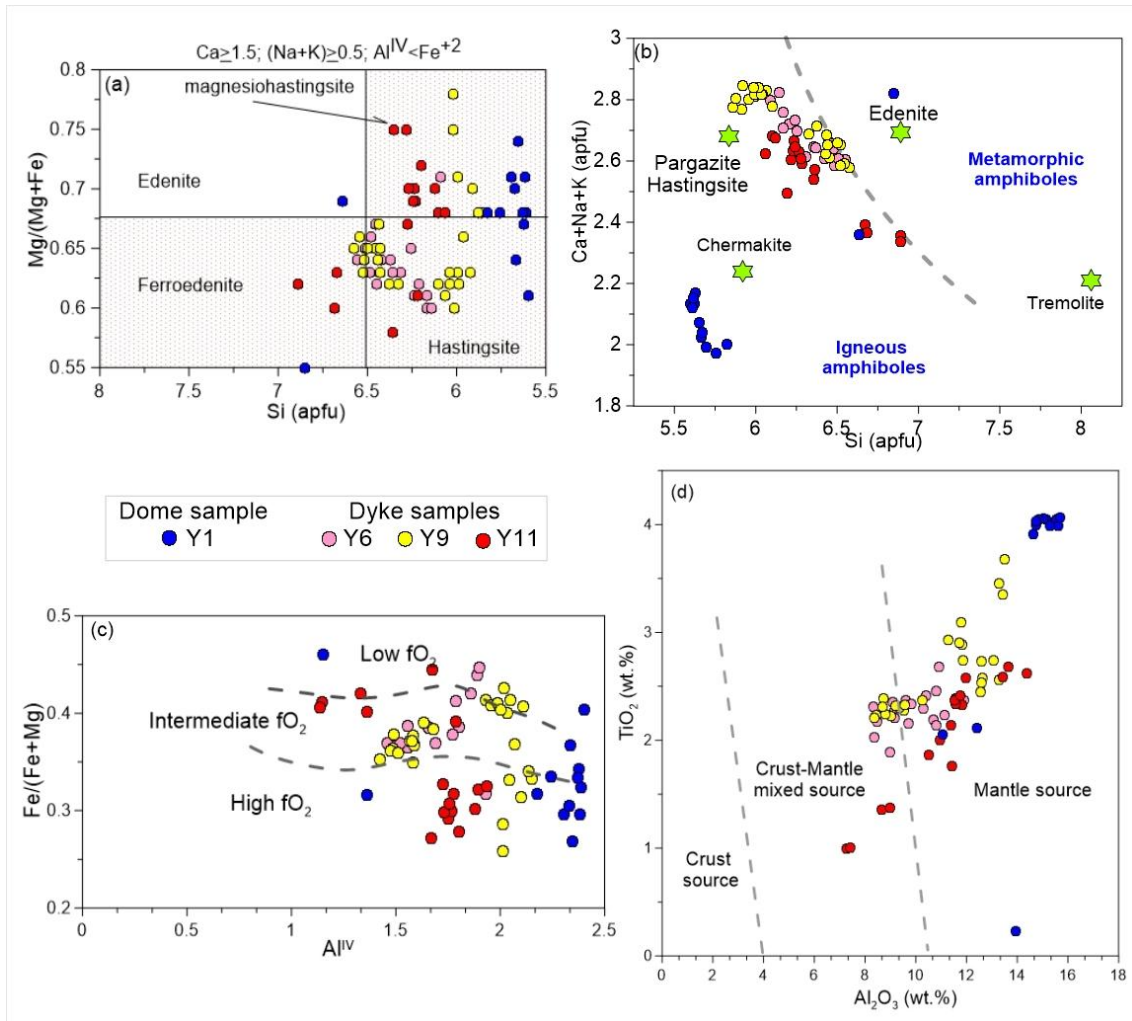


Figure 8. *a*) Plots of amphibole classification diagram (Leake et al., 1997), *b*) Discrimination of magmatic and metamorphic amphibole according to Si vs. (Ca+Na+K) diagram of the Ulukale porphyritic dome and Çağlarca radial dyke samples, *c*) Al^{IV} vs. Fe/(Fe+Mg) diagram (Anderson & Smith, 1995) showing the possible oxygen fugacity conditions during the crystallization, *d*) TiO₂ vs. Al₂O₃ magma source diagram for amphiboles (Jiang & An, 1984)

Accordingly, while the biotites subject to study are compatible with neoform biotites with Mg/Fe ratios varying between 1.4-2.5 they have the characteristics of magmatic biotite in terms of TiO₂ (>3% in all samples) and Al₂O₃ (dykes <15, dome samples generally <15) contents. In the FeO+MnO-MgO-10TiO₂ triangle diagram of biotites (Nachit et al., 1985), it is seen that they are primary and re-equilibrated primary biotites (Şekil 9b). Biotites were not affected by evolution or late-stage low-temperature hydrothermal fluids (secondary crystallization). The FeO/(FeO+MgO) vs. MgO diagram suggests that all of the dykes samples and dome-Y6 sample were derived from crust-mantle mixed source while dome-Y1 sample was derived from mantle source (Figure 9c).

The Ti concentration in biotite depends on the crystallization temperature and oxygen fugacity (fO₂) of biotite (Henry et al., 2005). Accordingly, low Ti content is associated with low crystallization temperature (Henry et al., 2005). According to Robert (1976) definition, the Ti content of biotite in primary magmas is generally high compared to re-equilibrated/hydrothermal/neo-formed and late-stage crystallizing magmas.

For this purpose, the Ti contents of our samples (dome and dykes 0.61-0.41) were compared with the Ti contents (0.24-0.15) of hydrothermal biotites (Tang et al., 2019). In the diagram created according to Ti, Mg and Fe contents to determine the formation temperatures of biotite (Deniz, 2022), it is seen that biotite has a pressure of 4-6 kbar and a crystallization temperature of 700-800°C (Figure 9d).

Biotite chemistry is considered to be important in elucidating the petrogenesis of rocks. For this purpose, in the diagram created according to MgO--Al₂O₃ contents [61], the samples are concentrated in the orogenic magma area with calc-alkaline characteristics (Figure 9e).

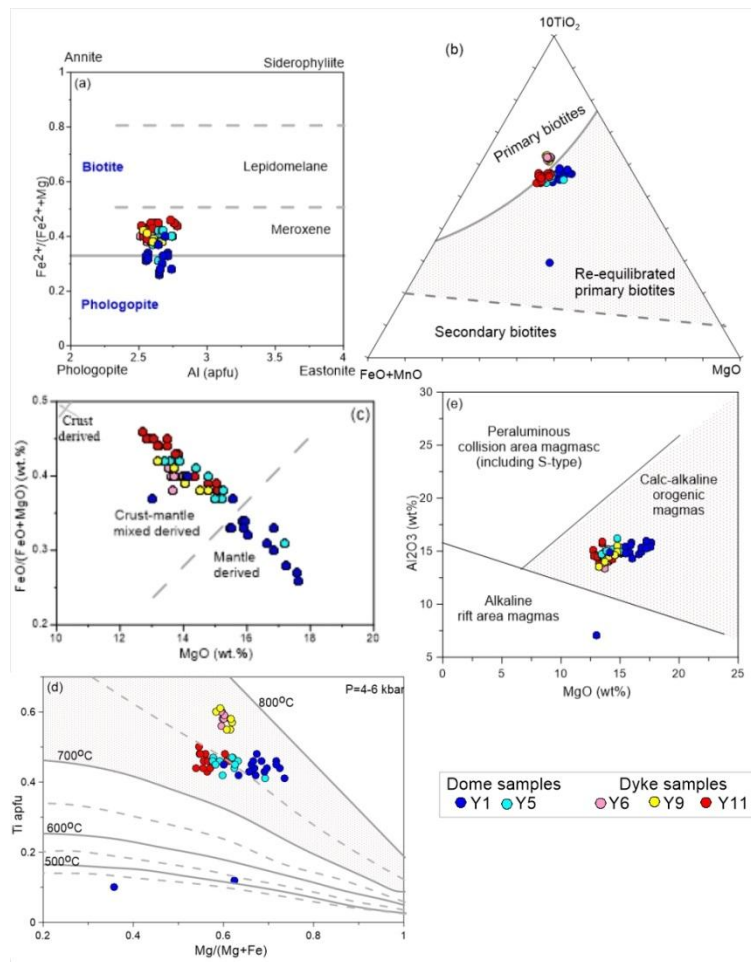


Figure 9. Diagrams commenting biotites belonging to the Ulukale dome and Çağlarca dykes. **a)** Nomenclature of biotite in the $Fe^{2+}/(Fe^{2+} + Mg)$ vs. Al (apfu) diagram **b)** $FeO+MnO-10xTiO_2-MgO$ triangular diagram (Nachit et al., 1985), **c)** Plots of $FeO/FeO+MgO$ vs. MgO for biotite (Zhou, 1986), **d)** Sample distribution in the temperature isotherm ($^{\circ}C$) diagram calculated according to Ti and $Mg/(Mg+Fe)$ (Tang et al., 2019), **e)** Plots of biotite composition in the MgO vs. Al_2O_3 diagram (Abdel-Rahman, 1994)

6. CONCLUSION

This study was conducted within the Late Miocene aged Tunceli Volcanics (Karabakır Formation), -with a dome with a height of approximately 300 m and a perimeter of 4800m- and reveals the petrography and mineral chemistry characteristics of dykes (seven) of different lengths, extending from a center at different angles to form a radial shape.

Petrographic investigations identified that rocks forming the dome had basic mineral composition of plagioclase and biotite with lower amounts of amphibole, quartz and sanidine, while the basic mineral composition of the dykes was plagioclase, amphibole and sanidine with lower amounts of biotite and quartz. Among the dome and dykes with porphyritic texture and trachyandesite composition, the rocks forming the dome have larger mineral sizes and more intense alteration than the dykes. Melting-dissolution structures in plagioclase and the presence of blade-shaped biotite minerals in dykes are petrographic features that indicate magma mixing.

Plagioclase belonging to porphyritic domes and dykes is in the composition of oligoclase and andesine. The compositional similarity of plagioclase in dome and dykes is also the same in the relationships between elements. Such distributions among the elements indicate the fractionation in plagioclase.

In the chemical analysis of two pyroxene minerals found only in dykes, pyroxenes are in the composition of augite and hypersthene (two samples). Element distributions are generally consistent (except for two examples). This compositional difference is caused by the presence of hypersthene mineral as an inclusion in the augite mineral. While hypersthene with more basic composition has high Al and Ti content, samples with augite composition contain lower Al and Ti. These pyroxenes, which have calc-alkaline properties, were affected by the equilibrium crystallization conditions that enable them to crystallize under low pressure conditions (upper crust + surface conditions).

The amphiboles are mainly composed of hastingsite and magnesiohastingsite. These minerals, which originate from the mantle and feature magmatic amphibole, have different oxygen fugacity (low-medium-high). Dome samples have characteristics with a more basic composition than dyke samples.

While biotites are meroxene in composition in dykes, they are phlogopite in dome samples. Element changes/contents in biotites indicate that these minerals are of magmatic origin and primary - re-equilibrated primary biotites. Although dome and dyke samples are generally similar in terms of element distribution, dome sample Y1 points to the mantle source area, while other samples point to a crust-mantle mixture. These biotites, which feature calc-alkaline orogenic magma, were formed in the temperature range of 700-800°C.

In conclusion; while one of the two dome analysis indicates a more basic composition and mantle source, while plagioclase, amphibole, and biotite minerals in and other dome and dykes specimens show generally similar properties. The elemental contents of these minerals indicate that these rocks are of magmatic origin and have not been affected by metamorphism. The fact that pyroxene mineral analysis was performed on only dyke samples makes it difficult to fully compare the domes and dykes in terms of this mineral and, accordingly, to interpret whether the magma forming the dome and dykes are the same/different. However, when all data are taken into account, the mantle-derived magma that started to form the dome, and later completed the development of both the dome and the dykes with the mantle and crust+mantle interaction. The formation of mantle+crust magma and temperature changes in biotite minerals (700-800°C) resulting

from these data can be considered as indicators of post-collision crustal thickening in the Eastern Anatolia Region.

AUTHOR CONTRIBUTIONS

Conceptualization, S.K, A.S and M.Y.Y.; project management, S.K.; fieldwork, S.K and M.Y.Y.; title, S.K. and A.S.; laboratory work, A.S and M.Y.Y.; formal analysis, S.K.; data curation, S.K. and A.S.; manuscript-original draft, S.K.; manuscript-review and editing, S.K.; visualization, S.K, A.S and M.Y.Y.; All authors have read and legally accepted the final version of the article published in the journal.” Authorship should be limited to those who contributed significantly to the article.

ACKNOWLEDGEMENT

The authors would like to thank the Firat University Scientific Research Projects Unit (FÜBAP) for research support (Project number FÜBAP-MF.20.22).

CONFLICT OF INTEREST

The authors declare that they have no conflicts of interest.

REFERENCES

- Abdel-Rahman, A.F.M. (1994). Nature of Biotites from Alkaline, Calc-Alkaline, and Peraluminous Magmas. *Journal of Petrology*, 35(2), 525-541. <https://doi.org/10.1093/petrology/35.2.525>
- Agostini, S., Savaşçın, M.Y., Di Giuseppe, P., Di Stefano, F., & et al. (2019). Neogene volcanism in Elazığ-Tunceli area (eastern Anatolia): geochronological and petrological constraints. *Ital. Jour. Geosci.*, vol. 138, 435-455. <https://doi.org/10.3301/IJG.2019.18>
- Anderson, J. L., & Smith, D. R. (1995). The Effects of Temperature and fO₂ on the Al-in Hornblende Barometer. *American Mineralogist*, 80, 549-559.
- Arger, J., Mitchel, J., & Westaway, R.W.C. (2000). Neogene and Quaternary volcanism of southeastern Turkey. *Geological Society, London, Special Publications*, 173(1), 459-487. <https://doi.org/10.1144/GSL.SP.2000.173.01.22>
- Atıcı, G., & Türkecan, A. (2017). Anadolu'nun volkanları, *Doğal Kay. Eko. Bült.*, 22, 1-18.
- Aydın, F., Karanlı, O., & Sadıklar, M.B., (2009). Compositional variations, zoning types and petrogenetic implications of low-pressure clinopyroxenes in the neogene alkaline volcanic rocks of northeastern Turkey. *Turkish J. Earth Sci.*, 18, 163-186. <https://doi.org/10.3906/yer-0802-2>
- Aydın, F., Schmitt, A.K., Siebel, W., Sönmez, M., & et al. (2014). Quaternary bimodal volcanism in the Niğde Volcanic Complex (Cappadocia, Central Anatolia-Turkey): age, petrogenesis and geodynamic implications. *Contributions to Mineralogy and Petrology*, 168, 2-24. <https://doi.org/10.1007/s00410-014-1078-3>

- Ball, J. L., Calder, E. S., Hubbard, B. E., & Bernstein, M. L. (2013). An assessment of hydrothermal alteration in the Santiaguito lava dome complex, Guatemala: implications for dome collapse hazards. *Bull. Volcanol.*, 75, 676. <https://doi.org/10.1007/s00445-012-0676-z>
- Beyarslan, M., & Bingöl, A.F. (2018). Zircon U-Pb age and geochemical constraints on the origin and tectonic implications of late cretaceous intra-oceanic arc magmatics in the Southeast Anatolian Orogenic Belt (SE-Turkey). *Journal of African Earth Sciences*, 147, 477-497. <https://doi.org/10.1016/j.jafrearsci.2018.07.001>
- Cassidy, M., Manga, M., Cashman, K., & Bachmann, O. (2018). Controls on explosive-effusive volcanic eruption styles. *Nat. Commun.*, 2839, <https://doi.org/10.1038/s41467-018-05293-3>
- Deer, W.A., Howie, R.A., & Zussman, J. (1992). An introduction to the rock forming minerals. 2nd ed. Harlow, Essex, England, New York, *Longman scientific and technical, London*.
- Deniz, K., (2022). Mica Types as Indication of Magma Nature, Central Anatolia, Turkey. *Acta Geologica Sinica*, 96(3), 844-857. <https://doi.org/10.1111/1755-6724.14670>
- Edmonds, M., Sides, I.R., Swanson, D.A., Werner, C., Martin, R.S., & et al. (2013). Magma storage, transport and degassing during the 2008-10 summit eruption at Kilauea volcano, Hawaii. *Geochim. Cosmochim. Acta*, 123, 284-301. <https://doi.org/10.1016/j.gca.2013.05.038>
- Fink, J.H., & Griffiths, R.W. (1998). Morphology, eruption rates, and rheology of lava domes: Insights from laboratory models. *J. Geophys. Res.*, 103, 527-545. <https://doi.org/10.1029/97JB02838>
- Fu, J.B. (1981). Chemical composition of biotite in porphyry copper deposits. *Geology and Prospecting*, 9, 16-19.
- Henry, D.J., Guidotti, C.V., & Thomson, J.A. (2005). The Ti saturation surface for low to medium pressure metapelitic biotite: Implications for geothermometry and Ti substitution mechanism. *Amer. Mineral.*, 90, 316-328. <https://doi.org/10.2138/am.2005.1498>
- Hibbard, M. J. (1991). Textural anatomy of twelve magma mixed granitoid systems. In: J. Didier, and B. Barbarin, (Eds.), *Enclaves and Granite Petrology. Development in Petrology*, (pp. 431-444). 6546968
- Horwell, C.J., Baxter, P.J., Hillman, S.E., Calkins, J.A., & et al. (2013). Physicochemical and toxicological profiling of ash from the 2010 and 2011 eruptions of Eyjafjallajökull and Grímsvötn volcanoes, Iceland using a rapid respiratory hazard assessment protocol. *Environ. Res.*, 127, 63-73. <https://doi.org/10.1016/j.envres.2013.08.011>
- Hu, J., Zhou, H., Peng, P.A., & Spiro, B. (2016). Seasonal variability in concentrations and fluxes of glycerol dialkyl glycerol tetraethers in Huguangyan Maar Lake, SE China: implications for the applicability of the MBT-CBT paleo temperature proxy in lacustrine settings. *Chem. Geol.*, 420, 200-212. <https://doi.org/10.1016/j.chemgeo.2015.11.008>
- İmer, A., Richards, J.P., Creaser, R.A., & Spell, T.L. (2015). The late Oligocene Cevizlidere Cu-AuMo deposit, Tunceli Province, eastern Turkey. *Mineralium Deposita*, 50, 245-263. <https://doi.org/10.1007/s00126-014-0533-4>

- Innocenti, F., Mazzuoli, R., Pasquar, G., Radicati Di Brozolo, F., & Villari, L. (1982). Tertiary and quaternary volcanism of the Erzurum-Kars area (Eastern Turkey): Geochronological data and geodynamic evolution. *J. Volcanol. Geotherm. Res.*, 13, 223-240. [https://doi.org/10.1016/0377-0273\(82\)90052-X](https://doi.org/10.1016/0377-0273(82)90052-X)
- Jacobs, D.C. & Parry, W.T. (1979). Geochemistry of biotite in the Santa Rita porphyry copper deposit, New Mexico. *Economic Geology*, 74(4), 860-887. <https://doi.org/10.2113/gsecongeo.74.4.860>
- Jiang, C. & An, S. (1984). On chemical characteristics of calcific amphiboles from igneous rocks and their petrogenesis significance. *Journal of Mineralogy and Petrology*, 3, 1-9.
- Karaoğlu, Ö., Browning, J., Bazargan, M., & Gudmundsson, A. (2016). Numerical modelling of triple-junction tectonics at Karlıova, Eastern Turkey, with implications for regional magma transport. *Earth and Planetary Science Letters*, 452, 157-170. <https://doi.org/10.1016/j.epsl.2016.07.037>
- Karaoğlu, O., Selçuk, A.S., & Gudmundsson, A. (2017). Tectonic controls on the Karlıova triple junction (Turkey): Implications for tectonic inversion and the initiation of volcanism. *Tectonophysics*, 694, 368-384. <https://doi.org/10.1016/j.tecto.2016.11.018>
- Karaoğlu, Ö., Gülmez, F., Göçmengil, G., Lustrino, M., & et al. (2020). Petrological evolution of Karlıova-Varto volcanism (Eastern Turkey): Magma genesis in a transtensional triple-junction tectonic setting. *Lithos*, 364-365, 105524. <https://doi.org/10.1016/j.lithos.2020.105524>
- Karlı, O., Chen, B., Uysal, I., Aydın, F., Wijbrans, J.R., & Kandemir, R. (2008). Elemental and Sr-Nd-Pb isotopic geochemistry of the most recent Quaternary volcanism in the Erzincan Basin, eastern Turkey: framework for the evaluation of basalt-lower crust interaction. *Lithos*, 106, 55-70. <https://doi.org/10.1016/j.lithos.2008.06.008>
- Kaygusuz, A. (2009). K/Ar Ages and geochemistry of the collision related volcanic rocks in the İlica (Erzurum) area, eastern Turkey, *Neues Jahrbuch für Mineralogie*, 186, 21-36. <https://doi.org/10.1127/0077-7757/2009/0134>
- Kaygusuz, A., Aslan, Z., Aydınçakır, E., Yücel, C., Gücer, M.A., & Şen, C. (2018). Geochemical and Sr-Nd-Pb isotope characteristics of the Miocene to Pliocene volcanic rocks from the Kandilli (Erzurum) area, Eastern Anatolia (Turkey): Implications for magma evolution in extension-related origin. *Lithos*, 296, 332-351. <https://doi.org/10.1016/j.lithos.2017.11.003>
- Keskin, M. (2005). Domal uplift and volcanism in a collision zone without a mantle plume: Evidence from Eastern Anatolia. [URL](#)
- Keskin, M., Pearce, J.A., & Mitchell, J. (1998). Volcano-stratigraphy and geochemistry of collision-related volcanism on the Erzurum-Kars Plateau, northeastern Turkey. *Journal of Volcanology and Geothermal Research*, 85, 355-404. [https://doi.org/10.1016/S0377-0273\(98\)00063-8](https://doi.org/10.1016/S0377-0273(98)00063-8)
- Kocaarslan, A., & Ersoy, E.Y. (2018). Petrologic evolution of Miocene-Pliocene mafic volcanism in the Kangal and Gürün basins (Sivas-Malatya), central east Anatolia: evidence for Miocene anorogenic magmas contaminated by continental crust. *Lithos*, 310-311, 392-408. <https://doi.org/10.1016/j.lithos.2018.04.021>

- Kuşçu, İ., Kuşçu, G.G., Tosdal, R., & Andrew, C.J. (2007). *Tectonomagmatic-metallogenic framework of mineralization events in the southern NeoTethyan arc, southeastern Turkey*. Digging Deeper. Proceedings of the 9th Biennial SGA Meeting, Dublin, (pp. 20-23).
- Kürkçüoğlu, B., Pickard, M., Şen, P., Hanan, B.B., Sayit, K. & et al. (2015). Geochemistry of mafic lavas from Sivas, Turkey and the evolution of Anatolian lithosphere. *Lithos*, 232, 229-241. <https://doi.org/10.1016/j.lithos.2015.07.006> [Get rights and content](#)
- Kürüm, S. (2011). K-Ar age, geochemical, and Sr-Pb isotopic compositions of Keban magmatics, Elazığ, Eastern Anatolia, Turkey. *National Sci.*, 3(9), 750-767. <https://doi.org/10.4236/ns.2011.39100>
- Kürüm, S., & Baykara, T. (2020). Geochemistry of Post-Collisional Yolçatı (Bingöl) Volcanic Rocks in Eastern Anatolia, Turkey. *African Earth Sciences*, 161, 103-153. <https://doi.org/10.1016/j.jafrearsci.2019.103653>
- Kürüm, S., Önal, A., Boztuğ, D., Spell, T., & Arslan, M. (2008). ⁴⁰Ar/³⁹Ar age and geochemistry of the post-collisional Miocene Yamadağ volcanics in the Arapkir area (Malatya Province), eastern Anatolia, Turkey. *Journal of Asian Earth Sciences*, 33, 229-251. <https://doi.org/10.1016/j.jseaes.2007.12.001>
- Kürüm S., Akgül B., Önal A.Ö., Boztuğ D., Harlavan Y., & Ural M. (2011). An Example for Arc-Type Granitoids along Collisional Zones: The Pertek Granitoid, Taurus Orogenic Belt, Turkey. *International Journal of Geosciences*, 2, 214-226. ISSN Online: 2156-8367
- Kürüm, S., Sar, A., Yurt, M.Y., & Yıldırım, İ. (2024). Petrological Features of Neogene Ulukale Porphyritic Dome and Çağlarca Radial Dykes in the Tunceli Volcanic, Eastern Turkey. *Doklady Earth Sciences*, 518(2), 1665-1678. ISSN 1028-334X.
- Lalonde, A.E., & Bernard, P. (1993). Composition and colour of biotite from granites: two useful properties in the characterization of plutonic suites from the Hepburn internal zone of the Wopmay orogen, Northwest Territories. *Canadian Mineralogist*, 31, 203-217.
- Leake, B.E. (1971). On aluminous and edenitic amphiboles. *Mineralogical Magazine* 38, 389-407. <https://doi.org/10.1180/minmag.1971.038.296.01>
- Leake, B.E., Woolley, A.R., Arps, C.E.S., Birch, W.D., Gilbert, M.C., & et al. (1997). Nomenclature of amphiboles Report of the Subcommittee on Amphiboles of the International Mineralogical Association Commission on New Minerals and Mineral Names. *European Journal of Mineralogy*, 9, 623-651. <https://doi.org/10.1127/ejm/9/3/0623>
- Lebedev, V., Sharkov, E., Ünal, E., & Keskin, M. (2016). Late Pleistocene Tendürek Volcano (Eastern Anatolia, Turkey): I. Geochronology and petrographic characteristics of igneous rocks. *Petrology*, 24, 127-152. <https://doi.org/10.1134/s0869591116030048>
- Leterrier, J., Maury, R.C., Thonon, P., Girard, D., & Marchal, M. (1982). Clinopyroxene composition as a method of identification of the magmatic affinities of paleo-volcanic series. *Earth and Planetary Science Letters*, 59, 139-154. [https://doi.org/10.1016/0012-821X\(82\)90122-4](https://doi.org/10.1016/0012-821X(82)90122-4)

- Lin, Y.C., Chung, S.L., Bingöl, A.F., Beyarslan, M., & Lee, H.Y. (2015). *Petrogenesis of late Cretaceous Elazığ magmatic rocks from SE Turkey: New age and geochemical and Sr-Nd-Hf isotopic constraints*. Goldschmidt, 16-21 August Prag, Abstracts, 1869
- Lustrino, M., Keskin, M., Mattioli, M., Lebedev, V.A., & Chugaev, A. (2010). Early activity of the largest Cenozoic shield volcano in the circum-Mediterranean area: Mt. Karacadağ, SE Turkey. *European Journal of Mineralogy*, 22, 343-362. <https://doi.org/10.1127/0935-1221/2010/0022-2024>
- Morimoto N., Fabries J., Ferguson A.K., Ginzburg I.V., Ross M., & et al. (1988). Nomenclature of pyroxenes. *Mineralogy and Petrology*, 39, 55-76.
- MTA. (2002). Geological map of Turkey. 1:500,000. MTA, Ankara, Turkey
- Nachit, H., Razafimahefa, N., Stussi, J.M., & Caron, J.P. (1985). Composition chimique des Biotites et typologie magmatique des granitoids. C.R. Academic Sciences Paris, Series 2, 301, 813-818. INIST identifier 9284353
- Nekvasil, H., Dondolini, A., Horn, J., Filiberto, J., Long, H., & Lindsley, D.H. (2004). The origin and evolution of silica-saturated alkalic suites: an experimental study. *Journal of Petro.* 45, 693-721. <https://doi.org/10.1093/petrology/egg103>
- Oyan, V., Keskin, M., Lebedev, V.A., Chugaev, A.V., & Sharkov, E.V. (2016). Magmatic evolution of the Early Pliocene Etrüsk stratovolcano, eastern Anatolian collision zone, Turkey. *Lithos*, 256, 88-108. <https://doi.org/10.1016/j.lithos.2016.03.017>
- Oyan, V., Keskin, M., Lebedev, V.A., Chugaev, A.V., Sharkov, E.V., & Ünal, E. (2017). Petrology and Geochemistry of the Quaternary Mafic Volcanism in the northeast of Lake Van, Eastern Anatolian Collision Zone, Turkey. *Journal of Petrology*, 58, 1701-1728. <https://doi.org/10.1093/petrology/egx070>
- Önal, A., Boztuğ, D., Arslan, M., Spell, T.L., & Kürüm, S. (2008). Petrology and ⁴⁰Ar-³⁹Ar age of the bimodal Orduzu Volcanics (Malatya) from the western end of the eastern Anatolian Neogene volcanism, Turkey. *Turkish Journal of Earth Sci.*, 17, 85-109. <https://journals.tubitak.gov.tr/earth/vol17/iss1/4>
- Özdemir, Y., Karaoğlu, Ö., Tolluoğlu, A.Ü., & Güleç, N. (2006). Volcanostratigraphy and petrogenesis of the Nemrut stratovolcano (East Anatolian high plateau): the most recent post-collisional volcanism in Turkey. *Chemical Geology*, 226, 189-211. <https://doi.org/10.1016/j.chemgeo.2005.09.020>
- Pearce, J., Bender, J., De Long, S., Kidd, W., Low, P., & et al. (1990). Genesis of collision volcanism in Eastern Anatolia, Turkey. *Journal of Volcanology and Geothermal Research*, 44, 189-229. [https://doi.org/10.1016/0377-0273\(90\)90018-B](https://doi.org/10.1016/0377-0273(90)90018-B)
- Rabayrol, F., Hart, C.J.R., & Thorkelson, D.J. (2019). Temporal, spatial and geochemical evolution of late Cenozoic post-subduction magmatism in central and eastern Anatolia, Turkey. *Lithos*, 336(337), 67-96. <https://doi.org/10.1016/j.lithos.2019.03.022>
- Rieder, M., Cavazzini, G., D'Yakonov, Y.S., Frankkamenetskii, V.A., Gottardi, G., & et al. (1998). Nomenclature of the mica. *Canadian Mineralogist* 36, 905-912.

- Robert, J.L. (1976). Titanium solubility in synthetic phlogopite solid solutions. *Chemical Geology*, 17(3): 213-227.
- Rosas-Carbajal, M., Komorowski, J.C. Nicollin, F., & Gibert, D. (2016). Volcano electrical tomography unveils edifice collapse hazard linked to hydrothermal system structure and dynamics, *Sci. Rep.*, 6, 29899.
- Sar, A., Ertürk, M.A., & Rizeli, M.E. (2019). Genesis of Late Cretaceous intra-oceanic arc intrusions in the Pertek area of Tunceli Province, eastern Turkey, and implications for the geodynamic evolution of the southern Neo-Tethys: Results of zircon U–Pb geochronology and geochemical and Sr-Nd isotopic analyses, *Lithos*, 105263, 350-351. <https://doi.org/10.1016/j.lithos.2019.105263>
- Sar, A., Rizeli, M.E., & Ertürk, M.A. (2022). Petrographic and Geochemical Characteristics of the Rocks Belonging to the Elazığ Magmatic Complex in the Geçityaka region (Tunceli). *El-Cezerî Journal of Science and Engineering*, 9(2), 680-694. <https://doi.org/10.31202/ecjse.993333>
- Tang, P., Yuchuan, Y., Tang, J., Wang, Y., Zheng, W., & et al. (2019). Advances in research of mineral chemistry of magmatic and hydrothermal biotites. *Acta Geologica Sinica*, 93(6), 1947-1966. <https://doi.org/10.1111/1755-6724.14395>
- Tröger, W.E. (1982). *Optische Bestimmung der gesteinsbildenden Minerale, Teil 2*. Schweizerbartsche Verlagsbuchhandlung, Stuttgart. (pp.822)
- Turner, M., Turner, S., Mironov, N., Portnyagin, M., & Hoernle, K. (2017). Can magmatic water contents be estimated from clinopyroxene phenocrysts in some lavas? A case study with implications for the origin of the Azores Islands. *Chem Geol.*, 466, 436-445. <https://doi.org/10.1016/j.chemgeo.2017.06.032>
- Xu, W., Zhao, Z., & Dai, L. (2020). Post-collisional mafic magmatism: Record of lithospheric mantle evolution in continental orogenic belt. *Science China Earth Sciences*, 63, 2029-2041. <https://doi.org/10.1007/s11430-019-9611-9>
- Yılmaz, Y., Güner, Y., & Şaroğlu, F. (1998). Geology of the quaternary volcanic centres of the east Anatolia. *Journal of Volc. and Geoth. Research*, 85, 173-210. [https://doi.org/10.1016/S0377-0273\(98\)00055-9](https://doi.org/10.1016/S0377-0273(98)00055-9)
- Zhang, J.Q., Li, S.R., Santosh, M., Wang, J-Z., & Li, Q. (2015). Mineral chemistry of high-Mg diorites and skarn in the Han-Xing Iron deposits of South Taihang Mountains, China: Constraints on mineralization process, *Ore Geology Reviews*, 64, 200-214. <https://doi.org/10.1016/j.oregeorev.2014.07.007>
- Zhou, Z.X. (1986). The origin of intrusive mass in Fengshandong, Hubei province. *Acta Petrol. Sin.*, 2 (1), 59-70 (in Chinese with English abstract).



Gazi University

Journal of Science

PART A: ENGINEERING AND INNOVATION

<http://dergipark.org.tr/guj.1592619>

Geochemical and Mineralogical Differentiation of Tepekent Basalts: A Multivariate Analysis Approach (NW of Konya-Central Anatolia)

Gülin GENCOGLU KORKMAZ^{1*} ¹ Konya Technical University, Engineering and Natural Sciences Faculty, Department of Geological Engineering, Türkiye

| Keywords | Abstract |
|---|--|
| Basalt Olivine PCA Pyroxene Replenishment UMAP | This study investigates the mineralogical, petrographic, and geochemical characteristics of Miocene-aged basaltic rocks from the Tepekent region to distinguish and correlate them with other members of the Sulutuş Volcanic Complex (SVC), particularly the Ulumuhsine and Yükselen basalts. Advanced geostatistical methods such as Principal Component Analysis (PCA), Uniform Manifold Approximation and Projection (UMAP), and k-medoids clustering analysis were applied to correlate the basaltic lava flows. While some overlaps were identified in whole-rock compositions, significant differences were observed in the mineral chemistry. The investigated basalts are primarily composed of plagioclase, with lesser amounts of olivine, pyroxene, and Fe-Ti oxides. Clinopyroxenes from the Tepekent basalts exhibit oscillatory zoning in MgO, CaO, Cr ₂ O ₃ , and TiO ₂ contents, indicating magma recharge from a more mafic mantle source. Olivine phenocrysts show disequilibrium with their host magma but are in equilibrium with the most mafic Ulumuhsine basalt, suggesting they were derived from earlier solidified phases and subsequently incorporated into the system during magma ascent or convective processes within the magma chamber. Irregular An fluctuations and sieve textures in plagioclase crystals further support the presence of magma replenishment processes. Although isotopic data are indispensable in provenance studies to definitively identify magma sources and establish genetic relationships in greater detail, this study demonstrates how mineral chemistry and geostatistical analyses can effectively differentiate basaltic lava flows and elucidate complex magma chamber processes. The findings highlight the interplay between crustal contamination, mantle-derived magma replenishment, and multi-stage magmatic evolution, providing valuable insights into the volcanic history of Central Anatolia. |

Cite
Gencoglu Korkmaz, G. (2025). Geochemical and Mineralogical Differentiation of Tepekent Basalts: A Multivariate Analysis Approach (NW of Konya-Central Anatolia). *GU J Sci, Part A, 12(1)*, 250-267. doi:10.54287/guj.1592619

| Author ID (ORCID Number) | Article Process |
|--------------------------|-----------------------------------|
| 0000-0003-0185-2806 | Gülin GENCOGLU KORKMAZ |
| | Submission Date 28.11.2024 |
| | Revision Date 08.01.2025 |
| | Accepted Date 20.01.2025 |
| | Published Date 26.03.2025 |

1. INTRODUCTION

Subduction zone volcanism is characterized by multi-stage, multi-source, and multi-process magmatism, resulting in the formation and coexistence of magmas with diverse origins and compositions. The Late Mesozoic-Neogene geology of Turkey is closely linked to the opening and closure of the Neotethys Ocean (Şengör, 1979; Şengör & Yılmaz, 1981). In Central Anatolia, widespread Cenozoic volcanism is related to these tectonic events, with several volcanic provinces and complexes, such as the Galatia Volcanic Province (GVP), the Cappadocia Volcanic Province (CVP), the Sulutaş Volcanic Complex (SVC), the Erenlerdağ-Alacadağ Volcanic Complex (EAVC), the Karapınar Volcanic Field (KPVF), and the Karacadağ Volcanic Complex (KCVC), forming key geological features of the region (Şengör & Yılmaz, 1981; Aydar & Gourgaud,

*Corresponding Author, e-mail: gkorkmaz@ktun.edu.tr

1998; Deniel et al., 1998; Uslular & Gençaliöđlu-Kuřcu, 2019; Asan et al., 2021; Gençođlu Korkmaz et al., 2022) (Figure 1).

The Sulutař Volcanic Complex (SVC), located in the northwest of Konya, is part of the Neogene bimodal volcanic activity in Central Anatolia (Figure 1). It exhibits a diverse composition, including shoshonitic, calc-alkaline, high-K calc-alkaline, and Na-alkaline magmas. Bimodal volcanism, dominated by mafic and felsic products with the scarcity of intermediate compositions, reflects complex tectonic and magmatic processes. Previous studies have indicated that both crustal contamination and source enrichment played significant roles in the compositional diversity of the SVC (Gençođlu Korkmaz et al., 2017; Asan et al., 2021). The SVC is situated within a graben-type extensional basin near Konya, bounded to the east by the Konya Fault Zone. This basin, filled with Neogene-aged sedimentary units, is underlain by Paleozoic and Mesozoic ophiolitic and metamorphic basement rocks. The extensional tectonics of the basin are linked to the rollback of a subduction zone associated with the Cyprus Arc, a result of the interaction between the African and Eurasian plates, which shaped the region's geodynamic evolution (Biryol et al., 2011; Delph et al., 2015; Gençođlu Korkmaz et al., 2017). Neogene volcanic rocks, particularly dacitic and basaltic lava flows, are exposed in the east and west of the study area, and include enclaves of varying sizes. Dacites occur as lava flows and volcanic necks, while basalts form lava flows, cutting through pre-Neogene units (Gençođlu Korkmaz et al., 2017).

Previous studies (Asan et al., 2021) yielded $^{40}\text{Ar}/^{39}\text{Ar}$ plateau and inverse isochron ages of 12.07 ± 0.06 Ma to 12.21 ± 0.32 Ma for the dacites and 11.01 ± 0.42 Ma to 11.05 ± 0.64 Ma for the calc-alkaline basalts in the Ulumuhsine-Küçükmuhsine region. On the other hand, a whole-rock sample from Yükselen basalts gave two plateau ages of 16.45 ± 0.76 Ma and 22.37 ± 0.65 Ma for the first and subsequent steps, respectively. These basalts are sodic alkaline, characterized by ocean island basalt (OIB)-like anorogenic geochemical signatures. Basaltic rocks with $\text{MgO} > 4$ wt% (Pecerrillo, 2005) are key in deciphering mantle source compositions as they represent primary mantle-derived melts. Typically, basalts with elevated Cr (1000 ppm), Ni (400 ppm), and MgO (~8 wt%) contents reflect derivation from a primary mantle source (Weaver, 1991; Best, 2003). However, in the Tepeken region, the studied basaltic rocks show lower MgO, Cr, and Ni values, indicating they are highly evolved and not representative of primary mantle melts (Eryiđit et al., 2022). Despite this, their enriched nature allows them to be plotted on Nb/La-La/Yb and Zr/Y-Zr/Nb diagrams to assess degrees of melting and enrichment. Low Zr/Y (4.8-10.9) and Zr/Nb (8.11-15.29) values suggest partial melting of a lithospheric mantle source, with the enrichment likely due to subduction-related recycling of ancient oceanic crust (Eryiđit et al., 2022).

In this study, the Miocene-aged basaltic rocks from the Tepeken region are classified and correlated with those from Ulumuhsine and Yükselen, using mineral chemistry data and geostatistical methods (PCA, UMAP, K-means clustering). By examining clinopyroxene and olivine mineral chemistry, relationships between the lava flows are established and their magmatic evolution is discussed. This integrated approach provides a deeper understanding of the Tepeken basalts and contributes to the broader knowledge of the Sulutař Volcanic

Complex, offering insights into the complex magmatic history of the Neogene volcanic activity in Central Anatolia.

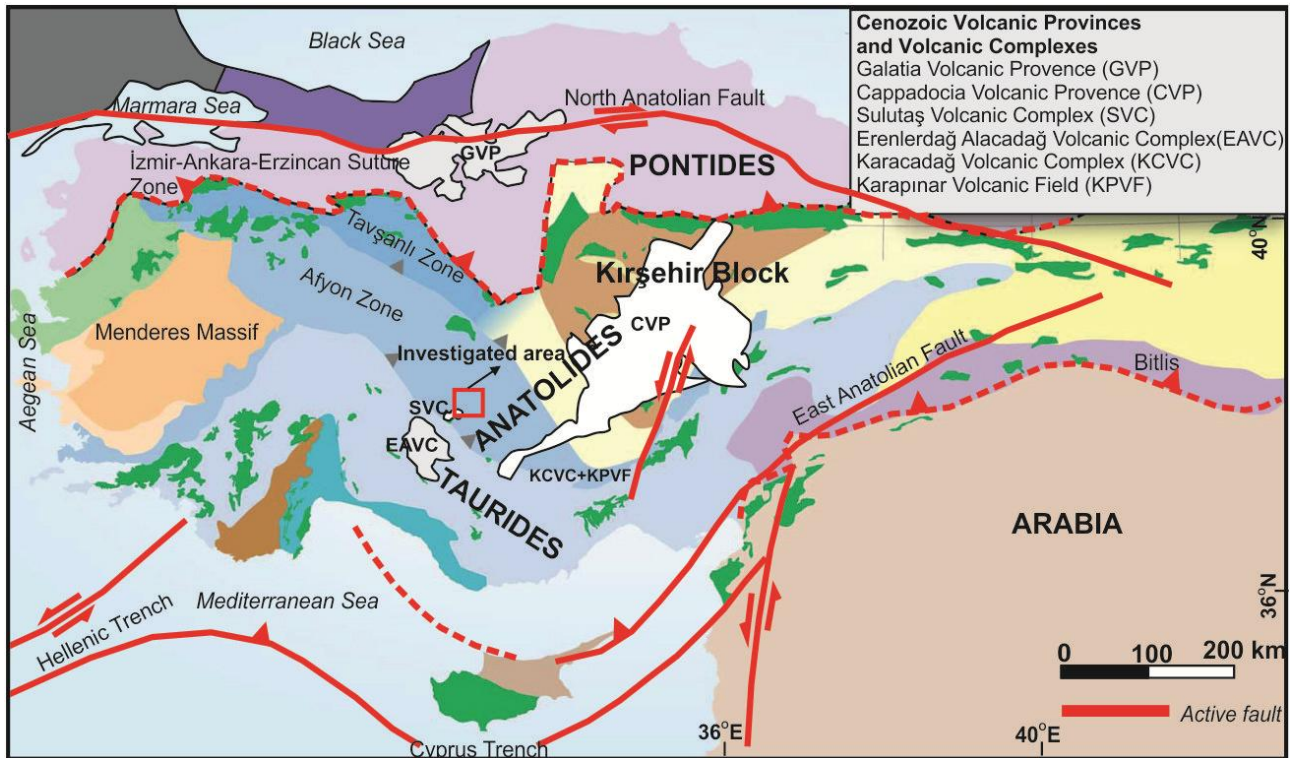


Figure 1. Active tectonic map of Turkey showing Cenozoic Volcanic Provinces was modified from Van Hinsbergen et al. (2016). Map was taken from Gençoglu Korkmaz and Kurt (2024)

2. MATERIAL AND METHOD

For petrographic and mineral chemistry analyses, approximately ten hand samples of basaltic rocks were collected from the Tepekent area (Konya, Central Anatolia). The sampling strategy was guided by whole-rock chemistry data published in Eryiğit et al. (2022). To strengthen the robustness of our analysis, additional data from the literature (Asan et al., 2021) were compiled and utilized for correlation and statistical evaluations.

Four carbon-coated, polished thin sections were prepared for mineral chemistry studies. The analyses were performed using a JEOL JXA-8600 electron microprobe at YEBIM (Ankara University), equipped with four wavelength-dispersive spectrometers (WDS) and an integrated energy-dispersive spectrometer (EDS) system. The operating parameters included a 20 nA beam current, 15 kV accelerating voltage, and a 20-second counting time per element. Detailed procedures for the analyses follow the methods described in Deniz and Kadioğlu (2019). Structural formulae for pyroxenes were calculated based on four cations and six oxygens, for olivines based on four oxygens, while for feldspars, calculations were based on eight oxygens.

Thermobarometric conditions were determined using multiple methods. The clinopyroxene-liquid thermobarometers by Neave and Putirka (2017) and Putirka (2008a) and Lindsley and Andersen's (1983) pyroxene thermometer were employed for P-T estimations. The plagioclase thermobarometer (Putirka, 2008b)

was also applied to evaluate geothermal conditions. Equilibrium conditions for clinopyroxene-glass pairs and olivine-glass pairs were verified using the $K_d(\text{Fe-Mg})$ value of 0.27 ± 0.03 (Putirka, 2008a) and 0.29 ± 0.03 (Matzen et al., 2011; Putirka, 2016), respectively. WinPyrox and WinPLtb software (Yavuz, 2013; Yavuz & Yildirim, 2018) were used for additional evaluations of hygrometric and depth conditions.

For geochemical interpretations, Iqpet software (Carr, 1990) was utilized. Moreover, statistical analysis (Principal Component Analysis (PCA), Uniform Manifold Approximation and Projection (UMAP) and k-medoids analysis) were generated to assess geostatistical variations and to enhance the overall geochemical analysis.

3. RESULTS AND DISCUSSION

3.1. Results

Petrography and Mineral chemistry of the Tepekent basalts

The investigated basalts outcrop as lava flows in a very restricted area (Figure 2a and 2b) near Karardi Tepe (Tepekent region). They predominantly display holocrystalline porphyritic texture, with olivine and clinopyroxene as the dominant mafic mineral phases (Figure 2c-2f). The rocks consist of approximately 65% plagioclase, 15% olivine, 10% clinopyroxene, 5% sanidine and 5% opaque minerals (Figure 2c-2f). Zeolitization is observed locally within the basalts (Figure 2e). Olivines are predominantly occur as microphenocrysts, with rare occurrences of phenocrysts. In certain areas, fracture-filling and crack-filling structures are noted, along with iddingsite alteration along the crystal boundaries (Figure 2c-2f). Clinopyroxenes are primarily observed as microphenocrysts, while plagioclases are observed as both microlith and microphenocrysts.

In the studied basalts, the feldspar minerals are predominantly represented by labradorite, with rare occurrences of sanidine (Figure 3). While plagioclases are primarily labradorite, their rims occasionally display compositions of andesine or bytownite. (Figure 3 and see Supplementary data). Normal, inverse, and oscillatory zoning patterns are observed in some plagioclases, as indicated by variations in MgO, TiO₂, CaO, and An contents. As well as anorthite contents range between (An₄₇₋₇₂) from the core to the rim (see Supplementary data). Moreover, some of the plagioclase microphenocrysts and phenocrysts show sieve textures.

Pyroxenes are augite and diopside based on Morimoto et al. (1988) (Figure 4a) and WinPyrox software Yavuz (2013). $Mg\#$ of the pyroxenes ranges between 64-85. Investigated pyroxenes exhibit normal, reverse and oscillatory zoning in terms of MgO, TiO₂, Cr₂O₃ and CaO (see Supplementary data). Reverse and oscillatory zoning within MgO -TiO₂ and Cr₂O₃ contents indicate reheating processes (magma mixing, new magma input and recharging) and mafic replenishment before the eruption (Gençoğlu Korkmaz, 2019; Ubide et al., 2014a;

2014b; 2014c). Using clinopyroxene-melt pairs that satisfy the conditions ($Kd_{Fe-Mg}=0.27\pm 0.03$), yielding temperatures between 973 and 1080 °C and pressures ranging from 1 to 5.7 kbar. Temperature estimates for clinopyroxenes were also calculated according to Lindsley and Andersen (1983) (Figure 4b). When the clinopyroxenes were plotted on the pyroxene quadrilateral, the sample points aligned with isotherms between 950 and 1300 °C (Figure 4b). Although these values represent a broader temperature range, they generally align with the temperature values obtained Putirka (2008a), suggesting consistency.

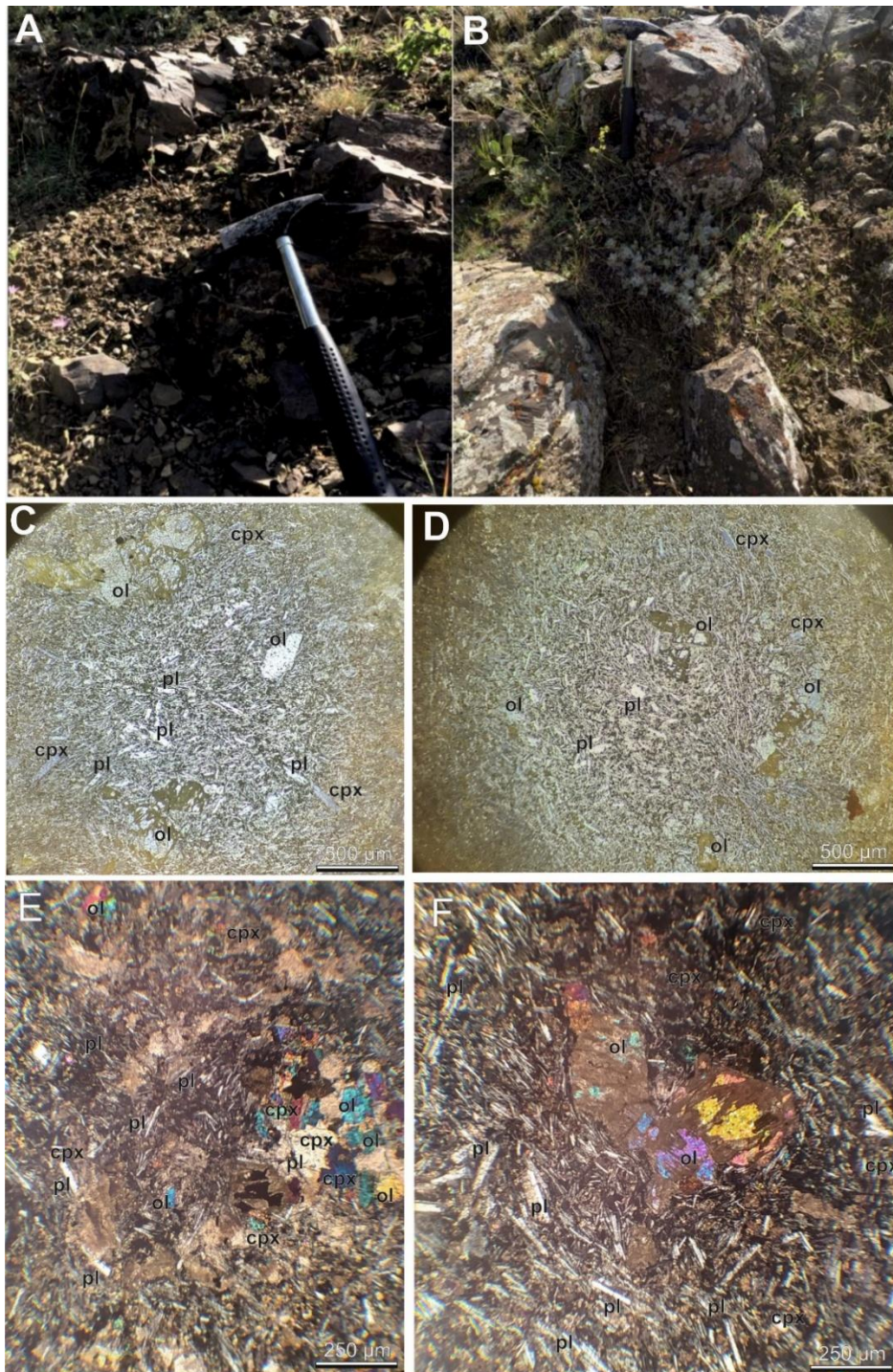


Figure 2. a), b) Field appearance of the Tepekent basalts; c), d), e), f) Microphotographs of the investigated basalts. Mineral abbreviations are based on Whitney and Evans (2009)

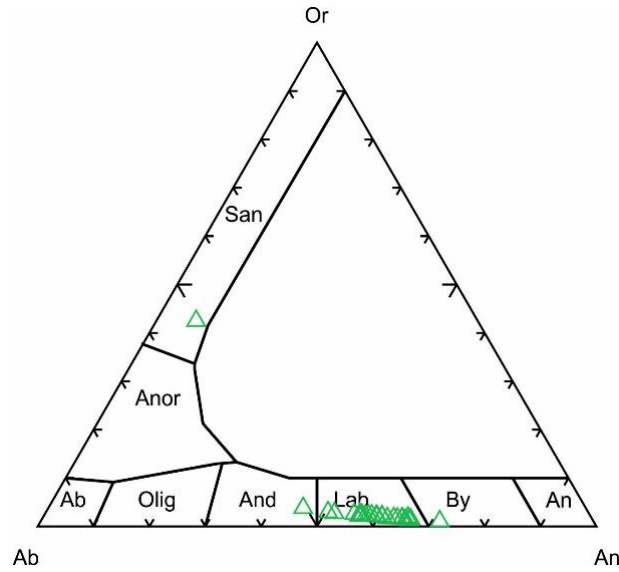


Figure 3. Ab-An-Or classification diagram (Deer et al., 1963) of the feldspars from the investigated rocks.

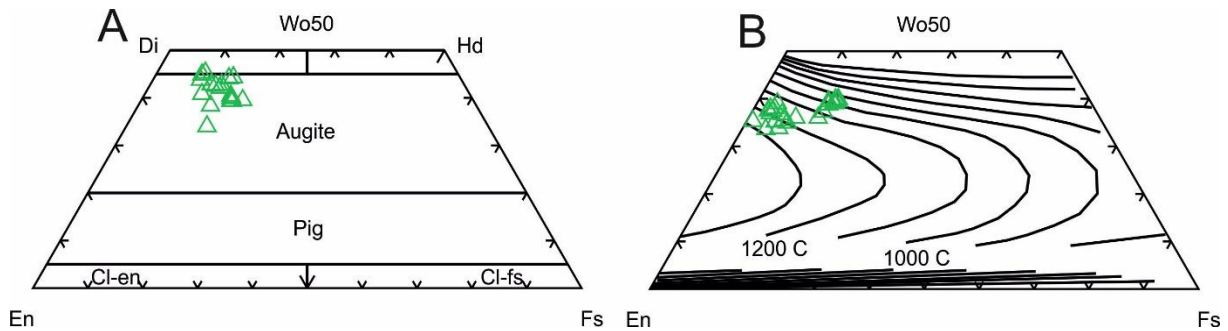


Figure 4. a) Morimoto et al. (1988) pyroxene classification diagram and b) Crystallization temperatures based on Lindsley and Andersen (1983)

Fo content [$Fo = 100 \times Mg/(Mg + Fe)$ in mol%] of the measured olivines ranges between 67-82. Major elements compositions were recorded in the olivine from the basalts: 0.001 to 0.014 wt%, Cr_2O_3 ; 0.16 to 0.5 wt%, CaO; 35-44 wt%, MgO. They are relatively homogeneous with Fo composition. Although many olivines in the same sample have been normal zoned in terms of Fo, some olivines have not displayed homogeneous distributions within Cr_2O_3 , TiO_2 and CaO contents (see Supplementary data). Using olivine-melt pairs that satisfy the conditions ($Kd_{Fe-Mg}=0.30\pm0.03$), the calculations were made for temperature values are around 1200°C.

3.2 Discussion

Chemical Relationship between the Miocene Basalts in the SVC

In the north-northwest of Konya, basaltic rocks are represented by a restricted basaltic sill or dike, which has previously been attributed to the Miocene-aged Sulutaş Volcanic Complex (Gençoğlu Korkmaz et al., 2017; Asan et al., 2021). In this study, the Tepekent basalts are examined alongside the previously reported Yükselen and Ulumuhsine basalts (Gençoğlu Korkmaz et al., 2017; Asan et al., 2021) to make correlation and perform the evaluation. The basaltic lavas in the Yükselen area, which outcrop over a restricted region, exhibit a distinct

whole-rock composition compared to the Ulumuhsine and Tepekent basalts. These lavas are alkaline basalts (Figure 5) and were previously classified as hawaiite-type sodic alkali basalts (Gençoğlu Korkmaz et al., 2017).

Silica versus major and trace element diagrams reveal a significant compositional distinction between the Yükselen hawaiites and the other basalts, with the former exhibiting a more mafic character. In contrast, no clear relationship indicating fractional crystallization (FC) is observed between the Ulumuhsine and Tepekent basalts (Figure 6 and 7). The major oxides and trace elements do not display homogeneous distributions, which suggests that the observed heterogeneity is better explained by assimilation-fractional crystallization (AFC) contamination processes rather than by FC alone (Figure 6 and 7). Nevertheless, certain trace elements, such as Zr, Yb, and Sr, exhibit similar concentrations across both basalt types, indicating underlying geochemical affinities.

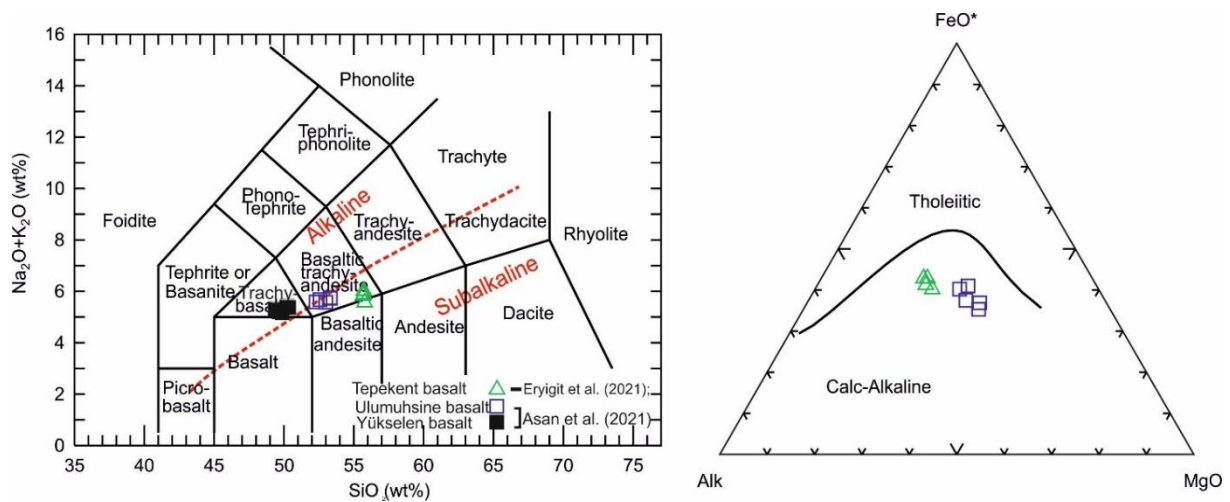


Figure 5. a) Total alkali-silica (TAS) rock classification diagram based on Irvine and Baragar (1971) and **b)** AFM diagram for subalkaline rocks (Irvine and Baragar, 1971) Whole-rock geochemistry data of Tepekent basalts were taken from Eryiğit et al. (2022). The other basalts were taken from Asan et al. (2021) to correlate the Miocene?-aged basaltic rocks outcropped the N-NW of Konya

Tectonic discrimination diagrams indicate that the Yükselen basalts display ocean island basalt (OIB) characteristics, whereas the Ulumuhsine and Tepekent basalts exhibit features consistent with enriched-mid-ocean ridge basalt (MORB) and crustal-contaminated arc basalts (Figure 8 and 9). The chondrite-normalized rare earth element (REE) diagram (Sun & McDonough, 1989) reveals a significant enrichment in light rare earth elements (LREEs), ranging from 20 to 200 times chondritic values. Notably, all three basalt types exhibit closely overlapping patterns, suggesting similar geochemical trends (Figure 8b).

As indicated by the diagrams (Figure 5-9), whole-rock geochemical data alone are insufficient to clearly distinguish calc-alkaline rocks outcropped around the investigated area. To address this limitation, this study incorporates mineral chemistry data and geostatistical interpretations to enhance the classification and understanding of petrogenetic processes.

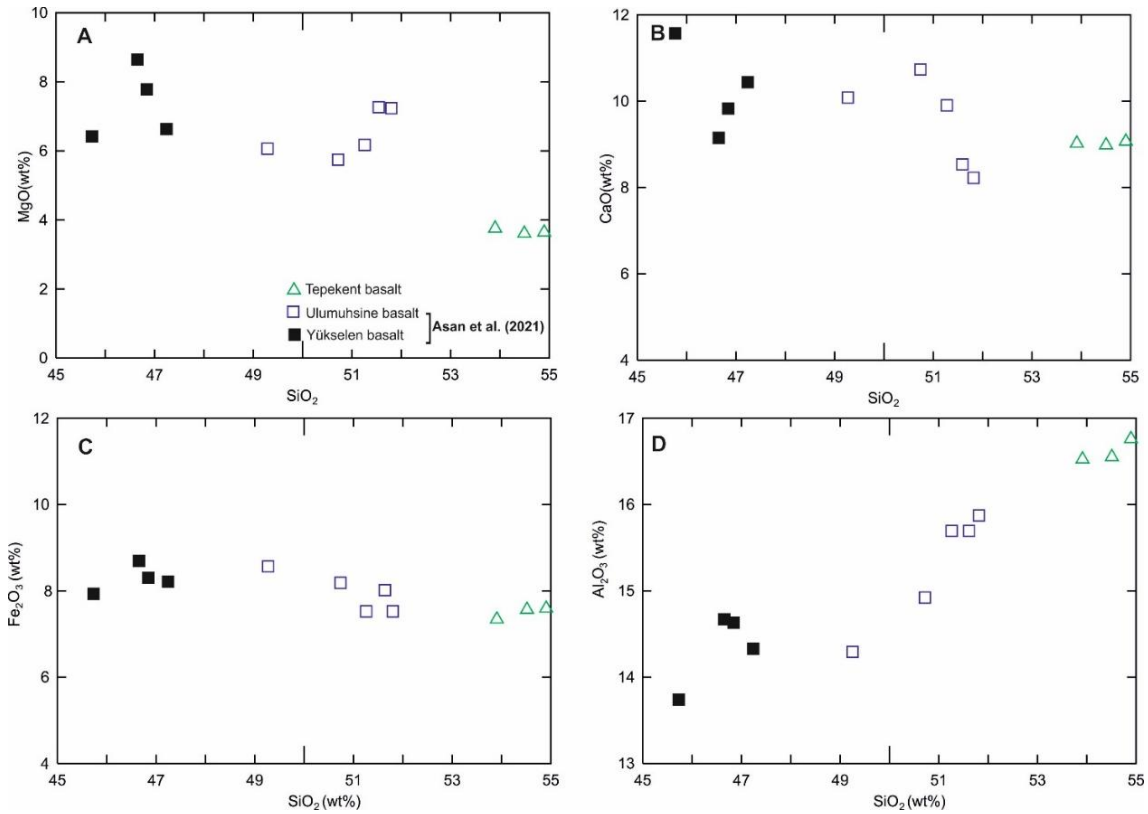


Figure 6. Silica versus selected major oxide variation diagrams for investigated basalts. Whole-rock geochemistry data of Tepekent basalts were taken from Eryiğit et al. (2022). The other basalts were taken from Asan et al. (2021) to correlate the Miocene?-aged basaltic rocks outcropped the N-NW of Konya

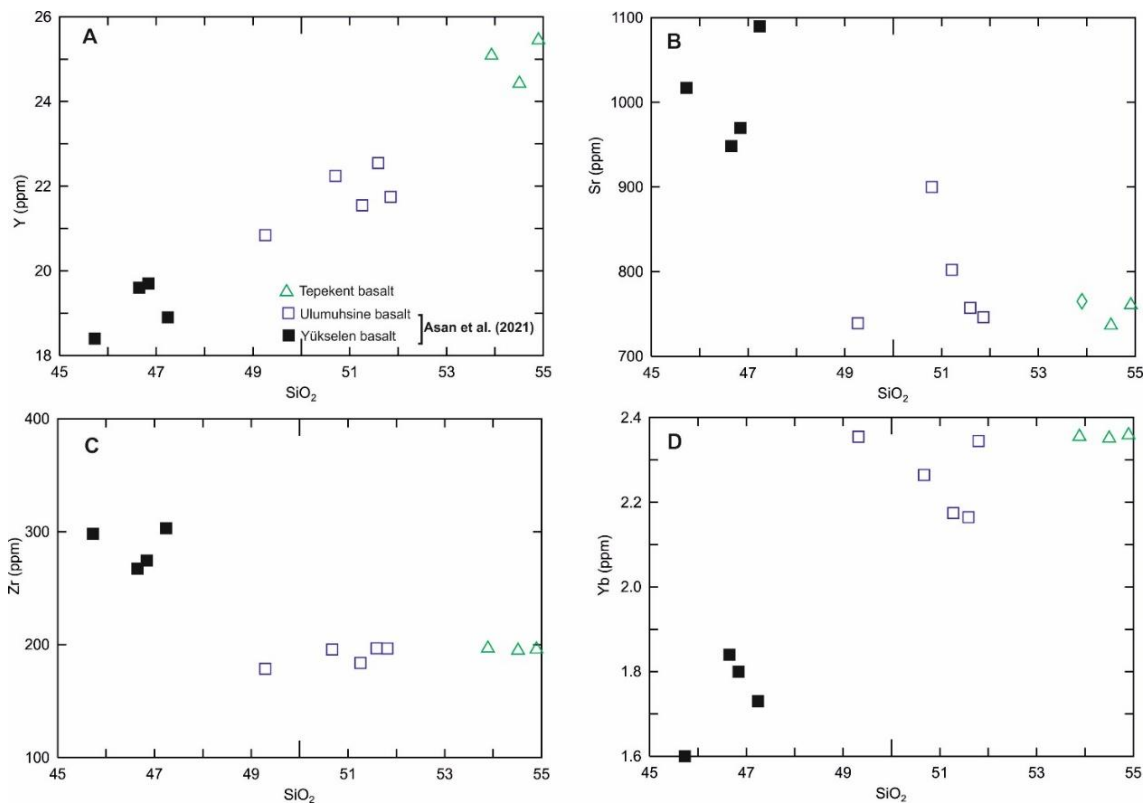


Figure 7. Silica versus selected trace element variation diagrams for investigated basalts. Whole-rock geochemistry data of Tepekent basalts were taken from Eryiğit et al. (2022). The other basalts were taken from Asan et al. (2021) to correlate the Miocene?-aged basaltic rocks outcropped the N-NW of Konya

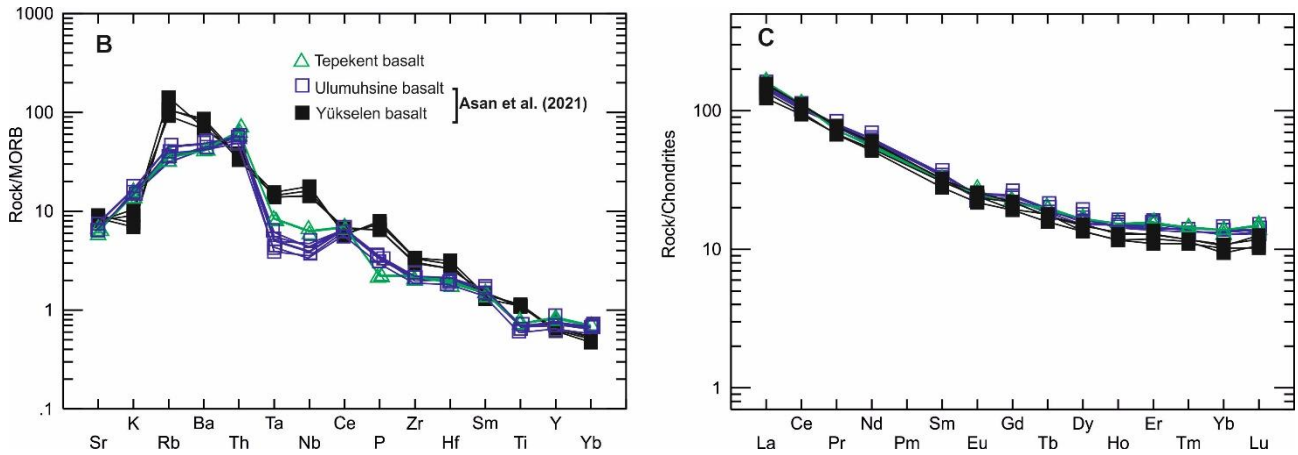


Figure 8. *a)* MORB-normalized spider diagram (Pearce, 1983); *b)* Chondrite-normalized (Sun & McDonough, 1989) spider diagram for investigated rocks.

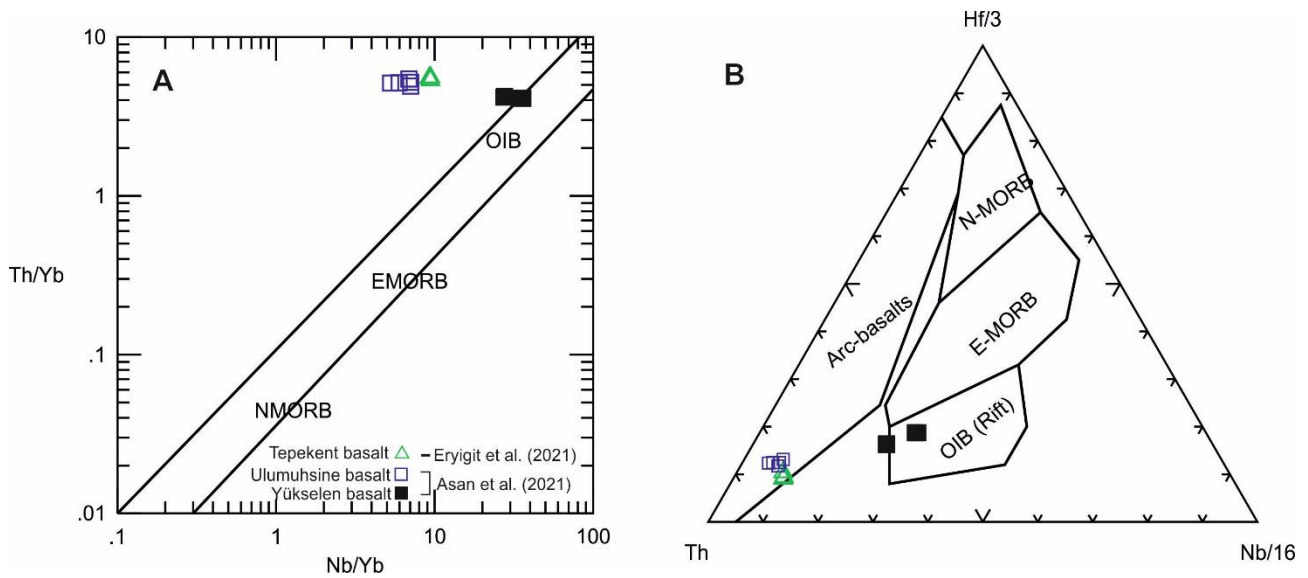


Figure 9. Tectonic setting diagrams based on *a)* Pearce (2008) and *b)* Wood (1980)

Complex Magma Chamber Process of the Tepekent Basalts

MnO, CaO and Cr₂O₃ compositions from the investigated olivines display nearly negative correlations with Mg# (Figure 10). The correlations of Mg# versus Cr₂O₃ and CaO align with fractional crystallization (Figure 10). In addition, olivine grains have CaO > 0.1, indicating being phenocryst rather than mantle xenocryst (Thompson & Gibson, 2000; Gençoğlu Korkmaz et al., 2019). However, the $Kd_{(Fe-Mg)}$ values of the olivines range from 0.105 to 0.204, which are lower than the expected $Kd_{(Fe-Mg)}$ equilibrium value of 0.29 ± 0.03 , suggesting that they are not in equilibrium with their host liquid (Figure 11a). Some of the olivine grains are in equilibrium with the most mafic basalt from Ulumuhsine (Figure 11b Sample Y7, (Asan et al., 2021)). These olivines may be antecrysts, representing earlier solidified phases that were transported into the system during magma ascent.

The reverse and oscillatory zoning observed in pyroxene minerals, with respect to MgO, Cr₂O₃, and TiO₂ from the core to the rim, suggests that the magma has been replenished by a more mafic mantle source (Gençoğlu Korkmaz, 2019; Ubide et al., 2014a; 2014b; 2014c). Some of pyroxenes can share the similar chemical

properties (see Supplementary data). They can be antecrysts formed before eruption phase and cropped from the magma wall and transferred the system. Moreover, the oscillatory variations in An content and the presence of sieve and dusty textures in plagioclase further support this interpretation indicating instability and complex magmatic processes during crystallization (Streck et al., 2002; 2005; Ginibre & Wörner, 2007; Streck, 2008; Gençoğlu Korkmaz & Kurt, 2021).

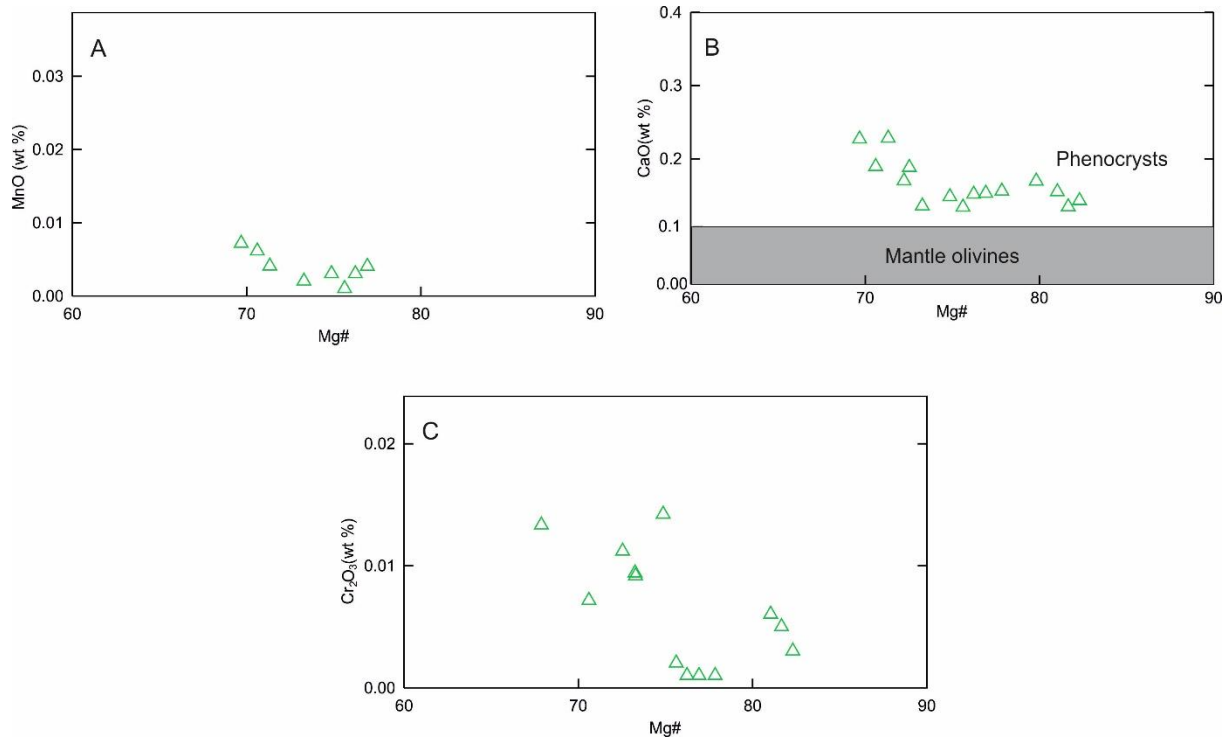


Figure 10. Mg versus selected major oxide diagrams for investigated olivines

Geostatistical Evaluation of the Basalts

In tephrochronology, occasionally Fe-Ti oxide pairs, biotite, amphibole, and pyroxene minerals are commonly used to correlate and associate tephra layers (Lowe, 2011). In this study, pyroxene minerals from the Tepekent basalts were specifically selected and utilized for correlation and classification purposes. To achieve this, classification and chemometric analyses, including PCA, UMAP, and k-medoids clustering, were performed.

Principal Component Analysis-PCA is a widely used linear dimensionality reduction method that transforms high-dimensional datasets into a lower-dimensional space while preserving as much variance as possible. It projects the data onto orthogonal axes, called principal components, which are aligned with the directions of maximum variance in the dataset. This method is particularly effective in datasets where variables are highly correlated, as it reduces redundancy by identifying uncorrelated linear combinations of the original features. PCA is often employed to simplify datasets for further analysis, including clustering and regression, by minimizing reconstruction error during the dimensionality reduction process (Jolliffe, 2002; Demšar et al., 2013). In volcanology, PCA has been applied to spatial and compositional data to differentiate volcanic units and interpret geochemical patterns (Prima & Yoshida, 2010; Mazzarini et al., 2016; Petrelli, 2021; Uslular et al., 2021).

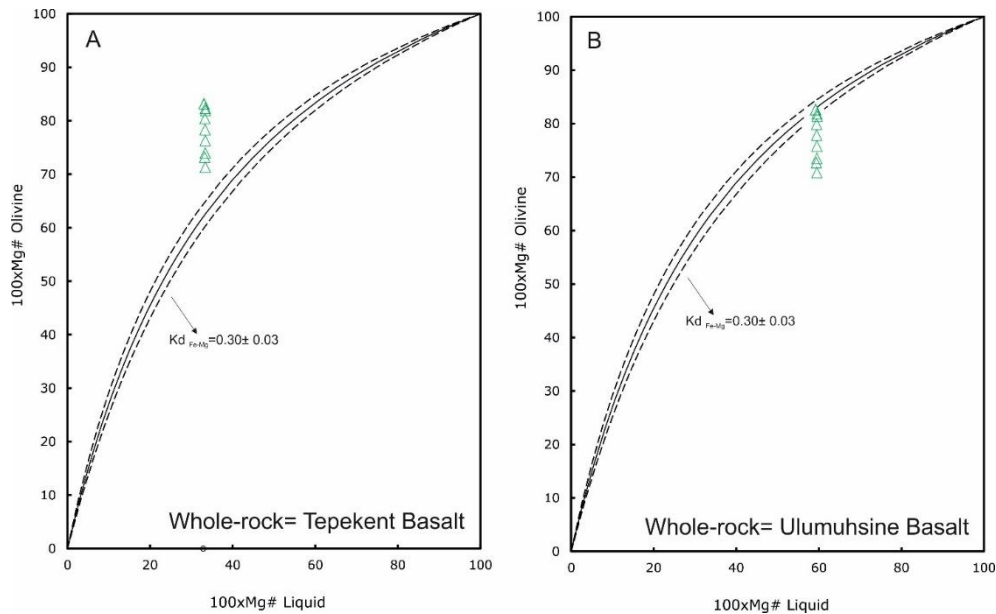


Figure 11. a) Rhodes diagrams illustrating disequilibrium conditions between Tepekent basalts and the analyzed olivines. **b)** Rhodes diagrams indicating equilibrium conditions for the most mafic basalt from Ulumuhsine and a subset of the analyzed olivines. The equilibrium field for Fe/Mg exchange between olivine and basaltic melt ($Kd_{(Fe-Mg)} = 0.29 \pm 0.03$) is based on Matzen et al. (2011) and Putirka (2016)

Uniform Manifold Approximation and Projection-UMAP is a nonlinear dimensionality reduction technique designed to preserve both global structure and local relationships in high-dimensional data. Unlike PCA, which relies on linear transformations, UMAP creates a low-dimensional manifold that retains the data's intrinsic topological properties. This makes UMAP particularly effective for datasets with nonlinear relationships, where preserving local neighborhoods is critical. UMAP has seen increased usage in Earth sciences for visualizing complex datasets, such as geochemical analyses of volcanic minerals, where its ability to distinguish subtle differences in composition is invaluable (McInnes et al., 2018; Becht et al., 2019). Moreover, k-medoids clustering is a robust partitioning algorithm that groups data into k-clusters using representative data points (medoids), which are actual data objects rather than centroids (Yousif & Yan, 2021). This method minimizes the sum of pairwise dissimilarities within each cluster, making it particularly effective in noisy or outlier-prone datasets (Yousif & Yan, 2021; Ren et al., 2022). It has significant applications across geosciences and biosciences, such as classifying fault systems, mineral assemblages, and spectral data in remote sensing, as well as clustering genomic sequences or ecological distributions. In tephrochronology, it can be used to classify volcanic ash layers and differentiate compositional variations in pyroclastic deposits by grouping similar geochemical signatures, aiding in the identification of volcanic sources and eruption dynamics. Clustering results obtained through k-medoids can be effectively visualized using UMAP, a nonlinear dimensionality reduction technique that preserves both global structure and local relationships in high-dimensional datasets. UMAP excels in representing the intrinsic topology of clusters, allowing clear differentiation of groups defined by k-medoids in a two- or three-dimensional space. To further validate and interpret clustering results, Principal Component Analysis (PCA) can be employed. PCA identifies the directions of maximum variance within the dataset, providing complementary insights into the overall structure

and confirming the robustness of the clustering. By combining k-medoids with UMAP for visualization and PCA for statistical verification, this approach offers a comprehensive framework for analyzing complex datasets. Such methodologies are particularly beneficial in fields like tephrochronology, where geochemical data of volcanic deposits can be clustered and visualized to discern compositional variations and eruption histories

The PCA and UMAP analyses of olivine minerals did not provide a clear distinction or correlation between the two calc-alkaline lava flows (Figure 12a and 12b). Investigated basalts and Ulumuhsine basalts can share common olivine grains or they can contain olivine grains within the similar composition. However, the PCA and UMAP diagrams and k-medoids clustering analysis (Table 1) for pyroxenes demonstrated a pronounced differentiation, suggesting that the two lava flows likely represent distinct magmatic events or magmatic episodes (Figure 13-14).

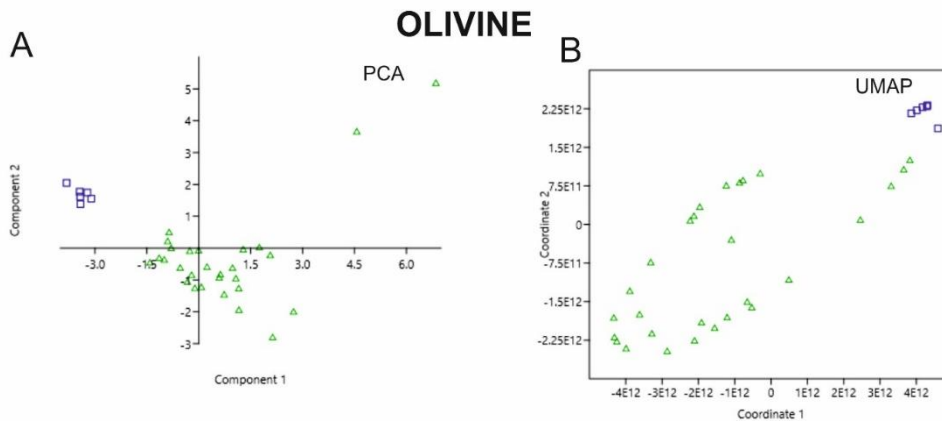


Figure 12. a) Principal Component Analysis (PCA) and b) Uniform Manifold Approximation and Projection (UMAP) diagrams of the investigated olivines. Green triangles represent olivines from the Tepekent basalts, while blue squares denote those from the Ulumuhsine basalts. Olivine data for the Ulumuhsine basalts were taken from Asan et al. (2021). Despite the analysis, PCA and UMAP results were insufficient to effectively distinguish the basaltic lava flows based on olivine compositions.

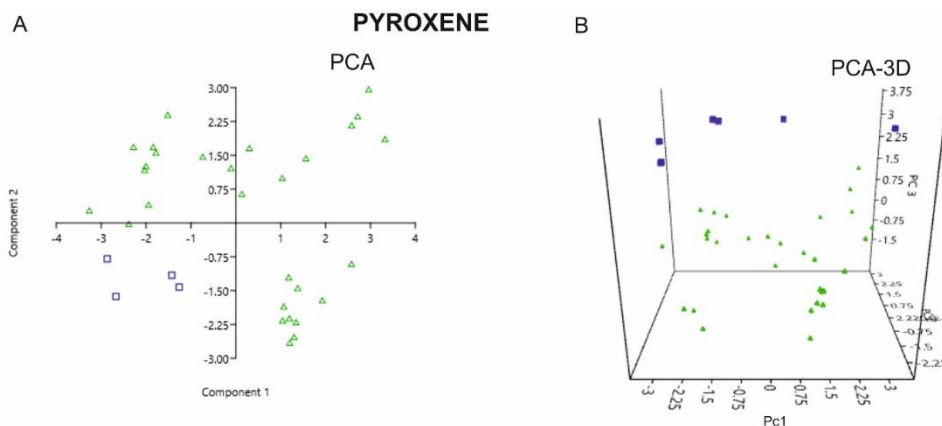


Figure 13. PCA diagrams of the investigated pyroxenes and pyroxenes from Ulumuhsine basalts. Green triangles represent clinopyroxenes from the Tepekent basalts, while blue squares denote those from the Ulumuhsine basalts. Clinopyroxene data for the Ulumuhsine basalts were taken from Asan et al. (2021)

Table 1. *K-medoids clustering analysis for pyroxenes*

| k-medoids | | | |
|-------------|---------|----------------|---------|
| Item | Cluster | Item | Cluster |
| BT43/C1-1/1 | 1 | BT44/C2/3 | 1 |
| BT43/C1-1/2 | 1 | BT44/C2/4 | 1 |
| BT43/C1-1/3 | 1 | BT44/C2/5 | 1 |
| BT43/C2-1/1 | 2 | BT44/C2/6 | 1 |
| BT43/C2-1/2 | 1 | BT44/C2/7 | 1 |
| BT43/C2-1/3 | 1 | BT43/C3-1/1 | 1 |
| BT43/C2-1/4 | 1 | BT43/C3-1/2 | 1 |
| BT43/C2-1/5 | 1 | BT43/C3-1/3 | 1 |
| BT43/C2-1/6 | 1 | BT44/C3/3 | 1 |
| BT43/C5-1/1 | 1 | BT44/C3/4 | 1 |
| BT43/C5-1/2 | 1 | BT44/C3/5 | 1 |
| BT43/C5-1/3 | 2 | BT44/C3/6 | 1 |
| BT43/C5-1/4 | 1 | *G-21B-1-px-5 | 2 |
| BT43/C5-1/5 | 1 | *G-21B-2-px6 | 2 |
| BT44/C1-1/1 | 1 | *G-21B-3-px-7a | 2 |
| BT44/C1-1/2 | 1 | *G-21B-3-px-7b | 2 |
| BT44/C1-1/3 | 1 | *G-21B-4-px-8a | 2 |
| BT44/C2/1 | 2 | *G-21B-4-px-8b | 2 |
| BT44/C2/2 | 1 | | |

* Sample data were taken from Asan et al. (2021).

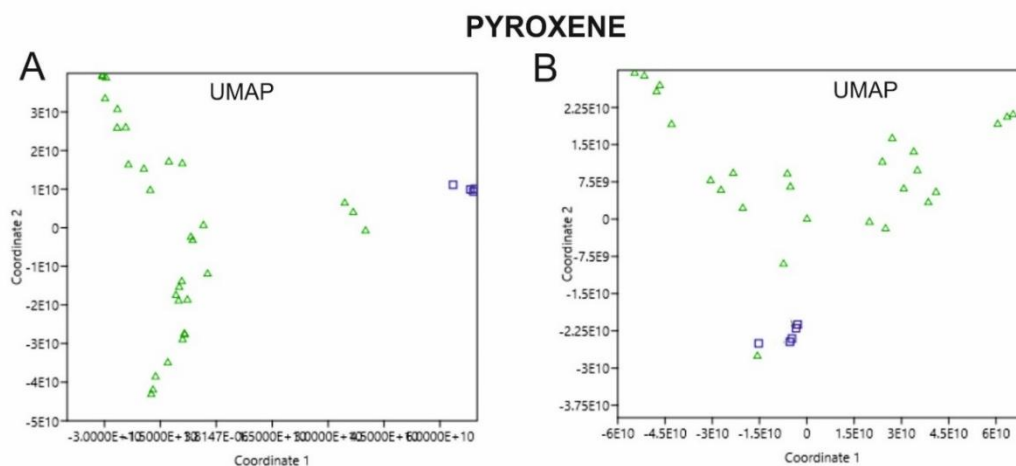


Figure 14. *a) UMAP (nonlinear, Euclidean distance) and b) UMAP (nonlinear, Bray-Curtis dissimilarity) visualizations of the investigated clinopyroxenes (green triangles) and clinopyroxenes from Ulumuhsine basalts (blue squares). The diagrams display the results of k-medoids clustering analysis, illustrating group separations based on compositional variations. These UMAP projections highlight how different distance metrics influence the clustering outcomes and the visualization of data relationships.*

4. CONCLUSION

This study underscores the efficacy of geostatistical interpretations of mineral chemistry in distinguishing between rocks with similar whole-rock geochemical characteristics, where bulk chemistry alone proves insufficient. Minerals such as Fe-Ti oxide pairs, amphibole, biotite, and pyroxene minerals play a critical role in tephrochronology for differentiating volcanic deposits. In this study, advanced geostatistical techniques, including Principal Component Analysis (PCA) and Uniform Manifold Approximation and Projection (UMAP), were applied to mineral chemistry data. PCA, a linear dimensionality reduction method, and UMAP, a nonlinear ordination technique, both proved instrumental in identifying subtle compositional differences between basaltic units with overlapping bulk compositions.

The Ulumuhsine and Tepekent basalts, despite their comparable whole-rock geochemical profiles, exhibit distinct pyroxene types based on mineral chemistry analyses. Notably, some olivines in the Tepekent basalts exhibit geochemical characteristics similar to those in the Ulumuhsine basalts. This resemblance suggests that these olivines may be antecrysts—minerals formed during earlier magmatic stages—that were incorporated into the Tepekent basalts during magma ascent through a complex magmatic plumbing system. This incorporation highlights the dynamic and multi-stage nature of magma evolution in the region. These differences suggest that the basalts are not products of the same lava flow and likely represent distinct basaltic products exposed different magmatic processes during their evolution. While mineral chemistry strongly supports this distinction, further geochronological and isotopic studies are necessary to confirm whether these basalts share a common origin or belong to the same eruptive episode.

This study emphasizes the value of combining mineral chemistry with both linear (PCA) and nonlinear (UMAP) ordination techniques to improve volcanic stratigraphy resolution. Such an approach provides a deeper understanding of magma evolution, particularly in cases where whole-rock geochemistry alone cannot adequately resolve genetic relationships between volcanic units.

ACKNOWLEDGEMENT

The author thanks Prof. Dr. Yusuf Kağan Kadioğlu and Assoc. Prof. Dr. Kıymet Deniz for EPMA analysis.

CONFLICT OF INTEREST

The author declares no conflict of interest.

REFERENCES

- Asan, K., Kurt, H., Gündüz, M., Gençoğlu Korkmaz, G., & Morgan, G. (2021) Geology, geochronology, and geochemistry of the Miocene Sulutas volcanic complex, Konya-Central Anatolia: genesis of orogenic and anorogenic rock associations in an extensional geodynamic setting. *International Geology Review*, 1-32.

- Aydar, E., & Gourgaud, A. (1998) The geology of Mount Hasan stratovolcano, central Anatolia, Turkey. *Journal of Volcanology and Geothermal Research*, 85, 129-152.
- Becht, E., McInnes, L., Healy, J., Dutertre, C.-A., Kwok, I.W., Ng, L.G., Ginhoux, F., & Newell, E.W. (2019) Dimensionality reduction for visualizing single-cell data using UMAP. *Nature biotechnology* 37, 38-44.
- Best, M.G. (2003) *Igneous and metamorphic petrology*, 2 ed. John Wiley & Sons.
- Biryol, C.B., Beck, S.L., Zandt, G., & Özacar, A.A. (2011) Segmented African lithosphere beneath the Anatolian region inferred from teleseismic P-wave tomography. *Geophysical Journal International* 184, 1037-1057.
- Carr, M. (1990) IGPET 3.0. Unpublished manual.—Terra Sofia, Somerset, New Jersey.
- Deer, W.A., Howie, R.A., & Zussman, J. (1963) *Rock-forming Minerals: Vol. 4: Framework Silicates*. Longman.
- Delph, J.R., Biryol, C.B., Beck, S.L., Zandt, G., & Ward, K.M. (2015) Shear wave velocity structure of the Anatolian Plate: anomalously slow crust in southwestern Turkey. *Geophysical Journal International* 202, 261-276.
- Demšar, U., Harris, P., Brunson, C., Fotheringham, A.S., & McLoone, S. (2013) Principal component analysis on spatial data: an overview. *Annals of the Association of American Geographers* 103, 106-128.
- Deniel, C., Aydar, E., & Gourgaud, A. (1998) The Hasan Dagi stratovolcano Central Anatolia, Turkey evolution from calc-alkaline to alkaline magmatism in a collision zone. *Journal of Volcanology and Geothermal Research* 87 275-302.
- Deniz, K., & Kadioğlu, Y.K. (2019) Investigation of feldspar raw material potential of alkali feldspar granites and alkali feldspar syenites within Central Anatolia. *Maden Tetkik ve Arama Dergisi* 158, 265-289.
- Eryiğit, B., Kurt, H., Asan, K., & Korkmaz, G.G. (2022) Petrography, Geochemistry, and Petrology of Volcanic Rocks in the Tepekent Region (Konya-Central Anatolia). *Konya Journal of Engineering Sciences* 10, 1002-1018.
- Gençoğlu Korkmaz, G. (2019) The Origin of the Enclaves in Emirgazi (Konya) and its Surrounding Volcanites and Their Petrological Importance in the Genesis of the Regional Volcanism Konya Technical University Graduate Education Institute. Konya Technical University (in Turkish), p. 321.
- Gençoğlu Korkmaz, G., Asan, K., Kurt, H., & Morgan, G. (2017) $^{40}\text{Ar}/^{39}\text{Ar}$ geochronology, elemental and Sr-Nd-Pb isotope geochemistry of the Neogene bimodal volcanism in the Yükselen area, NW Konya (Central Anatolia, Turkey). *Journal of African Earth Sciences* 129, 427-444.
- Gencoglu Korkmaz, G., & Kurt, H. (2024) Complex Magma Chamber Dynamics and Volcanic Activity in the Karapınar Volcanic Field: Insights from Mineral and Whole-Rock Chemistry – A Review, in: Dr. Károly, N. (Ed.), *A Comprehensive Study of Volcanic Phenomena*. IntechOpen, Rijeka, p. Ch. 0.

- Gençoğlu Korkmaz, G., & Kurt, H. (2021) Interpretation of the Magma Chamber Processes with the help of Textural Stratigraphy of the Plagioclases (Konya-Central Anatolia). *European Journal of Science and Technology*, 222-237.
- Gencoglu Korkmaz, G., Kurt, H., & Asan, K. (2019) Origin Of Olivines From The Karapınar-Karacadağ Volcanic Complex (Central Anatolia), in: KALIPCI, A.P.D.E. (Ed.), 4. International Conference on Civil, Environmental, Geology and Mining Engineering, Nevşehir, pp. 269-275.
- Gençoğlu Korkmaz, G., Kurt, H., Asan, K., & Leybourne, M. (2022) Ar-Ar Geochronology and Sr-Nd-Pb-O Isotopic Systematics of the Post-collisional Volcanic Rocks from the Karapınar-Karacadağ Area (Central Anatolia, Turkey): An Alternative Model for Orogenic Geochemical Signature in Sodic Alkali Basalts. *Journal of Geosciences* 67, 53-69.
- Ginibre, C., & Wörner, G. (2007) Variable parent magmas and recharge regimes of the Parinacota magma system (N. Chile) revealed by Fe, Mg and Sr zoning in plagioclase. *Lithos* 98, 118-140.
- Irvine, T., & Baragar, W.R.A. (1971) A Guide to the Chemical Classification of the Common Volcanic Rocks. *Canadian Journal of Earth Sciences* 8, 523-548.
- Jolliffe, I.T. (2002) Principal component analysis for special types of data. Springer.
- Lindsley, D.H., & Andersen, D.J. (1983) A two-pyroxene thermometer. *Journal of Geophysical Research: Solid Earth* 88, A887-A906.
- Lowe, D.J. (2011) Tephrochronology and its application: a review. *Quaternary Geochronology* 6, 107-153.
- Matzen, A.K., Baker, M.B., Beckett, J.R., & Stolper, E.M. (2011) Fe–Mg partitioning between olivine and high-magnesian melts and the nature of Hawaiian parental liquids. *Journal of Petrology* 52, 1243-1263.
- Mazzarini, F., Le Corvec, N., Isola, I., & Favalli, M. (2016) Volcanic field elongation, vent distribution, and tectonic evolution of a continental rift: The Main Ethiopian Rift example. *Geosphere* 12, 706-720.
- McInnes, L., Healy, J., & Melville, J. (2018) Umap: Uniform manifold approximation and projection for dimension reduction. arXiv preprint arXiv:1802.03426.
- Morimoto, N., Fabries, J., Ferguson, A.K., Ginzburg, I.V., Ross, M., Seifert, F.A., Zussman, J., Aoki, K., & Gottardi, G. (1988) Nomenclature of pyroxenes. *American Mineralogist* 73, 1123-1133.
- Neave, D.A., & Putirka, K.D. (2017) A new clinopyroxene-liquid barometer, and implications for magma storage pressures under Icelandic rift zones. *American Mineralogist* 102, 777-794.
- Pearce, J.A. (1983) Role of the sub-continental lithosphere in magma genesis at active continental margin. *Continental Basalts and Mantle Xenoliths*, 230-249.
- Pearce, J.A. (2008) Geochemical fingerprinting of oceanic basalts with applications to ophiolite classification and the search for Archean oceanic crust. *Lithos* 100, 14-48.
- Pecerrillo, A. (2005) Plio-Quaternary Volcanism in Italy: Petrology, Geochemistry, Geodynamics. . 370.
- Petrelli, M. (2021) Introduction to python in earth science data analysis: from descriptive statistics to machine learning. Springer Nature.
- Prima, O.D.A., & Yoshida, T. (2010) Characterization of volcanic geomorphology and geology by slope and topographic openness. *Geomorphology* 118, 22-32.

- Putirka, K.D. (2008a) Clinopyroxene thermobarometers.
- Putirka, K.D. (2008b) Thermometers and Barometers for Volcanic Systems. *Reviews in Mineralogy & Geochemistry* 69, 61-120.
- Putirka, K.D. (2016) Special Collection: Olivine: Rates and styles of planetary cooling on Earth, Moon, Mars, and Vesta, using new models for oxygen fugacity, ferric-ferrous ratios, olivine-liquid Fe-Mg exchange, and mantle potential temperature. *American Mineralogist* 101, 819-840.
- Ren, J., Hua, K., & Cao, Y. (2022) Global optimal k-medoids clustering of one million samples. *Advances in Neural Information Processing Systems* 35, 982-994.
- Şengör, A.C. (1979) Mid-Mesozoic closure of Permo–Triassic Tethys and its implications. *Nature* 279, 590-593.
- Şengör, A.M.C., & Yılmaz, Y. (1981) Tethyan evolution of Turkey: A plate tectonic approach. *Tectonophysics* 75, 181-241.
- Streck, M.J., Dungan, M.A., Malavassi, E., Reagan, M.K., & Bussy, F. (2002) The role of basalt replenishment in the generation of basaltic andesites of the ongoing activity at Arenal volcano, Costa Rica: evidence from clinopyroxene and spinel. *Bulletin of Volcanology* 64, 316-327.
- Streck, M.J., Dungan, M.A., Bussy, F., & Malavassi, E. (2005) Mineral inventory of continuously erupting basaltic andesites at Arenal volcano, Costa Rica: implications for interpreting monotonous, crystal-rich, mafic arc stratigraphies. *Journal of Volcanology and Geothermal Research* 140, 133-155.
- Streck, M.J. (2008) Mineral Textures and Zoning as Evidence for Open System Processes. *Reviews in Mineralogy and Geochemistry* 69, 595-622.
- Sun, S., & McDonough, W. (1989) Chemical and isotopic systematics of oceanic basalts: implications for mantle composition and processes. Geological Society, London, Special Publications 42, 313-345.
- Thompson, R.N., & Gibson, S.A. (2000) Transient high temperatures in mantle plume heads inferred from magnesian olivines in Phanerozoic picrites. *Nature* 407, 502.
- Ubide, T., Galé, C., Arranz, E., Lago, M., & Larrea, P. (2014a) Clinopyroxene and amphibole crystal populations in a lamprophyre sill from the Catalonian Coastal Ranges (NE Spain): A record of magma history and a window to mineral-melt partitioning. *Lithos* 184-187, 225-242.
- Ubide, T., Galé, C., Larrea, P., Arranz, E., & Lago, M. (2014b) Antecrysts and their effect on rock compositions: The Cretaceous lamprophyre suite in the Catalonian Coastal Ranges (NE Spain). *Lithos* 206-207, 214-233.
- Ubide, T., Galé, C., Larrea, P., Arranz, E., Lago, M., & Tierz, P. (2014c) The Relevance of Crystal Transfer to Magma Mixing: a Case Study in Composite Dykes from the Central Pyrenees. *Journal of Petrology* 55, 1535-1559.
- Uslular, G., & Gençlioğlu-Kuşcu, G. (2019) Mantle source heterogeneity in monogenetic basaltic systems: A case study of Eğrikuyu monogenetic field (Central Anatolia, Turkey). *Geosphere* 15, 29.
- Uslular, G., Le Corvec, N., Mazzarini, F., Legrand, D., & Gençlioğlu-Kuşcu, G. (2021) Morphological and multivariate statistical analysis of quaternary monogenetic vents in the Central Anatolian Volcanic

- Province (Turkey): Implications for the volcano-tectonic evolution. *Journal of Volcanology and Geothermal Research*, 107280.
- Van Hinsbergen, D.J., Maffione, M., Plunder, A., Kaymakçı, N., Ganerød, M., Hendriks, B.W., Corfu, F., Gürer, D., de Gelder, G.I., & Peters, K. (2016) Tectonic evolution and paleogeography of the Kırşehir Block and the Central Anatolian Ophiolites, Turkey. *Tectonics* 35, 983-1014.
- Weaver, B.L. (1991) Trace element evidence for the origin of ocean-island basalts. *Geology* 19, 123-126.
- Whitney, D.L., & Evans, B.W. (2009) Abbreviations for names of rock-forming minerals. *American Mineralogist* 95, 185-187.
- Wood, D.A. (1980) The application of a ThHfTa diagram to problems of tectonomagmatic classification and to establishing the nature of crustal contamination of basaltic lavas of the British Tertiary Volcanic Province. *Earth and Planetary Science Letters* 50, 11-30.
- Yavuz, F. (2013) WinPyrox: A Windows program for pyroxene calculation classification and thermobarometry†. *American Mineralogist* 98, 1338-1359.
- Yavuz, F., & Yıldırım, D.K. (2018) A Windows program for pyroxene-liquid thermobarometry. *Periodico di Mineralogia* 87.
- Yousif, S., & Yan, W. (2021) Application and evaluation of a K-Medoids-based shape clustering method for an articulated design space. *Journal of Computational Design and Engineering* 8, 935-948.



Gazi University

Journal of Science

PART A: ENGINEERING AND INNOVATION

<http://dergipark.org.tr/guj.1624298>

Quasi-Periodic Photonic Structures: Fibonacci Fractal-Based Optical Filter Design Using ZnO/MgF₂

Erman ÇOKDUYGULULAR^{1*} ¹ Istanbul University - Cerrahpaşa, Department of Engineering Sciences, Faculty of Engineering, TR-34320, Istanbul, Türkiye

| Keywords | Abstract |
|--|---|
| Fibonacci Photonic Crystals ZnO MgF ₂ Optical Filter | This study investigates the optical properties of one-dimensional photonic crystals based on ZnO/MgF ₂ , designed using Fibonacci fractal sequences. The effects of structures based on standard Fibonacci (FFPC), inverted Fibonacci (IFFPC), and mirror symmetry Fibonacci (MSFFPC) sequences on photonic band gaps and light-matter interactions were theoretically analyzed. Calculations were performed using the Transfer Matrix Method (TMM). The analyses revealed that lower-order sequences offer broad and uniform transmission, while higher-order sequences exhibit complex optical resonances with narrower bandwidths. MSFFPC structures, characterized by their regular configurations and narrow bandwidths, are ideal candidates for applications requiring precise color selection, such as sensors and narrow-band optical filters. Conversely, IFFPC structures provide advantages for wide spectral applications due to their broad transmission bands. FFPC structures, offering a balanced performance, can be employed in both wide-band and narrow-band optical systems. |

Cite

Çokduygular, E. (2025). Quasi-Periodic Photonic Structures: Fibonacci Fractal-Based Optical Filter Design Using ZnO/MgF₂. *GU J Sci, Part A, 12(1)*, 268-277. doi:10.54287/guj.1624298

| Author ID (ORCID Number) | Article Process |
|---|---|
| 0000-0003-3235-2919 Erman ÇOKDUYGULULAR | Submission Date 21.01.2025 Revision Date 06.02.2025 Accepted Date 13.02.2025 Published Date 26.03.2025 |

1. INTRODUCTION

Photonics technology advancement and the integration with optoelectronic devices have led to the development of devices whose electrical and optical properties can be tuned. Therefore, innovative photonics-based device designs have a critical role in future technologies. Designing these structures with optimal parameters has become a significant requirement, particularly for precisely adjusting optical properties. Integrated photonic systems offer solutions for controlling optical characteristics based on the principle of "light management engineering" by altering the propagation of electromagnetic waves. Among these solutions, the deposition of dielectric mirror layers with one-dimensional (1D) photonic crystal properties stands out as an effective method. 1D photonic crystals are structures where the dielectric constant periodically varies in only one direction, forming a photonic band gap and providing optical reflection at certain wavelengths.

*Corresponding Author, e-mail: erman.cokduygulular@iuc.edu.tr

Fibonacci photonic crystals, with their distinctive quasi-periodic structure, exhibit unique properties that differentiate them from conventional periodic photonic crystals. These structures, designed based on the Fibonacci sequence, offer exceptional advantages in fundamental optical processes such as light propagation and localization (Taherzadeh & Keshavarz, 2024). In addition to the diffraction and photonic band gaps observed in regular crystal arrangements, Fibonacci photonic crystals possess broad spectral sensitivity and a strong capacity for light confinement (Elsayed et al., 2024). These characteristics enable innovative solutions in various fields, including telecommunications, sensor technology, optical filters, and waveguides. For instance, the complexity offered by Fibonacci arrangements enhances light absorption at specific wavelengths, facilitating the development of efficient energy devices. Importantly, the optical properties of Fibonacci photonic crystals have been extensively examined through theoretical modeling and experimental studies. Research findings indicate that these arrangements have the potential to optimize light-matter interactions. Notably, the photonic band gaps achieved in aperiodic Fibonacci sequences provide an ideal platform for applications such as waveguides and sensors (Jiménez-Vivanco et al., 2024).

While knowledge about light wave propagation in completely ordered and disordered structures has rapidly advanced, the behavior of optical waves in the vast intermediate region between perfect order and disorder remains poorly understood. Fibonacci fractal photonic crystal (FFPC) structures, which can be described as non-Euclidean geometric configurations, exhibit fascinating optical properties. The transmission spectrum of Fibonacci systems includes forbidden frequency regions referred to as "pseudo band gaps," analogous to the band gaps of conventional photonic crystals (Capaz et al., 1990). Light waves are critically localized in the frequency regime outside these Fibonacci band gaps. In contrast to the completely disordered (Anderson-type) localization state, these critically localized states weaken non-exponentially, most likely by a power-law, and exhibit a rich, self-similar structure (Fujiwara et al., 1989). This makes these systems very interesting for light localization studies, as suggested by Kohmoto et al. (1987). Furthermore, FFPCs have been successfully utilized in the development of devices such as high-quality resonant microcavities (Escorcía-García & Mora-Ramos, 2009) and mirror with broad omni-directional photonic band gaps (Han & Wang, 2005; Srivastava et al., 2008). These applications underscore the versatility and potential of FFPCs in advancing photonic technologies (Tavakoli & Jalili, 2014).

ZnO/MgF₂ layered photonic crystals offer significant advantages in controlling light reflection and optimizing specific optical properties due to their multilayer structures. These systems are designed by alternately arranging MgF₂, with a low refractive index, and ZnO, with a high refractive index, resulting in a wide optical band gap. This characteristic makes them suitable for applications such as optical filters, sensors, and high-performance laser devices (Fujihara et al., 2001). The contrast between the low refractive index of MgF₂ and the high refractive index of ZnO creates wide omnidirectional photonic band gaps in these crystals. The layered structure is particularly optimized for anti-reflective coatings, creating a surface that minimizes energy loss and ensures high light transmission (Dai et al., 2006). MgF₂ provides thermal and mechanical durability,

making it stable for high-temperature applications. In contrast, ZnO's high optical absorption coefficient enhances the system's photonic performance. The fabrication of ZnO/MgF₂ layered structures commonly involves techniques such as physical vapor deposition or sol-gel processes, which ensure the homogeneity and structural precision of thin films.

The optical properties of ZnO/MgF₂ photonic crystals offer an ideal solution for applications requiring wavelength-dependent light control. For instance, they can regulate light transmission at different wavelengths in optical filters, enhancing precision in spectral selection. In anti-reflective coatings, these structures reduce reflection losses over a wide spectral range, thereby improving the efficiency of optical devices. Optimizes light transmission at narrow bandwidths, especially high-performance lasers (Fujihara et al., 2001; Dai et al., 2006).

In this study, the optical properties of ZnO/MgF₂-based quasi-periodic Fibonacci fractal photonic crystal (Fibonacci Fractal Photonic Crystal, FFPC) structures were theoretically investigated with respect to different sequence parameters. In addition to the conventional Fibonacci sequence, Fibonacci fractal photonic crystals with inverted and mirror symmetry (IFFPC and MSFFPC) are analyzed. The effects of these structures on the photonic band gap properties, which can be tuned to the visible spectral region, were examined in detail.

2. MATERIAL AND METHOD

This study uses various Fibonacci-based sequences to construct different fractal structures for application in 1D photonic crystals. The optical Transfer Matrix Method (TMM) was utilized to calculate the optical properties of Fibonacci photonic crystal structures, including transmission, reflection, and absorption. The details of TMM calculations and its fundamental operation have been presented in our previous studies (Çetinkaya et al., 2021; Çokduygular et al., 2023).

The FFPC structures created within the scope of this study are based on the classical Fibonacci sequence. The Fibonacci sequence can be defined as a particular ordering of binary digits (or symbols of any two-letter alphabet). Similar to Fibonacci numbers, the Fibonacci word is generated not through successive addition but by sequential concatenation. To describe this process, the initial sequences are set as $S_0 = "A"$ and $S_1 = "B"$. Here, A represents ZnO, and B represents MgF₂. Then, the sequence S_n is obtained by successive concatenation of the previous (S_{n-1}) and the preceding (S_{n-2}) sequences ($S_n = S_{n-1} + S_{n-2}$).

The IFFPC structures are based on the inverted Fibonacci sequence. The inverse code is simply the binary complement of a sequence, where all zeros are converted to ones and all ones to zeros. For example, if the binary representation of S_n is AAAABBAA, its inverted code, $(S_n)_{inv}$, becomes BBBBAABB. The inverted Fibonacci sequence is defined in this manner and is represented as a specific structural arrangement.

Lastly, MSFFPC structures are constructed based on the mirror-symmetry Fibonacci sequence. Mirror symmetry is a structure obtained by mirroring the binary code of a number and is constructed as follows: $S_n = S_{n-1} + (S_{n-2})_{ms}$. This approach generates distinct arrangement sets for FFPC, IFFPC, and MSFFPC, as provided in Table 1.

Table 1. Sequence sets for FFPC, IFFPC and MSFFPC.

| FFPC | | IFFPC | | MSFFPC | |
|-------|---------------------|-------|-----------------------------|--------|----------------------------|
| S_n | $S_{n-1} + S_{n-2}$ | S_n | $S_{n-1} + (S_{n-2})_{inv}$ | S_n | $S_{n-1} + (S_{n-2})_{ms}$ |
| S_0 | A | S_0 | A | S_0 | A |
| S_1 | B | S_1 | B | S_1 | B |
| S_2 | BA | S_2 | BB | S_2 | BA |
| S_3 | BAB | S_3 | BBA | S_3 | BAB |
| S_4 | BABBA | S_4 | BBAAA | S_4 | BABAB |
| S_5 | BABBABAB | S_5 | BBAAAAAB | S_5 | BABABBAB |
| S_6 | BABBABABBABBA | S_6 | BBAAAAABAABBB | S_6 | BABABBABBABAB |

In the investigated FFPC, IFFPC, and MSFFPC systems, the central wavelength is set to the middle of the visible region, i.e., $\lambda_0 = 550$ nm. Each layer of the Fibonacci-based photonic crystal is designed with a quarter-wave thickness, which is expected to reveal quasi-periodic effects more prominently, i.e., $n_A d_A = n_B d_B = \lambda_0/4$.

3. RESULTS AND DISCUSSION

The transmission spectra of ZnO/MgF₂-based FFPCs at different orders were analyzed to investigate their optical behavior as a function of the sequence order. The transmission spectra were calculated using the Transfer Matrix Method. Figure 1 presents the transmission spectra of ZnO/MgF₂-based FFPCs constructed at various orders.

The spectrum exhibits a single wide and symmetric transmission band in the third-order sequence, with maximum transmittance observed around 550 nm. This indicates that lower-order sequences possess simpler optical properties and demonstrate a straightforward light transmission behavior. Moving up to the fourth order, a single passband is retained, but this band appears sharper. This suggests that the optical properties become more pronounced as the sequence order increases. The transmission spectra display a more complex structure with the transition to the fifth and sixth orders. Two distinct transmission bands are observed in the fifth order, while in the sixth order, these bands increase to three. This indicates that the structure incorporates more optical modes and exhibits increasingly complex interactions with light. The behavior observed across the sequence orders in FFPC highlights the influence of the quasi-periodic nature of the Fibonacci sequence on the optical properties.

The maximum transmittance is around 100% for certain modes in all cases, and at higher orders, the transitions are concentrated in narrower bandwidths. These features indicate that optical selectivity and mode diversity are enhanced as the sequence order increases. This demonstrates the ability of higher-order sequences to support more precise and complex light manipulation.

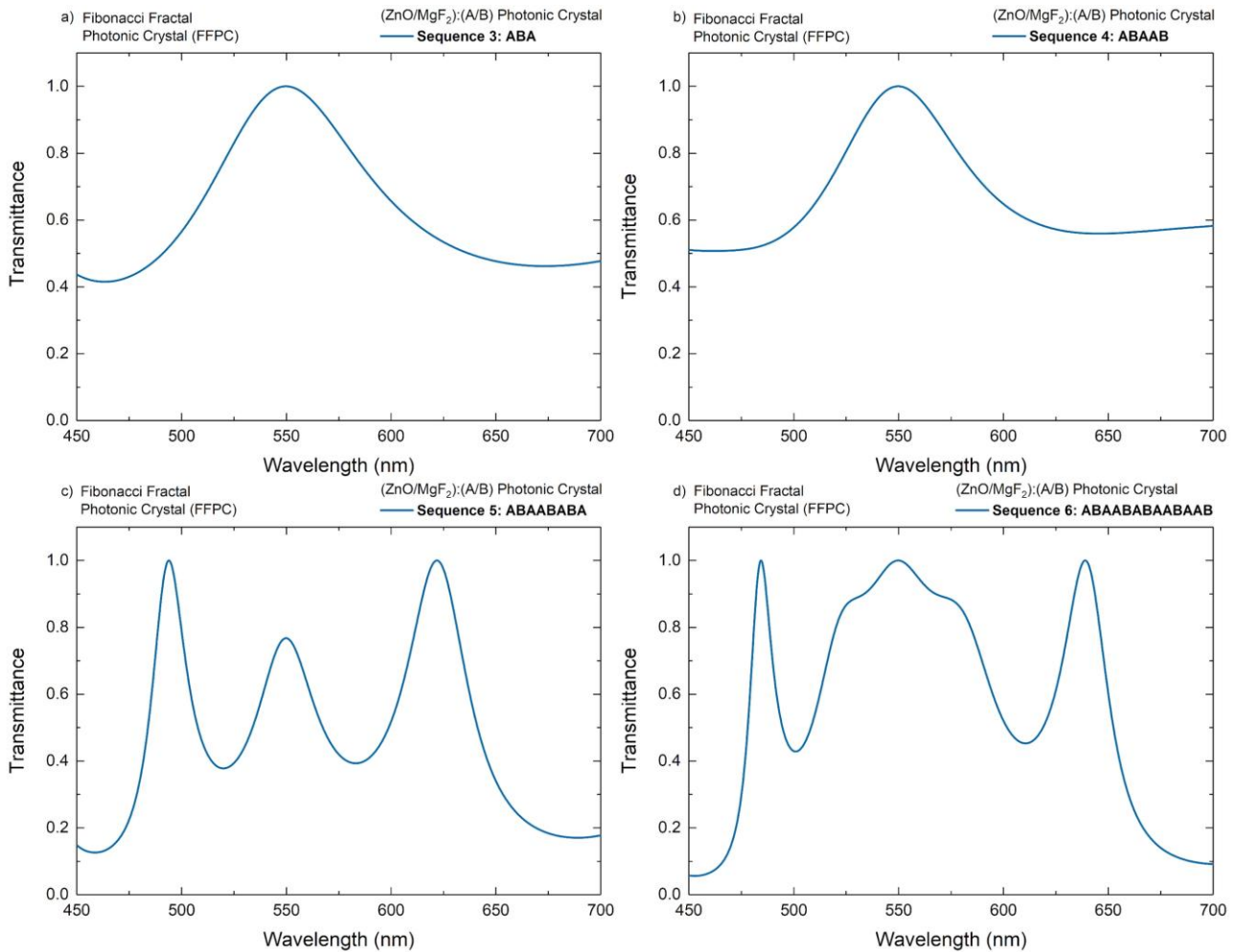


Figure 1. Transmittance spectra of ZnO/MgF₂ based Fibonacci fractal photonic crystals with a) 3rd, b) 4th, c) 5th, and d) 6th order alignments.

The transmission spectra of ZnO/MgF₂-based IFFPCs at different orders were analyzed to investigate their optical behavior as a function of the sequence order. The transmission spectra were calculated using the TMM. Figure 2 presents the transmission spectra of ZnO/MgF₂-based IFFPCs constructed at various orders.

The third-order structures of the IFFPC sequence are characterized by a wide transition band in the transmittance spectrum, with the maximum transmittance observed at a wavelength of approximately 550 nm. This indicates that lower-order sequences exhibit simpler and more uniform optical behavior. When transitioning to the fourth order, more defined features emerge in the spectrum, although the overall width of the transition band remains largely preserved. In the fifth order, the spectrum becomes more complex. The transmission spectrum splits into multiple narrow-band transition peaks, indicating an increase in the optical complexity of the structure. This complexity becomes even more pronounced in the sixth order, with the spectrum displaying sharp and well-defined transition peaks. This behavior demonstrates that higher-order IFFPC sequences interact more strongly with light at specific wavelengths, exhibiting multiple optical modes and enhanced spectral selectivity.

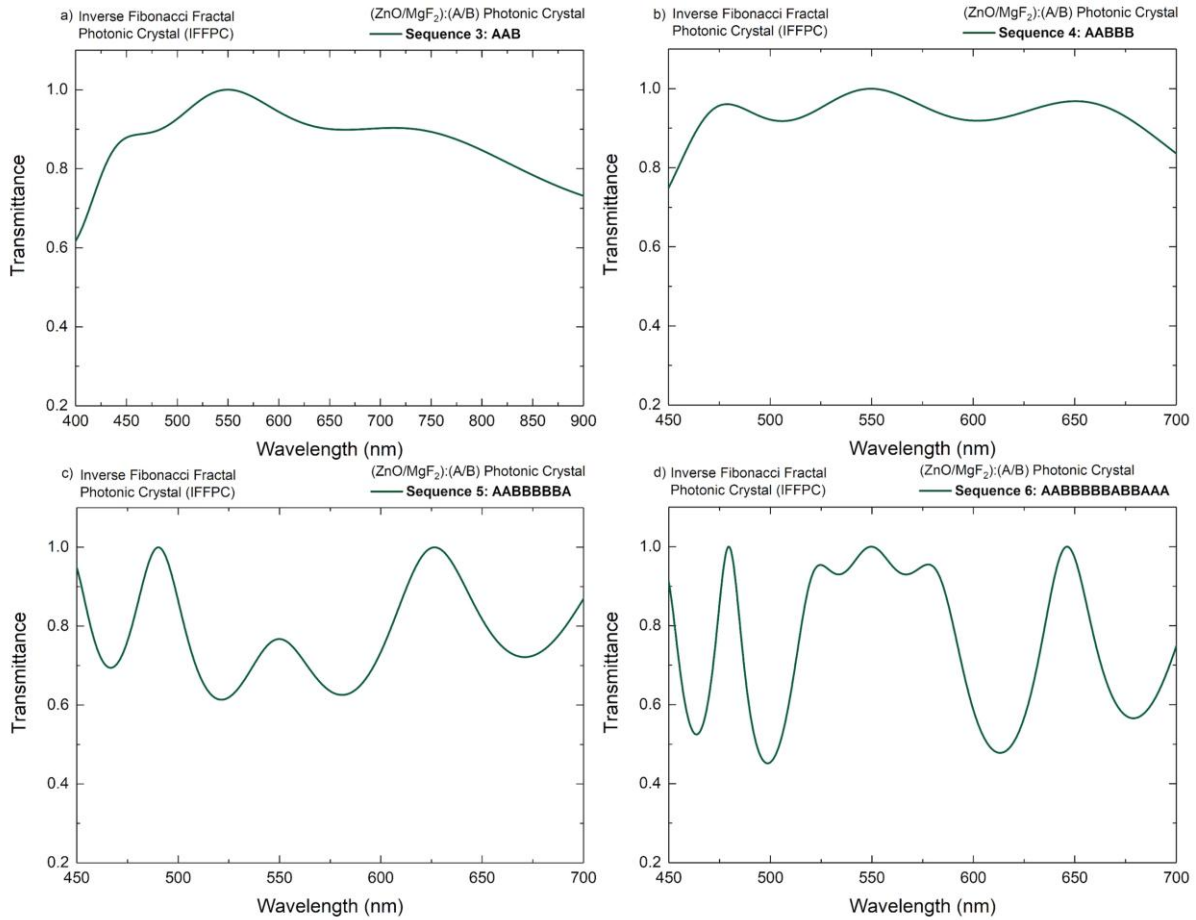


Figure 2. Transmittance spectra of ZnO/MgF₂ based Inverse Fibonacci fractal photonic crystals with a) 3rd, b) 4th, c) 5th, and d) 6th order alignments.

The transmittance spectra of ZnO/MgF₂-based MSFFPCs of different orders and their optical characteristics depending on the order of the sequence were investigated with the transmittance spectra calculated by TMM. Figure 3 shows the transmittance spectra of ZnO/MgF₂ based MSFFPCs of different orders.

For MSFFPC, a wide transition band is observed for third-order sequences, with the maximum transmittance occurring at a wavelength of about 550 nm. This indicates that lower-order sequences exhibit simpler and more fundamental optical behaviors. The spectrum transitions from a single broadband to two distinct transmission bands in the fourth order. This shift signifies that increasing the sequence order diversifies the optical modes and introduces more complex interactions between light and the structure. In the fifth order, this complexity increases further, with the spectrum displaying three primary transmission peaks. This demonstrates that higher-order sequences create more precise optical resonances. The transmission spectrum becomes highly intricate by the sixth order, with multiple narrow-band peaks emerging prominently. This highlights the growing impact of sequence order on the structure's optical properties, enabling more selective light guidance at specific wavelengths. Such photonic structures have significant potential in various applications, including wavelength-selective sensors, precision optical filters, and optoelectronic systems requiring advanced light management. High-order MSFFPCs generate complex optical resonances due to their increased diversity and density of optical modes, making them suitable for integration into advanced technologies.

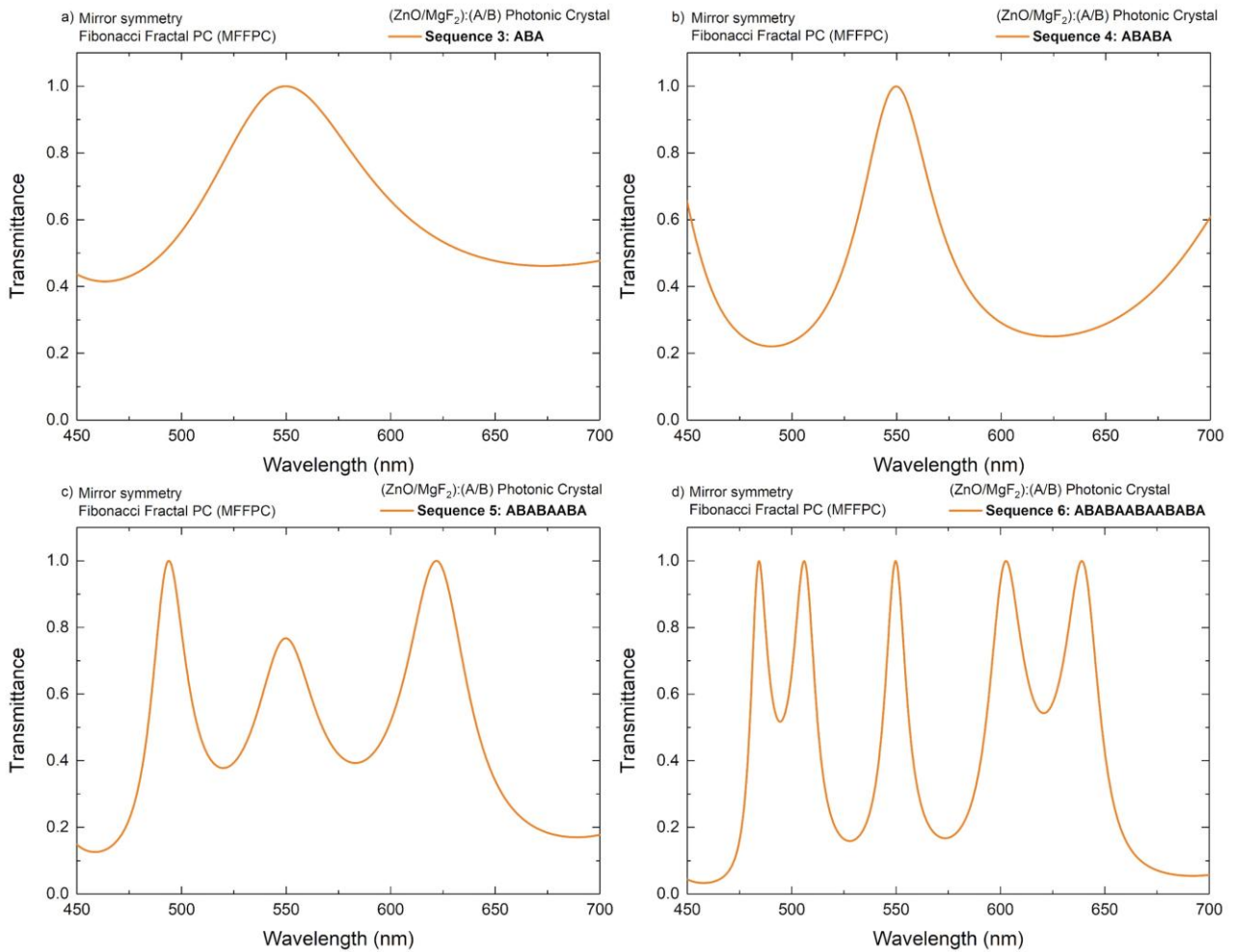


Figure 3. Transmittance spectra of ZnO/MgF₂ based Mirror Symmetry fibonacci fractal photonic crystals with a) 3rd, b) 4th, c) 5th, and d) 6th order sequences.

The optical properties of ZnO/MgF₂-based FFPC, IFFPC, and MSFFPC structures exhibit significant variations depending on the type of sequence. These structures address a wide range of applications by exhibiting different optical behaviors. FFPC can be used in wavelength-selective optical filters and general optical applications. IFFPC, with its wide transmission spectrum, stands out for use in general-purpose optical devices and applications requiring wide spectral filtering. Its characteristics make it particularly beneficial for systems demanding energy efficiency. MSFFPC, on the other hand, is distinguished by its orderly structure and narrow-band transmission peaks, making it the most suitable configuration for color-selective sensors and optical filters requiring high precision. This structure provides maximum selectivity at specific wavelengths, making it ideal for precise optical control applications. FFPC offers versatility; IFFPC is for broadband systems, and MSFFPC is for precision and specific optical applications.

FFPC, IFFPC, and MSFFPC optical characteristics are highly effective, particularly for optical applications requiring single-mode light management. The 3rd and 4th order transmittance spectrum of FFPC can be used in optical filtering applications. IFFPC, with its broader bandwidth in the 3rd and 4th orders, is better suited for general-purpose optical systems and applications requiring wide spectral coverage. The single-mode optical

characteristics with the narrowest half-width are achieved in third-order MSFFPC. This highly regular structure is ideal for precision color-selective sensors and laser systems, where high specificity and accuracy are critical. The color coordinates of the optical transitions corresponding to different orders of Fibonacci sequences (FFPC, IFFPC, MSFFPC) are presented in CIE color space in Figure 4. These graphs are particularly useful for visualizing how photonic crystals' optical transmittance influences the colors the human eye perceives.

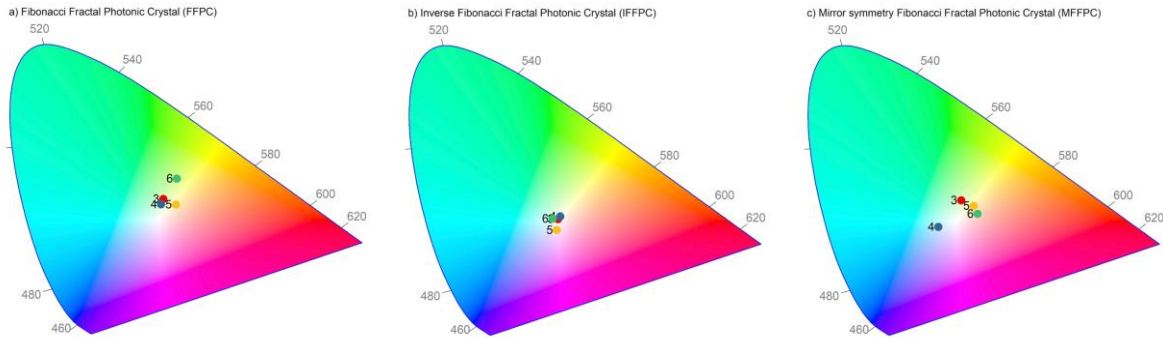


Figure 4. Different order CIE color coordinates of a) standard, b) inverse, and c) mirror symmetry Fibonacci fractal photonic crystals based on ZnO/MgF₂.

Although the color points corresponding to different Fibonacci sequence types are relatively close to one another, they exhibit slight shifts as the sequence order increases. For FFPC, the 3rd order is associated with warmer color coordinates. As the order increases, the color coordinates shift toward cooler tones (greenish-yellow). This behavior can be attributed to the more pronounced optical transitions at higher orders. In IFFPC structures, the 3rd and 4th orders concentrate around warm color tones (reddish-orange). By the 6th order, the coordinates shift toward more neutral tones (a green-yellow mix). This broader spread of colors in IFFPC is consistent with its wider transmission bandwidth.

For MSFFPC, the 3rd-order sequence (redpoint) indicates a warm color coordinate. A more regular transition is observed at higher orders (5th and 6th), with color points exhibiting less spread. This demonstrates that the mirror symmetry of the Fibonacci sequence results in more orderly optical behavior, offering more precise color selection. Among the Fibonacci-based structures, MSFFPC exhibits the most regular color distribution, making it the most suitable solution for color-selective applications. In contrast, IFFPC, with its broader color spectrum, is more appropriate for general-purpose wide-band applications.

4. CONCLUSION

In this study, the optical properties of one-dimensional photonic crystals based on ZnO/MgF₂, designed using Fibonacci fractal sequences, were thoroughly investigated. Analyses conducted on standard Fibonacci (FFPC), inverted Fibonacci (IFFPC), and mirror symmetry Fibonacci (MSFFPC) sequences revealed the significant effects of different sequence configurations and orders on photonic band gaps and optical light-matter interactions.

The results demonstrate that lower-order sequences exhibit wide and relatively simple transmission spectra, indicating their suitability for general optical filtering and wide spectral applications. However, spectral complexity was observed at higher sequence orders, characterized by the emergence of narrow-band transition peaks and enhanced selective optical behavior. Notably, MSFFPC sequences provide high spectral regularity and selectivity, making them ideal for precision applications such as color-selective sensors and narrow-band optical filters. IFFPC sequences, on the other hand, with their broad transmission bandwidths, offer advantages for wide spectral applications and systems requiring energy efficiency.

The results demonstrate that the optical properties of Fibonacci fractal photonic crystals can be effectively optimized through structural parameters such as sequence type and order selection. These findings open new opportunities for developing advanced photonic devices in telecommunications, optical sensing, color selection, and laser technologies. Furthermore, this research highlights the potential of Fibonacci sequences as a powerful tool for designing innovative photonic devices with high performance and customizable optical properties. In this context, photonic crystals based on Fibonacci sequences represent a significant research area with implications for fundamental scientific studies and industrial applications. These findings highlight the versatility of Fibonacci-based photonic crystal designs and their potential for tailored solutions across diverse optoelectronic and photonic technologies.

CONFLICT OF INTEREST

The author declares no conflict of interest.

REFERENCES

- Capaz, R. B., Koiller, B., & de Queiroz, S. L. A. (1990). Gap states and localization properties of one-dimensional Fibonacci quasicrystals. *Physical Review B*, 42(10), 6402–6407. <https://doi.org/10.1103/PhysRevB.42.6402>
- Çetinkaya, Ç., Çokduygulular, E., Kınacı, B., Güzelçimen, F., Özen, Y., Efkere, H. İ., Candan, İ., Emik, S., & Özçelik, S. (2021). Design and fabrication of a semi-transparent solar cell considering the effect of the layer thickness of MoO₃/Ag/MoO₃ transparent top contact on optical and electrical properties. *Scientific Reports*, 11(1), 13079. <https://doi.org/10.1038/s41598-021-92539-8>
- Çokduygulular, E., Çetinkaya, Ç., Emik, S., & Kınacı, B. (2023). In-depth analysis on PTB7 based semi-transparent solar cell employing MoO₃/Ag/WO₃ contact for advanced optical performance and light utilization. *Scientific Reports*, 13(1), 7548. <https://doi.org/10.1038/s41598-023-34507-y>
- Dai, X. F., Wang, H. Y., Chen, L. J., Duan, X. F., Chen, J. L., Wu, G. H., Zhu, H., & Xiao, J. Q. (2006). Growth and characterization of ferromagnetic shape memory alloy Co₅₀Ni₂₀FeGa₂₉ single crystals. *Journal of Crystal Growth*, 290(2), 626–630. <https://doi.org/10.1016/j.jcrysgro.2006.01.054>

- Elsayed, H. A., El-Sherbeeney, A. M., Nayak, S., Abukhadra, M. R., & Mehaney, A. (2024). Optical properties of the 1D quasiperiodic photonic crystals comprising gyroidal superconductor for THz applications. *Europhysics Letters*, 147(6), 65001. <https://doi.org/10.1209/0295-5075/ad7758>
- Escorcía-García, J., & Mora-Ramos, M. E. (2009). Study of optical propagation in hybrid periodic/quasiregular structures based on porous silicon. *PIERS Online*, 5(2), 167–170.
- Fujihara, S., Naito, H., & Kimura, T. (2001). Visible photoluminescence of ZnO nanoparticles dispersed in highly transparent MgF₂ thin-films via sol–gel process. *Thin Solid Films*, 389(1–2), 227–232. [https://doi.org/10.1016/S0040-6090\(01\)00893-8](https://doi.org/10.1016/S0040-6090(01)00893-8)
- Fujiwara, T., Kohmoto, M., & Tokihiro, T. (1989). Multifractal wave functions on a Fibonacci lattice. *Physical Review B*, 40(10), 7413–7416. <https://doi.org/10.1103/PhysRevB.40.7413>
- Han, P., & Wang, H. (2005). Criterion of omnidirectional reflection in a one-dimensional photonic heterostructure. *Journal of the Optical Society of America B*, 22(7), 1571. <https://doi.org/10.1364/JOSAB.22.001571>
- Jiménez-Vivanco, M. R., Lugo, E., Torres-Costa, V., Martín-Palma, R. J., Santana, M., & Herrera, R. (2024). Determination of the complex refractive index of free-standing porous silicon and oxidized porous silicon in the Visible and Ultraviolet range. *Applied Physics A*, 130(12), 952. <https://doi.org/10.1007/s00339-024-08129-8>
- Kohmoto, M., Sutherland, B., & Iguchi, K. (1987). Localization of optics: Quasiperiodic media. *Physical Review Letters*, 58(23), 2436–2438. <https://doi.org/10.1103/PhysRevLett.58.2436>
- Srivastava, R., Pati, S., & Ojha, S. P. (2008). Enhancement of omnidirectional reflection in photonic crystal heterostructures. *Progress In Electromagnetics Research B*, 1, 197–208. <https://doi.org/10.2528/PIERB07102903>
- Taherzadeh, S., & Keshavarz, A. (2024). Optical Bistability in Vanadium Dioxide Photonic Crystals Engineered with One-Dimensional Fibonacci Sequences. *Physics of Wave Phenomena*, 32(6), 401–409. <https://doi.org/10.3103/S1541308X24700407>
- Tavakoli, M., & Jalili, Y. S. (2014). One-dimensional Fibonacci fractal photonic crystals and their optical characteristics. *Journal of Theoretical and Applied Physics*, 8(1), 113. <https://doi.org/10.1007/s40094-014-0113-0>



Gazi University

Journal of Science

PART A: ENGINEERING AND INNOVATION

<http://dergipark.org.tr/guj.1565233>

Investigation of the Structural and Mechanical Properties of Pure Al-TiC Composites

Muharrem PUL¹ Tuncay ŞİMŞEK^{2*} Murat BILEN³ ¹ Department of Electricity and Energy, Kırıkkale Vocational School, Kırıkkale University, Türkiye² Department of Motor Vehicles and Transportation, Kırıkkale Vocational School, Kırıkkale University, Türkiye³ Department of Chemical Engineering, Faculty of Engineering, Gazi University, Türkiye

| Keywords | Abstract |
|-------------------|---|
| Aluminum | In this study, composites were prepared by powder metallurgy method by adding 5%, 10% and 20% by weight of TiC powder to 99.7% pure aluminum. The morphologies and elemental analysis of the prepared composite samples were carried out using scanning electron microscopy (SEM-EDX). The phase structures were then analyzed by X-ray diffraction (XRD). Finally, to investigate the mechanical properties of the composite structures, hardness measurements, compressive strength tests and abrasive wear tests were carried out. It was observed that the TiC ceramic particles added to the aluminum caused partial porosity within the structure. XRD analyses revealed peaks corresponding to Al and TiC phases in all composite structures, while no intermetallic phases or impurities associated with any phase were detected. It was observed that the addition of TiC, up to a certain amount, initially decreased and then increased the hardness of aluminum. In contrast to the hardness values, the compressive strength was found to increase with the addition of TiC. In the abrasive wear tests, wear initially increased with the addition of TiC, in parallel with the hardness values, but as the TiC content increased to 20%, the amount of wear decreased. Compared to the reference sample of pure aluminum as the matrix material, wear losses increased with the addition of TiC in all composite structures. |
| TiC | |
| Powder Metallurgy | |
| Microstructure | |
| Phase Analysis | |

Cite

Pul, M., Şimşek, T., Bilen, M. (2025). Investigation of the Structural and Mechanical Properties of Pure Al-TiC Composites. *GU J Sci, Part A, 12(1)*, 278-291. doi:10.54287/guj.1565233

| Author ID (ORCID Number) | Article Process |
|--------------------------|-----------------------------------|
| 0000-0002-0629-3516 | Muharrem PUL |
| 0000-0002-4683-0152 | Tuncay ŞİMŞEK |
| 0000-0003-3374-8173 | Murat BILEN |
| | Submission Date 11.10.2024 |
| | Revision Date 11.11.2024 |
| | Accepted Date 30.12.2024 |
| | Published Date 26.03.2025 |

1. INTRODUCTION

In metal matrix composites, various reinforcement materials such as ceramics, borides, nitrides, oxides, and high-entropy alloys have been used as additives (Tong & Ghosh, 2001; Kumar et al., 2024; Ravindran et al., 2022). Reinforcement materials are utilized in forms like fibers, platelets, whiskers, or particles. Among these structures, particle reinforcement is frequently preferred due to reasons such as the availability, microstructural uniformity, and homogeneity of the reinforcement materials. Particle-reinforced composite structures are generally successfully produced by powder metallurgy or liquid metallurgy methods (Ibrahim et al., 1991).

In metal matrix composites, ceramic reinforcements are commonly used in structural, aerospace, space, manufacturing, and mechanical applications due to their high mechanical properties, wear resistance, low density, and high-temperature performance (Song et al., 2008). Ceramic reinforcement materials are selected

*Corresponding Author, e-mail: tuncaysimsek@kku.edu.tr

based on their cost, elastic modulus, tensile strengths, densities, melting temperatures, thermal stabilities, coefficients of thermal expansion, sizes, morphologies, and compatibility with the metal matrix (Ibrahim et al., 1991; Rack., 1988). Among ceramic materials, TiC ceramics, when used as a reinforcement material, provide composite structures with mechanical properties such as high hardness and high elastic modulus. With a hardness of 28-35 GPa, a Young's modulus ranging from 410-510 GPa and a tensile strength of 258 MPa, TiC is a crucial reinforcement element known for its superior wear resistance. (Mhadhbi & Driss, 2020; Farid et al., 2023). Due to these properties, it is suitable for use in various engineering applications such as aerospace, automotive, and biomedical fields. Pandey et al. (2017) reported that TiC particles improve the wear resistance and mechanical properties of aluminum matrix composites in the composite structures they obtained with an Al6061 matrix reinforced with TiC. In another study, TiC reinforced Ti-Mo-Al intermetallic composite structures were successfully produced by powder metallurgy. In this study, composite structures were obtained by adding Ti+C₃Cr₂ in situ synthesis into the Ti-1.5Fe-2.25Mo-1.2Nd-0.3Al matrix. The incorporation of TiC led to a substantial enhancement in the mechanical properties of the composites at room and high temperatures and the wear resistance was also improved significantly (Liu et al., 2007). Saravanan et al. (2018) reinforced the Al7075 matrix with varying amounts of TiC using the powder metallurgy method. Their investigations showed that the reinforcement elements were homogeneously distributed within the main matrix and improved wear resistance. In another study, Al2024-TiC reinforced composite structures were produced, and the effects of wear resistance and thermally treated conditions on the structures were examined. The results showed that heat treatment enhanced both hardness and wear resistance, with oxidation and abrasion being the dominant wear mechanisms on composite structures (Bedolla-Becerril et al., 2023). Nyanor et al. (2024) produced hybrid composites by adding nano- and micron-sized TiC and carbon nanotube particles into aluminum materials. They reported improvements in tensile strength and ductility. Lin et al. (2021) investigated the production of Al2024 matrix composites reinforced with TiC nanoparticles and graphene nanoplatelets via powder metallurgy. Subsequently, the microstructural, microhardness, and tribological properties of the composites were analyzed. It was observed that the wear resistance of the composites significantly improved due to the synergistic effects of the TiC and graphene particles. Additionally, a shift in the wear mechanism from adhesive to abrasive wear was noted. In another study, the influence of nano-TiC on the properties of Al2024 metal matrix composites was investigated. The composites, containing varying amounts of TiC, were produced using the stir casting method, and their mechanical properties and hardness were evaluated. The results revealed that the ultimate tensile strength, yield strength, and hardness of the samples were proportionally enhanced with the increasing concentration of nano-TiC in the Al2024 matrix. In the study by Cabeza et al. (2017), the effect of ball milling on the properties of nano-TiC reinforced 6005A aluminum matrix composites were investigated. Various volume fractions of Nano-TiC and AA 6005A powders were milled using a horizontal attritor mill, with liquid methanol employed as a process control agent. The powder mixtures were milled for up to 10 hours. It was reported that the hardness of the composites increased with higher TiC content.

In this study, TiC ceramic was added to pure aluminum material at 5%, 10%, and 20% weight ratios using the powder metallurgy method, and then sintered. The phase structure, morphological, and mechanical properties of the composite structures were investigated. Additionally, the densities of the samples were determined. This study highlights the use of varying proportions of TiC reinforcement in a pure aluminum matrix to comprehensively analyze the relationship between reinforcement content and composite performance. The findings provide valuable insights into improving aluminum-based composites for advanced structural applications, particularly in industries requiring a balance of lightweight properties and high mechanical strength. Additionally, this research addresses critical gaps in understanding the effects of reinforcement distribution and porosity on the overall performance of metal matrix composites.

2. MATERIAL AND METHOD

In this study, aluminum powder with 99.7% commercial purity was used as the matrix material, and ceramic-based titanium carbide (TiC) powder was used as the reinforcing element. Composite samples were produced by adding 5%, 10%, and 20% by weight of TiC to aluminum. SEM images and mapping analyses showing the elemental distribution of the main matrix and reinforcing materials forming the composite structures are provided in Figure 1-2.

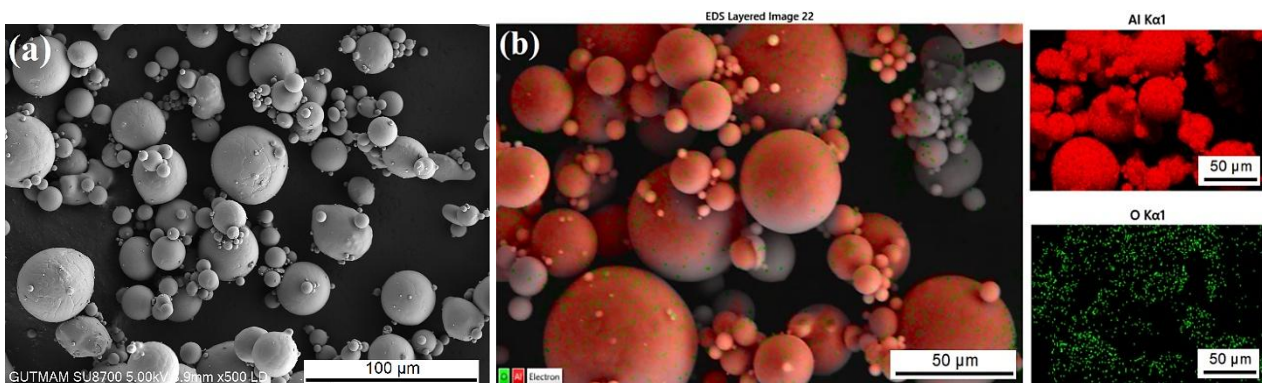


Figure 1. *a) SEM and b) Mapping images of the aluminum (Al) powder as the matrix material*

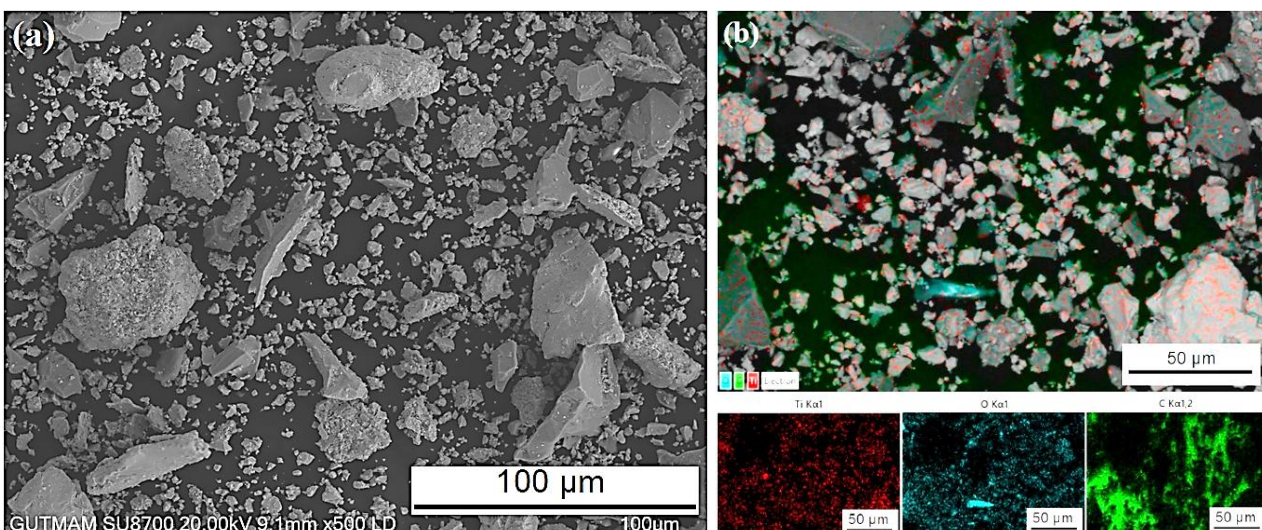


Figure 2. *a) SEM and b) Mapping images of the TiC powder as the reinforcing element.*

In the production of composite structures, the powder metallurgy method, one of the solid-phase techniques, was applied. For this purpose, in the first stage, Al 99.7% and TiC powders were weighed according to the specified weight ratios and mixed for 2 hours using a mechanical mixer. During this process in a rotary mixer, steel balls with a diameter of 8 mm, weighing 10 times the weight of the powder mixtures, were used. In the second stage of production, the mixture was compacted by applying 650 MPa of pressure in a 12 mm diameter steel mold. In the final stage of the powder metallurgy process, the compressed composite compacts were subjected to sintering. The sintering heat treatment was performed at a temperature of 570 ± 10 °C for 90 minutes in an air atmosphere, completing the production of Al/TiC composite samples.

In the second stage of the experimental study, phase analysis and mechanical tests were conducted along with SEM analysis. SEM and EDX analyses were performed using a Hitachi SU8700 model FE-SEM microscope. The phase structures were determined by X-ray diffraction (XRD). Phase identifications of each composite sample were analyzed using Jade 6.0 software. Measurements were taken with $\text{CuK}\alpha$ radiation ($\lambda=1.54\text{\AA}$), at 40 kV voltage and 30 mA current, in the 2θ range from 20° to 90° with a step size of 0.026° . In the mechanical tests, hardness measurements were first conducted using the Brinell method with a 2.5 mm steel indenter and a 15.625 kgf load. In the compression tests conducted in accordance with the ASTM C 109 standard, a compression testing machine with a capacity of 3000 kN and a loading rate of 0.9 kN/s was used. Finally, abrasive wear tests were performed. The abrasive wear tests were conducted using the pin-on-disk method on SiC-based 320 mesh sandpaper, applying a 10 N load, at a sliding rate of 0.8 m/s for 90 seconds.

3. RESULTS AND DISCUSSION

3.1. Microstructures

To examine the microstructures of the produced composite structures, SEM images were taken at different magnifications. Simultaneously, mapping and EDX elemental analyses were performed. Figure 3-5 present these images and analyses.

These figures provide detailed visual and compositional information about the distribution of TiC particles within the base aluminum matrix, as well as the interface between the matrix and the reinforcement, helping to understand the structural integrity and material properties of the composites.

When examining the SEM images in Figure 3, it was determined that a porous structure had formed in all samples. It was observed that the matrix material, aluminum, formed sufficient bonds during the sintering heat treatment, and there were not many voids between the aluminum powder particles. It can also be noted that aluminum smearing occurred during the surface polishing process. The soft structure of pure aluminum offers little resistance to such smearing. Additionally, it is understood that separations occurred between the grains in some areas. Although aluminum particles formed bonds with each other during the sintering heat treatment, the grinding process applied during polishing allowed the soft aluminum matrix to separate in certain regions and form cracks. It is also considered that another influential factor in the formation of these separations is the

presence of TiC particles used as the reinforcing material. Similar results are found in the literature (Kumar et al., 2017; Samal et al., 2019). This is because the TiC particles, positioned between the Al matrix powders, may have created interfacial regions acting as thermal barriers by partially obstructing heat transfer. It is well-known that ceramic-based TiC particles, which have significantly higher thermal resistance compared to aluminum, were unaffected by the 570°C temperature applied during the sintering process and maintained their structural integrity within the composite. Therefore, due to its very different thermal properties compared to aluminum, TiC exhibited different behavior during the heat treatment, influencing the structural properties of the regions where it was present. A similar result is presented in a study in the literature (Lu et al., 2020).

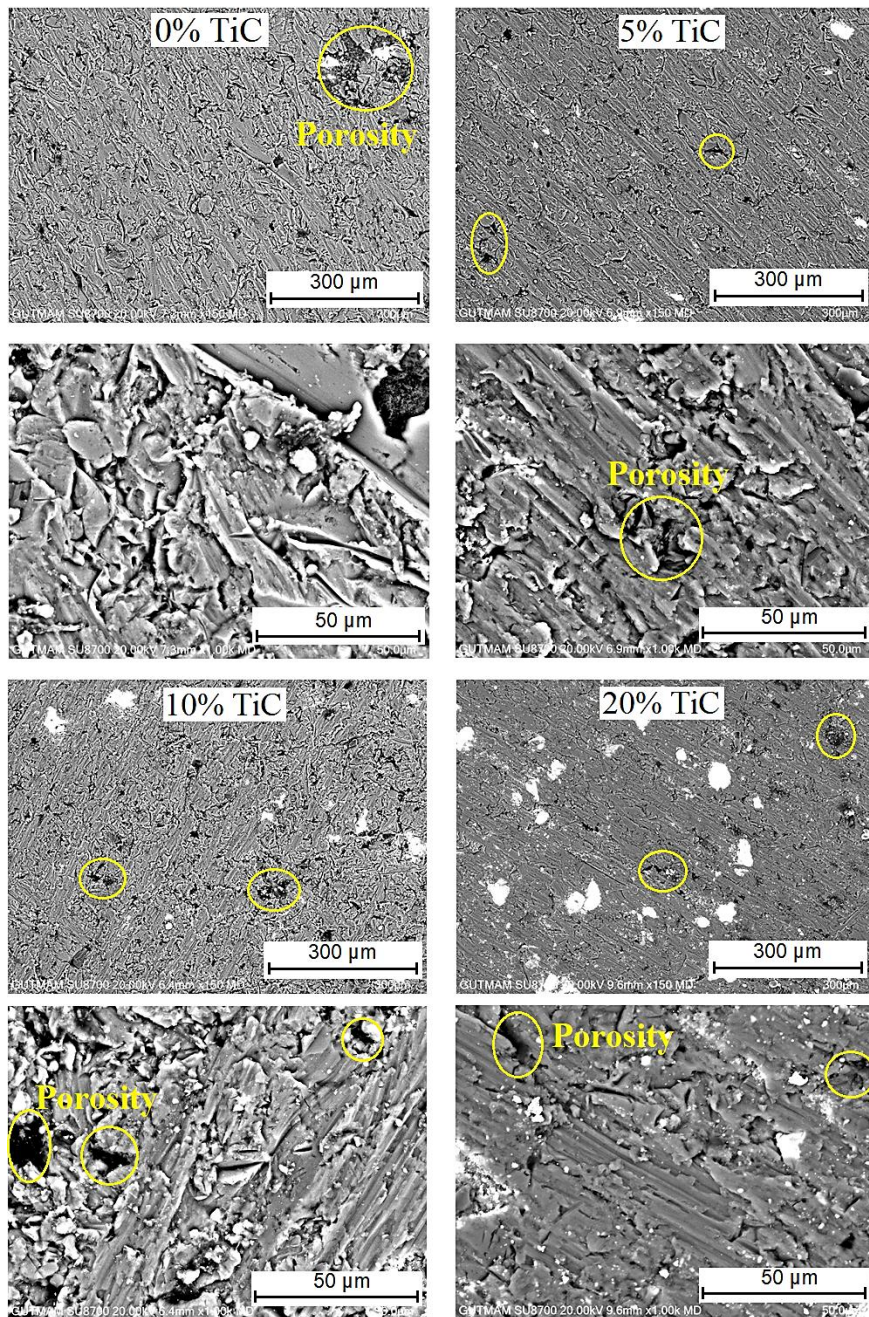


Figure 3. Microstructure images of aluminum composites with pure aluminum 0%, 5%, 10%, and 20% TiC content at 150× and 1000× magnifications.

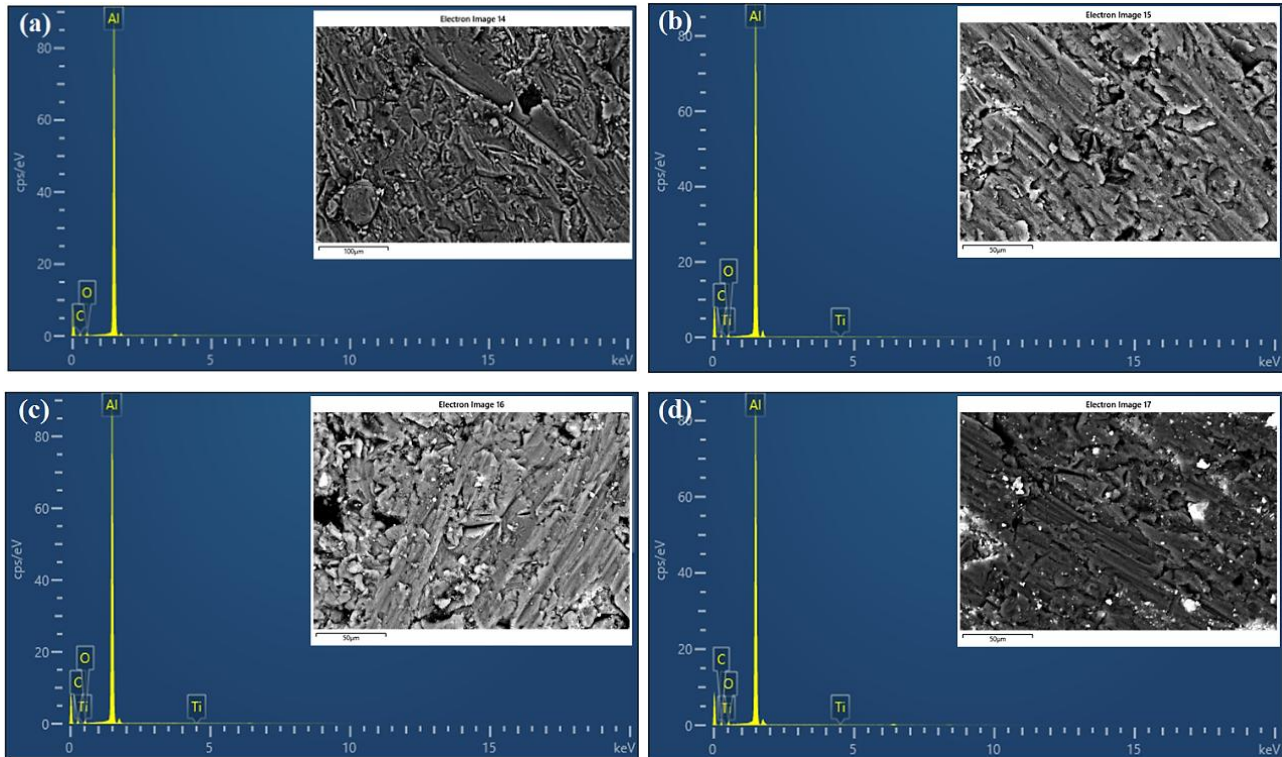


Figure 4. EDX analyses of pure aluminum and TiC-reinforced composite structures: Pure Al 99.7 (a), 5% TiC + Al 99.7 (b), 10% TiC + Al 99.7 (c), 20% TiC + Al 99.7 (d).

Upon examining the EDX analyses presented in Figure 4, the presence of titanium (Ti) and carbon (C) peaks associated with the TiC reinforcing element in the composite structure is evident. In the EDS analysis of the matrix material shown in Figure 4a, it is understood that only aluminum (Al), oxygen (O), and very small amounts of carbon are present. It is known that aluminum is highly sensitive to oxygen and reacts quickly, leading to oxidation. This phenomenon was observed in all EDX analyses. The carbon detected in the matrix material is believed to originate from the SiC-based sandpaper used during surface preparation. To verify and support the evaluations made based on the SEM images and EDX analyses related to the microstructures, mapping images of the composite structures are presented in Figure 5. Mapping analysis is an advanced analytical technique that visually shows the elemental distribution within the structure, performed during SEM imaging of the composite materials using a FE-SEM scanning electron microscope. When examining the images in Figure 5, the distribution of the titanium (Ti) and carbon (C) elements within the aluminum matrix and the TiC particles can be observed in all composite samples. Additionally, it is also understood that oxygen is present in all composite structures. In a mapping analysis conducted in a study in the literature, it was stated that TiC particles were dispersed homogeneously within the structure (Mohapatra et al., 2016). As indicated in the EDX analyses, the easy oxidation of aluminum means that oxidation formation cannot be prevented during processes carried out in non-inert environments.

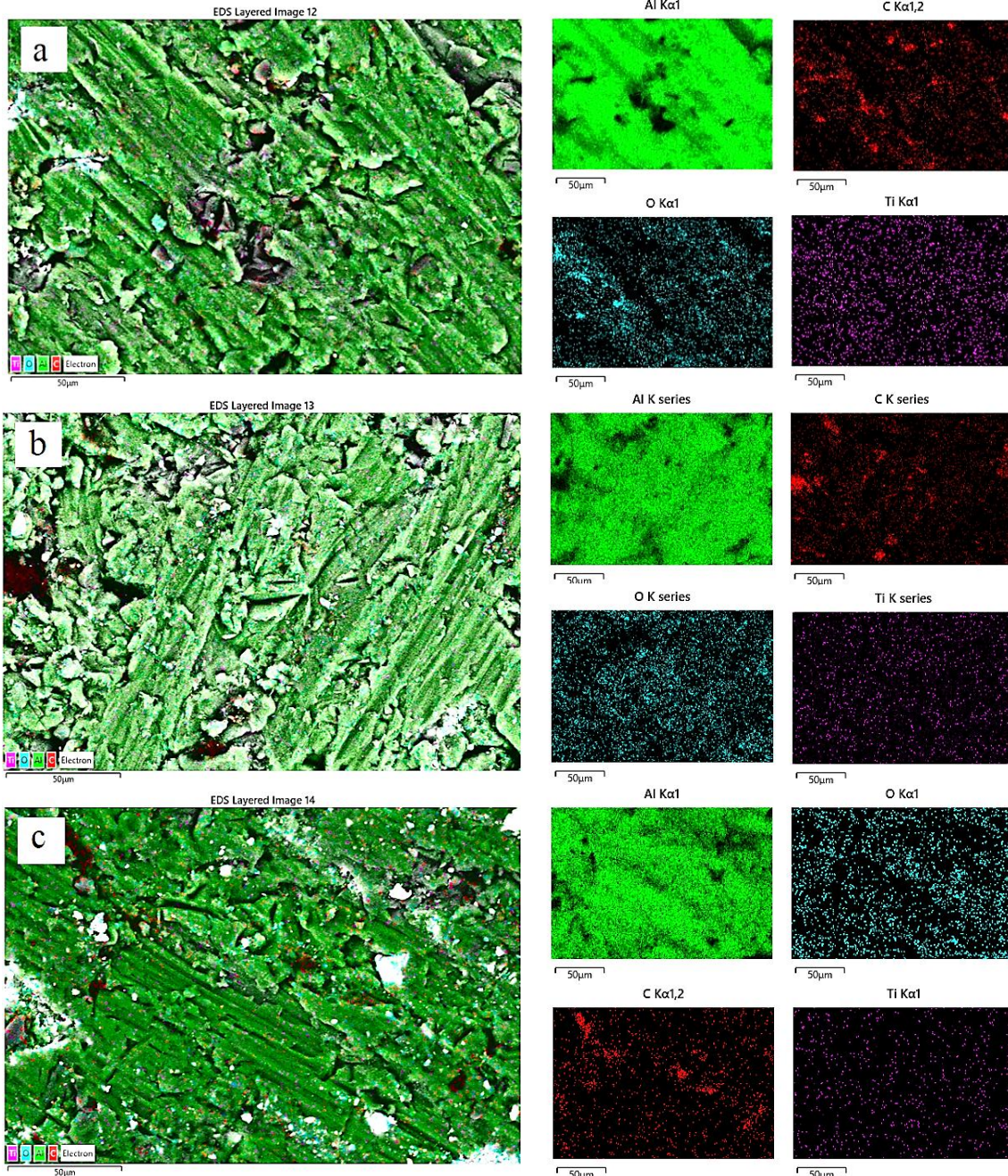


Figure 5. Mapping analyses of TiC-reinforced composite structures: 5% TiC + Al 99.7 (a), 10% TiC + Al 99.7 (b), 20% TiC + Al 99.7 (c).

3.2. XRD Analysis

Following the microstructure examinations, the phases of the sintered composite samples were identified using XRD. Figure 6 presents the XRD patterns of the pure aluminum matrix and the samples reinforced with 5%, 10%, and 20% TiC. Upon examining the figure, it can be observed that in the unreinforced pure Al material, peaks corresponding to the Al phase (ICDD: 85-1327, cubic, Fm-3m) appear at 2θ of 38.47° , 44.72° , 65.09° , 78.23° , and 82.43° . In the samples with the TiC addition, peaks corresponding to the TiC phase (ICDD: 71-0298, cubic, Fm-3m) were observed at 2θ of 35.90° and 41.50° . As the proportion of the reinforcing materials increased, a relative increase in the intensity of the TiC peaks was noted. The investigations revealed that after

the sample preparation, pressing, and sintering processes, no intermetallic phases or impurities were detected in the composite structures. This indicates that the addition of TiC did not introduce any unwanted phases and that the overall integrity of the composite materials was maintained (Ramkumar et al., 2019).

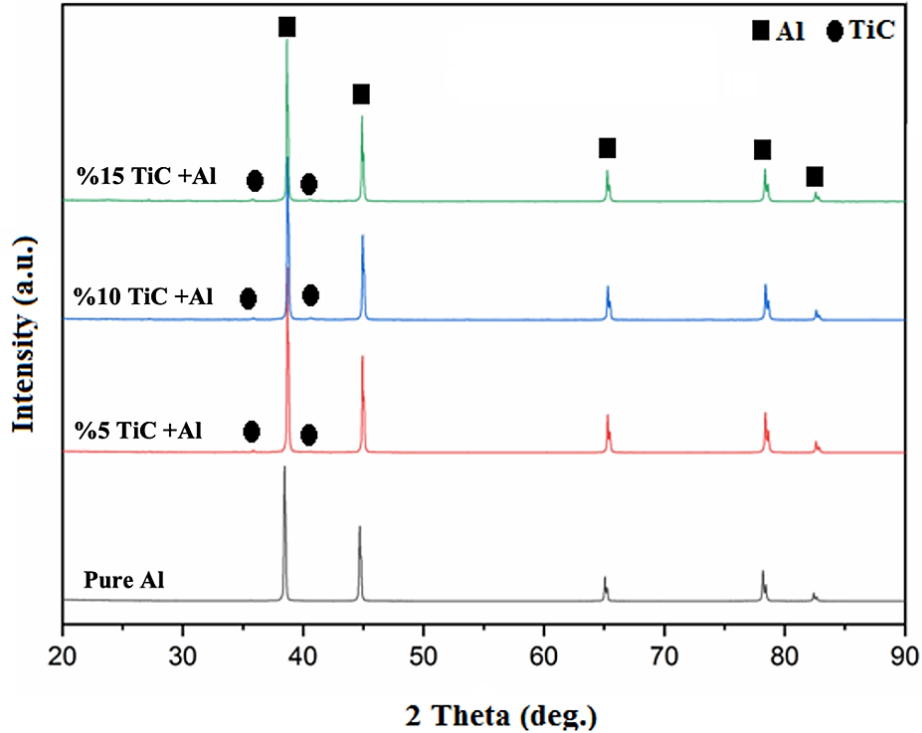


Figure 6. XRD graph of the pure aluminum matrix and samples reinforced with different proportions of TiC.

3.3. Mechanical Strength

To investigate the mechanical strength of the composite structures, hardness analyses were conducted, along with compressive strength, density measurements (based on Archimedes' principle), and abrasive wear tests were performed. The graphs of these mechanical tests are presented in Figure 7-9. These figures illustrate the relationship between the TiC reinforcement levels and the various mechanical properties of the composites, including hardness, density, compressive strength, and wear resistance. The results provide valuable insights into how the addition of TiC affects the mechanical performance of the aluminum matrix composites.

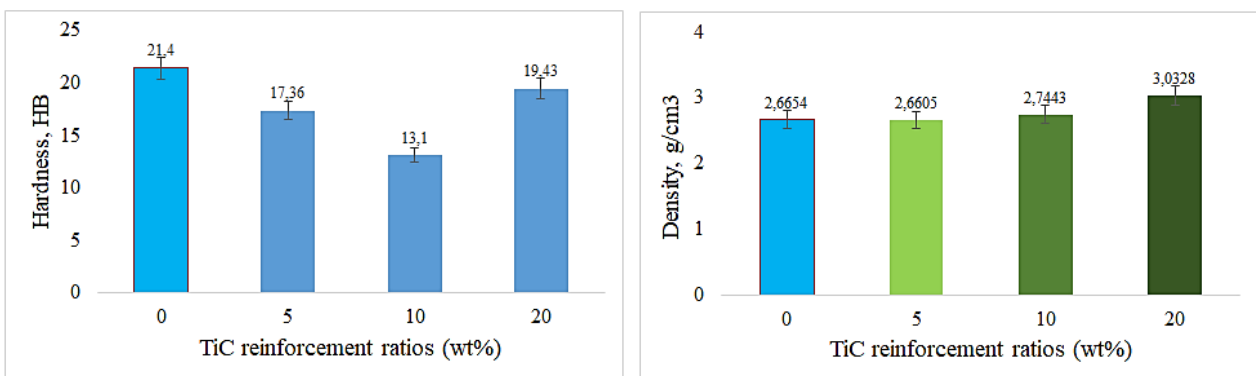


Figure 7. Hardness measurement and density values.

Upon examining the hardness measurement values presented in Figure 7, it is observed that the hardness values of all composite samples decreased with the addition of TiC. While an increase in the hardness of the composite structures was expected due to the much harder phase of TiC compared to aluminum, the opposite effect was noted. Such reductions in hardness can be encountered in some aluminum matrix composites with particle reinforcement. The primary reason for the decrease in hardness is believed to be the porosity present in the composite structure. However, as the amount of TiC within the composite structure increased, the initially decreased hardness values began to show a gradual improvement. This suggests that the hard TiC particles present in the structure, even in small amounts, begin to exhibit their reinforcing effect, reaching the highest value in the composite reinforced with 20% TiC. As the impact of porosity within the composite structure diminished, the hardness-enhancing effect of the TiC particles became more pronounced. As indicated by the microstructure images in Figure 3, a significantly porous structure had formed. Conversely, it is noted that the density values of the composite structures increased in proportion to the amount of TiC added. This is an expected outcome, given that the density of the aluminum matrix is 2.66 g/cm^3 , while the density of the TiC reinforcing element is 4.93 g/cm^3 . Thus, as the proportion of TiC within the composite structure increased, the density values also rose. Graphs illustrating the compressive strength and abrasive wear loss values obtained from tests conducted to examine the mechanical properties of the composite structures are presented in Figure 8. In the literature, Canakci and Varol (2014) used AA7075 chips obtained through turning operations in composites. A mixture of Al powder, AA7075 chips, and SiC particles was first cold-pressed at 100 MPa in a steel die and then hot-pressed at 300 MPa for 1 hour at 500°C . It was reported that Al powders were non-homogeneously distributed in the AA7075/Al-SiC powders. Furthermore, it was observed that increasing the amount of SiC particles enhanced the hardness of the recycled composites. Bodukuri et al. (2016) investigated the production of Al-SiC-B₄C metal matrix composites using powder metallurgy processes. Three compositions were designed with volume fractions of 90% Al, 8% SiC, and 2% B₄C; 90% Al, 5% SiC, and 5% B₄C; and 90% Al, 3% SiC, and 7% B₄C. The powders were ball-milled using an attrition mill and then compacted under a pressure of up to 150 MPa. Subsequently, the samples were sintered at 610°C with a heating rate of $20^\circ\text{C}/\text{min}$ and analyzed for their microstructural characteristics and hardness properties. It was observed that an increase in the amount of B₄C in the metal matrix composite significantly enhanced the microhardness, primarily due to the uniform distribution of the reinforcements. Recently, Barakat et al. (2023) fabricated Al-based nanocomposites using varying concentrations of Al₂O₃ nanoparticles. To enhance the wettability between the Al matrix and the reinforcement phase, the Al₂O₃ nanoparticles were coated with Ag and Cu using the electroless chemical deposition technique. The structural, microstructural, and mechanical properties of the hot-extruded nanocomposites were then characterized in detail. A significant improvement in mechanical properties was observed with increasing concentrations of Al₂O₃ nanoparticles. As can be seen from these studies in the literature, mechanical properties such as hardness in composite structures improve with the homogeneous distribution of reinforcement elements within the matrix.

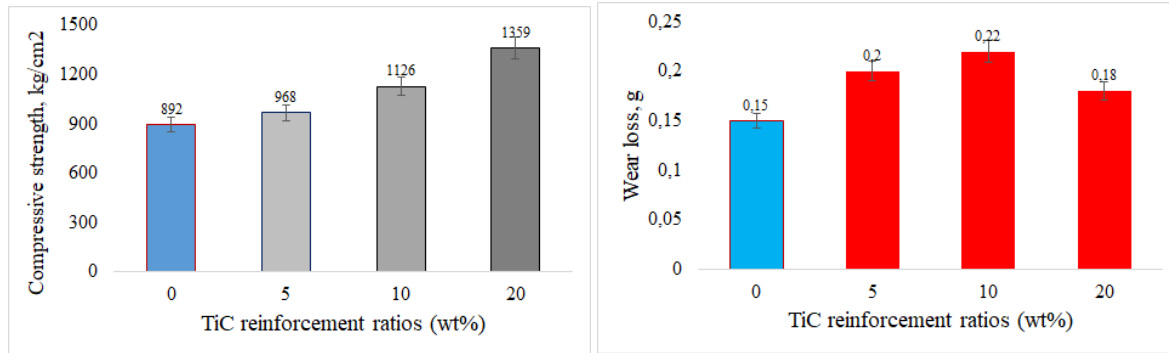


Figure 8. Compressive strength values and abrasive wear loss values.

Upon examining Figure 8, it is evident that the addition of TiC to the pure aluminum matrix material enhances the compressive strength of the composite samples. The ceramic properties of the TiC particles, which are significantly harder than aluminum, contribute to increasing the toughness of the composite structures, thereby raising their compressive strength. The graph indicates a proportional increase in strength with the amount of TiC added. Specifically, the compressive strength of the composite structure with 20% TiC reinforcement showed a 52% increase compared to the aluminum matrix material. Additionally, when looking at the graph depicting abrasive wear loss values within Figure 8, it can be seen that the reinforcement of TiC reduces the wear resistance of the composite structures. All composite samples exhibited greater wear losses than the pure aluminum matrix material. Initially, these wear loss values appear to correlate positively with the hardness values, which can be considered acceptable results. In other words, as the hardness of the material decreases, wear losses tend to increase. The highest wear loss occurred in the sample with 10% TiC reinforcement, which had the lowest hardness value. Conversely, the lowest wear loss was observed in the pure aluminum matrix material, which exhibited the highest hardness. Similar results are reported in a study by Pul (2019a). He stated that as the amount of hard-phase B₄C and SiC reinforcement elements increased in the aluminum composite, wear losses also progressively increased. This was attributed to poor wetting between the matrix and the reinforcements, as well as increased porosity. In another study conducted by Pul (2019b), the mechanical properties of Al2024-based composites reinforced with B₄C and TiB₂ particles were investigated. It was observed that, compared to the pure Al2024 reference material, the abrasive wear losses of the composites reinforced with B₄C and TiB₂ were higher, and the wear losses further increased with higher reinforcement content. Additionally, images of the worn surfaces captured using a digital microscope after the abrasive wear tests are presented in Figure 9.

A general examination of the images presented in Figure 9 reveals distinct wear lines formed on the surfaces of the materials. The regions that appear white or lighter in color in these images represent the grooved areas created during the abrasive wear tests. As shown in Figure 8, the most extensive wear regions are observed in the composites with 10% TiC reinforcement. This observation supports the findings related to wear loss values, indicating a strong correlation between the wear loss data and the worn surface images. Overall, the images illustrate the impact of TiC reinforcement on the wear characteristics of the composite materials, highlighting the increased wear loss associated with certain TiC concentrations.

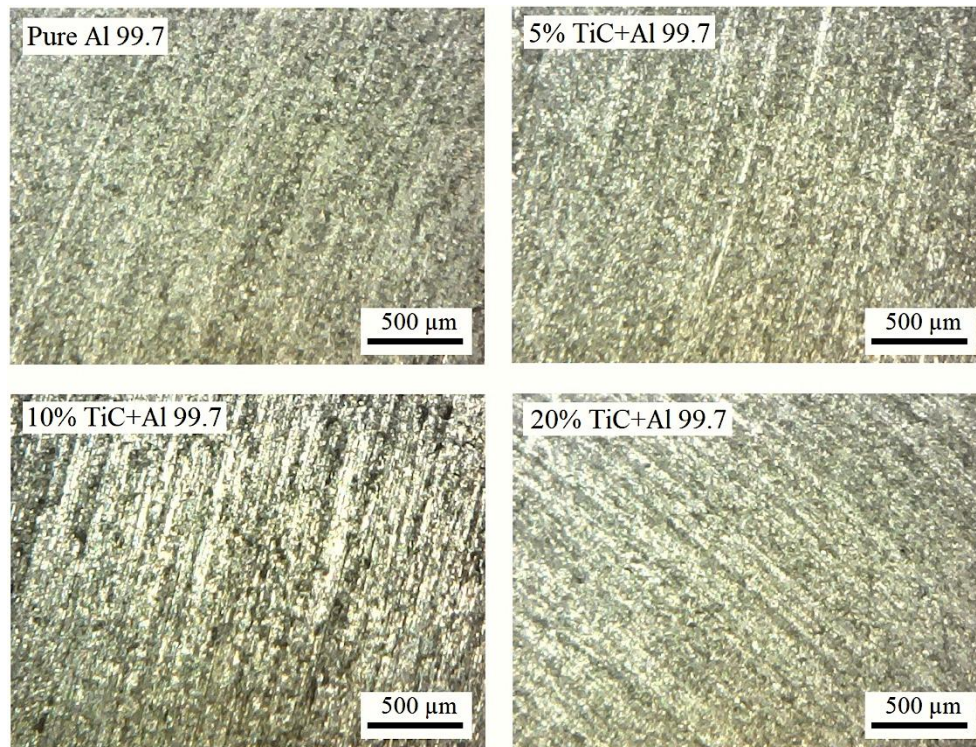


Figure 9. Surface Images of Experimental Samples After Abrasive Wear.

4. CONCLUSION

In this study, titanium carbide (TiC) powders were added as reinforcement materials in varying proportions to a pure aluminum matrix using the powder metallurgy method. The powders were homogeneously mixed in a tumbling mixer, pressed, and then characterized after sintering. Upon examining the microstructures, it was observed that the TiC ceramic particles contributed to partial porosity within the composite structures. Additionally, it was determined that the homogeneity of the structure improved progressively with the increasing TiC content. XRD analyses confirmed the presence of peaks corresponding to the aluminum (Al) and TiC phases. Notably, no impurities or intermetallic compounds were detected in any of the aluminum or TiC-reinforced samples. However, it was seen that with the increase in TiC content, the porosity within the structure led to a decrease in both the hardness of the aluminum composite materials and their resistance to abrasive wear. Conversely, the compressive strength values increased across all composite samples in proportion to the amount of TiC added. In conclusion, the physical properties of the TiC added to aluminum using the powder metallurgy technique, as well as the amount of reinforcement, were found to have a significant impact on the experimental values obtained. These findings demonstrate the potential of TiC-reinforced aluminum composites in applications where high compressive strength is a key requirement. However, the decrease in hardness and wear resistance with increasing TiC content suggests that further optimization of the processing parameters, such as sintering conditions or powder mixing techniques, is needed to minimize porosity and achieve a better balance of mechanical properties.

AUTHOR CONTRIBUTIONS

Conceptualization, M.P and T.Ş.; methodology, M.P, T.Ş, M.B.; title, M.P., T.Ş.; validation, M.P and T.Ş laboratory work, M.P and T.Ş.; formal analysis, M.P, T.Ş, M.B.; research, M.P, T.Ş, M.B.; sources, M.P, T.Ş, M.B.; data curation, M.P and T.Ş.; manuscript-original draft, M.P and T.Ş; manuscript-review and editing, M.P, T.Ş, M.B; visualization, M.P, T.Ş, M.B.; supervision, M.P; project management, M.P, T.Ş, M.B.; funding, M.P, T.Ş, M.B. All authors have read and legally accepted the final version of the article published in the journal.

CONFLICT OF INTEREST

The authors declare no conflict of interest.

REFERENCES

- Barakat, W.S., Habba, M. I.A., Ibrahim, A., Fathy, A., & Elkady, O.A., (2023). The effect of Cu coated Al₂O₃ particle content and densification methods on the microstructure and mechanical properties of Al matrix composites, *Journal of Materials Research and Technology*, 24, 6908-6922, <https://doi.org/10.1016/j.jmrt.2023.05.010>
- Bedolla-Becerril, E., Garcia-Guerra, J., Lopez-Morelos V.H., Garcia-Renteria, M.A, Falcon-Franco, L.A., Martinez-Landeros, V.H, Garcia-Villarreal, S., & Flores-Villaseñor, S.E. (2023). Tribological Behaviour of Al-2024/TiC Metal Matrix Composites. *Coatings* 13, 77. <https://doi.org/10.3390/coatings13010077>
- Bodukuri, A. K., Eswaraiyah, K., Rajendar, K., & Sampath, V. (2016). Fabrication of Al–SiC–B₄C metal matrix composite by powder metallurgy technique and evaluating mechanical properties, *Perspectives in Science*, 8, 428-431, <https://doi.org/10.1016/j.pisc.2016.04.096>
- Cabeza, M., Feijoo, I., Merino, P., Pena, G., Pérez, M.C., Cruz, S, Rey, P. (2017). Effect of high energy ball milling on the morphology, microstructure and properties of nano-sized TiC particle-reinforced 6005A aluminium alloy matrix composite, *Powder Technology*, 321, 31-43, <https://doi.org/10.1016/j.powtec.2017.07.089>
- Canakci, A., & Varol, T. (2014). Microstructure and properties of AA7075/Al–SiC composites fabricated using powder metallurgy and hot pressing, *Powder Technology*, 268, 72-79, <https://doi.org/10.1016/j.powtec.2014.08.016>
- Farid, W., Bah, T.M., Kong, C., & Yu, H. (2023). A novel way to fabricate high elastic modulus and high strength of TiC reinforced aluminum matrix composite, *Materials and Manufacturing Processes*, 38 (14), 1785-1797, <https://doi.org/10.1080/10426914.2023.2217886>
- Ibrahim, I.A., Mohamed, F.A. & Lavernia, E.J. (1991). Particulate reinforced metal matrix composites — a review. *Journal of Material Science*, 26, 1137–1156. <https://doi.org/10.1007/BF00544448>

- Kumar, R., Kiran, K., & Sreebalaji, V.S. (2017) Micro structural characteristics and mechanical behaviour of aluminium matrix composites reinforced with titanium carbide, *Journal of Alloys and Compounds*, 723, 795-801 <http://doi.org/10.1016/j.jallcom.2017.06.309>
- Kumar, D., Seetharam, R., & Ponappa, K. (2024). A review on microstructures, mechanical properties and processing of high entropy alloys reinforced composite materials. *Journal of Alloys and Compounds*, 972, 172732. <https://doi.org/10.1016/j.jallcom.2023.172732>
- Liu, B., Liu, Y., He, X. Y., Tang, H. P., Chen, L. F., & Huang, B. Y. (2007). Preparation And Mechanical Properties of Particulate-Reinforced Powder Metallurgy Titanium Matrix Composites, *Metallurgical and Materials Transactions A* 38, 2825-2831. <https://doi.org/10.1007/s11661-007-9329-9>
- Lin, F., Wang, J., Wu, H., Jia, F., Lu, Y., Ren, M., Yang, M., Chen, Z., & Jiang, Z. (2021). Synergistic effects of TiC and graphene on the microstructure and tribological properties of Al₂₀₂₄ matrix composites, *Advanced Powder Technology*, 32 (10), 3635-3649, <https://doi.org/10.1016/j.apt.2021.08.015>
- Lu, Y., Watanabe, M., Miyata, R., Nakamura, J., Yamada, J., Kato, H., & Yoshimi K. (2020) Microstructures and mechanical properties of TiC-particulate-reinforced Ti–Mo–Al intermetallic matrix composites, *Materials Science & Engineering A*, 790, 139523. <https://doi.org/10.1016/j.msea.2020.139523>
- Nyanor, P., Yehia, H.M., Bahador, A., Umeda, J., Kondoh, K., & Hassan, M.A. (2024) Microstructure and mechanical properties of hybrid nano-titanium carbide-carbon nanotubes (nano-TiC-CNT) reinforced aluminium matrix composite, *Advanced Composite Materials*, 33 (3), 305-323, <https://doi.org/10.1080/09243046.2023.2253097>
- Mhadhbi, M., & Driss, M. (2020). Titanium Carbide: Synthesis, Properties and Applications. *Brilliant Engineering*, 2 (2), 1–11. <https://doi.org/10.36937/ben.2021.002.001>
- Mohapatra, S., Chaubeya, A.K., Mishrab, D.K., & Singha, S.K. (2016) Fabrication of Al–TiC composites by hot consolidation technique: its microstructure and mechanical properties, *Journal of Materials Reserach and Technology*. 5(2):117–122. <http://doi.org/10.1016/j.jmrt.2015.07.001>
- Pandey, U., Purohit, R., Agarwal, P., Dhakad S.K., & Rana, R.S. (2017). Effect of TiC particles on the mechanical properties of aluminium alloy metal matrix composites (MMCs), *Materials Today: Proceedings*, 4, 5452–5460. <https://doi.org/10.1016/j.matpr.2017.05.057>
- Pul, M. (2019a). Effect of sintering on mechanical property of SiC/B₄C reinforced aluminum, *Materials Research Express*, 6: 016541 <https://doi.org/10.1088/2053-1591/aacee1>
- Pul, M. (2019b). The Effect on Mechanical Properties of Reinforcement Amount at B₄C + TiB₂ Reinforced Al 2024 Based Composites Produced by Powder Metallurgy, *International Journal of Engineering Research and Development*, 11(1), 87-99. <https://doi.org/10.29137/umagd.407488>
- Rack, H.J. (1988) *Processing and Properties of Powder Metallurgy Composites*", (P. Kumar, K. Vedula and A. Ritter, Eds.). The Metallurgical Society.
- Ramkumar, K.R., Sivasankaran, S., Al-Mufadi, F.A., Siddharth, S., & Raghu, R. (2019) Investigations on microstructure, mechanical, and tribological behaviour of AA 7075–x wt.% TiC composites for

- aerospace applications, *Archives of Civil and mechanical engineering*, 19428–19438. <https://doi.org/10.1016/j.acme.2018.12.003>
- Ravindran, S., Carolin, L.R., Gopal, V., Ramesh, K., Ravi, G., Sathya, S., (2022). Influence of nano-TiC content on the properties of Al2024 aluminium metal matrix composites, *Materials Today: Proceedings*, 69 (3), 922-926, <https://doi.org/10.1016/j.matpr.2022.07.371>
- Samal, P., Vundavilli, P. R., Meher, A., & Mahapatr, M.M. (2019) Fabrication and Mechanical Properties of Titanium Carbide Reinforced Aluminium Composites, *Materials Today: Proceedings*, 18 (7), 2649–2655. <https://doi.org/10.1016/j.matpr.2019.07.125>
- Saravanan, C., Subramanian K., Anandkrishnan V. & Sathish S., (2018). Tribological behavior of AA7075-TiC composites by powder metallurgy, *Industrial Lubrication and Tribology*, 70 (6), 1066–1071. <https://doi.org/10.1108/ILT-10-2017-0312>
- Song, M.S., Zhang, M.X., Zhang, S.G., Huang, B., & Li, J.G. (2008). In situ fabrication of TiC particulates locally reinforced aluminum matrix composites by self-propagating reaction during casting, *Materials Science and Engineering A*. 473, 166–171. <https://doi.org/10.1016/j.msea.2007.03.086>
- Tong, X. C., & Ghosh, A. K. (2001). Fabrication Of In Situ Tic Reinforced Aluminum Matrix Composites, *Journal of Materials Science*, 36, 4059-4069. <https://doi.org/10.1023/A:1017946927566>



The Effect of Proximity Sensor & Grip Sensor Use on Specific Absorption Rate (SAR) in Smartphones

Emirhan AYDIN^{1*} ¹ Mimar Sinan Mah., 103. Cad. No:72, Kapaklı, Tekirdağ, Türkiye

| Keywords | Abstract |
|--------------------------------|---|
| Smartphone | Today, with the contribution of the new generation of communication technologies, many smart devices are produced. Almost every electronic device, including smart phones, smart watches, wireless headphones, tablets, emits some form of radiation. While most of this electromagnetic radiation is harmless, some of it can have potential health effects, depending on the frequency of use over long periods of time and in close usage. Specific Absorption Rate is a measure of how much human body tissue absorbs energy when the body is exposed to radiation. This measurement helps determine whether a device is safe for regular use. The SAR value may vary depending on the antenna and schematic design of the smartphone. To support high band requirements for 5G smartphones, more RF antennas required to be added in PCB design. When designing smartphones, designers also need to design proximity-grip sensors that accurately meet the industry's Specific Absorption Rate (SAR) requirements. In this study, the effects of proximity and grip sensors used in smartphones on LTE and 5G NR SAR values are investigated. During these measurements, a combination of Grip and Proximity Sensors were alternately turned on and off. Although the proximity sensor and grip sensor are not mainly used to optimize SAR values, it is foreseen that they may have indirect effects on SAR. In this context, SAR measurements were made in 3D environment for different frequencies. As a result of this study, it was observed that the grip-proximity sensors used in smartphones significantly reduce the SAR value and transfer less energy to the users in close range use. The effect of using the proximity sensor on the SAR rate was measured to be approximately 8%, while the effect of using the Grip Sensor was observed to be approximately 10%. |
| Proximity Sensor | |
| Grip Sensor | |
| Specific Absorption Rate (SAR) | |
| Long Term Evolution (LTE) | |
| 5G New Radio | |

Cite

Aydın, E. (2025). The Effect of Proximity Sensor & Grip Sensor Use on Specific Absorption Rate (SAR) in Smartphones. *GU J Sci, Part A, 12(1)*, 292-306. doi:[10.54287/guj.1616086](https://doi.org/10.54287/guj.1616086)

Author ID (ORCID Number)

[0009-0007-7703-7054](https://orcid.org/0009-0007-7703-7054) Emirhan AYDIN

Article Process

| | |
|------------------------|------------|
| Submission Date | 09.01.2025 |
| Revision Date | 29.01.2025 |
| Accepted Date | 13.02.2025 |
| Published Date | 26.03.2025 |

1. INTRODUCTION

The wireless industry is driven not only by customer demand for services, but also by the technology available. In this respect, the wireless industry is one of the most rapidly changing industries in the world. New products and services are introduced as quickly as they are designed and developed. Changes in technology standards also force rapid change. The technology itself is divided and defined by different generations:

The first-generation cell phones used analog technology with frequency modulation. This was rapidly abandoned as it was determined that carriers could not provide enough services to meet the demand. As a result, the first generation was quickly replaced with a second-generation (2G) digital cell phone technology.

*Corresponding Author, e-mail: e.aydin@samsung.com

Multiple 2G standards were developed worldwide. These include GSM and the original CDMA. Although 2G technology is still in use today around the world, it is slowly fading away. This allows operators to repurpose their spectrum for greater subscriber capacity and higher data rates. Cell phones originally were designed primarily as voice telephones, but it was quickly discovered that it was possible to use them for data purposes. For 2G phones, data rates were slow, thereby limiting the functions to simple applications such as texting and e-mail.

Third-generation (3G) cell phones continued to use standard digital voice techniques but also developed high-speed data capability. New modulation and access methods were created and standards were ratified. Third-generation phones rapidly became popular, and over a period of several years' carriers adopted the new technology and built out their networks.

The fourth generation (4G) has brought about the creation of a single standard or family of standards that all carriers could adopt. This 4G technology is known as Long Term Evolution (LTE), and it is slowly being adopted in one form or another by all U.S. and worldwide carriers. The 4G systems and phones have led to much higher data rates and amazing new cell phone capabilities, particularly that of being able to receive and generate video. Technology advances have given us not only the high-speed data capability necessary for video but also large, color touch screens, making the cell phone a more popular consumer product than ever.

The main purpose of 5G is to make the cellular and data services available over a wider range and to provide even higher data speeds. 5G uses higher frequencies and wider bandwidths to achieve even higher data rates. (Rappaport et al, 2013). With semiconductor technology still viable at ever smaller IC feature sizes, operation well into the hundreds of GHz is possible. 5G frequency bands are categorized into two groups based on the frequency spectrum. Sub 6GHz range of the radio frequency spectrum is known as frequency range 1 (FR1). Any LTE/5G frequency band under the 6GHz range is categorized under the FR1 group. Frequency bands in the millimeter wave (above 24GHz) spectrum are categorized under FR2. Due to the higher bandwidth of millimeter waves, these bands can achieve gigabits per second speed on a 5G network (Morgado et al., 2018).

Although the radiation associated with 5G technology is non-ionizing (radio frequency (RF) waves, has a longer wavelength, frequency, and energy), with the increasing development of systems based on mmWave technologies, it has become important to assess any adverse health effects caused by electromagnetic fields (Wu et al., 2015; Morelli et al., 2021). To protect the human body from exposure to mmW radiation, many countries set safety guidelines standards, such as those set by the International Commission on Non-Ionizing Radiation Protection (ICNIRP) and the Institute of Electrical and Electronics Engineers (IEEE) and the Federal Communications Commission (FCC).

Most of the studies about the exposure assessment of the human body to RF radiation in complicated exposure conditions used numerical approaches such as numerical analysis based on the finite-difference time-domain method (Jeladze et al., 2019; Siervo et al., 2018). A large number of dosimetry studies above 6 GHz have been

conducted, with the main purpose to establish the correlation between different dosimetric parameters such as the specific absorption rate (SAR), absorbed power density, and the skin surface temperature elevation (Diao et al., 2020; Li et al., 2019; Nakae et al., 2020; Neufeld et al., 2018, Morelli et al., 2021).

Guraliuc et al. (2017) presented a detailed numerical dosimetry study with a 60GHz antenna module for two representative human body exposure scenarios in 5G small cells by using a numeric model of a human adult head and a human hand holding a smartphone. For the numerical analysis, the finite integration technique was implemented together with a finite element method which was used for a better characterization of the antenna. The SAR absorbed power and the equivalent incident power density were used as dosimetric parameters. It was found that maximum absorption occurs at users' ears during telephone conversation and fingertips during browsing on the internet.

Hamed and Maqsood (2018) evaluated SAR 1g and point SAR (without mass averaging) at frequencies of 28, 40, and 60 GHz to investigate the SAR distributions due to radiating source antennas in single and layered human tissues using the FDTD method. It was concluded from the results that at the radiated power of 20 and 24 dBm, the SAR levels without mass averaging in the tissues at 28 GHz were lower than those at 40 GHz and 60 GHz.

In recent work, Tian et al. (2023) set up mobile phone model with 5G/4G patch antenna, real human head and DBS model using COMSOL Multiphysics. They calculated the specific absorption rate (SAR) of different layers of head tissues with the mobile phone at different distances from the human head, as well as the temperature change rule of the head and the DBS irradiated by the antenna for 30 min. The simulation results showed that at the frequency of 3.5 GHz, the EMF radiation from the mobile phone to the head was usually greater than that at 2.4 GHz.

For smartphone manufacturers, SAR is important to consider when designing antennas. There are a number of factors that have an impact on the SAR value, such as the size, location, radiation power, and type of antenna being used. In addition to these, some of the hardware features used in smart phones allow the phone to consume less power while in use, which indirectly reduces the rate at which EM waves interact with the human body.

In this study, the 3D SAR test environment is used to simulate the functions of the proximity and grip sensors on mobile phones and their effects on SAR levels. Comparing the data obtained at the end of the study, it is observed that the use of external sensor structures has significant effects on the SAR value. The proximity sensor helps to reduce the amount of electromagnetic energy that is generated by thermal energy by turning off the screen of the smartphone when you bring the phone closer to your ear to make a call. This means the phone heats up less and transmits less EM energy to the human body. On the other hand, the Grip Sensor detects whether the user is holding the smartphone and limits the (Tx power) signal power sent from the

smartphone to the base station using the antenna sensing structures used in its design and working with a lower Tx signal power supports the generation of less EM wave energy on the user body and reduces SAR values.

2. MATERIAL AND METHOD

All mobile devices that use advanced antenna structures are sources of electromagnetic radiation to a greater or lesser extent. The source of this radiation is the antenna structures used in the mobile device. To understand the results of this study, it is important to explain the principles of antennas, electric and magnetic fields, and electromagnetic energy.

2.1. Antenna Structure and Electromagnetic Field

An RF signal generated by a transmitter is sent into free space and eventually picked up by a receiver in wireless communication systems. Since a radio signal consists of both electric and magnetic fields, it is called an electromagnetic wave. Whenever voltage is applied to the antenna, an electric field is created and, at the same time, a magnetic field is created by the flow of current in the antenna. These electric and magnetic fields are radiated out from the antenna and propagate through space at the speed of light.

In Figure 1, the half-wave dipole antenna is connected to the transmitter by the transmission line that was used to form the antenna. In most practical applications, the antenna is remote from the transmitter and receiver. A transmission line is used to transfer energy between the antenna and the transmitter or receiver.

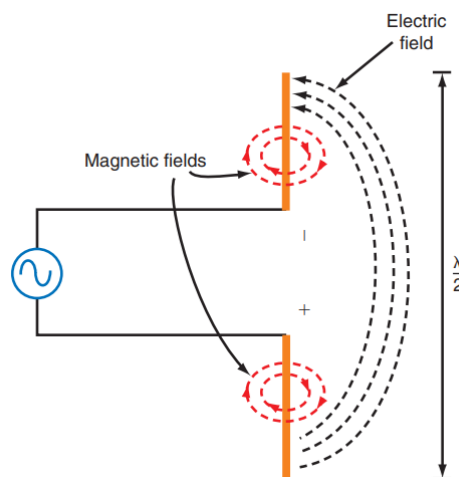


Figure 1. The electric and magnetic fields around the transmission line

The electric and magnetic fields produced by the antenna are at right angles to each other and both are perpendicular to the direction of wave propagation. Figure 2 shows the variation in the strength of the electric and magnetic fields as it moves out from the antenna.

2.2. Electromagnetic Radiation and EM Spectrum

Electromagnetic waves are oscillating signals whose electric and magnetic field amplitudes change at a certain rate. The strength of the field goes up and down, and the polarity of the field reverses a certain number of times

per second. The electromagnetic waves are in sinusoidal signal form. The frequency of these waves is measured in cycles per second (cps) or hertz (Hz). The electromagnetic spectrum is the range of electromagnetic signals which includes all frequencies. The full electromagnetic spectrum including frequency and wavelength is shown in Figure 2.

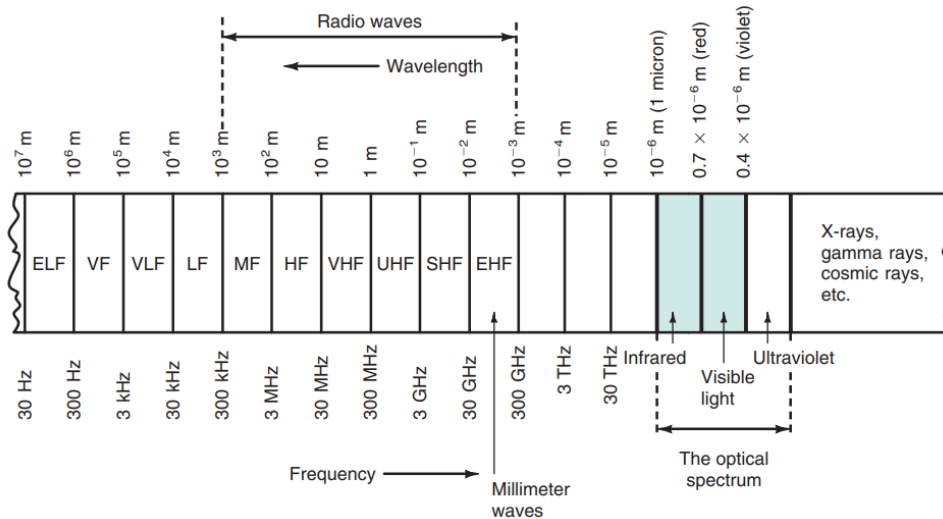


Figure 2. The electromagnetic spectrum

Ultra-High Frequency (UHF) is introduced from 300MHz to 3GHz and used for mobile telephony and services, as well as for military purposes. Electromagnetic signals with frequencies higher than 30 GHz are called millimeter waves. This range is increasingly used for satellite communications and mobile communications, although the equipment used to generate and receive signals in this range is extremely complex and expensive. EHF frequencies are also used for FR2 in 5G NR technology.

A photon has an energy (E) proportional to its frequency (f). This is given by Equation (1):

$$E = hf = \frac{hc}{\lambda}, \quad h = 6.62607015 \times 10^{-34} \text{ J}\cdot\text{s}, \quad c \cong 3 \times 10^8 \text{ m}\cdot\text{s}^{-1} \quad (1)$$

where the h is the Planck constant, λ is the wavelength, and c is the speed of light. This is also known as the Planck-Einstein equation. The energy of the photon will be proportional to the frequency of the electromagnetic waves, in other words, the high-frequency photon has more energy. The use of high-frequency communication technologies such as 4G (LTE) and 5G NR in smart phones leads to an excessive emission of electromagnetic energy during their use.

2.3. SAR Methodology and Global Regulations

The Specific Absorption Rate (SAR) is an exposure standard for wireless devices used to assess the hazards posed by radio frequency (RF) waves. It is a measure of the energy absorbed by human tissue when exposed to a radiofrequency (RF) electromagnetic field per unit mass (Hamed & Maqsood, 2018; Sabbah et al., 2011).

The SAR is proportional to the square of the value of the electric field strength induced in the body when the human body is exposed to a radio frequency field.

SAR values are calculated by averaging either the whole body or a small sample (1g or 10g of tissue). The higher the SAR, the more radiation is absorbed in the tissues and the greater the effect on the human body (Koukiou, 2024; Rosenqvist et al., 2021). The SAR is a measure of the energy absorbed by a mass placed in a volume with the same mass density (ρ) as the tissue and units of SAR are expressed in watts per kilogram (W/kg) (Hamed & Maqsood, 2018).

$$SAR_i = \frac{P_i}{\rho_i} = \sigma \frac{|E|^2}{\rho_i} \text{ W/kg} \quad (2)$$

When the antenna is close to the human model at low power levels, relatively high field strengths would be estimated in the vicinity of the antenna, as shown in Figure 3. When the antenna is very close to the human tissue, the field distribution on the human tissue is usually measured in the vicinity of the antenna (Hamed & Maqsood, 2018).



Figure 3. An overview of SAR measurement setup

There are two ways to calculate SAR: one is called Point SAR and the other called Mass or Volume Averaging SAR. The point SAR is not averaged and defines the maximum SAR of all meshes, and the point SAR for each mesh is calculated by dividing the absorbed power in each mesh by the mesh weight. In the case of averaged SAR values, a cube with a defined mass, e.g. 1 g or 10 g, is used for each point, and the power loss density is integrated over this cube. This is done by dividing the integrated power loss by the mass of the cube (Aly & Picket-May, 2014). The restriction limits of the SAR for the general public are given in Table 1.

Table 1. SAR exposure standards and limits

| Standard | SAR Limit (W/kg) | Averaging mass for SAR |
|-----------------|---------------------|------------------------|
| ICNIRP (Global) | 2.0 ($f < 10$ GHz) | 10 g of tissues |
| FCC/ANSI | 1.6 ($f < 6$ GHz) | 1 g of tissues |

2.4. Smartphone Sensing System Overview

To enhance functionality, user experience, and device performance, today's smartphones are equipped with a variety of sensors. The following technical information is provided for the proximity and grip sensors that are the focus of this study.

2.4.1. Proximity Sensor Overview

A proximity sensor in a smartphone is a type of sensor that detects the presence of objects or the distance between the phone and nearby objects, typically at very close ranges (~2 centimeters). It is often used to detect when the user brings the phone close to their face or ear, such as during a phone call. The proximity sensor helps to enhance the functionality of the smartphone by automatically adjusting the behavior of the device in response to a physical presence or movement.

Proximity sensors are generally based on the working principles of infrared (IR) or capacitive sensing. The most common type of proximity sensor used in smartphones uses infrared light to detect the presence of objects in the vicinity. An infrared transmitter emits infrared and an infrared detector receives the reflected light upon encountering an object. That allows the phone to register the closeness of the object. The sensor remains inactive when no object is detected.

Capacitive proximity sensing works on the basis of electrical capacitance. Proximity sensing works by detecting the change in capacitance caused by the proximity of a conductive subject. Even without direct contact, this allows the phone to sense the proximity of the object.

The proximity sensor is usually located below the screen as indicated in Figure 4. It is not visible to the user when looking at the screen. The proximity sensor helps conserve battery life by turning off the display when the phone is close to an object (such as your face). When you bring the phone closer to your ear, it has an indirect effect on the SAR values by reducing the heating problems on user's face that can occur due to the thermal energy.

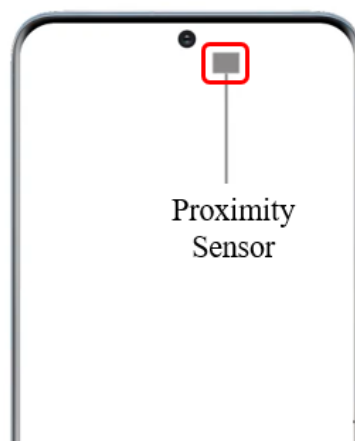


Figure 4. Enable Proximity Sensor by moving phone to the ear

2.4.2. Grip Sensor Overview

A grip sensor in a smartphone is a sensor that detects how the user holds or grips the device. It can measure pressure, position, or force exerted by the user's fingers on the device. It is typically located around the edges or frame of the device. Grip sensors are not as common as other smartphone sensors. However, they are becoming increasingly important in certain advanced smartphones.

A grip sensor's operating principle is based on detecting pressure or position changes from the user's hand. Pressure sensors measure the pressure that is applied to certain parts of the phone, often on the edges or the back of the phone. They can detect how firmly the user is holding the device and can trigger certain functions based on the amount of force that is being applied.

On the other hand, the use of the grip sensor in smart phones allows the recognition of the phone when it is in the hand of the user. During data and voice communication, the Tx power emitted by the device is limited and less Tx power will be emitted by smartphones. This has a positive effect on the SAR values. It also helps us to meet the specifications set by the regulations (Figure 5).

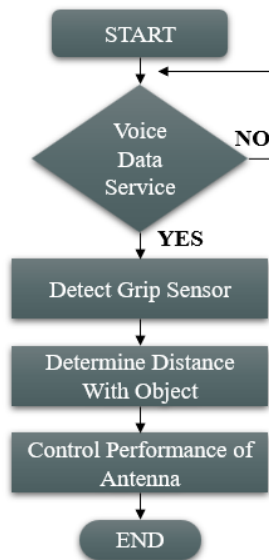


Figure 5. Flow diagram of controlling antenna performance by using a grip sensor

2.5. DUT (Device Under Test) Specifications

Antenna placement is a critical aspect of any device under test (DUT) because it has a significant impact on the performance of the antenna system. Antenna placement has an impact on how well the antenna can transmit or receive signals. Optimal antenna placement will ensure that the antenna is in a position where it can maintain an effective level of signal strength and signal quality. Poor antenna placement can result in reduced coverage, reduced reception (Rx) or signal interference.

The frequency response of the device can also be affected by antenna placement. In some cases, the performance at certain frequencies can be optimized by adjusting the placement. Antenna placement is critical

to ensuring that the device under test meets the required standards for regulatory testing (e.g. SAR testing, FCC compliance). Antenna placement must follow specific guidelines in order to simulate the real-world use scenarios that occur during certification testing. In this study, SAR (Specific Absorption Rate) was measured for 2G, 3G, 4G and 5G technologies by using a reference 5G model. Figure 6 shows the antenna placements of the tested model.

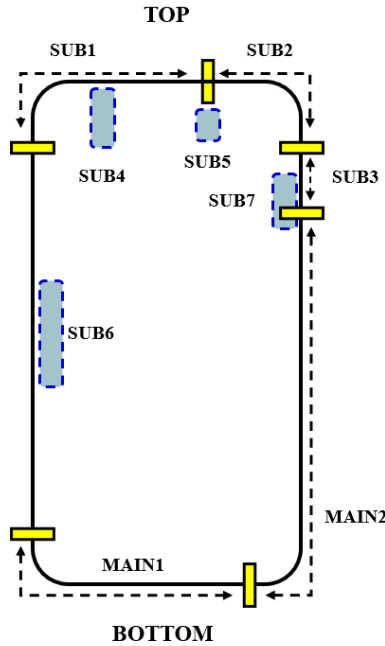


Figure 6. Rear (Back side) view of DUT, illustrate antenna placements

The above antenna structures are used for the following basic bands and technologies. The SAR measurements were also carried out based on the antenna patterns that were specified in Figure 6 and Table 2.

Table 2. Supported band list for DUT

| Antenna | Tx | Rx | PRx | DRx | Supported Band List |
|---------|-----|-----|-----|-----|--|
| MAIN1 | O | O | N/A | N/A | GSM 850/900, WCDMA B5/8, LTE B5/8/12/17/20/26/28, NR n5/8/20/26/28/71 |
| MAIN2 | O | O | N/A | O | GSM 1800/1900, WCDMA B1/2/4, LTE B1/2/3/7/25/38/40/41, NR n1/3/7/38/40/41/66/77/78 |
| SUB1 | N/A | N/A | N/A | O | GSM 850/900, WCDMA B5/8, LTE B5/8/12/17/20/26/28/38/40/41, NR n5/7/8/20/28/38/40/41 |
| SUB2 | O | O | O | O | GSM 1800/1900, WCDMA B1/2/4, GPS, Wi-Fi1_5G, LTE B1/2/3/4/7/25/38/40/41, NR n1/3/7/38/40/41/66/77/78 |
| SUB3 | N/A | N/A | O | N/A | LTE B1/3/4/66, NR n1/3/7/38/40/41/66, Wi-Fi1_2.4G |
| SUB4 | N/A | N/A | N/A | O | NR n77/78 |
| SUB5 | O | O | N/A | N/A | Wi-Fi2_2.4G / 5G |
| SUB6 | N/A | N/A | N/A | O | LTE B1/3/4/66, NR n1/3/66 |
| SUB7 | N/A | N/A | O | N/A | NR n77/78 |

3. RESULTS AND DISCUSSION

In Türkiye, the Information and Communication Technologies Authority (ICTA), known as BTK (Bilgi Teknolojileri ve İletişim Kurumu), regulates the Specific Absorption Rate (SAR) standard for mobile phones and wireless devices. Türkiye's SAR limits are consistent with international standards, primarily based on International Commission on Non-Ionizing Radiation Protection (ICNIRP) guidelines, which are widely accepted worldwide, including the European Union. Türkiye is not a member of the EU. However, Türkiye aligned its regulations with the EU standards, which are similar to the ICNIRP standards. Compliance with these SAR limits for telecommunications equipment in Türkiye is monitored and regulated by the BTK. Manufacturers are required to ensure that their products are in compliance with the SAR limits before they can be sold in Türkiye.

In this study, SAR measurements were performed by simulating the following combinations with introduced bads listed in Table 2. The combinations that are used for the grip sensor and the proximity sensor are the following. We used MT8821C Radio Communication Analyzer and E5515C 8960 Series 10 Wireless Communications Test Set in our measurements.

- a. Grip Sensor ON, Proximity Sensor ON
- b. Grip Sensor OFF, Proximity Sensor ON
- c. Grip Sensor ON, Proximity Sensor OFF
- d. Grip Sensor OFF, Proximity Sensor OFF

GSM900 SAR measurement results in W/kg included in Table 3. GSM900 operates in the frequency range of 890 MHz to 915 MHz (uplink) and 935 MHz to 960 MHz (downlink). According to the measured values, having the Grip Sensor OFF has a negative effect on SAR, if Grip sensor in OFF state, SAR increasing around 0,02 W/kg. The SAR values measured for both the grip sensor and the proximity sensor in the "ON" state are the minimum values as expected.

Table 3. GSM900 & DCS1800 SAR measurement results

| Mode | Antenna | | Sensor Mode | Measurement | | Improvement | |
|-------|---------|---------|--------------------------|-------------|---------|-------------|---------|
| | GSM900 | DCS1800 | | GSM900 | DCS1800 | GSM900 | DCS1800 |
| Voice | MAIN1 | MAIN2 | Grip On - Proximity ON | 0,353 | 0,303 | 6% | 4% |
| | | | Grip OFF - Proximity ON | 0,378 | 0,328 | | |
| | | | Grip On - Proximity OFF | 0,367 | 0,316 | | |
| | | | Grip OFF - Proximity OFF | 0,416 | 0,346 | | |

DCS1800 operates in the frequency range of 1710 MHz to 1785 MHz (uplink) and 1805 MHz to 1880 MHz (downlink). Lower frequencies (such as GSM 900MHz) tend to go deeper into the human body, particularly near the skin. Signals at higher frequencies (such as DCS1800) tend to be absorbed more strongly at the surface

of the skin, resulting in a shallower penetration depth. Handsets operating at 1800 MHz typically operate at lower power, which results in lower SAR levels.

UMTS Band 1, also known as WCDMA Band 1, operates in the frequency range of 1920 MHz to 1980 MHz for the uplink and 2110 MHz to 2170 MHz for the downlink. This band is typically used for 3G (Universal Mobile Telecommunications System) communication. UMTS devices have higher transmitting power compared to 2G, as they are designed to provide higher data rates and support more advanced services. However, UMTS operates at higher frequencies than GSM (especially in Band 1, which is around 2 GHz). This means that the energy tends to be absorbed closer to the skin rather than deeper into the tissue. Due to these reasons, it measured very closer to DCS1800 SAR values, as shown in Table 4.

UMTS Band 8 (WCDMA Band 8) operates in the frequency range of 880 MHz to 915 MHz for uplink and 925 MHz to 960 MHz for downlink. UMTS Band 8 (B8) operates at a lower frequency (about 900MHz), typically causing more penetration. The lower frequency allows the signal to travel further and pass through tissue more effectively than higher frequency. Table 4 shows the UMTS Band 8 SAR measurement results. UMTS Band 8 has deeper tissue penetration, leading to more energy absorption by the body.

Table 4. UMTS B1 & UMTS B8 SAR Measurement results

| Mode | Antenna | | Sensor Mode | Measurement | | Improvement | |
|-------|---------|---------|--------------------------|-------------|---------|-------------|---------|
| | UMTS B1 | UMTS B8 | | UMTS B1 | UMTS B8 | UMTS B1 | UMTS B8 |
| Voice | MAIN2 | MAIN2 | Grip On - Proximity ON | 0,296 | 0,388 | 3% | 8% |
| | | | Grip OFF - Proximity ON | 0,318 | 0,436 | | |
| | | | Grip On - Proximity OFF | 0,307 | 0,417 | | |
| | | | Grip OFF - Proximity OFF | 0,329 | 0,463 | | |

LTE B1 operates in the frequency range of 1920 MHz to 1980 MHz for uplink and 2110 MHz to 2170 MHz for downlink. LTE B1 operates at a higher frequency. This means that it tends to have slightly worse propagation (range and indoor coverage) due to higher path loss. However, it compensates with better data throughput and more efficient frequency reuse. According to measurement result, LTE B1 has higher SAR value compared to 2G and UMTS network (Table 5).

Table 5. LTE B1 SAR Measurement results

| Band | Mode | Antenna | Sensor Mode | Measurement | DIFF | Improvement |
|--------|-------|---------|--------------------------|-------------|-------|-------------|
| LTE B1 | Voice | MAIN2 | Grip ON - Proximity ON | 0,517 | 0,112 | 11% |
| | | | Grip OFF - Proximity ON | 0,598 | | |
| | | | Grip ON - Proximity OFF | 0,563 | | |
| | | | Grip OFF - Proximity OFF | 0,629 | | |

In order to overcome propagation losses, mobile devices typically use higher output power at lower frequency bands. Higher frequencies generally result in a higher power density in the tissues of the human body. LTE B3 operates in the 1.7 GHz to 1.8 GHz range, which is lower than LTE B1. While the mobile phone is operating in the LTE B3 mode, it emits slightly less power, which results in a lower SAR value as shown in Table 6.

Table 6. LTE B3 SAR Measurement results

| Band | Mode | Antenna | Sensor Mode | Measurement | DIFF | Improvement |
|--------|-------|---------|--------------------------|-------------|-------|-------------|
| LTE B3 | Voice | MAIN2 | Grip ON - Proximity ON | 0,545 | 0,066 | 7% |
| | | | Grip OFF - Proximity ON | 0,588 | | |
| | | | Grip ON - Proximity OFF | 0,577 | | |
| | | | Grip OFF - Proximity OFF | 0,611 | | |

LTE B8 operates in the 900MHz band, commonly deployed in 4G-LTE in Europe, parts of Asia and Africa. Both LTE B8 (900 MHz) and LTE B5 (850 MHz) operate at relatively low frequencies, and devices using these bands typically transmit at similar power levels. Table 7 shows SAR measurement results for LTE B8.

Table 7. LTE B8 SAR Measurement results

| Band | Mode | Antenna | Sensor Mode | Measurement | DIFF | Improvement |
|--------|-------|---------|--------------------------|-------------|-------|-------------|
| LTE B8 | Voice | MAIN1 | Grip ON - Proximity ON | 0,461 | 0,075 | 8% |
| | | | Grip OFF - Proximity ON | 0,521 | | |
| | | | Grip ON - Proximity OFF | 0,492 | | |
| | | | Grip OFF - Proximity OFF | 0,536 | | |

LTE B40 is used for time division duplex (TDD) LTE deployments and operates in the 2.3 GHz to 2.4 GHz frequency range. LTE B40 is a higher band, 2,3GHz-2,4GHz, than lower band frequencies, such as Band 5 or Band 8. This means that the radio waves in LTE B40 are more superficially absorbed by the skin and outer layers of the body than they are more deeply penetrating (Table 8).

Table 8. LTE B40 SAR Measurement results

| Band | Mode | Antenna | Sensor Mode | Measurement | DIFF | Improvement |
|---------|-------|---------|--------------------------|-------------|-------|-------------|
| LTE B40 | Voice | MAIN2 | Grip ON - Proximity ON | 0,688 | 0,073 | 7% |
| | | | Grip OFF - Proximity ON | 0,733 | | |
| | | | Grip ON - Proximity OFF | 0,705 | | |
| | | | Grip OFF - Proximity OFF | 0,761 | | |

NR n78 is a part of the mid-band spectrum (also referred to as Sub-6 GHz) and is commonly used for 5G services in many regions worldwide. n78 band operates between 3.3 GHz and 3.8 GHz, tend to lead to higher surface absorption of radio waves compared to lower-frequency bands like LTE Band 40. Higher frequencies

are absorbed more by the skin and outer layers of the body, while lower frequencies penetrate deeper into the body tissue. Since 5G NR typically operates at higher frequencies, n78 bands generally results in higher surface absorption of radio waves. Devices operating in this band often have to transmit at higher power to cover urban areas and provide high-speed internet, leading to potentially higher SAR values (Table 9).

Table 9. NR n78 SAR Measurement results

| Band | Mode | Antenna | Sensor Mode | Measurement | DIFF | Improvement |
|-----------|-------|---------|--------------------------|-------------|------|-------------|
| NR n78 | Voice | SUB2 | Grip ON - Proximity ON | 0,844 | 0,09 | 9% |
| | | | Grip OFF - Proximity ON | 0,901 | | |
| | | | Grip ON - Proximity OFF | 0,867 | | |
| | | | Grip OFF - Proximity OFF | 0,934 | | |

4. CONCLUSION

Specific absorption rate (SAR) measurements play a critical role in the assessment of potential risks to human health from electromagnetic radiation, particularly from high-frequency devices such as cell phones, wireless communication systems, and other emerging technologies. At high frequencies, including the millimeter wave and 5G bands, the interaction between RF radiation and biological tissue is different from that at lower frequencies, raising concerns about potential health effects such as thermal heating, tissue damage, and long-term exposure risks.

While the current evidence from scientific studies suggests that exposure levels within established safety limits do not pose a significant risk to human health, there are still uncertainties about the cumulative effects of long-term exposure, particularly in vulnerable populations such as children and pregnant women. The increasing prevalence and use of higher-frequency devices requires continued research to better understand the biological effects of RF radiation. Therefore, all design parameters must be carefully considered before the introduction of a new mobile phone to the market. Some sensors used in mobile phones ensure that devices operating at high frequencies emit less radiation, resulting in lower SAR levels for users.

In this study, the effects of the use of the grip sensor and the proximity sensor on the SAR values are realized in 4 different scenarios for different communication technologies. Both grip sensors and proximity sensors contribute indirectly to reducing SAR in mobile phones. However, their effect is primarily through optimized power management. Specifically, proximity sensing can actively reduce transmission power when the phone is near the head of the user, directly reducing SAR. Grip sensors, while helpful in managing the behavior of the phone, have a less direct impact on SAR, but they can contribute to power adjustment based on the way the device is being held. As shown in Figure 7, we achieved best case with both sensors are in ON state, provides from 5% to 11% improvement on SAR values with different frequencies. It is important to use these sensors in future smartphones as a standard hardware component.

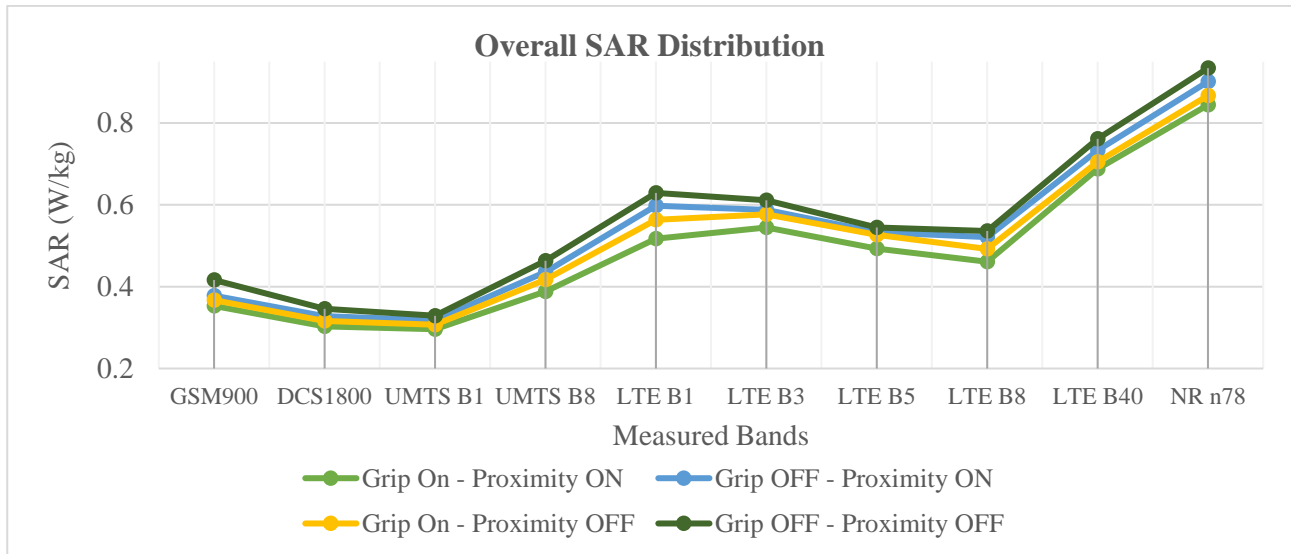


Figure 7. Overall SAR measurement results, for 2G, UMTS, LTE and 5G NR

ACKNOWLEDGEMENT

This study was supported by Samsung Electronics Türkiye within the scope of Samsung Electronics Turkey R&D Center activities.

CONFLICT OF INTEREST

The author declares no conflict of interest.

REFERENCES

- Aly, A., & Picket-May, M. (2014). FDTD Computation for Sar Induced in Human Head Due to Exposure to EMF from Mobile Phone. *Advanced Computing: An International Journal*, 5, 01-12. <https://doi.org/10.5121/acij.2014.5601>
- Diao, Y., Rashed, E. A., & Hirata, A. (2020). Assessment of absorbed power density and temperature rise for nonplanar body model under electromagnetic exposure above 6 GHz. *Physics in medicine and biology*, 65(22), 224001. <https://doi.org/10.1088/1361-6560/abdbb7>
- Guraliuc, A. R., Zhadobov, M., Sauleau, R., Marnat, L., & Dussopt, L. (2017). Near-Field User Exposure in Forthcoming 5G Scenarios in the 60 GHz Band. *IEEE Transactions on Antennas and Propagation*, 65(12, 1), 6606–6615. <https://doi.org/10.1109/TAP.2017.2754473>
- Hamed, T.B., & Maqsood, M. (2018). SAR Calculation & Temperature Response of Human Body Exposure to Electromagnetic Radiations at 28, 40 and 60 GHz mmWave Frequencies. *Progress in Electromagnetics Research M*, 73, 47-59. <https://doi.org/10.2528/PIERM18061102>
- Jeladze, V., Nozadze, T., Petoev-Darsavelidze, I., & Partsvania, B. (2019). Mobile phone antenna-matching study with different finger positions on an inhomogeneous human model. *Electromagnetic biology and medicine*, 38(4), 297–306. <https://doi.org/10.1080/15368378.2019.1641721>
- Koukiou, G. (2024). SAR Features and Techniques for Urban Planning—A Review. *Remote Sensing*, 16(11), 1923. <https://doi.org/10.3390/rs16111923>

- Li, K., Sasaki, K., Watanabe, S., & Shirai, H. (2019). Relationship between power density and surface temperature elevation for human skin exposure to electromagnetic waves with oblique incidence angle from 6 GHz to 1 THz. *Physics in medicine and biology*, 64(6), 065016. <https://doi.org/10.1088/1361-6560/ab057a>
- Morelli, M. S., Gallucci, S., Siervo, B., & Hartwig, V. (2021). Numerical Analysis of Electromagnetic Field Exposure from 5G Mobile Communications at 28 GHz in Adults and Children Users for Real-World Exposure Scenarios. *International Journal of Environmental Research and Public Health*, 18(3), 1073. <https://doi.org/10.3390/ijerph18031073>
- Morgado, A., Huq, K. M. S., Rodriguez, J., & Mumtaz, S. (2018). A survey of 5G technologies: regulatory, standardization and industrial perspectives. *Digital Communications and Networks*, 4(2), 87-97. <https://doi.org/10.1016/j.dcan.2017.09.010>
- Nakae, T., Funahashi, D., Higashiyama, J., Onishi, T., & Hirata, A. (2020). Skin temperature elevation for incident power densities from dipole arrays at 28 GHz. *IEEE Access*, 8, 26863-26871. <https://doi.org/10.1109/ACCESS.2020.2970219>
- Neufeld, E., Carrasco, E., Murbach, M., Balzano, Q., Christ, A., & Kuster, N. (2018). Theoretical and numerical assessment of maximally allowable power-density averaging area for conservative electromagnetic exposure assessment above 6 GHz. *Bioelectromagnetics*, 39(8), 617–630. <https://doi.org/10.1002/bem.22147>
- Rappaport, T.T., Sun, S., Mayzus, R., Zhao, H., Azar, Y., Wang, K., Wong, G.N., Schulz, J.K., Samimi, M., & Gutierrez, F. (2013). Millimeter Wave Mobile Communications for 5G Cellular: It Will Work! *IEEE Access*, 1, 335-349. <https://doi.org/10.1109/ACCESS.2013.2260813>
- Rosenqvist, A., Jones, C. E., Rignot, E., Simons, M., Siqueira, P., & Tadono, T. (2021). A review of SAR observation requirements for global and targeted science applications. In *2021 IEEE International Geoscience and Remote Sensing Symposium IGARSS* (pp. 1745-1748). IEEE. <https://doi.org/10.1109/IGARSS47720.2021.9553966>
- Sabbah, A.I., Dib, N.I., & Al-Nimr, M.A. (2011). Evaluation of specific absorption rate and temperature elevation in a multi-layered human head model exposed to radio frequency radiation using the finite-difference time domain method. *Iet Microwaves Antennas & Propagation*, 5, 1073-1080. <https://doi.org/10.1049/iet-map.2010.0172>
- Siervo, B., Morelli, M. S., Landini, L., & Hartwig, V. (2018). Numerical evaluation of human exposure to WiMax patch antenna in tablet or laptop. *Bioelectromagnetics*, 39(5), 414-422. <https://doi.org/10.1002/bem.22128>
- Tian, R., Wu, Y. -Q., Lu, M., & Miao, X. -F. (2023). Specific Absorption Rate and Temperature Distributions in the Human Head with Implanted Deep Brain Stimulation Subjected to Mobile Phone Electromagnetic Radiation. *Electronics*, 12(21), 4389. <https://doi.org/10.3390/electronics12214389>
- Wu, T., Rappaport, T. S., & Collins, C. M. (2015). Safe for Generations to Come. *IEEE microwave magazine*, 16(2), 65–84. <https://doi.org/10.1109/MMM.2014.2377587>



Gazi University

Journal of Science

PART A: ENGINEERING AND INNOVATION

<http://dergipark.org.tr/guj.1559050>

Design of 8-Elements Linear Dipole Antenna Array to Suppress Sidelobe Signals by Using Genetic Optimization

Emirhan AYDIN^{1*} ¹ Mimar Sinan mah. 103. Cad. No:72, Kapaklı, Tekirdağ, Türkiye

| Keywords | Abstract |
|---|---|
| Antenna Arrays Genetic Optimization Sidelobe Suppression Linear Dipole Antenna | High sidelobe levels can result in unwanted interference or "noise" from signals arriving from directions other than the desired main lobe. These signals can degrade the overall performance of a system by reducing the signal-to-noise ratio, making it more difficult to distinguish the intended signal from background noise. In systems like radar or satellite communication, sidelobes can cause interference to other users or systems operating in adjacent frequency bands or directions. Suppressing the sidelobes helps minimize this cross-talk and interference. When the sidelobes are suppressed, more of the transmitted power is concentrated in the main lobe, improving the efficiency of power usage. This is important in communication systems where conserving power is essential, such as in satellites or mobile devices. In environments where signals may bounce off objects (such as in urban areas for wireless communication or radar), sidelobes can pick up signals reflected from various surfaces. By suppressing sidelobes, the system becomes less susceptible to multipath interference, which can degrade signal quality and accuracy. To sum up, sidelobe suppression is crucial for ensuring the efficiency, accuracy, and reliability of many systems, particularly in radar and communications. It minimizes interference, reduces false detections, improves directional sensitivity, and ensures that resources (e.g., power and bandwidth) are used effectively. In this paper, 8-element linear dipole antenna array designed to suppress sidelobe signals, which causes interference on the communication system. One of the key parameter is the distance between the each antenna. In this simulation, we defined the distance between each antenna as $0.6 \cdot \lambda$, for 3GHz operating frequency. Another optimization parameter is the magnitude of each antenna element, aimed to optimize magnitudes of each antenna element's sidelobe levels by using Genetic Algorithm (GA), where theta angle between 40-60 degrees. The antenna array design done in CST Studio environment, but amplitude tuning with GA performed using MATLAB. We compared our design results for each simulation, observed the change of directivity for antenna array by using GA. As a result, the sidelobe level between the desired theta 40 and 60 degrees suppressed from -17dB to -28.2dB but it observed that the directivity of the main antenna radiation pattern decreased from 13dBi to 10dBi. |

| Cite |
|---|
| Aydın, E. (2025). Design of 8-Elements Linear Dipole Antenna Array to Suppress Sidelobe Signals by Using Genetic Optimization. <i>GU J Sci, Part A, 12(1)</i> , 307-318. doi:10.54287/guj.1559050 |

| Author ID (ORCID Number) | Article Process |
|-----------------------------------|---|
| 0009-0007-7703-7054 Emirhan AYDIN | Submission Date 01.10.2024 Revision Date 25.11.2024 Accepted Date 30.12.2024 Published Date 26.03.2025 |

1. INTRODUCTION

The radiation of antennas produces some undesirable effects, such as side lobe level (SLL). In most antenna array applications, especially the first SLL is an undesirable effect because it causes too much electromagnetic interference (Liang et al., 2017). Due to emerging high frequency techniques, SLL suppression is a very important issue for antenna arrays operating in the FR1 and FR2 region. The main parameters of a selected antenna model (radiation pattern, impedance, half power beamwidth, main bandwidth, directivity, radiation

*Corresponding Author, e-mail: e.aydin@samsung.com

efficiency etc.) are calculated by methods known in the literature (Panduro et al., 2006). The main objective of antenna array analysis is to determine the number of antenna array elements and the spacing between antenna elements that can produce the expected radiation pattern for the center operating frequency with the best approximation and maximum directivity (Katoch et al., 2021).

In general, antenna pattern studies are classified into the three main groups. The first group is the studies that generate radiation diagrams with zeros in predetermined directions. An example of the first group is the Schelkunoff method. The second group includes the design of an antenna that can approximate the desired radiation pattern over the entire visible region. Woodward and Fourier transform by Taylor (1955), are the techniques used for this purpose.

The third group includes techniques that produce radiation patterns with narrow main beam and low side auricle levels. Binomial method by Taylor (1955), Dolph-Chebyshev by Taylor (1955) are examples of this third group.

In the literature, the tuning of main beamwidth and sidelobe levels has been frequently emphasized for pattern shaping in array antennas. For example, Dolph calculated the excitation coefficients of the equally spaced array elements that give the minimum main beamwidth for a given maximum sidelobe level, showed that radiation diagrams with equal sidelobe levels obtained with these coefficients can also be obtained with Chebyshev polynomial, developed a new formulation for the design of Chebyshev arrays that expresses the array factor in terms of cosine and hyperbolic-cosine functions without using Chebyshev polynomials directly (Satılmış, 2022).

The genetic algorithm, used as an improvement method in the study of sequence analysis, is one of the so-called heuristic algorithms, algorithms that include rules based on experience and training. The concept of genetic algorithm is inspired by the science of genetics. There are several studies in the literature where genetic algorithms have been used for antenna pattern synthesis, most of these studies have used linear arrays. For example, organized the placement of linear array elements using a genetic algorithm. In subsequent studies, calculated the antenna amplitude excitation coefficients for linear antennas for pattern shaping using a genetic algorithm (Lambora et al., 2019; Aydin & Erdem Aykac, 2023; Zhang & Li, 2023). More traditional optimization methods such as particle swarm optimization and ant colony algorithm generally used to suppress the side lobe levels of antenna arrays, with the developing artificial intelligence applications, sidelobe suppression techniques with increased accuracy are also used (Yang et al., 2021; Xiang et al., 2024).

In this study, Genetic Algorithm (GA) is selected to optimize the amplitude parameters of linearly spaced antenna arrays, while keeping the distance between antennas constant. In this antenna array design, since all antennas are positioned at equal distances, genetic optimization is only applied on the radiation amplitudes of the antennas (Singh et al., 2022; Nie et al., 2024; Xiang et al., 2024). In this way, it is aimed to calculate the

optimum radiation amplitudes for each antenna. For the antenna radiation amplitude calculation, the optimum value of the radiation amplitude is calculated with a coding in MATLAB, as a matrix form.

In this case, the antenna radiation amplitudes are optimized using the genetic optimization algorithm. With the new antenna radiation amplitude values obtained, the antenna array designed on CST Studio is updated and the radiation directivity of the new radiation amplitude and the suppression at the side lobe level are evaluated. The array of 8 dipole antennas positioned in the x-axis with a distance of $0.6 \cdot \lambda$ between them is designed using the CST Studio Suite program. For the 3 GHz center frequency, the λ value was calculated as 96 mm with an optimization margin of 4.5% and the $0.6 \cdot \lambda$ distance was defined as 57.60 mm (Aydin & Erdem Aykac, 2023).

2. MATERIAL AND METHOD

The genetic algorithm was developed by J. H. Holland, showed that complex structures can be coded using simple data sequences. The genetic algorithm (GA) is an optimization algorithm inspired by natural selection; it is a method for solving optimization problems based on a natural selection process. Genetic algorithms act as a biological metaphor and use some of the methods observed in natural evolution (Dhiman & Kaur, 2019; Ma et al., 2019). GA aims to yield solutions for the consecutive generations (Lambora et al., 2019). Genetic algorithms are widely used to generate high-quality solutions to optimization and search problems based on biologically inspired operators. Once the genetic representation and fitness function defined, a GA proceeds to initialize a population of solutions and then evolve it through repeated application of mutation, crossover, inversion and selection operators. GA changes the process of searching for the optimum solution adaptively, check the probabilities and reaches the optimal solution.

The main advantage of genetic algorithms is that they do not require any knowledge of the general nature of the problem they are trying to optimize. They can easily find an ideal general solution in a complex multidimensional search space. Genetic algorithms are particularly effective in finding the approximate maximum or minimum value in a high-dimensional, multi-model function set.

The fitness function defined on the genetic representation and measures the quality of the represented solution. GA can be applied to the genetic algorithm to solve problems which are not well suited with standard optimization algorithms, including problems where the objective function is discontinuous, non-differentiable, stochastic or highly nonlinear. It uses a group search technology and the evolutionary population represents a set of problem solutions such as increasing data rate, reducing power consumption, optimize interference effect of communication channel and improving spectrum efficiency (Liang et al., 2020; Durmus & Kurban, 2022).

The flow diagram of a simple genetic algorithm is given in Figure 1. In the algorithm, an initial population is first created, then genetic processors are used to generate the solutions in the next generation through reproduction, crossover and mutation. The fitness assessment process is applied to each individual in order to

perform the selection process applied during the reproduction event. The cycle of development and evaluation of successive generations continues until the best solution is found. A simple genetic algorithm consists of five basic steps. Each of these significantly affects the performance of the algorithm (Liu et al., 2014; Durmus & Kurban, 2022).

These steps are:

- a. Representation of solutions
- b. How to create an initial ensemble
- c. Fitness or quality assessment criteria
- d. Genetic processors
- e. Control parameters

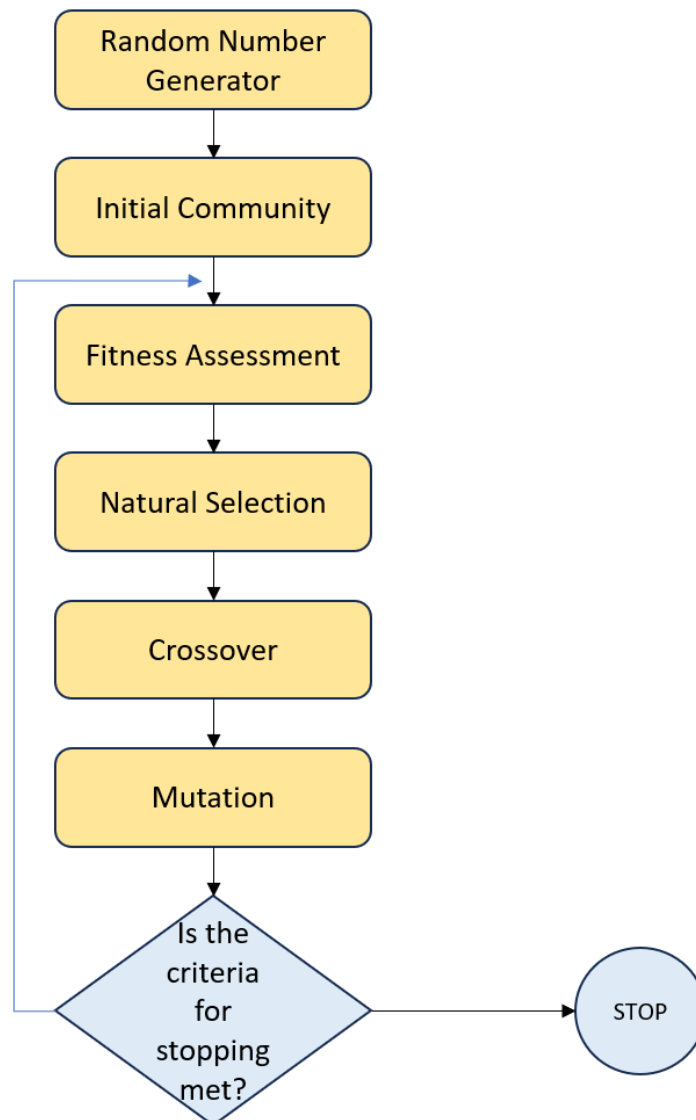


Figure 1. A simple flowchart of a genetic algorithm

The genetic algorithm differs from the classical, derivative-based optimization algorithm in two main ways, as summarized in Table 1.

Table 1. Comparison between the Classical Algorithm and Genetic Algorithm

| Classical Algorithm | Genetic Algorithm |
|--|---|
| It generates a single point in each iteration. The sequence of points converges to the optimum solution. | In each iteration, a point forms the population; the best point in the population is an optimal solution. |
| It selects the next point in the sequence with a deterministic calculation. | It selects the next population through computation using random number generators. |

The basic control variables of a simple genetic algorithm are density size, crossover and mutation rate. The density of a genetic algorithm affects its performance in two ways. Reducing the density will lead to under-sampling, making divergence difficult to achieve and the search will drift towards a sub-optimal point. Conversely, if the number of densities is too large, a one-generation evolution will require a very long time. This is especially undesirable when solving real-time problems. According to the simulation results, the population size is set to 512 in this study to achieve the best directionality on radiation pattern.

Mutation is an important as it allows new regions to enter the search space. The mutation rate should be well controlled to design an efficient genetic algorithm. For example, a high mutation rate will introduce randomness into the search, which will divergence processes too quickly. Conversely, a very low mutation rate will reduce the divergence too much, causing the search to find a non-ideal point as a solution. Therefore, the mutation rate is set to 0.01 in this study. The crossover rate is a parameter used to determine the frequency of the crossover processor applied to the structures (individuals of the density). A low crossover rate will cause too few new structures to enter the generation, making the algorithm inefficient and the search will become bogged down at a certain point. A high crossover rate will cause the search space to be explored very quickly, thus reducing the performance of the algorithm. In this study, the crossover rate is used as 0.5 to get optimum achievement.

3. ANTENNA ARRAY STRUCTURES AND APPLICATIONS

Antenna arrays are antenna systems formed by combining different or similar antennas in different ways. The first practical use of arrays was realized in 1937 in the light of previous work in this field. Studies in the literature show that antenna arrays can produce radiation patterns with desired characteristics by adjusting the amplitude and phase of the feed applied to the antennas. If all antennas in the array are fed in the same phase, the main beam of the radiation diagram is perpendicular to the array plane. In other cases, the main beam can be oriented in different directions such as θ_1 , θ_2 , θ_3 . Since the phases can be changed electronically, the main beam can be formed in any desired direction within the field of view defined by the radiation pattern of the antennas in the array (Amaireh et al., 2019).

In general, the radiation diagram of a single element has large apertures and each element provides a low gain. In most applications it is necessary to design antennas with very high gain for long distance communication. The high gain is proportional to the physical structure of the antenna. Increasing the size of the individual elements can provide higher gain. Another way to increase the gain of the antenna without increasing the size of the individual elements is to match the radiating elements with the appropriate electrical and geometrical structure. This new antenna consisting of multiple elements is called an array. In most applications, the elements of the array are chosen identically. In order to obtain high gain radiation diagrams, it is necessary to add the element areas in the desired directions and cancel each other in the remaining directions, but this is difficult to achieve in practice. The factors affecting the total radiation pattern of the antenna in an array of identical elements are as follows (Taylor, 1955):

- a. Geometric structure of the entire array (linear, circular, etc.)
- b. Distance between antenna elements
- c. Excitation amplitudes of elements
- d. Excitation phases of elements
- e. Radiation diagrams of elements

N elements in the array can be placed with N-1 different range values, as shown in Figure 2.

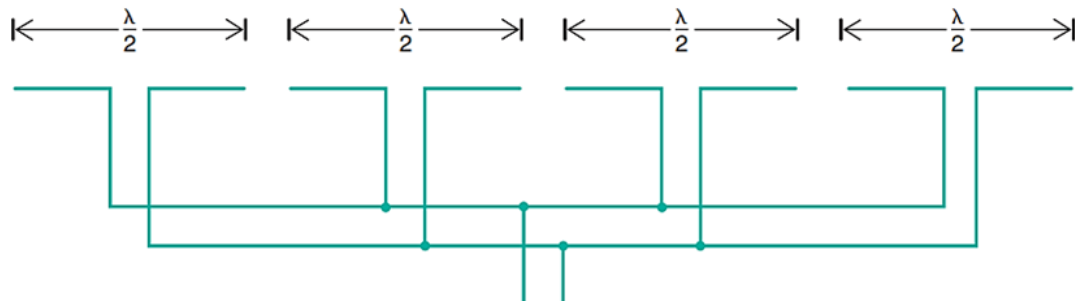


Figure 2. Linear $\lambda/2$ dipole antenna array structure

In this antenna array design, since all antennas are positioned at equal distances, genetic optimization is applied on the radiation amplitudes of the antennas, aimed to calculate the optimum radiation amplitudes for each antenna, by using 8-element antenna array shown in Figure 3.

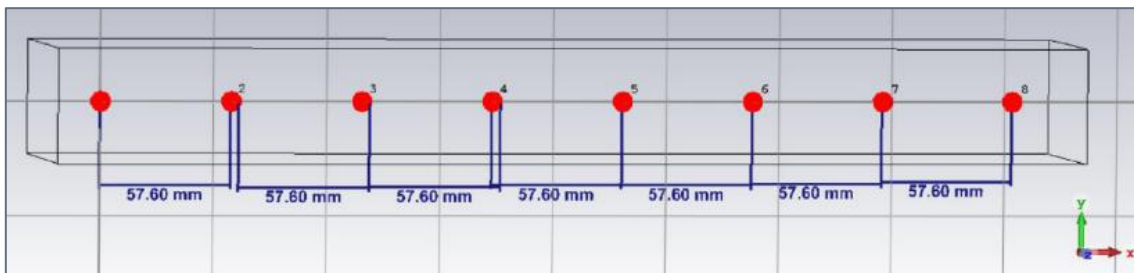


Figure 3. Linear antenna array structure

4. RESULTS AND DISCUSSION

The radiation pattern of dipole antenna arrays can be plotted on a 2D graph with axes Θ (theta) and ϕ (phi) or on a 3D graph in cartesian coordinate system. The cartesian and polar representations of the far-field radiation obtained at a central operating frequency of 3GHz shared in Figure 4.

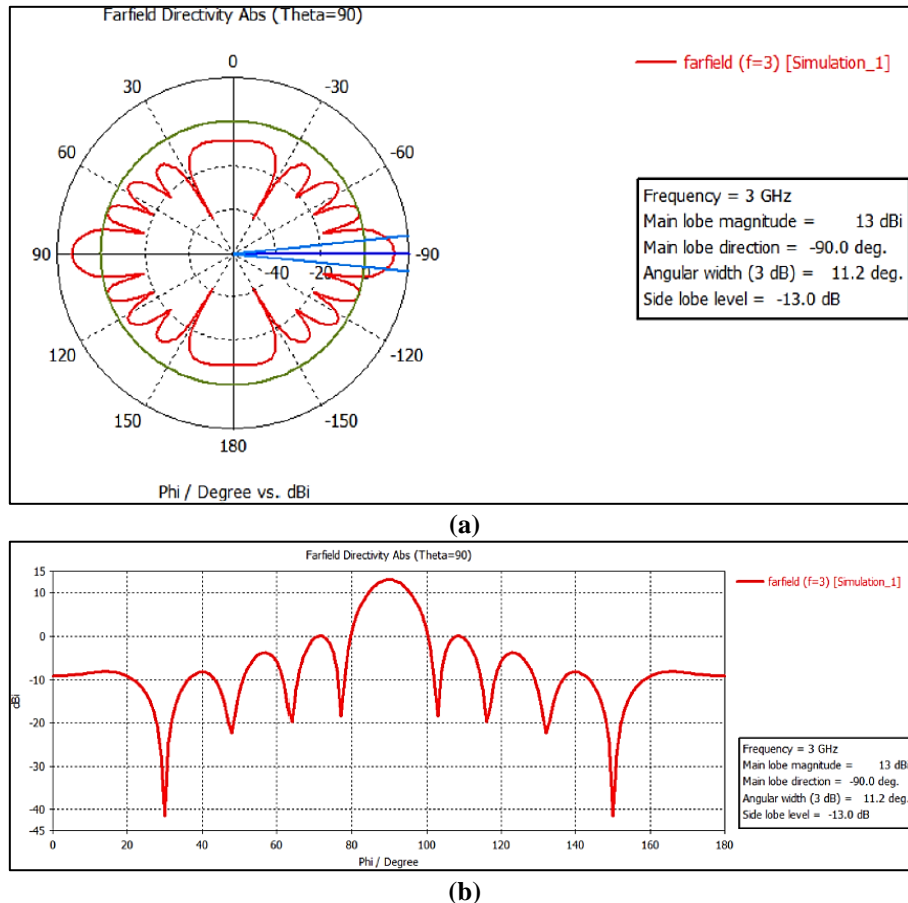


Figure 4. a) Polar representation of the far-field radiation, b) Cartesian representations of the far-field radiation

In the Matlab environment, genetic calculations have been performed to calculate updated amplitude values for the new pattern, and an attempt has been made to simulate them. Since the number of elements is 8, the N value has been updated to 8. Correspondingly, in order to meet the dimensions, the A amplitude matrix has also been updated and defined as a matrix with 8 elements, all having an amplitude of 1.

$N=8;$

$A= [1 \ 1 \ 1 \ 1 \ 1 \ 1 \ 1 \ 1];$

$D= [0.576 \ 1.152 \ 1.728 \ 2.304 \ 2.88 \ 3.456 \ 4.032 \ 4.608];$

The radiation pattern of an 8-element planar dipole antenna array shared in Figure 5. As can be understood from this graph, for the value of theta between 40 and 60 degrees, the side lobe level we want to suppress is approximately around -17 dB.

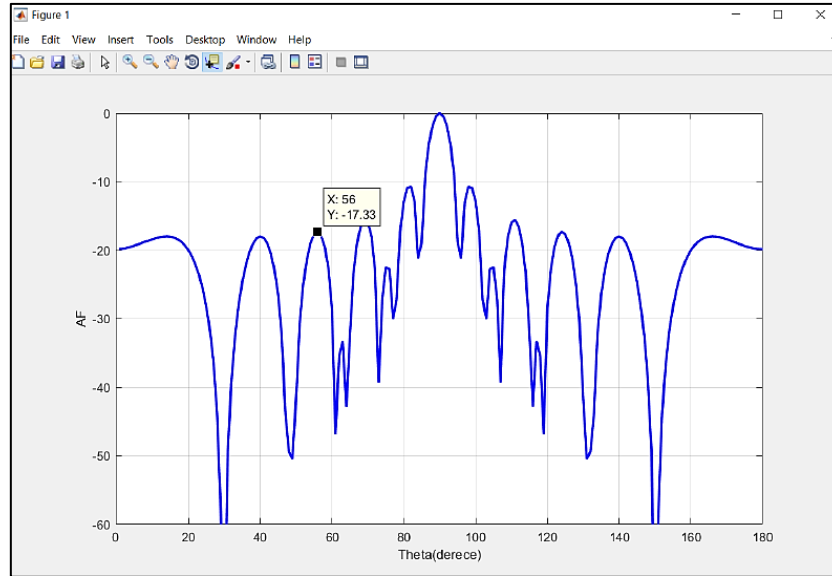


Figure 5. The radiation pattern of an 8-element planar dipole antenna array in MATLAB

It has been determined that the best side lobe value that can be obtained using genetic algorithm optimization for the existing side lobe between 40 and 60 is -28.2 dB. The results of the genetic algorithm run shown in Figure 6.

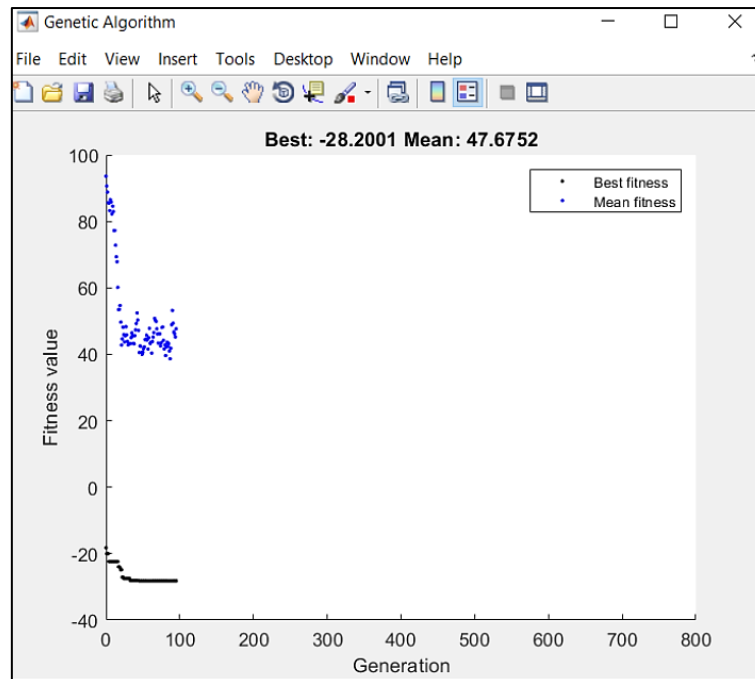


Figure 6. Results of the genetic algorithm in MATLAB

The values belonging to the new generated matrix [B] obtained with the genetic algorithm are shared.

$$B=[1.11 \ -0.92 \ 5.83 \ 9.49 \ 11.13 \ 4.13 \ 1.78 \ -0.14];$$

The far-field radiation of the optimized amplitude values obtained at the working frequency is shown in Cartesian and polar representation in Figure 7.

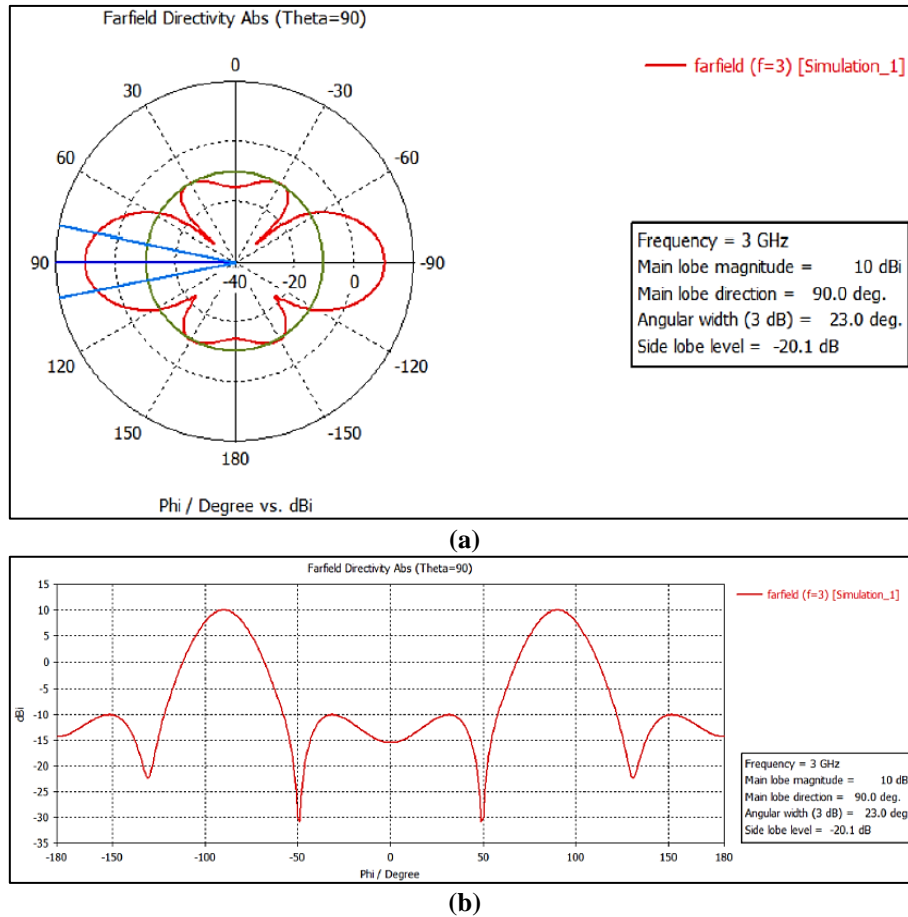


Figure 7. a) Polar representation of the far-field radiation, b) Cartesian representations of the far-field radiation

5. CONCLUSION

In this study, GA algorithm is used to suppress side lobe signals for 8-element linear dipole antenna arrays. The 8-element linear dipole antenna array is designed using CTS Studio and GA optimization is implemented in Matlab. As can be seen from the cartesian representation in Figure 4, multiple dominant sidelobe signal levels are observed in the system with a center operating frequency of 3GHz.

The Matlab representation for the case where the phi angle is varied between 40 and 60 degrees is shown in Figure 5. With the Genetic Optimization algorithm applied to the model, the new amplitude matrix [B] was obtained. The iterations of this GA learning are shown in Figure 6, best value detected around -28dB.

The conclusions regarding the overlapping of the initial state and the optimized radiation patterns are shown in Figure 7. According to the results obtained, the side lobe level has been suppressed with the new amplitude values, but the main lobe directivity has weakened by approximately 3 dB, and the beam width (BW) has increased.

Initial Condition BW: 24 degrees

Optimized Amplitude Value BW: 64 degrees

As a result, the desired theta has been suppressed from -17 dB levels to -28.2 dB levels in the side lobe level occurring between 40-60 degrees. However, it has been observed that the directivity value of the main radiation pattern has decreased from 13 dBi to 10 dBi as shown in Figure 8.

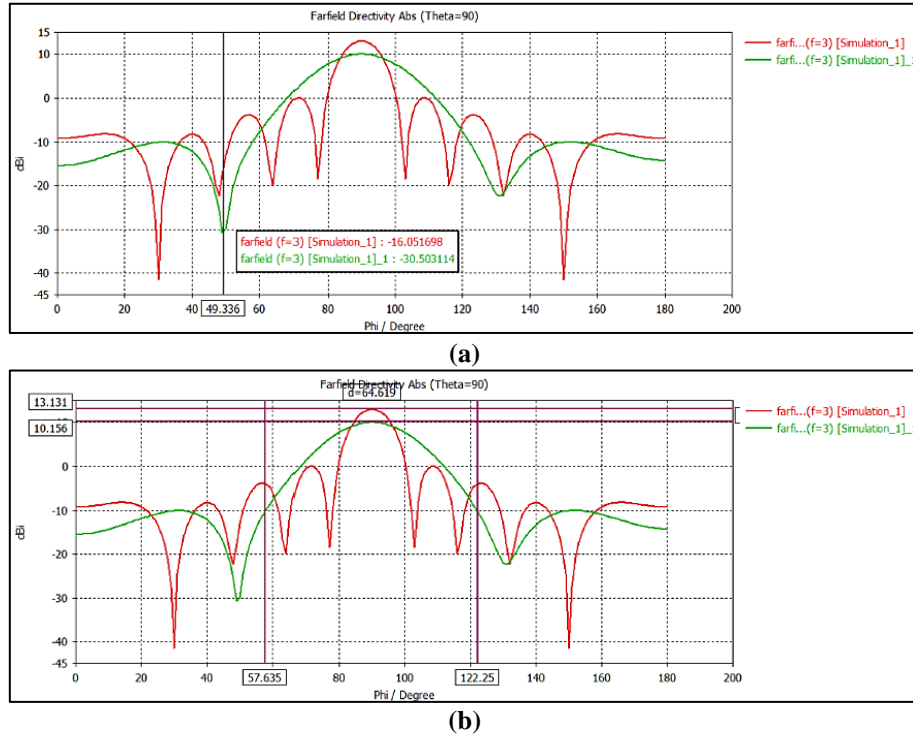


Figure 8. *a) Directivity comparison of initial and optimized design, b) Optimized beamwidth measure*

Literature researches shows that the use of the Genetic Optimization algorithm with linear array antennas gives more efficient results compared to the use of planar and circular antenna arrays. When the radiation diagram obtained by re-arranging the distance between antennas with Genetic Optimization is examined, it is observed that it has the versatility that can be achieved with more complex systems both in terms of the number of iterations and the average crossover rates. In applications where beam directivity is not a primary parameter, suppressing side lobe signals by using genetic optimization provides a useful solution.

ACKNOWLEDGEMENT

This study was supported by Samsung Electronics Türkiye within the scope of Samsung Electronics Turkey R&D Center activities.

CONFLICT OF INTEREST

The authors declare no conflict of interest.

REFERENCES

- Amaireh, A. A., Al-Zoubi, A. Sh., & Dib, N. I. (2019). Sidelobe-Level Suppression for Circular Antenna Array via New Hybrid Optimization Algorithm Based on Antlion and Grasshopper Optimization Algorithms. *Progress in Electromagnetics Research C*, 93, 49-63. <https://doi.org/10.2528/PIERC19040909>

- Aydin, E., & Erdem Aykac, R. (2023). The Effect of Antenna Spacing on Active S-Parameters in Planar Array Antennas. *The Eurasia Proceedings of Science Technology Engineering and Mathematics*, 24, 29-36. <https://doi.org/10.55549/epstem.1406213>
- Dhiman, G., & Kaur, A. (2019). STOA: A bio-inspired based optimization algorithm for industrial engineering problems. *Engineering Applications of Artificial Intelligence*, 82, 148-174. <https://doi.org/10.1016/j.engappai.2019.03.021>
- Durmus, A., & Kurban, R. (2022). Optimal synthesis of concentric circular antenna arrays using political optimizer. *IETE Journal of Research*, 68(1), 768-777. <https://doi.org/10.1080/03772063.2021.1902871>
- Katoch, S., Chauhan, S. S., & Kumar, V. (2021). A review on genetic algorithm: past, present, and future, *Multimedia Tools and Applications* 80.5: 8091-8126. <https://doi.org/10.1007/s11042-020-10139-6>
- Lambora, A., Gupta, K., & Chopra, K. (2019) Kriti Chopra. Genetic Algorithm—A Literature Review. 2019 *International Conference on Machine Learning, Big Data, Cloud and Parallel Computing (COMITCon), Faridabad, 14-16 February 2019*, 380-384. <https://doi.org/10.1109/COMITCon.2019.8862255>
- Liang, S., Feng, T., & Sun, G. (2017). Sidelobe-level suppression for linear and circular antenna arrays via the cuckoo search–chicken swarm optimisation algorithm. *IET Microwaves, Antennas & Propagation*, 11(2), 209-218. <https://doi.org/10.1049/iet-map.2016.0083>
- Liang, S. Fang, Z. Sun, G. Liu, Y. Qu, G. & Zhang, Y. (2020). Sidelobe reductions of antenna arrays via an improved chicken swarm optimization approach. *IEEE Access*, 8, 37664-37683. <https://doi.org/10.1109/ACCESS.2020.2976127>
- Liu, J., Zhao, Z., Yang, K., & Liu, Q. H. (2014). A hybrid optimization for pattern synthesis of large antenna arrays. *Progress In Electromagnetics Research*, 145, 81-91. <http://doi.org/10.2528/PIER13121606>
- Ma, Y., Yang, S., Chen, Y., Qu, S. W., & Hu, J. (2019). Pattern synthesis of 4-D irregular antenna arrays based on maximum-entropy model. *IEEE transactions on antennas and propagation*, 67(5), 3048-3057. <https://doi.org/10.1109/TAP.2019.2896730>
- Nie, Y., Liu, Y., Zhao, W., & Li, J. (2024, May). Optimizing Linear Antenna Arrays with The Chaotic Gold Rush Optimizer. In 2024 *IEEE 14th International Conference on Electronics Information and Emergency Communication (ICEIEC)*, 31-34. IEEE. <https://doi.org/10.1109/ICEIEC61773.2024.10561817>
- Panduro, M. A., Mendez, A. L., Dominguez, R., & Romero, G. (2006). Design of non-uniform circular antenna arrays for side lobe reduction using the method of genetic algorithms. *AEU-International Journal of Electronics and Communications*, 60.10: 713-717. <https://doi.org/10.1016/j.aeue.2006.03.006>
- Satılmış, G. (2022). Genetik Algoritma Kullanarak Dipol Dizi Antenlerde Yan Lob Bastırma. *Muş Alparslan Üniversitesi Mühendislik Mimarlık Fakültesi Dergisi*, 3(2), 50-56.
- Singh, H., Mittal, N., Singh, U., & Salgotra, R. (2022). Synthesis of non-uniform circular antenna array for low side lobe level and high directivity using self-adaptive Cuckoo search algorithm. *Arabian Journal for Science and Engineering*, 47(3), 3105-3118. <https://doi.org/10.1007/s13369-021-06059-8>

- Taylor, T. T. (1955). Design o Line Source Antennas for Narrow Beamwidth and Low Sidelobe, *IRE Trans. Antennas Propag.*, 3, 16-28. <http://doi.org/10.1109/TPGAP.1955.5720407>
- Xiang, L., Pei, F., & Klein, A. (2024). Joint Optimization of Beamforming and 3D Array Steering for Multi-Antenna UAV Communications, *IEEE Wireless Communications and Networking Conference (WCNC), Dubai, United Arab Emirates*, 1-6, <https://doi.org/10.1109/WCNC57260.2024.10570943>
- Yang, G., Zhang, Y., & Zhang, S. (2021). Wide-band and wide-angle scanning phased array antenna for mobile communication system. *IEEE Open Journal of Antennas and Propagation*, 2, 203-212. <https://doi.org/10.1109/OJAP.2021.3057062>
- Zhang, J., & Li, J. (2023). Cognitive engine design based on artificial intelligence. *Spatial Cognitive Engine Technology*, Academic Press, 51-63. <https://doi.org/10.1016/B978-0-323-95107-4.00009-3>



Gazi University

Journal of Science

PART A: ENGINEERING AND INNOVATION

<http://dergipark.org.tr/guj.1611750>

Controlling 2D Porous Media Characteristics Through Topology Manipulation

Mohammed A. BORAHEY^{1*} ¹ Mechanical Power Engineering Department, Zagazig University, Zagazig, 44519, Egypt

| Keywords | Abstract |
|--------------------|--|
| Model Porous Media | A systematic approach for controlling different 2D porous media (PM) characteristics is presented. Through the manipulation of the topology of the PM grain size, shape and distribution, different PM characteristics can be controlled/tailored as required. The presented approach is tested using a test 2D porous media to achieve a specific target porosity value and offers the possibility of tuning other fluid/solid dependent characteristics like the pressure gradient and maximum velocity. The demonstrated approach can be further extended to include other target characteristics through the inclusion of more topological parameters. It can also be extended to any generic PM structure. This approach opens many possibilities for the use of model 2D porous media in different applications and as a surrogate model for naturally occurring PM. |
| 2D Porous Media | |
| Topology | |
| Grain | |

Cite

Boraey, M. A. (2025). Controlling 2D Porous Media Characteristics Through Topology Manipulation. *GU J Sci, Part A, 12(1)*, 318-330. doi:10.54287/guj.1611750

| Author ID (ORCID Number) | Article Process |
|---|-----------------------------------|
| 0000-0001-5231-769X Mohammed A. BORAHEY | Submission Date 02.01.2025 |
| | Revision Date 29.01.2025 |
| | Accepted Date 13.02.2025 |
| | Published Date 26.03.2025 |

1. INTRODUCTION

Porous media are encountered in many natural and industrial situations. Examples include oil reservoirs, heat exchangers, energy recovery systems, waste management, soil mechanics, composites for different machine components etc (Liu et al., 2017; Kumar & Muniamuthu, 2024). Due to this, different approaches have been proposed and used to study different phenomena in porous media. The most basic of these approaches is the fully experimental one. In which a sample of the physical system under consideration is brought to the lab where it gets tested under controlled experimental conditions then different conclusions can be drawn from the measured variables (Anguy et al., 1996; Mosser et al., 2017; Kharrat et al., 2022). On the other side of the spectrum lays the fully computational methods which can be divided into models that replicate the exact PM geometry (through a CT scan or a similar approach) and lumped models that only use the main PM properties like porosity without considering the exact geometry of the grains and their distribution (Miah et al., 2018; Di Palma et al., 2019; Yan et al., 2022).

Several studies have argued that computational models that do not consider the exact PM geometry may fail in predicting some features which are sensitive to the grain geometry such as the displacement interface geometry in the case of two-phase flow (Akhlaghi Amiri & Hamouda, 2014; Yong et al., 2014; Lu et al.,

*Corresponding Author, e-mail: maboraey@gmail.com

2018). The price paid to reflect the effect of the PM exact geometry is a detailed representation of the actual system through a CT scan or a similar approach (Di Palma et al., 2019). This approach, despite being more accurate, has two downsides. First, it is expensive since it is not fully computational as it needs a measurement part to get the full PM grain/bore geometry. Second, the obtained results cannot be generalized, or a sensitivity analysis cannot be done since the obtained results are specific to the tested PM sample.

A hybrid approach between these two extremes is the use of a model porous media that replicate some of the real PM under consideration without the need for a detailed description of the actual grain/bore geometry (Akhlaghi Amiri & Hamouda, 2014; Meinicke et al., 2020). Many studies adopted this approach while replicating the important parameters of the PM like porosity, grain size and shape (Rokhfrouz & Akhlaghi Amiri, 2019). Based on this approach, a recent emphasis has been placed on 2D porous media which, in addition to being used as model for real porous media, are gaining popularity in many applications due to its unique properties and simplicity (Akhlaghi Amiri & Hamouda, 2014; Yan et al., 2022; Sun et al., 2023).

Synthetic porous media is another terminology widely used in scientific literature to reflect the use of different chemical and physical processes to produce porous media with desired target properties like specific surface area (Pfeiffer et al., 2016; Abdelrahman, 2018; Di Palma et al., 2019). Many studies have used model 2D and synthetic porous media to investigate its use for a specific application (Akhlaghi Amiri & Hamouda, 2014; Abdelrahman, 2018; Jahanshahi Javaran et al., 2010; Muniamuthu et al., 2016; Sun et al., 2023; Kumar & Muniamuthu, 2024) like waste management (Abdelrahman, 2018; Kumar & Muniamuthu, 2024), noise and vibration reduction (Kumar et al., 2016; Letaieff et al., 2017; Yuan et al., 2020; Sunil Kumar et al., 2024), control of thermal stresses in machine components (Kumar et al., 2023) and hydrogen storage (Pfeiffer et al., 2016). However, there is still no general approach/methodology that is generic enough to allow the determination of the 2D PM geometric parameters to fulfill a specific set of design targets.

The aim of this study is to show the possibility of designing/tailoring the 2D PM geometric parameters to achieve target properties (whether these properties are specified by the intended use of the 2D PM or they are used to replicate a physical PM) like a specific porosity value or other solid/fluid specific characteristics like the maximum velocity and the pressure gradient. The used approach relies on manipulating different topological parameters of the 2D porous media to achieve the required design targets. This approach can be made more sophisticated by controlling more topological parameters in order to achieve more PM characteristics. The approach is demonstrated through the study of the flow in a sample 2D porous media and how different target goals can be achieved through the change of the PM grain size, shape and size distribution.

2. PARAMETERS OF A 2D POROUS MEDIA

A model 2D porous media is normally used for one of two goals. To replicate a physical porous media which allows an easier way of analyzing its characteristics or to be used in a specific application. In both cases, a

set of properties/characteristics needs to be replicated/achieved in the designed 2D PM. Some of these properties can be geometry related like porosity while others can be related to the used fluid/solid interaction like the required pressure gradient to pump the fluid through the PM with a certain flow rate/velocity or the maximum velocity in the bores between the PM grains.

Assume a simplified 2D PM model as shown in Figure 1. The model porosity depends on the number of grains and their size. In this case, for a target porosity value, many options can be tuned to achieve the required porosity, which include some or all of the following topological parameters:

- 1- Grain shape (e.g. circular, square, ... etc)
- 2- Grain size and distribution (e.g. equal size, two or more sizes with specific size ratio, distribution ... etc)
- 2- Grain relative arrangement to each other (e.g. inline, staggered, random ... etc).

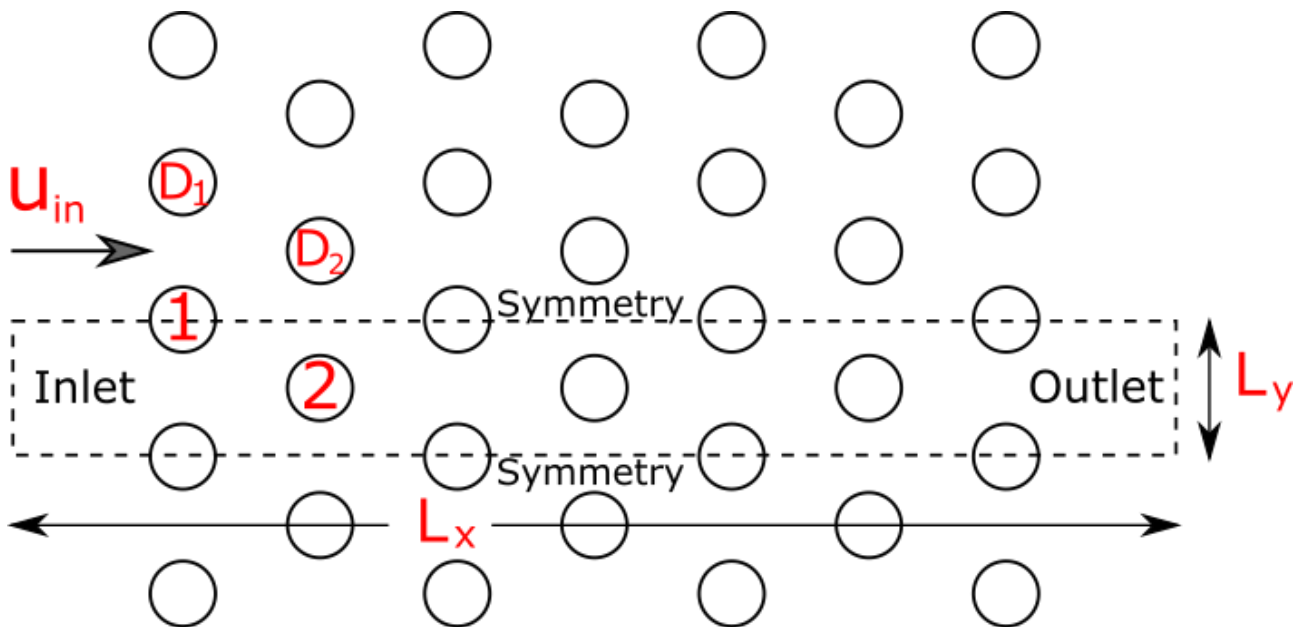


Figure 1. Sample 2D porous media geometry

Since the target porosity value can be achieved using any of these combinations, this adds more degrees of freedom to achieve other target design goals as well. If these goals are geometry-dependent (e.g. min. or max. throat diameter), the tuning of these topological parameters is enough. For other PM hydrodynamic characteristics that are solid/fluid dependent like the pressure gradient or the maximum velocity, a detailed numerical solution is needed to map the topological parameters space to the hydrodynamic parameters space. Once this mapping is done, the specific geometric configuration can be easily determined.

3. DESIGN OF A MODEL 2D POROUS MEDIA

Now let us consider a test 2D porous media for a certain application. The first parameter that needs to be replicated is the porosity. A generic representation for one of the many options that can be used to achieve this goal is the one depicted in Figure 1. In this model we only consider a staggered arrangement of grains

(other arrangements can be considered as well). Another parameter that can be used is the grain shape. In the current study, we consider two shapes only cylinder and square. In addition to this we also add another geometric parameter that allows the use of different sizes of the grains in consecutive rows. Based on this we can have many combinations as shown in Table 1

where:

D_1 : is the characteristic length of grains in row 1 (Diameter for a cylinder or side length for a square).

D_2 : is the characteristic length of grains in row 2 (Diameter for a cylinder or side length for a square).

CC: denotes a configuration where both rows 1 and 2 contain cylindrical grains.

CS: denotes a configuration where row 1 has cylindrical grains while row 2 has square ones.

L_x : is the model 2D PM length parallel to the flow.

L_y : is the model 2D PM length in the normal to the flow direction.

Table 1. Tuning of 2D porous media geometric parameters

| $[D_1^2/(L_x L_y)] \times 1000$ | D_2/D_1 | Porosity % (CC) | Porosity % (CS) |
|---------------------------------|-----------|-----------------|-----------------|
| 1.2 | 1.0 | 15 | 17 |
| 0.9 | 1.7 | 14 | 17 |
| 0.8 | 2.1 | 14 | 17 |
| 1.3 | 1.0 | 17 | 19 |
| 1.0 | 1.5 | 17 | 20 |
| 0.8 | 2.4 | 17 | 22 |
| 1.9 | 1.0 | 32 | 37 |
| 1.6 | 1.3 | 32 | 37 |
| 1.4 | 1.6 | 31 | 37 |
| 2.0 | 1.0 | 37 | 42 |
| 1.9 | 1.2 | 37 | 42 |
| 1.7 | 1.3 | 37 | 43 |

It is clear from Table 1 that a specific porosity value (like 17% or 37%) can be obtained with many combinations of the three main geometric parameters. Namely, the size of the grain with respect to the characteristic PM size, the ratio of the grain size between the two rows 1 and 2 and the shape of the grain. If the main objective is to design a PM with a target porosity then we have six options for each of these two porosity values.

Now, since we have six options, we can choose one of them according to other design targets. We can move to hydrodynamic design targets but before doing so we need to model the flow field of all the cases presented in the table above.

4. THE NUMERICAL MODEL

Due to the symmetry of the considered PM geometry, we only need to consider the part of the domain in the dashed box shown in Figure 1. The left boundary is set as velocity inlet while the right boundary is an outlet. The top and bottom boundaries are symmetry BCs and the solid grains are dealt with using the no slip BC.

Due to its computational efficiency especially for parallel processing, the Lattice Boltzmann Method (LBM) is used for the simulation of the flow field in the considered 2D PM for the cases considered above (He & Luo, 1997; Jahanshahi Javaran et al., 2010; Yan et al., 2022). The details of the used LBM model are given in Appendix A.

For all the test cases, the flow is assumed to be a steady-state laminar flow of a Newtonian fluid. The inlet velocity u_{in} is fixed for all cases to give a flow Reynolds number of 10 based on L_y .

$$Re = \frac{\rho u_{in} L_y}{\mu} \quad (1)$$

where: ρ is the fluid density and μ is the dynamic viscosity.

The normalized pressure gradient is calculated as follows:

$$\frac{dp}{dx} = \frac{\Delta p L_y}{L_x p_0} \quad (2)$$

where: p_0 is the initial pressure in the domain.

Δp is the pressure drop along the porous media length L_x .

The normalized maximum velocity is the maximum velocity in the domain normalized by the inlet velocity.

$$V_{max} = \frac{u_{max}}{u_{in}} \quad (3)$$

where: u_{max} is the maximum velocity magnitude in the simulation domain.

For all cases, the simulation was run until a steady-state solution is reached. For the used Reynolds number, no oscillatory solution was observed for any of the tested cases.

5. RESULTS AND DISCUSSION

This section shows and discusses the results obtained following the proposed approach and simulation discussed in the previous section. The reported velocity fields are normalized by the inlet velocity u_{in} and the density fields are normalized by the initial density ρ_0 .

Figure 2 shows the normalized velocity field for some of the test cases. The magnitude of the maximum velocity and its location seem to depend on both the grain shape configuration and the grain size ratio.

Figure 3 shows the density contours for the same cases. On average, the variation of the density on the cross stream-wise direction is limited to the neighbor of the grains and in some cases (case a) is almost constant across the PM cross section. It is also clear that the CS configuration in general results in higher pressure gradient due to the larger difference in the density between the front and rear stagnation points of the square grains compared to the smoother variation in case of the cylindrical grains. For cases where the shape, size and configuration of the PM grains are more random/generic, the velocity and density fields will be less uniform.

The previous two figures show that the change of the topological parameters of the 2D PM, for the same porosity value, has a profound effect on the resulting flow field (i.e. velocity and density fields). As will be shown, this will subsequently affect the 2D PM hydrodynamic characteristics which allows more freedom in selecting the appropriate set of geometric parameters that fulfills other hydrodynamic design targets.

Table 2 shows the calculated normalized pressure gradient and the normalized maximum velocity in all tested 2D PM configurations presented in Table 1. The highlighted cells show the normalized pressure gradient and normalized maximum velocity for PM configurations with the same porosity value.

The normalized pressure gradient and normalized maximum velocity for the configurations with a porosity value of 17% show almost no sensitivity to the grain shape configuration (CC vs. CS) with weak dependence on the grain size ratio (D_1/D_2). For other PM grain configurations/shapes, these parameters can be more sensitive to different size parameters.

On the other side, cases with a porosity value of 37% show strong dependence of both the normalized pressure gradient and normalized maximum velocity on the grain configuration and grain size ratio. Based on this a specific configuration can be chosen or tailored to meet a specific pressure gradient and maximum velocity for the given porosity value.

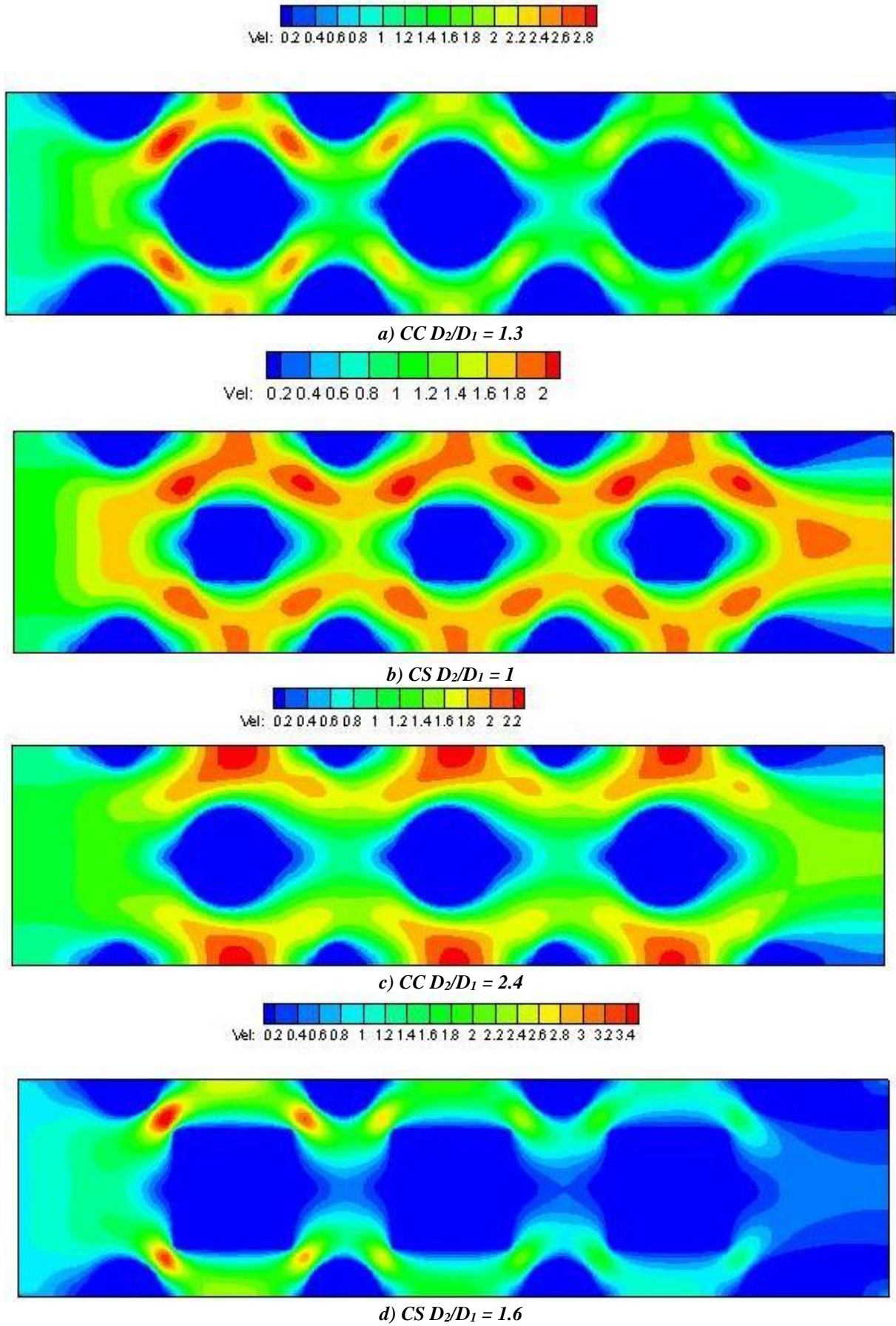


Figure 2. The normalized velocity field for some of the test cases

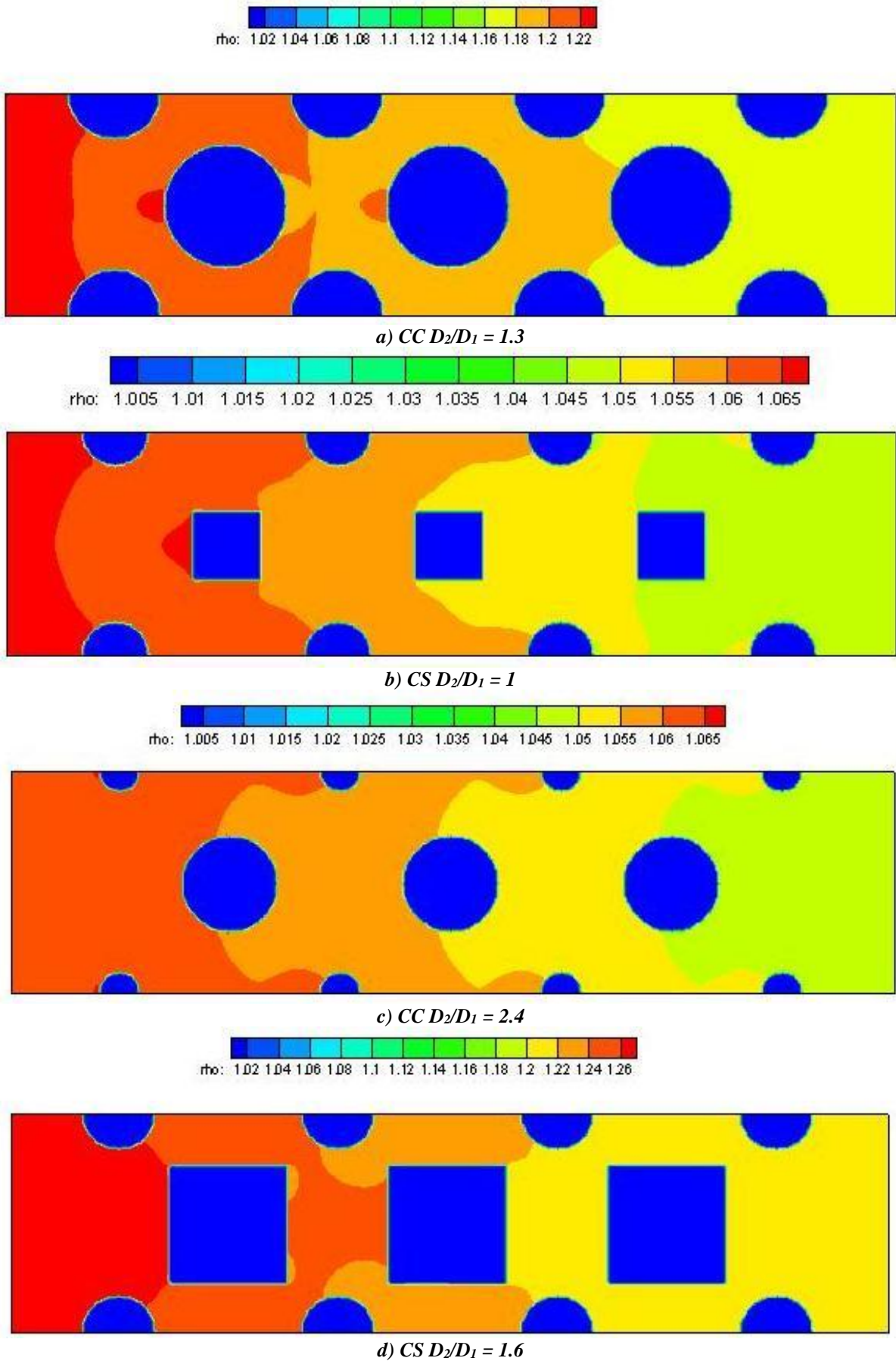


Figure 3. The normalized density field for some of the test cases

This sample set of test cases shows that by controlling only three topological parameters (grain shape, size ratio and grain configuration) three target parameters (porosity, pressure gradient and maximum velocity) can be fulfilled in the designed model 2D PM. Inclusion of other topological parameters like the type and parameters of the grains size distribution and a more generic grains arrangement will allow the control of more target design parameters like the max. and min. throat area in addition to other hydrodynamic parameters.

Table 2. Hydrodynamic parameters of the tested cases

| Porosity % (CC) | Porosity % (CS) | dp/dx (CC) | dp/dx (CS) | V _{max} (CC) | V _{max} (CS) |
|-----------------|-----------------|------------|------------|-----------------------|-----------------------|
| 15 | 17 | 0.47 | 0.58 | 2.04 | 2.08 |
| 14 | 17 | 0.44 | 0.58 | 2.03 | 2.24 |
| 14 | 17 | 0.41 | 0.56 | 2.11 | 2.34 |
| 17 | 19 | 0.51 | 0.66 | 2.06 | 2.18 |
| 17 | 20 | 0.50 | 0.70 | 2.05 | 2.28 |
| 17 | 22 | 0.48 | 0.70 | 2.35 | 2.55 |
| 32 | 37 | 1.23 | 2.03 | 2.65 | 3.62 |
| 32 | 37 | 1.21 | 2.17 | 2.63 | 3.75 |
| 31 | 37 | 1.10 | 2.06 | 2.67 | 3.62 |
| 37 | 42 | 1.57 | 2.78 | 2.95 | 4.42 |
| 37 | 42 | 1.57 | 2.97 | 2.93 | 4.59 |
| 37 | 43 | 1.59 | 3.15 | 2.91 | 4.79 |

6. CONCLUSION

In this work, a simple and systematic approach is proposed for the design of model 2D porous media. The approach relies on achieving the required design targets (whether geometric or hydrodynamic) through the manipulation of the PM topological parameters. The proposed approach is tested by a set of sample test cases to show how the topological parameters can be used in tuning the required 2D PM in order to achieve a predefined set of design targets. Geometric design targets can be fulfilled by just tuning the topological parameters of the PM while the hydrodynamic targets need the extra step of numerically modeling the flow field in the model PM to properly select the best configuration. The presented approach can be used to meet more design targets by including more topological parameters in the design of the model 2D PM. In addition to this, the proposed approach can be extended to more generic PM structures.

CONFLICT OF INTEREST

The author declares no conflict of interest

APPENDIX A:

The LBM solves the discrete Boltzmann equation on a lattice like the 2DQ9 which is used in the current work (Krüger et al., 2017).

$$g_i(x_i + c\Delta t, t + \Delta t) - g(x_i, t) = \Omega(g) \tag{1A}$$

where: g_i is a probability distribution function in lattice direction i , c is the lattice speed $c = \Delta x / \Delta t$ and $\Omega(g)$ is a collision operator. The lattice velocities c_i for the used D2Q9 lattice (Figure 1A) configurations are:

$$c_i = \begin{cases} (0,0) & i = 0 \\ (\pm 1,0)c, (0, \pm 1)c & i = 1:4 \\ (\pm 1, \pm 1)c & i = 5:8 \end{cases} \tag{2A}$$

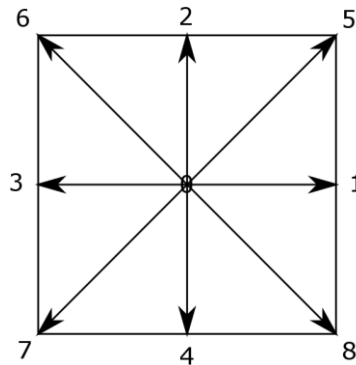


Figure 1A. the D2Q9 lattice velocity set

The single relaxation time (SRT) LBM uses the BGK collision operator but in the current work, the multiple relaxation time MRT LBM (Krüger et al., 2017) is utilized due to it improved stability especially for complex geometries. For this model, the collision operator is expressed as:

$$\Omega(g) = -N^{-1} \cdot S \cdot [n - n^{eq}] \tag{3A}$$

Where N is a matrix to transform g from the velocity space to the moment space $n = N \cdot g$. The equilibrium distribution function g^{eq} is also transformed to $n^{eq} = N \cdot g^{eq}$.

$$N = \begin{bmatrix} 1 & 1 & 1 & 1 & 1 & 1 & 1 & 1 & 1 \\ -4 & -1 & -1 & -1 & -1 & 2 & 2 & 2 & 2 \\ 4 & -2 & -2 & -2 & -2 & 1 & 1 & 1 & 1 \\ 0 & 1 & 0 & -1 & 0 & 1 & -1 & -1 & 1 \\ 0 & -2 & 0 & 2 & 0 & 1 & -1 & -1 & 1 \\ 0 & 0 & 1 & 0 & -1 & 1 & 1 & -1 & 1 \\ 0 & 0 & -2 & 0 & 2 & 1 & 1 & -1 & -1 \\ 0 & 1 & -1 & 1 & -1 & 0 & 0 & 0 & 0 \\ 0 & 0 & 0 & 0 & 0 & 1 & -1 & 1 & -1 \end{bmatrix} \tag{4A}$$

S is a diagonal matrix with diagonal elements representing the relaxation rate for each moment.

$$S = \text{diag}(0, s_1, s_2, 0, s_4, 0, s_6, s_v, s_v) \quad (5A)$$

The speed of sound for the D2Q9 is given by:

$$c_s = \frac{c}{\sqrt{3}} \quad (6A)$$

s_v is related to the fluid kinematic viscosity as follows:

$$v = c_s^2 \left(\frac{1}{s_v} - \frac{1}{2} \right) \quad (7A)$$

The equilibrium probability distribution function g^{eq} is:

$$g_i^{eq} = w_i \frac{p}{c_s^2} \left[1 + \frac{c_i \cdot v}{c_s^2} + \frac{(c_i \cdot v)^2}{2c_s^4} - \frac{v \cdot v}{2c_s^2} \right] \quad (8A)$$

Pressure p and velocity v are calculated from the moments of g :

$$p(x, t) = c_s^2 \sum_i g_i(x, t) \quad (9A)$$

$$v_j(x, t) = \frac{c_s^2}{p(x, t)} \sum_i c_{ij} g_i(x, t) \quad (10A)$$

REFERENCES

- Abdelrahman, E. A. (2018). Synthesis of zeolite nanostructures from waste aluminum cans for efficient removal of malachite green dye from aqueous media. *Journal of Molecular Liquids*, 253, 72-82. <https://doi.org/10.1016/j.molliq.2018.01.038>
- Akhlaghi Amiri, H. A., & Hamouda, A. A. (2014). Pore-scale modeling of non-isothermal two phase flow in 2D porous media: Influences of viscosity, capillarity, wettability and heterogeneity. *International Journal of Multiphase Flow*, 61, 14-27. <https://doi.org/10.1016/j.ijmultiphaseflow.2014.01.001>
- Anguy, Y., Bernard, D., & Ehrlich, R. (1996). Towards realistic flow modelling. Creation and evaluation of two-dimensional simulated porous media: An image analysis approach. *Surveys in Geophysics*, 17(3), 265-287. <https://doi.org/10.1007/BF01904044>
- Di Palma, P. R., Guyennon, N., Parmigiani, A., Huber, C., Heße, F., & Romano, E. (2019). Impact of Synthetic Porous Medium Geometric Properties on Solute Transport Using Direct 3D Pore-Scale Simulations. *Geofluids*, 2019(1), 6810467. <https://doi.org/10.1155/2019/6810467>
- He, X., & Luo, L.-S. (1997). Theory of the lattice Boltzmann method: From the Boltzmann equation to the lattice Boltzmann equation. *Physical review E*, 56(6), 6811.
- Jahanshahi Javaran, E., Gandjalikhan Nassab, S. A., & Jafari, S. (2010). Thermal analysis of a 2-D heat recovery system using porous media including lattice Boltzmann simulation of fluid flow.

- International Journal of Thermal Sciences, 49(6), 1031-1041.
<https://doi.org/10.1016/j.ijthermalsci.2009.12.004>
- Kharrat, A., Brandstätter, B., Borji, M., Ritter, R., Arnold, P., Fritz-Popovski, G., . . . Ott, H. (2022). Development of foam-like emulsion phases in porous media flow. *Journal of Colloid and Interface Science*, 608, 1064-1073. <https://doi.org/10.1016/j.jcis.2021.10.022>
- Krüger, T., Kusumaatmaja, H., Kuzmin, A., Shardt, O., Silva, G., & Viggen, E. M. (2017). The lattice Boltzmann method. Springer International Publishing, 10(978-3), 4-15.
- Kumar, K. S., Arun, S., Mohan, A., & Muniamuthu, S. (2016). Experimental analysis of noise and vibration reduction in windmill gear box for 5MW wind turbine. *International Journal of Mechanical Engineering and Technology*, 7(6), 76-85.
- Kumar, K. S., & Muniamuthu, S. (2024). Design and fabrication of nickel-chromium reinforced 2-stage energy efficient pyrolysis reactor for waste plastics applications. *International Journal of Ambient Energy*, 45(1), 2288148. <https://doi.org/10.1080/01430750.2023.2288148>
- Kumar, K. S., Muniamuthu, S., Raja, P., & Mohan, K. R. (2023). Measurement of temperature flow analysis by condition monitoring system for WTG gear box to evaluate the thermal performance associated with plant load factor. *Journal of Thermal Engineering*, 9(4), 979-987. <https://doi.org/10.18186/thermal.1332437>
- Letaieff, M. R., Walha, L., Taktak, M., Chaari, F., & Haddar, M. (2017). Porous material effect on gearbox vibration and acoustic behavior. *Journal of Theoretical and Applied Mechanics*, 55(4), 1381-1395.
- Liu, T., Ding, J., Su, Z., & Wei, G. (2017). Porous two-dimensional materials for energy applications: Innovations and challenges. *Materials Today Energy*, 6, 79-95. <https://doi.org/10.1016/j.mtener.2017.08.006>
- Lu, X., Xie, P., Ingham, D. B., Ma, L., & Pourkashanian, M. (2018). A porous media model for CFD simulations of gas-liquid two-phase flow in rotating packed beds. *Chemical Engineering Science*, 189, 123-134. <https://doi.org/10.1016/j.ces.2018.04.074>
- Meinicke, S., Dobil, K., Wetzel, T., & Dietrich, B. (2020). Characterization of heat transfer in consolidated, highly porous media using a hybrid-scale CFD approach. *International Journal of Heat and Mass Transfer*, 149, 119201. <https://doi.org/10.1016/j.ijheatmasstransfer.2019.119201>
- Miah, M. I., Elhaj, M. A., Ahmed, S., & Hossain, M. E. (2018). Modeling of temperature distribution and oil displacement during thermal recovery in porous media: A critical review. *Fuel*, 226, 423-440. <https://doi.org/10.1016/j.fuel.2018.04.018>
- Mosser, L., Dubrule, O., & Blunt, M. J. (2017). Reconstruction of three-dimensional porous media using generative adversarial neural networks. *Physical review E*, 96(4), 043309. <https://doi.org/10.1103/PhysRevE.96.043309>
- Muniamuthu, S., Raju, N. L., Sathishkumar, S., & Kumar, K. S. (2016). Investigation on mechanical properties of Al 7075-Al₂O₃ metal matrix composite. *International Journal of Mechanical Engineering and Technology*, 7(6), 474-482.

- Pfeiffer, W. T., al Hagrey, S. A., Köhn, D., Rabbel, W., & Bauer, S. (2016). Porous media hydrogen storage at a synthetic, heterogeneous field site: numerical simulation of storage operation and geophysical monitoring. *Environmental Earth Sciences*, 75(16), 1177. <https://doi.org/10.1007/s12665-016-5958-x>
- Rokhforouz, M. R., & Akhlaghi Amiri, H. A. (2019). Effects of grain size and shape distribution on pore-scale numerical simulation of two-phase flow in a heterogeneous porous medium. *Advances in Water Resources*, 124, 84-95. <https://doi.org/10.1016/j.advwatres.2018.12.008>
- Sun, J., Xu, Y., & Wang, L. (2023). Evaluation of the Elastic Modulus and Plateau Stress of a 2D Porous Aluminum Alloy Based on a Convolutional Neural Network. *Metals*, 13(2). <https://doi.org/10.3390/met13020284>
- Sunil Kumar, K., Kamalakar, V., Palani, S., Muniamuthu, S., & Belinda, C. M. (2024). Design of K-Type Propeller Optimized with Lightweight Aluminum Material and Its CFD Analysis for Marine-Based Applications. Paper presented at the Recent Trends in Thermal and Fluid Sciences, Singapore.
- Yan, G., Li, Z., Bore, T., Galindo Torres, S. A., Scheuermann, A., & Li, L. (2022). A lattice Boltzmann exploration of two-phase displacement in 2D porous media under various pressure boundary conditions. *Journal of Rock Mechanics and Geotechnical Engineering*, 14(6), 1782-1798. <https://doi.org/10.1016/j.jrmge.2022.05.003>
- Yong, Y., Lou, X., Li, S., Yang, C., & Yin, X. (2014). Direct simulation of the influence of the pore structure on the diffusion process in porous media. *Computers & Mathematics with Applications*, 67(2), 412-423. <https://doi.org/10.1016/j.camwa.2013.08.032>
- Yuan, Y., Xu, K., & Zhao, K. (2020). Numerical analysis of transport in porous media to reduce aerodynamic noise past a circular cylinder by application of porous foam. *Journal of Thermal Analysis and Calorimetry*, 141(5), 1635-1646. <https://doi.org/10.1007/s10973-019-08619-5>



Gazi University

Journal of Science

PART A: ENGINEERING AND INNOVATION

<http://dergipark.org.tr/guj.1588040>

Application of Decision Tree Algorithms for Predicting Trip Purposes in Makurdi, Nigeria

Emmanuel Okechukwu NWAFOR^{1*}  Folake Olubunmi AKINTAYO¹ ¹ Department of Civil Engineering, Faculty of Technology, University of Ibadan, Nigeria

| Keywords | Abstract |
|---|---|
| Decision Tree Algorithm Trip Purpose Intelligent Transport Sustainable Transport | Decision tree models are versatile and interpretable machine learning algorithms widely used for both classification and regression tasks in transportation planning. This research focuses on analysing the suitability of decision tree algorithms in predicting trip purposes in Makurdi, Nigeria. The methodology involves formalizing household demographic and trip information datasets obtained through an extensive survey process. Modelling and prediction were conducted using Python programming language, and evaluation metrics such as R-squared and Mean Absolute Error (MAE) were used to assess the model's performance. The results indicate that the model performed well, achieving accuracies of 84% and 68% and low MAE values of 0.188 and 0.314 on training and validation data, respectively. These findings suggest the model's reliability for future predictions. The study concludes that the decision tree-based model provides actionable insights for urban planners, transportation engineers, and policymakers to make informed decisions for improving transportation planning and management in Makurdi, Nigeria. |

Cite
Akintayo, F. O., & Nwafor, E. O. (2025). Application of Decision Tree Algorithms for Predicting Trip Purposes in Makurdi, Nigeria. *GU J Sci, Part A, 12(1)*, 332-346. doi:10.54287/guj.1588040

| Author ID (ORCID Number) | Article Process |
|---|-----------------------------------|
| 0000-0002-5177-4941 Emmanuel Okechukwu NWAFOR | Submission Date 19.11.2024 |
| 0000-0001-6494-9811 Folake Olubunmi AKINTAYO | Revision Date 29.01.2025 |
| | Accepted Date 13.02.2025 |
| | Published Date 26.03.2025 |

1. INTRODUCTION

Urbanization has led to rapid changes in travel behaviour and transportation needs across cities, especially in developing regions (Lyons et al., 2018; Pradhan et al., 2021). Makurdi, Nigeria, is experiencing significant urban expansion, creating challenges for effective transportation planning. Understanding trip purposes, why people travel is critical for optimizing transportation infrastructure and services (Cruz & Sarmiento, 2020; Khan et al., 2022). Insights into trip purposes provide a foundation for developing policies that alleviate congestion, improve access, and enhance overall mobility (Gallo & Marinelli, 2020). However, in developing cities like Makurdi, limited access to detailed data complicates traditional approaches to transportation planning, necessitating innovative, data-driven methods. According to Klaus and Wegener (2004), when the demography, socioeconomic status and the spatial configuration of land-use changes, the pattern of travel demand changes, both in the amount and spatial distribution of the demand. For developing travel demand/prediction models, extensive data on current travel patterns is required. Forecasting future travel demand is an important part of the long-term transport planning process for determining strategies for meeting

*Corresponding Author, e-mail: engineerkeb@gmail.com

future needs. Land-use policies, pricing programs, and the expansion of transportation supply-highway and transit service are examples of such strategies. However, what works in one city may not work in another, necessitating the development of localized travel behavior models or the calibration of current ones to suit cities for efficient and sustainable infrastructure development (Bauriedl & Strüver, 2020; Lovelace, 2021; Cheng et al., 2022; Koumetio Tekouabou et al, 2023; Alghamdi, 2024)

Studies in Nigerian cities, including those focusing on urban centres such as Ilorin, Ibadan, Makurdi, Lagos, Abuja, and Port Harcourt, have often used traditional methods for understanding travel behaviour. These typically involve household surveys, traffic counts, and modal split studies (Akintayo & Adibeli, 2022; Adeke et al., 2018). While these studies provide valuable insights, they often face limitations in terms of data availability and accuracy. As in the case of Makurdi, the availability of structured transportation data in many Nigerian cities is limited, which makes it challenging to implement traditional methods effectively. Similar to the approach in this study, some research has relied on surveys to gather trip characteristics and demographic data (Biala et al., 2024). However, a key difference is that many studies in Nigeria still rely heavily on simple statistical methods, which may not fully capture the complexity of travel demand, especially in rapidly urbanizing areas like Makurdi. The application of machine learning methods, particularly decision trees, as in this study, is relatively novel for Nigerian cities. These methods, as demonstrated in the current study, can provide more accurate predictions and insights, which is especially important in regions where data is scarce and transportation planning needs to be more adaptive to rapid changes in urban dynamics. A few recent studies in Nigerian cities have begun to explore machine learning and AI for transportation modelling and optimization (Biala et al., 2024; Olugbade et al., 2022; Otuoze et al., 2021).

Machine learning algorithms, particularly decision tree models, have demonstrated significant potential in analysing and predicting travel behaviours (Kashifi et al., 2022). Decision trees are widely recognized for their versatility and interpretability, making them ideal for analysing complex datasets in transportation (Nair, 2023; Koushik et al., 2020). Unlike other machine learning algorithms that act as "black boxes," decision trees provide clear insights into the relationships between variables, such as household demographics and trip purposes (Barri et al., 2022). Studies have shown that decision tree algorithms can efficiently model urban travel demand, offering insights critical for urban planning. For instance, An et al. (2022) applied decision tree models to predict peak travel times in dense urban settings, achieving significant accuracy and interpretability in their results. Similarly, Lee et al. (2022) used decision tree regression techniques to analyse small-city travel patterns, highlighting the model's ability to function effectively in data-scarce environments. To create an intelligent transportation system that can handle traffic congestion and road safety to prevent accidents, artificial intelligence (AI) and machine learning (ML) can be used (Choudhary et al, 2021). According to Bharadiya (2023), machine learning and artificial intelligence (AI) are important in many facets of smart cities, especially when it comes to intelligent transportation systems. Intelligent traffic control, dynamic routing, congestion management, and modeling and simulation are just a few of the applications for these technologies.

Díaz et al. (2018) address the issue of air pollution caused by road traffic in large cities by using an Intelligent Transportation System model based on Complex Event Processing technology and Colored Petri Nets (CPNs). Pulugurta et al. (2013) employed AI techniques for travel demand forecasting. The procedure focused on the mode choice step of the major 4-stages of transport modelling – trip generation, trip distribution, mode choice and traffic assignment. The fuzzy logic technique of AI was used to overcome challenges associated with the traditional regression models as its harness human knowledge as linguistic variables in the form of IF-THEN rules. Also, based on the Victorian Integrated Survey of Travel and Activity, several machine learning algorithms were used to model mode choice decisions in the greater Melbourne area (Richards & Zill, 2019). According to the results of the revealed preference household travel survey, certain machine learning models perform better than the traditional discrete choice model. Sun et al. (2021) contributes to the advancement of travel behavior analysis by showcasing how machine learning algorithms effectively identify trip purposes using mobile signaling data, sampling surveys, and point of interest (POI) data. Further, Zhang and Zhao (2022) discuss how ML models outperform traditional statistical methods in transportation analysis due to their ability to capture complex interdependencies among demographic, socioeconomic, and spatial variables. This underscores the need for adopting advanced ML models in developing cities like Makurdi, where traditional data collection and analysis methods face resource and accuracy constraints. Makurdi presents a unique case for applying decision tree models due to its distinctive urban challenges, including a rapidly growing population and limited transportation infrastructure. The city's reliance on informal transport systems, combined with a lack of structured transportation data, makes predictive modelling essential for effective planning. By leveraging machine learning, this research seeks to fill critical gaps in understanding urban mobility in Makurdi, contributing to both academic discourse and practical urban planning.

2. MATERIAL AND METHOD

2.1. Description of Study Area

Makurdi, Nigeria is the capital city of Benue state situated on latitudes $7^{\circ}37'60''\text{N}$ to $7^{\circ}50'20''\text{N}$ and longitudes $8^{\circ}19'30''\text{E}$ to $8^{\circ}40'20''\text{E}$ at 93meters above the sea level. The town is primarily drained by the Benue River, which divides it into Makurdi North and South and is connected by two bridges. Residents of Makurdi metropolis, Nigeria work primarily in civil service, business, and agrarian peasantry. The human population of Makurdi metropolis, Nigeria is estimated at 500,797 persons (NPC, 2006); with highest concentration of people in the high level, Wadata and Wurukum districts (Abah, 2012). Location of the study area is as shown in Figure 1.

2.2. Source of Data

Data for the study were sourced through a household questionnaire interview survey carried out in the study area between January 2021 and December 2022. the study area was divided into nine traffic analysis zones (TAZ) based on the geopolitical council wards of the city, which include the following; Bar, Walumayo, Fiide, Modern Market, Wadata/Ankpa, Central South, Clerk/Market, North Bank, North Bank 2. Revealed

preference questionnaires was administered to households within Makurdi metropolis to capture information on travel demand based on demographic characteristics of households. The survey considered various data collection methods ranging from the use of web-page (Google form or Survey Monkey and WhatsApp), Email and personal interview at home. The Systematic Random Sampling Technique was used in carrying out the travel survey. In using this method, every 3rd household along a street of a study location was selected for the survey. The questionnaire consists of questions which are designed to achieve the socioeconomic and current travel information of respondents. The essential attributes and data type required for the study is as Gender, age, economic status, number of household members, Number of cars available for use by household members, the number and type of driving licenses owned by household members and other household attributes which are the dependent variables while the target variables are the trip purposes such as home-based work (HBW), home-based education (HBE), home-based shopping (HBS), home-based leisure (HBL), non home-based (NHB) and home-based other trip (HBO).

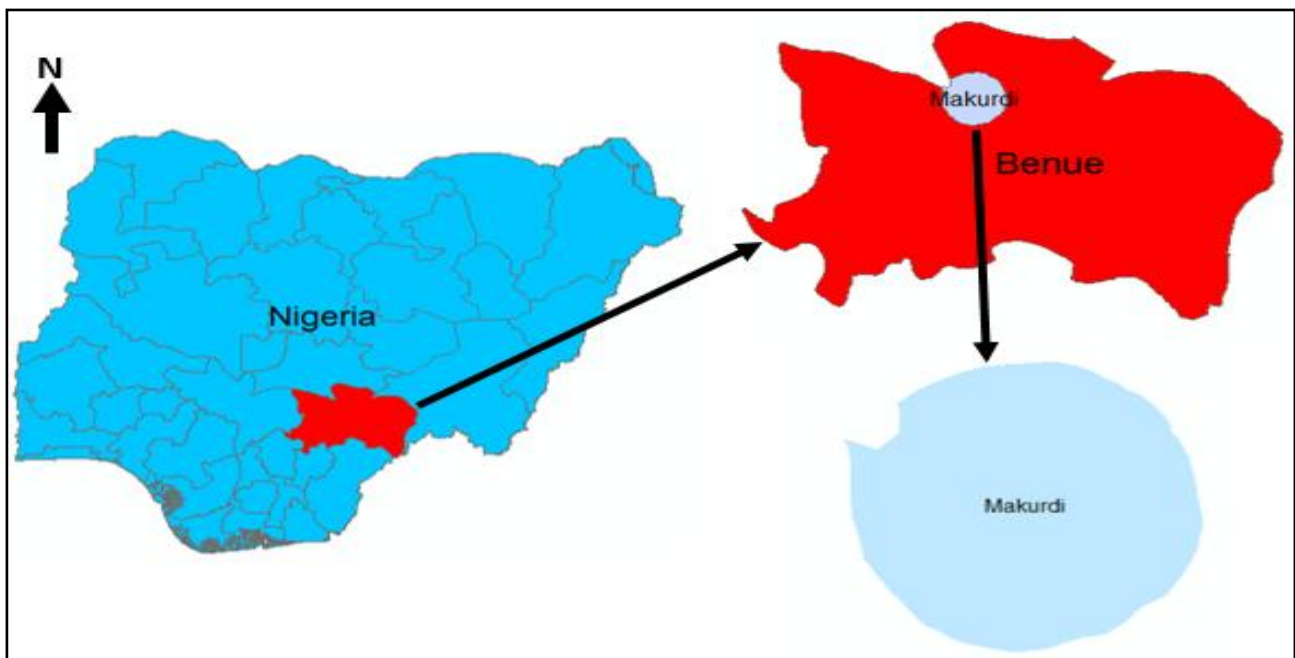


Figure 1. Location of Study Area

2.3. Machine Learning (ML) Trip Purpose Predictive Modelling

2.3.1. Decision Tree Model using Python Programming

To analyse the collected data, a Decision Tree Algorithm was employed as the core machine learning (ML) model. The decision tree was chosen due to its ability to handle both categorical and continuous data, which is essential for this study, given the diversity of trip purposes and household characteristics. The model was developed using the Python programming language within the Google Collaboratory environment, which provides a flexible and accessible platform for running and visualising machine learning models. Python's versatility, combined with the power of libraries such as Scikit-learn and Pandas, enabled robust data processing and model training. This model predicted six different trip purposes simultaneously, leveraging

household demographic and trip data obtained from the extensive survey. By using a decision tree, the model is able to clearly illustrate the decision-making process for each type of trip purpose, making it easier to interpret the results.

2.3.2. Model Training and Validation

More specifically, a Multioutput decision tree model or regressor was used. Multi Output Regressor is used when there are multiple target variables to predict simultaneously. It extends the concept of simple Decision Tree regression to handle multiple target variables. Each target variable is predicted independently but simultaneously by the model. In this case, we are predicting values for each of 6 trip purposes simultaneously. The dataset used for modelling contains the input parameters for the modelling and prediction processes. The dataset was divided into training and testing sets – 80% for model training and 20% for model testing. The division was achieved using ‘train_test_split’ function in a Python Library called Sklearn. Other Python Libraries/functions used in the course of the modelling include Pandas, Seaborn, Numpy, Google.colab, and Matplotlib.

2.3.3. Models Evaluation and Visualisations

The performance of the Decision Tree model was evaluated using three key evaluation metrics: Mean Squared Error (MSE), Mean Absolute Error (MAE), and R-squared (R^2). These metrics provided insights into the model’s accuracy, precision, and explanatory power. In addition to these quantitative measures, visualisations were utilised to gain a deeper understanding of the model’s performance. Tools such as feature importance plots were particularly helpful in evaluating how well the model performed for each trip purpose and in highlighting the significance of different input features.

3. RESULTS AND DISCUSSION

3.1. Summary of Dataset for Modelling

From the survey carried out about 1802 households were interviewed and 25 households trip characteristics were collected from each household. 19 of the variables (trip characteristics) were dependent variables while 6 of the variables were the target variables. The travel diary yielded a total of 23102 trips from the households survey. Table 1 shows the data obtained from the household interview survey. The mean and standard deviation of these data are as shown.

The results showed that the average household size is 3.65, mean employment per household is 2.01, mean number of students per household is 1.43, mean number of male and female per household is 2.03 and 1.62, respectively, among other insights that can be seen from the statistics of the data.

Table 1. Descriptive statistics of dataset obtained from questionnaire survey

| Variables | mean | SD | Min. | Max. | Sum |
|---|-------------|-----------|-------------|-------------|------------|
| Number of household members | 3.65 | 1.28 | 1 | 12 | 6581 |
| Number of Employed household members | 2.01 | 0.8 | 0 | 6 | 3628 |
| Number of vehicles in household | 0.22 | 0.42 | 0 | 4 | 1191 |
| number of household members less than 5 years | 0.13 | 0.38 | 0 | 2 | 229 |
| number of household members > 5 but < 20 years | 0.94 | 0.98 | 0 | 5 | 1692 |
| number of household members > 21 but < 66 years | 2.56 | 0.97 | 0 | 8 | 4607 |
| number of household members > 66 years | 0.03 | 0.19 | 0 | 2 | 56 |
| Number of males in household | 2.02 | 0.92 | 0 | 7 | 3634 |
| number of females in household | 1.62 | 0.81 | 0 | 5 | 2927 |
| Number of students in household | 1.43 | 1.1 | 0 | 6 | 2562 |
| Number of driver's license holders in household | 0.22 | 0.42 | 0 | 4 | 1186 |
| Total number of household daily trips generated | 12.9 | 4.15 | 0 | 32 | 23102 |
| Number of daily Non-Home-based trips by household (NHB) | 0.82 | 1.08 | 0 | 4 | 1478 |
| Number of Work/Business Trips (HBW) | 4.19 | 1.74 | 0 | 12 | 7494 |
| Number of Shopping Trips (HBS) | 3.11 | 1.68 | 0 | 8 | 5564 |
| Number of School Trips (HBE) | 2.77 | 2.17 | 0 | 10 | 4956 |
| Number of Recreation/social/religious trips (HBL) | 0.98 | 1.3 | 0 | 8 | 1784 |
| Number of Private Car Trips | 3.49 | 1.12 | 0 | 9 | 6296 |
| Number of Keke Trips | 0.82 | 0.34 | 0 | 2 | 1466 |
| Number of Motorcycle Trips | 5.56 | 1.78 | 0 | 14 | 10028 |
| Number of Bus Trips | 2.46 | 0.79 | 0 | 6 | 4423 |
| Number of Walking Trips | 0.49 | 0.19 | 0 | 1 | 890 |
| Number of daily Home-based-other trips by household (HBO) | 1.04 | 1.11 | 0 | 4 | 1856 |

Source: Survey Data

3.2. Pearson's Correction Analysis

Correlation analysis was done for each pair of variables in the dataset using Python correlation function. Due to the large dimension of the correlation matrix table, a heat map (Figure 2) was used to represent the correlation analysis results for better visualisation. The analysis showed that the correlation coefficients of the overall dataset lie between -0.3 and 1.0. The bar at the right-hand side of the heat map explains the colour code used to represent the correlation coefficients of each pair of variables.

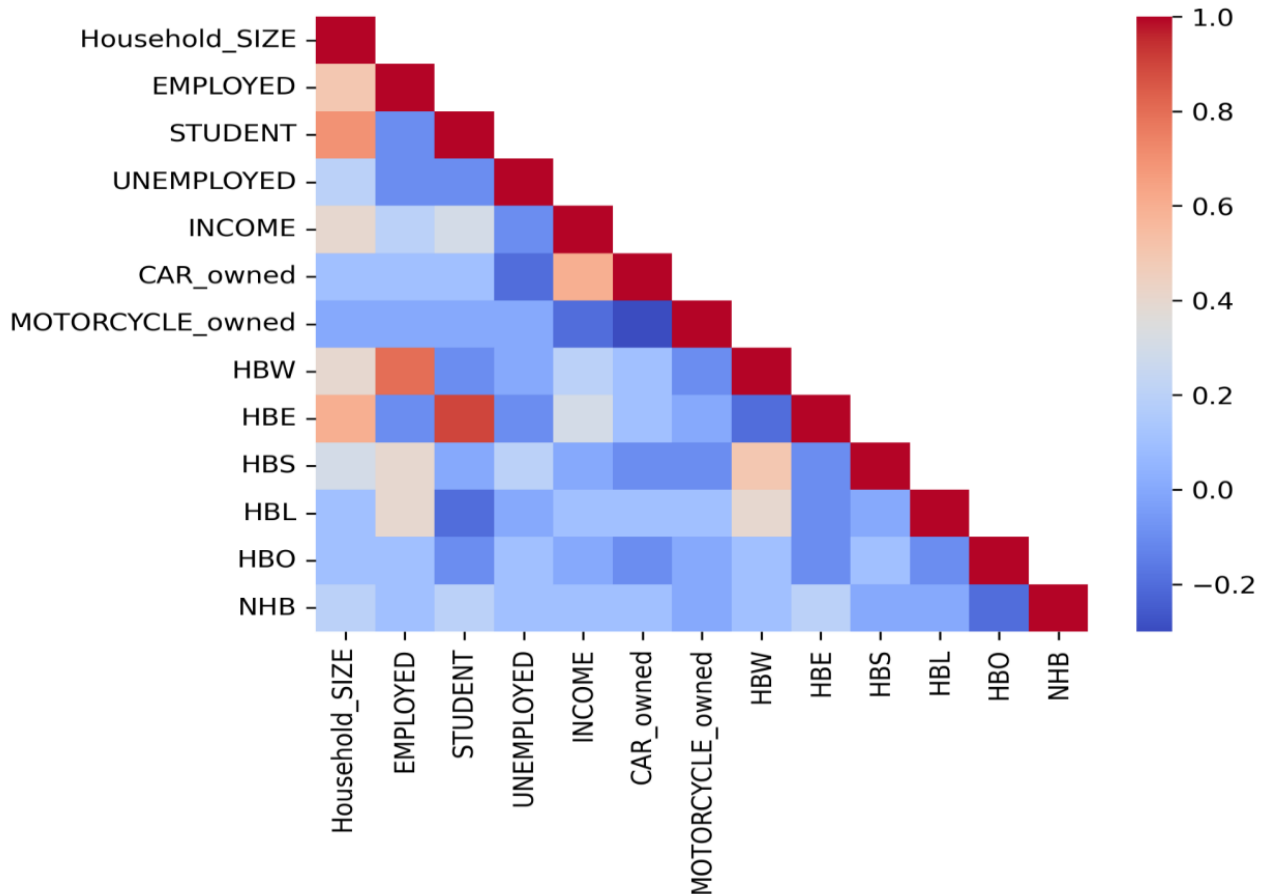


Figure 2: Heat map of correlation analysis

3.3. Decision Tree Model

After the data had been pre-processed and split into dependent and independent variables, and split into 80% training and 20% testing datasets, the decision tree model was initiated and built (or trained) on the training data. The optimal decision tree architecture was gotten by evaluating various decision trees based on 'Max_Depth' parameter using R-squared and MAE as accuracy and error metrics, respectively. It was observed that due to the unique characteristics of the data being considered in this study, the accuracy of prediction of the decision tree models increased while the error decreased with increasing value of 'Max_depth' parameter until a Max_depth of 16 (and upward) when the accuracy and error values remained constant or can be said to have converged. This shows that at this point, the number depth is enough to make the most accurate prediction decisions. Hence, a 'max_depth' value of 16 was used in building the decision

tree model for this study. Figure 3 shows the structure of the first two (depths of 2) of the decision tree model built in this study.

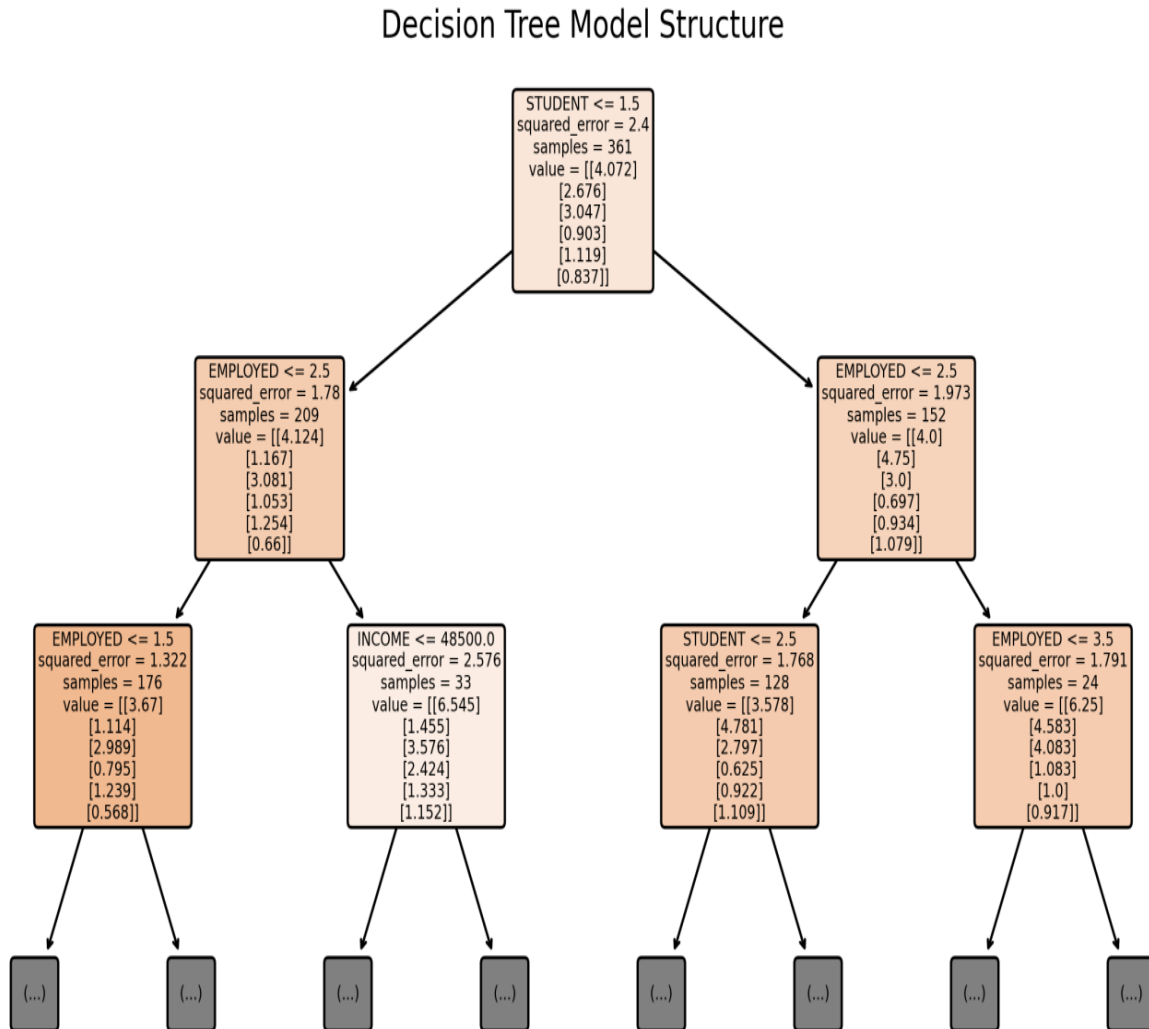


Figure 3. Decision tree model structure (from the root node to the second level)

From Figure 3, the mean square error (MSE) on each node represents the minimum value of mean square error that gives the best split on that node while the sample represent the number of training samples that reach that node. The value in each node represents the predictions for all the target variables.

3.4. Model Performance Evaluation and Visualisations

The performance of the trained Decision tree model was then evaluated using R-squared, MAE and MSE. The trained model was also evaluated (validated) by using it to predict previously unseen data (the 20% test data), and the performance measured using the same metrics as shown in Table 2.

Table 2. Performance of the Decision Tree model for Training and Validation

| Performance Metrics | Training | Validation |
|---------------------------|----------|------------|
| R-squared value | 0.841978 | 0.681508 |
| Mean Absolute Error (MAE) | 0.187717 | 0.313950 |
| Mean Squared Error (MSE) | 0.301527 | 0.615197 |

These accuracy results show that the Decision Tree model for trip purposes prediction performed satisfactorily well giving an accuracy of 84% and 68%, and MAE values of 0.188 and 0.314, on training and validation data, respectively. This means that the model can be relied upon for future estimations involving trip purpose decisions of households. The application of machine learning, particularly decision tree models, as a method for predicting travel behaviour is consistent with the work of Kashifi et al. (2022) and An et al. (2022), who both demonstrated the success of machine learning algorithms in urban travel demand modelling. However, what differentiates this study is its context in Makurdi, where data availability is limited. Studies like Lee et al. (2022) also used decision trees in data-scarce environments, showing that decision trees can function effectively with limited data. The results of this study (84% accuracy and 68% MAE) are similar to those achieved in these other studies, demonstrating the robustness of decision tree models in predicting trip purpose. Studies like Sun et al. (2021) have shown that machine learning models, particularly decision trees, can perform well in urban mobility analysis, but the exact depth or configuration needed to optimize performance can vary across datasets. In Makurdi, the fact that this depth resulted in a significant drop in MAE suggests that this model was well-suited for the data's specific characteristics.

3.5. Plotting the actual and predicted values for Trip Purposes

In order to further examine the performance of the trained model, the first 20 rows of both the actual dataset and predicted dataset were plotted on a chart as shown in Figure 4.

Examining the plots suggest that the model predicted trip purpose values similar to actual values of trip purposes in the original data. This further confirms the reliability of the Decision Tree model for application in predicting trip purposes.

3.6. Features Importance or Sensitivity Analysis Plot

Feature importance indicates how much each feature contributes to the model's predictions. The higher the importance, the more influential the feature. This doesn't give a traditional mathematical equation, but it provides a sense of which features are more influential in the predictions. The importance scores show how often a feature is used for decision-making in the tree. Feature Importance analysis was carried out using Python programming. The code snippet generates a horizontal bar plot using Seaborn to visualize the feature importance's. The features are sorted based on their importance, and the corresponding importance values are

represented by the lengths of the bars. Figure 5 shows the plot of feature importance analysis for the Decision Tree model for the combined 6 targets (trip purposes). The plot provides a clear visualization of the relative importance of each feature in the Decision Tree model.

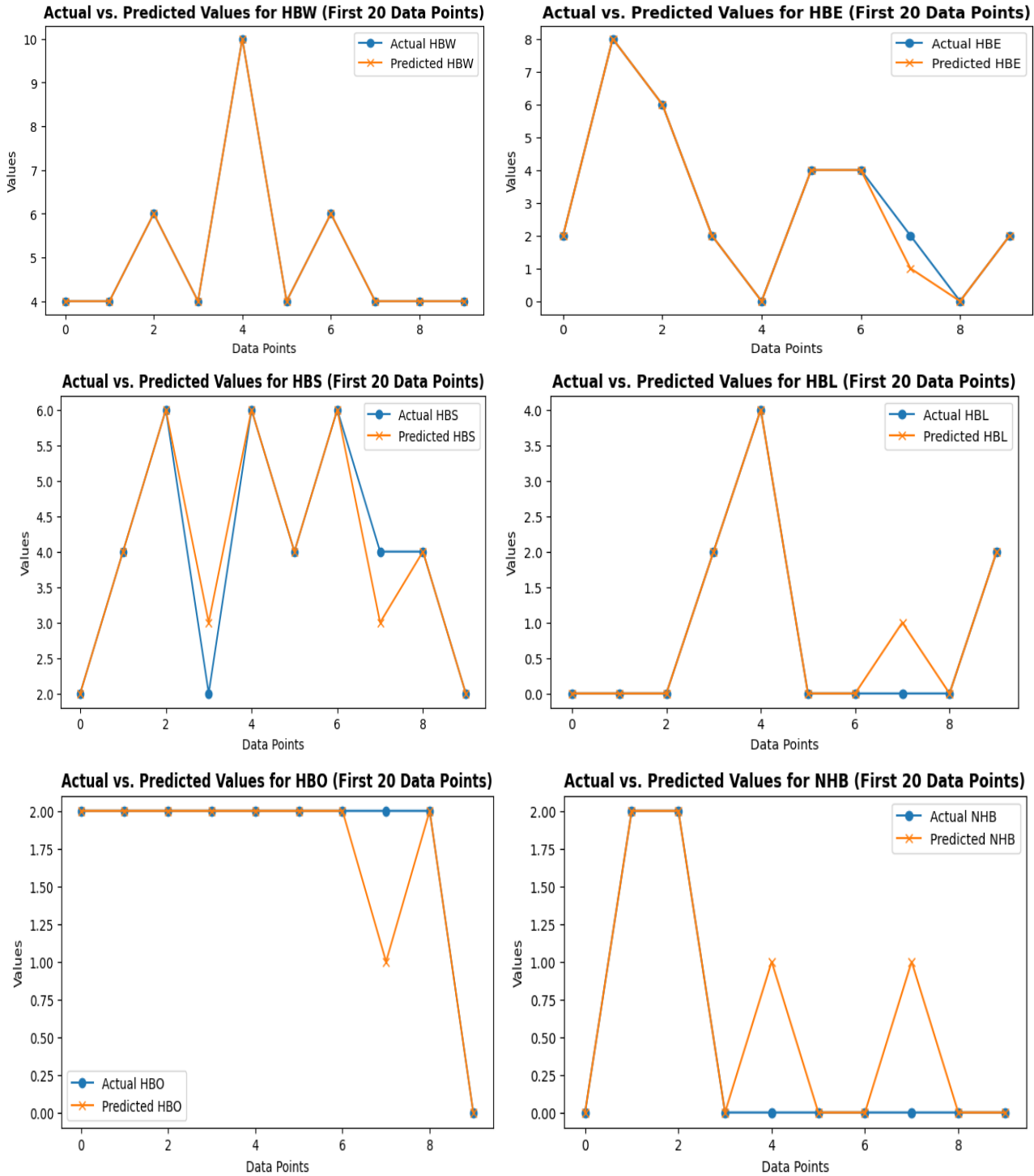


Figure 4. Actual vs Predicted values for HBW, HBE HBS, HBL, HBO and NHB (first 20 Data Point)

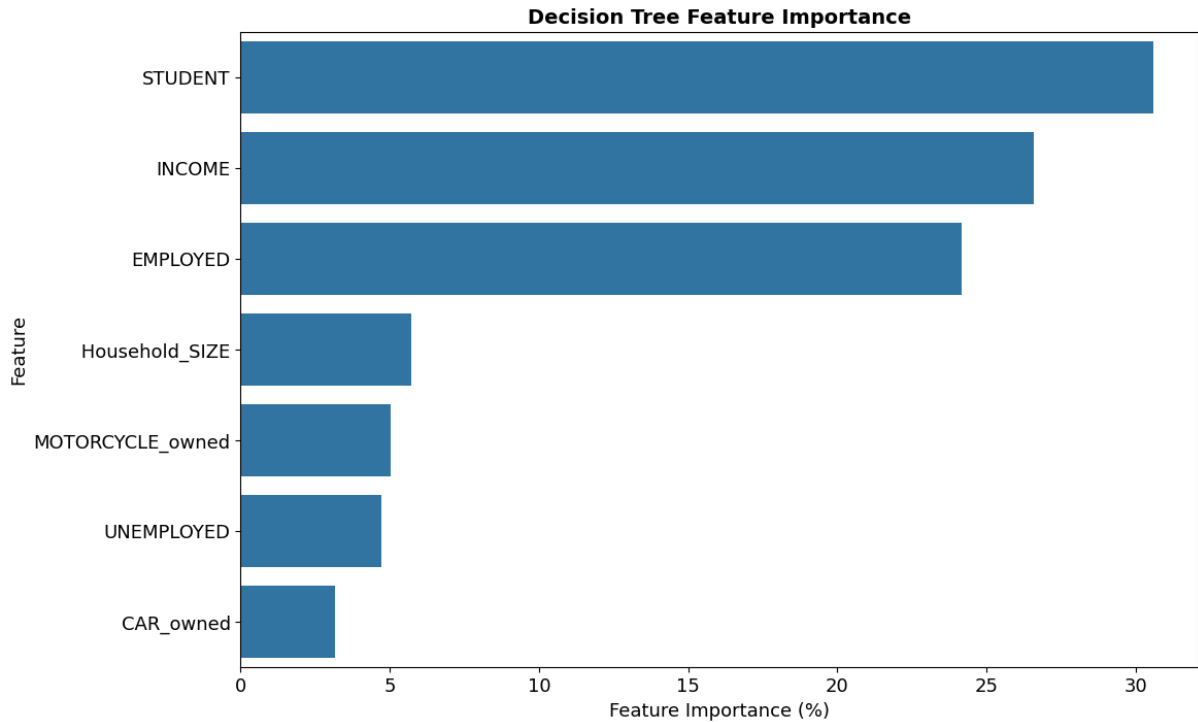


Figure 5. Feature Importance Analysis for the Decision Tree Model for the Combined 6 Target Trip Purposes

4. CONCLUSION

This study examined the application of decision tree algorithms for predicting trip purposes in Makurdi, Nigeria. In recent years, machine learning techniques, especially decision trees, have gained prominence in transportation planning due to their ability to manage complex datasets and deliver interpretable results. Decision trees are particularly effective for modelling trip purposes as they can capture non-linear relationships between various input factors, making them ideal for understanding the diverse influences on travel behaviour in Makurdi. The main objective of this research was to evaluate the performance of the decision tree algorithm in accurately predicting trip purposes based on demographic and travel data. The application of this algorithm offers significant potential for enhancing transportation planning and management in Makurdi, contributing to more efficient and sustainable urban mobility systems. The model's success in predicting trip purposes provides valuable insights that can guide the development of improved transportation systems in the city.

The study found that the decision tree algorithm performed exceptionally well in predicting trip purposes, with accuracy rates of 84% and 68% on the training and validation datasets, respectively, alongside low Mean Absolute Error (MAE) values of 0.188 and 0.314. These results confirm the algorithm's robustness and reliability in making future predictions regarding household travel decisions. Visualizing the predictions of the model versus the actual dataset shows a close similarity between the prediction curve and actual data curve, further corroborating the model's reliability. The feature importance analysis of the Decision Tree model for predicting trip purposes reveals that attributes such as "STUDENT," "INCOME," and "EMPLOYED" play crucial roles, contributing approximately 30.60%, 26.59%, and 24.17% respectively. Conversely, factors like

"Household_SIZE," "MOTORCYCLE_owned," "UNEMPLOYED," and "CAR_owned" have lower predictive significance, ranging from 3.17% to 5.73%. Overall, demographic and socioeconomic factors, notably student status, income, and employment, greatly influence trip purpose predictions. Decision tree algorithm offers several advantages for trip purpose prediction. It is easy to interpret, allowing transportation planners to understand the factors that influence trip purposes. By embracing digital innovation, cities can create more efficient, sustainable, and resilient transportation systems that meet the needs of a rapidly urbanizing world.

AUTHOR CONTRIBUTIONS

Conceptualization, Emmanuel Okechukwu Nwafor and Dr. Folake Olubunmi Akintayo; methodology, Emmanuel Okechukwu Nwafor and Dr. Folake Olubunmi Akintayo.; fieldwork, Emmanuel Okechukwu Nwafor; software, Emmanuel Okechukwu Nwafor; title, Emmanuel Okechukwu Nwafor and Dr. Folake Olubunmi Akintayo; validation, Emmanuel Okechukwu Nwafor and Dr. Folake Olubunmi Akintayo; laboratory work, Emmanuel Okechukwu Nwafor and Dr. Folake Olubunmi Akintayo; formal analysis, Emmanuel Okechukwu Nwafor and Dr. Folake Olubunmi Akintayo; research, Emmanuel Okechukwu Nwafor and Dr. Folake Olubunmi Akintayo; sources, Emmanuel Okechukwu Nwafor and Dr. Folake Olubunmi Akintayo; data curation, Emmanuel Okechukwu Nwafor and Dr. Folake Olubunmi Akintayo; manuscript-original draft Emmanuel Okechukwu Nwafor; manuscript-review and editing, Dr. Folake Olubunmi Akintayo; visualization, Emmanuel Okechukwu Nwafor and Dr. Folake Olubunmi Akintayo; supervision, Dr. Folake Olubunmi Akintayo; project management, Emmanuel Okechukwu Nwafor and Dr. Folake Olubunmi Akintayo; funding, Emmanuel Okechukwu Nwafor and Dr. Folake Olubunmi Akintayo. All authors have read and legally accepted the final version of the article published in the journal.

ACKNOWLEDGEMENT

I would like to express my deepest appreciation to everyone who contributed to the completion of this research and the preparation of this paper. My sincere thanks go to the University of Ibadan for providing the necessary resources and a conducive environment for this study. I am particularly grateful to my advisors and colleagues whose insightful feedback and guidance were instrumental in shaping this work. I also extend my heartfelt thanks to Dr. Akintayo F.B. for her expert advice, which significantly enhanced the quality of this research. Lastly, I would like to acknowledge the Journal of Science Part A: Engineering and Innovation for providing me with the opportunity to submit this work.

CONFLICT OF INTEREST

The authors declare no conflict of interest

REFERENCES

- Adeke, P. T., Ato, A. A., & Zava, A. E. (2018). Traffic signal design and performance assessment of 4-leg intersections using Webster's model: A case of 'SRS' and 'B-division' Intersections in Makurdi Town. *Traffic*, 5(05).
- Alghamdi, M. (2024). Smart city urban planning using an evolutionary deep learning model. *Soft Comput* **28**, 447–459. <https://doi.org/10.1007/s00500-023-08219-4>
- Akintayo, F.O., & Adibeli, S.A., (2022). Safety performance of selected bus stops in Ibadan Metropolis, Nigeria, *Journal of Public Transportation*, Volume 24, <https://doi.org/10.1016/j.jpuptr.2022.100003>
- An, R., Tong, Z., Ding, Y., Tan, B., Wu, Z., Xiong, Q., & Liu, Y. (2022). Examining non-linear built environment effects on injurious traffic collisions: A gradient boosting decision tree analysis. *Journal of Transport & Health*, 24, 101296.
- Barri, E. Y., Farber, S., Jahanshahi, H., & Beyazit, E. (2022). Understanding transit ridership in an equity context through a comparison of statistical and machine learning algorithms. *Journal of Transport Geography*, 105, 103482.
- Bauriedl, S., & Strüver, A. (2020). Platform Urbanism: Technocapitalist Production of Private and Public Spaces. *Urban Planning*, 5(4), 267-276. <https://doi.org/10.17645/up.v5i4.3414>
- Bharadiya, J. (2023). Artificial Intelligence in Transportation Systems: a Critical Review. *American Journal of Computing and Engineering*, 6(1), 34 - 45. <https://doi.org/10.47672/ajce.1487>
- Biala, O. T., Aderinlewo O. O., Asonja, C. O., Titiloye O. D. Ojekunle, M. O., & Nwafor E. O. (2024): Comparative Analysis of Linear Regression and Multilayer Perceptron Neural Network (MLPNN) Models for Trip Generation Modelling of Ilorin City, Nigeria . *Journal of Engineering and Engineering Technology* /18(1),65-72.
- Cheng, Y. D., Yang, L. K. & Deng, S. (2022). Nonprofit density and distributional equity in public service provision: Exploring racial/ethnic disparities in public park access across U.S. cities. *Public Administration Review*, 82(3): 473–486. <https://doi.org/10.1111/puar.13465>
- Choudhary, A., Agrawal, A. P., Logeswaran, R. & Unhelkar, B. (Eds.). (2021). Applications of Artificial Intelligence and Machine Learning. *Lecture Notes in Electrical Engineering*. <https://doi.org/10.1007/978-981-16-3067-5>
- Cruz, C. O., & Sarmiento, J. M. (2020). "Mobility as a service" platforms: A critical path towards increasing the sustainability of transportation systems. *Sustainability*, 12(16), 6368.
- Díaz, G., Macià, H., Valero, V., Boubeta-Puig, J. & Cuartero, F. (2018). An Intelligent Transportation System to control air pollution and road traffic in cities integrating CEP and Colored Petri Nets. *Neural Computing and Applications*. <https://doi.org/10.1007/s00521-018-3850-1>
- Gallo, M., & Marinelli, M. (2020). Sustainable mobility: A review of possible actions and policies. *Sustainability*, 12(18), 7499.

- Kashifi, M. T., Jamal, A., Kashefi, M. S., Almoshaogeh, M., & Rahman, S. M. (2022). Predicting the travel mode choice with interpretable machine learning techniques: A comparative study. *Travel Behaviour and Society*, 29, 279-296.
- Khan, M. A., Etmnani-Ghasrodashti, R., Shahmoradi, A., Kermanshachi, S., Rosenberger, J. M., & Foss, A. (2022). Integrating shared autonomous vehicles into existing transportation services: evidence from a paratransit service in Arlington, Texas. *International Journal of Civil Engineering*, 20(6), 601-618.
- Klaus, S. & Wegener M. (2004). Evaluating Urban Sustainability Using Land-Use Transport Interaction Models, Spiekermann & Wegener Urban and Regional Research (S&W), EJTIR, 4, no. 3, (2004), pp.251-272
- Koumetio Tekouabou, S. C., Diop, E. B., Azmi, R. *et al.* (2023). Artificial Intelligence Based Methods for Smart and Sustainable Urban Planning: A Systematic Survey. *Arch Computat Methods Eng* 30, 1421–1438. <https://doi.org/10.1007/s11831-022-09844-2>
- Koushik, A. N., Manoj, M., & Nezamuddin, N. (2020). Machine learning applications in activity-travel behaviour research: a review. *Transport reviews*, 40(3), 288-311.
- Lee, S., Lee, J., Hiemstra-van Mastrigt, S., & Kim, E. (2022). What cities have is how people travel: Conceptualizing a data-mining-driven modal split framework. *Cities*, 131, 103902. <https://doi.org/10.1016/j.cities.2022.103902>
- Lovelace, R. (2021). Open source tools for geographic analysis in transport planning. *J Geogr Syst* 23, 547–578. <https://doi.org/10.1007/s10109-020-00342-2>
- Lyons, G., Mokhtarian, P., Dijst, M., & Böcker, L. (2018). The dynamics of urban metabolism in the face of digitalization and changing lifestyles: Understanding and influencing our cities. *Resources, Conservation and Recycling*, 132, 246-257.
- Nair, R. (2023). Unraveling the Decision-making Process Interpretable Deep Learning IDS for Transportation Network Security. *Journal of Cybersecurity & Information Management*, 12(2).
- NPC, National Population Commission. (2006). National Population Census of Federal Republic of Nigeria Official Gazette, 96 (2).
- Olugbade, S., Ojo, S., Imoize, A. L., Isabona, J., & Alaba, M. O. (2022). A review of artificial intelligence and machine learning for incident detectors in road transport systems. *Mathematical and Computational Applications*, 27(5), 77.
- Otuoze, S. H., Hunt, D. V., & Jefferson, I. (2021). Neural network approach to modelling transport system resilience for major cities: case studies of lagos and kano (Nigeria). *Sustainability*, 13(3), 1371.
- Pradhan, R. P., Arvin, M. B., & Nair, M. (2021). Urbanization, transportation infrastructure, ICT, and economic growth: A temporal causal analysis. *Cities*, 115, 103213.
- Pulugurta, S., Arun, A. & Errampalli, M. (2013). Use of Artificial Intelligence for Mode Choice Analysis and Comparison with Traditional Multinomial Logit Model. *Procedia - Social and Behavioral Sciences*, 104, 583–592. <https://doi.org/10.1016/j.sbspro.2013.11.152>

- Richards, M. J. & Zill, J. C., (2019). Modelling Mode Choice with Machine Learning Algorithms, Australasian Transport Research Forum 2019 Proceedings 30 September 2, October, Canberra, Australia.
- Sun, H., Chen, Y., Wang, Y. & Liu, X. (2021). Correction to: Trip purpose inference for tourists by machine learning approaches based on mobile signaling data. *Journal of Ambient Intelligence and Humanized Computing*. <https://doi.org/10.1007/s12652-021-03443-y>
- Zhang, X., & Zhao, X. (2022). Machine learning approach for spatial modeling of ridesourcing demand. *Journal of Transport Geography*, 100(C).

JOURNAL OF SCIENCE

PART A: ENGINEERING AND INNOVATION



| Correspondence Address |

Gazi University
Graduate School of Natural and Applied Sciences
Emniyet Neighborhood, Bandırma Avenue
No:6/20B, 06560, Yenimahalle - ANKARA
B Block, Auxiliary Building

| e-mail |

gujsa06@gmail.com

| web page |

<https://dergipark.org.tr/tr/pub/gujsa>

e-ISSN 2147-9542